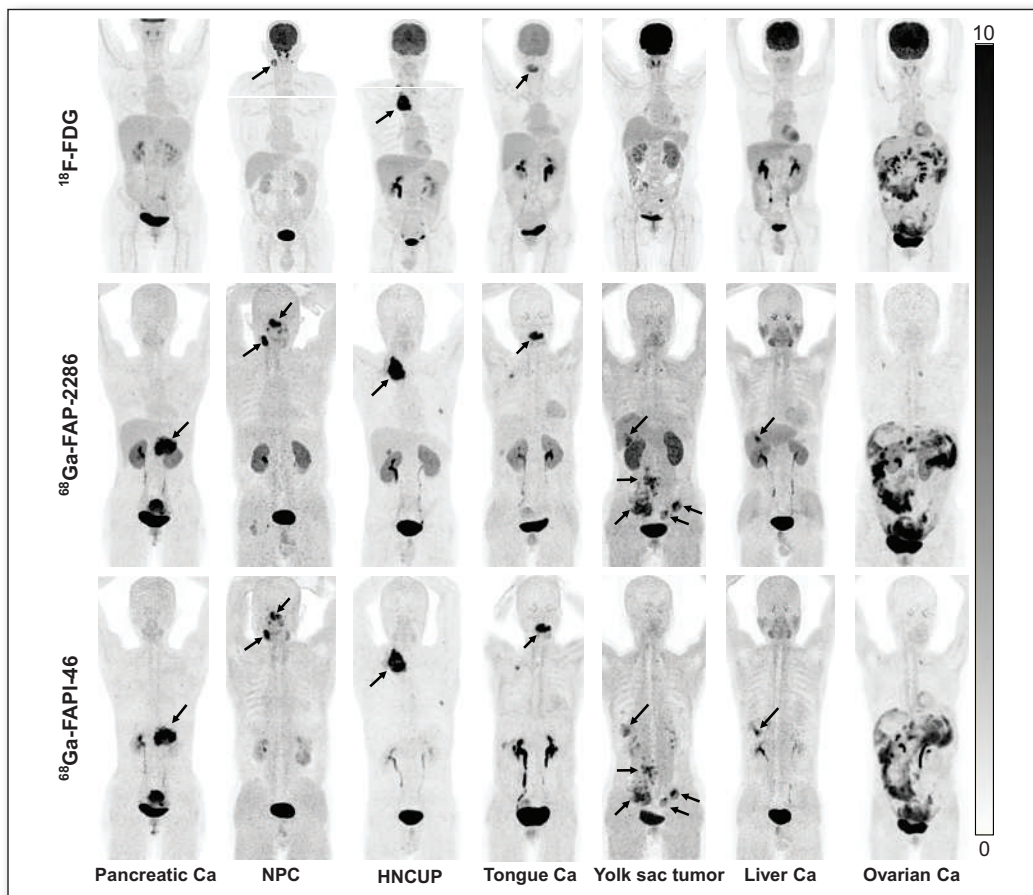


FEATURED ARTICLE

PET Imaging of Fibroblast Activation Protein in Various Types of Cancer Using ^{68}Ga -FAP-2286: Comparison with ^{18}F -FDG and ^{68}Ga -FAPI-46 in a Single-Center, Prospective Study. Yizhen Pang et al. See page 386.



Cellular-level resolution: introducing lensless radiomicroscopy for in vitro radionuclide imaging. Justin Klein et al. See page 479.

EARLY-BIRD DEADLINE: APRIL 27, 2023



Register Today

WWW.SNMMI.ORG/AM2023



Tc 99m: The **core** of nuclear medicine imaging^{1,2}

EFFICIENT AND RELIABLE³

- Greater than 50 years of TechneLite[®] generator manufacturing expertise³
- Our 5th generation of dry-column technetium-99m generator advances³
- 100% Assay and Mo-99 breakthrough testing³
- 100% terminal sterilization following filling and in-process test elutions³



INDICATIONS AND USAGE:

The TechneLite[®] generator is a source of sodium pertechnetate Tc 99m for use in the preparation of FDA-approved diagnostic radiopharmaceuticals, as described in the labeling of these diagnostic radiopharmaceutical kits.

Sodium Pertechnetate Tc 99m Injection is used IN ADULTS as an agent for:

- Thyroid Imaging
- Salivary Gland Imaging
- Urinary Bladder Imaging (direct isotopic cystography) for the detection of vesico-ureteral reflux
- Nasolacrimal Drainage System Imaging

Sodium Pertechnetate Tc 99m Injection is used IN CHILDREN as an agent for:

- Thyroid Imaging
- Urinary Bladder Imaging (direct isotopic cystography) for the detection of vesico-ureteral reflux

CONTRAINDICATIONS: None known.

Important Safety Information:

Allergic reactions including anaphylaxis have been reported infrequently following the administration of Sodium Pertechnetate Tc 99m Injection.

WARNINGS:

Radiation risks associated with the use of Sodium Pertechnetate Tc 99m Injection are greater in children than in adults and, in general, the younger the child, the greater the risk owing to greater absorbed radiation doses and longer life expectancy. These greater risks should be taken firmly into account in all benefit-risk assessments involving children. Long-term cumulative radiation exposure may be associated with an increased risk of cancer.

PRECAUTIONS:

Since the eluate does not contain an antimicrobial agent, it should not be used after 12 hours from the time of TechneLite[®], Technetium Tc 99m Generator, elution. After the termination of the nasolacrimal imaging procedure, blowing the nose and washing the eyes with sterile distilled water or an isotonic sodium chloride solution will further minimize the radiation dose. As in the use of any radioactive material, care should be taken to minimize radiation exposure to patients and occupational workers. Radiopharmaceuticals should be used only by physicians who are qualified by training and experience and who are licensed in the safe handling of radionuclides.

Please see following page(s) for brief Prescribing Information. Full Prescribing Information may be accessed at <https://www.lantheus.com/assets/TechneLite-PI-513160-0719mktg.pdf>

References:

1. World Nuclear Association, <http://www.world-nuclear.org/information-library/non-power-nuclear-applications/radioisotopes-research/radioisotopes-in-medicine.aspx> Accessed April 1, 2019 2. FDA News Release, February 8, 2018, <https://www.fda.gov/news-events/newsroom/press-announcements/ucm595990.htm> Accessed April 1, 2019 3. Quality data on file, Lantheus Medical Imaging, Inc.

TechneLite[®]
Technetium Tc 99m Generator

FOR DIAGNOSTIC USE

BRIEF SUMMARY

Please see Full Prescribing Information available at https://www.lantheus.com/assets/TechneLite-PI-_513160-0719mktg.pdf for complete information.

INDICATIONS AND USAGE:

The Technelite generator is a source of sodium pertechnetate Tc 99m for use in the preparation of FDA-approved diagnostic radiopharmaceuticals, as described in the labeling of these diagnostic radiopharmaceutical kits.

Sodium Pertechnetate Tc 99m Injection is used IN ADULTS as an agent for:

- Thyroid Imaging
- Salivary Gland Imaging
- Urinary Bladder Imaging (direct isotopic cystography) for the detection of vesico-ureteral reflux.
- Nasolacrimal Drainage System Imaging

Sodium Pertechnetate Tc 99m Injection is used IN CHILDREN as an agent for:

- Thyroid Imaging
- Urinary Bladder Imaging (direct isotopic cystography) for the detection of vesico-ureteral reflux.

CONTRAINDICATIONS: None known.

WARNINGS: Radiation risks associated with the use of Sodium Pertechnetate Tc 99m Injection are greater in children than in adults and, in general, the younger the child, the greater the risk owing to greater absorbed radiation doses and longer life-expectancy. These greater risks should be taken firmly into account in all benefit-risk assessments involving children.

Long-term cumulative radiation exposure may be associated with an increased risk of cancer.

PRECAUTIONS:

General

As in the use of any radioactive material, care should be taken to minimize radiation exposure to the patient consistent with proper patient management and to ensure minimum radiation exposure to occupational workers.

Since the eluate does not contain an antimicrobial agent, it should not be used after 12 hours from the time of TECHNELITE[®], Technetium Tc 99m Generator elution.

After the termination of the nasolacrimal imaging procedure, blowing the nose and washing the eyes with sterile distilled water or an isotonic sodium chloride solution will further minimize the radiation dose.

Radiopharmaceuticals should be used only by physicians who are qualified by training and experience in the safe handling of radionuclides and whose experience and training have been approved by the appropriate government agency authorized to license the use of radionuclides.

Carcinogenesis, Mutagenesis, Impairment of Fertility

No animal studies have been performed to evaluate carcinogenic potential or whether Sodium Pertechnetate Tc 99m affects fertility in males or females.

Pregnancy

Animal reproductive studies have not been conducted with Sodium Pertechnetate Tc 99m. It is also not known whether Sodium Pertechnetate Tc 99m can cause fetal harm when administered to a pregnant woman or can affect reproduction capacity. Sodium Pertechnetate Tc 99m Injection should be given to a pregnant woman only if clearly needed.

Ideally examinations using radiopharmaceuticals, especially those elective in nature, of a woman of childbearing capability should be performed during the first few (approximately 10) days following the onset of menses.

Nursing Mothers

Sodium Pertechnetate Tc 99m is excreted in human milk during lactation; therefore formula feedings should be substituted for breast feeding.

This radiopharmaceutical preparation should not be administered to pregnant or lactating women unless expected benefits to be gained outweigh the potential risks.

Pediatric Use

See INDICATIONS and DOSAGE AND ADMINISTRATION sections. Also see the description of additional risks under WARNINGS.

Geriatric Use

Clinical studies of Technelite[®] did not include sufficient numbers of subjects aged 65 and over to determine whether they respond differently from younger subjects. Other reported clinical experience has not identified differences in responses between the elderly and younger patients. In general, dose selection for an elderly patient should be cautious, usually starting at the low end of the dosing range, reflecting the greater frequency of decreased hepatic, renal, or cardiac function, and of concomitant disease or other drug therapy.

ADVERSE REACTIONS: Allergic reactions including anaphylaxis have been reported infrequently following the administration of Sodium Pertechnetate Tc 99m Injection.

Lantheus Medical Imaging

331 Treble Cove Road

N. Billerica, MA 01862 USA

For Ordering Call Toll-Free: 800-299-3431

All other business: 800-362-2668

(In Massachusetts and International, call 978-667-9531)

Patent: <http://www.lantheus.com/patents/index.html>



LANTHEUS[™]

513160-0719
PM-US-TE-0004

Printed in U.S.A.

July 2019

EDITOR'S PAGE

- 343** The ¹⁷⁷Lu-PSMA-617 (Pluvicto) Supply Problem Will Be Solved by Competition
Johannes Czernin and Jeremie Calais

DISCUSSIONS WITH LEADERS

- 344** Focusing on Whole-Person Health: A Conversation Between H el ene Langevin and Ramsey Badawi
H el ene Langevin and Ramsey Badawi

HOT TOPICS

- 347** Tackling the Last Mile: A Major Component to Successfully Establish Radioligand Therapy
Kelsey L. Pomykala, Marcus W urker, and Ken Herrmann

EDITORIAL

- 349** Clinical Implementation of ¹⁷⁷Lu-PSMA-617 in the United States: Lessons Learned and Ongoing Challenges
Praful Ravi, Bridget Whelpley, Emma Kelly, Andrew Wolanski, Jolivet ette Ritzer, Matthew Robertson, Hina Shah, Alicia K. Morgans, Xiao X. Wei, Rajitha Sunkara, et al.

APPROPRIATE USE CRITERIA

- 351** Summary: Appropriate Use Criteria for Estrogen Receptor-Targeted PET Imaging with ^{16 } -¹⁸F-Fluoro-^{17 } -Fluoroestradiol
Gary A. Ulaner, David A. Mankoff, Amy S. Clark, Amy M. Fowler, Hannah M. Linden, Lanell M. Peterson, Farrokh Dehdashti, Brenda F. Kurland, Joanne Mortimer, Jason Mouabbi, et al.

ONCOLOGY

Clinical

- 355** Response Monitoring in Metastatic Breast Cancer: A Prospective Study Comparing ¹⁸F-FDG PET/CT with Conventional CT
Marianne Vogsen, Frederik Harbo, Nick M. Jakobsen, Henriette J. Nissen, Sara E. Dahlsgaard-Wallenius, Oke Gerke, Jeanette D. Jensen, Jon T. Asmussen, Anne Marie B. Jylling, Poul-Erik Braad, et al.
- 362** ¹⁸F-FDG PET/CT Prediction of Treatment Outcomes in Human Papillomavirus-Positive, Locally Advanced Oropharyngeal Cancer Patients Receiving Deintensified Therapy: Results from NRG-HN002
Rathan M. Subramaniam, Lyudmila DeMora, Min Yao, Sue S. Yom, Maura Gillison, Jimmy J. Caudell, John Waldron, Ping Xia, Christine H. Chung, Minh Tam Truong, et al.

- 368** ■ **BRIEF COMMUNICATION.** Novel ⁶⁸Ga-FAPI PET/CT Offers Oncologic Staging Without COVID-19 Vaccine-Related Pitfalls
Tristan T. Demmert, Ines Maric, Kelsey L. Pomykala, Katharina Lueckerath, Jens Siveke, Benedikt M. Schaarschmidt, Rainer Hamacher, Ken Herrmann, and Wolfgang P. Fendler

THERANOSTICS

Clinical

- 372** PSMA-Directed Imaging and Therapy of Salivary Gland Tumors: A Single-Center Retrospective Study
Caner Civan, Stefan Kasper, Christoph Berliner, Pedro Fragoso-Costa, Viktor Gr unwald, Michael Pogorzelski, Benedikt Michael Schaarschmidt, Stephan Lang, David Kersting, Michael Nader, et al.
- 379** Comparison of ⁶⁸Ga-PSMA-617 PET/CT and ⁶⁸Ga-RM2 PET/CT in Patients with Localized Prostate Cancer Who Are Candidates for Radical Prostatectomy: A Prospective, Single-Arm, Single-Center, Phase II Study
Romain Schollhammer, Gr egoire Robert, Julien Asselineau, Mokrane Yacoub, Delphine Vimont, Nicolas Balamoutoff, Franck Bladou, Antoine B enard, Elif Hindi e, Henri de Clermont Gallerande, et al.
- 386** ■ **FEATURED ARTICLE OF THE MONTH.** PET Imaging of Fibroblast Activation Protein in Various Types of Cancer Using ⁶⁸Ga-FAP-2286: Comparison with ¹⁸F-FDG and ⁶⁸Ga-FAPI-46 in a Single-Center, Prospective Study
Yizhen Pang, Liang Zhao, Tinghua Meng, Weizhi Xu, Qin Lin, Hua Wu, Jingjing Zhang, Xiaoyuan Chen, Long Sun, and Haojun Chen
- 395** Predicting Outcomes of Indeterminate Bone Lesions on ¹⁸F-DCFPyL PSMA PET/CT Scans in the Setting of High-Risk Primary or Recurrent Prostate Cancer
Tim E. Phelps, Stephanie A. Harmon, Esther Mena, Liza Lindenberg, Joanna H. Shih, Deborah E. Citrin, Peter A. Pinto, Bradford J. Wood, William L. Dahut, James L. Gulley, et al.
- 402** ¹⁷⁷Lu-PSMA-I&T for Treatment of Metastatic Castration-Resistant Prostate Cancer: Prognostic Value of Scintigraphic and Clinical Biomarkers
Amir Karimzadeh, Matthias Heck, Robert Tauber, Karina Knorr, Bernhard Haller, Calogero D'Alessandria, Wolfgang A. Weber, Matthias Eiber, and Isabel Rauscher
- 410** ¹⁷⁷Lu-PSMA SPECT Quantitation at 6 Weeks (Dose 2) Predicts Short Progression-Free Survival for Patients Undergoing ¹⁷⁷Lu-PSMA-I&T Therapy
Nikeith John, Sarennya Pathmanandavel, Megan Crumbaker, William Counter, Bao Ho, Andrew O. Yam, Peter Wilson, Remy Niman, Maria Ayers, Aron Poole, et al.

CARDIOVASCULAR

Clinical

- 416** Exploring Vessel Wall Biology In Vivo by Ultrasensitive Total-Body PET
Thorsten Derlin, Benjamin A. Spencer, Martin Mamach, Yasser Abdelhafez, Lorenzo Nardo, Ramsey D. Badawi, Simon R. Cherry, and Frank M. Bengel

PULMONARY

Clinical

- 423** PET Imaging of Neutrophil Elastase with ¹¹C-GW457427 in Acute Respiratory Distress Syndrome in Pigs
Emmi Puuvuori, Elena Chiodaroli, Sergio Estrada, Pierre Cheung, Norbert Lubenow, Jonathan Sigfridsson, Hampus Romelin, Sofie Ingvast, Mathias Elgland, Francesco Liggieri, et al.

NEUROLOGY

Clinical

430 ⁶⁸Ga-DOTA PET for Diagnosis of Spinal Cerebrospinal Fluid Leaks

Petros Evangelou, Mohamed Aymen Omrane, Johannes Thurow, Michael Mix, Christian Fung, Niklas Lützen, Ganna Blazhenets, Horst Urbach, Jürgen Beck, and Philipp T. Meyer

437 A Head-to-Head Comparison Between Plasma pTau181 and Tau PET Along the Alzheimer's Disease Continuum

Emma M. Coomans, Inge M.W. Verberk, Rik Ossenkoppele, Sander C.J. Verfaillie, Denise Visser, Mariam Gouda, Hayel Tuncel, Emma E. Wolters, Tessa Timmers, Albert D. Windhorst, et al.

444 A Visual Interpretation Algorithm for Assessing Brain Tauopathy with ¹⁸F-MK-6240 PET

John P. Seibyl, Jonathan M. DuBois, Annie Racine, Jessica Collins, Qi Guo, Dustin Wooten, Eddie Stage, David Cheng, Roger N. Gunn, Lilly Porat, et al.

452 The Association of Age-Related and Off-Target Retention with Longitudinal Quantification of [¹⁸F]MK6240 Tau PET in Target Regions

Cécile Tissot, Stijn Servaes, Firoza Z. Lussier, João Pedro Ferrari-Souza, Joseph Therriault, Pâmela C.L. Ferreira, Gleb Bezgin, Bruna Bellaver, Douglas Teixeira Leffa, Sulantha S. Mathotaarachchi, et al.

460 Evaluation of Tau Radiotracers in Chronic Traumatic Encephalopathy

Cassis Varlow and Neil Vasdev

Basic

466 Neurovascular Uncoupling: Multimodal Imaging Delineates the Acute Effects of 3,4-Methylenedioxymethamphetamine

Tudor M. Ionescu, Mario Amend, Tadashi Watabe, Jun Hatazawa, Andreas Maurer, Gerald Reischl, Bernd J. Pichler, Hans F. Wehrli, and Kristina Herfert

AI/ADVANCED IMAGE ANALYSIS

Translational

472 Deep Learning-Based Attenuation Correction Improves Diagnostic Accuracy of Cardiac SPECT

Aakash D. Shanbhag, Robert J.H. Miller, Konrad Pieszko, Mark Lemley, Paul Kavanagh, Attila Feher, Edward J. Miller, Albert J. Sinusas, Philipp A. Kaufmann, Donghee Han, et al.

PHYSICS AND INSTRUMENTATION

Basic

479 ■ FEATURED BASIC SCIENCE ARTICLE. Development of a Lensless Radiomicroscope for Cellular-Resolution Radionuclide Imaging

Justin S. Klein, Tae Jin Kim, and Guillem Pratx

RADIOPHARMACEUTICALS

Clinical

485 Adverse Clinical Events at the Injection Site Are Exceedingly Rare After Reported Radiopharmaceutical Extravasation in Patients Undergoing ^{99m}Tc-MDP Whole-Body Bone Scintigraphy: A 12-Year Experience

Ashwin Singh Parihar, Lisa R. Schmidt, John Crandall, Farrokh Dehdashti, and Richard L. Wahl

491 ■ INVITED PERSPECTIVE. Extravasation of Diagnostic Radiopharmaceuticals: A Wolf in Sheep's Clothing?

Jochem A.J. van der Pol and Felix M. Mottaghy

RADIOBIOLOGY/DOSIMETRY

Basic

493 A Realistic Multiregion Mouse Kidney Dosimetry Model to Support the Preclinical Evaluation of Potential Nephrotoxicity of Radiopharmaceutical Therapy

Clarita Saldarriaga Vargas, Lara Struelens, Matthias D'Huyvetter, Vicky Cavelliers, and Peter Covens

ILLUSTRATED POST

Clinical

500 Progression or Response: New Liver Lesions in a Patient with Responding Hodgkin Lymphoma

Ashwin Singh Parihar, Adeel Haq, Richard L. Wahl, and Amin H. Jahromi

LETTERS TO THE EDITOR

501 Theranostic Digital Twins: An Indispensable Prerequisite for Personalized Cancer Care

Julia Brosch-Lenz, Carlos Uribe, Arman Rahmim, and Babak Saboury

DEPARTMENTS

8A This Month in JNM

490 Erratum

The Official Publication of **SNMMI**

Publications Committee

TODD E. PETERSON, PhD, FSNMMI
Chair

CAROLYN J. ANDERSON, PhD, FSNMMI

PAIGE B. BENNETT, MD

JOYITA DUTTA, PhD

MICHAEL M. GRAHAM, PhD, MD, FACR,
FSNMMI

HOSSEIN JADVAR, MD, PhD, FACNM,
FSNMMI

STEVEN M. LARSON, MD, FACNM

HEINRICH R. SCHELBERT, MD, PhD, FSNMMI

HEIKO SCHÖDER, MD, MBA, FSNMMI

DAVID M. SCHUSTER, MD

JESSICA WILLIAMS, CNMT, RT(N),
FSNMMI-TS

HARVEY A. ZIESSMAN, MD, FSNMMI

Ex officio

JOHANNES CZERNIN, MD, FSNMMI

MUNIR GHESANI, MD, FACNM, FACR

ARNOLD M. STRASHUN, MD, FSNMMI

KATHY S. THOMAS, MHA, CNMT,
PET, FSNMMI-TS

HENRY F. VANBROCKLIN, PhD, FSNMMI

Associate Director of Communications

SUSAN ALEXANDER

Senior Copyeditor

SUSAN NATH

Senior Publications & Marketing Service Manager

STEVEN KLEIN

Editorial Production Manager

PAULETTE MCGEE

Editorial Project Manager

MARK SUMIMOTO

Director of Communications

REBECCA MAXEY

CEO

VIRGINIA PAPPAS

MISSION STATEMENT: *The Journal of Nuclear Medicine* advances the knowledge and practice of molecular imaging and therapy and nuclear medicine to improve patient care through publication of original basic science and clinical research.

JNM (ISSN 0161-5505 [print]; ISSN 2159-662X [online]) is published monthly by SNMMI, 1850 Samuel Morse Drive, Reston, VA 20190-5316. Periodicals postage is paid at Herndon, VA, and additional mailing offices. Postmaster, send address changes to *The Journal of Nuclear Medicine*, 1850 Samuel Morse Drive, Reston, VA 20190-5316. The costs of publication of all nonsolicited articles in *JNM* were defrayed in part by the payment of page charges. Therefore, and solely to indicate this fact, these articles are hereby designated "advertisements" in accordance with 18 USC section 1734.

DISCLOSURE OF COMMERCIAL INTEREST: Johannes Czernin, MD, editor-in-chief of *The Journal of Nuclear Medicine*, has indicated that he is a founder of Sofie Biosciences and holds equity in the company and in intellectual property invented by him, patented by the University of California, and licensed to Sofie Biosciences. He is also a founder and board member of Trethera Therapeutics and holds equity in the company and in intellectual property invented by him, patented by the University of California, and licensed to Triangle. He also serves on the medical advisory board of Actinium Pharmaceuticals and on the scientific advisory boards of POINT Biopharma, RayzeBio, and Jubilant Pharma and is a consultant for Amgen. No other potential conflicts of interest were reported. Manuscripts submitted to *JNM* with potential conflicts are handled by a guest editor.

EDITORIAL COMMUNICATIONS should be sent to: Editor-in-Chief, Johannes Czernin, MD, *JNM* Office, SNMMI, 1850 Samuel Morse Drive, Reston, VA 20190-5316. Phone: (703) 326-1185; Fax: (703) 708-9018. To submit a manuscript, go to <https://submit-jnm.snmjournals.org>.

BUSINESS COMMUNICATIONS concerning permission requests should be sent to the publisher, SNMMI, 1850 Samuel Morse Drive, Reston, VA 20190-5316; (703) 708-9000; home page address: jnm.snmjournals.org. Subscription requests and address changes should be sent to Membership Department, SNMMI at the address above. Notify the Society of change of address and telephone number at least 30 days before date of issue by sending both the old and new addresses. Claims for copies lost in the mail are allowed within 90 days of the date of issue. Claims are not allowed for issues lost as a result of insufficient notice of change of address. For information on advertising, contact Team SNMMI (Kevin Dunn, Rich Devanna, and Charlie Meitner; (201) 767-4170; fax: (201) 767-8065; TeamSNMMI@cunnasso.com). Advertisements are subject to editorial approval and are restricted to products or services pertinent to nuclear medicine. Closing date is the first of the month preceding the date of issue.

INDIVIDUAL SUBSCRIPTION RATES for the 2023 calendar year are \$633 within the United States and Canada; \$680 elsewhere. Make checks payable to the SNMMI. CPC IPM Sales Agreement No. 1415158. Sales of individual back copies from 1999 through the current issue are available for \$60 at <http://www.snmfi.org/subscribe> (subscriptions@snmfi.org; fax: (703) 667-5134). Individual articles are available for sale online at <http://jnm.snmjournals.org>.

COPYRIGHT © 2023 by the Society of Nuclear Medicine and Molecular Imaging. All rights reserved. No part of this work may be reproduced or translated without permission from the copyright owner. Individuals with inquiries regarding permission requests, please visit <http://jnm.snmjournals.org/site/misc/permission.xhtml>. Because the copyright on articles published in *The Journal of Nuclear Medicine* is held by the Society, each author of accepted manuscripts must sign a statement transferring copyright (available for downloading at <http://jnm.snmjournals.org/site/misc/ifafora.xhtml>). See Information for Authors for further explanation (available for downloading at <http://www.snmjournals.org/site/misc/ifafora.xhtml>).

The ideas and opinions expressed in *JNM* do not necessarily reflect those of the SNMMI or the Editors of *JNM* unless so stated. Publication of an advertisement or other product mentioned in *JNM* should not be construed as an endorsement of the product or the manufacturer's claims. Readers are encouraged to contact the manufacturer with any questions about the features or limitations of the products mentioned. The SNMMI does not assume any responsibility for any injury or damage to persons or property arising from or related to any use of the material contained in this journal. The reader is advised to check the appropriate medical literature and the product information currently provided by the manufacturer of each drug to be administered to verify the dosage, the method and duration of administration, and contraindications.

EDITOR-IN-CHIEF

Johannes Czernin, MD
University of California at Los Angeles
Los Angeles, California

IMMEDIATE PAST EDITOR

Dominique Delbeke, MD, PhD
Vanderbilt University Medical Center
Nashville, Tennessee

ASSOCIATE EDITORS, CONTINUING EDUCATION

Hossein Jadvar, MD, PhD, MPH, MBA, FACNM, FSNMMI
University of Southern California
Los Angeles, California
Lale Kostakoglu, MD, MPH
University of Virginia Health System
Charlottesville, Virginia

ASSOCIATE EDITORS

Ramsey Derek Badawi, PhD
UC Davis Medical Center
Sacramento, California
Henryk Barthel, MD, PhD
Leipzig University
Leipzig, Germany
Frank M. Bengel, MD
Hannover Medical School
Hannover, Germany
Lisa Bodei, MD, PhD
Memorial Sloan Kettering Cancer Center
New York, New York

Irene Buvat, PhD
Université Paris Sud
Orsay, France
Jérémie Calais, MD
University of California at Los Angeles
Los Angeles, California
Sharmila Dorbala, MBBS
Brigham and Women's Hospital
Lexington, Massachusetts
Alexander E. Drzezga, MD
University Hospital of Cologne
Cologne, Germany

Jan Grimm, MD, PhD
Memorial Sloan Kettering Cancer Center
New York, New York
Ken Herrmann, MD, MBA
Universitätsklinikum Essen
Essen, Germany

Thomas A. Hope, MD
University of California, San Francisco
San Francisco, California

Jason S. Lewis, PhD
Memorial Sloan Kettering Cancer Center
New York, New York

David A. Mankoff, MD, PhD
University of Pennsylvania
Philadelphia, Pennsylvania

Heiko Schöder, MD
Memorial Sloan Kettering Cancer Center
New York, New York
Wolfgang Weber, MD
Technical University of Munich
München, Germany

SERIES EDITOR, FOCUS ON MI

Carolyn J. Anderson, PhD
University of Missouri
Columbia, Missouri

SERIES EDITOR, HOT TOPICS

Heinrich R. Schelbert, MD, PhD
University of California at Los Angeles
Los Angeles, California

CONSULTING EDITORS

Nancy Knight, PhD
University of Maryland School of Medicine
Baltimore, Maryland
Barry A. Siegel, MD
Mallinckrodt Institute of Radiology
St. Louis, Missouri
Arnold M. Strashun, MD
SUNY Downstate Medical Center
Scarsdale, New York
H. William Strauss, MD
Memorial Sloan Kettering Cancer Center
New York, New York

ASSOCIATE EDITORS (INTERNATIONAL)

Gerald Antoch, MD
Dusseldorf, Germany

Richard P. Baum, MD, PhD

Bad Berka, Germany
Ambros J. Beer, MD
Ulm, Germany
François Bénard, MD, FRCPC
Vancouver, Canada
Thomas Beyer, PhD
Vienna, Austria

Andreas K. Buck, MD, PhD

Würzburg, Germany
Ignasi Carrió, MD
Barcelona, Spain
June-Key Chung, MD
Seoul, Korea
Stefano Fanti, MD
Bologna, Italy

Markus Hacker, MD

Wien, Austria
Rodney J. Hicks, MD, FRACP

Melbourne, Australia
Michael S. Hofman, MBBS, FRACP
Melbourne, Australia
Ora Israel, MD

Haifa, Israel
Andreas Kjaer, MD, PhD, DMSc

Copenhagen, Denmark
Adriaan A. Lammertsma, PhD

Amsterdam, The Netherlands
Michael Lassman, PhD

Würzburg, Germany
Helmut R. Mäcke, PhD

Freiburg, Germany
Wim J.G. Oyen, MD, PhD

Milan, Italy
John O. Prior, MD, PhD

Lausanne, Switzerland
Osman Ratib, MD, PhD

Geneva, Switzerland
Mike Sathekge, MBChB, MMed, PhD

Pretoria, South Africa
Markus Schwaiger, MD

München, Germany
Andrew M. Scott, MD

Heidelberg, Australia
Nagara Tamaki, MD, PhD

Kyoto, Japan
Jia-He Tian, PhD

Beijing, China
Mei Tian, MD, PhD

Hangzhou, China

EDITORIAL CONSULTANTS

Martin S. Allen-Auerbach, MD

Los Angeles, California
Magnus Dahlbom, PhD

Los Angeles, California
Andrew Quon, MD

Los Angeles, California
Christiaan Schiepers, MD, PhD

Los Angeles, California
Daniel H. Silverman, MD, PhD

Los Angeles, California
Roger Slavik, PhD

Winterthur, Switzerland

EDITORIAL BOARD

Diane S. Abou, PhD

St. Louis, Missouri
Hojjat Ahmadzadehfar, MD

Dortmund, Germany
Valentina Ambrosini, MD, PhD

Bologna, Italy
Norbert Avril, MD

Cleveland, Ohio
Shadfar Bahri

Los Angeles, California
Jacques Barbet, PhD

Saint-Herbalin, France
Bradley Jay Beattie, PhD

New York, New York
Matthias Richard Benz, MD

Los Angeles, California
Elie Besserer-Offroy, PhD, FACSC

Los Angeles, California
Pradeep Bhambhvani, MD

Birmingham, Alabama
Angelika Bischof-Delaloye, MD

Lausanne, Switzerland

Christina Bluemel, MD

Würzburg, Germany
Ronald Boellaard, PhD

Groningen, The Netherlands
Nicolaas Bohnen, MD

Ann Arbor, Michigan
Wesley E. Bolch, PhD

Gainesville, Florida
Elias H. Botvinick, MD

San Francisco, California
Winfried Brenner, MD, PhD

Berlin, Germany
Richard C. Brunken, MD

Cleveland, Ohio
Ralph Buchert, PhD

Hamburg, Germany
Alfred Buck, MD

Menzingen, Switzerland
Denis B. Buxton, PhD

Bethesda, Maryland
Weibo Cai, PhD

Madison, Wisconsin
Federico Caobelli, MD

Basel, Switzerland
Giuseppe Carlucci, PhD

Los Angeles, California
Richard E. Carson, PhD

New Haven, Connecticut
Paolo Castellucci, MD

Bologna, Italy
Francesco Ceci, MD, PhD

Turin, Italy
Juliano J. Cerci

Curitiba, Brazil
Delphine Chen, MD

Seattle, Washington
Xiaoyuan Chen, PhD

Singapore
Simon R. Cherry

Davis, California
Arturo Chiti, MD

Rozzano, Italy
Peter M. Clark, PhD

Los Angeles, California
Christian Cohade, MD

Montreal, Canada
Ekaterina (Kate) Dadachova, PhD

Saskatoon, Canada
Issa J. Dahabreh, MD

Boston, Massachusetts
Heike Elisabeth Daldrop-Link, MD, PhD

Stanford, California
Farrokh Dehdashti, MD

St. Louis, Missouri
Robert C. Delgado-Bolton, MD, PhD

Logroño, Spain
Thorsten Derlin, MD

Hannover, Germany
Elisabeth G.E. de Vries, PhD

Groningen, The Netherlands
Marcelo F. Di Carli, MD

Boston, Massachusetts
David W. Dick, PhD

Iowa City, Iowa
Vasken Dilsizian, MD

Baltimore, Maryland
Jacob Dubroff, MD, PhD

Philadelphia, Pennsylvania
Janet F. Eary, MD

Bethesda, Maryland
W. Barry Edwards, PhD

Columbia, Missouri
Matthias Eiber, MD

Munich, Germany
David Eidelberg, MD

Manhasset, New York
Georges El Fakhri, PhD

Boston, Massachusetts
Peter J. Ell, MD

London, United Kingdom
Keigo Endo, MD

Nantan, Japan
Einat Even-Sapir, MD, PhD

Tel Aviv, Israel
Frederic H. Fahey, DSc

Boston, Massachusetts

EDITORIAL BOARD, continued**Melpomeni Fani, PhD, MSc**

Basel, Switzerland

Andrea Farolfi, MD

Bologna, Italy

Wolfgang Peter Fendler, MD

Essen, Germany

James W. Fletcher, MD

Indianapolis, Indiana

Amy M. Fowler, MD, PhD

Madison, Wisconsin

Kirk A. Frey, MD, PhD

Ann Arbor, Michigan

Andrei Gafita

Los Angeles, California

Victor H. Gerbaudo, PhD, MSHCA

Boston, Massachusetts

Frederik L. Giesel, MD, PhD, MBA

Düsseldorf, Germany

Karolien Goffin, MD, PhD

Leuven, Belgium

Serge Goldman, MD, PhD

Brussels, Belgium

Stanley J. Goldsmith, MD

New York, New York

Martin Gotthardt, MD, PhD

Nijmegen, The Netherlands

Michael Graham, MD, PhD

Iowa City, Iowa

David Groheux, MD, PhD

Paris, France

Uwe A. Haberkorn, MD

Heidelberg, Germany

Mathieu Hatt, PhD, HDR

Brest, France

Wolf-Dieter Heiss, MD

Cologne, Germany

Karl Herholz, MD

Manchester, United Kingdom

Thomas F. Heston, MD

Las Vegas, Nevada

John M. Hoffman, MD

Salt Lake City, Utah

Carl K. Hoh, MD

San Diego, California

Jason P. Holland, DPhil

Zurich, Switzerland

Roland Hustinx, MD, PhD

Liege, Belgium

Andrei H. Iagaru, MD

Stanford, California

Masanori Ichise, MD

Chiba, Japan

Heather A. Jacene, MD

Boston, Massachusetts

Francois Jamar, MD, PhD

Brussels, Belgium

Jae Min Jeong, PhD

Seoul, Korea

John A. Katzenellenbogen, PhD

Urbana, Illinois

Zohar Keidar, MD, PhD

Haifa, Israel

Kimberly A. Kelly, PhD

Charlottesville, Virginia

Laura M. Kenny, MD, PhD

London, United Kingdom

Fabian Kiessling, MD

Aachen, Germany

E. Edmund Kim, MD, MS

Orange, California

Francoise Kraeber-Bodéré, MD, PhD

Nantes, France

Clemens Kratochwil, MD

Heidelberg, Germany

Kenneth A. Krohn, PhD

Portland, Oregon

Brenda F. Kurland, PhD

Pittsburgh, Pennsylvania

Constantin Lapa, MD

Augsburg, Germany

Suzanne E. Lapi, PhD

Birmingham, Alabama

Steven M. Larson, MD

New York, New York

Dong Soo Lee, MD, PhD

Seoul, Korea

Jeffrey Leyton, PhD

Sherbrooke, Canada

Xiang-Guo Li, PhD

Turku, Finland

Hannah M. Linden, MD

Seattle, Washington

Martin A. Lodge, PhD

Baltimore, Maryland

Katharina Lückerath, PhD

Los Angeles, California

Susanne Lütje, MD, PhD

Bonn, Germany

Umar Mahmood, MD, PhD

Boston, Massachusetts

H. Charles Manning, PhD

Nashville, Tennessee

Giuliano Mariani, MD

Pisa, Italy

Chester A. Mathis, PhD

Pittsburgh, Pennsylvania

Alan H. Maurer, MD

Philadelphia, Pennsylvania

Jonathan McConathy, MD, PhD

Birmingham, Alabama

Alexander J.B. McEwan, MD

Edmonton, Canada

Yusuf Menda, MD

Iowa City, Iowa

Philipp T. Meyer, MD, PhD

Freiburg, Germany

Matthias Miederer, MD

Mainz, Germany

Erik Mittra, MD, PhD

Portland, Oregon

Christine E. Mona, PhD

Los Angeles, California

Dae Hyuk Moon, MD

Seoul, Korea

Jennifer Murphy, PhD

Los Angeles, California

Helen Nadel, MD, FRCPC

Stanford, California

Matthias Nahrendorf, MD, PhD

Boston, Massachusetts

Yuji Nakamoto, MD, PhD

Kyoto, Japan

David A. Nathanson, PhD

Los Angeles, California

Nghi C. Nguyen, MD, PhD

Dallas, Texas

Sridhar Nimmagadda, PhD

Baltimore, Maryland

Egbert U. Nitzsche, MD

Aarau, Switzerland

Daniela E. Oprea-Lager, MD, PhD

Amsterdam, The Netherlands

Medhat M. Osman, MD, PhD

Saint Louis, Missouri

Christopher J. Palestro, MD

New Hyde Park, New York

Miguel Hernandez Pampaloni, MD, PhD

San Francisco, California

Neeta Pandit-Taskar, MD

New York, New York

Ashwin Singh Parihar, MBBS, MD

Saint Louis, Missouri

Michael E. Phelps, PhD

Los Angeles, California

Gerold Porenta, MD, PhD

Vienna, Austria

Sophie Poty, PhD

Montpellier, France

Edwin (Chuck) Pratt, PhD, MS Eng

New York, New York

Daniel A. Pryma, MD

Philadelphia, Pennsylvania

Valery Radchenko, PhD

Vancouver, Canada

Caius G. Radu, MD

Los Angeles, California

Isabel Rauscher, MD

Munich, Germany

Nick S. Reed, MBBS

Glasgow, United Kingdom

Mark Rijpkema, PhD

Nijmegen, The Netherlands

Steven P. Rowe, MD, PhD

Baltimore, Maryland

Mehran Sadeghi, MD

West Haven, Connecticut

Orazio Schillaci, MD

Rome, Italy

Charles Ross Schmidtlein, PhD

New York, New York

David M. Schuster, MD

Atlanta, Georgia

Travis Shaffer, PhD

Stanford, California

Sai Kiran Sharma, PhD

New York, New York

Anthony F. Shields, MD, PhD

Detroit, Michigan

Barry L. Shulkin, MD, MBA

Memphis, Tennessee

Yu Shyr, PhD

Nashville, Tennessee

Albert J. Sinusas, MD

New Haven, Connecticut

Riemer H.J.A. Slart, MD, PhD

Groningen, The Netherlands

Piotr Slomka, PhD, FACC

Los Angeles, California

Simon John Christoph Soerensen, MD

Stanford, California

Ida Sonni, MD

Los Angeles, California

Michael G. Stabin, PhD

Richland, Washington

Lisa J. States, MD

Philadelphia, Pennsylvania

Sven-Erik Strand, PhD

Lund, Sweden

Rathan M. Subramaniam, MD, PhD, MPH

Dunedin, New Zealand

John Sunderland, PhD

Iowa City, Iowa

Suleman Surti, PhD

Philadelphia, Pennsylvania

Julie Sutcliffe, PhD

Sacramento, California

David Taieb, MD, PhD

Marseille, France

Laura H. Tang, MD, PhD

New York, New York

Ukihide Tateishi, MD, PhD

Tokyo, Japan

James T. Thackeray, PhD

Hannover, Germany

Mathew L. Thakur, PhD

Philadelphia, Pennsylvania

Alexander Thiel, MD

Montreal, Canada

Daniel L.J. Thorek, PhD

St. Louis, Missouri

David W. Townsend, PhD

Singapore

Timothy Turkington, PhD

Durham, North Carolina

Gary A. Ulaner, MD, PhD

Irvine, California

David Ulmert, MD, PhD

Los Angeles, California

Christopher H. van Dyck, MD

New Haven, Connecticut

Douglas Van Nostrand, MD

Washington, District of Columbia

Patrick Veit-Haibach, MD

Toronto, Canada

Nerissa Viola-Villegas, PhD

Detroit, Michigan

John R. Votaw, PhD

Atlanta, Georgia

Richard L. Wahl, MD

St. Louis, Missouri

Anne Marie Wallace, MD

La Jolla, California

Martin A. Walter, MD

Geneva, Switzerland

Rudolf A. Werner, MD

Wuerzburg, Germany

Andreas G. Wibmer, MD

New York, New York

Anna M. Wu, PhD

Duarte, California

Randy Yeh, MD

New York, New York

Hyewon (Helen) Youn, PhD

Seoul, Korea

Pat B. Zanzonico, PhD

New York, New York

Brian M. Zeglis, PhD

New York, New York

Robert Zeiser, MD

Freiburg, Germany

Hong Zhang, MD, PhD

Hangzhou, China

Hongming Zhuang, MD, PhD

Philadelphia, Pennsylvania

Sibylle I. Ziegler, PhD

Munich, Germany

ASSISTANT TO THE EDITOR**Joshua N. Wachtel**

Los Angeles, California

Addressing Pluvicto supply issues: Czernin and Calais comment on potential solutions to insufficient supply and slowed access to ^{177}Lu -PSMA-617 and preview a related editorial in this issue of *JNM*. **Page 343**

Discussions with leaders: Ramsey Badawi talks with H el ene Langevin, director of the National Center for Complementary and Integrative Health, about her career-long perspective on medical treatment for the “whole patient.” **Page 344**

“Last mile” for radioligand therapy: Pomykala and colleagues look at elements required to translate newly approved nuclear theranostics into routine clinical use, including the challenges of supply chain and distribution logistics. . . . **Page 347**

^{177}Lu -PSMA in prostate cancer: Ravi and colleagues describe the process of clinical implementation of ^{177}Lu -PSMA-617 at a major academic center, highlighting successes and hurdles, including referrals, supply issues, and patient selection. **Page 349**

ER-targeted ^{18}F -FES PET AUC: Ulaner and colleagues from an SNMMI-convened expert work group provide a brief summary of recently published appropriate use criteria for ^{18}F -FES PET detection of estrogen receptor–positive breast cancer, including clinical scenarios. **Page 351**

PET/CT or CE-CT in breast cancer: Vogsen and colleagues compare contrast-enhanced CT and ^{18}F -FDG PET/CT for response monitoring in metastatic breast cancer using standardized response evaluation criteria, focusing on early detection of progressive disease. **Page 355**

PET/CT negative predictive value: Subramaniam and colleagues report on the negative predictive value of a 12- to 14-wk posttreatment PET/CT for 2-y progression-free survival and locoregional control in patients with p16-positive locoregionally advanced oropharyngeal cancer. . . **Page 362**

^{68}Ga -FAPI PET and COVID-19 pitfalls: Demmert and colleagues assess ^{18}F -FDG and ^{68}Ga -FAPI-46 PET/CT tumor staging in a series of patients after COVID vaccination and discuss the potential of FAPI to avoid confounding postvaccination findings and provide superior tumor localization. **Page 368**

PSMA targeting in salivary gland tumors: Civan and colleagues analyze the diagnostic performance of PSMA PET/CT and the dosimetry, efficacy, and safety of ^{177}Lu -PSMA-617 radioligand therapy in salivary gland malignancies. **Page 372**

PSMA vs. GRP-R PET/CT in prostate cancer: Schollhammer and colleagues describe a prospective

head-to-head comparison of PSMA- and gastrin-releasing peptide receptor–targeted imaging at initial prostate cancer staging to understand how these can be used or combined in clinical practice. **Page 379**

^{68}Ga -FAP-2286 in various cancers: Pang and colleagues assess the diagnostic accuracy of ^{68}Ga -FAP-2286, compared with ^{18}F -FDG and ^{68}Ga -FAPI-46, to detect primary and metastatic lesions in patients with various types of cancer. . . **Page 386**

Predicting IBLs on PSMA PET/CT: Phelps and colleagues define variables that predict whether indeterminate bone lesions in patients with high-risk primary or biochemically recurrent prostate cancer are likely malignant or benign using features on ^{18}F -DCFPyL PET/CT. **Page 395**

^{177}Lu -PSMA-I&T for mCRPC: Karimzadeh and colleagues detail prostate-specific antigen response and progression-free and overall survival in patients with metastatic castration-resistant prostate cancer treated with ^{177}Lu -PSMA-I&T and identify clinical and imaging prognostic factors. **Page 402**

SPECT and ^{177}Lu -PSMA response: John and colleagues evaluate changes in ^{177}Lu -PSMA SPECT/CT quantitative parameters to monitor ^{177}Lu -PSMA treatment response in men with progressive metastatic castration-resistant prostate cancer. **Page 410**

Vessel wall total-body PET: Derlin and colleagues use ultrasensitive, extended-field-of-view total-body PET to explore biologic hallmarks of previously difficult-to-evaluate low-signal cardiac vessel wall pathology and crosstalk with other organs. **Page 416**

PET and neutrophil elastase: Puuvuori and colleagues assess the novel neutrophil elastase inhibitor ^{11}C -GW457427 in a pig model of acute respiratory distress syndrome, for PET detection and quantification of neutrophil activity in the lungs. **Page 423**

^{68}Ga -DOTA CSF PET: Evangelou and colleagues evaluate ^{68}Ga -DOTA PET imaging of the cerebrospinal fluid space as a state-of-the-art approach to radionuclide cisternography in patients with suspected intracranial hypotension resulting from spinal CSF leaks. **Page 430**

Plasma pTau181 vs. tau PET: Coomans and colleagues compare plasma tau phosphorylated at threonine-181 PET and tau PET in participants along the Alzheimer disease continuum, including evaluation of staging and progression. . . **Page 437**

Visual interpretation of ^{18}F -MK-6240: Seibyl and colleagues describe development of a visual

assessment method for ^{18}F -MK-6240 PET that provides both an overall assessment of brain tauopathy and regional characterization of abnormal tau deposition. **Page 444**

Age and off-target retention of [^{18}F]MK6240: Tissot and colleagues look at common reference region estimates in the cerebellum over time and evaluate the effects of age-related and off-target retention on longitudinal PET quantification of [^{18}F]MK6240 in target regions. **Page 452**

Tau PET tracers in CTE: Varlow and Vasdev conduct a head-to-head in vitro evaluation of 5 tau PET radiotracers in subjects pathologically diagnosed with chronic traumatic encephalopathy. **Page 460**

MDMA and neurovascular uncoupling: Ionescu and colleagues delineate the acute effects of 3,4-methylenedioxymethamphetamine using simultaneous PET/fMRI in rats, with a goal of identifying more robust measures for pharmacologic research. **Page 466**

AI-based SPECT attenuation correction: Shanbhag and colleagues develop and validate a deep-learning model to generate simulated attenuation correction myocardial perfusion images directly from non-corrected SPECT, without the need for CT. **Page 472**

Lensless radiomicroscope: Klein and colleagues describe development of the lensless radiomicroscope, a new imaging modality, for in vitro cellular-resolution imaging of β - and α -emitting radionuclides. **Page 479**

Adverse events after extravasation: Parihar and colleagues study the occurrence of short- and long-term clinical adverse events in patients after $^{99\text{m}}\text{Tc}$ -methylene diphosphonate whole-body bone scintigraphy with reported radiopharmaceutical extravasation. **Page 485**

Perspective on diagnostic RPE: van der Pol and Mottaghy comment on radiopharmaceutical extravasation and a related article in this issue of *JNM*. **Page 491**

Multiregion mouse kidney model: Vargas and colleagues describe development of a multiregion model of a mouse kidney based on high-resolution MRI data, with utility in calculating reference dose factors for specific mouse kidney tissues. **Page 493**

Progression or response: Parihar and colleagues offer a case study in a patient with responding Hodgkin lymphoma and new liver lesions on ^{18}F -FDG PET/CT. **Page 500**

The ¹⁷⁷Lu-PSMA-617 (Pluvicto) Supply Problem Will Be Solved by Competition

Johannes Czernin and Jeremie Calais

Ahmanson Translational Theranostics Division, Department of Molecular and Medical Pharmacology, David Geffen School of Medicine at UCLA, Los Angeles, California

An editorial in this issue of *The Journal of Nuclear Medicine* by the theranostics teams of Dana–Farber Cancer Institute and Brigham and Women’s Hospital addresses ongoing challenges with the rollout of ¹⁷⁷Lu-PSMA-617 (¹⁷⁷Lu-vipivotide tetraxetan; Pluvicto [Novartis]) (1). The authors highlight several major problems: insufficient and slow supply remains a daunting problem for patients, their families, caregivers, and treating physicians. Most alarmingly, 5% of the authors’ patients died while waiting for treatment, as this can be delayed by 2 mo or even longer (1). These observations match our own experience. The authors point to additional consequences, including long intervals between pretreatment prostate-specific membrane antigen (PSMA) PET/CT scans and therapy rendering patient stratification and treatment monitoring unreliable (1).

The U.S. Food and Drug Administration approved the new-drug application for Pluvicto 9 mo ago. The Centers for Medicare and Medicaid Services has reimbursed for it since October 2022. Novartis halted production of Pluvicto in Ivrea, Italy, and Milburn, New Jersey, in May 2022 and resumed production and delivery at the Ivrea site in June 2022. Yet, Pluvicto availability has remained a significant problem because only one of the two previous sites is currently operational for Pluvicto production.

Drugs are usually considered a failure if they do not meet revenue and profit expectations, which is one suggested reason for the market withdrawal of the CD20 antibody ¹³¹I-tositumomab (Bexxar; GlaxoSmithKline) (2). But commercialization starts with successful and compliant drug production and delivery. Patients and their treatment teams lose trust in products that are much talked about but remain largely unavailable. The last-mile requirements for radioligand therapies are specified by Pomykala et al. in this issue (3) and include having a proficient drug supply, meeting infrastructure and regulatory requirements, training competent staff and having them available (including authorized users), establishing reliable reimbursement, and having a sufficient patient referral base. If the first of these requirements remains the key problem, then the rest of the requirements are no longer relevant. Past mistakes in rolling out molecular radiotherapies also included tedious drug-ordering processes, as was the case for another CD20-directed radiotherapeutic antibody, ibritumomab tiuxetan (Zevalin; Acrotech Biopharma) (4).

Novartis recently announced that “Pluvicto demonstrated a statistically significant and clinically meaningful improvement in radiographic progression-free survival... in a randomized trial of patients with PSMA-positive metastatic castration-resistant prostate cancer... after treatment with androgen-receptor pathway inhibitor (ARPI) therapy, compared to a change in ARPI” (PSMAfore,

NCT04689828) (5). This, and several ongoing investigator- or industry-initiated late-stage randomized clinical trials, place PSMA-targeted therapies at various stages of prostate cancer, suggesting that indications will broaden and demand will increase dramatically.

What are the solutions? Novartis added a new production site at Purdue Research Park near Indianapolis, and it is hoped that this and the Milburn site will be fully operational later this year. Novartis needs to create further back-up solutions to guarantee a drug supply for new patients whose waiting times are unacceptable and for those who are already undergoing treatment and are waiting for the subsequent therapy cycles. Competition will certainly contribute to solving the supply problem. Several compounds are undergoing testing in phase 3 clinical trials, including SPLASH (NCT0464752, POINT Biopharma/Lantheus) and ECLIPSE (NCT05204927, Curium), and are likely to meet endpoints. These are going to shake up the market in 2024.

As Friedrich von Hayek stated, “A monopoly based on superior efficiency, on the other hand, does comparatively little harm so long as it is assured that it will disappear as soon as anyone else becomes more efficient in providing satisfaction to the consumers.” (6).



Johannes Czernin



Jeremie Calais

REFERENCES

1. Ravi P, Whelpley B, Kelly E, et al. Clinical implementation of ¹⁷⁷Lu-PSMA-617 in the United States: lessons learned and ongoing challenges. *J Nucl Med.* 2023;64:349–350.
2. Prasad V. The withdrawal of drugs for commercial reasons: the incomplete story of tositumomab. *JAMA Intern Med.* 2014;174:1887–1888.
3. Pomykala KL, Würker M, Herrmann K. Tackling the last mile: a major component to successfully establish radioligand therapy. *J Nucl Med.* 2023;64:347–348.
4. Ordering information for ZEVALIN administration facilities. Zevalin website. <https://zevalin.com/hcp/zevalin-dosing-and-administration/ordering-information-for-zevalin-administration-facilities/>. Accessed January 17, 2023.
5. Novartis Pluvicto™ shows statistically significant and clinically meaningful radiographic progression-free survival benefit in patients with PSMA-positive metastatic castration-resistant prostate cancer. Novartis website. <https://www.novartis.com/news/media-releases/novartis-pluvictotm-shows-statistically-significant-and-clinically-meaningful-radiographic-progression-free-survival-benefit-patients-psma-positive-metastatic-castration-resistant-prostate-cancer>. Published December 5, 2022. Accessed January 17, 2023.
6. Hayek FA. *Individualism and Economic Order*. University of Chicago Press; 1948:92.

Focusing on Whole-Person Health

A Conversation Between H el ene Langevin and Ramsey Badawi

H el ene Langevin¹ and Ramsey Badawi²

¹National Center for Complementary and Integrative Health, Bethesda, Maryland; and ²University of California Davis Medical Center, Davis, California

Ramsey Badawi, from the University of California Davis, talked with H el ene Langevin, director of the National Center for Complementary and Integrative Health (NCCIH) at the National Institutes of Health (NIH; Bethesda, MD), about her career-long perspective on the ways in which medical treatment should address the whole patient. She is currently the chair of the Interagency Pain Research Coordinating Committee and has been a prime mover in engaging the NIH community in research in the whole-person health initiative.

Dr. Langevin received her medical degree from McGill University (Montreal, Canada). She completed a postdoctoral research fellowship in neurochemistry at the Medical Research Council Neurochemical Pharmacology Unit (Cambridge, U.K.) and a residency in internal medicine and fellowship in endocrinology and metabolism at the Johns Hopkins Hospital (Baltimore, MD). She was a professor of neurologic sciences at the University of Vermont Larner College of Medicine (Burlington) until 2012, when she became director of the Osher Center for Integrative Medicine (Boston, MA) and a professor of medicine in residence at Harvard Medical School (Boston, MA). She became director of NCCIH in 2018. As the principal investigator of several NIH-funded studies, Dr. Langevin has centered her research around the role of connective tissue in chronic musculoskeletal pain and the mechanisms of acupuncture, manual, and movement-based therapies. Her more recent work has focused on the effects of stretching on inflammation resolution mechanisms within connective tissue.

Dr. Badawi: You studied music as well as biology as a student. I was curious: what was your instrument of choice? Do you still play?

Dr. Langevin: Piano. I still play. I find it so relaxing. I love classical music—it takes you back to a different epoch. My favorite period is the turn of the 20th century, when things were getting deconstructed in art and music. That’s an interesting time.

Dr. Badawi: You spent quite some time as a practicing physician. How did that inform your choices of scientific inquiry?

Dr. Langevin: I was an endocrinologist, and I also practiced internal medicine. I ended up seeing a lot of people who had pain—chronic pain, specifically. You can’t be a doctor without encountering patients who are dealing with chronic pain. I felt so frustrated by how little I could offer. That’s what got me interested in nonpharmacologic methods for pain management, of which there were very few at the time.

Dr. Badawi: You have had a tremendously successful scientific career. What would you describe as your most significant contribution?

Dr. Langevin: I was part of a group of people who, around 20 years ago, started seriously thinking about the role of connective tissue in the body: how important it is, how understudied it is, how it interfaces with all of the other systems in the body, and how much more we need to understand. We needed to study the connection between biochemistry and biomechanics and the whole field of mechanical transduction. We developed a very simple model in my lab, which used acupuncture needles to deliver a force into the tissue. By simply stretching the tissue, we could look at the impact of this force on cells and cascades of signaling pathways. But much remains to be done. At the cellular level, we think about connective tissue as the extracellular matrix, but at the whole-organ and whole-body levels, huge gaps remain in our understanding of the role connective tissue plays.

Dr. Badawi: When we think of vigorous aerobic or resistance training, the metabolic pathways and the outcomes of the signaling are understood even by lay people, but significant benefits are associated with other exercise modalities, such as yoga. Is this related to what you are talking about?

Dr. Langevin: Absolutely. If you’re doing a less vigorously aerobic exercise, such as gentle yoga, your heart rate may not go up very much. But what may happen is that you move your body in directions that are not habitual. At the same time, you are relaxing your body and removing some of the connective tissue restrictions by gentle stretching. It’s a very different effect physiologically. Doing yoga for 30 min or running for 30 min can both be beneficial but in very different ways.

Dr. Badawi: May I ask about your own exercise habits?

Dr. Langevin: I do about 15 min of stretching every morning, because I know that if I don’t, I tend to stiffen, get more pain, and be more injury-prone. I also always try to do something aerobic. I don’t run any more, but I ride my bicycle to work. I’ll swim in the summer and do cross-country skiing in the winter. I also like canoeing—anything that’s outside. I like to challenge my body in different ways. I think aerobic exercise is important for your general health, but it’s not enough by itself. The stretching is necessary to maintain my capability to do the aerobic exercise.

Dr. Badawi: Changing the topic, how did you make the transition from practicing scientist to leadership at NIH, and what drove that career choice?



H el ene Langevin, MD

Dr. Langevin: One of the nice things about being at NIH is that I'm able to have a lab in the NIH intramural space. I'm still able to do research, although I have less time for it. Having the opportunity to also be the director of NCCIH has opened up a whole other aspect of science for me. In this role, I can impact the kinds of questions that researchers can address in a much larger sense. For example, the NIH Helping to End Addiction Long-Term (HEAL) Initiative is aimed at addressing the opioid epidemic. This has 2 components: the opioid problem and the related crisis of pain. So many people live with chronic pain. A lot of it is musculoskeletal, and in many cases, we don't understand the pathophysiology. Together with the HEAL Initiative, we launched an effort aimed at developing imaging and other methods to quantify abnormalities within the musculoskeletal tissues that may underlie myofascial pain. These are areas in which we have historically done very little research. As NCCIH director, I have a wonderful opportunity to help researchers make a tremendous impact.

Dr. Badawi: *I once attended a lecture by a hand surgeon, John Agee. He mentioned the opioid epidemic and the pain crisis. He opined that a direct cause of a large fraction of the problem was not a deficit of medicine, it was a deficit of love—that many of these people who find themselves dependent on opioids for pain management actually have a lack of meaningful human connection in their lives. He said that human connection is enormously important in reducing the impact of pain. What is your thought about that statement?*

Dr. Langevin: I think that you're talking about the psychosocial component of what we call the biopsychosocial model of pain.

not always supported with robust scientific evidence of utility. This is important work, and we still support this kind of research.

But as part of the new strategic plan, we decided to create a framework for studying these in the context of what we call whole-person health. We define this in a way that empowers individuals, families, communities, and whole populations to improve their health in multiple interconnected domains. We want to stop thinking about biologic, behavioral, social, and environmental factors as separate and instead look at them all together. Even within the biologic domain, we tend to compartmentalize: we look separately at the nervous system, cardiovascular system, and digestive system. The point of whole-person health is to think about the integration of the whole person.

My role involved not just developing the new strategic plan but also publicizing and implementing it and overseeing new funding opportunities. We're starting to see people submitting grant applications in response to this, which is very gratifying. Part of my job is also to go out to speak with people from other NIH institutes that are more focused on specific body systems or diseases and advocate for collaboration on whole-person health. So far this has been very successful. We have an internal NIH working group on whole-person health in which many other institutes and centers participate.

We also participate in several trans-NIH initiatives. One of these is the Pragmatic Trials Collaboratory, which focuses on research in health-care settings. Conducting trials that are embedded within health-care systems can help disseminate knowledge and address obstacles in implementation of proven approaches that

“... when I came to NIH, I really wanted to start thinking about what we call whole-person health. Instead of focusing on diseases a single organ system at a time, we need to understand health better, which is a whole-body phenomenon.”

The muscles, the connective tissue that I was talking about earlier in terms of the myofascial pain, are the bio part. That's hugely important, but the psychosocial component is enormously important as well. Thirty years ago, if you had back pain, you went to see an orthopedic surgeon, who decided whether you needed surgery. If you didn't need surgery, your back pain was called nonspecific and not much could be done for you, which led to huge frustration. However, the pendulum has now swung toward the psychologic components of pain. We have begun to understand the processes involving the central nervous system, emotional distress, stress responses, and behaviors that go along with having pain. We have begun to understand the negative consequences of, for example, loneliness in this context. But we have yet to fully connect the psychologic and social contexts of pain with what's going on in the physiologic space and the tissues. I think that's the big challenge now.

Dr. Badawi: *That sounds like a tremendously exciting paradigm to explore.*

Dr. Langevin: Indeed!

Dr. Badawi: *Tell us a bit about your current role as director of NCCIH.*

Dr. Langevin: When I came to NIH, one of the big things that I presided over was mapping out the new strategic plan for NCCIH. In the past, NCCIH had focused on a few very important areas, such as pain, mind-and-body practices (such as yoga and meditation), and natural products, which are in widespread use but

aren't being used. We know, for example, that opiates should not be the first-line treatment for pain. Yet if you look at health-care systems, they're often still used in this way. Nonpharmacologic methods, however, can be tricky to implement, because they require different expertise, different people. This initiative is aimed at changing that.

I also do a lot of outreach and external talks. For example, I spoke at the September 2022 Total-Body PET Conference in Edinburgh, U.K. It was great fun to be able to interact with a completely different scientific community that I did not know before.

Dr. Badawi: *Can you tell us a bit about how your whole-person health research effort came about?*

Dr. Langevin: It goes back all the way to when I did my very first research fellowship after medical school. My area of study was the hypothalamus, which is a really interesting part of the body. It's very small and difficult to image, but packed inside that little hypothalamus is control of the autonomic nervous system, the endocrine system, sleep, appetite, growth, reproductive function, and more. I always think it is like the orchestra conductor for the whole body. Subsequently, when I was practicing internal medicine, my subspecialty was endocrinology. The endocrine system is a whole-body system that impacts all the organs. Then I got interested in connective tissue, which in a completely different way also has its fingers over all these different organ systems. So, this idea of whole-body research was kind of in my head for a long time.

Then, when I came to NIH, I really wanted to start thinking about what we call whole-person health. Instead of focusing on diseases a single organ system at a time, we need to understand health better, which is a whole-body phenomenon. Imagine you're not so healthy; perhaps you've had an unhealthy lifestyle for a couple of years, gained a few pounds, your blood pressure might be starting to creep up, your blood sugar might be a bit less controlled, your lipids a little high. This is the beginning of what we call the metabolic syndrome. It's a very, very common problem, but it's reversible up to a point. So if you do the right interventions (eating a good diet, getting some exercise, and especially managing stress), the entire thing can be reversed. All of these abnormalities can improve at the same time, because it's a whole-body intervention. You can see that this is all connected: exercise ties into the musculoskeletal system, diet and nutrition tie into metabolism and endocrinology, and then stress and sleep tie into the nervous system and the hypothalamus. For me, this represents much of what I have been thinking about pretty much my whole career.

Dr. Badawi: *We've been talking about the potential role of molecular imaging and, in particular, total-body PET in whole-person research. What do you think are the key areas in which total-body PET might be able to contribute?*

Dr. Langevin: We talked a little bit already about the relationship between the structure of the body and its biochemistry. When we think about biochemistry, we tend to think about these molecules sort of floating around in liquid—but that's not right. All biochemistry occurs in a structural environment. What PET imaging and total-body PET in particular allow you to do is to look at biochemistry in this greater context. So I'm very intrigued. I think there's a lot of potential here. This is a really wonderful new way to look at how the different organs and systems communicate with

one another. Some of the presentations that I saw at the Edinburgh conference last fall showed me that this new technique really encourages integrative thinking. Sometimes it takes the development of a new technology to allow the generation of a different kind of hypothesis or a different way to look at a problem.

Dr. Badawi: *I think the field is beginning to see that the mathematic and analytic tools for molecular imaging that we've been using quite successfully for the last 40 years are not really adequate for addressing the whole-person health problem. As a result, people are starting to reach out to others who have expertise that can help us. I think that is very positive.*

Dr. Langevin: I agree. And, if I may, I would like to mention the trans-NIH Methodologic Approaches for Whole Person Research Workshop that NCCIH hosted in summer 2021. Our goal was to identify expertise in all kinds of fields that could be brought to bear on studying whole-person health. The discussion was very encouraging. We have a new generation of researchers who are not afraid to tackle big data and complex questions. They have the necessary computational tools, the networks, and the analytic tools. They also have new technologies that can collect and analyze these kinds of data, and we have new thoughts on how to design studies properly to look at complex systems. We looked at how to study interconnected systems and how to study the impact of multicomponent interventions on these interconnected systems. I would encourage anyone who is interested to watch the conference [on-demand at <https://www.nccih.nih.gov/news/events/methodological-approaches-for-whole-person-research>]. It really showed us that the field is ready to tackle this.

Dr. Badawi: *Dr. Langevin, thank you so much for a fascinating conversation!*

Dr. Langevin: My pleasure. This has been very fun!

Tackling the Last Mile: A Major Component to Successfully Establish Radioligand Therapy

Kelsey L. Pomykala¹, Marcus Würker², and Ken Herrmann³

¹*Institute for Artificial Intelligence in Medicine, University Hospital Essen, Essen, Germany;* ²*Deutsche Post DHL Group, Bonn, Germany;* and ³*Department of Nuclear Medicine, University of Duisburg–Essen, and German Cancer Consortium–University Hospital Essen, Essen, Germany*

The term *last mile* originates from the telecommunication industry and describes the difficulty of connecting the end customer to the main telecommunication networks (1). Successfully tackling the last mile is associated with economic success in several different industries in addition to telecommunications, in particular within the supply chain and logistics industry. Translating this concept to the anticipated expansion of radioligand therapy automatically shifts the focus to the delivery of the therapy to the patients. The first difficult 25 miles of the marathon have been run by discovering and developing new therapies, investigating them in well-designed clinical trials, and gaining government approval. To complete the last mile is to successfully deliver the therapy to patients.

With 2 promising radioligand therapies recently approved by the Food and Drug Administration—¹⁷⁷Lu-DOTATATE (Lutathera; Advanced Accelerator Applications) and ¹⁷⁷Lu-PSMA-617 (Pluvicto; Advanced Accelerator Applications)—the stage is set for a radioligand therapy renaissance, especially with the abundance of convincing clinical data in support of Pluvicto (2–5), leading to a huge buzz. However, early lessons were learned from Lutathera after the Food and Drug Administration approval in 2018. There was an initial steep rise in demand, but sales plateaued far earlier than expected, never fully reaching the anticipated revenue potential. One can infer why this occurred. First, there were not enough hospitals prepared to offer Lutathera. Next, with neuroendocrine tumors being a specialized disease often treated in dedicated centers, sometimes these neuroendocrine tumor centers did not have nuclear medicine departments organized to deliver this new therapy. Additionally, overall, there are low numbers of neuroendocrine tumors, with approximately 12,000 patients diagnosed each year in the United States (6). When starting with a relatively low number of patients, and adding not having enough centers to provide Lutathera treatment, economies of scale, or an average cost decrease as output increases, was not allowed to occur. Will the story be different for Pluvicto? One advantage is that prostate cancer is more common, with over 260,000 new cases per year in the United States (7). But how can we make sure that all patients can be reached and that the last mile does not prevent sustainable success of radioligand therapy?

Securing patient access clearly depends on scaling up the delivery of radioligand therapy to many more clinical institutions capable of administering the therapy. Conservative estimates predict that 70–280 theranostic centers will be needed in the United States to treat neuroendocrine and prostate cancer alone, depending on how many treatments are performed per day per site (8). In addition, with more studies under way to investigate the utility of radioligand therapy as earlier-line therapy and in other cancers, even more centers may be required. The 5 key pillars of successfully implementing radioligand therapy include drug supply, infrastructure and regulatory requirements (e.g., radioactive material program license), staff (including authorized users), reimbursement, and referred patients. The first pillar, drug supply, is not without challenges. Production can be affected by several issues, including ¹⁷⁷Lu shortages due to reactor shutdowns, inability to meet increasing governmental requirements, and site contamination. Although the pharmaceutical companies handle the first pillar, our field, nuclear medicine, has to pay attention to the remaining pillars. To identify eligible patients, experts in radioligand therapy should be present in multidisciplinary tumor boards, form reliable collaborations and patient referral pathways, and ensure that patients then return to the primary leading physician for further follow-up care. To ensure that there is enough staff to care for the patients, specialty training will be required for nurses, technologists, pharmacists, medical doctors, medical physicists, and more professionals. To guarantee high-quality training for all subspecialties involved, curricula need to be established and to some degree standardized. Another important aspect is to overcome financial disincentives for patient-referring collaborators by potentially considering revenue share options.

Infrastructure investment (e.g., infusion chairs, shielding, and waste management systems), as well as reimbursement, require the buy-in of major stakeholders such as payers, hospital administrations, and government organizations (requiring coordinated lobbying on behalf of patient interests). Reimbursement needs to include not only payment for the drug but also payment for all associated procedures such as administration, dosimetry, and imaging required for patient selection. Without a clear pathway to pay off the investment into new infrastructure, the required ramp-up of theranostic centers will not be successful. Advocacy, collaboration, consistency, and hard work are needed to build these 5 strong pillars. Recent joint efforts by the European Association of Nuclear Medicine, Society of Nuclear Medicine and Molecular Imaging, and International Atomic Energy Agency have been

Received Oct. 13, 2022; revision accepted Dec. 21, 2022.

For correspondence or reprints, contact Kelsey L. Pomykala (kelsey.herrmann@uk-essen.de).

Published online Dec. 22, 2022.

COPYRIGHT © 2023 by the Society of Nuclear Medicine and Molecular Imaging.

DOI: 10.2967/jnumed.122.264900

initiated to ignite the establishment of theranostic centers, but this is only the beginning (9).

After reviewing the essential pillars for radioligand therapy delivery, what are the concrete necessary action items that need to be completed? Each center needs to create an individual viable business plan including strategies for infrastructure development, staff preparation, and creation of revenue with reimbursements. A regulatory framework must be locally established such as licensing, proper storage, and waste management and disposal. Contracts need to be established, with the availability of vendors on site for assistance. Educational sessions ought to be organized to inform nuclear medicine staff, referring clinicians, and patients about the new therapies. Patient acceptance is also an important part of success, and with education, this should be attainable because of high patient convenience (intravenous therapy) and low side effects.

For those who are not yet convinced of the importance of the last mile, let us turn to the logistics giant Deutsche Post DHL Group for an example. The company encompasses a vast portfolio of logistics services and is thereby suited to analyze the significance of last-mile businesses in terms of barriers to entry and financial attractiveness. Deutsche Post DHL Group's services range from international door-to-door express services to domestic and international parcel networks, forwarding of freight over international air, sea, and ground routes (door-to-port and port-to-door services), warehousing, and customer-dedicated domestic transport. The group's published financial figures (10) consistently suggest higher returns for business models including last-mile activities. In 2021, the activities with less of a focus on the last mile generated between a 5.1% and 5.7% earnings-before-interest-and-taxes margin, whereas the divisions including distributed last-mile services generated up to a 17.4% margin in the same year.

Whereas successfully tackling the last mile goes along with a significant economic upside in the logistics industry, it is a prerequisite to turn theranostics into a major oncologic therapy option. However, distributing specific therapies with a limited shelf-life around the globe in a secure and traceable way is considered the most challenging task in this industry, often performed by highly specialized niche players.

The renaissance of theranostics brings along one of the most exciting times in our field. Apart from the clinical effectiveness and the regulatory approval, successfully establishing the winning

pillars of radioligand therapy's last mile will determine the sustainable success of theranostics.

DISCLOSURE

Ken Herrmann reports personal fees from Bayer, Sofie Biosciences, SIRTEX, Adacap, Curium, Endocyte, BTG, IPSEN, Siemens Healthineers, GE Healthcare, Amgen, Novartis, ymabs, Aktis Oncology, Theragnostics, Pharma15, Debiopharm, AstraZeneca, and Janssen; other fees from Sofie Biosciences; nonfinancial support from ABX; and grants from BTG outside the submitted work. Kelsey Pomykala reports personal fees from ABX outside the submitted work. Marcus Würker is an employee of Deutsche Post DHL Group not involved in the delivery of radiopharmaceuticals. No other potential conflict of interest relevant to this article was reported.

REFERENCES

1. Hayes A. Last mile: what it means in reaching customers. Investopedia website. <https://www.investopedia.com/terms/l/lastmile.asp>. Published May 5, 2022. Accessed November 7, 2022.
2. Hofman MS, Violet J, Hicks RJ, et al. [¹⁷⁷Lu]-PSMA-617 radionuclide treatment in patients with metastatic castration-resistant prostate cancer (LuPSMA trial): a single-centre, single-arm, phase 2 study. *Lancet Oncol*. 2018;19:825–833.
3. Kim YJ, Kim Y-I. Therapeutic responses and survival effects of ¹⁷⁷Lu-PSMA-617 radioligand therapy in metastatic castrate-resistant prostate cancer: a meta-analysis. *Clin Nucl Med*. 2018;43:728–734.
4. Hofman MS, Emmett L, Sandhu S, et al. [¹⁷⁷Lu]Lu-PSMA-617 versus cabazitaxel in patients with metastatic castration-resistant prostate cancer (TheraP): a randomised, open-label, phase 2 trial. *Lancet*. 2021;397:797–804.
5. Sartor O, de Bono J, Chi KN, et al. Lutetium-177-PSMA-617 for metastatic castration-resistant prostate cancer. *N Engl J Med*. 2021;385:1091–1103.
6. Neuroendocrine tumors: statistics. American Society of Clinical Oncology website. February 2022. <https://www.cancer.net/cancer-types/neuroendocrine-tumors/statistics>. Published February 2022. Accessed January 9, 2023.
7. Key statistics for prostate cancer. American Cancer Society website. <https://www.cancer.org/cancer/prostate-cancer/about/key-statistics.html>. Published January 2022. Accessed January 9, 2023.
8. Czernin J, Calais J. How many theranostics centers will we need in the United States? *J Nucl Med*. 2022;63:805–806.
9. Herrmann K, Giovanella L, Santos A, et al. Joint EANM, SNMMI and IAEA enabling guide: how to set up a theranostics centre. *Eur J Nucl Med Mol Imaging*. 2022;49:2300–2309.
10. 2021 Annual Report. Deutsche Post DHL Group; 2022.

Clinical Implementation of ^{177}Lu -PSMA-617 in the United States: Lessons Learned and Ongoing Challenges

Praful Ravi¹, Bridget Whelpley¹, Emma Kelly¹, Andrew Wolanski^{1,2}, Jolivette Ritzer^{1,2}, Matthew Robertson^{1,2}, Hina Shah^{1,2}, Alicia K. Morgans¹, Xiao X. Wei¹, Rajitha Sunkara¹, Mark Pomerantz¹, Mary-Ellen Taplin¹, Kerry L. Kilbridge¹, Atish D. Choudhury¹, and Heather Jacene^{1,2}

¹Dana-Farber Cancer Institute, Boston, Massachusetts; and ²Brigham and Women's Hospital, Boston, Massachusetts

In March 2022, ^{177}Lu -PSMA-617 (^{177}Lu -vipivotide tetraxetan) received Food and Drug Administration approval for treatment of metastatic castration-resistant prostate cancer (mCRPC) in men with prostate-specific membrane antigen (PSMA)-avid disease who have received prior chemotherapy and a novel androgen receptor-directed therapy (1). Approval followed the VISION trial, which demonstrated a median 4-mo overall survival benefit for ^{177}Lu -PSMA-617 plus best supportive care versus best supportive care alone (2). ^{177}Lu -PSMA-617 is the first theranostic agent for prostate cancer and a clinically meaningful addition to the therapeutic armamentarium. Here, we describe the process of clinical implementation of ^{177}Lu -PSMA-617 at a major academic center, highlighting successes and challenges.

Between May and October 2022, 146 patients with a median age of 73 y were referred for ^{177}Lu -PSMA-617 therapy at Dana-Farber Cancer Institute. Cognizant of potential access issues, once ^{177}Lu -PSMA-617 was Food and Drug Administration-approved, we developed a standard operating process as the only gateway to receiving therapy. This involved practitioners ordering ^{68}Ga -PSMA-11 PET/CT and noting on the requisition that the patient was being considered for ^{177}Lu -PSMA-617. Once the PSMA PET/CT was performed, cases were reviewed at a weekly multidisciplinary tumor board (TB) meeting with representation from the Genitourinary Medical Oncology Department and the Nuclear Medicine Department. The median duration between PSMA PET/CT and TB review was 11 d (interquartile range, 6–20 d). Of the cohort, 127 (88%) were approved for therapy, 10 (7%) were deferred, and 8 (6%) were declined for reasons such as no prior chemotherapy, lack of PSMA-avid disease, poor performance status, or poor organ function. All approved patients had received a prior taxane and a novel androgen receptor-directed agent. As of October 31, 2022, 52 patients (41% of those approved) had received at least 1 cycle of ^{177}Lu -PSMA-617. The median duration between TB review and cycle 1 was 59 d (range, 32–129 d), with the median delay increasing from 41 d in May 2022 to 96 d in October 2022. Due to the delay, 45 patients (35%) continued existing therapy or started a new line of therapy between baseline PSMA PET/CT and cycle 1

of ^{177}Lu -PSMA-617. Six patients (5%) died before receiving ^{177}Lu -PSMA-617.

Our experiences highlight several issues. First, establishing a referral process for ^{177}Lu -PSMA-617, including a multidisciplinary TB, has been key in managing volume and coordinating care. TBs facilitate open dialog for selecting patients for therapy on the basis of PSMA PET/CT imaging and clinical judgment at the individual-patient level about the broader therapeutic options available at the specific point in the disease.

Second, supply issues, currently causing more than a 3-mo delay in ^{177}Lu -PSMA-617 administration, have had a notable impact, with 5% of patients dying while waiting for treatment. These delays have led to delivery of bridging therapy (chemotherapy, novel androgen receptor-directed agents, radiotherapy), which dilutes the impact of ^{177}Lu -PSMA-617 as a theranostic agent and increases toxicity risks. Since decisions on proceeding with ^{177}Lu -PSMA-617 therapy are being based on PSMA PET/CT performed 3–4 mo beforehand, and with patients receiving bridging therapies, it is likely that disease differs in terms of extent of PSMA-negative disease, visceral metastases, or other poor-prognosis factors between the time of PSMA PET/CT and ^{177}Lu -PSMA-617 administration. This also impacts how disease is followed radiographically during therapy, especially if PSMA PET/CT is used to monitor therapy response.

Finally, these issues serve as a reminder about selecting patients for ^{177}Lu -PSMA-617. The fact that a patient has PSMA-avid disease (as >90% of patients with mCRPC will, per the VISION trial criteria) (2) should not automatically mean that ^{177}Lu -PSMA-617 treatment is indicated. At our center, we treat patients per the Food and Drug Administration label and VISION population, with no exceptions for patients who have not had both prior chemotherapy and novel androgen receptor-axis inhibitor treatment. Additionally, for those with limited PSMA-avid disease, we consider metastasis-directed therapy given encouraging results from prospective trials in hormone-sensitive prostate cancer (3–5) and retrospective data suggesting utility in mCRPC (6). Furthermore, second-line chemotherapy (cabazitaxel) is a valid option in patients who have received prior docetaxel, with the THERA-P trial showing similar overall survival between ^{177}Lu -PSMA-617 and cabazitaxel in the post-docetaxel setting (7,8). There are prognostic nomograms available that may help select patients (9). However, unfortunately, those least likely to benefit from ^{177}Lu -PSMA-617 are often those in most need of a new line of therapy (i.e., heavily pretreated, visceral disease, poorer organ function).

Received Nov. 14, 2022; revision accepted Jan. 4, 2023.

For correspondence or reprints, contact Praful Ravi (praful_ravi@dfci.harvard.edu).

Published online Jan. 26, 2023.

COPYRIGHT © 2023 by the Society of Nuclear Medicine and Molecular Imaging. DOI: 10.2967/jnumed.122.265194

While radiopharmaceutical therapy is not new to prostate cancer (^{223}Ra is used in bone-predominant mCRPC (10)), and though the wider acceptance and use of theranostics is promising, the clinical roll-out of ^{177}Lu -PSMA-617 has posed unique challenges due to the need for selection by PSMA PET/CT, supply shortages of drug, and the time between imaging and treatment administration. We believe that close collaboration between medical oncology and nuclear medicine, multidisciplinary TBs, and careful patient selection can address these challenges through streamlined processes, which will be necessary as the demands for treatment are likely to increase pending data from trials evaluating ^{177}Lu -PSMA-617 in earlier settings of prostate cancer disease (PSMAddition, NCT04720157; PSMAfore, NCT04689828).

DISCLOSURE

No potential conflict of interest relevant to this article was reported.

REFERENCES

1. FDA approves Pluvicto for metastatic castration-resistant prostate cancer. FDA website. <https://www.fda.gov/drugs/resources-information-approved-drugs/fda-approves-pluvicto-metastatic-castration-resistant-prostate-cancer>. Published March 23, 2022. Accessed January 9, 2023.
2. Sartor O, de Bono J, Chi KN, et al. Lutetium-177-PSMA-617 for metastatic castration-resistant prostate cancer. *N Engl J Med*. 2021;385:1091–1103.
3. Ost P, Reynders D, Decaestecker K, et al. Surveillance or metastasis-directed therapy for oligometastatic prostate cancer recurrence: a prospective, randomized, multicenter phase II trial. *J Clin Oncol*. 2018;36:446–453.
4. Phillips R, Shi WY, Deek M, et al. Outcomes of observation vs stereotactic ablative radiation for oligometastatic prostate cancer: the ORIOLE phase 2 randomized clinical trial. *JAMA Oncol*. 2020;6:650–659.
5. Hölscher T, Baumann M, Kotzerke J, et al. Toxicity and efficacy of local ablative, image-guided radiotherapy in gallium-68 prostate-specific membrane antigen targeted positron emission tomography-staged, castration-sensitive oligometastatic prostate cancer: the OLI-P phase 2 clinical trial. *Eur Urol Oncol*. 2022;5:44–51.
6. Brennan V, Spektor A, Sweeney C, et al. Evaluating the role of stereotactic body radiation therapy with respect to androgen receptor signaling inhibitors for oligometastatic prostate cancer. *Adv Radiat Oncol*. 2021;7:100808.
7. Hofman MS, Emmett L, Sandhu S, et al. [^{177}Lu]Lu-PSMA-617 versus cabazitaxel in patients with metastatic castration-resistant prostate cancer (TheraP): a randomised, open-label, phase 2 trial. *Lancet*. 2021;397:797–804.
8. Hofman MS, Emmett L, Sandhu S, et al. TheraP: ^{177}Lu -PSMA-617 (LuPSMA) versus cabazitaxel in metastatic castration-resistant prostate cancer (mCRPC) progressing after docetaxel—overall survival after median follow-up of 3 years (ANZUP 1603) [abstract]. *J Clin Oncol*. 2022;40(suppl):5000.
9. Gafita A, Calais J, Grogan TR, et al. Nomograms to predict outcomes after ^{177}Lu -PSMA therapy in men with metastatic castration-resistant prostate cancer: an international, multicentre, retrospective study. *Lancet Oncol*. 2021;22:1115–1125.
10. Parker C, Nilsson S, Heinrich D, et al. Alpha emitter radium-223 and survival in metastatic prostate cancer. *N Engl J Med*. 2013;369:213–223.

Summary: Appropriate Use Criteria for Estrogen Receptor–Targeted PET Imaging with 16α - ^{18}F -Fluoro- 17β -Fluoroestradiol

Gary A. Ulaner¹, David A. Mankoff², Amy S. Clark³, Amy M. Fowler⁴, Hannah M. Linden⁵, Lanell M. Peterson⁶, Farrokh Dehdashti⁷, Brenda F. Kurland, Joanne Mortimer⁸, Jason Mouabbi⁹, Dae Hyuk Moon¹⁰, and Elisabeth G.E. de Vries¹¹

¹Molecular Imaging and Therapy, Hoag Family Cancer Institute, Newport Beach, California; ²Department of Radiology, University of Pennsylvania, Philadelphia, Pennsylvania; ³Department of Medical Oncology, University of Pennsylvania, Philadelphia, Pennsylvania; ⁴Department of Radiology, University of Wisconsin–Madison, Madison, Wisconsin; ⁵Department of Medical Oncology, University of Washington, Seattle, Washington; ⁶Department of Nuclear Medicine, University of Washington, Seattle, Washington; ⁷Department of Radiology, Washington University of St. Louis, St. Louis, Missouri; ⁸Department of Medical Oncology, City of Hope, Duarte, California; ⁹Department of Medical Oncology, University of Texas M.D. Anderson Cancer Center, Houston, Texas; ¹⁰Department of Nuclear Medicine, Asan Medical Center, University of Ulsan College of Medicine, Seoul, South Korea; and ¹¹Department of Medical Oncology, University Medical Center Groningen, University of Groningen, Groningen, The Netherlands

PET imaging with 16α - ^{18}F -fluoro- 17β -fluoroestradiol (^{18}F -FES), a radiolabeled form of estradiol, allows whole-body, noninvasive evaluation of estrogen receptor (ER). ^{18}F -FES is approved by the U.S. Food and Drug Administration as a diagnostic agent “for the detection of ER-positive lesions as an adjunct to biopsy in patients with recurrent or metastatic breast cancer.” The Society of Nuclear Medicine and Molecular Imaging (SNMMI) convened an expert work group to comprehensively review the published literature for ^{18}F -FES PET in patients with ER-positive breast cancer and to establish appropriate use criteria (AUC). The findings and discussions of the SNMMI ^{18}F -FES work group, including example clinical scenarios, were published in full in 2022 and are available at <https://www.snmmi.org/auc>. Of the clinical scenarios evaluated, the work group concluded that the most appropriate uses of ^{18}F -FES PET are to assess ER functionality when endocrine therapy is considered either at initial diagnosis of metastatic breast cancer or after progression of disease on endocrine therapy, the ER status of lesions that are difficult or dangerous to biopsy, and the ER status of lesions when other tests are inconclusive. These AUC are intended to enable appropriate clinical use of ^{18}F -FES PET, more efficient approval of FES use by payers, and promotion of investigation into areas requiring further research. This summary includes the rationale, methodology, and main findings of the work group and refers the reader to the complete AUC document.

Key Words: 16α - ^{18}F -fluoro- 17β -fluoroestradiol; appropriate use criteria; estrogen receptor–targeted PET imaging

J Nucl Med 2023; 64:351–354
DOI: 10.2967/jnumed.123.265420

Estrogen receptor (ER) status is currently routinely determined by immunohistochemistry of tissue samples (1). However, biopsy

is invasive, and the lesion may be in a location that is difficult to biopsy (2). Because ER expression may vary spatially and temporally, the results obtained from a tissue sample may incompletely represent a patient’s ER receptor distribution (2–9). Moreover, not all tumors that are ER-positive by immunohistochemistry respond to ER-targeted therapy (10,11). Alternative methods for evaluation of ER status are needed.

16α - ^{18}F -fluoro- 17β -fluoroestradiol (^{18}F -FES) is a radiolabeled form of estrogen that binds to ER. PET imaging with ^{18}F -FES allows noninvasive identification of functional ER distribution (10,11). ^{18}F -FES uptake measured by PET correlates with ER immunohistochemistry (7,12–17), successfully demonstrates ER heterogeneity within individual patients (4–6,18,19), serves as a prognostic biomarker (9,19–21), provides high diagnostic accuracy for detection of ER-positive metastases (2,7,10,15,17,22–24), and can assess the efficacy of ER blockade (25–28).

The Society of Nuclear Medicine and Molecular Imaging (SNMMI) in 2021 convened an ^{18}F -FES PET appropriate use criteria (AUC) work group made up of a multidisciplinary panel of health-care providers and researchers with substantive knowledge of breast cancer and breast cancer imaging. In addition to SNMMI members, representatives from the American College of Nuclear Medicine, the Korean Society of Nuclear Medicine, and the Lobular Breast Cancer Society were included in the work group. The purpose of these AUC is to provide expert opinion on clinical scenarios in which ^{18}F -FES PET will have an impact on management of patients with ER-positive breast cancer. The complete “Appropriate Use Criteria for Estrogen Receptor-Targeted PET Imaging with 16α - ^{18}F -Fluoro- 17β -Fluoroestradiol,” with extensive reference documentation and other supporting material, is freely available on the SNMMI website at www.snmmi.org/auc.

METHODOLOGY

AUC Development

The work group identified 14 clinical scenarios for patients with ER-positive breast cancer for which physicians may want guidance on whether ^{18}F -FES PET would be considered appropriate.

Received Jan. 6, 2023; accepted Jan. 6, 2023.
For correspondence or reprints, contact Gary Ulaner (gary.ulaner@hoag.org).
COPYRIGHT © 2023 by the Society of Nuclear Medicine and Molecular Imaging.

The work group then conducted a systematic review of evidence related to these scenarios and determined an appropriateness score for each scenario using a modified Delphi process (29).

The protocol for this guideline was reviewed and approved by the SNMMI guidance oversight committee and the U.S. Food and Drug Administration. The PubMed, MEDLINE, Embase, Web of Science, and Cochrane Collaboration Library electronic databases were searched for evidence that reported on outcomes of interest, with updates in the literature through June 2022.

After a complex consensus-based rating process as outlined in the complete AUC, final appropriate use scores were summarized for each clinical scenario as “appropriate,” “may be appropriate,” or “rarely appropriate” on a scale from 1 to 9 (Table 1). The work group emphasized that ¹⁸F-FES PET is a unique imaging test that is independent from other clinically available radiotracers, such as ¹⁸F-FDG PET.

Clinical Scenarios

The complete AUC document provides the evidence and data limitations for each of the 14 clinical scenarios. Summarized here is the evidence for 4 clinical scenarios for which the work group determined ¹⁸F-FES PET as “appropriate” and 1 scenario deemed “may be appropriate” with substantial current investigation.

Clinical Scenario 8: Assessing ER Status in Lesions That Are Difficult to Biopsy or When Biopsy Is Nondiagnostic (Score: 8—Appropriate). The work group regarded the use of ¹⁸F-FES PET as appropriate to assess ER status when the lesions are difficult to biopsy. Published examples on the use of ¹⁸F-FES PET for this clinical indication are available (2). Lesions may be in locations that make biopsy difficult or impose substantial risk. Examples include brain lesions, spinal lesions deep to the spinal cord, or lesions adjacent to major vascular structures. In these cases, the high correlation of ¹⁸F-FES PET with ER immunohistochemistry (2,7,10,24) may favor noninvasive imaging over the risks of biopsy.

TABLE 1
Clinical Scenarios for ER-Targeted PET with ¹⁸F-FES

Scenario number	Description	Appropriateness	Score*
Diagnosis			
1	Diagnosing primary breast cancer	Rarely appropriate	2
2	Diagnosing malignancy of unknown primary when biopsy is not feasible or is nondiagnostic	May be appropriate	5
Staging			
3	Routine staging of primary tumor (T staging)	Rarely appropriate	1
4	Routine staging of axillary nodes	Rarely appropriate	3
5	Routine staging of extraaxillary nodes and distant metastases	May be appropriate	5
6	Staging ILC and low-grade IDC	May be appropriate	5
Biopsy			
7	Assessing ER status, in lieu of biopsy, in lesions that are easily accessible for biopsy	May be appropriate	5
8	Assessing ER status in lesions that are difficult to biopsy or when biopsy is nondiagnostic	Appropriate	8
Selection of therapy			
9	After progression of metastatic disease, for considering second line of endocrine therapy	Appropriate	8
10	At initial diagnosis of metastatic disease, for considering endocrine therapy	Appropriate	8
11	At initial diagnosis of primary breast cancer, for considering endocrine therapy	Rarely appropriate	1
Other			
12	Measuring response to therapy	Rarely appropriate	1
13	Detecting lesions in patients with suspected/known recurrent or metastatic breast cancer	May be appropriate	5
14	Detecting ER status when other imaging tests are equivocal or suggestive	Appropriate	8

*Work group scored each clinical scenario on scale from 1 to 9: scores of 7–9 indicate that procedure is appropriate for specific scenario and is generally considered acceptable; scores of 4–6 indicate that procedure may be appropriate for specific scenario and may imply that more evidence is needed to definitively classify scenario; and scores of 1–3 indicate that procedure is rarely appropriate for specific clinical scenario and is generally not considered acceptable. Division of scores into 3 general levels of appropriateness is partially arbitrary, and numeric designations should be viewed as continuum. ER = estrogen receptor; IDC = invasive ductal carcinoma; ILC = invasive lobular carcinoma.

Clinical Scenario 9: After Progression of Metastatic Disease, for Considering Second Line of Endocrine Therapy (Score: 8—Appropriate) and Clinical Scenario 10: At Initial Diagnosis of Metastatic Disease, for Considering Endocrine Therapy (Score: 8—Appropriate). There are several endocrine axis therapies for patients with breast cancer. These therapies act by decreasing available estrogens, degrading ER, blocking estrogen binding to ER, or decreasing downstream effects of ER signaling (30). The presence of ER by immunohistochemistry may not be the optimal predictive biomarker for the success of endocrine axis therapies. Patients with recurrent or metastatic ER-positive breast cancer may develop endocrine resistance despite remaining ER-positive on immunohistochemistry (31). Several investigators have studied ¹⁸F-FES PET as a potentially superior predictive biomarker for determining whether patients with breast cancer will be successfully treated by endocrine axis therapies. To date, at least 17 prospective trials have demonstrated ¹⁸F-FES PET to be successful in this role (19–21,25,26,32–43), as reviewed by Ulaner (44). These trials represent 547 subjects with ER-positive breast cancer undergoing endocrine axis therapies ranging from the earlier agents, such as tamoxifen, to the more recent introduction of aromatase inhibitors and inhibitors of cyclin-dependent kinases 4 and 6. The work group stated that this body of evidence provided strong support for the use of ¹⁸F-FES PET to assist with treatment selection for patients with metastatic ER-positive breast cancer considering endocrine axis therapies. Given that more than 100,000 patients live with ER-positive metastatic breast cancer (45), the use of ¹⁸F-FES PET for this clinical scenario has the potential to prevent large numbers of patients from receiving ineffective courses of endocrine therapies, to save time, and to reduce unnecessary side effects and the costs of ineffective treatments.

Clinical Scenario 14: Detecting ER Status When Other Imaging Tests Are Equivocal or Suggestive (Score: 8—Appropriate). It is not uncommon for imaging studies to be inconclusive or equivocal. Several studies have evaluated the ability of ¹⁸F-FES PET to solve clinical dilemmas when findings on other imaging modalities were equivocal or inconclusive (46–49). These 4 studies include ¹⁸F-FES PET scans on 181 patients with breast cancer, with more than half of ¹⁸F-FES PET scans leading to alterations in patient treatment based on knowledge gained from ¹⁸F-FES PET. The work group was unanimous that ¹⁸F-FES was appropriate for patients with an ER-positive breast cancer and equivocal prior imaging studies, if assessment of ER status by ¹⁸F-FES could change patient management.

Clinical Scenario 6: Staging Invasive Lobular Carcinoma (ILC) and Low-Grade Invasive Ductal Carcinoma (IDC) (Score: 5—May Be Appropriate). ILC is a disease distinct from the more common IDC, with unique genetic, molecular, and pathologic features (50). Interpretation of breast cancer imaging is influenced by tumor histology. For example, primary ILC is more difficult to detect than IDC on mammography, ultrasound, MRI, and ¹⁸F-FDG PET (51,52). Low-grade IDC and ILC malignancies are more likely to display metastases with lower ¹⁸F-FDG avidity (52–54). ¹⁸F-FDG PET/CT has lower rates of detecting distant metastases in ILC than in IDC (55). Because low-grade IDC and ILC are nearly always ER-positive (50,56), investigators have suggested that ER-targeted imaging may be of value for patients with these malignancies, particularly when disease is not appreciable on ¹⁸F-FDG PET. A head-to-head comparison of patients with metastatic ILC lesions found more than twice as many ¹⁸F-FES-avid lesions as ¹⁸F-FDG-avid lesions in patients who underwent

both scans (57). The work group believes this is an area in which larger prospective trials are needed.

SUMMARY

¹⁸F-FES is a radiolabeled form of estrogen that binds to ER. PET imaging with ¹⁸F-FES allows noninvasive and whole-body evaluation of ER that is functional for binding. The full AUC document described in this summary represents the expert opinions of a work group convened by the SNMMI to evaluate clinical scenarios for use of ¹⁸F-FES PET in patients with ER-positive breast cancer, based on a comprehensive review of the published literature. The work group concluded that the most appropriate uses of ¹⁸F-FES PET are for scenarios in which clinicians are considering endocrine therapy, either after progression on a prior line of endocrine therapy or at initial diagnosis of metastatic disease; for assessing the ER status of lesions that are difficult or dangerous to biopsy; and for determining the ER status of lesions when other imaging tests have inconclusive results. The complete findings and discussions of the SNMMI ¹⁸F-FES work group are available at <https://www.snmmi.org/auc>.

REFERENCES

- Allison KH, Hammond MEH, Dowsett M, et al. Estrogen and progesterone receptor testing in breast cancer: ASCO/CAP guideline update. *J Clin Oncol*. 2020;38:1346–1366.
- Kurland BF, Wiggins JR, Coche A, et al. Whole-body characterization of estrogen receptor status in metastatic breast cancer with 16 α -¹⁸F-fluoro-17 β -estradiol positron emission tomography: meta-analysis and recommendations for integration into clinical applications. *Oncologist*. 2020;25:835–844.
- Kurland BF, Peterson LM, Lee JH, et al. Between-patient and within-patient (site-to-site) variability in estrogen receptor binding, measured in vivo by ¹⁸F-fluoroestradiol PET. *J Nucl Med*. 2011;52:1541–1549.
- Yang Z, Sun Y, Xu X, et al. The assessment of estrogen receptor status and its intratumoral heterogeneity in patients with breast cancer by using ¹⁸F-fluoroestradiol PET/CT. *Clin Nucl Med*. 2017;42:421–427.
- Nienhuis HH, van Kruchten M, Elias SG, et al. ¹⁸F-fluoroestradiol tumor uptake is heterogeneous and influenced by site of metastasis in breast cancer patients. *J Nucl Med*. 2018;59:1212–1218.
- Currin E, Peterson LM, Schubert EK, et al. Temporal heterogeneity of estrogen receptor expression in bone-dominant breast cancer: ¹⁸F-fluoroestradiol PET imaging shows return of ER expression. *J Natl Compr Canc Netw*. 2016;14:144–147.
- Chae SY, Ahn SH, Kim SB, et al. Diagnostic accuracy and safety of 16 α -[¹⁸F]fluoro-17 β -oestradiol PET-CT for the assessment of oestrogen receptor status in recurrent or metastatic lesions in patients with breast cancer: a prospective cohort study. *Lancet Oncol*. 2019;20:546–555.
- Lindström LS, Karlsson E, Wilking UM, et al. Clinically used breast cancer markers such as estrogen receptor, progesterone receptor, and human epidermal growth factor receptor 2 are unstable throughout tumor progression. *J Clin Oncol*. 2012;30:2601–2608.
- Bottoni G, Piccardo A, Fiz F, et al. Heterogeneity of bone metastases as an important prognostic factor in patients affected by oestrogen receptor-positive breast cancer. The role of combined [¹⁸F]fluoroestradiol PET/CT and [¹⁸F]fluoro-deoxyglucose PET/CT. *Eur J Radiol*. 2021;141:109821.
- van Kruchten M, de Vries EGE, Brown M, et al. PET imaging of oestrogen receptors in patients with breast cancer. *Lancet Oncol*. 2013;14:e465–e475.
- Katzenellenbogen JA. The quest for improving the management of breast cancer by functional imaging: the discovery and development of 16 α -[¹⁸F]fluoroestradiol (FES), a PET radiotracer for the estrogen receptor, a historical review. *Nucl Med Biol*. 2021;92:24–37.
- Mintun MA, Welch MJ, Siegel BA, et al. Breast cancer: PET imaging of estrogen receptors. *Radiology*. 1988;169:45–48.
- McGuire AH, Dehdashti F, Siegel BA, et al. Positron tomographic assessment of 16 α -[¹⁸F] fluoro-17 β -estradiol uptake in metastatic breast carcinoma. *J Nucl Med*. 1991;32:1526–1531.
- Peterson LM, Mankoff DA, Lawton T, et al. Quantitative imaging of estrogen receptor expression in breast cancer with PET and ¹⁸F-fluoroestradiol. *J Nucl Med*. 2008;49:367–374.

15. Seenu V, Sharma A, Kumar R, et al. Evaluation of estrogen expression of breast cancer using ^{18}F -FES PET CT: a novel technique. *World J Nucl Med.* 2020;19:233–239.
16. Takahashi M, Maeda H, Tsujikawa T, et al. ^{18}F -fluoroestradiol tumor uptake is influenced by structural components in breast cancer. *Clin Nucl Med.* 2021;46:884–889.
17. Venema CM, Mammatas LH, Schröder CP, et al. Androgen and estrogen receptor imaging in metastatic breast cancer patients as a surrogate for tissue biopsies. *J Nucl Med.* 2017;58:1906–1912.
18. Yang Z, Sun Y, Xue J, et al. Can positron emission tomography/computed tomography with the dual tracers fluorine-18 fluoroestradiol and fluorodeoxyglucose predict neoadjuvant chemotherapy response of breast cancer?—A pilot study. *PLoS One.* 2013;8:e78192.
19. Kurland BF, Peterson LM, Lee JH, et al. Estrogen receptor binding (^{18}F -FES PET) and glycolytic activity (^{18}F -FDG PET) predict progression-free survival on endocrine therapy in patients with ER+ breast cancer. *Clin Cancer Res.* 2017;23:407–415.
20. Liu C, Xu X, Yuan H, et al. Dual tracers of $^{16}\alpha$ - ^{18}F fluoro-17 β -estradiol and ^{18}F fluorodeoxyglucose for prediction of progression-free survival after fulvestrant therapy in patients with HR+/HER2- metastatic breast cancer. *Front Oncol.* 2020;10:580277.
21. He M, Liu C, Shi Q, et al. The predictive value of early changes in ^{18}F -fluoroestradiol positron emission tomography/computed tomography during fulvestrant 500 mg therapy in patients with estrogen receptor-positive metastatic breast cancer. *Oncologist.* 2020;25:927–936.
22. Evangelista L, Guameri V, Conte PF. ^{18}F -fluoroestradiol positron emission tomography in breast cancer patients: systematic review of the literature & meta-analysis. *Curr Radiopharm.* 2016;9:244–257.
23. Mo JA. Safety and effectiveness of F-18 fluoroestradiol positron emission tomography/computed tomography: a systematic review and meta-analysis. *J Korean Med Sci.* 2021;36:e271.
24. van Geel JLL, Boers J, Elias SG, et al. Clinical validity of $^{16}\alpha$ - ^{18}F fluoro-17 β -estradiol positron emission tomography/computed tomography to assess estrogen receptor status in newly diagnosed metastatic breast cancer. *J Clin Oncol.* 2022;40:3642–3652.
25. Linden HM, Kurland BF, Peterson LM, et al. Fluoroestradiol positron emission tomography reveals differences in pharmacodynamics of aromatase inhibitors, tamoxifen, and fulvestrant in patients with metastatic breast cancer. *Clin Cancer Res.* 2011;17:4799–4805.
26. van Kruchten M, de Vries EG, Glaudemans AW, et al. Measuring residual estrogen receptor availability during fulvestrant therapy in patients with metastatic breast cancer. *Cancer Discov.* 2015;5:72–81.
27. Wang Y, Ayres KL, Goldman DA, et al. ^{18}F -fluoroestradiol PET/CT measurement of estrogen receptor suppression during a phase I trial of the novel estrogen receptor-targeted therapeutic GDC-0810: using an imaging biomarker to guide drug dosage in subsequent trials. *Clin Cancer Res.* 2017;23:3053–3060.
28. Bardia A, Chandralapaty S, Linden HM, et al. AMEERA-1 phase 1/2 study of amcenestrant, SAR439859, in postmenopausal women with ER-positive/HER2-negative advanced breast cancer. *Nat Commun.* 2022;13:4116.
29. Niederberger M, Spranger J. Delphi technique in health sciences: a map. *Front Public Health.* 2020;8:457.
30. Eggersmann TK, Degenhardt T, Gluz O, Wuerstlein R, Harbeck N. CDK4/6 inhibitors expand the therapeutic options in breast cancer: palbociclib, ribociclib and abemaciclib. *BioDrugs.* 2019;33:125–135.
31. Hoefnagel LD, van de Vijver MJ, van Slooten HJ, et al. Receptor conversion in distant breast cancer metastases. *Breast Cancer Res.* 2010;12:R75.
32. Mortimer JE, Dehdashti F, Siegel BA, Katzenellenbogen JA, Fracasso P, Welch MJ. Positron emission tomography with 2- ^{18}F fluoro-2-deoxy-D-glucose and $^{16}\alpha$ - ^{18}F fluoro-17 β -estradiol in breast cancer: correlation with estrogen receptor status and response to systemic therapy. *Clin Cancer Res.* 1996;2:933–939.
33. Dehdashti F, Flanagan FL, Mortimer JE, Katzenellenbogen JA, Welch MJ, Siegel BA. Positron emission tomographic assessment of “metabolic flare” to predict response of metastatic breast cancer to antiestrogen therapy. *Eur J Nucl Med.* 1999;26:51–56.
34. Mortimer JE, Dehdashti F, Siegel BA, Trinkaus K, Katzenellenbogen JA, Welch MJ. Metabolic flare: indicator of hormone responsiveness in advanced breast cancer. *J Clin Oncol.* 2001;19:2797–2803.
35. Linden HM, Stekhova SA, Link JM, et al. Quantitative fluoroestradiol positron emission tomography imaging predicts response to endocrine treatment in breast cancer. *J Clin Oncol.* 2006;24:2793–2799.
36. Dehdashti F, Mortimer JE, Trinkaus K, et al. PET-based estradiol challenge as a predictive biomarker of response to endocrine therapy in women with estrogen-receptor-positive breast cancer. *Breast Cancer Res Treat.* 2009;113:509–517.
37. Peterson LM, Kurland BF, Schubert EK, et al. A phase 2 study of $^{16}\alpha$ - ^{18}F fluoro-17 β -estradiol positron emission tomography (FES-PET) as a marker of hormone sensitivity in metastatic breast cancer (MBC). *Mol Imaging Biol.* 2014;16:431–440.
38. van Kruchten M, Glaudemans A, de Vries EFJ, Schroder CP, de Vries EGE, Hospers GAP. Positron emission tomography of tumour [^{18}F]fluoroestradiol uptake in patients with acquired hormone-resistant metastatic breast cancer prior to oestradiol therapy. *Eur J Nucl Med Mol Imaging.* 2015;42:1674–1681.
39. Park JH, Kang MJ, Ahn JH, et al. Phase II trial of neoadjuvant letrozole and lapatinib in Asian postmenopausal women with estrogen receptor (ER) and human epidermal growth factor receptor 2 (HER2)-positive breast cancer [Neo-ALL-IN]: highlighting the TILs, ER expressional change after neoadjuvant treatment, and FES-PET as potential significant biomarkers. *Cancer Chemother Pharmacol.* 2016;78:685–695.
40. Chae SY, Kim SB, Ahn SH, et al. A randomized feasibility study of ^{18}F -fluoroestradiol PET to predict pathologic response to neoadjuvant therapy in estrogen receptor-rich postmenopausal breast cancer. *J Nucl Med.* 2017;58:563–568.
41. Boers J, Venema CM, de Vries EFJ, et al. Molecular imaging to identify patients with metastatic breast cancer who benefit from endocrine treatment combined with cyclin-dependent kinase inhibition. *Eur J Cancer.* 2020;126:11–20.
42. Peterson LM, Kurland BF, Yan F, et al. ^{18}F -fluoroestradiol PET imaging in a phase II trial of vorinostat to restore endocrine sensitivity in ER+/HER2- metastatic breast cancer. *J Nucl Med.* 2021;62:184–190.
43. Su Y, Zhang Y, Hua X, et al. High-dose tamoxifen in high-hormone-receptor-expressing advanced breast cancer patients: a phase II pilot study. *Ther Adv Med Oncol.* 2021;13:1758835921993436.
44. Ulaner GA. $^{16}\alpha$ - ^{18}F -fluoro-17 β -fluoroestradiol (FES): clinical applications for patients with breast cancer. *Semin Nucl Med.* 2022;52:574–583.
45. Mariotto AB, Etzioni R, Hurlbert M, Penberthy L, Mayer M. Estimation of the number of women living with metastatic breast cancer in the United States. *Cancer Epidemiol Biomarkers Prev.* 2017;26:809–815.
46. van Kruchten M, Glaudemans AW, de Vries EF, et al. PET imaging of estrogen receptors as a diagnostic tool for breast cancer patients presenting with a clinical dilemma. *J Nucl Med.* 2012;53:182–190.
47. Sun Y, Yang Z, Zhang Y, et al. The preliminary study of $^{16}\alpha$ - ^{18}F fluoroestradiol PET/CT in assisting the individualized treatment decisions of breast cancer patients. *PLoS One.* 2015;10:e0116341.
48. Yang Z, Xie Y, Liu C, et al. The clinical value of ^{18}F -fluoroestradiol in assisting individualized treatment decision in dual primary malignancies. *Quant Imaging Med Surg.* 2021;11:3956–3965.
49. Boers J, Loudini N, Brunsch CL, et al. Value of ^{18}F -FES PET in solving clinical dilemmas in breast cancer patients: a retrospective study. *J Nucl Med.* 2021;62:1214–1220.
50. Ciriello G, Gatz ML, Beck AH, et al. Comprehensive molecular portraits of invasive lobular breast cancer. *Cell.* 2015;163:506–519.
51. Berg WA, Gutierrez L, NessAiver MS, et al. Diagnostic accuracy of mammography, clinical examination, US, and MR imaging in preoperative assessment of breast cancer. *Radiology.* 2004;233:830–849.
52. Bos R, van Der Hoeven JJ, van Der Wall E, et al. Biologic correlates of ^{18}F fluorodeoxyglucose uptake in human breast cancer measured by positron emission tomography. *J Clin Oncol.* 2002;20:379–387.
53. Ueda S, Tsuda H, Asakawa H, et al. Clinicopathological and prognostic relevance of uptake level using ^{18}F -fluorodeoxyglucose positron emission tomography/computed tomography fusion imaging (^{18}F -FDG PET/CT) in primary breast cancer. *Jpn J Clin Oncol.* 2008;38:250–258.
54. Dashevsky BZ, Goldman DA, Parsons M, et al. Appearance of untreated bone metastases from breast cancer on FDG PET/CT: importance of histologic subtype. *Eur J Nucl Med Mol Imaging.* 2015;42:1666–1673.
55. Hogan MP, Goldman DA, Dashevsky B, et al. Comparison of ^{18}F -FDG PET/CT for systemic staging of newly diagnosed invasive lobular carcinoma versus invasive ductal carcinoma. *J Nucl Med.* 2015;56:1674–1680.
56. Perou CM, Sorlie T, Eisen MB, et al. Molecular portraits of human breast tumours. *Nature.* 2000;406:747–752.
57. Ulaner GA, Jhaveri K, Chandralapaty S, et al. Head-to-head evaluation of ^{18}F -FES and ^{18}F -FDG PET/CT in metastatic invasive lobular breast cancer. *J Nucl Med.* 2021;62:326–331.

Response Monitoring in Metastatic Breast Cancer: A Prospective Study Comparing ¹⁸F-FDG PET/CT with Conventional CT

Marianne Vogsen¹⁻⁵, Frederik Harbo⁶, Nick M. Jakobsen², Henriette J. Nissen², Sara E. Dahlsgaard-Wallenius², Oke Gerke^{2,3}, Jeanette D. Jensen¹, Jon T. Asmussen⁶, Anne Marie B. Jylling^{3,7}, Poul-Erik Braad², Werner Vach⁸, Marianne Ewertz³, and Malene G. Hildebrandt^{2,3,5,9}

¹Department of Oncology, Odense University Hospital, Odense, Denmark; ²Department of Nuclear Medicine, Odense University Hospital, Odense, Denmark; ³Department of Clinical Research, University of Southern Denmark, Odense, Denmark; ⁴Odense Patient Data Explorative Network (OPEN), Odense University Hospital, Odense, Denmark; ⁵Centre for Personalized Response Monitoring in Oncology (PREMIO), Odense University Hospital, Odense, Denmark; ⁶Department of Radiology, Odense University Hospital, Odense, Denmark; ⁷Department of Pathology, Odense University Hospital, Odense, Denmark; ⁸Basel Academy for Quality and Research in Medicine, Basel, Switzerland; and ⁹Centre for Innovative Medical Technology, Odense University Hospital, Odense, Denmark

This study aimed to compare contrast-enhanced CT (CE-CT) and ¹⁸F-FDG PET/CT for response monitoring in metastatic breast cancer using the standardized response evaluation criteria RECIST 1.1 and PERCIST. The objective was to examine whether progressive disease was detected systematically earlier by one of the modalities. **Methods:** Women with biopsy-verified metastatic breast cancer were enrolled prospectively and monitored using combined CE-CT and ¹⁸F-FDG PET/CT every 9–12 wk to evaluate response to first-line treatment. CE-CT scans and RECIST 1.1 were used for clinical decision-making without accessing the ¹⁸F-FDG PET/CT scans. At study completion, ¹⁸F-FDG PET/CT scans were unmasked and assessed according to PERCIST. Visual assessment was used if response criteria could not be applied. The modality-specific time to progression was defined as the time from the baseline scan until the first scan demonstrating progression. Paired comparative analyses for CE-CT versus ¹⁸F-FDG PET/CT were applied, and the primary endpoint was earlier detection of progression by one modality. Secondary endpoints were time to detection of progression, response categorization, visualization of changes in response over time, and measurable disease according to RECIST and PERCIST. **Results:** In total, 87 women were evaluable, with a median of 6 (1–11) follow-up scans. Progression was detected first by ¹⁸F-FDG PET/CT in 43 (49.4%) of 87 patients and first by CE-CT in 1 (1.15%) of 87 patients ($P < 0.0001$). Excluding patients without progression ($n = 32$), progression was seen first on ¹⁸F-FDG PET/CT in 78.2% (43/55) of patients. The median time from detection of progression by ¹⁸F-FDG PET/CT to that of CE-CT was 6 mo (95% CI, 4.3–6.4 mo). At baseline, 76 (87.4%) of 87 patients had measurable disease according to PERCIST and 51 (58.6%) of 87 patients had measurable disease according to RECIST 1.1. Moreover, ¹⁸F-FDG PET/CT provided improved visualization of changes in response over time, as seen in the graphical abstract. **Conclusion:** Disease progression was detected earlier by ¹⁸F-FDG PET/CT than by CE-CT in most patients, with a potentially clinically relevant median 6-mo delay for CE-CT. More patients had measurable disease according to PERCIST than according to RECIST 1.1. The magnitude of the final benefit for patients is a perspective for future research.

Key Words: metastatic breast cancer; response monitoring; ¹⁸F-FDG PET/CT; CE-CT; PERCIST

J Nucl Med 2023; 64:355–361

DOI: 10.2967/jnumed.121.263358

Response monitoring modalities are used to guide clinical decision-making to optimize treatment strategy. However, no specific modalities for monitoring response in metastatic breast cancer (MBC) are recommended by clinical guidelines (1,2), and contrast-enhanced CT (CE-CT) is used widely in clinical practice. RECIST guidelines (RECIST 1.1) (3) are typically required when patients are monitored in clinical trials. However, CE-CT has low sensitivity for bone metastases and low specificity for liver metastases (4–6).

¹⁸F-FDG PET/CT and PERCIST have been suggested to overcome the shortcomings of CE-CT (4,6–8). Changes in metabolic activity may appear before morphologic changes can be seen (4,9), giving ¹⁸F-FDG PET/CT excellent potential to monitor treatment response in bone and liver metastases and detect treatment failure early (4,10,11). Further, more patients may be classified as having measurable disease using ¹⁸F-FDG PET/CT and PERCIST than CE-CT and RECIST 1.1 (6).

Studies have demonstrated that ¹⁸F-FDG PET/CT is promising for measuring and detecting early response in MBC (4,12–14), and its use for monitoring may improve survival for patients with MBC (15). But to our knowledge, no prospective studies have compared CE-CT and RECIST 1.1 with ¹⁸F-FDG PET/CT and PERCIST for longitudinal response monitoring in MBC.

Several treatment options are available for women with MBC, and their priorities concerning survival, quality of life, and toxicity influence shared decision-making (1). A precondition for any clinical decision-making is accurate diagnosis of disease progression. The earlier this can be achieved, the more a patient can benefit from treatment adaptations.

This study compared ¹⁸F-FDG PET/CT and CE-CT for longitudinal response monitoring in women with MBC. The objective was to examine whether progressive disease (PD) was detected systematically earlier by one of the modalities, with the primary endpoint

Received Dec. 20, 2021; revision accepted Sep. 14, 2022.

For correspondence or reprints, contact Marianne Vogsen (marianne.vogsen@rsyd.dk).

Published online Oct. 7, 2022.

COPYRIGHT © 2023 by the Society of Nuclear Medicine and Molecular Imaging.

TABLE 1
Time-Related Detection of Progression by CE-CT and ¹⁸F-FDG PET/CT for 87 Patients

Distribution of progression	n	Difference
Progression seen first on ¹⁸ F-FDG PET/CT	43 (49.4%)	48%; 95% CI, 36%–60%; <i>P</i> < 0.0001
Progression on both modalities, seen first on ¹⁸ F-FDG PET/CT	26 (29.9%)	
Progression on ¹⁸ F-FDG PET/CT only	17 (19.5%)	
Progression seen first on CE-CT	1 (1.15%)	48%; 95% CI, 36%–60%; <i>P</i> < 0.0001
Progression on both modalities, seen first on CE-CT	0 (0.00%)	
Progression on CE-CT only	1 (1.15%)	
Progression on both modalities simultaneously	11 (12.6%)	
No progression on any modality	32 (36.8%)	

being the first detection of progression. Secondary endpoints were comparisons of time until detection of progression, response categorization, measurable disease according to RECIST 1.1 and PERCIST, and visualization of changes in response over time.

MATERIALS AND METHODS

Study Design and Patients

A prospective cohort study compared response assessment using CE-CT and ¹⁸F-FDG PET/CT in MBC patients who served as their

own controls. The institutional review board (the Danish Ethics Committee, S-20170019) approved this study, and all subjects gave written informed consent. The study was registered at ClinicalTrials.gov (NCT03358589) and followed the Declaration of Helsinki. Research Electronic Data Capture (RedCap; Vanderbilt University) and SharePoint (Microsoft) were used for data storage and management, and the results were reported using the Strengthening of Reporting of Observational Studies in Epidemiology guideline (16).

Women were eligible if diagnosed with de novo or recurrent MBC (17) and fit for systemic oncologic treatment. They were excluded if MBC was not biopsy-verified or if they left the study or died before the first follow-up scan.

Data Collection

Patients were included before initiating first-line treatment. They were followed until progression leading to change to second-line treatment, death, loss of follow-up, or the end of trial by November 30, 2020. Hence, in cases of change of oncologic treatment for reasons other than progression (i.e., toxicity or maximum dose of chemotherapy), the patient was still followed as mentioned. Data were derived from medical records, scan images, pathology, and scan reports.

Image Techniques

¹⁸F-FDG PET/CT, including CE-CT imaging from top of skull to mid thigh, was performed 60 ± 5 min after intravenous injection of 4 MBq of ¹⁸F-FDG per kilogram of body weight. Blood sugar levels were measured routinely, and patients fasted at least 4 h before ¹⁸F-FDG injection. All scans were performed according to the European Association of Nuclear Medicine guideline (18).

The PERCIST standardization criteria (8) were registered prospectively and are listed with supplemental image techniques in Supplemental Table 1 (supplemental materials are available at <http://jnm.snmjournals.org>).

Image Interpretation

A diagnostic ¹⁸F-FDG PET combined with CE-CT was performed, with ¹⁸F-FDG PET images available at baseline (19,20). ¹⁸F-FDG PET/CT and CE-CT scans were performed simultaneously for each follow-up scan, but treatment decisions were based on CE-CT with masked ¹⁸F-FDG PET images. Hence, women were monitored with CE-CT using RECIST 1.1 (3) if the disease was measurable at baseline; otherwise, a visual assessment was used based on the radiologist's discretion. One of 2 experienced radiologists made the CE-CT assessments used for clinical decision-making. In cases of uncertainty, consensus on the response category was reached in a multidisciplinary conference.

The response categorization from CE-CT scans used in daily clinical practice was registered for research purposes. Follow-up ¹⁸F-FDG PET/CT scans were unmasked at the end of the trial and assessed by one-lesion PERCIST (8) in patients with measurable disease at baseline

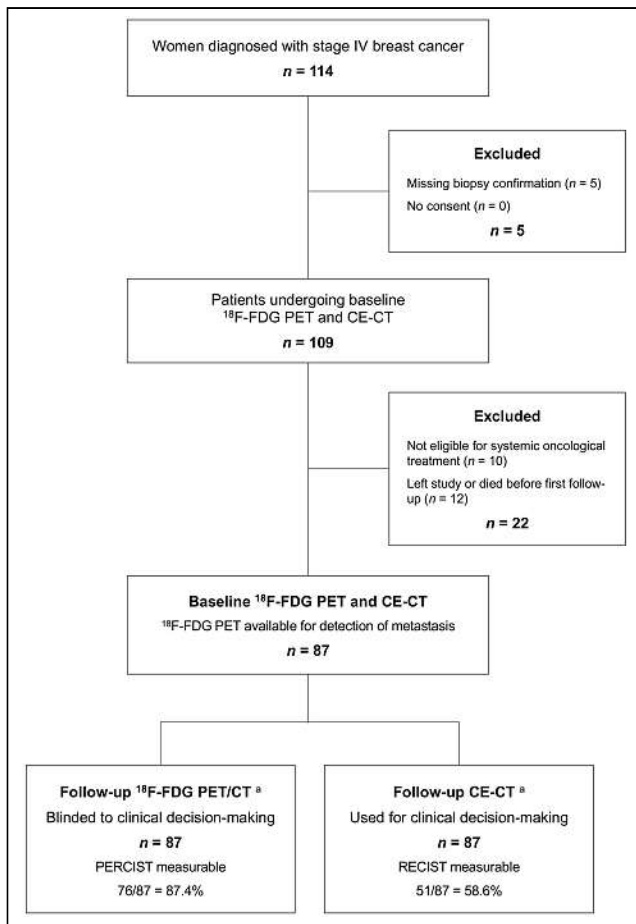


FIGURE 1. Flowchart of 87 women monitored by ¹⁸F-FDG PET/CT and CE-CT during first-line treatment for MBC. ^aCombined ¹⁸F-FDG PET/CT and CE-CT every 9–12 wk. ¹⁸F-FDG PET images not available during study period.

and when follow-up scans were comparable according to PERCIST (Supplemental Table 2). Otherwise, a visual assessment based on the discretion of the nuclear medicine specialist was used. One of 3 nuclear medicine physicians assessed the scans. In cases of uncertainty, consensus was reached between the observer and a senior physician in nuclear medicine. Assessors of ¹⁸F-FDG PET/CT were unaware of the CE-CT scan report and the clinical decision-making. The nadir scan was used as a reference in the PERCIST assessment to allow meaningful comparison with RECIST 1.1 (Supplemental Table 2).

Outcome Measures

The rate of earlier detection by one of the modalities was the primary endpoint. Progression was assigned in cases of new lesions, a 20% increase in the sum lesion diameter (CE-CT), a 30% increase in SUV normalized by lean body mass (SUL_{peak}, ¹⁸F-FDG PET/CT), or unequivocal progression of nontarget lesions (Supplemental Table 2).

The secondary endpoint of modality-specific time until detection of the first progression was defined as the time from baseline until the first scan with an assessment of PD or progressive metabolic disease. In 18 instances (in 13 patients), progression was regarded as false-positive because PD was reported by CE-CT without clinical change of management and the following scan did not reveal further progression (*n* = 9) or because progressive metabolic disease was reported by ¹⁸F-FDG PET/CT without further progression or resolution of ¹⁸F-FDG uptake on the following scan (*n* = 9). A detailed description of these instances is provided in Supplemental Figure 1. They were not counted as progressions in the time-related analyses of detection of progression.

For patients with progression on one modality only, a consistency check was performed by follow-up with medical records in June 2021. Change in treatment because of a clinically or image-guided identified progression or a confirmation on subsequent scans was considered a sign of consistency.

The distribution of patients with measurable disease at baseline and response categories on follow-up scans were registered as secondary endpoints. Changes in treatment response over time were visualized in selected patients.

Statistical Analysis

Descriptive statistics are presented as frequencies and respective percentages. The relative timing of progression was classified by assigning each patient to 1 of the 6 categories shown in Table 1. We report the 2 relative frequencies of ¹⁸F-FDG PET/CT detecting progression first and CE-CT detecting progression first. We estimated the difference between them with a 95% CI and conducted a McNemar test for paired binary data (type I error, 5%, 2-sided).

The modality-specific time until detection of progression for both modalities was visualized by a Kaplan–Meier plot. The significance of the difference between the 2 modalities was analyzed using a shared-frailty model. Censoring was performed at the time point of the last available scan for patients reaching the end of follow-up (November 2020) without progression, loss to follow-up between scans, or death. As the data were paired, this was the same time point for both modalities.

For patients in whom progression was detected earlier by ¹⁸F-FDG PET/CT than by CE-CT, the median time from detection by ¹⁸F-FDG PET/CT until detection by CE-CT was estimated with 95% CI. Results were visualized by a Kaplan–Meier plot, treating loss to follow-up, death, and final study scan as censoring events.

A preplanned interim analysis was conducted but had no impact on further study conduct. It can be seen with the sample size calculation in Supplemental Table 3.

Analyses were performed using Stata/IC 15.0 (StataCorp) and Excel (Microsoft).

TABLE 2
Baseline Characteristics of 87 Patients with MBC

Characteristic	Data
Age at diagnosis of MBC (y)	72.7 (41.1–89.4)
Time from primary breast cancer to MBC (y)	5.13 (0.00–38.1)
MBC diagnosis	
De novo MBC	27 (31.0%)
First distant relapse of MBC	60 (69.0)
ER status*	
Negative, 0%	12 (13.8)
Positive, 1%–100%	75 (86.2)
HER2 status*	
Normal	80 (92.0)
Positive	5 (5.75)
Unknown	2 (2.30)
Molecular subtype*	
ER+/HER2–	71 (81.6)
ER+/HER2 unknown	2 (2.30)
HER2+ (ER±)	5 (5.75)
Triple-negative	9 (10.3)
First-line treatment	
Endocrine therapy [†]	10 (11.5)
Endocrine therapy [†] + cyclin-dependent kinase 4/6 [‡]	60 (69.0)
Chemotherapy [§]	12 (13.8)
Chemotherapy [§] + trastuzumab + pertuzumab	4 (4.60)
Chemotherapy + pembrolizumab	1 (1.15)
Number of metastases	
1	1 (1.15)
2–4	7 (8.05)
≥5	79 (90.8)
Organs involved	
Bone only [¶]	23 (26.4)
Lymph node only	4 (4.60)
Visceral involvement	22 (25.3)
Mixed (not visceral) [#]	38 (43.7)

*Biomarker profile of metastatic lesion or concurrent local recurrence.

[†]Aromatase inhibitor or fulvestrant.

[‡]Palbociclib, ribociclib, or abemaciclib.

[§]Epirubicin, cyclophosphamide, taxanes, carboplatin, gemcitabine, vinorelbine, or capecitabine.

^{||}Combined CE-CT and ¹⁸F-FDG PET/CT assessment.

[¶]Bone-only metastasis ± breast ± axillary lymph nodes.

[#]Mixed bone, lymph node, lung, skin, or other metastases. ER = estrogen receptor; HER2 = human epidermal growth receptor 2. Qualitative data are number and percentage; continuous data are median and range.

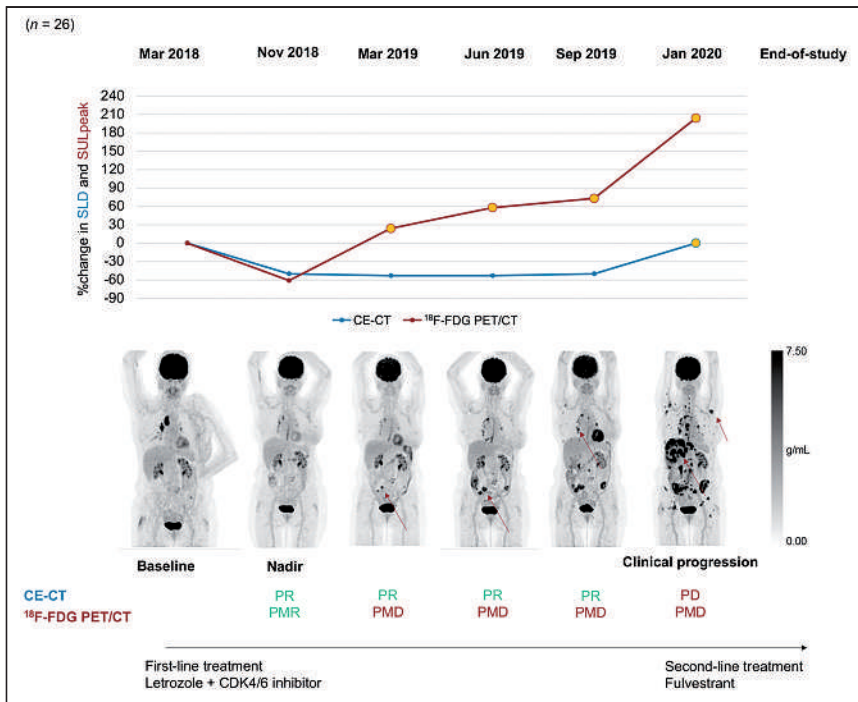


FIGURE 2. Illustration of progression detected by CE-CT and ^{18}F -FDG PET/CT but seen first on ^{18}F -FDG PET/CT. Shown are maximum-intensity projection images and percentage change in sum of diameters for CE-CT and RECIST 1.1 (blue line) and SUL_{peak} for ^{18}F -FDG PET/CT and PERCIST (red line). New lesions are shown as yellow dots. CDK4/6 = cyclin-dependent kinase 4/6; PMD = progressive metabolic disease; PMR = partial metabolic response; PR = partial response; SLD = sum of lesion diameter.

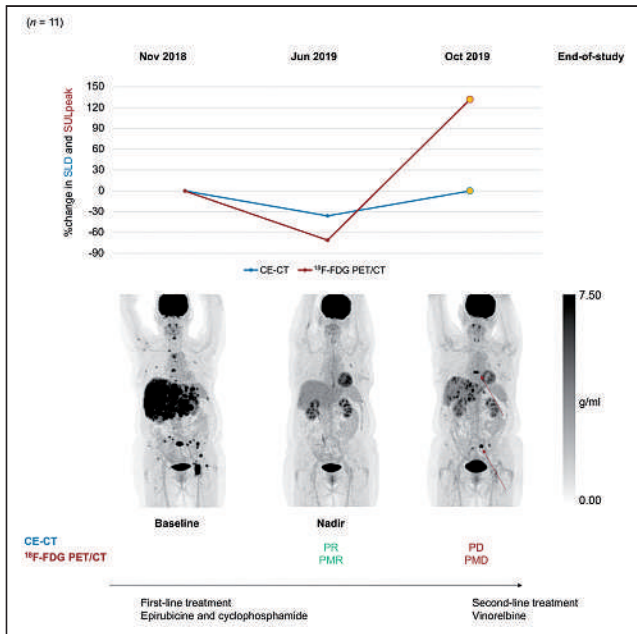


FIGURE 3. Illustration of progression detected by CE-CT and ^{18}F -FDG PET/CT simultaneously. Shown are maximum-intensity projection images and percentage change in sum of diameters for CE-CT and RECIST 1.1 (blue line) and SUL_{peak} for ^{18}F -FDG PET/CT and PERCIST (red line). New lesions are shown as yellow dots. PMD = progressive metabolic disease; PMR = partial metabolic response; PR = partial response; SLD = sum of lesion diameter.

RESULTS

Between September 1, 2017, and August 31, 2019, 114 patients were diagnosed with MBC at Odense University Hospital, Denmark. As seen in Figure 1, 27 patients were excluded. In total, 87 patients had 517 follow-up CE-CT scans performed as part of ^{18}F -FDG PET/CT scans (unaware of ^{18}F -FDG PET). A median of 6 scans (range, 1–11 scans) was performed per patient. The median follow-up time was 15.9 mo (range, 1.94–37.5 mo), 55 patients (63.2%) experienced a progression, and 1 patient died.

Baseline characteristics of included patients appear in Table 2 and Supplemental Table 4. HER2 was overexpressed in 5.75% of patients, and most metastases were estrogen receptor–positive, compatible with most patients (80.5%) receiving endocrine therapy. Bone-only disease was present in 26.4% of patients.

Detection of First Progression

Progression was detected first by ^{18}F -FDG PET/CT in 43 (49.4%) of 87 patients and first by CE-CT in 1 (1.15%) of 87 patients ($P < 0.0001$). Excluding 32 patients with no progression while involved in the study, progression was seen first on ^{18}F -FDG PET/CT in 78.2% (43/55) of patients and by CE-CT in 1.82% (1/55) of patients. Further results on time-related detection of progression for the 2 modalities are seen in

Table 1 and Figures 2–5. Reasons for the first progression were almost equally distributed between the 2 modalities (Table 3).

Among 17 patients for whom progression was detected by ^{18}F -FDG PET/CT only, the consistency check after 7 mo revealed a subsequent change in treatment because of clinically or image-guided progression in 9 patients (52.9%; Fig. 4; Supplemental Fig. 2A). No treatment change had appeared in the remaining 8 patients, but (slow) progression could be confirmed on the subsequent scans (Supplemental Fig. 2B).

The detection of progression by CE-CT without detection by ^{18}F -FDG PET/CT in 1 patient led to a change in management (Fig. 5).

The median time to the detection of first progression was 24.3 mo (95% CI, 15.9 mo to infinity) and 14.9 mo (95% CI, 11.4–20.8 mo) for CE-CT and ^{18}F -FDG PET/CT assessment, respectively. Thus, a statistically significant difference was observed between the 2 modalities ($P < 0.001$; Fig. 6A). The median time from detection of progression by ^{18}F -FDG PET/CT to detection by CE-CT was 5.98 mo (95% CI, 4.27–6.41 mo; Fig. 6B).

Measurable Disease and Response Categories

Measurable disease at baseline was present in 51 (58.6%) and 76 (87.4%) of 87 patients for RECIST 1.1 and PERCIST, respectively. Of 11 patients not being measurable according to PERCIST, 7 patients (63.4%) had invasive lobular carcinomas.

Figure 7 illustrates the distribution of response categories during the study period. Complete metabolic responses and progressive metabolic disease were reported more frequently by ^{18}F -FDG PET/CT, whereas stable disease was reported more often by CE-CT. Progression was detected by visual assessment in 18%

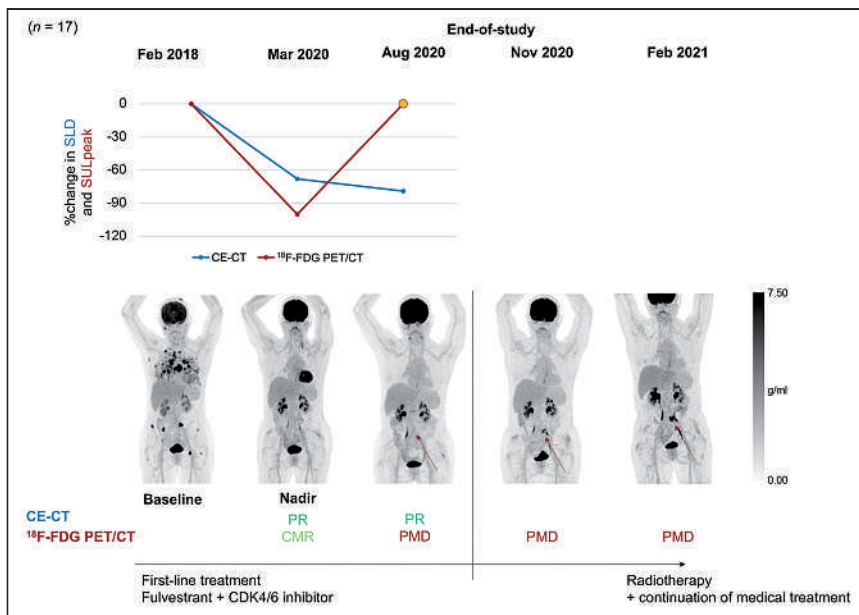


FIGURE 4. Illustration of progression detected by ¹⁸F-FDG PET/CT only. Shown are maximum-intensity projection images and percentage change in sum of diameters for CE-CT and RECIST 1.1 (blue line) and SUL_{peak} for ¹⁸F-FDG PET/CT and PERCIST (red line). New lesions are shown as yellow dots. CDK4/6 = cyclin-dependent kinase 4/6; PMD = progressive metabolic disease; PMR = partial metabolic response; PR = partial response; SLD = sum of lesion diameter.

(24/136) and 45% (21/47) of the total number of progressions detected by ¹⁸F-FDG PET/CT and CE-CT, respectively.

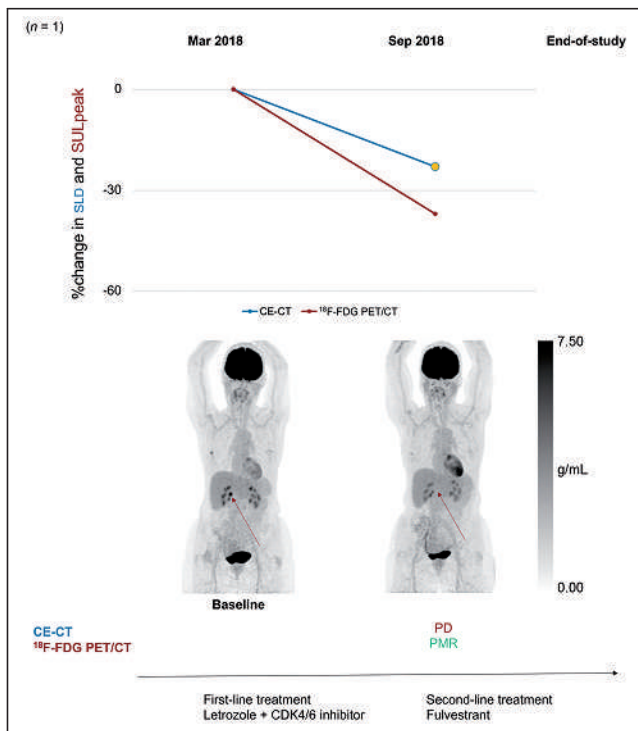


FIGURE 5. Illustration of progression detected by CE-CT only. Shown are maximum-intensity projection images and percentage change in sum of diameters for CE-CT and RECIST 1.1 (blue line) and SUL_{peak} for ¹⁸F-FDG PET/CT and PERCIST (red line). New lesions are shown as yellow dots. CDK4/6 = cyclin-dependent kinase 4/6; PMR = partial metabolic response; SLD = sum of lesion diameter.

Changes in response over time are illustrated in Figure 2 and Supplemental Figure 3 for patients with measurable disease at baseline for whom progression was detected by both modalities but seen first on ¹⁸F-FDG PET/CT.

DISCUSSION

In this prospective study of longitudinal response monitoring in MBC, progression was detected earlier by ¹⁸F-FDG PET/CT than by CE-CT in most patients ($P < 0.0001$). A median delay of 6 mo was observed for CE-CT compared with ¹⁸F-FDG PET/CT, which seems clinically relevant. In addition, more patients had measurable disease by PERCIST than RECIST 1.1, and ¹⁸F-FDG PET/CT provided improved visualization of changes in response over time.

Detection of Progression

A high proportion of PET-detected PDs could be observed as continuous progression until detection by CE-CT. This implied that a true PD was present and that earlier detection could potentially impact clinical practice. In cases of progression seen only on ¹⁸F-FDG PET/CT, a consistency check was made after the end of the trial. This revealed a clinical or image-guided change in management among half of these patients, thus suggesting true progression. The progression detected by ¹⁸F-FDG PET/CT in the remaining patients generally presented as small, solitary, but slow-progressing lesions of which the long-term clinical impact could not be assessed.

We considered lesions that could not be confirmed on the subsequent scan to indicate false progression since the progressing lesion resolved. The frequency of such findings was limited and equally distributed in both modalities.

TABLE 3

Reasons for First Progression Detected by CE-CT and ¹⁸F-FDG PET/CT in Patients with Measurable Disease

Reason for first progression	CE-CT (n)	¹⁸ F-FDG PET/CT (n)
New lesions only	13 (48.1%)	24 (55.8%)
Increase in SLD* or SUL _{peak} [†] only	7 (25.9%)	10 (23.3%)
New lesions and increase in SLD* or SUL _{peak} [†] (combined)	5 (18.5%)	6 (14.0%)
Unequivocal progression of nontarget lesions	2 (7.40%)	3 (6.98%)
Total	27 (100%)	43 (100%)

*Increase of 20% in SLD.

†Increase of 30% in SUL_{peak}.

SLD = sum of lesion diameter.

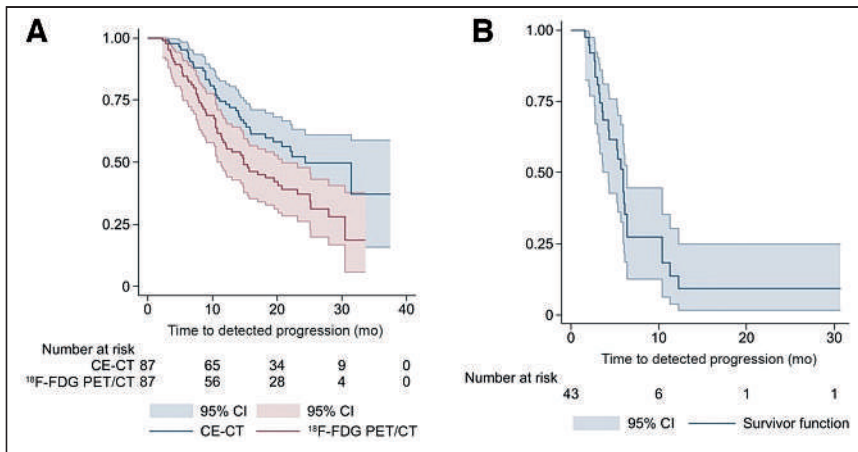


FIGURE 6. Kaplan-Meier estimates of time to detection of progression by CE-CT and ¹⁸F-FDG PET/CT (*n* = 87) (A) and from detection of progression by ¹⁸F-FDG PET/CT to detection by CE-CT (*n* = 43) (B).

¹⁸F-FDG PET/CT for Response Monitoring

¹⁸F-FDG PET/CT has been suggested to be less useful in patients with invasive lobular cancers with a predilection site for metastatic spread in the gastrointestinal tract, peritoneal carcinomatosis, and bones (21). These subtypes often encounter low Ki-67 and low ¹⁸F-FDG uptake (22,23), confirmed by this study with 7 of 11 patients who had no measurable disease of a lobular subtype.

The lack of standardization criteria has been suggested as a barrier to introducing ¹⁸F-FDG PET/CT for response monitoring in MBC in clinical trials (4,24), but PERCIST has been suggested as promising and feasible (6,25–27). In this study, PERCIST was

applied using the one-lesion method, with cutoff values of $\pm 30\%$ for PD or regressive disease, as suggested in PERCIST.

(29), and treatment response is reported more frequently by ¹⁸F-FDG PET/CT than by CE-CT (14). Therefore, treatment effect might be underestimated by CE-CT and RECIST 1.1 in current clinical practice (8,14).

Strengths and Limitations

A major strength is the prospective, paired study design, in which patients served as their own controls. The study included patients from daily clinical practice, with no strict inclusion criteria regarding measurability or molecular subtypes. The study provides clinically relevant knowledge and compares the standardized response evaluation criteria RECIST 1.1 and PERCIST for longitudinal response monitoring in MBC. We used the PERCIST criteria with strict acquisition to the suggested image conditions, allowing images to be compared between baseline and follow-up ¹⁸F-FDG PET/CT scans (8).

With other limitations, this was a nonrandomized single-center observational study. The nadir level of SUL_{peak} was used without international consensus. The follow-up time was relatively short such that no progression was observed in approximately one third of the patients. This could be explained by most patients having estrogen receptor-positive disease, for whom new treatment options have improved survival (30).

Perspectives

¹⁸F-FDG PET/CT has been suggested to improve treatment decisions by detecting non-response earlier than conventional methods and preventing patients from receiving ineffective, potentially toxic treatments (31,32). In this study, progression was detected earlier by ¹⁸F-FDG PET/CT. However, we cannot make firm conclusions about the long-term survival benefit of introducing ¹⁸F-FDG PET/CT. We consider this and data on MR scans and circulation tumor DNA collected in the present study (NCT03358589) to be perspectives for

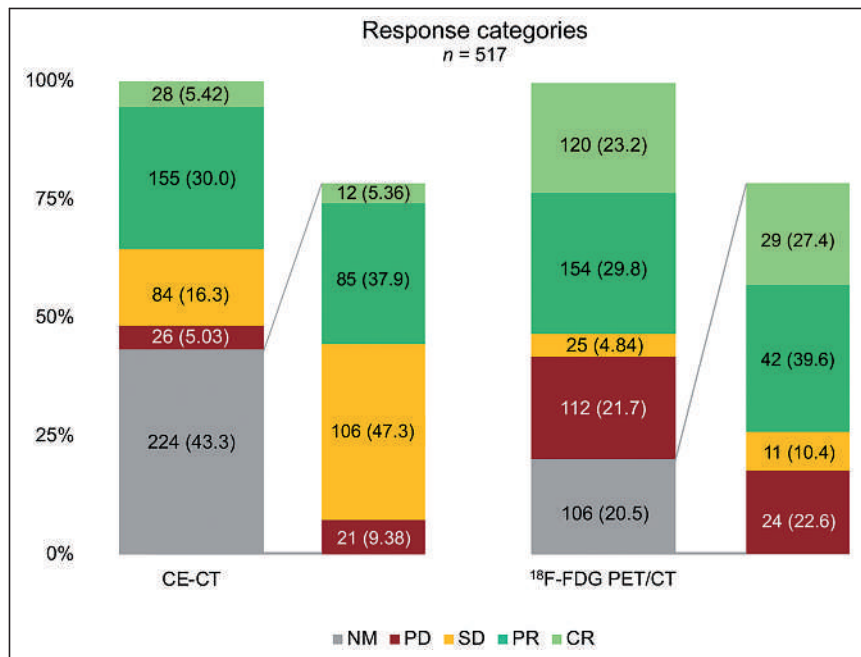


FIGURE 7. Response categories for CE-CT and ¹⁸F-FDG PET/CT for 517 follow-up scans. Response categories from visual assessments are in gray. CR = complete (metabolic) response; NM = not measurable; PR = partial (metabolic) response; SD = stable (metabolic) disease.

future research. Furthermore, stratified analyses within breast cancer-directed treatments could be relevant when comparing the 2 modalities.

CONCLUSION

Disease progression was detected earlier by ^{18}F -FDG PET/CT than by CE-CT in most patients, with a potentially clinically relevant 6-mo delay for CE-CT. More patients had measurable disease according to PERCIST than according to RECIST 1.1, and visualization of changes over time was improved by ^{18}F -FDG PET/CT. The magnitude of the final benefit for patients is a perspective for future research.

DISCLOSURE

This work was supported by a Qvesehls grant, a Mrs. Astrid Thaysens grant, the Independent Research Fund Denmark (7016-00359), the University of Southern Denmark, Odense University Hospital, and PREMIO. No other potential conflict of interest relevant to this article was reported.

ACKNOWLEDGMENTS

We thank Marie Lykke Rasmussen and Susanne Geneser, who served as patient representatives and coresearchers in this study.

KEY POINTS

QUESTION: Is PD detected earlier by CE-CT or ^{18}F -FDG PET/CT used for response monitoring in MBC?

PERTINENT FINDINGS: Disease progression was detected earlier by ^{18}F -FDG PET/CT than by CE-CT in most patients ($P < 0.0001$).

IMPLICATIONS FOR PATIENT CARE: ^{18}F -FDG PET/CT may improve treatment decisions by detecting progression earlier than CE-CT, preventing patients from receiving ineffective, potentially toxic treatments.

REFERENCES

- Cardoso F, Paluch-Shimon S, Senkus E, et al. 5th ESO-ESMO international consensus guidelines for advanced breast cancer (ABC 5). *Ann Oncol*. 2020;31:1623–1649.
- NCCN clinical practice guidelines: breast cancer, version 4.2021. National Comprehensive Cancer Network website. https://www.nccn.org/professionals/physician_gls/pdf/breast.pdf. Published May 1, 2021. Accessed January 12, 2023.
- Eisenhauer EA, Therasse P, Bogaerts J, et al. New response evaluation criteria in solid tumours: revised RECIST guideline (version 1.1). *Eur J Cancer*. 2009;45:228–247.
- Groheux D. Role of fludeoxyglucose in breast cancer: treatment response. *PET Clin*. 2018;13:395–414.
- Hildebrandt MG, Gerke O, Baun C, et al. ^{18}F -fluorodeoxyglucose (FDG)-positron emission tomography (PET)/computed tomography (CT) in suspected recurrent breast cancer: a prospective comparative study of dual-time-point FDG-PET/CT, contrast-enhanced CT, and bone scintigraphy. *J Clin Oncol*. 2016;34:1889–1897.
- Pinker K, Riedl C, Weber WA. Evaluating tumor response with FDG PET: updates on PERCIST, comparison with EORTC criteria and clues to future developments. *Eur J Nucl Med Mol Imaging*. 2017;44:55–66.
- Wahl RL, Jacene H, Kasamon Y, Lodge MA. From RECIST to PERCIST: evolving considerations for PET response criteria in solid tumors. *J Nucl Med*. 2009;50(suppl 1):122S–150S.
- Joo Hyun O, Lodge MA, Wahl RL. Practical PERCIST: a simplified guide to PET response criteria in solid tumors 1.0. *Radiology*. 2016;280:576–584.
- Ulaner GA. PET/CT for patients with breast cancer: where is the clinical impact? *AJR*. 2019;213:254–265.
- Du Y, Cullum I, Illidge TM, Ell PJ. Fusion of metabolic function and morphology: sequential ^{18}F -fluorodeoxyglucose positron-emission tomography/computed tomography studies yield new insights into the natural history of bone metastases in breast cancer. *J Clin Oncol*. 2007;25:3440–3447.
- Tateishi U, Gamez C, Dawood S, Yeung HW, Cristofanilli M, Macapinlac HA. Bone metastases in patients with metastatic breast cancer: morphologic and metabolic monitoring of response to systemic therapy with integrated PET/CT. *Radiology*. 2008;247:189–196.
- Lin NU, Guo H, Yap JT, et al. Phase II study of lapatinib in combination with trastuzumab in patients with human epidermal growth factor receptor 2-positive metastatic breast cancer: clinical outcomes and predictive value of early ^{18}F -fluorodeoxyglucose positron emission tomography imaging (TBCRC 003). *J Clin Oncol*. 2015;33:2623–2631.
- Taralli S, Lorusso M, Scolozzi V, Masiello V, Marazzi F, Calcagni ML. Response evaluation with ^{18}F -FDG PET/CT in metastatic breast cancer patients treated with palbociclib: first experience in clinical practice. *Ann Nucl Med*. 2019;33:193–200.
- Riedl CC, Pinker K, Ulaner GA, et al. Comparison of FDG-PET/CT and contrast-enhanced CT for monitoring therapy response in patients with metastatic breast cancer. *Eur J Nucl Med Mol Imaging*. 2017;44:1428–1437.
- Naghavi-Behzad M, Vogsen M, Vester RM, et al. Response monitoring in metastatic breast cancer: a comparison of survival times between FDG-PET/CT and CE-CT. *Br J Cancer*. 2022;126:1271–1279.
- von Elm E, Altman DG, Egger M, Pocock SJ, Gøtzsche PC, Vandenbroucke JP. The Strengthening of Reporting of Observational studies in Epidemiology (STROBE) statement: guidelines for reporting observational studies. *Lancet*. 2007;370:1453–1457.
- Giuliano AE, Connolly JL, Edge SB, et al. Breast cancer: major changes in the American Joint Committee on Cancer eighth ed.—cancer staging manual. *CA Cancer J Clin*. 2017;67:290–303.
- Boellaard R, Delgado-Bolton R, Oyen WJ, et al. FDG PET/CT: EANM procedure guidelines for tumour imaging—version 2.0. *Eur J Nucl Med Mol Imaging*. 2015;42:328–354.
- Vogsen M, Jensen JD, Christensen IY, et al. FDG-PET/CT in high-risk primary breast cancer: a prospective study of stage migration and clinical impact. *Breast Cancer Res Treat*. 2021;185:145–153.
- Vogsen M, Jensen JD, Gerke O, et al. Benefits and harms of implementing ^{18}F -FDG-PET/CT for diagnosing recurrent breast cancer: a prospective clinical study. *EJNMMI Res*. 2021;11:93.
- El-Hage A, Ruel C, Afif W, et al. Metastatic pattern of invasive lobular carcinoma of the breast: emphasis on gastric metastases. *J Surg Oncol*. 2016;114:543–547.
- Groheux D, Giacchetti S, Moretti JL, et al. Correlation of high ^{18}F -FDG uptake to clinical, pathological and biological prognostic factors in breast cancer. *Eur J Nucl Med Mol Imaging*. 2011;38:426–435.
- Koolen BB, Vrancken Peeters MJ, Wesseling J, et al. Association of primary tumour FDG uptake with clinical, histopathological and molecular characteristics in breast cancer patients scheduled for neoadjuvant chemotherapy. *Eur J Nucl Med Mol Imaging*. 2012;39:1830–1838.
- Harbeck N, Penault-Llorca F, Cortes J, et al. Breast cancer. *Nat Rev Dis Primers*. 2019;5:66.
- Young H, Baum R, Cremerius U, et al. Measurement of clinical and subclinical tumour response using ^{18}F -fluorodeoxyglucose and positron emission tomography: review and 1999 EORTC recommendations. European Organization for Research and Treatment of Cancer (EORTC) PET Study Group. *Eur J Cancer*. 1999;35:1773–1782.
- Vogsen M, Bulow JL, Ljungstrom L, et al. FDG-PET/CT for response monitoring in metastatic breast cancer: the feasibility and benefits of applying PERCIST. *Diagnostics (Basel)*. 2021;11:723.
- Pinker K, Riedl CC, Ong L, et al. The impact that number of analyzed metastatic breast cancer lesions has on response assessment by ^{18}F -FDG PET/CT using PERCIST. *J Nucl Med*. 2016;57:1102–1104.
- Kono M, Fujii T, Matsuda N, et al. Somatic mutations, clinicopathologic characteristics, and survival in patients with untreated breast cancer with bone-only and non-bone sites of first metastasis. *J Cancer*. 2018;9:3640–3646.
- Weber WA. Assessing tumor response to therapy. *J Nucl Med*. 2009;50(suppl 1):1S–10S.
- Gao JJ, Cheng J, Bloomquist E, et al. CDK4/6 inhibitor treatment for patients with hormone receptor-positive, HER2-negative, advanced or metastatic breast cancer: a US Food and Drug Administration pooled analysis. *Lancet Oncol*. 2020;21:250–260.
- Avril S, Muzic RF Jr, Plecha D, Traugber BJ, Vinayak S, Avril N. ^{18}F -FDG PET/CT for monitoring of treatment response in breast cancer. *J Nucl Med*. 2016;57(suppl 1):34S–39S.
- Dose Schwarz J, Bader M, Jenicke L, Hemminger G, Janicke F, Avril N. Early prediction of response to chemotherapy in metastatic breast cancer using sequential ^{18}F -FDG PET. *J Nucl Med*. 2005;46:1144–1150.

¹⁸F-FDG PET/CT Prediction of Treatment Outcomes in Human Papillomavirus–Positive, Locally Advanced Oropharyngeal Cancer Patients Receiving Deintensified Therapy: Results from NRG-HN002

Rathan M. Subramaniam^{1,2}, Lyudmila DeMora³, Min Yao⁴, Sue S. Yom⁵, Maura Gillison⁶, Jimmy J. Caudell⁷, John Waldron⁸, Ping Xia⁹, Christine H. Chung⁷, Minh Tam Truong¹⁰, Michelle Echevarria⁷, Jason W. Chan⁵, Jessica L. Geiger¹¹, Loren Mell¹², Samantha Seaward¹³, Wade L. Thorstad¹⁴, Jonathan Jay Beitler¹⁵, Khalil Sultanem¹⁶, Diagjin Blakaj¹⁷, and Quynh-Thu Le¹⁸

¹Otago Medical School, University of Otago, Otago, New Zealand; ²Duke University, Durham, North Carolina; ³NRG Oncology Statistics and Data Management Center, Philadelphia, Pennsylvania; ⁴University Hospitals Cleveland, Cleveland, Ohio; ⁵University of California, San Francisco, California; ⁶University of Texas MD Anderson Cancer Center, Houston, Texas; ⁷Moffitt Cancer Center, Tampa, Florida; ⁸Princess Margaret Hospital, Toronto, Oneida, Canada; ⁹Cleveland Clinic, Cleveland, Ohio; ¹⁰Boston Medical Center, Boston, Massachusetts; ¹¹Case Western Reserve University, Cleveland, Ohio; ¹²UC San Diego Moores Cancer Center, San Diego, California; ¹³Kaiser Permanente NCI Community Oncology Research Program, Vallejo, California; ¹⁴Washington University School of Medicine, St. Louis, Missouri; ¹⁵Emory University/Winship Cancer Institute, Atlanta, Georgia; ¹⁶Jewish General Hospital, Montreal, Canada; ¹⁷Ohio State University Comprehensive Cancer Center, Columbus, Ohio; and ¹⁸Stanford University, Stanford, California

The purpose of this study was to determine the negative predictive value (NPV) of a 12- to 14-wk posttreatment PET/CT for 2-y progression-free survival (PFS) and locoregional control (LRC) in patients with p16-positive locoregionally advanced oropharyngeal cancer (LA-OPC). Study was a secondary endpoint in NRG-HN002, a noncomparative phase II trial in p16-positive LA-OPC, stage T1-T2, N1-N2b or T3, N0-N2b, and ≤ 10 pack-year smoking. Patients were randomized in a 1:1 ratio to reduced-dose intensity-modulated radiotherapy (IMRT) with or without cisplatin. **Methods:** PET/CT scans were reviewed centrally. Tumor response evaluations for the primary site, right neck, and left neck were performed using a 5-point ordinal scale (Hopkins criteria). Overall scores were then assigned as negative, positive, or indeterminate. Patients with a negative score for all 3 evaluation sites were given an overall score of negative. The hypotheses were NPV for PFS and LRC at 2-y posttreatment $\leq 90\%$ versus $>90\%$ (1-sided P value, 0.10). **Results:** A total of 316 patients were enrolled, of whom 306 were randomized and eligible. Of these, 131 (42.8%) patients consented to a posttherapy PET/CT, and 117 (89.3%) patients were eligible for PET/CT analysis. The median time from the end of treatment to PET/CT scan was 94 d (range, 52–139 d). Estimated 2-y PFS and LRC rates in the analysis subgroup were 91.3% (95% CI, 84.6, 95.8%) and 93.8% (95% CI, 87.6, 97.5%), respectively. Posttreatment scans were negative for residual tumor for 115 patients (98.3%) and positive for 2 patients (1.7%). NPV for 2-y PFS was 92.0% (90% lower confidence bound [LCB] 87.7%; $P = 0.30$) and for LRC was 94.5% (90% LCB 90.6%; $P = 0.07$). **Conclusion:** In the context of deintensification with reduced-dose radiation, the NPV of a 12- to 14-wk posttherapy PET/CT for 2-y LRC is estimated to be $>90\%$, similar to that reported for patients receiving standard chemoradiation. However, there is insufficient evidence to conclude that the NPV is $>90\%$ for PFS.

Key Words: PET/CT negative predictive value; p16-positive oropharyngeal cancer; NRG-HN002

J Nucl Med 2023; 64:362–367

DOI: 10.2967/jnumed.122.264424

Head and neck squamous cell cancer (HNSCC) is the ninth most common malignant tumor worldwide, responsible for about 2% of all cancer-related deaths (1). Human papillomavirus (HPV)–associated HNSCC is rising in incidence and affects a younger population (2,3). This subgroup of patients harbors HPV in their tumor cells, predominantly HPV-16, and the tumors occur mostly in the oropharynx. The prognosis for these patients is better, with overall survival (OS) at 3 y being about 82% in locally advanced HPV-positive HNSCC (4). Standard therapy for locoregionally advanced oropharyngeal SCC (OPSCC) is a combination of 70-Gy radiation therapy (RT) and concurrent platinum chemotherapy (5). Because of the better survival outcomes in the HPV-associated OPSCC patient population and to reduce treatment-related short- and long-term toxicities, various deintensification treatment strategies are currently being explored (6,7) for patients with HPV-associated OPSCC.

¹⁸F-FDG PET/CT has been shown to be a valuable imaging test in assessing treatment response in HNSCC. In a phase III randomized controlled study ($n = 564$), an ¹⁸F-FDG PET/CT–based surveillance strategy was noninferior in survival and also cost-effective when compared with routine neck dissection (8), after standard chemoradiation therapy. Therefore, it is recommended that ¹⁸F-FDG PET/CT be performed, usually about 12 wk or later from completion of chemoradiation therapy (9), to minimize false-positive results from radiation-induced inflammation.

The 5-point Hopkins criteria for posttherapy ¹⁸F-FDG PET/CT interpretation was established and validated to standardize the interpretation and reduce variability (10). Its reported accuracy is

Received May 25, 2022; revision accepted Aug. 24, 2022.

For correspondence or reprints, contact Rathan M. Subramaniam (rathan.subramaniam@otago.ac.nz).

Published online Sep. 2, 2022.

COPYRIGHT © 2023 by the Society of Nuclear Medicine and Molecular Imaging.

86.4% (95% CI, 79.3%, 91.3%) with a negative predictive value (NPV) of 92.1% (95% CI, 86.9%, 95.3%) (9). The Hopkins scale is a standardized qualitative interpretation method designed for routine clinical practice. It has been recently shown to be equivalent in its performance compared with a more complex quantitative assessment method (11). It also predicts survival outcomes, both OS and progression-free survival (PFS) in HNSCC patients (9,10).

The Hopkins criteria was internally and externally validated (9,10) using mixed patient populations of HPV-positive and HPV-negative HNSCC. This study evaluates its performance metrics in HPV-positive, locally advanced oropharyngeal cancer patients receiving deintensified therapy. Specifically, we determine the NPV of 12- to 14-wk posttreatment ¹⁸F-FDG PET/CT for PFS and locoregional control (LRC) at 2 y in this population.

MATERIALS AND METHODS

NRG-HN002 is a multiinstitutional, noncomparative randomized phase II clinical trial (ClinicalTrials.gov identifier: NCT02254278). The trial determined the acceptability of 2 curative-intent strategies incorporating reduced-dose RT with or without cisplatin. This trial was designed to select the arm(s) meeting PFS (primary objective) and swallowing-related quality of life criteria (as measured by the M.D. Anderson Dysphagia Inventory [MDADI]; co-primary objective) for advancement to a definitive trial. The trial design, patients, inclusion/exclusion criteria, trial oversight, and definitions have already been described (6).

¹⁸F-FDG PET/CT Substudy and Patients

All patients eligible for NRG-HN002 were offered to participate in an optional study to assess treatment response at 2 y based on 12- to 14-wk posttreatment ¹⁸F-FDG PET/CT scans. Of the 306 eligible patients for the parent study, 131 consented to participate. Of these, 117 patients received protocol treatment and had acceptable-quality scans and thus were eligible for analysis. Fourteen patients were excluded from these analyses (1 did not receive protocol treatment, 1 had the scan in the wrong format, and 12 had no scan).

¹⁸F-FDG PET/CT Imaging

All sites were instructed to follow an ¹⁸F-FDG PET/CT imaging protocol. A serum glucose level of < 200 mg/dL before the study, an uptake time of 60 ± 10 min, and dedicated head and neck (orbits to the upper thorax) and whole-body (orbits to upper thigh) acquisitions were obtained. Recommended PET acquisition parameters were 6 bed positions and an acquisition of 2–5 min per bed position. The dedicated head and neck PET/CT typically followed the body examination. It included 2 bed positions (6 min per bed position), and the images were reconstructed into a 30-cm field of view with a 256 × 256 matrix. The recommended acquisition parameters for the low-dose CT scan were as follows: kV = 120; effective mAs = 90–150; gantry rotation time < 0.5 s; maximum reconstructed slice width = 2.5 mm (overlap acceptable); standard reconstruction algorithm, maximum reconstruction diameter = 30 cm; and without iodinated contrast. The PET/CT data were corrected for dead time, scatter, randoms, and attenuation using standard algorithms provided by the scanner manufacturers. For the dedicated head and neck views, a postprocessing filter with a full-width at half maximum in the range of 5 mm was recommended.

¹⁸F-FDG PET/CT Image Interpretation: Hopkins Criteria

PET/CT scans were reviewed both centrally and locally by participating institutions. Tumor response evaluations for the primary site, right neck, and left neck were performed using a 5-point ordinal scale (Hopkins criteria) (10): score 1—definite complete metabolic response; score 2—likely complete metabolic response; score 3—likely inflammatory; score 4—likely residual metabolic disease; and score 5—definite residual

metabolic disease. A score of 1 or 2 was interpreted as negative, 3 as indeterminate, and 4 or 5 as positive. An overall score was assigned using this collapsed 3-point categorization, with the highest score at any anatomic site determining the overall score.

In the central review, if at least 1 evaluation site was positive, the assigned overall score was positive. Patients with a negative score for all 3 evaluation sites were given an overall score of negative. This is a visual, qualitative analysis using internal jugular vein and liver uptake as internal controls.

In the local review, 6 patients had at least 1 evaluation site as positive and were assigned an overall positive score; 1 patient had a site score of positive and was given an overall score of indeterminate. Seven patients had site and overall scores of indeterminate; 3 patients had a site score of indeterminate and were ultimately given an overall score of negative. Patients with a negative score for all 3 evaluation sites were all given an overall score of negative.

Statistical Analysis

Distributions of patients' characteristics for those who did and did not consent to PET/CT imaging were compared using the χ^2 test with a significance level of 0.05. Hazard ratios (HRs) for PFS and locoregional failure (LRF) for these 2 subgroups were estimated using the Cox proportional hazards models. Primary analyses included eligible patients who consented to PET/CT imaging and had a posttreatment PET/CT scan submitted for analysis regardless of timing. Sensitivity analyses included patients with scans 10–16 wk after the end of RT. Overall central scan review results were used in the primary analyses of the NPV. The level of agreement between overall local and central PET/CT reads on the 3-point scale was assessed using percent agreement and Brennan–Prediger's and Gwet's coefficients. The level of agreement for primary site, right neck, and left neck scores was measured using the weighted versions of the same coefficients with linear weights to account for different levels of disagreement between categories of Hopkins criteria.

The primary purpose of analyzing ¹⁸F-FDG PET/CT in NRG-HN002 was to determine the NPV of 12- to 14-wk posttherapy ¹⁸F-FDG PET/CT for 2-y PFS and 2-y LRC. Failure for PFS endpoint was defined as local, regional, or distant progression or death due to any cause; rates were calculated by the Kaplan–Meier method. The LRF endpoint was defined as local or regional progression, salvage surgery of the primary tumor with tumor present or unknown, salvage neck dissection with tumor present or unknown > 20 wk after the end of RT, death due to study cancer without documented progression, or death due to unknown causes without documented progression; rates were calculated by the cumulative incidence method.

NPV was calculated as the proportion of PET/CT-negative patients who remained progression-free at 2 y and, separately, for those who maintained LRC (remained free of LRF) at 2 y. The binomial NPV estimates and exact CIs were calculated. The null hypothesis of NPV ≤ 90% for PFS was tested against the alternative of NPV > 90% with a 1-sided binomial test at the 0.10 level. The power for these hypotheses was calculated under the alternative hypothesis of 95% NPV. With an estimated 140 available scans, the statistical power to reject the null hypothesis of NPV ≤ 90% was 76% per protocol-specified design.

RESULTS

Patients

NRG-HN002 opened to accrual on October 27, 2014, and completed accrual on February 7, 2017, with 316 patients enrolled, of whom 308 were randomized (306 eligible). A total of 117 patients consented and were eligible for PET/CT analysis (Supplemental Fig. 1; supplemental materials are available at <http://jnm.snmjournals.org>).

Supplemental Table 1 summarizes patient and tumor characteristics by PET/CT consent status. Overall, 131 eligible patients (42.8%) consented to the posttherapy PET/CT exam. The consent rate was comparable between arms. No significant differences in patient and tumor characteristics were found between consent status groups.

Supplemental Figure 2 summarizes the PFS analysis by consent status. The estimated HR (no consent vs. consent) was 1.77 (95% CI, 0.91, 3.41). Supplemental Figure 3 summarizes the LRF analysis by consent status; the estimated HR (no consent vs. consent) was 1.41 (95% CI, 0.65, 3.09).

Patient and Tumor Characteristics

Of 131 patients who consented to PET/CT imaging, 117 (89.3%) were eligible for analysis. Supplemental Table 2 shows patient and tumor characteristics for these patients. The median age of patients was 62 y (minimum–maximum, 39–84 y); 87.2% of patients were male, 90.6% were white, 81.2% had a Zubrod performance status 0, 54.7% had tonsil primary site, 64.1% had T2–3 disease, 76.9% had N2 disease, and 79.5% had bilateral RT planning. The mean time from the end of treatment to the PET/CT scan was 13.6 wk (SD = 1.9 wk; range and interquartile range, 7.4–19.8 and 12.7–14.4 wk, respectively).

Study Endpoints

PET/CT Central Review. Supplemental Table 3 summarizes the PET/CT scan central review results. Three patients had a site score of indeterminate but were ultimately given an overall score of negative. Overall, posttreatment scans for 115 of 117 patients (98.3%) were negative for residual tumor, and 2 (1.7%) were positive for residual tumor. For the primary site, posttreatment scans for 113 patients (96.6%) had “definite complete metabolic response”; 1 patient (0.9%) had “likely complete metabolic response”; 2 patients (1.7%) were assessed as “likely inflammatory”; 1 patient (0.9%) had “definite residual metabolic disease.” Similar results were found for the right and left neck (Supplemental Table 3).

NPV of PET/CT for 2-y PFS. Table 1 summarizes the results for NPV for PFS at 2 y using central review results. Overall, the NPV for 2-y PFS was 92.0% (90% lower confidence bound [LCB], 87.7%; 95% CI, 85.4%, 96.3%) with $P = 0.3$ not rejecting the null hypothesis of the NPV for 2-y PFS $\leq 90\%$. With $P > 0.10$, these results indicate that there is not enough evidence to conclude that

the NPV of PET/CT for 2-y PFS is $> 90\%$, but were able to (with a 90% confidence) rule out an NPV below 87.7%. Comparable NPV results were found by treatment arm. On the intensity-modulated radiotherapy (IMRT) + cisplatin and IMRT arms, 57 and 58 patients were evaluable for NPV for PFS, respectively; 1 patient on each arm was censored for PFS. For patients with an overall PET/CT score of “positive for residual tumor,” 1 patient (50.0%) had a failure for 2-y PFS, and 1 patient (50.0%) did not have failure for 2-y PFS (Table 1).

A sensitivity analysis to estimate the NPV was completed using evaluable patients with PET/CT scans completed 10–16 wk after RT. A total of 104 patients were included, with a resulting overall NPV for 2-y PFS equal to 92.2% (90% LCB, 87.6%; 95% CI, 85.1%, 96.6%) and $P = 0.3$. Again, given $P > 0.10$, there is not enough evidence to conclude that NPV of PET/CT for 2-y PFS is $> 90\%$ (Supplemental Table 4).

NPV of PET/CT for 2-Y LRC. Table 2 summarizes the results for NPV for LRC at 2 y using central review results. The NPV for 2-y LRC was 94.5% (90% LCB, 90.6%) with $P = 0.07$, rejecting the null hypothesis of the NPV for 2-y LRC $\leq 90\%$ in favor of the alternative hypothesis of NPV $> 90\%$. A 90% LCB for the NPV for 2-y LRC was 90.6%, a number above the hypothesized (null) NPV of 90% (95% CI, 88.5%, 98.0%). The NPV for 2-y LRC for the IMRT + cisplatin arm was 94.6% (90% LCB 88.5%). The NPV for 2-y LRC for the IMRT arm was 94.4% (90% LCB 88.0%). Results by the treatment arm are also shown in Table 2. Of the 58 patients on the IMRT + cisplatin arm eligible for PET/CT analysis, 56 were evaluable for NPV for LRC; 2 patients were censored for LRC before the 2-y time point. Of the 59 patients on the IMRT arm eligible for PET/CT analysis, 56 were evaluable for NPV for LRC; 3 patients were censored for LRC before the 2-y time point. For patients with an overall PET/CT score of “positive for residual tumor,” 1 patient (50.0%) had failure for 2-y LRC and 1 patient (50.0%) did not have failure for 2-y LRC.

A sensitivity analysis to estimate the NPV was completed using evaluable patients with PET/CT scans completed 10–16 wk after RT. A total of 101 patients were included, with a resulting overall NPV for 2-y LRC equal to 94.9% (90% LCB, 90.8%; 95% CI, 88.6%, 98.3%) and $P = 0.06$, again rejecting the null hypothesis of the NPV for 2-y LRC $\leq 90\%$ in favor of the alternative hypothesis of NPV $> 90\%$ (1-sided α -level 0.10) (Supplemental Table 5).

TABLE 1
NPV per Central Review for 2-Year PFS

PET/CT result and outcome	IMRT + cisplatin	IMRT	Total
PET overall interpretation			
Positive for residual tumor	0 (0.0%)	2 (3.4%)	2 (1.7%)
Negative for residual tumor	57 (100.0%)	56 (96.6%)	113 (98.3%)
2-y PFS status in PET-negative			
Failure	4 (7.0%)	5 (8.9%)	9 (8.0%)
Nonfailure	53 (93.0%)	51 (91.1%)	104 (92.0%)
NPV of 2-y PFS	93.0%	91.1%	92.0%
95% exact CI	83.0%–98.1%	80.4%–97.0%	85.4%–96.3%
One-sided 90% exact LCB	86.5%	84.1%	87.7%
H0: NPV $\leq 90\%$ vs. HA: NPV $> 90\%$			
<i>P</i> value (exact)			0.2964

TABLE 2
NPV per Central Review for 2-Year LRC

PET/CT result and outcome	IMRT + cisplatin	IMRT	Total
PET overall interpretation			
Positive for residual tumor	0 (0.0%)	2 (3.6%)	2 (1.8%)
Negative for residual tumor	56 (100.0%)	54 (96.4%)	110 (98.2%)
2-y LRC status in PET-negative			
Failure	3 (5.4%)	3 (5.6%)	6 (5.5%)
Nonfailure	53 (94.6%)	51 (94.4%)	104 (94.5%)
NPV of 2-y LRC			
95% exact CI	85.1%–98.9%	84.6%–98.8%	88.5%–98.0%
One-sided 90% exact LCB	88.5%	88.0%	90.6%
H0: NPV ≤ 90% vs HA: NPV > 90%			
<i>P</i> value (exact)			0.0682

PET/CT Local Assessment. When local assessment results were used, the NPV for 2-y PFS was 91.8% (90% LCB, 86.5%; 95% CI, 83.8%, 96.6%; $P = 0.4 > 0.10$). The NPV for 2-y LRC was 95.1% (90% LCB, 90.5%; 95% CI, 88.0%, 98.7%; $P = 0.08 < 0.10$). Therefore, there is evidence that the NPV > 90% for 2-y LRC. Results from the sensitivity analysis, using only scans completed 10–16 wk after RT, are similar for both endpoints (Supplemental Tables 6 and 7).

Local and central assessments by neck site and overall are shown in Supplemental Table 8. The percent agreement and Brennan–Prediger’s and Gwet’s agreement coefficients between overall local and central interpretation were 0.87 (95% CI, 0.80, 0.94), 0.80 (95% CI, 0.70, 0.91), and 0.86 (95% CI, 0.78, 0.94), respectively (Supplemental Table 8). The agreement coefficient estimates for primary site and right and left neck are also shown in Supplemental Table 8. These values suggest substantial agreement between local and central PET/CT interpretation for overall, primary site, left and right neck. Disagreements mainly consisted of patients who were classified with a definite metabolic disease by central reviews but were assigned a likely complete metabolic response or likely inflammatory by local assessments.

DISCUSSION

In this study, testing a reduced-dose of RT for patients with p16-positive, T1-T2 N1-N2b M0, or T3 N0-N2b M0 OPSCC (seventh edition staging) with ≤ 10 pack-years of smoking, we estimated the performance characteristics of the Hopkins criteria for the predictive ability of 12- to 14-wk posttreatment ¹⁸F-FDG PET/CT for patient outcomes at 2 y. On the basis of the central review, most posttreatment scans (98.3%) were negative for residual tumor, and the NPV for LRC was 94.5% and PFS was 92.0%. Similar NPVs were obtained on the basis of local site analysis.

The study population of this trial had a distinctly more favorable outcome profile than the study population of the original development and internal (10) and subsequent external validation (9) of the Hopkins criteria for interpretation of the 12- to 14-wk posttreatment ¹⁸F-FDG PET/CT. The study population from the original derivation study ($n = 214$) included many subsites of HNSCC patients (oropharynx 63.1%, oral cavity 5.1%, larynx 18.7%, and other sites 13.1%; 57.5% HPV-positive) who had higher progression and

death rates (median follow up of 27 mo; 17.7% died and 29.4% had progression). The external validation study (ECLYPS) had a study population similar to the original derivation study, including various subsites (oropharynx 54.7%, oral cavity 6.3%, larynx 16.8%, and other sites 22.2%; 29.6% HPV-positive) and poorer outcome rates (13.6% died and LRF 20.8% at 2 y) (9). Compared with these 2 study populations, the NRG-HN002 population analyzed in this substudy included only patients with HPV-positive oropharyngeal cancer, and 2-y PFS was 87.6% or above and OS was 96.7% or above. Hence, this trial provides the performance characteristic (NPV) of the Hopkins criteria for posttreatment ¹⁸F-FDG PET/CT in a favorable deintensified outcome group.

One of the Hopkins criteria characteristics is decreasing the number of intermediate readings and uncertainty about inflammatory uptake. The number of patients with intermediate score (score 3, likely inflammatory) was low in this study ($n = 1$ for left neck, $n = 0$ for right neck, and $n = 2$ for the primary site), which is similar to that in the prior studies (9,12–14). This is most likely due to the standardized qualitative reads and subsiding radiation-induced inflammation by 12–14 wk after therapy. Compared with other interpretation criteria (such as NI-RADS, Porceddu, Deauville), the Hopkins criteria has been demonstrated to reduce the intermediate interpretation to the lowest (14). In addition, unlike the prior studies, the number of patients with scores representing residual disease is extremely low (1.7%) in this study, compared with the other studies (9,10), due to the favorable HPV (2) oropharyngeal SCC population in this study who responded well for the treatment.

This study establishes the value of Hopkins criteria in a multi-center clinical trial setting. The advantage of standardized qualitative interpretation criteria is the ease and rapid deployment in a clinical practice setting (15) while maintaining similar accuracy of semiquantitative interpretation methods such as PERCIST (16) and other methods (11), which require more stringent standard methods of performing the scans and complex analyses. The analysis suggests substantial agreement between local and central interpretation for overall, primary site, left, and right neck interpretation. In future studies, the level of agreement could be further optimized by including a training program or training set for site reads. Further, the added value of performing a PET/CT 3 mo after therapy in a favorable population could be established by performing a clinical examination and therapy response judgment first,

before performing a PET/CT, then comparing these results or revealing them to the clinical team and estimating the final clinical judgment at 3 mo after therapy. This would have demonstrated the true added value of performing a PET/CT to the clinical judgment, at this time point.

There are limitations to this secondary endpoint analysis of NRG-HN002. First, PET/CT was an optional method for therapy response assessment at the time this study was designed, and the actual sample size was slightly lower than the projected sample size (113 vs. 140 patients). Second, presumably higher risk patients did not opt-in for PET/CT. However, this apparent finding was not statistically significant and was not explained by differences in tumor and patient characteristics between participants and non-participants in the PET/CT substudy. Third, although the protocol specified a posttreatment PET/CT at 12–14 wk, the actual PET/CT time varied around 12–14 wk after treatment. However, the sensitivity analysis, which included PET/CT scans obtained at 10–16 wk after treatment (89%), led to the same conclusions regarding NPV of PET/CT as the analysis using all scans. Fourth, our study was not designed to compare either clinical evaluation or CT imaging versus PET/CT imaging, so we cannot comment on the relative adequacy of various follow-up methods in this low-risk group. Furthermore, NPV estimates close to 2-y PFS and LRC rates suggest that marginal additional information on 2-y posttreatment outcomes is gained using PET/CT around 12–14 wk after treatment. However, as discussed earlier, this result alone should not be used to determine the adequacy of PET/CT in this population. Other metrics such as specificity, sensitivity, and positive predictive value should be considered; none of these metrics can be properly and accurately estimated from this substudy.

CONCLUSION

Within the context of deintensification with reduced-dose radiation, the NPV around 12- to 14-wk posttherapy PET/CT for 2-y LRC is statistically $> 90\%$, similar to that reported for patients receiving standard chemoradiation. However, there is insufficient evidence to conclude that the NPV is $> 90\%$ for PFS.

DISCLOSURE

The National Cancer Institute sponsored the study. This project was supported by grants U10CA180868 (NRG Oncology Operations), U10CA180822 (NRG Oncology SDMC), U24CA180803 (IROC), and UG1CA189867 (NRG Oncology NCORP) from the National Cancer Institute (NCI). This project is funded, in part, under a grant with the Pennsylvania Department of Health. The Department specifically disclaims responsibility for any analyses, interpretations or conclusions. Dr. Caudell reports grants and honoraria from Varian Medical Systems and honoraria from Galera. Dr. Chung reports participation on the Advisory Board for Bristol-Myers Squibb, CUE, Sanofi, Mirati, Merck, Brooklyn Immunotherapeutics, and Exelixis. Dr. Geiger reports consulting fees from Merck, Exelis, and Regeneron. Dr. Gillison reports grants from Kura Oncology, Agenus, Genocoe Biosciences, Inc., Roche, and Bristol Myers Squibb; consulting fees from Kura Oncology, Shattuck Labs, Inc., Nektar Therapeutics, Ispen Biopharmaceuticals Inc., EMD Serono, Inc., Gilead Sciences, Inc., Eisai Medical Research Inc., Istari Oncology, Inc., LLX Solutions, LLC, Onclive, Seagen, Debiopharm, Mirati Therapeutics, Sensei Biotherapeutics, Inc., BioNTech AG, and Coherus; participation on the Advisory Board for Kura DSMB, SQZ Biotech, and BioMimetix;

and stock options from Sensei. Dr. Mell reports grants from Radiation Therapy Oncology Group Foundation, Merck Sharp & Dohme Corp., Syneos Health Inc., and NCI and consulting fees from Cel-Sci. Dr. Le reports consulting fees from Nanobiotix, Roche, and Coherus and honoraria from Johns Hopkins, 2021 China International Exchange and Promotive Association for Medical and Health Care (CPAM), Nasopharyngeal Cancer Branch Inaugural Conference and Minimally Invasive Surgery Training Course of Nasopharyngeal Cancer. No other potential conflict of interest relevant to this article was reported.

KEY POINTS

QUESTION: What is the NPV of 12- to 14-wk posttreatment ^{18}F -FDG PET/CT for PFS and LRC at 2 y in HPV-positive, locally advanced oropharyngeal cancer receiving deintensified therapy?

PERTINENT FINDINGS: NRG-HN002 is a multiinstitutional, noncomparative randomized phase II clinical trial (ClinicalTrials.gov identifier: NCT02254278). The primary endpoint of the study was the NPV for PFS and LRC at 2 y. The NPV of around 12- to 14-wk posttherapy PET/CT for 2-y LRC is statistically $> 90\%$, similar to that reported for patients receiving standard chemoradiation. However, there is insufficient evidence to conclude that the NPV is $> 90\%$ for PFS.

IMPLICATIONS FOR PATIENT CARE: ^{18}F -FDG PET/CT performed around 12–14 wk after therapy has very high NPV for PFS and LRC in HPV-positive, locally advanced oropharyngeal cancer receiving deintensified therapy.

REFERENCES

1. Siegel RL, Miller KD, Fuchs HE, Jemal A. Cancer statistics, 2021. *CA Cancer J Clin*. 2021;71:7–33.
2. Gillison ML, Chaturvedi AK, Anderson WF, Fakhry C. Epidemiology of human papillomavirus-positive head and neck squamous cell carcinoma. *J Clin Oncol*. 2015;33:3235–3242.
3. Ang KK, Harris J, Wheeler R, et al. Human papillomavirus and survival of patients with oropharyngeal cancer. *N Engl J Med*. 2010;363:24–35.
4. Sun Y, Wang Z, Qiu S, Wang R. Therapeutic strategies of different HPV status in head and neck squamous cell carcinoma. *Int J Biol Sci*. 2021;17:1104–1118.
5. Bourhis J, Sire C, Graff P, et al. Concomitant chemoradiotherapy versus acceleration of radiotherapy with or without concomitant chemotherapy in locally advanced head and neck carcinoma (GORTEC 99-02): an open-label phase 3 randomised trial. *Lancet Oncol*. 2012;13:145–153.
6. Yom SS, Torres-Saavedra P, Caudell JJ, et al. Reduced-dose radiation therapy for HPV-associated oropharyngeal carcinoma (NRG Oncology HN002). *J Clin Oncol*. 2021;39:956–965.
7. Strohl MP, Wai KC, Ha PK. De-intensification strategies in HPV-related oropharyngeal squamous cell carcinoma - a narrative review. *Ann Transl Med*. 2020;8:1601.
8. Mehanna H, Wong W-L, McConkey CC, et al. PET-CT Surveillance versus neck dissection in advanced head and neck cancer. *N Engl J Med*. 2016;374:1444–1454.
9. Van den Wyngaert T, Helsen N, Carp L, et al. Fluorodeoxyglucose-positron emission tomography/computed tomography after concurrent chemoradiotherapy in locally advanced head-and-neck squamous cell cancer: the ECLYPS study. *J Clin Oncol*. 2017;35:3458–3464.
10. Marcus C, Ciarallo A, Tahari AK, et al. Head and neck PET/CT: therapy response interpretation criteria (Hopkins criteria)—interreader reliability, accuracy, and survival outcomes. *J Nucl Med*. 2014;55:1411–1416.
11. Helsen N, Van den Wyngaert T, Carp L, et al. Quantification of ^{18}F -fluorodeoxyglucose uptake to detect residual nodal disease in locally advanced head and neck squamous cell carcinoma after chemoradiotherapy: results from the ECLYPS study. *Eur J Nucl Med Mol Imaging*. 2020;47:1075–1082.
12. Van den Wyngaert T, De Schepper S, Carp L. Quality Assessment in FDG-PET/CT imaging of head-and-neck cancer: one home run is better than two doubles. *Front Oncol*. 2020;10:1458.

13. Kendi AT, Brandon D, Switchenko J, et al. Head and neck PET/CT therapy response interpretation criteria (Hopkins criteria): external validation study. *Am J Nucl Med Mol Imaging*. 2017;7:174–180.
14. Zhong J, Sundersingh M, Dyker K, et al. Post-treatment FDG PET-CT in head and neck carcinoma: comparative analysis of 4 qualitative interpretative criteria in a large patient cohort. *Sci Rep*. 2020;10:4086.
15. Peacock JG, Christensen CT, Banks KP. RESISTing the need to quantify: putting qualitative FDG-PET/CT tumor response assessment criteria into daily practice. *AJNR*. 2019;40:1978–1986.
16. Wahl RL, Jacene H, Kasamon Y, Lodge MA. From RECIST to PERCIST: evolving considerations for PET response criteria in solid tumors. *J Nucl Med*. 2009;50(suppl 1):122S–150S.

Novel ^{68}Ga -FAPI PET/CT Offers Oncologic Staging Without COVID-19 Vaccine–Related Pitfalls

Tristan T. Demmert^{1,2}, Ines Maric^{1,2}, Kelsey L. Pomykala³, Katharina Lueckerath^{1,2}, Jens Siveke^{2,4}, Benedikt M. Schaarschmidt⁵, Rainer Hamacher^{2,6}, Ken Herrmann^{1,2}, and Wolfgang P. Fendler^{1,2}

¹Department of Nuclear Medicine, West German Cancer Center, University of Duisburg–Essen, Essen, Germany; ²German Cancer Consortium, Partner Site Essen University Hospital, and German Cancer Research Center, Essen, Germany; ³Institute for AI in Medicine, University Medicine Essen, Essen, Germany; ⁴Bridge Institute of Experimental Tumor Therapy, West German Cancer Center, Essen University Hospital, Essen, Germany; ⁵Department of Diagnostic and Interventional Radiology and Neuroradiology, Essen University Hospital, University of Duisburg–Essen, Essen, Germany; and ⁶Department of Medical Oncology, West German Cancer Center, Essen University Hospital, Essen, Germany

In the setting of ongoing coronavirus disease 2019 vaccination, vaccine-related tracer uptake in locoregional lymph nodes has become a well-known issue in tumor staging by ^{18}F -FDG PET/CT. ^{68}Ga -fibroblast-activation protein inhibitor (FAPI) PET/CT is a new oncologic imaging tool that may overcome this limitation. **Methods:** We assessed postvaccine head-to-head and same-day ^{18}F -FDG and ^{68}Ga -FAPI-46 PET/CT findings in a series of 11 patients from a large, prospective imaging registry. All patients with documented tracer uptake in locoregional lymph nodes on PET/CT or PET/MRI, after vaccination within 6 wk, were eligible for investigation. **Result:** Significant visual lymph node uptake adjacent to the injection site was noted in 11 of 11 (100%) patients with ^{18}F -FDG PET/CT, versus 0 of 11 (0%) with ^{68}Ga -FAPI PET/CT. ^{18}F -FDG detected 73% and ^{68}Ga -FAPI PET/CT 94% of all tumor lesions. **Conclusion:** In this case-series study, ^{68}Ga -FAPI showed its potential to avoid ^{18}F -FDG PET/CT postvaccination pitfalls and presented superior tumor localization.

Key Words: PET; PET/CT; COVID-19; tumor staging; vaccine-related pitfalls

J Nucl Med 2023; 64:368–371
DOI: 10.2967/jnumed.122.264872

Since the outbreak of the coronavirus disease 2019 (COVID-19) pandemic in 2019 and the start of global mass vaccination in November 2020, several clinical studies have addressed the issue of reactive tracer accumulation in locoregional lymph nodes and upper-arm muscles (*J*). At local sites, ^{18}F -FDG is taken up by immune cells responding to the messenger RNA inflammatory stimulus (2–4). This observation is concerning because vulnerable groups, such as oncologic patients, undergo both regular booster shots and medical imaging. False-positive findings on ^{18}F -FDG

PET due to uptake in inflammatory cells may trigger false management decisions.

^{68}Ga -fibroblast-activation protein inhibitor (FAPI) PET/CT is a novel imaging test directed at cancer-associated fibroblasts in the tumor stroma. Because of its unique mechanism targeting only activated fibroblasts and subtypes of cancer-associated fibroblasts, ^{68}Ga -FAPI PET/CT may be able to avoid false-positive postvaccine uptake. ^{68}Ga -FAPI PET/CT has emerged as a potential alternative to ^{18}F -FDG PET/CT in many tumor types and may avoid locoregional pitfalls caused by vaccination. Here, we assess same-day head-to-head postvaccine ^{18}F -FDG and ^{68}Ga -FAPI PET/CT uptake in patients from a large, prospective registry of oncologic imaging collected during the ongoing mass vaccination campaign in Germany.

MATERIALS AND METHODS

We selected 11 patients with ^{68}Ga -FAPI and ^{18}F -FDG PET/CT (May 2021 to April 2022) from our prospective database, which is part of a large, prospective observational study (NCT04571086). Enrollment is offered to all patients who undergo ^{68}Ga -FAPI-46 PET in our department. Eleven patients met the following criteria: same-day ^{68}Ga -FAPI and ^{18}F -FDG PET for oncologic staging or restaging, with ^{18}F -FDG at least 4 h after ^{68}Ga -FAPI PET; ^{68}Ga -FAPI or ^{18}F -FDG tracer uptake in local soft tissue or nodes, with a visually positive target-to-background ratio on PET/CT; COVID-19 vaccination within 6 wk; and no change in treatment between PET and vaccination (Fig. 1).

The study was approved by the ethics committee (approvals 20-9485-BO and 19-8991-BO), and all patients gave written informed consent for enrollment into a prospective observational trial (NCT04571086).

Lymph nodes were considered positive when demonstrating visually focal uptake above the background level. Visual readings were performed by 2 nuclear medicine physicians in consensus. The median injected dose was 333 MBq (interquartile range [IQR], 245–421 MBq) for ^{18}F -FDG and 102 MBq (IQR, 79–125 MBq) for ^{68}Ga -FAPI. Follow-up data included imaging and clinical information. All patients fasted for 6 h before the ^{18}F -FDG scan, and blood glucose level (<200 mg/dL) was measured. Descriptive statistics are provided. An ANOVA was applied for assessing differences in SUV among the different time frames after vaccination. The SUV was measured in the center of each lymph node, determined on PET/CT images.

Six (55%) patients underwent imaging on a Siemens Biograph Vision and 5 (45%) on a Siemens Biograph mCT device. SUV_{peak} was selected on the basis of phantom cross-calibration for the PET/CT devices to achieve reproducible results.

Received Sep. 5, 2022; revision accepted Oct. 27, 2022.

For correspondence or reprints, contact Wolfgang P. Fendler (wolfgang.fendler@uk-essen.de).

Published online Nov. 17, 2022.

Immediate Open Access: Creative Commons Attribution 4.0 International License (CC BY) allows users to share and adapt with attribution, excluding materials credited to previous publications. License: <https://creativecommons.org/licenses/by/4.0/>. Details: <http://jnm.snmjournals.org/site/misc/permission.xhtml>.

COPYRIGHT © 2023 by the Society of Nuclear Medicine and Molecular Imaging.

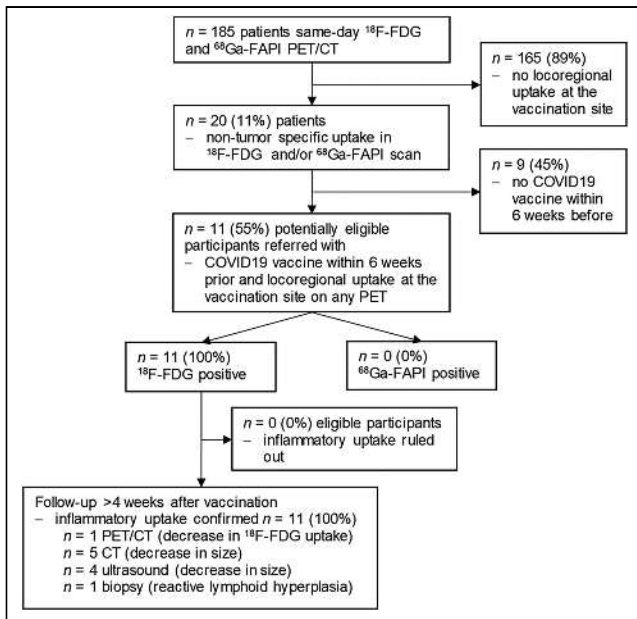


FIGURE 1. Patient flowchart.

RESULTS

Patient characteristics are shown in Supplemental Table 1 (supplemental materials are available at <http://jnm.snmjournals.org>). After database screening, 11 patients (5 men and 6 women) were included. The mean age was 44 y (IQR, 34–54 y). Three (27%) underwent PET for staging and 8 (73%) for restaging. Five (45%) patients had sarcoma, and 6 (55%) patients had carcinoma. When combined findings from ^{68}Ga -FAPI and ^{18}F -FDG scans were considered, 3 (27%) patients showed primary lesions only, 1 (9%) patient showed locoregional lesions, and 7 (64%) patients showed distant metastases. Distant metastatic disease was noted in visceral organs, bone, and soft tissue in 5 (45%), 1 (9%), and 1 (9%) patients, respectively. The thoracic cavity was tumor-free in 7 (64%) patients. Before chemotherapy, 2 (18%) of 11 patients had a thoracic primary tumor, that is, lung ($n = 1$) and breast cancer ($n = 1$), which have a higher likelihood of axillary nodal involvement (Supplemental Table 2).

Ten (91%) patients received BNT162b2 vaccine and 1 (9%) received messenger RNA1273 vaccine at a median interval of 19 d (IQR, 8–30 d) before PET/CT. Eleven (100%) patients demonstrated focal ^{18}F -FDG tracer uptake in axillary lymph nodes on PET/CT; none of the patients had focal ^{68}Ga -FAPI uptake. Details are listed in Supplemental Table 3. SUV at different times after vaccination (Fig. 2A) demonstrated the highest ^{18}F -FDG accumulation in lymph nodes at 2–4 wk after vaccination (ANOVA $P = 0.002$), whereas no increase in uptake on ^{68}Ga -FAPI was observed at any of the time points (Fig. 2B, ANOVA $P = 0.79$).

Imaging follow-up data at an average of 120 d (IQR, 44–196 d) confirmed reactive nodal uptake in all patients: a decrease in

uptake was documented in all 4 (100%) lymph nodes of the patient who underwent follow-up ^{18}F -FDG PET/CT. A decrease in lymph node size was documented for all patients (on CT, $n = 5$ [100%]; on ultrasound, $n = 4$ [100%]). One patient underwent a biopsy confirming reactive lymphoid hyperplasia with no evidence of malignancy (Supplemental Fig. 1). Further tracer accumulation at the injection site in the deltoid muscle was detected in 5 (45%) patients (Supplemental Fig. 2.2). Another patient showed generalized tracer accumulation in the bone marrow on ^{18}F -FDG PET in addition to splenic uptake above the level of liver uptake, indicating reactive bone marrow and splenic activation by a vaccine-induced immune response (Supplemental Fig. 3). According to combined ^{18}F -FDG and ^{68}Ga -FAPI PET/CT reports, none of the patients had tumor involvement of the arm or axillary lymph nodes. One patient with breast cancer demonstrated new bone metastases 4 y after initial therapy. Local recurrence was not noted, and focal nodal uptake was seen ipsilateral to the vaccination site and contralateral to the former tumor site.

The combined analysis of ^{68}Ga -FAPI and ^{18}F -FDG scans detected, in total, 102 (100%) tumor lesions (primary, 6 [6%]; locoregional, 26 [25%]; distant nodal, 10 [10%]; lung, 7 [7%]; liver, 18 [18%]; bone, 28 [27%]; and soft tissue, 7 [7%]). Lesion detection efficacy was higher for ^{68}Ga -FAPI than for ^{18}F -FDG PET (96 [94%] vs. 74 [73%]). ^{68}Ga -FAPI PET detected additional tumor lesions in the lung (7 [100%] vs. 5 [71%]), liver (17 [94%] vs. 9 [50%]), and bone (28 [100%] vs. 23 [82%]). The superior efficacy was based on a higher detection rate in 3 patients with different tumor entities (ovarian cancer, solitary fibrous tumor, and breast cancer). There was no ^{18}F -FDG–positive, ^{68}Ga -FAPI–negative primary tumor lesion (Supplemental Table 4).

Representative images are shown for all included patients in Supplemental Figures 1–11.

DISCUSSION

The COVID-19 pandemic is active globally, with an estimated 12.8 billion vaccine doses given and 627.1 million registered infections as of October 21, 2022 (5). Vaccines aim to decrease COVID-19 spread and severe disease, protecting vulnerable groups, including cancer patients (6). Repeat vaccinations have been endorsed by the

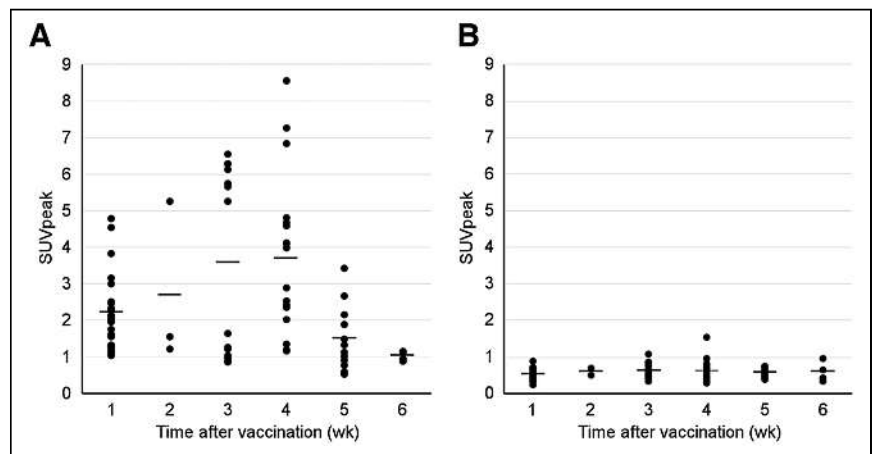


FIGURE 2. SUV_{peak} over time for 78 locoregional lymph nodes for ^{18}F -FDG (ANOVA $P = 0.002$) (A) and ^{68}Ga -FAPI (ANOVA $P = 0.791$) (B) PET/CT. Average SUV_{peak} for weeks 1, 2, 3, 4, 5, and 6 was 2.2, 2.7, 3.6, 3.7, 1.5, and 1.0, respectively, for ^{18}F -FDG PET and 0.5, 0.6, 0.6, 0.6, 0.6, and 0.6, respectively, for ^{68}Ga -FAPI PET.

Centers for Disease Control and many national infection agencies (7). Thus, most cancer patients underwent 3 vaccinations within the last year (7). On the basis of current knowledge about decreasing protection over time and the emergence of new variants, vaccination at least annually is the likely scenario (8–10). For vulnerable groups, repeat COVID-19 vaccination will come in addition to annual flu shots.

Postvaccination lymph node uptake on ^{18}F -FDG PET has been demonstrated in prior case reports or case series on COVID-19 and flu vaccine for a variety of tumor entities (1–4, 11–16). An increase in annual vaccination will put oncologic patients at considerable risk of false-positive ^{18}F -FDG PET findings. Here, we confirmed ^{18}F -FDG uptake within 6 wk of vaccination in a case series of oncologic patients. Nonspecific ^{18}F -FDG uptake will adversely influence staging and restaging procedures in oncology patients (3). Patients are at risk of false-positive lymph node findings when undergoing ^{18}F -FDG PET/CT within 6 wk of vaccination. Therefore, PET/CT appointments for patients at risk must be planned carefully with consideration of any vaccination. In addition, bone marrow uptake was seen in 1 patient, pointing to an additional pitfall in patients with myeloproliferative disease (2).

The regulation of fibroblast activation protein α in cancer is not completely understood. Transforming growth factor β , associated with epithelial–mesenchymal transition, angiogenesis, or immune suppression, participates in the upregulation of fibroblast activation protein α expression, suggesting a lower susceptibility of ^{68}Ga -FAPI PET to acute inflammation (17). Fittingly, none of the patients demonstrated focal ^{68}Ga -FAPI uptake in locoregional lymph nodes after vaccination. In addition, ^{68}Ga -FAPI PET demonstrated higher detection efficacy when compared with ^{18}F -FDG PET/CT both for locoregional and for distant staging. Tumor detection was based on the PET/CT findings; however, lesions were not verified by imaging follow-up, and findings are limited by a low sample size. Superior detection for ^{68}Ga -FAPI versus ^{18}F -FDG PET is in line with previous reports on carcinoma of unknown primary, sarcoma, and breast carcinoma imaging (18). Our findings indicate that ^{68}Ga -FAPI PET delivers oncologic staging with accuracy equal or superior to that of ^{18}F -FDG PET but with no risk of a false diagnosis after vaccination (19).

An ongoing prospective trial at our institution aims to assess accuracy and correlation with histopathology for various types of cancer (clinicaltrials.gov, NCT05160051). Our study was limited by a low number of patients and a low histopathologic confirmation rate for lymph node findings.

CONCLUSION

Increased annual vaccinations are expected for vulnerable groups, including cancer patients. ^{18}F -FDG may trigger costly follow-up investigations and false management decisions. In our study, ^{68}Ga -FAPI PET, a promising novel imaging tool, avoided postvaccination lymph node and bone marrow pitfalls and provided accurate oncologic staging. ^{68}Ga -FAPI PET should be assessed as an alternative to ^{18}F -FDG PET in ongoing (NCT05160051) and future prospective studies.

DISCLOSURE

Katharina Lueckerath reports fees from SOFIE Bioscience (consultant) and Enlaza Therapeutics (consultant). Rainer Hamacher is supported by the Clinician Scientist Program of the University Medicine Essen Clinician Scientist Academy sponsored by the

faculty of medicine and Deutsche Forschungsgemeinschaft (DFG) and has received travel grants from Lilly, Novartis, and PharmaMar, as well as fees from Lilly and PharmaMar. Jens Siveke received honoraria as a consultant or for continuing medical education presentations from AstraZeneca, Bayer, Bristol-Myers Squibb, Eisbach Bio, Immunocore, Novartis, Roche/Genentech, and Servier; his institution receives research funding from Bristol-Myers Squibb, Celgene, Eisbach Bio, and Roche/Genentech; he holds ownership and serves on the board of directors of Pharma15. Benedikt Schaarschmidt received a research grant from PharmaCep for an ongoing investigator-initiated study not related to this paper. Ken Herrmann reports personal fees from Bayer, Sofie Biosciences, SIRTEX, Adacap, Curium, Endocyte, BTG, IPSEN, Siemens Healthineers, GE Healthcare, Amgen, Novartis, ymabs, Aktis Oncology, Theragnostics, and Pharma15; other fees from Sofie Biosciences; nonfinancial support from ABX; and grants from BTG. Wolfgang P. Fendler reports fees from Sofie Biosciences (research funding), Janssen (consultant, speakers' bureau), Calyx (consultant), Bayer (consultant, speakers' bureau, research funding), Parexel (image review), and AAA (speakers' bureau). All disclosures were outside the submitted work. No other potential conflict of interest relevant to this article was reported.

ACKNOWLEDGMENTS

We thank the patients who volunteered to participate in this trial and the investigators and staff who cared for them.

KEY POINTS

QUESTION: Can ^{68}Ga -FAPI PET prevent COVID-19 vaccine-related reactive lymph node uptake?

PERTINENT FINDINGS: We compared ^{18}F -FDG and ^{68}Ga -FAPI PET/CT acquired on the same day within 6 wk of COVID-19 vaccination in 11 oncology patients. Although ^{18}F -FDG was visually positive in 11 patients, ^{68}Ga -FAPI had higher tumor detection efficacy and showed no vulnerability to vaccine-related tracer uptake in any patients. Additionally, the ^{18}F -FDG uptake intensity was time-dependent on the vaccination interval. ^{68}Ga -FAPI was visually negative at all time points.

IMPLICATIONS FOR PATIENT CARE: ^{68}Ga -FAPI avoids vaccine-associated reactive lymph node uptake and is therefore superior to ^{18}F -FDG in tumor staging up to 6 wk after COVID-19 vaccination.

REFERENCES

1. Eifer M, Eshet Y. Imaging of COVID-19 vaccination at FDG PET/CT. *Radiology*. 2021;299:E248.
2. Nawwar AA, Searle J, Lyburn ID. Features of systemic immune response from COVID-19 vaccination on ^{18}F -FDG PET/CT. *Clin Nucl Med*. 2022;47:e89–e90.
3. Becker AS, Perez-Johnston R, Chikarmane SA, et al. Multidisciplinary recommendations regarding post-vaccine adenopathy and radiologic imaging: radiology scientific expert panel. *Radiology*. 2021;300:E323–E327.
4. Adin ME, Isufi E, Kulon M, Pucar D. Association of COVID-19 mRNA vaccine with ipsilateral axillary lymph node reactivity on imaging. *JAMA Oncol*. 2021;7:1241–1242.
5. COVID-19 dashboard by the Center for Systems Science and Engineering (CSSE) at Johns Hopkins University (JHU), Johns Hopkins website. <https://coronavirus.jhu.edu/map.html>. Accessed October 21, 2022.
6. Wang Q, Berger NA, Xu R. Analyses of risk, racial disparity, and outcomes among US patients with cancer and COVID-19 infection. *JAMA Oncol*. 2021;7:220–227.
7. Barrière J, Carles M, Audigier-Valette C, et al. Third dose of anti-SARS-CoV-2 vaccine for patients with cancer: should humoral responses be monitored? A position article. *Eur J Cancer*. 2022;162:182–193.

8. Rubin R. COVID-19 vaccine makers plan for annual boosters, but it's not clear they'll be needed. *JAMA*. 2021;326:2247–2249.
9. Chudasama RV, Khunti K, Ekezie WC, et al. COVID-19 vaccine uptake and hesitancy opinions from frontline health care and social care workers: Survey data from 37 countries. *Diabetes Metab Syndr*. 2022;16:102361
10. Bar-On YM, Goldberg Y, Mandel M, et al. Protection by 4th dose of BNT162b2 against omicron in Israel. medRxiv website. <https://www.medrxiv.org/content/10.1101/2022.02.01.22270232v1>. Published February 1, 2022. Accessed December 8, 2022.
11. Treglia G, Cuzzocrea M, Giovanella L, Elzi L, Muoio B. Prevalence and significance of hypermetabolic lymph nodes detected by 2-[¹⁸F]FDG PET/CT after COVID-19 vaccination: a systematic review and a meta-analysis. *Pharmaceuticals*. 2021;14:762.
12. Özütemiz C, Krystosek LA, Church AL, et al. Lymphadenopathy in COVID-19 vaccine recipients: diagnostic dilemma in oncologic patients. *Radiology*. 2021;300: E296–E300.
13. Thomassen A, Lerberg Nielsen A, Gerke O, Johansen A, Petersen H. Duration of ¹⁸F-FDG avidity in lymph nodes after pandemic H1N1v and seasonal influenza vaccination. *Eur J Nucl Med Mol Imaging*. 2011;38:894–898.
14. Weeks JK, O'Brien SR, Rosenspire KC, Dubroff JG, Pantel AR. Evolving bilateral hypermetabolic axillary lymphadenopathy on FDG PET/CT following 2-dose COVID-19 vaccination. *Clin Nucl Med*. 2021;46:1011–1012.
15. Indini A, Costa S, Ierardi AM, Rijavec E, Passoni E, Grossi F. COVID-19 vaccination mimicking lymph-node progression in a patient with melanoma: a case report. *Melanoma Res*. 2021;31:490–493.
16. Andresciani F, Ricci M, Grasso RF, Zobel BB, Quattrocchi CC. COVID-19 vaccination simulating lymph node progression in a patient with prostate cancer. *Radiol Case Rep*. 2022;17:2996–2999.
17. Krepela E, Vanickova Z, Hrabal P, et al. Regulation of fibroblast activation protein by transforming growth factor beta-1 in glioblastoma microenvironment. *Int J Mol Sci*. 2021;22:1046.
18. Giesel FL, Kratochwil C, Schlittenhardt J, et al. Head-to-head intra-individual comparison of biodistribution and tumor uptake of ⁶⁸Ga-FAPI and ¹⁸F-FDG PET/CT in cancer patients. *Eur J Nucl Med Mol Imaging*. 2021;48:4377–4385.
19. Çermik TF, Ergü L N, Yilmaz BA, Mercanoğ Lu GL. Tumor imaging with ⁶⁸Ga-DOTA-FAPI-04 PET/CT: comparison with ¹⁸F-FDG PET/CT in 22 different cancer types. *Clin Nucl Med*. 2022;47:e333–e339.

PSMA-Directed Imaging and Therapy of Salivary Gland Tumors: A Single-Center Retrospective Study

Caner Civan^{1,2}, Stefan Kasper^{2,3}, Christoph Berliner^{1,2}, Pedro Fragoso-Costa^{1,2}, Viktor Grünwald^{2,3}, Michael Pogorzelski^{2,3}, Benedikt Michael Schaarschmidt^{2,4}, Stephan Lang^{2,5}, David Kersting^{1,2}, Michael Nader¹, Katharina Lückerath^{1,2}, Ken Herrmann^{1,2}, Wolfgang P. Fendler^{*1,2}, and Manuel Weber^{*1,2}

¹Department of Nuclear Medicine, University Hospital Essen, Essen, Germany; ²German Cancer Consortium, partner site Essen, Essen, Germany; ³Department of Medical Oncology, West German Cancer Center, University Hospital Essen, Essen, Germany;

⁴Institute of Diagnostic and Interventional Radiology and Neuroradiology, University of Duisburg–Essen, Essen, Germany; and

⁵Head and Neck Surgery, Department of Otorhinolaryngology, University Hospital Essen, University Duisburg–Essen, Essen, Germany

We analyzed the diagnostic performance of prostate-specific membrane antigen (PSMA) PET/CT and the dosimetry, efficacy, and safety of ¹⁷⁷Lu-PSMA-617 radioligand therapy (RLT) in salivary gland malignancies (SGMs). **Methods:** We identified 28 SGM patients with PSMA PET/CT from our database. CT and PSMA PET/CT images were evaluated separately by 3 masked readers in joint reading sessions. Pathologic findings were grouped into 6 TNM regions, and lesion-based disease extent was classified as no disease ($n = 1$, 4%), unifocal ($n = 2$, 7%), oligometastatic ($n = 9$, 32%), multifocal ($n = 3$, 11%), or disseminated ($n = 13$, 47%). For each region, the SUV_{max} of the lesion with the highest uptake was measured and the visual PSMA expression score was evaluated on a per-patient basis using PROMISE criteria. The association between PSMA expression and clinical and histopathologic markers was tested using the Student *t* test. Five patients underwent PSMA RLT with intratherapeutic dosimetry. Response was assessed using RECIST 1.1, and adverse events were graded according to version 5.0 of the Common Terminology Criteria for Adverse Events. **Results:** Compared with CT, PSMA PET/CT demonstrated additional metastatic lesions in 11 of 28 (39%) patients, leading to upstaging of TNM and lesion-based disease extent in 3 (11%) and 6 (21%) patients, respectively. PSMA PET/CT detected CT-occult local tumor, regional lymph nodes, nonregional lymph nodes, and bone metastases in 1 (4%), 4 (14%), 2 (7%), and 4 (14%) patients, respectively; no additional lesions were detected in the other predefined regions. PSMA expression level was higher than liver in 6 patients (25%). A significantly higher SUV_{max} was observed in male than female patients (15.8 vs. 8.5, $P = 0.007$) and in bone than lung lesions (14.2 vs. 6.4, $P = 0.006$). PSMA RLT was discontinued after 1 cycle in 3 of 5 patients because of insufficient tumor doses. No adverse events of grade 4 or higher occurred. **Conclusion:** In SGMs, PSMA PET/CT demonstrated a superior detection rate and led to upstaging in about one third of patients when compared with CT. The male sex and the presence of bone metastases were associated with significantly higher PSMA expression. PSMA RLT was well tolerated, but most patients did not have more than 1 cycle because of insufficient tumor doses.

Key Words: ¹⁷⁷Lu-PSMA; ⁶⁸Ga-PSMA; PET/CT; theranostics; salivary gland malignancies

J Nucl Med 2023; 64:372–378

DOI: 10.2967/jnumed.122.264342

Salivary gland malignancies (SGMs) are rare head and neck tumors that encompass 24 different histologic subtypes, with mucoepidermoid carcinoma and adenoid cystic carcinoma (ACC) being the most frequent (1–3). SGMs most commonly originate from the parotid, submandibular, and sublingual glands and are characterized by slow growth and an indolent course but tend to show multiple recurrences and distant metastases (4). Although survival outcomes have improved with surgery and postoperative radiotherapy in early and locally advanced stages of the disease, there is no consensus on systemic treatments in recurrent or metastatic disease (5). No further standard treatment has yet been established for recurrent or metastatic disease. SGMs show a high intrinsic resistance to classic cytotoxic drugs. Recently, small phase II trials demonstrated the tyrosine kinase inhibitors lenvatinib or axitinib to have activity in ACC (6,7). Further, for a subset of patients with such specific genetic alteration as NTRK fusions, BRAF mutations, or Her2/neu amplifications, molecule-targeted therapies are available (8,9). However, for most patients, no molecule-targeted therapies are available, and those patients are treated mostly with the cytotoxic drugs cisplatin, taxanes, anthracyclines, cyclophosphamide, or 5-fluorouracil, with only a moderate response rate. Taken together, there is a huge unmet medical need to improve the palliative treatment of patients with recurrent or metastatic SGMs.

Routine imaging is performed using MRI and CT (10). Additional ¹⁸F-FDG PET can increase sensitivity, especially with regard to N or M stage, impacting therapy management in 12.5% of cases (11). Furthermore, recent immunohistochemical and PET imaging studies have shown increased prostate-specific membrane antigen (PSMA) expression in ACC, implying that PSMA-targeted imaging may improve staging accuracy and that ¹⁷⁷Lu-PSMA-617 radioligand therapy (RLT) can be feasible in a theranostic setup (12–15).

The aim of this study was to investigate the diagnostic role of PSMA PET/CT and the safety, feasibility, and efficacy of PSMA RLT in patients with SGM.

MATERIALS AND METHODS

Eligibility Criteria

Our institutional database was screened for SGM patients undergoing PSMA PET/CT from May 2015 to October 2021. All patients gave written informed consent to undergo clinical PSMA imaging or therapy. The retrospective analysis of available data was approved by the local institutional review board, and the requirement to obtain informed

Received Apr. 27, 2022; revision accepted Sep. 16, 2022.
For correspondence or reprints, contact Manuel Weber (manuel.weber@uk-essen.de).

*Contributed equally to this work.

Published online Sep. 22, 2022.

COPYRIGHT © 2023 by the Society of Nuclear Medicine and Molecular Imaging.

consent was waived (University of Duisburg–Essen, medical faculty, protocol 21-10370-BO).

PSMA PET/CT Image Acquisition

Values are presented as median and interquartile range. Images were acquired in accordance with the joint procedure guidelines of the European Association of Nuclear Medicine and the Society of Nuclear Medicine and Molecular Imaging: 63 min (26 min) or 98 min (21 min) after the administration of 116 MBq (44.5 MBq) of ^{68}Ga -PSMA-11 ($n = 21$, 75%) or 281 MBq (97 MBq) of ^{18}F -PSMA-1007 ($n = 7$, 25%), respectively (16). Images were acquired on a Biograph mCT (11/28, 39%) or Biograph Vision 600 (17/28, 61%) PET/CT system (Siemens Healthineers).

Image Interpretation

CT and PSMA PET/CT scans were analyzed separately 2 wk apart by 2 masked nuclear medicine physicians in joint consensus sessions and an additional board-certified radiologist for the CT reading session. The CT scans were read first, and for TNM-based analysis, pathologic findings were grouped into the following categories: local tumor, regional lymph nodes, nonregional lymph nodes, lung, bone, and other regions.

To assess the lesion-based disease extent, CT and PSMA PET/CT analysis results were each grouped into the following disease categories: no evidence of disease, unifocal disease (1 lesion), oligometastatic disease (2–5 lesions), multifocal disease (6–10 lesions), and disseminated disease (>10 lesions). For PSMA PET/CT analysis, the SUV_{max} of the lesion of each region with the highest uptake was measured. The PSMA expression score was assessed visually in accordance with PROMISE criteria on a per-patient level (17).

^{177}Lu -PSMA-617 RLT

PSMA RLT was performed as therapy after exhaustion of established treatment options following the decision of a multidisciplinary tumor board. An overview of patient selection is provided in Figure 1. Key eligibility criteria were adequate bone marrow and kidney function in accordance with the procedure guidelines of the European Association of Nuclear Medicine and Society of Nuclear Medicine and Molecular Imaging for PSMA RLT (18) and a PSMA expression level of at least 2 (17). Each cycle, 6.8 ± 1.4 GBq of ^{177}Lu -PSMA-617 were

administered intravenously, with a 6-wk interval between cycles. Progression-free survival was defined as the interval from treatment start until death or progressive disease according to RECIST, version 1.1, as analyzed by 2 readers in joint consensus sessions (19).

Blood count, creatinine, transaminases, and symptoms were monitored before and during PSMA RLT, and toxicity was graded according to the Common Terminology Criteria for Adverse Events, version 5.0 (20).

Dosimetry

Posttherapeutic dosimetry of tumor lesions and kidneys was performed for all patients undergoing PSMA RLT and calculated according to OLINDA/MIRD recommendations (21). SPECT/CT imaging was performed on a Siemens Intevo SPECT/CT system using the xQuant reconstruction algorithm, allowing for quantitative ^{177}Lu imaging as previously described (22). The chosen imaging schedule was set to include 4 time points (4, 24, 48, and 120–144 h) after injection, with

TABLE 1
Patient Characteristics

Characteristic	Data
Sex	
Male	11 (39%)
Female	17 (61%)
Age (y)	
Median	59
Range	30–75
Primary location	
Major salivary gland	18 (64%)
Parotid gland	8 (29%)
Submandibular gland	7 (25%)
Sublingual gland	3 (11%)
Minor salivary gland	10 (36%)
Clinical indications	
Staging	2 (7%)
Restaging	12 (43%)
Evaluation for RLT	14 (50%)
Previous treatments	
Primary surgery	25 (89%)
Multiple surgeries	12 (43%)
Radiotherapy	24 (86%)
Chemotherapy	7 (25%)
Metastasectomy	9 (32%)
Palliative radiotherapy	6 (21%)
Disease sites at ^{68}Ga -PSMA PET/CT	
Local tumor	8 (29%)
Locoregional lymph node metastases	5 (18%)
Nonlocoregional lymph node metastases	4 (14%)
Lung metastases	14 (50%)
Bone metastases	10 (36%)
Other metastases	10 (36%)

Data are number and percentage, except for age.

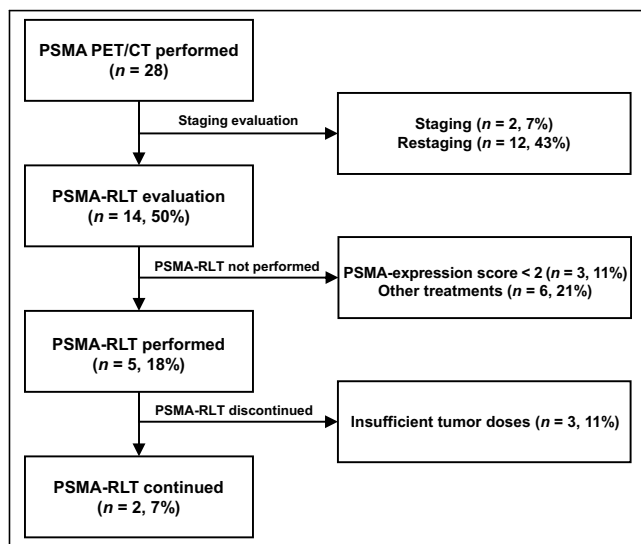


FIGURE 1. CONSORT (Consolidated Standards of Reporting Trials) diagram describing SGM patient selection for PSMA-directed imaging and PSMA RLT.

TABLE 2
Characteristics of PSMA RLT Cohort

Characteristic	Patient 1	Patient 2	Patient 3	Patient 4	Patient 5
Age (y)	50	42	40	56	65
Sex	M	F	F	F	M
Histology	ACC	ACC	ACC	ACC	Acinic cell carcinoma
Initial diagnosis to RLT (y)	8	2	4	3	16
Prior treatments	Surgery*; radiotherapy; axitinib; chemotherapy	Surgery; radiotherapy	Surgery; radiotherapy*; metastasectomy	Surgery; radiotherapy	Surgery*; radiotherapy*; denosumab
Primary location	Paranasal sinus (minor salivary gland)	Parotid gland	Upper jaw (minor salivary gland)	Parotid gland	Parotid gland
Metastatic sites	Local; lung	Lung	Bone	Lung; soft tissue	Locoregional LN; bone
PSMA expression score	3	2	3	2	3
RECIST 1.1 response	PD	NA [†]	NA [†]	SD	SD
TTP after PSMA RLT	3 mo	12 mo [†]	6 mo [†]	Lost to follow-up	12 mo

*Repeated treatments.

[†]Systemic treatment started immediately after PSMA RLT.

LN = lymph nodes; PD = progressive disease; NA = not applicable; SD = stable disease; TTP = time to progression.

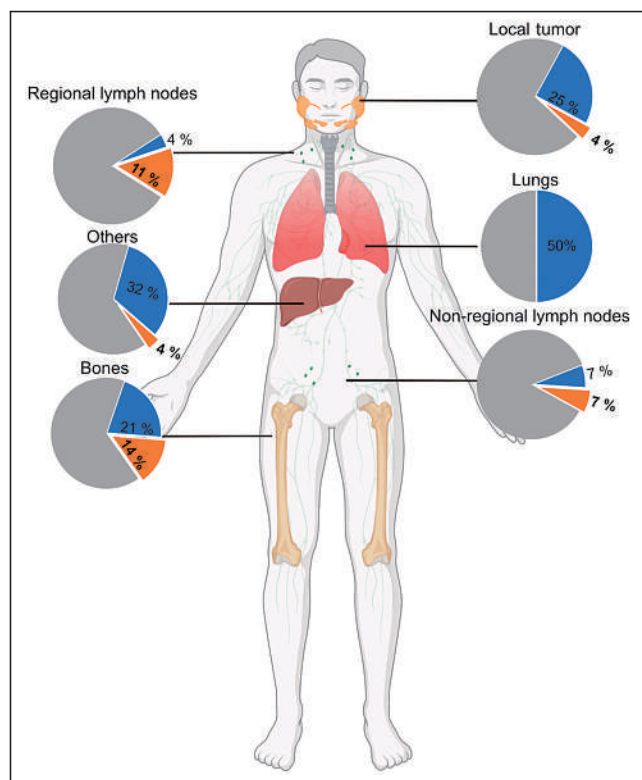


FIGURE 2. Pie charts demonstrating additional detection of diseased regions by PSMA PET/CT (orange) when compared with standalone CT (blue). Charts demonstrate percentage positive patients among 28 patients, separately for each region.

at least 2 time points considered necessary to determine lesion or kidney doses. For logistic reasons, 2 or 3 time points were acquired for each cycle, respectively.

Statistical Analysis

The statistical analyses were performed using SPSS (version 27.0; IBM). The Student *t* test was used to assess differences in SUV_{max} dependent on sex, location of the primary, and disease site (bone vs. lung).

RESULTS

Patient Characteristics

The study included 28 patients (11 men, 39%; 17 women, 61%). Histopathologic subtypes were ACC (24/28, 86%), adenocarcinoma (2/28, 7%), acinic cell carcinoma (1/28, 4%), and sebaceous carcinoma (1/28, 4%). The median age was 59 y (range, 30–75 y). The clinical indication for PSMA PET/CT was initial staging for 2 patients (7%), restaging for 12 (43%), and evaluation for PSMA RLT for 14 (50%). Five patients (18%) underwent PSMA RLT. Detailed patient characteristics are provided in Table 1.

Five of these patients (3 female, 2 male) received a total of 11 cycles of PSMA RLT (range, 1–6 cycles). The median age of PSMA RLT patients was 50 y (range, 40–65 y). Demographic and clinical information on the treatment cohort is provided in Table 2.

CT Versus PSMA PET/CT Detection Accuracy

CT detected any disease in 25 of 28 (89%) patients, local tumor in 7 (25%), regional lymph nodes in 1 (4%), and distant metastases in 22 (79%). PSMA PET was positive in 27 (96%) patients and visualized local tumor in 8 (29%), regional lymph nodes in 5 (18%), and distant metastases in 25 (89%) (Fig. 2). PSMA PET/CT demonstrated additional metastatic lesions in 11 (39%) patients; in 8 (29%)

TABLE 3
Analysis of Lesion-Based Disease Extent

CT	PSMA				
	No disease	Unifocal	Oligometastatic	Multifocal	Disseminated
No disease	1 (4%)	0	1 (4%)*	0	1 (4%)*
Unifocal	0	2 (7%)	1 (4%)*	0	0
Oligometastatic	0	0	7 (25%)	2 (7%)*	1 (4%)*
Multifocal	0	0	0	1 (4%)	0
Disseminated	0	0	0	0	11 (39%)

*Upstaging.

Data are number. Extent shifted toward higher disease burden in 6 of 28 (21%) patients after PSMA PET (oligometastatic disease, 2–5 metastases; multifocal disease, 6–10; disseminated disease, ≥ 11).

patients, CT-negative regions were rated positive on PSMA PET/CT. PSMA PET/CT detected additional bone metastases in 2 patients (7%) and nonregional lymph node metastases in 1 patient (4%), with no disease shown on CT (TNM upstaging). PSMA PET/CT led to an up-shift of lesion-based disease extent in 6 (21%) patients (Table 3). Figure 3 shows an example SGM patient, in whom additional bone lesions were detected by PSMA PET/CT.

In 6 (21%) patients ^{18}F -FDG and PSMA PET/CT were performed within a 3-mo interval without interim progression on morphologic imaging. Of the 6 patients, 2 had higher detection efficacy for PSMA PET/CT, 2 had higher detection efficacy for ^{18}F -FDG PET/CT, and 2 had equal detection efficacy for both modalities.

PSMA Ligand Uptake

PSMA expression score was 0 ($n = 2$, 7%), 1 ($n = 4$, 15%), 2 ($n = 15$, 56%), and 3 ($n = 6$, 22%), respectively (Fig. 4). The male sex (15.8 vs. 8.5, $P = 0.007$) was significantly associated with a higher SUV_{max} (Table 4). The mean SUV_{max} in tumor sites of

patients with a primary tumor in the minor salivary glands was 12.8, versus 9.0 in those with a primary in the major salivary glands, without statistical significance ($P = 0.31$). SUV_{max} was significantly higher in bone than lung metastases (14.2 vs. 6.4, $P = 0.006$).

PSMA RLT Absorbed Dose and Efficacy

In total, 5 patients received PSMA RLT. Dosimetry was performed for the kidneys and a total of 13 tumor lesions over 7 therapy cycles. The highest lesion-absorbed dose was 0.68 Gy/GBq (mean, 0.41 Gy/GBq; range, 0.06–0.68 Gy/GBq). The highest lesion uptake ratio after 24 h was 0.44 (mean, 0.16; range, 0.004–0.44). The mean effective half-life of the lesions was 7.7 min (range, 0.32–30.98 min). The mean kidney-absorbed dose was 0.37 Gy/GBq (range, 0.32–0.41 Gy/GBq). Dosimetry results for each cycle are shown in Table 5.

PSMA RLT was discontinued in 3 patients after 1 cycle because visual lesion uptake was below liver uptake on the 24-h posttreatment ^{177}Lu -PSMA scintigraphy. In these 3 patients, systemic treatment was initiated before progression occurred. Progression-free survival was 3 mo ($n = 1$) or not reached ($n = 1$, last follow-up: 12 mo) after initiation of PSMA RLT in the 2 patients remaining with more than 1 treatment cycle. The long-term response was observed in the only patient with acinic cell carcinoma, with the remainder having ACC. Supplemental Figure 1 shows a patient example (supplemental materials are available at <http://jnm.snmjournals.org>).

PSMA RLT Adverse Events and Follow-up

Changes in blood parameters did not meet the adverse-event criteria of the Common Terminology Criteria for Adverse Events, version 5.0. Xerostomia that was less than serious was reported by both patients undergoing more than 1 cycle of PSMA RLT, without worsening under treatment.

DISCUSSION

The results of our study indicate a superior detection rate for PSMA PET/CT in

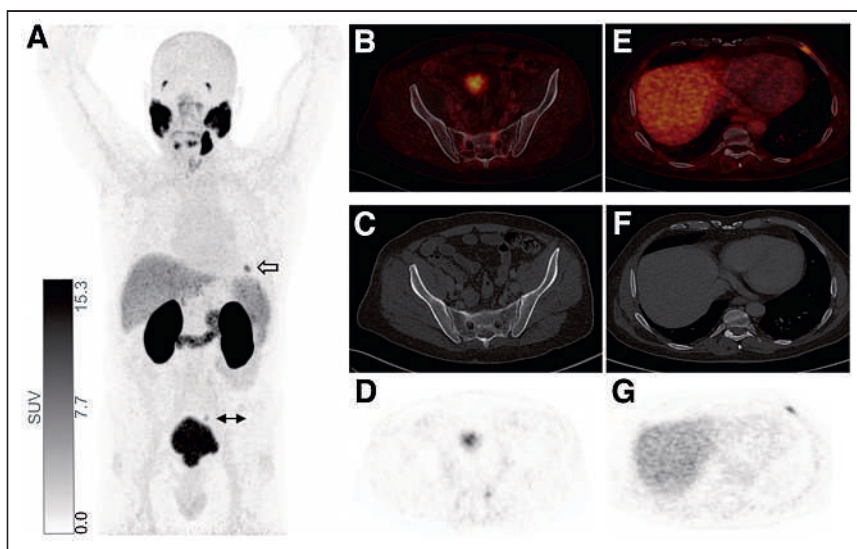


FIGURE 3. ^{68}Ga -PSMA PET/CT of 69-y-old man with adenoid-cystic carcinoma of right submandibular gland after primary resection. Maximum-intensity projection (A) and axial slices (B–E) of ^{68}Ga -PSMA PET/CT reveal bone metastases in sixth left rib (white arrow) and sacral bone (black arrow) without CT correlate (F and G), confirmed by follow-up imaging 6 mo later.

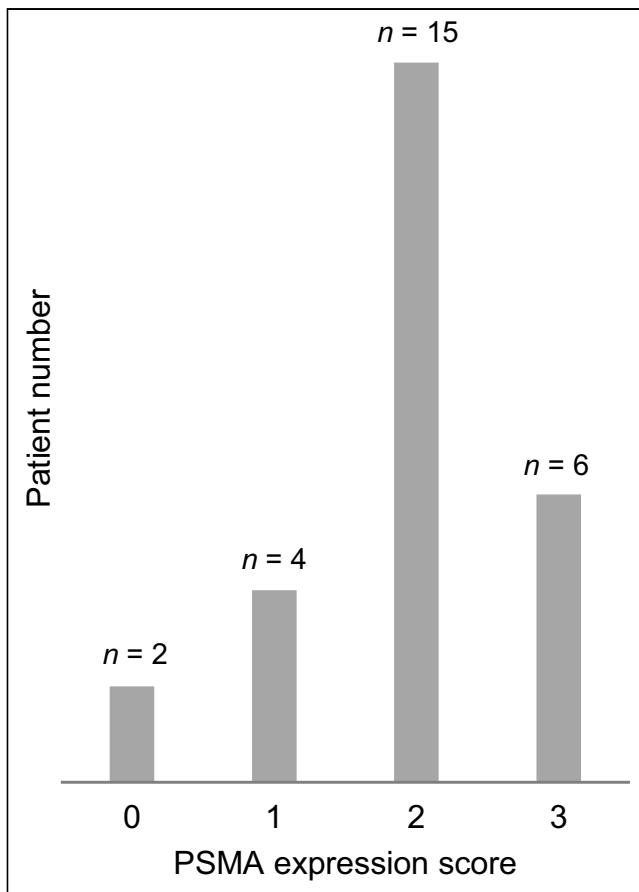


FIGURE 4. PSMA expression score by PROMISE criteria for 27 patients. One patient without any detected lesion was excluded.

SGMs, with additional localization of lesions in 11 of 28 patients (39%) and TNM upstaging in 3 (11%) patients through the detection of CT-occult oligometastatic bone metastases. Therefore, in salivary gland tumors PSMA PET/CT may be a possible alternative to other hybrid imaging modalities such as ^{18}F -FDG PET/CT or PET/MRI (11,23). In addition, PSMA PET/CT identifies candidates for PSMA RLT, which was well tolerated and induced a tumor response.

PSMA PET/CT revealed oligometastatic disease in 9 of 28 (32%) patients (Table 3). Accurate localization of disease supports planning of metastasis-directed therapy. Metastasis-directed therapy of oligometastatic head and neck cancer, including SGMs, has been shown to result in high disease-control rates (24), which underline the importance of sensitive imaging to further optimize this treatment option. PSMA PET/CT revealed multifocal or disseminated disease in 3 of 9 (33%) patients with CT oligometastatic disease. Detection of multifocal or disseminated disease may thereby more accurately identify patient candidates for systemic therapy not likely to benefit from local treatment alone.

Seventy-five percent of patients had at least 1 lesion with PSMA uptake equal to or higher than liver uptake, with significantly higher PSMA expression occurring in male patients and bone lesions (Table 4). Boxel et al. likewise demonstrated high tumor uptake (13). Higher PSMA expression in male patients is not supported by current knowledge of PSMA regulation pathways, since high androgen levels suppress the PSMA encoding gene folate hydrolase 1, potentially reducing PSMA expression levels (25). This finding has been demonstrated in prostate cancer patients, in whom prolonged androgen-deprivation therapy was linked to increases in PSMA expression (26). Likewise, the androgen axis can be active in patients with SGMs, and the efficacy and safety of androgen receptor-targeted treatment is currently being investigated in a prospective single-arm clinical trial (NCT04325828). In line with this

TABLE 4

Comparison of SUV_{max} for Sex, Primary Location at Initial Diagnosis, Bone Metastasis vs. Lung Metastasis, and Subtype

Parameter	<i>n</i>	Average SUV_{max}	<i>P</i>
Total patients	28 (100%)	10.7 (SD, 7.8)	
Sex			
Male	11 (39%)	15.8 (SD, 9.8)	
Female	17 (61%)	8.5 (SD, 4.9)	0.001*
Primary location at primary diagnosis			
Major salivary glands	18 (64%)	9 (SD, 4.4)	
Minor salivary glands	10 (36%)	12.8 (SD, 8.4)	0.308
Metastasis sites			
Bone	14 (50%)	14.2 (SD, 10.2)	
Lung	16 (57%)	6.4 (SD, 4.2)	
Other	7 (25%)	8.8 (SD, 2.8)	0.006*
Subtype			
ACC	24 (86%)	10.1 (SD, 5.9)	
Other	4 (14%)	14.2 (SD, 16)	0.352

**P* < 0.05, assessed by Student *t* test.

TABLE 5
Results of Individual Patient Dosimetry

Patient no.	Cycle no.	Activity (GBq)	Lesion 1			Lesion 2			Renal AD (Gy/GBq)		
			Type	AD (Gy/GBq)	SUV _{max}	SUV _{mean}	Type	AD (Gy/GBq)		SUV _{max}	SUV _{mean}
1	1	7.6	Lung	0.06	11.9	6.1	Recurrent	0.42	22.9	14.6	0.35
	2	7.5	Lung	0.08	11.9	6.1	Recurrent	0.23	22.9	14.6	0.32
2	1	7.5	Lung	0.26	9	5					
3	1	6.1	Bone	0.68	11.2	7.7	Bone	0.22	16.4	10.4	0.38
4	1	5.8	Lung	0.42	7.2	4	Lung	0.65	13.7	7	
5	1	6.1	Bone	0.41	27.1	14.9	Bone	0.49	30	17.4	0.39
	2	7.5	Bone	0.17	27.1	14.9	Bone	0.25	30	17.4	0.34

AD = absorbed dose.

possibility, an immunohistochemistry study by Boxtel et al. showed higher PSMA expression in tumor cells of SGMs in women than in men, attributed to lower levels of circulating androgens (27). In contrast to immunohistochemistry findings, PSMA PET/CT allows for the in vivo noninvasive assessment of target PSMA expression in entire lesions and at multiple tumor sites. PSMA PET/CT indicates that male patients may be more suitable candidates for PSMA RLT. However, because the small sample size is conducive to the occurrence of type 1 errors, further analyses of larger cohorts are warranted.

In our case series, PSMA RLT was well tolerated. Events grade 3 or higher in the Common Terminology Criteria for Adverse Events were not noted. There was no treatment-limiting xerostomia. In line with this finding, side effects of PSMA RLT were grade 1–2 in a study by Klein Nulent et al., and only 1 patient experienced grade 3 thrombocytopenia (28). However, tumor-absorbed doses in our patients were unsatisfactory. Although high PSMA expression was noted on both PSMA PET/CT and early posttreatment SPECT/CT, retention times of PSMA uptake were short, resulting in lower absorbed doses than in prostate cancer. A potential explanation is the low detection threshold of PSMA PET/CT, resulting in a high target-to-background signal that may lead to an overestimation of PSMA expression (29).

To our knowledge, this was the largest study so far to evaluate the dosimetry of PSMA RLT in SGMs. Uijen et al. reviewed a total of 15 cycles of PSMA RLT in 10 non-prostate cancer patients, also including 2 patients with SGMs (30). Klein Nulent et al. demonstrated the first case of ACC treated with PSMA RLT, but treatment response or dosimetry data were not reported (14). Has Simsek et al. reported 1 ACC patient treated with PSMA RLT, revealing intense metastatic PSMA uptake on posttreatment imaging performed after 24 h (15). Klein Nulent et al. reported the first cohort study to evaluate the efficacy and safety of PSMA RLT in SGMs (28). Six patients with SGMs were treated with PSMA RLT, which resulted radiologically stable disease in 2 patients after 4 cycles and a clinical response such as pain relief, less dyspnea, and less fatigue in 4 patients after 2 or 4 cycles of PSMA RLT (28).

In our study, tumor stabilization over more than 1 y was observed for only 1 of 5 PSMA RLT patients, indicating that further improvement is needed. In the future, RLT may be improved by more stringent patient selection, application of higher-activity

regimens, or introduction of α -based RLT. Further research focusing on histopathologic subtypes, specifically on PSMA RLT in acinic cell carcinoma, may be of interest.

Limitations of this study include its retrospective, single-center design and small sample size.

CONCLUSION

PSMA PET/CT demonstrated superior tumor detection and led to upstaging in about one third of SGM patients when compared with CT. The male sex and the presence of bone metastases were associated with significantly higher PSMA expression. PSMA RLT was tolerated well and stabilized disease in 1 patient. However, frequent discontinuation after 1 PSMA RLT cycle and low tumor-absorbed doses indicate that PSMA RLT for SGM needs further improvement.

DISCLOSURE

Wolfgang Fendler received financial support from the German Research Foundation (Deutsche Forschungsgemeinschaft grant FE1573/3-1/659216) and Wiedenfeld-Stiftung/Stiftung Krebsforschung Duisburg. Manuel Weber reports fees from Boston Scientific, Terumo, Eli Lilly, and Advanced Accelerator Applications, outside the submitted work. Christoph Berliner reports personal fees from Janssen (speakers' bureau), ABX (image review), and Roche (image review) outside the submitted work. Ken Herrmann reports personal fees from Bayer, Sofie Biosciences, SIRTEX, Adapcap, Curium, Endocyte, BTG, IPSEN, Siemens Healthineers, GE Healthcare, Amgen, Novartis, ymabs, Aktis Oncology, Theragnostics, and Pharma15; other fees from Sofie Biosciences; nonfinancial support from ABX; and grants from BTG, outside the submitted work. David Kersting is supported by the Universitätsmedizin Essen Clinician Scientist Academy/German Research Foundation and reports research funding from Pfizer outside the submitted work. Benedikt Schaarschmidt is supported by a research grant from PharmaCept, outside the submitted work. Wolfgang Fendler reports fees from Sofie Biosciences (research funding), Janssen (consultant, speakers' bureau), Calyx (consultant), Bayer (consultant, speakers' bureau), and Parexel (image review) outside the submitted work. No other potential conflict of interest relevant to this article was reported.

KEY POINTS

QUESTION: Is PSMA a potential target for theranostic applications in SGMs?

PERTINENT FINDINGS: In SGMs, PSMA PET/CT has a higher detection rate than conventional imaging and led to upstaging in about one third of patients. ¹⁷⁷Lu-PSMA-617 treatment was tolerable and resulted in disease stabilization in 1 patient with acinic cell carcinoma.

IMPLICATIONS FOR PATIENT CARE: Preliminary findings demonstrate a superior detection rate for PSMA PET/CT compared with CT in SGMs and a potential role for PSMA RLT in a subset of patients. Prospective studies on larger collectives are warranted.

REFERENCES

1. El-Naggar AK, Chan JKC, Grandis JR, Takata T, Slootweg PJ, eds. *WHO Classification of Head and Neck Tumours*. International Agency for Research on Cancer; 2017:162–185.
2. Atallah S, Casiraghi O, Fakhry N, et al. A prospective multicentre REFCOR study of 470 cases of head and neck adenoid cystic carcinoma: epidemiology and prognostic factors. *Eur J Cancer*. 2020;130:241–249.
3. Binesh F, Akhavan A, Masumi O, Mirvakili A, Behniafard N. Clinicopathological review and survival characteristics of adenoid cystic carcinoma. *Indian J Otolaryngol Head Neck Surg*. 2015;67:62–66.
4. Lorini L, Ardighieri L, Bozzola A, et al. Prognosis and management of recurrent and/or metastatic head and neck adenoid cystic carcinoma. *Oral Oncol*. 2021;115:105213.
5. Colevas AD, Yom SS, Pfister DG, et al. NCCN guidelines insights: head and neck cancers, version 1.2018. *J Natl Compr Canc Netw*. 2018;16:479–490.
6. Kang EJ, Ahn MJ, Ock CY, et al. Randomized phase II study of axitinib versus observation in patients with recurrent or metastatic adenoid cystic carcinoma. *Clin Cancer Res*. 2022;27:5272–5279.
7. Tchekmedyian V, Sherman EJ, Dunn L, et al. Phase II study of lenvatinib in patients with progressive, recurrent or metastatic adenoid cystic carcinoma. *J Clin Oncol*. 2019;37:1529–1527.
8. Kurzrock R, Bowles D, Kang H, et al. Targeted therapy for advanced salivary gland carcinoma based on molecular profiling: results from MyPathway, a phase IIa multiple basket study. *Ann Oncol*. 2020;31:412–421.
9. Hong DS, DuBois SG, Kummer S, et al. Larotrectinib in patients with TRK fusion-positive solid tumours: a pooled analysis of three phase 1/2 clinical trials. *Lancet Oncol*. 2020;21:531–540.
10. Wang X, Luo Y, Li M, Yan H, Sun M, Fan T. Management of salivary gland carcinomas: a review. *Oncotarget*. 2017;8:3946–3956.
11. Ruhlmann V, Poeppel TD, Veit J, et al. Diagnostic accuracy of ¹⁸F-FDG PET/CT and MR imaging in patients with adenoid cystic carcinoma. *BMC Cancer*. 2017;17:887.
12. De Keizer B, Krijger GC, Ververs FT, Van Es RJ, De Bree R, Willems S. ⁶⁸Ga-PSMA PET-CT imaging of metastatic adenoid cystic carcinoma. *Nucl Med Mol Imaging*. 2017;51:360–361.
13. van Boxtel W, Lütje S, van Engen-van Grunsven IC, et al. ⁶⁸Ga-PSMA-HBED-CC PET/CT imaging for adenoid cystic carcinoma and salivary duct carcinoma: a phase 2 imaging study. *Theranostics*. 2020;10:2273–2283.
14. Klein Nulent TJ, van Es RJ, Krijger GC, de Bree R, Willems SM, de Keizer B. Prostate-specific membrane antigen PET imaging and immunohistochemistry in adenoid cystic carcinoma: a preliminary analysis. *Eur J Nucl Med Mol Imaging*. 2017;44:1614–1621.
15. Has Simsek D, Kuyumcu S, Agaoglu FY, Unal SN. Radionuclide therapy with ¹⁷⁷Lu-PSMA in a case of metastatic adenoid cystic carcinoma of the parotid. *Clin Nucl Med*. 2019;44:764–766.
16. Fendler WP, Eiber M, Beheshti M, et al. ⁶⁸Ga-PSMA PET/CT: joint EANM and SNMMI procedure guideline for prostate cancer imaging—version 1.0. *Eur J Nucl Med Mol Imaging*. 2017;44:1014–1024.
17. Eiber M, Herrmann K, Calais J, et al. Prostate cancer molecular imaging standardized evaluation (PROMISE): proposed miTNM classification for the interpretation of PSMA-ligand PET/CT. *J Nucl Med*. 2018;59:469–478.
18. Kratochwil C, Fendler WP, Eiber M, et al. EANM procedure guidelines for radionuclide therapy with ¹⁷⁷Lu-labelled PSMA-ligands (¹⁷⁷Lu-PSMA-RLT). *Eur J Nucl Med Mol Imaging*. 2019;46:2536–2544.
19. Eisenhauer EA, Therasse P, Bogaerts J, et al. New response evaluation criteria in solid tumours: revised RECIST guideline (version 1.1). *Eur J Cancer*. 2009;45:228–247.
20. Common terminology criteria for adverse events (CTCAE), version 5.0. Cancer Therapy Evaluation Program website. https://ctep.cancer.gov/protocoldevelopment/electronic_applications/docs/ctcae_v5_quick_reference_5x7.pdf. Published November 27, 2017. Accessed December 15, 2022.
21. Stabin MG, Sparks RB, Crowe E. OLINDA/EXM: the second-generation personal computer software for internal dose assessment in nuclear medicine. *J Nucl Med*. 2005;46:1023–1027.
22. Tran-Gia J, Lassmann M. Characterization of noise and resolution for quantitative ¹⁷⁷Lu SPECT/CT with xSPECT Quant. *J Nucl Med*. 2019;60:50–59.
23. Kirchner J, Schaarschmidt BM, Sauerwein W, et al. ¹⁸F-FDG PET/MRI vs MRI in patients with recurrent adenoid cystic carcinoma. *Head Neck*. 2019;41:170–176.
24. Franzese C, Badalamenti M, Teriaca A, et al. Metastasis-directed stereotactic body radiation therapy in the management of oligometastatic head and neck cancer. *J Cancer Res Clin Oncol*. 2021;147:1307–1313.
25. Watt F, Martorana A, Brookes DE, et al. A tissue-specific enhancer of the prostate-specific membrane antigen gene, FOLH1. *Genomics*. 2001;73:243–254.
26. Bakht MK, Oh SW, Youn H, Cheon GJ, Kwak C, Kang KW. Influence of androgen deprivation therapy on the uptake of PSMA-targeted agents: emerging opportunities and challenges. *Nucl Med Mol Imaging*. 2017;51:202–211.
27. van Boxtel W, Uijen MJ, Verhaegh GW, et al. Prognostic value of PSMA, c-MET and E-cadherin in salivary duct carcinoma. *Oral Oncol*. 2020;110:105018.
28. Klein Nulent TJ, van Es RJ, Willems SM, et al. First experiences with ¹⁷⁷Lu-PSMA-617 therapy for recurrent or metastatic salivary gland cancer. *EJNMMI Res*. 2021;11:126.
29. Lückerrath K, Stuparu AD, Wei L, et al. Detection threshold and reproducibility of ⁶⁸Ga-PSMA11 PET/CT in a mouse model of prostate cancer. *J Nucl Med*. 2018;59:1392–1397.
30. Uijen MJ, Derks Y, Merckx R, et al. PSMA radioligand therapy for solid tumors other than prostate cancer: background, opportunities, challenges, and first clinical reports. *Eur J Nucl Med Mol Imaging*. 2021;48:4350–4368.

Comparison of ^{68}Ga -PSMA-617 PET/CT and ^{68}Ga -RM2 PET/CT in Patients with Localized Prostate Cancer Who Are Candidates for Radical Prostatectomy: A Prospective, Single-Arm, Single-Center, Phase II Study

Romain Schollhammer^{1,2}, Grégoire Robert³, Julien Asselineau⁴, Mokrane Yacoub⁵, Delphine Vimont², Nicolas Balamoutoff¹, Franck Bladou³, Antoine Bénard⁴, Elif Hindié^{1,2,6}, Henri de Clermont Gallerande^{1,2}, and Clément Morgat^{1,2}

¹Nuclear Medicine Department, Bordeaux University Hospital, Bordeaux, France; ²INCLIA, University of Bordeaux, CNRS, EPHE, UMR 5287, Bordeaux, France; ³Department of Urology, Bordeaux University Hospital, Bordeaux, France; ⁴CHU Bordeaux, Public Health Department, Clinical Epidemiology Unit, Bordeaux, France; ⁵Department of Pathology, Bordeaux University Hospital, Bordeaux, France; and ⁶Institut Universitaire de France, Paris, France

Considering the wide range of therapeutic options for localized prostate cancer (e.g., active surveillance, radiation-beam therapy, focal therapy, and radical prostatectomy), accurate assessment of the aggressiveness and localization of primary prostate cancer lesions is essential for treatment decision making. National Comprehensive Cancer Network guidelines recognize prostate-specific membrane antigen (PSMA) PET/CT for use in initial staging of high-risk primary prostate cancer. The gastrin-releasing peptide receptor (GRP-R) is a neuropeptide receptor overexpressed by low-risk prostate cancer cells. We aimed to perform the first (to our knowledge) prospective head-to-head comparison of PSMA- and GRP-R-targeted imaging at initial staging to understand how PSMA PET and GRP-R PET can be used or combined in clinical practice. **Methods:** This was a prospective, single-center, diagnostic cross-sectional imaging study using anonymized, masked, and independent interpretations of paired PET/CT studies in 22 patients with ^{68}Ga -PSMA-617 (a radiolabeled PSMA inhibitor) and ^{68}Ga -RM2 (^{68}Ga -DOTA-4-amino-1-carboxymethylpiperidine-D-Phe-Gln-Trp-Ala-Val-Gly-His-Sta-Leu-NH₂, a radiolabeled GRP-R antagonist). We enrolled patients with newly diagnosed, biopsy-proven prostate cancer. None had received neoadjuvant hormone therapy or chemotherapy, and all underwent extended pelvic lymph node dissection. Histologic findings served as a reference. **Results:** On a lesion-based analysis (including lesions < 0.1 cm³), ^{68}Ga -PSMA-617 PET/CT detected 74.3% (26/35) of all tumor lesions and ^{68}Ga -RM2 PET/CT detected 78.1% (25/32); 1 patient could not be offered ^{68}Ga -RM2 PET/CT. Paired examinations showed positive uptake of the 2 tracers in 21 of 32 lesions (65.6%), negative uptake in 5 of 32 lesions (15.6%), and discordant uptake in 6 of 32 lesions (18.8%). Uptake of ^{68}Ga -PSMA-617 was higher when the International Society of Urological Pathology (ISUP) score was at least 4 versus at least 1 ($P < 0.0001$) or 2 ($P = 0.0002$). There were no significant differences in uptake between ISUP scores for ^{68}Ga -RM2. Median ^{68}Ga -RM2 SUV_{max} was significantly higher than median ^{68}Ga -PSMA-617 SUV_{max} in the ISUP-2 subgroup ($P = 0.01$). **Conclusion:** ^{68}Ga -PSMA-617 PET/CT is useful to depict higher, more clinically significant ISUP score lesions, and ^{68}Ga -RM2 PET/CT has a higher detection rate for low-ISUP tumors.

Combining PSMA PET and GRP-R PET allows for better classification of intraprostatic lesions.

Key Words: GRP-R; PSMA; PET; prostate cancer; imaging

J Nucl Med 2023; 64:379–385

DOI: 10.2967/jnumed.122.263889

Prostate cancer is the most common cancer in men and the third cause of cancer-related deaths (1). The range of therapeutic options for localized prostate cancer varies from active surveillance or focal therapy to radiation-beam therapy or radical prostatectomy, depending on the local extension and risk classification of tumor progression. Therefore, the initial assessment of primary-tumor aggressiveness is critical to treatment decision making. In combination with clinical examination, PSA level, and prostatic MRI, the risk classification of the primary tumor depends mainly on appropriate sampling by prostatic biopsies and on precise evaluation of the International Society of Urological Pathology (ISUP) score.

Prostate-specific membrane antigen (PSMA) is a type 2 glycoprotein expressed in secretory cells of prostatic epithelium. Several radiolabeled PSMA inhibitors have been developed (^{68}Ga -PSMA-11, ^{68}Ga -PSMA-617, ^{68}Ga -PSMAI&T, and ^{18}F -PSMA1007 (2)). Uptake of radiolabeled PSMA inhibitors correlates well with ISUP score and PSA level (3). Recently, National Comprehensive Cancer Network guidelines considered the use of PSMA PET/CT for the initial staging of high-risk primary prostate cancer (4). However, the ability of PSMA PET/CT to also identify lower-grade lesions is unclear.

The gastrin-releasing peptide receptor (GRP-R) is a G-protein-coupled receptor of the bombesin receptor family (5) that can be targeted with radiolabeled antagonists such as ^{68}Ga -RM2 (^{68}Ga -DOTA-4-amino-1-carboxymethylpiperidine-D-Phe-Gln-Trp-Ala-Val-Gly-His-Sta-Leu-NH₂) (6), ^{68}Ga -NeoBOMB1 (7), or ^{68}Ga -RM26 (8) for PET imaging. Unlike PSMA, GRP-R is overexpressed in low-risk prostate cancers (low Gleason score, low prostate-specific antigen [PSA] value, and small tumor) (9–11). A study of the diagnostic performance of ^{68}Ga -RM2 PET/CT for initial staging of prostate cancer in 41 patients reported a detection rate of 93%, a sensitivity of 98%, and a specificity of 65% (6).

Received Jan. 27, 2022; revision accepted Aug. 23, 2022.

For correspondence or reprints, contact Clément Morgat (clement.morgat@chu-bordeaux.fr).

Published online Sep. 2, 2022.

COPYRIGHT © 2023 by the Society of Nuclear Medicine and Molecular Imaging.

In preclinical work, we compared in vitro GRP-R and PSMA expression in primary prostate cancer samples by means of ^{111}In -RM2 and ^{111}In -PSMA-617. Our results suggested that PSMA- and GRP-R-based imaging may have a complementary role in fully characterizing the local extent and aggressiveness of prostate cancer (with GRP-R being a valuable target in patients with a low metastatic risk and PSMA being a valuable target in patients with a higher risk (12)).

Additionally, a pilot clinical study using ^{68}Ga -PSMA-11 PET/CT and ^{68}Ga -RM2 PET/CT on 8 patients also suggested a complementary role for these imaging modalities in the initial staging of prostate cancer (13).

Here, we present a prospective head-to-head comparison between ^{68}Ga -PSMA-617 PET/CT and ^{68}Ga -RM2 PET/CT for the initial assessment of localized primary prostate cancer tumors. Our primary objective was to assess uptake intensity (SUV_{max}) with ^{68}Ga -PSMA-617 and ^{68}Ga -RM2 PET/CT at the level of prostatic lesions and to compare SUV_{max} between ISUP score categories. Secondary objectives were to compare ^{68}Ga -PSMA-617 and ^{68}Ga -RM2 uptake stratified by ISUP score, to compare SUV_{max} at 2 acquisition times (60 and 120 min after injection), and to evaluate for an association between the immunohistochemistry scores of the targets (PSMA and GRP-R) and ^{68}Ga -PSMA-617 and ^{68}Ga -RM2 uptake.

MATERIALS AND METHODS

Study Design and Participants

This was a prospective, single-center, diagnostic cross-sectional imaging study using anonymized, masked, and independent interpretations of paired ^{68}Ga -PSMA-617 PET/CT and ^{68}Ga -RM2 PET/CT scans (EudraCT 2017-000490-36, NCT03604757). ^{68}Ga -PSMA-617 PET/CT and ^{68}Ga -RM2 PET/CT were performed before prostatectomy in no specific order and with no consideration of patient characteristics. We prospectively enrolled 22 patients with newly diagnosed, biopsy-proven prostate cancer. The French ethical committee approved this study (approval 2017/62), and all subjects gave written informed consent.

The inclusion criteria were an age greater than 18 y, a diagnosis of prostate cancer confirmed by biopsy, and an indication for prostatectomy. No patient had received neoadjuvant hormone therapy or chemotherapy. All patients underwent extended pelvic lymph node dissection.

Radiopharmaceuticals and PET/CT Protocol

^{68}Ga -PSMA-617 and ^{68}Ga -RM2 were produced according to our previous description (12), with minor modifications (^{68}Ga was used as the radionuclide, and 10 μg of PSMA-617 were used). The Discovery RX PET/CT device (GE Healthcare) at the University Hospital of Bordeaux was used. Whole-body PET/CT images were acquired from vertex to mid thighs, with 2.5-min emission scans per bed position, at 60 and 120 min after intravenous administration of 2 MBq/kg (range, 80–200 MBq) of ^{68}Ga -PSMA-617 or ^{68}Ga -RM2. Images were reconstructed using an ordered-subset expectation maximization algorithm with 2 iterations and 21 subsets (matrix size, 256×256 ; 47 slices corresponding to a 15.6-cm transaxial field of view; voxel size, $2.376 \times 2.376 \times 3.27$ mm). The CT acquisition was performed for attenuation correction, in helical mode, using 120 kV, mAs modulation to optimally reduce the dose, and a 512×512 matrix (voxel size, $0.9766 \times 0.9766 \times 2$ mm).

PET/CT Image Analysis

PET/CT and multiparametric MR (when available) images were analyzed using Pmod software (version 3.5; PMOD Technologies LLC). A manual registration was performed between each modality, using a linear transformation, to aid visual analysis and accurate positioning of the tumor lesion. Then, manual segmentation was performed by 2

experienced nuclear physicians masked to the histologic findings, radiopharmaceutical, and patient characteristics. Supravesical sections were removed because of physiologic renal uptake of ^{68}Ga -PSMA-617 and physiologic pancreatic uptake of ^{68}Ga -RM2. A consensus was reached in cases of discrepancy between the 2 interpretations. Uptake of ^{68}Ga -PSMA-617 and ^{68}Ga -RM2 was quantified according to SUV_{max} and described for each lesion.

Histology

Prostatectomy samples were fixed and embedded in paraffin blocks. Tissue slices 5 μm thick were stained with hematoxylin, eosin, and safran, and an experienced pathologist manually surrounded tumor lesions under microscopic examination and reported the ISUP score and size of each lesion. Lesions smaller than 0.1 cm^2 were included in the analysis. Histologic samples were then digitized using a slide scanner (NDP.scan; Hamamatsu). The obtained images were arranged and reoriented to facilitate comparison between histology and PET imaging.

Immunohistochemistry

The immunohistochemical study was performed as previously described for GRP-R (14) and PSMA (15). Immunohistochemistry results were expressed as an immunoreactive score (IRS) that considered staining intensity and the percentage of stained tumor cells, as previously described (14). The final IRS score (product of staining intensity score and percentage-of-positive-cells score) thus ranged from 0 to 12. No PSMA or GRPR expression was categorized as IRS 0–1, weak PSMA or GRP-R expression was categorized as IRS 2–3, moderate PSMA or GRP-R expression was categorized as IRS 4–8, and strong PSMA or GRP-R expression was categorized as IRS 9–12. Immunohistochemistry results were dichotomized into 2 groups: low PSMA or GRP-R expression (absent/weak expression) and high PSMA or GRP-R expression (moderate/strong expression).

Cross-Sectional Analysis of PET Signal and Histology

For each tumor lesion, SUV_{max} for ^{68}Ga -PSMA-617 and ^{68}Ga -RM2 was compared with histology (cancer or noncancer area), allowing determination of concordance and discordance of findings.

Cross-Sectional Analysis of PET Signal and Immunohistochemistry Staining

For each tumor lesion, SUV_{max} for ^{68}Ga -PSMA-617 and ^{68}Ga -RM2 SUV_{max} was compared with the immunohistochemistry score for the whole tumor compartment.

Statistical Analysis

The sample size was fixed at 6 patients for each metastatic risk group defined at enrollment, before surgery (ISUP-1 and cT1-T2a and PSA < 10 ng/mL, Briganti < 5%; ISUP-2 or cT2b or PSA = 10–20 ng/mL; ISUP-3 or cT2b or PSA = 10–20 ng/mL; ISUP4–5 or cT2c or PSA > 20 ng/mL).

Quantitative variables are described as mean and SD, median and first to third quartiles, or minimum to maximum. Qualitative variables are described as frequency and percentage. SUV_{max} was compared at the patient level in normal tissues and at the lesion level in pathologic tissues. All comparisons of SUV_{max} (between ISUP scores, radiopharmaceuticals, and acquisition times) used univariable mixed linear regression models, including a random intercept to consider the inpatient correlation (with a variance component structure). The models' hypotheses (normality and heteroscedasticity of residuals) were systematically checked, leading us to transform SUV_{max} in pathologic tissues by the natural logarithm. Exponential of parameters estimated with these last models can be expressed as a multiplicative factor: less than 1 means a decreased value compared with the other group, and more than 1 means an increased value compared with the other group.

TABLE 1
Patient Characteristics (n = 22)

Variable	At diagnosis	Histopathology
ISUP score (n)		
1 (Gleason 6)	5 (22.7%)	1 (4.5%)
2 (Gleason 7 [3 + 4])	6 (27.3%)	9 (40.9%)
3 (Gleason 7 [4 + 3])	4 (18.2%)	2 (9.1%)
4 (Gleason 8)	2 (9.1%)	3 (13.6%)
5 (Gleason > 8)	5 (22.7%)	7 (31.8%)
TNM stage (n)		
T2a	19 (86.4%)	0 (0.0%)
T2c	3 (13.6%)	6 (27.3%)
T3a	0 (0.0%)	11 (50.0%)
T3b	0 (0.0%)	5 (22.7%)
N ₀	0 (0.0%)	20 (90.9%)
N ₁	0 (0.0%)	1 (4.5%)
N _x	22 (100.0%)	1 (4.5%)
Age (y)		
Mean	64.0 (SD, 5.9)	
Median	65 (Q1–Q3, 59–68)	
Minimum–maximum	52–75	
PSA (ng/mL)		
Mean	8.3 (SD, 4.0)	
Median	7 (Q1–Q3, 6–9)	
Minimum–maximum	3–21	

Comparisons of SUV_{max} in normal and pathologic tissues between 60 and 120 min were performed first to select the adequate acquisition time for other analyses. Comparison of SUV_{max} between negative and positive immunochemistry scores used nonparametric Wilcoxon tests. For the 2 primary outcomes only, if the global statistical test was significant at 2.5%, 2-by-2 comparison tests between ISUP scores were

interpreted using a 0.4% significance level (Bonferroni method). Statistical analyses used SAS software (version 9.4; SAS Institute).

RESULTS

Radiopharmaceuticals, Patient Characteristics, and Lesion Characteristics

Twenty-two men with newly diagnosed prostate cancer were enrolled in the study between April 25, 2018, and November 19, 2019. The demographic and clinicopathologic characteristics of the population are presented in Table 1. The median interval between the 2 PET/CT examinations was 6 d (Q1–Q3, 3–8 d). The median interval between the last PET/CT examination and surgery was 6 d (Q1–Q3, 1–15 d). Nine (41%) patients underwent ⁶⁸Ga-PSMA-617 PET/CT first, and 13 (59%) patients underwent ⁶⁸Ga-RM2 PET/CT first. One patient could not undergo ⁶⁸Ga-RM2 PET/CT. The median injected activity was 167.2 MBq (range, 118.7–210.2 MBq) for ⁶⁸Ga-PSMA-617 and 149.5 MBq (range, 84.5–198.5 MBq) for ⁶⁸Ga-RM2. All images were acquired at 1 and 2 h after injection, except in 1 patient, who underwent ⁶⁸Ga-RM2 imaging at 1 h only.

Thirty-five lesions (including lesions < 0.1 cm³) were identified by histology on prostatectomy samples: 9 ISUP-1 (25.7%), 13 ISUP-2 (37.1%), 3 ISUP-3 (8.6%), 3 ISUP-4 (8.6%), and 7 ISUP-5 (20.0%).

The dynamics of ⁶⁸Ga-PSMA-617 and ⁶⁸Ga-RM2 uptake were then analyzed in normal and pathologic prostatic tissues. In the normal prostate, the median SUV_{max} with ⁶⁸Ga-RM2 was 3.20 (Q1–Q3, 2.40–3.80) at 1 h and 2.40 (range, 1.85–3.85) at 2 h. ⁶⁸Ga-RM2 uptake was significantly lower at 2 h ($\beta = -0.59$; 95% CI, -0.95 to -0.24 ; $P = 0.003$). For ⁶⁸Ga-PSMA-617 in the normal prostate, the median SUV_{max} was 2.55 (range, 2.20–3.40) at 1 h and 2.50 (range, 2.00–3.10) at 2 h, with no differences between the 2 acquisition times ($\beta = -0.10$; 95% CI, -0.31 – 0.10 ; $P = 0.31$).

In tumor areas, the median SUV_{max} with ⁶⁸Ga-RM2 was 5.20 (range, 3.30–8.30) at 1 h and 5.40 (Q1–Q3, 3.75–7.90) at 2 h ($\exp(\beta) = 0.99$; 95% CI, 0.81–1.23; $P = 0.96$). For ⁶⁸Ga-PSMA-617 uptake in tumor lesions, the median SUV_{max} was 4.20 (range, 3.00–6.10) at 1 h and 4.10 (range, 2.90–7.30) at 2 h, with no significant differences between the 2 acquisition times ($e^{\beta} = 1.00$; 95% CI, 0.78–1.30; $P = 0.98$).

TABLE 2
ISUP-Based Stratification of Lesions Detected by ⁶⁸Ga-PSMA-617 PET/CT or ⁶⁸Ga-RM2 PET/CT

Lesion on imaging	Total	ISUP-1	ISUP-2	ISUP-3	≥ISUP-4
⁶⁸Ga-PSMA-617 PET/CT*					
n	35	9	13	3	10
No	9 (25.7%)	6 (66.7%)	3 (23.1%)		
Yes	26 (74.3%)	3 (33.3%)	10 (76.9%)	3 (100%)	10 (100%)
⁶⁸Ga-RM2 PET/CT†					
n‡	32 (3)	8 (1)	13	3	8 (2)
No	7 (21.9%)	4 (50.0%)	2 (15.4%)		1 (12.5%)
Yes	25 (78.1%)	4 (50.0%)	11 (84.6%)	3 (100%)	7 (87.5%)

*60 min after intravenous administration.

†120 min after intravenous administration.

‡One lesion is missing for patient who did not benefit from ⁶⁸Ga-RM2 PET/CT, and 2 other missing lesions correspond to failure of PET/CT device at 2 h after injection for another patient.

TABLE 3
Comparison of ^{68}Ga -PSMA-617 and ^{68}Ga -RM2 Uptake with ISUP Score

ISUP score	Median SUV _{max}	
	^{68}Ga -RM2	^{68}Ga -PSMA-617
1	3.45 (2.50–4.70)	3.00 (2.60–3.50)
2	6.30 (5.30–7.50)	3.60 (3.40–4.50)
3	8.30 (3.80–9.80)	6.80 (5.10–7.10)
≥4	7.35 (3.25–9.05)	7.45 (5.90–12.50)

Data in parentheses are Q1–Q3.

Therefore, given the lower uptake of ^{68}Ga -RM2 in normal prostate tissue at 2 h and the equivalent uptake in tumor lesions at 1 and 2 h, an analysis was conducted using PET/CT data obtained 2 h after injection. For ^{68}Ga -PSMA-617, as no differences in uptake were seen either in normal prostate or in tumor area, the 1-h uptake time recommended by the joint guidelines of the European Association of Nuclear Medicine and the Society of Nuclear Medicine and Molecular Imaging for ^{68}Ga -PSMA PET/CT was applied (16).

Lesion-Based PET/CT Imaging

Of the 35 prostatic lesions evaluated with ^{68}Ga -PSMA-617 PET/CT, 26 (74.3%) were detected. Undetected lesions had an ISUP score of no more than 2 (6 ISUP-1 and 3 ISUP-2).

Of the 32 prostatic lesions evaluated with ^{68}Ga -RM2 PET/CT, 25 (78.1%) were detected by ^{68}Ga -RM2 PET/CT. The undetected lesions included 4 that were ISUP-1, 2 that were ISUP-2, and 1 that was ISUP-4 (Table 2).

Concordance and Discordance in PET/CT Imaging

Twenty-one (65.6%) of 32 histology-proven lesions (whatever their volume) showed uptake of both ^{68}Ga -PSMA-617 and ^{68}Ga -RM2, 4 (12.5%) were seen only on ^{68}Ga -RM2, 2 (6.3%) were seen only on ^{68}Ga -PSMA-617, and 5 (15.6%) were negative on both ^{68}Ga -PSMA-617 and ^{68}Ga -RM2.

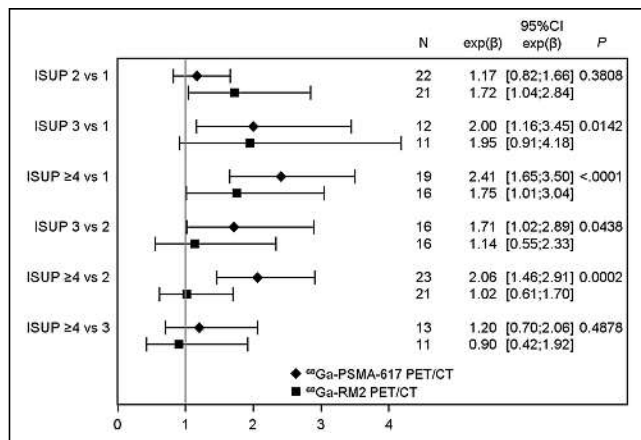


FIGURE 1. Comparison of ^{68}Ga -PSMA-617 and ^{68}Ga -RM2 uptake with ISUP score. Estimates of >1 and <1 indicated higher and lower SUV_{max} in higher ISUP, respectively.

Association with Pathologic Parameters

Regarding uptake of the radiopharmaceuticals according to histology parameters, ^{68}Ga -PSMA-617 SUV_{max} differed according to ISUP score ($P = 0.003$), with a higher SUV_{max} for increasing ISUP scores (Tables 2 and 3). Especially, uptake of ^{68}Ga -PSMA-617 was higher for ISUP scores of at least 4 than for an ISUP score of 1 ($e^{\beta} = 2.41$; 95% CI, 1.65–3.50; $P < 0.0001$) or 2 ($e^{\beta} = 2.06$; 95% CI, 1.46–2.91; $P = 0.002$).

There were no significant differences in uptake between ISUP scores for ^{68}Ga -RM2 ($P = 0.11$).

Median ^{68}Ga -RM2 SUV_{max} was significantly higher than median ^{68}Ga -PSMA-617 SUV_{max} in the ISUP-2 subgroup (6.30 [Q1–Q3, 5.30–7.50] vs. 3.60 [Q1–Q3, 3.40–4.50], $P = 0.01$). In other ISUP groups, no differences in uptake were seen between ^{68}Ga -PSMA-617 and ^{68}Ga -RM2 (Table 3; Figs. 1 and 2).

Immunohistochemistry was also conducted on prostatectomy samples from patients included in this study. Sixteen samples were available for GRP-R staining and 18 for PSMA staining (the remaining samples were considered noncontributive by the pathologist and were excluded from the analyses). GRP-R staining was considered positive (IRS ≥ 4) in 11 (68.8%) of 16 lesions. The median GRP-R IRS score was 4 (Q1–Q3, 3–6). The PSMA IRS was considered positive (IRS ≥ 4) in 15 (83.3%) of 18 lesions. The median PSMA IRS score was 11 (interquartile range, 6–12). The median ^{68}Ga -RM2 SUV_{max} was 6.40 (interquartile range, 3.70–7.50) in samples low for GRP-R, versus 7.35 (interquartile range, 5.30–9.00) for samples positive for GRP-R ($P = 0.50$) (Fig. 3; Supplemental Fig. 1; supplemental materials are available at <http://jnm.snmjournals.org>). The median ^{68}Ga -PSMA-617 SUV_{max} was 3.60 (Q1–Q3, 3.00–5.30) for PSMA-negative samples and 6.80 (Q1–Q3, 4.50–8.50) for PSMA-positive samples ($P = 0.12$) (Fig. 3; Supplemental Fig. 2).

DISCUSSION

Several radiopharmaceuticals have been developed to help in the staging of prostate cancer. ^{11}C -acetate, marking lipid metabolism, cannot reliably distinguish between benign prostatic hyperplasia and prostate tumors. Moreover, the radiolabeled amino acid ^{18}F -fluciclovine has not shown good diagnostic performance for characterization of primary lesions (17). Finally, ^{11}C - and ^{18}F -choline, also marking lipid

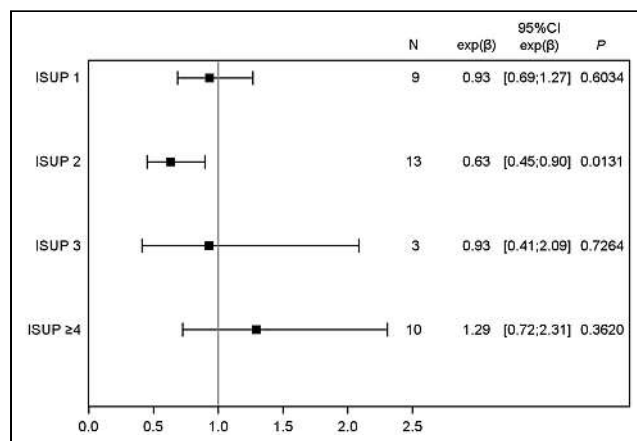


FIGURE 2. ^{68}Ga -PSMA-617 SUV_{max} compared with ^{68}Ga -RM2 SUV_{max}, according to ISUP groups. Estimates of >1 and <1 indicated higher and lower SUV_{max}, respectively, with ^{68}Ga -PSMA-617. For ISUP ≥ 4 group, when patient who had only ^{68}Ga -PSMA-617 was excluded, values were 1.32 (95% CI, 0.72–2.44) ($P = 0.3459$).

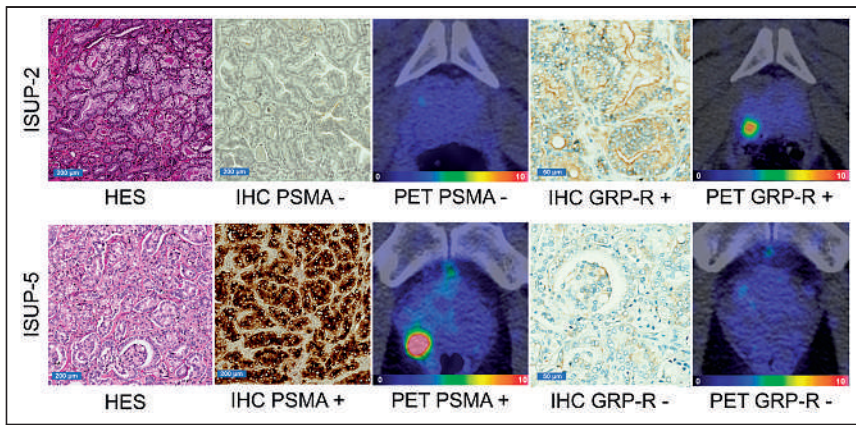


FIGURE 3. Representative GRP-R and PSMA immunohistochemistry with corresponding ^{68}Ga -RM2 and ^{68}Ga -PSMA-617 PET/CT images for 2 patients. (Top) Hematoxylin, eosin, and saffron staining of ISUP-2 sample ($\times 5$ magnification), negative PSMA immunohistochemistry ($\times 5$ magnification), negative ^{68}Ga -PSMA-617 PET/CT, positive GRP-R immunohistochemistry ($\times 20$ magnification), and positive ^{68}Ga -RM2 PET/CT. (Bottom) Hematoxylin, eosin, and saffron staining of ISUP-5 sample ($\times 5$ magnification), positive PSMA immunohistochemistry ($\times 5$ magnification), positive ^{68}Ga -PSMA-617 PET/CT, negative GRP-R immunohistochemistry ($\times 20$ magnification), and negative ^{68}Ga -RM2 PET/CT. HES = hematoxylin, eosin, and saffron; IHC = immunohistochemistry. Intensity-scale bars indicate SUV.

metabolism, have shown lower sensitivity than multiparametric MRI for primary detection of prostate cancer (18). Thus, improvements in current molecular imaging for prostate cancer appear necessary to initially assess the aggressiveness of the primary tumor.

PSMA and GRP-R are differently overexpressed in prostate cancer, raising hope for precise molecular imaging of tumor lesions within the prostate gland. Few studies have prospectively investigated the role of these radiopharmaceuticals at initial staging, before surgery. In a prospective study enrolling 56 patients with intermediate-grade prostate cancer before prostatectomy, PSMA

the lower uptake of ^{68}Ga -RM2 in nonpathologic prostate tissue at 2 h after injection despite equivalent results on tumor lesion uptake at 1 and 2 h. This result can be extracted from preclinical studies (20) but has never, to our knowledge, been translated into PET/CT studies. This observation suggests that results from previous studies using a time point of 1 h after injection for ^{68}Ga -RM2 PET/CT imaging are not optimal. Surprisingly, uptake of ^{68}Ga -PSMA-617 was similar between 1 and 2 h—a result that contrasts with a previous publication that reported increasing uptake between 1 and 3 h, but the study populations were different (21).

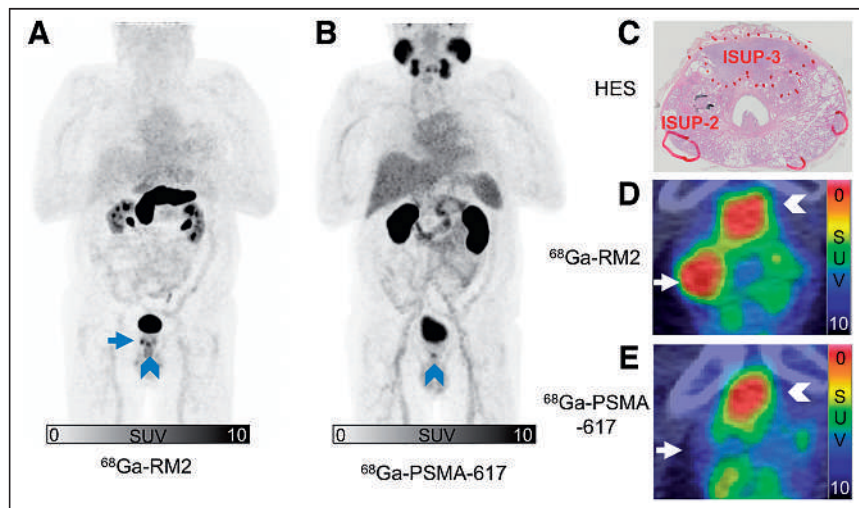


FIGURE 4. ^{68}Ga -RM2 maximum-intensity projection (A), ^{68}Ga -PSMA-617 maximum-intensity projection (B); hematoxylin, eosin, and saffron staining of histologic slice from prostatectomy of patient 7 with manual demarcation of tumor lesions (C); ^{68}Ga -RM2 transaxial PET/CT image (D); and ^{68}Ga -PSMA-617 transaxial PET/CT image (E). Anterior ISUP-3 lesion and right basal ISUP-2 lesion were seen on histology, with 2 small lesions $< 0.1 \text{ cm}^3$ (C). ^{68}Ga -RM2 PET/CT and ^{68}Ga -PSMA-617 PET/CT showed similar uptake on ISUP-3 lesion: SUV_{max} was 6.7 for ^{68}Ga -RM2 and 6.8 for ^{68}Ga -PSMA-617 (arrowheads). ^{68}Ga -RM2 was the only radiopharmaceutical able to detect ISUP-2 lesion well (arrows): SUV_{max} was 7.3 for ^{68}Ga -RM2 and 3.4 for ^{68}Ga -PSMA-617. HES = hematoxylin, eosin, and saffron.

PET was to be accurate in detecting intraprostatic lesions that had an ISUP score of at least 2. In contrast, the detection rate of PSMA PET was low for ISUP-1 lesions. Touijer et al. prospectively investigated ^{68}Ga -RM2 PET/CT in 16 patients before radical prostatectomy. The performance of ^{68}Ga -RM2 PET/CT imaging did not significantly differ from that of multiparametric MRI in terms of sensitivity, specificity, and accuracy (19). Therefore, the objective of this work was to perform a head-to-head comparison of PSMA and GRP-R targeting, covering various metastatic risks, at the initial staging of prostate cancer using ^{68}Ga -PSMA-617 and ^{68}Ga -RM2 radiopharmaceuticals. Our aim was to better understand how PSMA PET and GRP-R PET can map progression risk and how they might be used or combined in clinical practice. Because of the exploratory nature of this study, we were not aiming at assessing the diagnostic performance of the radiopharmaceuticals.

An interesting finding of our work was the lower uptake of ^{68}Ga -RM2 in nonpathologic prostate tissue at 2 h after injection despite equivalent results on tumor lesion uptake at 1 and 2 h. This result can be extracted from preclinical studies (20) but has never, to our knowledge, been translated into PET/CT studies. This observation suggests that results from previous studies using a time point of 1 h after injection for ^{68}Ga -RM2 PET/CT imaging are not optimal. Surprisingly, uptake of ^{68}Ga -PSMA-617 was similar between 1 and 2 h—a result that contrasts with a previous publication that reported increasing uptake between 1 and 3 h, but the study populations were different (21).

On a lesion-based analysis and using histologic results as a reference, detection of primary lesions by ^{68}Ga -RM2 PET/CT was fairly good, compared with ^{68}Ga -PSMA-617 PET/CT. A previous study evaluating the diagnostic potential of ^{68}Ga -RM2 PET/CT for primary prostate cancer found a higher sensitivity of ^{68}Ga -RM2 PET/CT than found in our work (0.98) (6). This difference can be explained by exclusion of all lesions 0.1 cm^3 or smaller. When these very small lesions, which are below the spatial resolution of PET scanners, were removed for our study population, ^{68}Ga -RM2 PET/CT detected 86% of lesions and ^{68}Ga -PSMA-617 PET/CT detected 83% of lesions. The high uptake of ^{68}Ga -PSMA-617 in tumor lesions of high ISUP score correlates with the known efficacy of PSMA imaging of intraprostatic tumors in patients with newly diagnosed high-risk prostate cancer (3). Additionally, ^{68}Ga -RM2 PET/CT outperformed ^{68}Ga -PSMA-617 PET/CT for the detection of ISUP-2 lesions (Fig. 4).

Therefore, to better classify intraprostatic lesions, we propose that both PSMA PET and GRP-R PET be performed, as discordant

uptake occurs in 6 of 32 (18.8%) lesions. We suggest that PSMA PET be performed first for staging high-risk lesions. Next, the addition of GRP-R PET would allow a more extensive characterization of lower-risk prostate cancer lesions. Indeed, a low ^{68}Ga -PSMA-617 uptake associated with a high ^{68}Ga -RM2 uptake would suggest a low-grade prostatic tumor lesion. This double-PET strategy might also be used for guidance of biopsies to decrease the discordance rate between biopsy staging and final staging on prostatectomy samples (22). Finally, the possibility of precision detection and characterization of intraprostatic lesions opens new avenues for radiotherapy planning or focal treatments.

^{68}Ga -PSMA-617 PET/CT was the only imaging modality able to detect the single metastatic lymph node confirmed by histology (ISUP-5) in our study. No significant uptake in this lymph node was seen on ^{68}Ga -RM2 PET/CT or on previously ordered ^{18}F -choline PET/CT (23). This result illustrates the higher sensitivity of PSMA PET for depicting metastatic disease in high-risk or recurrent prostate cancer (24).

Overall, most intraprostatic lesions were detected by PSMA or GRP-R PET. It should be stressed, however, that there still were some lesions (5/32, 15.6%) unseen by both modalities.

Results from this molecular imaging PET study were consolidated by GRP-R and PSMA immunohistochemistry conducted on surgical samples. A meaningfully higher tracer uptake was seen on immunohistochemistry-positive samples for PSMA, but this was not confirmed statistically. Other immunohistochemistry scores should also be considered (11).

A limitation of our monocentric phase II institutional study is obviously the limited number of patients enrolled. The small sample size may have led to underpowered results. Moreover, the SUV of ^{68}Ga -PSMA-617 might not be directly transferable to the ^{68}Ga -PSMA-11 used in clinics. Finally, visual analysis between histology and PET imaging can be suboptimal. Methods for accurate spatial registration of PET images and histopathologic images, using fiducial markers, have been developed (25) and deserve to be implemented.

CONCLUSION

This prospective head-to-head comparison showed the remarkable potential of the combination of ^{68}Ga -RM2 PET/CT and ^{68}Ga -PSMA-617 PET/CT to evaluate different aspects of prostate cancer biology. ^{68}Ga -PSMA-617 PET/CT is useful to depict lesions with a higher, more clinically significant, ISUP score. ^{68}Ga -RM2 has a higher detection rate than ^{68}Ga -PSMA-617 in lower ISUP scores but uptake similar to that of ^{68}Ga -PSMA-617 in higher ISUP scores. Importantly, almost 20% of lesions were seen only on GRP-R PET (~13%) or PSMA PET (~6%), revealing the complementary role of these imaging procedures. Combining PSMA PET and GRP-R PET allows better classification of intraprostatic lesions.

DISCLOSURE

This was an investigator-initiated trial with institutional academic funding. The study was funded and promoted by the University Hospital of Bordeaux (grant AOI 2016; recipient, Clément Morgat). Life Molecular Imaging provided the RM2 precursor and the reference compound but had no role in the study design. Clément Morgat reports consulting activities for IRE Elit and research support from IRE Elit and Life Molecular Imaging

outside the submitted work. The corresponding author had full access to all data and final responsibility to submit for publication. No other potential conflict of interest relevant to this article was reported.

ACKNOWLEDGMENTS

We thank all the patients for their participation, and we thank the entire staff of the PET research center (Pessac, France), whose hard work made this study possible. Sandrine Fouchet is warmly thanked for all her administrative work. We also want to thank Frédérique Sgoifo and Tiziri Aoudjit for data management.

KEY POINTS

QUESTION: What is the role of GRP-R targeting in initial staging of localized prostate cancer in the context of PSMA PET/CT?

PERTINENT FINDINGS: In a prospective, head-to-head comparison of 22 paired PET/CT examinations using ^{68}Ga -RM2 (a radiolabeled GRP-R antagonist) and ^{68}Ga -PSMA-617, the median ^{68}Ga -RM2 SUV_{max} was significantly higher than the median ^{68}Ga -PSMA-617 SUV_{max} in the ISUP-2 subgroup. As expected, ^{68}Ga -PSMA-617 PET/CT was useful for initial staging of tumors with a high ISUP score.

IMPLICATIONS FOR PATIENT CARE: Combining PSMA PET and GRP-R PET allows better classification of intraprostatic lesions.

REFERENCES

1. Siegel RL, Miller KD, Jemal A. Cancer statistics, 2017. *CA Cancer J Clin*. 2017; 67:7–30.
2. Schwarzenboeck SM, Rauscher I, Bluemel C, et al. PSMA ligands for PET imaging of prostate cancer. *J Nucl Med*. 2017;58:1545–1552.
3. Uprimny C, Kroiss AS, Decristoforo C, et al. ^{68}Ga -PSMA-11 PET/CT in primary staging of prostate cancer: PSA and Gleason score predict the intensity of tracer accumulation in the primary tumour. *Eur J Nucl Med Mol Imaging*. 2017;44:941–949.
4. Acute lymphoblastic leukemia. National Comprehensive Cancer Network website. <https://www.nccn.org/guidelines/guidelines-detail?category=1&id=1459>. Published 2022. Accessed December 5, 2022.
5. Mansi R, Fleischmann A, Mäcke HR, Reubi JC. Targeting GRPR in urological cancers: from basic research to clinical application. *Nat Rev Urol*. 2013;10:235–244.
6. Duan H, Baratto L, Fan RE, et al. Correlation of ^{68}Ga -RM2 PET with postsurgery histopathology findings in patients with newly diagnosed intermediate- or high-risk prostate cancer. *J Nucl Med*. 2022;63:1829–1835.
7. Nock BA, Kaloudi A, Lymperis E, et al. Theranostic perspectives in prostate cancer with the gastrin-releasing peptide receptor antagonist NeoBOMB1: preclinical and first clinical results. *J Nucl Med*. 2017;58:75–80.
8. Zhang J, Niu G, Fan X, et al. PET using a GRPR antagonist ^{68}Ga -RM26 in healthy volunteers and prostate cancer patients. *J Nucl Med*. 2018;59:922–928.
9. Beer M, Montani M, Gerhardt J, et al. Profiling gastrin-releasing peptide receptor in prostate tissues: clinical implications and molecular correlates. *Prostate*. 2012; 72:318–325.
10. Körner M, Waser B, Rehm R, Reubi JC. Early over-expression of GRP receptors in prostatic carcinogenesis. *Prostate*. 2014;74:217–224.
11. Faviana P, Boldrini L, Erba PA, et al. Gastrin-releasing peptide receptor in low grade prostate cancer: can it be a better predictor than prostate-specific membrane antigen? *Front Oncol*. 2021;11:650249.
12. Schollhammer R, De Clermont Gallerande H, Yacoub M, et al. Comparison of the radiolabeled PSMA-inhibitor ^{111}In -PSMA-617 and the radiolabeled GRP-R antagonist ^{111}In -RM2 in primary prostate cancer samples. *EJNMMI Res*. 2019;9:52.
13. Fassbender TF, Schiller F, Zamboglou C, et al. Voxel-based comparison of [^{68}Ga]Ga-RM2-PET/CT and [^{68}Ga]Ga-PSMA-11-PET/CT with histopathology for diagnosis of primary prostate cancer. *EJNMMI Res*. 2020;10:62.

14. Morgat C, MacGrogan G, Brouste V, et al. Expression of gastrin-releasing peptide receptor in breast cancer and its association with pathologic, biologic, and clinical parameters: a study of 1,432 primary tumors. *J Nucl Med*. 2017;58:1401–1407.
15. Woythal N, Arsenic R, Kempkensteffen C, et al. Immunohistochemical validation of PSMA expression measured by ⁶⁸Ga-PSMA PET/CT in primary prostate cancer. *J Nucl Med*. 2018;59:238–243.
16. Fendler WP, Eiber M, Beheshti M, et al. ⁶⁸Ga-PSMA PET/CT: joint EANM and SNMMI procedure guideline for prostate cancer imaging—version 1.0. *Eur J Nucl Med Mol Imaging*. 2017;44:1014–1024.
17. Parent EE, Schuster DM. Update on ¹⁸F-fluciclovine PET for prostate cancer imaging. *J Nucl Med*. 2018;59:733–739.
18. Nitsch S, Hakenberg OW, Heuschkel M, et al. Evaluation of prostate cancer with ¹¹C- and ¹⁸F-choline PET/CT: diagnosis and initial Staging. *J Nucl Med*. 2016(suppl 3);57:38S–42S.
19. Touijer KA, Michaud L, Alvarez HAV, et al. Prospective study of the radiolabeled GRPR antagonist BAY86-7548 for positron emission tomography/computed tomography imaging of newly diagnosed prostate cancer. *Eur Urol Oncol*. 2019;2:166–173.
20. Mansi R, Wang X, Forrer F, et al. Development of a potent DOTA-conjugated bombesin antagonist for targeting GRPr-positive tumours. *Eur J Nucl Med Mol Imaging*. 2011;38:97–107.
21. Afshar-Oromieh A, Hetzheim H, Kratochwil C, et al. The theranostic PSMA ligand PSMA-617 in the diagnosis of prostate cancer by PET/CT: biodistribution in humans, radiation dosimetry, and first evaluation of tumor lesions. *J Nucl Med*. 2015;56:1697–1705.
22. Qiu D-X, Li J, Zhang J-W, et al. Dual-tracer PET/CT-targeted, mpMRI-targeted, systematic biopsy, and combined biopsy for the diagnosis of prostate cancer: a pilot study. *Eur J Nucl Med Mol Imaging*. 2022;49:2821–2832.
23. Schollhammer R, de Clermont Gallerande H, Robert G, et al. ⁶⁸Ga-PSMA-617 compared with ⁶⁸Ga-RM2 and ¹⁸F-Fcholine PET/CT for the initial staging of high-risk prostate cancer. *Clin Nucl Med*. 2019;44:e535–e536.
24. Minamimoto R, Hancock S, Schneider B, et al. Pilot comparison of ⁶⁸Ga-RM2 PET and ⁶⁸Ga-PSMA-11 PET in patients with biochemically recurrent prostate cancer. *J Nucl Med*. 2016;57:557–562.
25. Puri T, Chalkidou A, Henley-Smith R, et al. A method for accurate spatial registration of PET images and histopathology slices. *EJNMMI Res*. 2015;5:64.

PET Imaging of Fibroblast Activation Protein in Various Types of Cancer Using ^{68}Ga -FAP-2286: Comparison with ^{18}F -FDG and ^{68}Ga -FAP-46 in a Single-Center, Prospective Study

Yizhen Pang^{*1,2}, Liang Zhao^{*1,2}, Tinghua Meng^{*1}, Weizhi Xu¹, Qin Lin², Hua Wu¹, Jingjing Zhang^{3,4}, Xiaoyuan Chen⁴⁻⁶, Long Sun¹, and Haojun Chen¹

¹Department of Nuclear Medicine and Minnan PET Center, First Affiliated Hospital of Xiamen University, School of Medicine, Xiamen University, Xiamen, China; ²Department of Radiation Oncology, First Affiliated Hospital of Xiamen University, Xiamen, China; ³Department of Diagnostic Radiology, National University of Singapore, Singapore; ⁴Clinical Imaging Research Centre, Centre for Translational Medicine, Yong Loo Lin School of Medicine, National University of Singapore, Singapore; ⁵Departments of Diagnostic Radiology, Surgery, Chemical and Biomolecular Engineering, and Biomedical Engineering, Yong Loo Lin School of Medicine and Faculty of Engineering, National University of Singapore, Singapore; and ⁶Nanomedicine Translational Research Program, NUS Center for Nanomedicine, Yong Loo Lin School of Medicine, National University of Singapore, Singapore

PET imaging that targets fibroblast activation protein (FAP) on the surface of cancer-associated fibroblasts has yielded promising tumor diagnostic results. FAP-2286 contains cyclic peptides as FAP-binding motifs to optimize tumor retention compared with the small-molecule FAP inhibitor (FAPi) series (FAPi-04/46). The aim of this study was to evaluate the diagnostic accuracy of ^{68}Ga -FAP-2286 to detect primary and metastatic lesions in patients with various types of cancer, compared with ^{18}F -FDG and ^{68}Ga -FAP-2286. **Methods:** Sixty-four patients with 15 types of cancer underwent ^{68}Ga -FAP-2286 PET/CT for initial assessment or detection of recurrence. For comparison, 63 patients underwent paired ^{68}Ga -FAP-2286 and ^{18}F -FDG PET/CT and 19 patients underwent paired ^{68}Ga -FAP-2286 and ^{68}Ga -FAPi-46 PET/CT. Lesion uptake was quantified as SUV_{max} and tumor-to-background ratio. The Wilcoxon matched-pairs signed-rank test was used to compare SUV_{max} between PET modalities, and the McNemar test was used to compare lesion detectability. **Results:** Uptake of ^{68}Ga -FAP-2286 was significantly higher than that of ^{18}F -FDG in primary tumors (median SUV_{max} , 11.1 vs. 6.9; $P < 0.001$), lymph node metastases (median SUV_{max} , 10.6 vs. 6.2; $P < 0.001$), and distant metastases, resulting in improved image contrast and lesion detectability. All primary tumors (46/46) were clearly visualized by ^{68}Ga -FAP-2286 PET/CT, whereas 9 of the 46 lesions could not be visualized by ^{18}F -FDG PET/CT. The lesion detection rate of ^{68}Ga -FAP-2286 PET/CT was superior to that of ^{18}F -FDG PET/CT for involved lymph nodes (98% [105/107] vs. 85% [91/107], $P = 0.001$) and bone and visceral metastases (95% [162/171] vs. 67% [114/171], $P < 0.001$). ^{68}Ga -FAP-2286 yielded tumor uptake and lesion detection rates similar to those of ^{68}Ga -FAPi-46 in a subcohort of 19 patients. **Conclusion:** ^{68}Ga -FAP-2286 is a promising FAP-inhibitor derivative for safe cancer diagnosis, staging, and restaging. It may be a better alternative to ^{18}F -FDG for the cancer types that exhibit low-to-moderate uptake of ^{18}F -FDG, which include gastric, pancreatic, and hepatic cancers. In addition, ^{68}Ga -FAP-2286 and ^{68}Ga -FAPi-46 yielded comparable clinical results.

Key Words: fibroblast activation protein; FAP-2286; FAPi-46; PET/CT

J Nucl Med 2023; 64:386–394

DOI: 10.2967/jnumed.122.264544

The glucose analog ^{18}F -FDG is extensively used for tumor metabolic imaging. Cancer-associated fibroblasts, one of the most abundant components of the tumor stroma, are alternative targets for the imaging of solid tumors (1). Considering the high expression of fibroblast activation protein (FAP) on the cell surfaces of activated cancer-associated fibroblasts and its limited expression in normal tissue, PET imaging of cancer-associated fibroblasts with radiolabeled FAP inhibitors (FAPi) is an active field in nuclear medicine (2).

^{68}Ga - and ^{18}F -radiolabeled FAPi variants (including FAPi-04, FAPi-46, and FAPi-74) have yielded promising results in the diagnosis of various cancers (3–5). Furthermore, FAPi has been reported to be superior to ^{18}F -FDG in PET/CT imaging of, for example, hepatic, gastric, and pancreatic cancer, as well as peritoneal carcinomatosis (6–9). However, these FAPi molecules are normally retained in tumors for a relatively short time, potentially limiting their use for radionuclide therapy (10,11).

FAP-2286 is a low-molecular-weight, FAP-targeted polypeptide linked to the chelator DOTA, which allows for the attachment of radionuclides for imaging and therapeutic use. FAP-2286, developed using a cyclic peptide as a binding motif, is reported to be potent, highly selective for FAP, and stable in human plasma (12). In addition, it has a long retention time in tumors, translating to the robust antitumor efficacy of ^{177}Lu -FAP-2286 as demonstrated in a preclinical study (12). In this study, FAP-2286 had a half-maximal effective concentration comparable to that of FAPi-46 (4.9 vs. 1.7 nM), as well as better cellular internalization, longer retention, and higher uptake on PET/CT scans at all time points in human embryonic kidney FAP cells. Moreover, ^{177}Lu -FAP-2286 had a significantly higher tumor retention than ^{177}Lu -FAPi-46 at 24 and 72 h after injection, resulting in excellent antitumor efficacy in human

Received Jun. 20, 2022; revision accepted Aug. 30, 2022.

For correspondence or reprints, contact Haojun Chen (leoehen0821@foxmail.com), Long Sun (13178352662@163.com), or Xiaoyuan Chen (chen.shawn@nus.edu.sg).

*Contributed equally to this work.

Published online Sep. 2, 2022.

COPYRIGHT © 2023 by the Society of Nuclear Medicine and Molecular Imaging.

embryonic kidney FAP xenografts. The results of a recent pilot study in which ^{177}Lu -FAP-2286 was used for peptide-targeted radionuclide therapy in patients with diverse advanced adenocarcinomas exhibited acceptable side effects and prolonged retention and activity (13). The preliminary results from the LuMIERE trial (NCT04939610) reported that ^{177}Lu -FAP-2286 demonstrated a manageable safety profile with some promising efficacy in 9 patients with 7 types of cancer (partial response was observed in 1 patient who completed 6 cycles of ^{177}Lu -FAP-2286 in a 3.7-GBq dose cohort) (14). When these results are taken together, FAP-2286 exhibits promising characteristics as a targeting vector, with potent and selective FAP binding that leads to intense tumor accumulation and substantial therapeutic efficacy.

In this study, we aimed to investigate the diagnostic accuracy of the novel imaging agent ^{68}Ga -FAP-2286 for detecting primary and metastatic lesions in patients with various types of cancer, and we compared the results with those of ^{18}F -FDG and ^{68}Ga -FAPI-46.

MATERIALS AND METHODS

Participant Enrollment

This is a preliminary report of an ongoing, single-center, prospective study of the diagnostic accuracy of ^{68}Ga -FAP-2286 for PET/CT imaging of solid tumors. The institutional review board approved the study (approval 2022KY013), and all subjects gave written informed consent. The study was registered at ClinicalTrials.gov (NCT05392205). The inclusion criteria were as follows: adult patients (aged 18 y or older), patients with newly diagnosed or previously treated malignant tumors (to avoid the treatment impact on radiotracer uptake, the interval between the completion of therapy and the PET scan was > 6 mo), and patients who were able to provide informed consent or assent according to the guidelines of the Clinical Research Ethics Committee. Exclusion criteria were as follows: patients with nonmalignant disease; patients who were pregnant; and patients, their parents, or their legal representatives who were unable or unwilling to provide written informed consent.

Radiolabeling

FAP-2286 and FAPI-46 were obtained from Yantai Dongcheng Pharmaceutical Group Co., Ltd., and Jiangsu Huayi Technology Co., Ltd., respectively. Both compounds were used for research purposes. ^{18}F -FDG was manufactured according to the standard method of our laboratory (15,16) using the coincidence ^{18}F -FDG synthesis module (TracerLab FxFN; GE Healthcare). The FAPI-46 ligands were radiolabeled with ^{68}Ga according to a previous protocol (17). Briefly, 925–1,110 MBq of $^{68}\text{GaCl}_3$ eluted from the $^{68}\text{Ge}/^{68}\text{Ga}$ generator (ITG) were reacted with 25 μg (28.2 nmol) of FAPI-46 in 1 mL of 0.25 M sodium acetate buffer for 10 min at 100°C and purified before use. FAP-2286 ligands were radiolabeled with ^{68}Ga in a similar protocol (925–1,110 MBq of $^{68}\text{GaCl}_3$ reacted with 25 μg [17.0 nmol] of FAP-2286). The synthesis of the radiopharmaceutical is detailed in the supplemental materials (available at <http://jnm.snmjournals.org>).

PET/CT Imaging and Evaluation

The dose of intravenously injected ^{68}Ga -FAP-2286 was calculated according to the participants' body weight (1.8–2.2 MBq/kg). At 1 h after intravenous administration, the participants underwent PET/CT via a hybrid scanner (Discovery MI; GE Healthcare). All obtained data were transferred to the Advantage Workstation (version AW 4.7; GE Healthcare) and reconstructed using the Bayesian penalized-likelihood reconstruction algorithm (Q.clear; GE Healthcare). For patients with malignant disease, additional ^{18}F -FDG or ^{68}Ga -FAPI-46 PET/CT was performed for comparative purposes, depending on the patients' willingness. The PET/CT imaging protocols for ^{18}F -FDG and ^{68}Ga -FAPI-46 were the same as those for ^{68}Ga -FAP-2286, except

that 6 h of fasting were required before the ^{18}F -FDG PET/CT scan (the supplemental materials provide details) (18).

All PET images were evaluated by 2 board-certified nuclear medicine physicians, each with at least 10 y of experience in PET/CT imaging; the 2 physicians were not masked to the study. Disagreements in opinion were resolved via discussion and consensus. In addition to visual evaluation, lesions were evaluated semiquantitatively by selection of regions of interest. The SUV_{max} was calculated automatically

TABLE 1
Patients' Characteristics ($n = 64$)

Characteristic	Data
Number of patients	64
Patients with paired ^{68}Ga -FAP-2286 and ^{18}F -FDG PET/CT	63
Days between ^{68}Ga -FAP-2286 and ^{18}F -FDG PET/CT	1–7
Patients with paired ^{68}Ga -FAP-2286 and ^{68}Ga -FAPI-46 PET/CT	19
Days between ^{68}Ga -FAP-2286 and ^{68}Ga -FAPI-46 PET/CT	1–4
Median age (y)	57.5 (range, 32–85)
Sex	
Male	38
Female	26
Types of cancer	
Head and neck	15
Hepatic	12
Gastric	10
Pancreatic	7
Ovarian	5
Esophageal*	4
Breast	3
Non-small cell lung*	2
Renal	2
Glioblastoma	1
Thymic	1
Colorectal	1
Yolk sac tumor	1
Gastrointestinal stromal tumor	1
Clinical reason for PET/CT	
Detection of unknown primary tumor	3
Staging of cancer	39
Evaluation of doubtful lesions	2
Identification of disease recurrence	20
Final diagnosis	
Histopathologic confirmation (via biopsy or surgery)	58
Diagnostic imaging/follow-up	6

*One patient was diagnosed with synchronous double cancer (esophageal and lung adenocarcinoma).

Data are numbers, unless indicated otherwise.

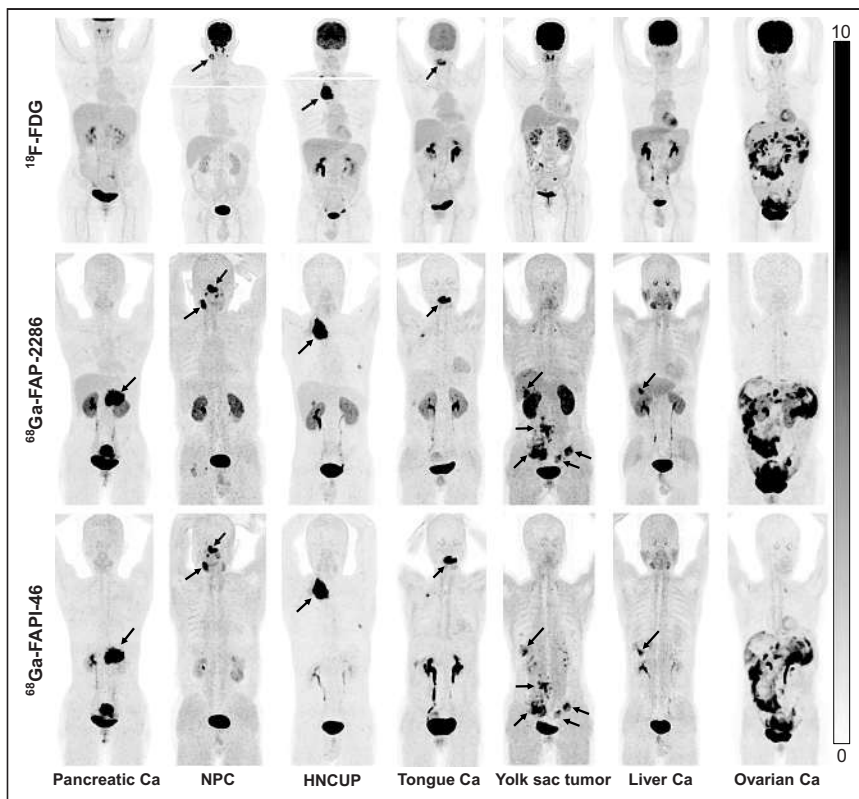


FIGURE 1. Maximum-intensity projections of ^{18}F -FDG, ^{68}Ga -FAP-2286, and ^{68}Ga -FAPI-46 PET/CT imaging in 7 patients with different types of cancer (histologically confirmed). Tumor lesions are indicated with arrows. Ca = carcinoma; HNCUP = head and neck carcinoma of unknown primary; NPC = nasopharyngeal carcinoma.

using the Advantage Workstation. Regions with radiotracer uptake higher than the background activity in primary tumors, lymph nodes, the lungs, the liver, peritoneal surfaces, and other body parts were considered pathologic. Tracer uptake in normal organs (background) was quantified on the basis of SUV_{mean} , which was delineated with a sphere 1 cm in diameter (for the small organs, including thyroid, salivary gland, pancreas) to 2 cm

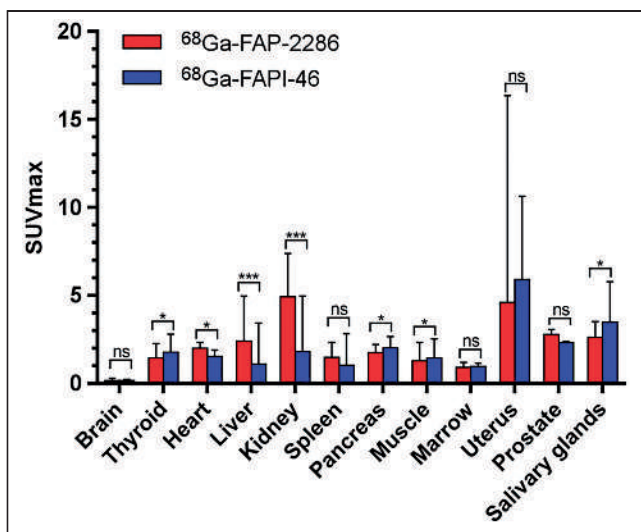


FIGURE 2. PET-based biodistribution analysis of ^{68}Ga -FAP-2286 and ^{68}Ga -FAPI-46 in normal organs at 1 h after injection. Results are shown as means and SDs from 19 patients. * $P < 0.05$. *** $P < 0.001$. ns = not statistically significant.

in diameter (for the other organs, including brain, heart, liver, kidney, spleen, muscle, and bone marrow) placed inside the organ parenchyma. The tumor-to-background ratio (TBR) was calculated as the ratio of the tumor SUV_{max} to the background SUV_{mean} . Physiologic uptake of ^{68}Ga -FAP-2286 and ^{68}Ga -FAPI-46 in normal organs was determined by calculating the SUV_{mean} of the background measurements in the heart, liver, spleen, lungs, kidneys, muscles, prostate, and uterus. Histopathologic results obtained via surgery or biopsy served as the gold standard for the final diagnosis. If tissue-based diagnosis was not possible, comprehensive evaluations of multimodal imaging characteristics were used as the reference standard.

Statistical Analysis

Statistics were analyzed using SPSS, version 22.0 (IBM). The Wilcoxon matched-pairs signed-rank test was used to compare SUVs derived from ^{68}Ga -FAP-2286, ^{68}Ga -FAPI-46, and ^{18}F -FDG PET/CT images. The McNemar test was used to compare the lesion detectability of different PET scans. The paired-sample t test was used to evaluate differences in normal-organ uptake between ^{68}Ga -FAP-2286 and ^{68}Ga -FAPI-46 PET/CT. Statistical significance was defined as a P value of less than 0.05.

RESULTS

Patient Characteristics

From March 1, 2022, to May 31, 2022, 64 patients with malignant disease (38 men; median age, 57.5 y; range, 32–85 y) who underwent ^{68}Ga -FAP-2286 PET/CT were enrolled in this prospective study (Table 1). Among the 64 patients, 44 (9 types of cancer) underwent PET/CT for initial assessment (lesion detection and staging) and the other 20 (9 types of cancer) for detection of tumor recurrence and metastases (restaging). The final diagnosis was based on histopathologic results ($n = 58$) and diagnostic radiology (comprehensive considerations of imaging findings, $n = 6$). For comparison, 63 patients underwent paired ^{68}Ga -FAP-2286 and ^{18}F -FDG PET/CT and 19 patients underwent paired ^{68}Ga -FAP-2286 and ^{68}Ga -FAPI-46 PET/CT. Representative images from the 3 types of PET scans are shown in Figure 1.

Adverse Events and Biodistribution

All patients tolerated the ^{68}Ga -FAP-2286 PET/CT scans. There were no signs of any drug-related pharmacologic effects or other adverse physiologic responses. All observed vital signs (including temperature, blood pressure, and heart rate) were normal at the 4-h follow-up. No abnormal symptoms were reported by the patients.

The in vivo distribution pattern of ^{68}Ga -FAP-2286 was evaluated and compared with that of ^{68}Ga -FAPI-46 in 19 patients who underwent both scans. ^{68}Ga -FAP-2286 exhibited an in vivo distribution pattern similar to that of ^{68}Ga -FAPI-46, except for a slightly higher physiologic uptake in the liver and kidneys (Fig. 2). Semiquantitative analysis demonstrated that ^{68}Ga -FAP-2286 uptake in the kidneys (5.3 ± 1.5 vs. 2.3 ± 1.2 , $t = 8.959$, $P < 0.001$), liver (2.8 ± 1.0 vs. 1.5 ± 0.9 , $t = 8.582$, $P < 0.001$), and heart (1.9 ± 0.4 vs. 1.4 ± 0.3 , $t = 6.557$, $P < 0.001$) were higher than that of ^{68}Ga -FAPI-46. In contrast, background uptake of ^{68}Ga -FAP-2286 in the thyroid

TABLE 2
Comparison of SUV_{max} on ⁶⁸Ga-FAP-2286 and ¹⁸F-FDG PET/CT Images in Primary and Metastatic Tumors

Tumor type	n	Size (cm)	⁶⁸ Ga-FAP-2286			¹⁸ F-FDG PET/CT			P
			Positive tumors	SUV _{max}	TBR	Positive tumors	SUV _{max}	TBR	
Primary									
Total [§]	46	3.2 (0.9–11.3)	46	11.1 (2.5–28.9)	9.2 (1.1–31.5)	37	6.9 (1.5–19.1)	3.0 (0.9–13.2)	<0.001
HNC	7	1.7 (1.5–3.4)	7	16.8 (11.0–20.2)	13.7 (8.1–15.3)	7	11.0 (4.0–15.6)	7.0 (2.9–13.1)	0.043
Breast cancer*	6	1.5 (0.9–7.0)	6	9.9 (6.0–18.3)	10.1 (3.9–22.3)	4	6.4 (1.5–17.3)	5.0 (1.1–13.2)	0.249
Esophageal cancer	4	4.1 (2.1–9.0)	4	22.9 (10.0–26.4)	13.6 (6.3–19.4)	4	11.6 (7.9–18.4)	5.8 (4.7–8.6)	0.068
Lung adenocarcinoma	2	2.9 (1.1–4.7)	2	7.5 (5.7–9.3)	10.0 (9.2–10.9)	2	6.1 (3.3–8.9)	7.1 (4.2–10.0)	NA
Gastric cancer	6	2.0 (1.2–4.5)	6	9.1 (4.1–13.0)	9.2 (4.9–12.7)	3	3.4 (1.7–7.9)	2.0 (0.9–4.1)	0.028
Hepatic cancer	8	5.2 (0.9–11.3)	8	11.3 (2.5–28.9)	5.2 (1.5–9.4)	5	4.8 (3.1–9.7)	1.5 (1.0–3.5)	0.028
Pancreatic cancer	7	3.4 (2.4–5.7)	7	13.0 (10.7–22.7)	12.2 (5.7–23.3)	6	6.5 (3.0–8.1)	2.9 (1.1–4.4)	0.018
Renal cancer	1	4.5 (NA)	1	6.1 (NA)	1.5 (NA)	1	4.1 (NA)	2.0 (NA)	NA
Ovarian cancer	5	4.8 (1.7–6.2)	5	10.8 (6.0–25.6)	11.0 (5.0–31.5)	5	9.6 (5.3–12.2)	6.9 (2.8–9.3)	0.138
Recurrence/mets									
Recurrent tumor (total [†])	9	2.9 (0.7–5.1)	9	5.8 (2.9–16.5)	4.7 (2.2–15.7)	3	3.8 (2.2–7.6)	1.1 (0.8–5.4)	0.008
LN mets (total)	107	1.2 (0.5–6.6)	105	10.6 (3.0–20.1)	9.0 (2.2–30.0)	91	6.2 (1.3–21.2)	3.7 (1.0–13.0)	<0.001
Lung mets	21	0.9 (0.4–1.3)	16	3.4 (0.6–10.2)	4.9 (0.9–14.5)	19	3.5 (0.7–7.1)	5.0 (1.0–10.2)	0.931
Hepatic mets	30	2.6 (0.9–10.7)	27	6.9 (2.4–12.2)	4.1 (0.9–8.4)	22	6.8 (2.1–10.8)	2.2 (0.9–3.9)	<0.001
Peritoneal mets	70	NA [‡]	69	8.6 (2.4–15.4)	6.7 (1.8–27.0)	46	4.6 (1.5–11.4)	2.4 (0.8–8.1)	<0.001
Subcutaneous mets	12	0.9 (0.6–2.0)	12	8.1 (5.2–12.4)	9.3 (6.3–20.4)	5	1.4 (0.7–7.4)	1.3 (1.0–11.6)	0.002
Bone mets	38	1.0 (0.4–3.1)	38	6.6 (3.8–13.3)	10.1 (2.9–26.7)	22	2.7 (0.9–11.4)	2.4 (0.9–19.3)	<0.001

*One patient was diagnosed with multifocal breast cancer (4 primary tumors).

[†]Local recurrent tumors included glioblastoma (n = 1), HNC (n = 4), hepatic cancer (n = 3), and gastric cancer (n = 1).

[‡]Lesion size cannot be calculated because of diffuse type of peritoneal metastases (irregular shape).

[§]Primary tumors were not located in 2 patients with head and neck cancer of unknown primary etiology; 2 patients were therefore excluded from analysis. Two patients were diagnosed with synchronous double cancer (one with esophageal and lung adenocarcinoma, the other with HNC and renal cancer).

HNC = head and neck cancer; NA = not applicable; mets = metastases; LN = lymph node.

Qualitative data are number; continuous data are median and range.

(1.6 ± 0.5 vs. 1.9 ± 0.5 , $t = -3.537$, $P = 0.01$), pancreas (1.8 ± 0.3 vs. 2.1 ± 0.5 , $t = -2.559$, $P = 0.038$), muscles (1.3 ± 0.5 vs. 1.5 ± 0.5 , $t = -2.515$, $P = 0.04$), and salivary glands (2.5 ± 0.6 vs. 3.6 ± 1.0 , $t = -3.356$, $P = 0.012$) were lower than that of $^{68}\text{Ga-FAPI-46}$ (Fig. 2).

$^{68}\text{Ga-FAP-2286}$ and $^{18}\text{F-FDG}$ Uptake in Cancer Patients

Among the 44 patients who underwent paired $^{68}\text{Ga-FAP-2286}$ and $^{18}\text{F-FDG}$ PET/CT for initial diagnosis, 1 was diagnosed with a synchronous double cancer (esophageal cancer and lung adenocarcinoma) and 1 was diagnosed with multifocal breast cancer (4 primary tumors in the same breast). In addition, the primary tumors could not be located in 2 patients with head and neck cancers of unknown primary. Thus, in total, 46 primary tumor lesions (all confirmed by histopathology) were evaluated in this study (Table 2). All primary tumors were clearly visualized with intense radiotracer uptake on $^{68}\text{Ga-FAP-2286}$ PET/CT, whereas 9 of the 46 lesions could not be visualized via $^{18}\text{F-FDG}$ PET/CT. Primary tumor lesions exhibiting no pathologic uptake on $^{18}\text{F-FDG}$ PET/CT images were gastric cancer ($n = 3$), hepatic cancer ($n = 3$), breast cancer ($n = 2$), and pancreatic cancer ($n = 1$) (Supplemental Fig. 1). The SUV_{max} of all primary tumor lesions derived from $^{68}\text{Ga-FAP-2286}$ PET/CT was significantly higher than that derived from $^{18}\text{F-FDG}$ PET/CT (11.1 vs. 6.9 , $P < 0.001$). Moreover, lesions exhibited a 3-fold higher TBR on $^{68}\text{Ga-FAP-2286}$ PET/CT images than they did on $^{18}\text{F-FDG}$ PET/CT images (9.2 vs. 3.0 , $P < 0.001$), thus improving the image contrast for tumor

detection and delineation. Representative images are shown in Supplemental Figure 2.

We investigated tumor uptake over time by performing $^{68}\text{Ga-FAP-2286}$ PET at multiple time points (0.5, 1, and 3 h after injection) in patients 33 and 54. The SUV_{max} in patient 33 (nasopharyngeal carcinoma with lymph node and bone metastases) increased from 0.5 to 3 h in the primary tumor (by 72.1%, from 8.6 to 14.8), involved lymph nodes (by 5.2%–69.1%), and 1 bone metastasis (by 64.4%) (Fig. 3). Similar results were observed in patient 54 (metastatic colon cancer); the hepatic metastases demonstrated stable $^{68}\text{Ga-FAP-2286}$ uptake but an increased TBR from 1 to 3 h (Supplemental Fig. 3).

Among the 19 patients who underwent paired $^{68}\text{Ga-FAP-2286}$ and $^{18}\text{F-FDG}$ PET/CT for cancer restaging, $^{68}\text{Ga-FAP-2286}$ demonstrated significantly higher lesion detection rates than $^{18}\text{F-FDG}$ PET/CT (100% [9/9] vs. 33% [3/9], $P = 0.031$) in 9 locally recurrent tumors (all confirmed by histopathology) (Supplemental Fig. 2B). Among the 63 patients who underwent paired $^{68}\text{Ga-FAP-2286}$ and $^{18}\text{F-FDG}$ PET/CT for initial staging or restaging, 107 lymph node metastases and 171 bone and visceral metastases were evaluated. Among these, 66 metastatic lesions (12 lymph nodes and 54 bone and visceral metastases) were confirmed by histopathology, and 212 lesions (95 lymph nodes and 117 bone and visceral metastases) were confirmed by diagnostic radiology. $^{68}\text{Ga-FAP-2286}$ yielded significantly higher radiotracer uptake (SUV_{max} , 10.6 vs. 6.2 ; $P < 0.001$) and TBR (9.0 vs. 3.7 , $P < 0.001$) than did $^{18}\text{F-FDG}$ in the metastatic lymph nodes. Therefore, $^{68}\text{Ga-FAP-2286}$ PET/CT had a significantly higher detection rate (98% [105/107] vs. 85% [91/107], $P = 0.001$)

than $^{18}\text{F-FDG}$ PET/CT in the diagnosis of lymph node metastases. Interestingly, the $^{18}\text{F-FDG}$ uptake was positive and the $^{68}\text{Ga-FAP-2286}$ uptake was negative in the enlarged mediastinal lymph nodes in 1 patient with gastric cancer; these lymph nodes were confirmed to be inflammatory on endobronchial ultrasound-guided transbronchial needle aspiration (Supplemental Fig. 2C). Regarding PET/CT imaging of bone and visceral metastases, $^{68}\text{Ga-FAP-2286}$ yielded a greater number of positive lesions (95% [162/171] vs. 67% [114/171], $P < 0.001$) and a higher radiotracer uptake and TBR than $^{18}\text{F-FDG}$ in most lesions (hepatic, peritoneal, subcutaneous, and bone metastases). Interestingly, no significant difference in hepatic metastasis SUV_{max} was observed between $^{68}\text{Ga-FAP-2286}$ and $^{18}\text{F-FDG}$, even though the TBR yielded by $^{68}\text{Ga-FAP-2286}$ (4.1) was twice that yielded by $^{18}\text{F-FDG}$ in those lesions (2.2, $P < 0.001$).

With the new lymph node and visceral metastases detected by $^{68}\text{Ga-FAP-2286}$ PET/CT, TNM staging was upgraded in 3 patients (3/44, 7%), including 1 with gastric cancer (from IIA to IIB), 1 with esophageal cancer (from IIIA to IIIB), and 1 with nasopharyngeal cancer (from IVA to IVB). Compared with $^{18}\text{F-FDG}$, $^{68}\text{Ga-FAP-2286}$ PET/CT detected a greater number of metastatic lesions or a larger disease extent in

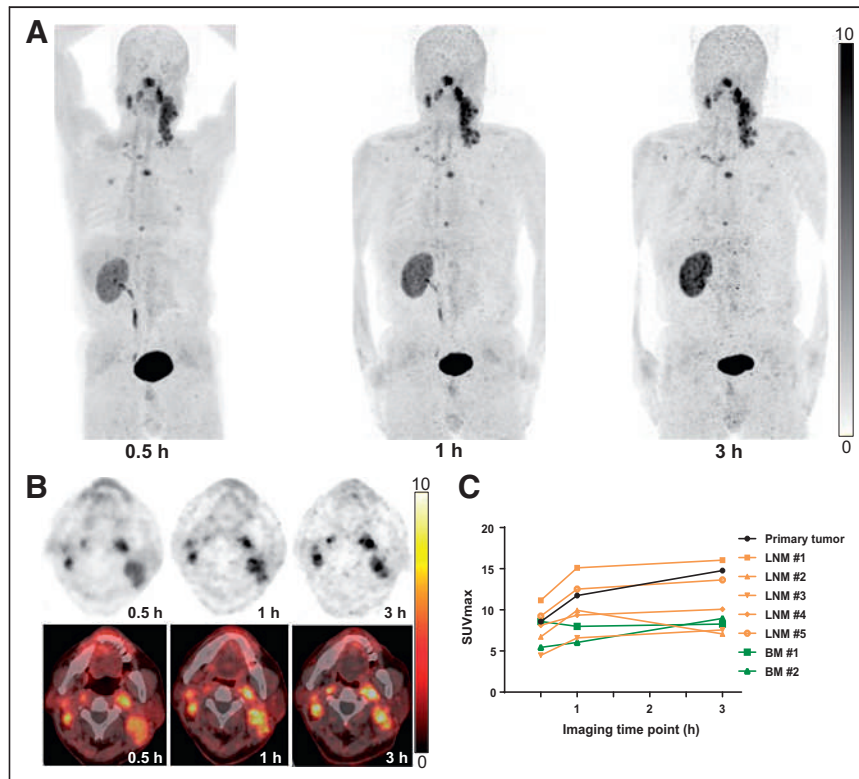


FIGURE 3. A 66-y-old man with nasopharyngeal carcinoma who underwent $^{68}\text{Ga-FAP-2286}$ PET/CT at different time points after injection. Rapid and stable radiotracer uptake was observed in both primary and metastatic lesions. Semiquantitative analysis demonstrated SUV_{max} increase at 0.5–3 h in primary tumor (by 72.1% [from 8.6 to 14.8]), involved lymph nodes (by 5.2%–69.1%), and 1 bone metastasis (by 64.4%). BM = bone metastasis; LNM = lymph node metastasis.

12 patients (12/44, 27%), including 4 with pancreatic cancer, 2 with hepatic cancer, 2 with nasopharyngeal cancer, 1 with esophageal cancer, 2 with ovarian cancer, and 1 with gastric cancer. Among the other 19 patients in whom recurrence was detected, ⁶⁸Ga-FAP-2286 PET/CT detected ¹⁸F-FDG–negative locally recurrent tumors in 6 patients (6/19, 32%) and ¹⁸F-FDG–negative metastatic lesions in 7 patients (7/19, 37%). The patients with new lesions or a larger disease extent detected by ⁶⁸Ga-FAP-2286 PET/CT are presented in Supplemental Table 1.

⁶⁸Ga-FAP-2286 and ⁶⁸Ga-FAPI-46 Uptake in Patients with Cancer

Among the 19 patients who underwent paired ⁶⁸Ga-FAP-2286 and ⁶⁸Ga-FAPI-46 PET/CT, 11 did so for initial staging and 8 for restaging. The ⁶⁸Ga-FAP-2286–derived SUV_{max} was comparable to that derived from ⁶⁸Ga-FAPI-46 in 13 primary tumor lesions (13.6 vs. 13.3, *P* = 0.53; Table 3), 4 recurrent tumors (11.2 vs. 9.6, *P* = 0.47), and 33 metastatic lymph nodes (8.3 vs. 8.2, *P* = 0.28). Too few patients with each cancer type underwent paired analyses with these modalities to allow for comparisons of radiotracer uptake per tumor type. Regarding visceral and bone metastases, the quantitative tumor uptake of ⁶⁸Ga-FAP-2286 was not inferior to that of ⁶⁸Ga-FAPI-46 in the lung (4.0 vs. 3.9), liver (4.6 vs. 4.4), peritoneum (9.8 vs. 11.4), or bone (6.9 vs. 5.8) (all *P* > 0.05; Table 3). Interestingly, in 1 patient with metastatic cholangiocarcinoma, the median SUV_{max} of ⁶⁸Ga-FAP-2286 was

significantly higher than that of ⁶⁸Ga-FAPI-46 (8.1 vs. 6.0, *P* = 0.022) in the widespread subcutaneous metastases, and ⁶⁸Ga-FAP-2286 PET/CT detected a greater number of subcutaneous metastases than ⁶⁸Ga-FAPI-46 (25 vs. 16). Representative images are shown in Figures 4–6.

DISCUSSION

In this study, we conducted clinical investigations using ⁶⁸Ga-FAP-2286 for PET/CT imaging in patients with different types of cancer. We aimed to investigate whether ⁶⁸Ga-FAP-2286 could be used for cancer imaging, and we compared it with ¹⁸F-FDG and ⁶⁸Ga-FAPI-46.

The encouraging results from a preclinical study and a first-in-humans study (12,13) warranted further clinical evaluation of ⁶⁸Ga-FAP-2286. Therefore, we are in the process of investigating the diagnostic accuracy of ⁶⁸Ga-FAP-2286 for the identification of FAP-positive solid tumors via PET/CT. First, we evaluated the in vivo distribution pattern of ⁶⁸Ga-FAP-2286 and compared it with that of ⁶⁸Ga-FAPI-46. The physiologic uptake of ⁶⁸Ga-FAP-2286 was lower than that of ⁶⁸Ga-FAPI-46 in the muscles, salivary glands, thyroid, and pancreas. However, ⁶⁸Ga-FAP-2286 uptake in the kidneys, liver, and heart was higher than that of ⁶⁸Ga-FAPI-46, thus suggesting that the cyclopeptide structure of FAP-2286 may lead to altered in vivo pharmacokinetics. Cyclic peptides may have improved biologic properties compared with the small-molecule

TABLE 3
Comparison of SUV_{max} on FAP-2286 and FAPI-46 PET/CT Images in Primary and Metastatic Lesions

Parameter	<i>n</i>	Tumor size (cm)	Tracer	Positive lesions	SUV _{max}	<i>P</i>
Primary tumors (total)*	13	3.6 (1.0–6.2)	FAP-2286		13.6 (2.5–25.8)	0.53
			FAPI-46		13.3 (2.4–21.8)	
Recurrence/mets						
Recurrent tumor (total)†	4	3.1 (2.6–5.1)	FAP-2286	4	11.2 (2.7–14.4)	0.465
			FAPI-46	4	9.6 (2.9–13.6)	
Lymph node mets (total)	33	1.2 (0.6–4.6)	FAP-2286	33	8.3 (3.4–15.6)	0.28
			FAPI-46	33	8.2 (4.0–15.4)	
Lung mets	2	0.9 (0.8–1.0)	FAP-2286	2	4.0 (3.8–4.2)	NA
			FAPI-46	2	3.9 (3.6–4.2)	
Hepatic mets	6	2.0 (0.9–11.8)	FAP-2286	6	4.6 (2.7–7.2)	0.345
			FAPI-46	6	4.4 (2.9–8.5)	
Subcutaneous mets	10	0.8 (0.6–2.0)	FAP-2286	10	8.1 (7.4–10.3)	0.022
			FAPI-46	10	6.0 (3.6–8.6)	
Peritoneal mets	22	NA‡	FAP-2286	22	9.8 (6–15.4)	0.18
			FAPI-46	22	11.4 (7.4–19.2)	
Bone mets	10	1.3 (0.7–2.5)	FAP-2286	10	6.9 (3.9–12.2)	0.074
			FAPI-46	10	5.8 (2.9–11.4)	

*Primary tumors included head and neck cancer (*n* = 2), esophageal cancer (*n* = 1), lung adenocarcinoma (*n* = 1), hepatic cancer (*n* = 2), gastric cancer (*n* = 1), pancreatic cancer (*n* = 4), renal cancer (*n* = 1), and ovarian cancer (*n* = 1).

†Including glioblastoma, tongue cancer, hepatic cancer, and gastric cancer.

‡Because peritoneal metastases were statistically analyzed according to peritoneal cancer index score, size of lesions could not be obtained.

Mets = metastases; NA = not applicable.

Qualitative data are number; continuous data are median and range.

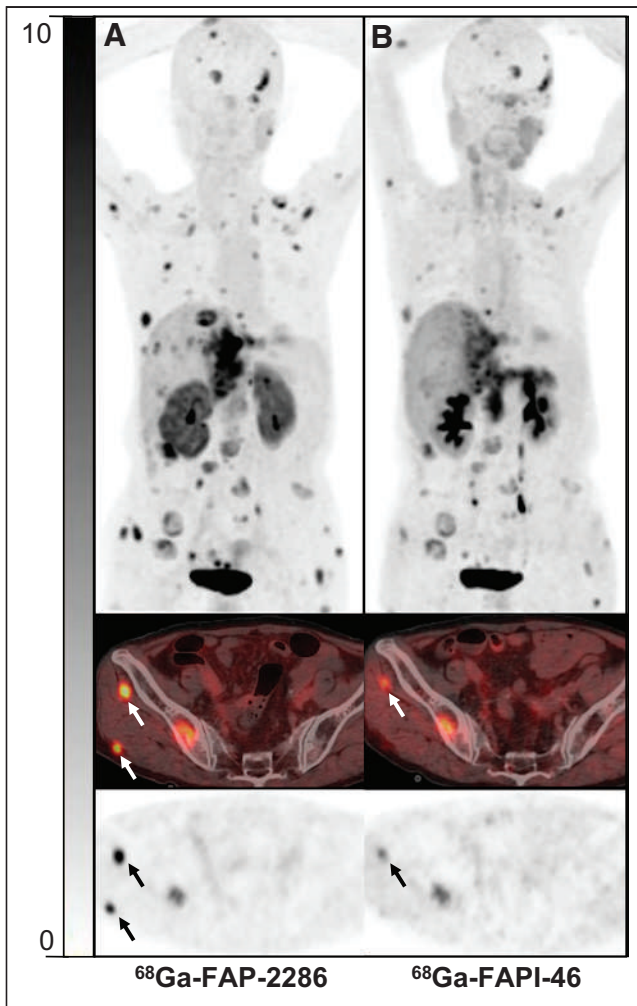


FIGURE 4. A 65-y-old woman with metastatic intrahepatic cholangiocarcinoma who underwent imaging for cancer restaging. ^{68}Ga -FAP-2286 (A) revealed greater number of metastases and higher uptake than ^{68}Ga -FAPI-46 (B) in widespread subcutaneous metastases (arrows).

FAP series (19), including stronger receptor selectivity and binding affinity, because of increased plasma stability and conformational rigidity. Indeed, ^{177}Lu -FAP-2286 had a long effective half-life in the first-in-humans study (35 ± 9 h in the entire body and 44 ± 25 h in bone metastases) (13). Moreover, tumor uptake in our study increased in one patient and remained stable in the other from 0.5 to 3 h after injection. In preclinical studies, FAP-2286 demonstrated longer tumor retention than FAPI-46 at later time points (12), and greater antitumor efficacy was observed in tumor xenografts with ^{177}Lu -FAP-2286 than with ^{177}Lu -FAPI-46. When these results are taken together, an increased FAP-binding affinity, improved tumor accumulation, and longer tumor retention are seen to be the main potential advantages of FAP-2286 compared with other FAPI variants. In our study, the results from PET imaging demonstrated that tumor uptake of ^{68}Ga -FAPI-46 and ^{68}Ga -FAP-2286 was comparable at earlier time points, thus indicating that both compounds can be used for imaging of FAP-positive tumors. Further studies with a larger patient population are needed to test the role of ^{68}Ga -FAP-2286 among the existing FAPI derivatives.

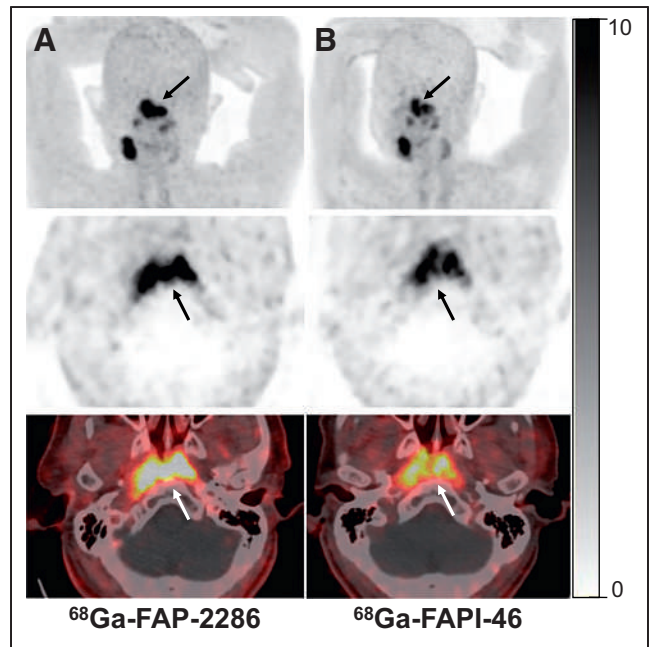


FIGURE 5. A 72-y-old man with newly diagnosed nasopharyngeal carcinoma who underwent PET/CT for tumor staging. ^{68}Ga -FAP-2286 PET/CT (A) showed higher radiotracer uptake in primary tumor (SUV_{max} , 17.4 vs. 12.2; arrows) than ^{68}Ga -FAPI-46 (B).

Another aim of the present study was to compare tumor uptake and lesion detectability between ^{68}Ga -FAP-2286 and ^{18}F -FDG PET/CT. With respect to primary tumor lesions, the quantitative tumor uptake and TBR were significantly higher with ^{68}Ga -FAP-2286 than with ^{18}F -FDG. This finding corresponds to the results showing that all primary tumors (46/46) were identified with ^{68}Ga -FAP-2286 whereas 9 were missed with ^{18}F -FDG (Supplemental Fig. 1). Consistent with previous FAPI-based imaging studies (7–9), ^{68}Ga -FAP-2286 PET/CT was superior to ^{18}F -FDG PET/CT in gastrointestinal malignancies, including gastric, pancreatic, and hepatic cancer. This result suggests that ^{68}Ga -FAP-2286 PET/CT is promising in the diagnosis of these cancer types for which ^{18}F -FDG PET/CT is inadequate. Regarding the detection of lymph node and visceral metastases, ^{68}Ga -FAP-2286 yielded a higher radiotracer uptake and TBR than ^{18}F -FDG and an improved lesion detectability, particularly of hepatic, bone, and peritoneal metastases. Interestingly, we noted that 1 patient (Supplemental Fig. 2C) with reactive lymph nodes did not exhibit increased ^{68}Ga -FAP-2286 uptake, whereas false-positive ^{18}F -FDG uptake was observed in these nodules. Similar findings have been reported in previous studies (20). Thus, we speculate that ^{68}Ga -FAP-2286 may be more suitable than ^{18}F -FDG for differentiating reactive lymph nodes from tumor metastatic lymph nodes. However, tumor and inflammation differentiation by ^{68}Ga -FAP-2286 PET/CT was not the main aim of this study, although this question should be investigated in future clinical trials.

Overall, the results from this study suggest that ^{68}Ga -FAP-2286 is a promising FAPI molecule for cancer diagnosis, staging, and restaging. Therefore, ^{68}Ga -FAP-2286 PET/CT may contribute to the diagnosis of solid tumors, especially in malignant tumors with low-to-moderate uptake on ^{18}F -FDG PET/CT. The specific cancer types that showed ^{68}Ga -FAP-2286 to be superior to ^{18}F -FDG

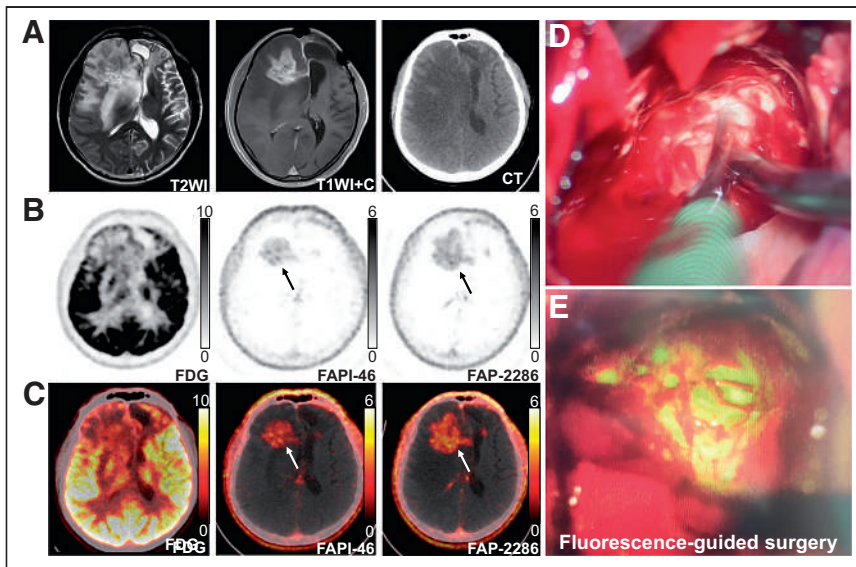


FIGURE 6. A 44-y-old man with glioblastoma who underwent surgical resection 1 y before images were obtained. (A) MRI revealed suggestive recurrent lesions in right frontal lobe adjacent to surgical margin (arrow). (B [axial PET image] and C [fused PET/CT image]) ^{68}Ga -FAP-2286 PET/CT yielded higher radiotracer uptake (SUV_{max} , 4.2 vs. 2.7; arrows) and TBR (70.0 vs. 45.0) than ^{68}Ga -FAP-46 in these lesions. (D [intraoperative view] and E [fluorescence-guided surgery]) Patient subsequently underwent surgical resection, and postoperative pathology confirmed diagnosis of recurrent glioblastoma. T1WI+C = T1-weighted imaging with contrast enhancement; T2WI = T2-weighted imaging.

include gastric, pancreatic, and hepatic cancers; the respective findings were in line with those described in previous publications (7). Specifically, pancreatic and hepatic cancers (especially intrahepatic cholangiocarcinoma) are characterized by intense stromal desmoplastic reactions surrounding cancer cells, and cancer-associated fibroblasts are the main effector cells in the desmoplastic reaction (21,22). Furthermore, because of the low background uptake in hepatic parenchyma, FAP imaging was able to detect hepatic tumors with favorable tumor-to-background contrast. Gastric cancer evokes the production and deposition of activated fibroblasts in the submucosa wall (23), resulting in increased ^{68}Ga -FAP uptake in gastric tumor lesions. Unlike ^{18}F -FDG, very low ^{68}Ga -FAP uptake was observed in the gastric wall and gastrointestinal tract, which further improved the detectability of gastric cancer. Taken together, high FAP expression and low background activity in abdominal organs are the main reasons and explain why ^{68}Ga -FAP-2286 PET/CT is superior to ^{18}F -FDG in terms of tumor detectability in these tumor entities. Improved tumor detectability may lead to changes in clinical staging and optimization of therapeutic strategies. Moreover, the favorable TBR may improve delineation of gross tumors in radiotherapy and evaluation of the effectiveness of therapy (24,25).

Our study was associated with several limitations. First, few patients underwent paired ^{68}Ga -FAP-2286 and ^{18}F -FDG PET/CT, rendering subgroup analysis of radiotracer uptake per tumor type impracticable. Second, as the subcohort of patients who underwent paired ^{68}Ga -FAP-2286 and ^{68}Ga -FAP-46 PET/CT was also small ($n = 19$), only a descriptive comparison was possible. Furthermore, as only 2 patients underwent ^{68}Ga -FAP-2286 PET/CT at multiple time points, we could not fully investigate radiotracer retention in tumors. Prospective studies with a larger patient population are warranted to better explore the role of ^{68}Ga -FAP-2286 in cancer diagnosis and the potential superiority of FAP-2286 with respect to other FAPI derivatives.

CONCLUSION

^{68}Ga -FAP-2286 is a promising FAPI derivative for safe cancer diagnosis, staging, and restaging. It may be superior to ^{18}F -FDG in selected cases, especially for cancers that exhibit low-to-moderate uptake of ^{18}F -FDG, including gastric, pancreatic, and hepatic cancers. In addition, ^{68}Ga -FAP-2286 and ^{68}Ga -FAP-46 yielded comparable clinical results.

DISCLOSURE

This work was funded by the National Natural Science Foundation of China (82071961), the Key Scientific Research Program for Young Scholars in Fujian (2021ZQNZD016), the Fujian Natural Science Foundation for Distinguished Young Scholars (2022D005), Key Medical and Health Projects in Xiamen (3502Z20209002), and National University of Singapore start-up grants (NUHSRO/2020/133/Startup/08, NUHSRO/2021/097/Startup/13). No other potential conflict of interest relevant to this article was reported.

KEY POINTS

QUESTION: Is ^{68}Ga -FAP-2286 an efficacious alternative for the imaging of FAP-positive tumors?

PERTINENT FINDINGS: In this preliminary report of a single-center, prospective study of the diagnostic accuracy of ^{68}Ga -FAP-2286 PET/CT of solid tumors, all 46 primary tumors in 9 types of cancer were identified with ^{68}Ga -FAP-2286, whereas 9 were missed with ^{18}F -FDG. ^{68}Ga -FAP-2286 yielded a higher radiotracer uptake and TBR than ^{18}F -FDG. ^{68}Ga -FAP-2286 and ^{68}Ga -FAP-46 yielded comparable clinical results.

IMPLICATIONS FOR PATIENT CARE: ^{68}Ga -FAP-2286 is a promising FAP-inhibitor derivative for safe cancer diagnosis, staging, and restaging.

REFERENCES

- Backhaus P, Gierse F, Burg MC, et al. Translational imaging of the fibroblast activation protein (FAP) using the new ligand [^{68}Ga]Ga-OncoFAP-DOTAGA. *Eur J Nucl Med Mol Imaging*. 2022;49:1822–1832.
- Kratochwil C, Flechsig P, Lindner T, et al. ^{68}Ga -FAP-2286 PET/CT: tracer uptake in 28 different kinds of cancer. *J Nucl Med*. 2019;60:801–805.
- Li M, Younis MH, Zhang Y, Cai W, Lan X. Clinical summary of fibroblast activation protein inhibitor-based radiopharmaceuticals: cancer and beyond. *Eur J Nucl Med Mol Imaging*. 2022;49:2844–2868.
- Pang Y, Zhao L, Luo Z, et al. Comparison of ^{68}Ga -FAP-2286 and ^{18}F -FDG uptake in gastric, duodenal, and colorectal cancers. *Radiology*. 2021;298:393–402.
- Zhao L, Chen J, Pang Y, et al. Fibroblast activation protein-based theranostics in cancer research: a state-of-the-art review. *Theranostics*. 2022;12:1557–1569.
- Shi X, Xing H, Yang X, et al. Comparison of PET imaging of activated fibroblasts and ^{18}F -FDG for diagnosis of primary hepatic tumours: a prospective pilot study. *Eur J Nucl Med Mol Imaging*. 2021;48:1593–1603.
- Chen H, Pang Y, Wu J, et al. Comparison of [^{68}Ga]Ga-DOTA-FAP-04 and [^{18}F]FDG PET/CT for the diagnosis of primary and metastatic lesions in patients with various types of cancer. *Eur J Nucl Med Mol Imaging*. 2020;47:1820–1832.

8. Pang Y, Zhao L, Shang Q, et al. Positron emission tomography and computed tomography with [⁶⁸Ga]Ga-fibroblast activation protein inhibitors improves tumor detection and staging in patients with pancreatic cancer. *Eur J Nucl Med Mol Imaging*. 2022;49:1322–1337.
9. Qin C, Shao F, Gai Y, et al. ⁶⁸Ga-DOTA-FAPI-04 PET/MR in the evaluation of gastric carcinomas: comparison with ¹⁸F-FDG PET/CT. *J Nucl Med*. 2022;63:81–88.
10. Loktev A, Lindner T, Burger EM, et al. Development of fibroblast activation protein-targeted radiotracers with improved tumor retention. *J Nucl Med*. 2019;60:1421–1429.
11. Fu K, Pang Y, Zhao L, et al. FAP-targeted radionuclide therapy with [¹⁷⁷Lu]Lu-FAPI-46 in metastatic nasopharyngeal carcinoma. *Eur J Nucl Med Mol Imaging*. 2022;49:1767–1769.
12. Zboralski D, Hoehne A, Bredenbeck A, et al. Preclinical evaluation of FAP-2286 for fibroblast activation protein targeted radionuclide imaging and therapy. *Eur J Nucl Med Mol Imaging*. 2022;49:3651–3667.
13. Baum RP, Schuchardt C, Singh A, et al. Feasibility, biodistribution, and preliminary dosimetry in peptide-targeted radionuclide therapy of diverse adenocarcinomas using ¹⁶⁶Lu-FAP-2286: first-in-humans results. *J Nucl Med*. 2022;63:415–423.
14. McConathy J, Dhawan M, Goenka A, et al. ¹⁷⁷Lu-FAP-2286 in patients with advanced or metastatic solid tumors: initial data from a phase 1/2 study investigating safety, pharmacokinetics, dosimetry, and preliminary antitumor activity (LuMI-ERE) [abstract]. *J Nucl Med*. 2022;63(suppl 2):2271.
15. Zhao L, Zhuang Y, Fu K, et al. Usefulness of [¹⁸F]fluorodeoxyglucose PET/CT for evaluating the PD-L1 status in nasopharyngeal carcinoma. *Eur J Nucl Med Mol Imaging*. 2020;47:1065–1074.
16. Yu S. Review of F-FDG synthesis and quality control. *Biomed Imaging Interv J*. 2006;2:e57.
17. Meyer C, Dahlbom M, Lindner T, et al. Radiation dosimetry and biodistribution of ⁶⁸Ga-FAPI-46 PET imaging in cancer patients. *J Nucl Med*. 2020;61:1171–1177.
18. Boellaard R, Delgado-Bolton R, Oyen WJ, et al. FDG PET/CT: EANM procedure guidelines for tumour imaging: version 2.0. *Eur J Nucl Med Mol Imaging*. 2015;42:328–354.
19. Parker MFL, Blecha J, Rosenberg O, Ohliger M, Flavell RR, Wilson DM. Cyclic ⁶⁸Ga-labeled peptides for specific detection of human angiotensin-converting enzyme 2. *J Nucl Med*. 2021;62:1631–1637.
20. Zhou X, Wang S, Xu X, et al. Higher accuracy of [⁶⁸Ga]Ga-DOTA-FAPI-04 PET/CT comparing with 2-[¹⁸F]FDG PET/CT in clinical staging of NSCLC. *Eur J Nucl Med Mol Imaging*. 2022;49:2983–2993.
21. Guo W, Pang Y, Yao L, et al. Imaging fibroblast activation protein in liver cancer: a single-center post hoc retrospective analysis to compare [⁶⁸Ga]Ga-FAPI-04 PET/CT versus MRI and [¹⁸F]-FDG PET/CT. *Eur J Nucl Med Mol Imaging*. 2021;48:1604–1617.
22. Nielsen MF, Mortensen MB, Detlefsen S. Key players in pancreatic cancer-stroma interaction: cancer-associated fibroblasts, endothelial and inflammatory cells. *World J Gastroenterol*. 2016;22:2678–2700.
23. Zhang J, Li S, Zhao Y, et al. Cancer-associated fibroblasts promote the migration and invasion of gastric cancer cells via activating IL-17a/JAK2/STAT3 signaling. *Ann Transl Med*. 2020;8:877.
24. Windisch P, Zwahlen DR, Koerber SA, et al. Clinical results of fibroblast activation protein (FAP) specific PET and implications for radiotherapy planning: systematic review. *Cancers (Basel)*. 2020;12:2629.
25. Zhao L, Pang Y, Zheng H, et al. Clinical utility of [⁶⁸Ga]Ga-labeled fibroblast activation protein inhibitor (FAPI) positron emission tomography/computed tomography for primary staging and recurrence detection in nasopharyngeal carcinoma. *Eur J Nucl Med Mol Imaging*. 2021;48:3606–3617.

Predicting Outcomes of Indeterminate Bone Lesions on ^{18}F -DCFPyL PSMA PET/CT Scans in the Setting of High-Risk Primary or Recurrent Prostate Cancer

Tim E. Phelps¹, Stephanie A. Harmon¹, Esther Mena¹, Liza Lindenberg¹, Joanna H. Shih², Deborah E. Citrin³, Peter A. Pinto⁴, Bradford J. Wood^{5,6}, William L. Dahut⁷, James L. Gulley⁷, Ravi A. Madan⁷, Peter L. Choyke¹, and Baris Turkbey¹

¹Molecular Imaging Branch, National Cancer Institute, National Institutes of Health, Bethesda, Maryland; ²Biometric Research Program, National Cancer Institute, National Institutes of Health, Rockville, Maryland; ³Radiation Oncology Branch, National Cancer Institute, National Institutes of Health, Bethesda, Maryland; ⁴Urologic Oncology Branch, National Cancer Institute, National Institutes of Health, Bethesda, Maryland; ⁵Radiology and Imaging Sciences, Clinical Center, National Institutes of Health, Bethesda, Maryland; ⁶Center for Interventional Oncology, National Cancer Institute, National Institutes of Health, Bethesda, Maryland; and ⁷Genitourinary Malignancies Branch, National Cancer Institute, National Institutes of Health, Bethesda, Maryland

Indeterminate bone lesions (IBLs) on prostate-specific membrane antigen (PSMA) PET/CT are common. This study aimed to define variables that predict whether such lesions are likely malignant or benign using features on PSMA PET/CT. **Methods:** ^{18}F -DCFPyL PET/CT imaging was performed on 243 consecutive patients with high-risk primary or biochemically recurrent prostate cancer. IBLs identified on PSMA PET/CT could not definitively be interpreted as benign or malignant. Medical records of patients with IBLs were reviewed to determine the ultimate status of each lesion. IBLs were deemed malignant or benign on the basis of evidence of progression or stability at follow-up, respectively, or by biopsy results; IBLs were deemed equivocal when insufficient or unclear evidence existed. Post hoc patient, lesion, and scan variables accounting for clustered data were evaluated using Wilcoxon rank-sum and χ^2 tests to determine features that favored benign or malignant interpretation. **Results:** Overall, 98 IBLs within 267 bone lesions (36.7%) were identified in 48 of 243 patients (19.8%). Thirty-seven of 98 IBLs were deemed benign, and 42 were deemed malignant, of which 8 had histologic verification; 19 remained equivocal. Location and SUV_{max} categorical variables were predictive of IBL interpretation ($P = 0.0201$ and $P = 0.0230$, respectively). For IBLs with new interpretations, 34 of 37 (91.9%) considered benign showed an SUV_{max} of less than 5 or exhibited focal uptake without coexisting bone metastases; 37 of 42 (88.1%) deemed malignant demonstrated an SUV_{max} of at least 5 or were present with coexisting bone metastases. Logistic regression predicted IBLs with a high SUV_{max} (univariable: odds ratio [OR], 9.29 [$P = 0.0016$]; multivariable: OR, 13.87 [$P = 0.0089$]) or present with other bone metastases (univariable: OR, 9.87 [$P = 0.0112$]; multivariable: OR, 11.35 [$P = 0.003$]) to be malignant. **Conclusion:** IBLs on PSMA PET/CT are concerning; however, characterizing their location, SUV, and additional scan findings can aid interpretation. IBLs displaying an SUV_{max} of at least 5 or present with other bone metastases favor malignancy. IBLs without accompanying bone metastases that exhibit an SUV_{max} of less than 5 and are observed only in atypical locations favor benign processes. These guidelines may assist in the interpretation of IBLs on PSMA PET/CT.

Key Words: prostate cancer; PET/CT; PSMA; bone metastases; indeterminate bone lesions

J Nucl Med 2023; 64:395–401
DOI: 10.2967/jnumed.122.264334

Prostate-specific membrane antigen (PSMA) PET/CT is a highly sensitive and specific diagnostic tool enabling early detection of primary and metastatic prostate cancer (PCa) (1). PSMA overexpression is observed in nearly 95% of all cases of primary PCa, and PSMA expression on histology correlates with tumor aggressiveness (2). The recent Food and Drug Administration approval of ^{18}F -DCFPyL has increased the use of PSMA PET/CT in staging and in suspected early metastatic involvement of patients with high-risk PCa and biochemically recurrent (BCR) PCa (3). However, ^{18}F -DCFPyL and other PSMA PET tracers commonly demonstrate nonspecific and indeterminate PSMA uptake in soft tissue or bones with unclear or no anatomic correlation on CT (4–6). To interpret lesions with PSMA uptake, several PSMA PET/CT reporting systems, including the European Association of Nuclear Medicine standardized reporting criteria (E-PSMA), the PSMA Reporting and Data System (PSMA-RADS), and the Prostate Cancer Molecular Imaging Standardized Evaluation (PROMISE), were developed with structured categories for lesions that are benign, likely benign, indeterminate or equivocal, likely malignant, and malignant (7–9). Lesion classification is based on location, size, SUV_{max} , relative uptake compared with expected physiologic uptake, number of lesions with PSMA uptake, and scan-based regional distribution (7); however, lesions classified as indeterminate require follow-up for definitive assessment. Since metastatic PCa commonly involves bones, PSMA uptake in indeterminate bone lesions (IBLs) that are benign processes, such as fibrous dysplasia, Paget disease, and hemangiomas, can easily be mistaken for bone metastases and lead to inappropriate changes in patient management (10–14). On the other hand, IBLs interpreted as benign when they are true metastases may delay necessary treatment. Recent PSMA PET/CT imaging studies using ^{18}F -PSMA-1007 (5,15,16), ^{68}Ga -PSMA-11 (6,16–18), and ^{18}F -DCFPyL (4) tracers have investigated indeterminate PSMA-avid uptake in soft-tissue and bone lesions. Although these studies associate certain imaging features with IBLs that are usually benign—specifically, a single IBL located in the rib with subtle PSMA uptake and no

Received Apr. 25, 2022; revision accepted Sep. 13, 2022.
For correspondence or reprints, contact Tim E. Phelps (tim.phelps@nih.gov).
Published online Oct. 20, 2022.
COPYRIGHT © 2023 by the Society of Nuclear Medicine and Molecular Imaging.

additional metastases—there lacks consensus regarding features that predict which IBLs are likely malignant. In this study, we defined features of ^{18}F -DCFPyL PET/CT that predict IBLs as benign or malignant.

MATERIALS AND METHODS

Patient Population

Between July 2017 and October 2021, ^{18}F -DCFPyL PET/CT imaging was performed on 243 consecutive patients with histologically confirmed high-risk PCa or BCR PCa without prior evidence of metastatic disease. All patients gave written informed consent before participating in a prospective clinical trial (NCT03181867). In a post hoc subanalysis, patients included in this study had at least 1 IBL in the presence or absence of other soft-tissue or bone lesions suggestive of metastatic PCa on ^{18}F -DCFPyL PET/CT. Patients without an IBL were excluded.

^{18}F -DCFPyL PET/CT Imaging

^{18}F -DCFPyL was synthesized under good manufacturing practices as previously described (19). Patients received an intravenous injection of ^{18}F -DCFPyL (mean, 262.7 ± 37.9 MBq [7.10 ± 1.02 mCi]; range, 167.6–317.8 MBq [4.53 – 8.59 mCi]) and underwent whole-body PET/CT after a 2-h uptake period (3 min/bed position) using a 3-dimensional time-of-flight Discovery MI DR scanner (GE Healthcare) with a 20-cm coronal and a 70-cm axial field of view. Image reconstruction applied an attenuation-corrected 3-dimensional iterative maximum-likelihood expectation-maximization algorithm using 29 subsets, 3 iterations, time-of-flight, a point spread function regularization parameter of 6.0, and a gaussian postprocessing filter with a 4.1-cm kernel. A low-dose unenhanced CT scan (120 kV, 60 mAs) was acquired with each PET scan for attenuation correction and anatomic coregistration.

Assessment of PSMA-Avid IBLs

^{18}F -DCFPyL PET/CT images were prospectively interpreted by 2 expert nuclear medicine physicians (both with 5 y of experience reading PSMA PET/CT images). Scans of patients with at least 1 PSMA-avid IBL, defined as focal radiotracer uptake in bone without correlative sclerotic or lytic features on CT, or not clearly benign—equivalent to the definition of the PSMA-RADS-3B category (9)—were further analyzed. Two different readers retrospectively reviewed each IBL using medical records until January 2022, including other pre-PSMA and post-PSMA follow-up imaging, therapeutic interventions, and laboratory or biopsy-based pathology, to provide an updated interpretation as benign, malignant, or equivocal based on the following criteria.

Benign findings were, first, no evidence of progression (i.e., a stable lesion without morphologic changes) between pre-PSMA and PSMA imaging for patients without follow-up or between pre-PSMA and post-PSMA imaging for patients with follow-up; second, PCa-negative biopsy findings for the lesion; or third, stable lesion uptake before therapeutic intervention at follow-up ^{18}F -DCFPyL PET/CT.

Malignant findings were, first, evidence of progression (i.e., new lesions, sclerotic changes, or lytic changes) between pre-PSMA and PSMA imaging for patients without follow-up or between pre-PSMA and post-PSMA imaging for patients with follow-up; second, PCa-positive biopsy findings for the lesion; or third, evidence of lesion regression after therapeutic intervention based on a significantly reduced SUV_{max} at follow-up ^{18}F -DCFPyL PET/CT imaging.

TABLE 1
Clinical Characteristics of Patients with IBLs

Characteristic	Data
Patients with IBL	48
Age (y)	
Median	66
Range	53–79
PSA (ng/mL)	
Median	4.00
Range	0.44–203.8
Disease phase	
BCR PCa	35
High-risk PCa	13
TNM stage	
Not available	5
T1	10
T2	13
T3	15
T2 N1	1
T3 N1	3
T4 N1	1
Gleason grade group	
1	2
2	14
3	10
4	7
5	15

Data are number of events unless otherwise indicated.

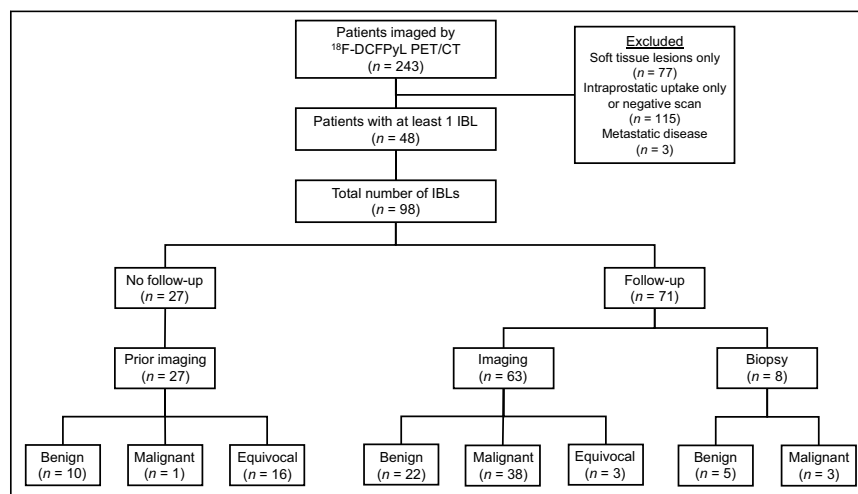


FIGURE 1. Flowchart of patient selection criteria and lesion-level follow-up for patients with at least 1 IBL. Interpretations (benign, malignant, or equivocal) are shown for IBLs with no follow-up (prior imaging) and follow-up (imaging or biopsy).

TABLE 2
Histopathologic Assessment of IBL Biopsy Specimens

Location of biopsied IBL	SUV _{max}	CT morphology	Histopathologic result	
			Finding	Features
Fifth rib	4.1	Sclerotic	Benign	Fibrous replacement of bone marrow
Third rib	3.6	Sclerotic	Benign	Trabecular bone with trilineage hematopoiesis
Sixth rib	2.9	Sclerotic	Benign	Fragments of bone marrow fibrosis
Ischium bone	17.4	Mixed sclerotic/lytic	Malignant	Metastatic prostate adenocarcinoma involving bone and bone marrow
Iliac bone	1.3	Negative	Malignant	Metastatic moderately differentiated prostate adenocarcinoma
Clavicle bone	3.1	Negative	Benign	Bone marrow with trilineage hematopoiesis
Seventh rib	2.8	Sclerotic	Benign	Bone with hematopoietic bone marrow
Fifth rib	15.2	Mixed sclerotic/lytic	Malignant	Metastatic poorly differentiated prostate adenocarcinoma

Equivocal findings were insufficient evidence for either a benign or a malignant interpretation due to a short follow-up duration or unclear imaging features.

Statistical Analysis

The association of IBL characteristics with an updated interpretation was evaluated using the Wilcoxon rank-sum test for clustered data (20) in continuous variables and the χ^2 test for clustered data (21) in categorical variables to account for multiple lesions sampled per patient. The characteristics evaluated included SUV_{max}, anatomic location; CT features (including no CT abnormality in bone sclerotic, lytic, and mixed sclerotic and lytic bone morphologies; and the presence or absence of other suggestive findings on PSMA imaging (including lymph node or bone uptake). Tests were repeated considering distribution of benign versus malignant lesion assignments as well as benign versus malignant versus equivocal categorizations. Logistic regression analysis, using weighted generalized estimation equations with working independence correlation structure to account for the correlation of multiple lesions per patient, was performed to evaluate the association of IBL characteristics with a malignant interpretation. Lesions with an equivocal clinical or pathologic interpretation were excluded from logistic regression analysis. Weights were calculated as $100 \times (1/N_p)$, where N_p is the number of lesions sampled per patient. *P* values of less than 0.05 were considered significant for all statistical analyses. Receiver-operating-characteristic curve and Youden index ([sensitivity + specificity - 1]) analyses were evaluated for the SUV_{max} of IBLs to be interpreted as benign or malignant. The SUV_{max} threshold with the highest sensitivity and lowest false positive rate was selected to differentiate lesions likely to be malignant.

RESULTS

Incidence and Interpretation of IBLs

Overall, 98 IBLs within 267 total bone lesions (36.7%) were identified in 48 of 243

patients (19.8%). Patient characteristics are shown in Table 1, and patient selection criteria with lesion-level follow-up and IBL interpretation based on review are shown in Figure 1. Median patient follow-up was 7.5 mo (range, 0.0–54.0 mo); median lesion follow-up was 4.8 mo (range, 1.1–54.0 mo) in patients with post-PSMA follow-up and 9.1 mo (range, 0.0–54.0 mo) in patients with prior imaging only. Detailed patient follow-up information was used to interpret each IBL as benign, malignant, or equivocal (Supplemental Fig. 1; Supplemental Table 1; supplemental materials are available at <http://jnm.snmjournals.org>).

The 98 IBLs had a median SUV_{max} of 3.6 (interquartile range, 2.3–9.8) and were identified in the pelvis (28.6%), spine (21.4%), ribs (39.8%), or other atypical locations including the scapula, clavicle, skull, sternum, and extremities (10.2%). Only 8 of 98 (8.2%) IBLs had biopsy confirmation—3 were malignant (metastatic prostate adenocarcinoma) and 5 were benign (Table 2). At the lesion level, 42 of 98 (42.9%) IBLs were considered malignant, 37 (37.7%) were benign, and 19 (19.4%) remained equivocal. Most IBLs were assessed as equivocal (18/19, 94.7%) because of short follow-up (<7 mo). At the

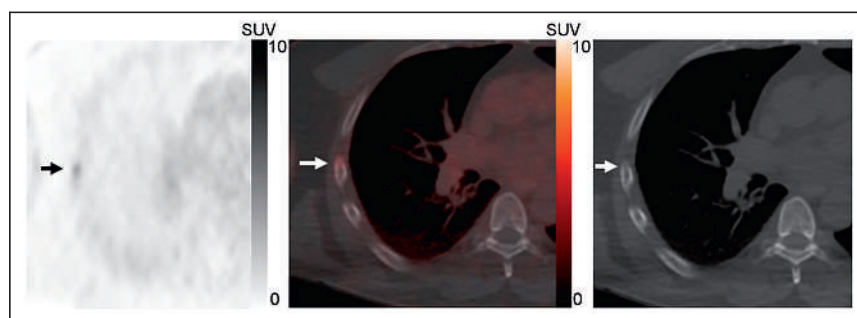


FIGURE 2. A 63-y-old patient with BCR PCa and PSA of 0.46 ng/mL. Axial ¹⁸F-DCFPyL PET (left), ¹⁸F-DCFPyL PET/CT (middle), and CT (right) images show a single area of subtle PSMA-avid uptake with SUV_{max} of 2.4 in the right fifth rib and no CT correlate (arrows). This IBL was determined to be benign based on negative 17-mo follow-up bone scintigraphy findings.

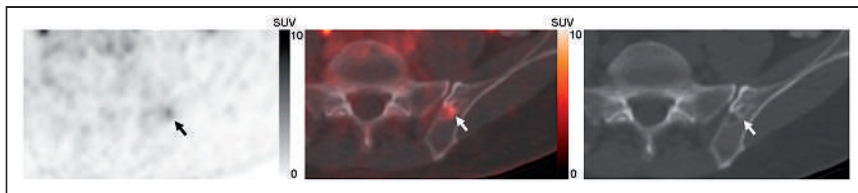


FIGURE 3. A 60-y-old patient with BCR PCa and PSA of 3.9 ng/mL. Axial ^{18}F -DCFPyL PET (left), ^{18}F -DCFPyL PET/CT (middle), and CT (right) images show a single area of subtle PSMA-avid uptake with SUV_{max} of 3.9 in left iliac bone and mixed sclerotic and lytic CT features (arrows). This IBL was stable for 4 mo and negative on 4 other staging modalities; thus, the IBL was interpreted as benign.

patient-level, 11 of 48 (22.9%) had a malignant IBL, 24 (50.0%) had a benign IBL, and 13 (27.1%) had equivocal findings; 1 patient with multiple IBLs had mixed determinations. Examples are given of patients with IBLs on ^{18}F -DCFPyL PET/CT which demonstrate benign (Figs. 2 and 3) or malignant (Fig. 4; Supplemental Fig. 2) characteristics based on their location, SUV_{max} , and CT morphology. PSMA PET/CT features in the pelvis (Fig. 3) and spine (Fig. 4) can show similarity but have different interpretations; thus, additional follow-up may assist with assessment.

Imaging Features of IBLs That Predict for Malignancy or Benignancy

Two lesion-based categorical variables were predictors for malignancy or benignancy: lesion location ($P = 0.0201$)—categorized as spine, pelvis, ribs, and other regions (e.g., skull, sternum, and scapula)—and lesion SUV_{max} ($P = 0.0230$)—categorized as less than 5 versus 5 or more (Table 3). No other ^{18}F -DCFPyL PET/CT-based continuous and categorical variables were predictive (Supplemental Table 2). Logistic regression analysis for benign versus malignant findings ($n = 79$) revealed that a high SUV_{max} (univariable: odds ratio [OR], 9.29 [95% CI, 3.19–24.75; $P = 0.0016$]; multivariable: OR, 13.87 [95% CI, 1.91–100.9; $P = 0.0089$]) and the presence of additional bone metastases on the PSMA PET/CT scan (univariable: OR, 9.87 [95% CI, 2.00–48.82; $P = 0.0112$]; multivariable: OR, 11.35 [95% CI, 3.05–42.25; $P = 0.0030$]) were associated with malignancy (Table 4). Selection of an SUV_{max}

threshold of at least 5 was based on receiver-operating-characteristic curve and Youden index analyses that maximized the sensitivity (71.4%, 30/42) for predicting IBLs as malignant with the fewest false positives (2.7%, 1/37) (Supplemental Fig. 3). Although this SUV_{max} threshold missed 12 of 42 (28.6%) IBLs with an SUV_{max} of less than 5 that were deemed malignant, 7 of these 12 IBLs were identified in the presence of other bone metastases. Therefore, a model incorporating all 3 ^{18}F -DCFPyL PET/CT imaging variables that predicted for malignancy or benignancy ($n = 79$) was developed to assess the likelihood that an IBL would be benign or malignant based on a single PSMA PET/CT scan (Fig. 5). Overall, 89.9% of the model's predictions agreed with our assessment, but 10.1% disagreed, including 5 false negatives and 3 false positives (Table 5). Although our model suggests that a single IBL located in the pelvis or spine with an SUV_{max} of less than 5 is probably benign, these are common sites for PCa bone metastases and represented a greater number of false negatives, such as the example in Figure 4. Ultimately, the relationship of these predictive variables may improve IBL interpretation on PSMA PET/CT scans (Fig. 6).

DISCUSSION

PSMA PET/CT can impact management decisions in patients with high-risk primary and BCR PCa, and multiple studies have demonstrated that up to 68% of predetermined interventions can change after PSMA PET/CT (22,23). Although the PSMA-RADS, PROMISE, and E-PSMA structured PSMA PET/CT reporting systems have improved lesion classification and interpretation based on particular imaging features, several lesions with PSMA uptake categorized as indeterminate or equivocal have been shown to be false positives (11–13) whereas some have been shown to be true positives at follow-up (4,18). A particular issue with PSMA PET/CT is the incidence of indeterminate lesions with mild focal uptake in bone

and unclear or negative anatomic features; currently, these lesions require biopsy or follow-up imaging for definitive assessment. Interpreting such lesions as metastatic without sufficient evidence can have far-reaching implications for patients and lead to unnecessary interventions that alter a patient's quality of life. Understanding specific features that increase the certainty of interpreting IBLs as probably benign or probably malignant is, therefore, of great clinical importance.

Our study demonstrated that 3 PSMA PET/CT-based features predict IBL interpretation: the presence or absence of other bone metastases on the scan, IBL SUV_{max} , and IBL location. Prior studies investigating IBLs using a variety of PSMA PET tracers have mentioned that these particular features may predict interpretation or are important. Specifically, a follow-up ^{18}F -PSMA-1007 PET/CT study by Arnfield et al. monitoring 159 IBLs for more than 12 mo in 77 patients suggested that IBLs were likely benign when

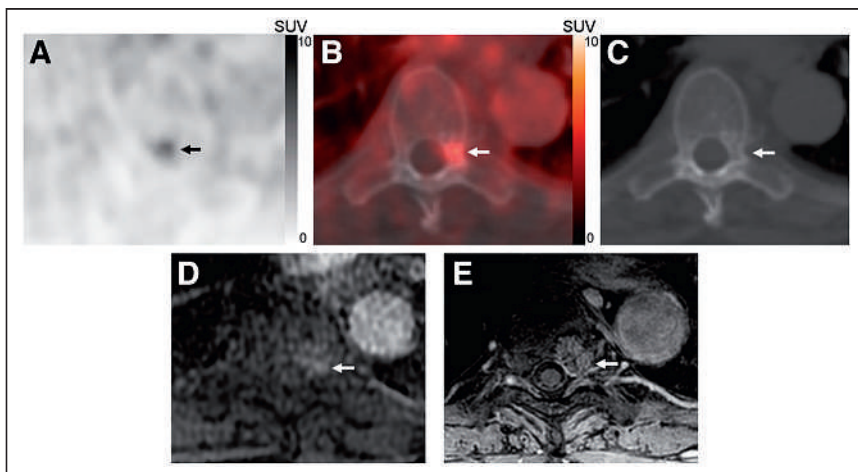


FIGURE 4. A 73-y-old patient with BCR PCa and PSA of 4.9 ng/mL. Axial ^{18}F -DCFPyL PET (A), ^{18}F -DCFPyL PET/CT (B), CT (C), pre-PSMA MRI (D), and follow-up MRI (E) images show a single area of subtle PSMA-avid uptake with SUV_{max} of 3.3 in left T8 lamina and subtle sclerotic CT features (arrows). This IBL became more prominent and enhanced over a 3-y period between retrospective MRI (D) and follow-up MRI (E) and was determined to be malignant.

TABLE 3
¹⁸F-DCFPyL PSMA PET/CT-Based Variables That Predict IBL Interpretation (*n* = 98)

Predictive variable	Incidence (<i>n</i> = 98)	IBL interpretation			<i>P</i> *
		M (<i>n</i> = 42)	B (<i>n</i> = 37)	E (<i>n</i> = 19)	
Location					0.0201
Spine	28 (28.6%)	16	12	0	
Pelvis	21 (21.4%)	12	7	2	
Rib	39 (39.8%)	8	14	17	
Other	10 (10.2%)	6	4	0	
SUV _{max}					0.0230
<5	64 (65.3%)	12	36	16	
≥5	34 (34.7%)	30	1	3	

*For 3-way assessment (M vs. B vs. E) statistical significance is evaluated using χ^2 test for clustered data.
M = malignant; B = benign; E = equivocal.

showing an SUV_{max} of less than 7.2 in the absence of other definite bone metastases (15). In contrast, a multicenter ¹⁸F-PSMA-1007 PET/CT study analyzing 351 IBLs with an SUV_{max} of less than 10 determined that SUV_{max} did not predict interpretation (5). Moreover, a follow-up ⁶⁸Ga-PSMA-11 PET/CT study by Chen et al. reported that 61 of 62 patients with primary PCa and a single rib IBL with a mean SUV_{max} of 3.0 were benign; however, 1 lesion showing an SUV_{max} of 2.2 later proved to be a metastasis (18). Lastly, a ¹⁸F-DCFPyL PET/CT longitudinal follow-up study found that 3 of 14 IBLs showed changes indicative of malignancy (4). These prior studies collectively demonstrate that a single IBL in an atypical location in the absence of metastases is meaningful for predicting IBLs as benign but that SUV_{max} is not reliable. In addition, our findings agree with previous studies that no patient variables (including age, primary PCa, Gleason grade group, TNM stage, and serum prostate-specific antigen [PSA]) predict IBL interpretation.

There are some similarities between these prior studies and our findings regarding which IBLs favor benign outcomes; however, we expand on the current understanding of imaging features that predict IBLs for malignancy. First, we suggest that IBLs are likely malignant

in the presence of other bone metastases, independent of SUV_{max} and location, but not necessarily with accompanying soft-tissue metastases. In our cohort, 7 of 48 patients with an IBL had no more than 3 other bone metastases, of which 3 of 7 also had lymph node involvement and 4 of 7 had no PSMA-avid lymph nodes. On the basis of our predictive model, 3 of the 4 patients with no PSMA-avid lymph nodes could be classified as oligometastatic and might have had the option to undergo local PCa interventions. Second, IBLs with an SUV_{max} of at least 5 after 2 h of ¹⁸F-DCFPyL uptake increased the likelihood of malignancy. Of the 34 IBLs showing an SUV_{max} of at least 5, 30 of 34 (88.2%) were deemed malignant, and only 1 of 34 (2.9%) was a false positive lesion deemed benign whereas 3 of 34 (8.8%) were equivocal because of insufficient evidence. However, IBLs with an increased SUV_{max} can result from inflammatory events such as trauma or hemangiomas (13), as well as from benign bone remodeling processes such as fibrous dysplasia (10) or Paget disease (24). Although the SUV_{max} threshold of at least 5 after 2 h of uptake was feasible to classify 88.2% of IBLs as malignant for our cohort, this SUV_{max} threshold requires validation in separate cohorts receiving ¹⁸F-DCFPyL PET/CT. Third, IBLs in typical locations were more

TABLE 4
Logistic Regression Analysis Showing OR at 95% CI for Clinically Relevant ¹⁸F-DCFPyL PET/CT-Based Features That Predict IBLs as Benign vs. Malignant (*n* = 79)

¹⁸ F-DCFPyL PET/CT feature	Univariable analysis		Multivariable analysis	
	OR	<i>P</i>	OR	<i>P</i>
IBL located in pelvis	1.68 (0.48–5.96)	0.516	—	—
IBL located in spine	1.42 (0.55–3.65)	0.613	—	—
IBL located in ribs	0.38 (0.14–1.03)	0.170	—	—
IBL SUV _{max}	9.29 (3.49–24.75)	0.0016	13.87 (1.91–100.9)	0.0089
Other bone metastases	9.87 (2.00–48.82)	0.0112	11.35 (3.05–42.25)	0.0030
Other lymph node metastases	2.26 (0.62–8.26)	0.315	—	—

Data in parentheses are 95% CI. Features significantly associated with malignant interpretation were included in multivariable analysis.

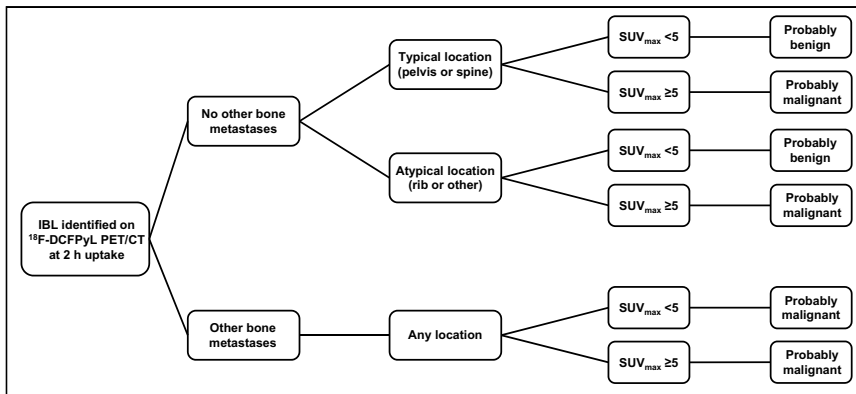


FIGURE 5. Model assessing the likelihood that an IBL is benign or malignant based on ^{18}F -DCFPyL PET/CT imaging variables that predicted for benignity or malignancy ($n = 79$).

commonly malignant based on follow-up review, but the association of lesion location with SUV_{max} and other PSMA scan bone findings, particularly whether lesions are solitary, multifocal, or present with other bone metastases, can improve assessment as displayed in Figures 5 and 6.

Although these predictors can guide interpretation, follow-up imaging may be necessary when insufficient evidence is available or conflicting imaging features are present on other studies. In this scenario, equivocal interpretation avoids misdiagnosis, and follow-up imaging can assist with assessment. Of the 19 of 98 (19.4%) IBLs that remained equivocal in our study, 16 had no available post-PSMA follow-up records, 2 had short follow-up (<3 mo), and 1 had sufficient follow-up (12 mo) but CT changes were not clear enough for a definitive interpretation. Overall, most IBLs that were determined to be equivocal (14/19, 74%) showed an SUV_{max} of less than 5 and were located in the ribs without other bone metastases.

IBLs showing subtle PSMA uptake only outside the pelvis or spine in the absence of definite bone metastases are likely benign; however, malignancy is always possible. For example, in the ^{68}Ga -PSMA-11 PET/CT study mentioned earlier, 1 of 62 (1.6%) single rib IBLs with an SUV_{max} of 2.2 in the absence of other metastases demonstrated evidence of malignancy on follow-up imaging (18).

12.5 (range, 5.1–26.0) were benign, indicating that several lesions were not clinically concerning despite exceeding a prior proposed SUV_{max} threshold of 7.2–11.1 after 2 h of uptake (15,25). Thus, standardized imaging protocols for each class of PSMA tracer are necessary before SUV_{max} can reliably serve as a predictor of risk of malignancy. Ultimately, pairing detailed patient history with these predictive imaging features may increase the predictive value of IBL categorization among different PSMA agents and scanning conditions.

Our study had 3 main limitations. First, the follow-up time for our patients was short (mean, 7.5 mo; range, 0.0–54.0 mo); thus, nearly 20% of the IBLs remained equivocal because of insufficient evidence. Second, only a minority of IBLs were biopsied (8%, 8/98) since biopsy was not always safe to obtain or accepted by patients; however, all biopsy results supported our predictive model. Despite careful analysis of imaging and clinical findings, the lack of pathology confirmation may misrepresent the true nature of some IBLs deemed benign or malignant. Third, our results are limited to one type of PSMA-targeted PET tracer, ^{18}F -DCFPyL, after 2 h of uptake, and quantitative SUV_{max} PET findings may not apply to other tracers scanned under different conditions. However, other variables such as location and additional bone findings may still be relevant with other tracers.

TABLE 5
Model Predicting the Likelihood That IBLs Identified on ^{18}F -DCFPyL PET/CT at 2 Hour of Uptake Are Benign or Malignant ($n = 79$)

Other PSMA-avid bone findings	IBL location	IBL SUV_{max}	Likelihood of interpretation	Interpretation accuracy
No bone metastases	Typical	<5	81.0% benign	True positive ($n = 17$); false negative ($n = 4$)
No bone metastases	Typical	≥ 5	94.7% malignant	True positive ($n = 18$); false positive ($n = 1$)
No bone metastases	Atypical	<5	94.4% benign	True negative ($n = 17$); false negative ($n = 1$)
No bone metastases	Atypical	≥ 5	100% malignant	True positive ($n = 8$)
Bone metastases	Any	<5	77.8% malignant	True positive ($n = 7$); false positive ($n = 2$)
Bone metastases	Any	≥ 5	100% malignant	True positive ($n = 4$)

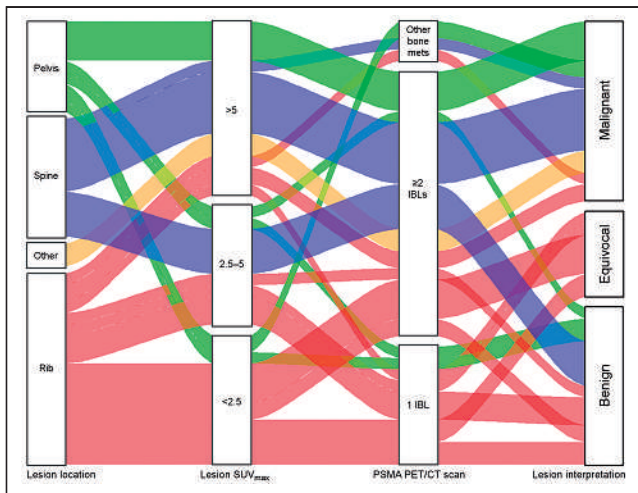


FIGURE 6. Sankey diagram showing the relationship of multiple predictive ^{18}F -DCFPyL features ($n = 98$). Specifically, lesion location, lesion SUV_{max} , and type of bone findings on a PSMA PET/CT scan are more likely associated with a particular lesion interpretation (right). Pathways with 1 lesion have been removed for clarity.

CONCLUSION

IBLs on PSMA PET/CT are concerning in patients with high-risk primary and BCR PCa; however, IBL location, SUV, and additional scan findings can aid interpretation. IBLs in any location with an SUV_{max} of at least 5 or with coexisting bone metastases irrespective of location and SUV_{max} have an increased risk for malignancy. Conversely, IBLs with an SUV_{max} of less than 5 that are present only in atypical locations such as the ribs without accompanying bone metastases are likely benign. These predictors may assist in decreasing the number of bone lesions on PSMA PET/CT that are truly indeterminate.

DISCLOSURE

No potential conflict of interest relevant to this article was reported.

KEY POINTS

QUESTION: Can imaging-based features on PSMA PET/CT predict the likelihood that an IBL is benign or malignant?

PERTINENT FINDINGS: Categorizing IBL location and SUV_{max} can predict for malignancy versus benignancy in ^{18}F -DCFPyL PET/CT scans. An IBL with coexisting bone metastases or an IBL with an SUV_{max} of at least 5 after 2 h of uptake, independent of location, is suggestive of malignancy. An IBL in an atypical location such as the rib with an SUV_{max} of less than 5 after 2 h of uptake and without accompanying bone metastases is usually benign.

IMPLICATIONS FOR PATIENT CARE: Considering the location and SUV_{max} of IBLs and other findings on PSMA PET/CT scans can reduce the number of patients with an IBL by reassigning such lesions to either the benign or malignant category.

REFERENCES

- Rowe SP, Macura KJ, Mena E, et al. PSMA-based [^{18}F]DCFPyL PET/CT is superior to conventional imaging for lesion detection in patients with metastatic prostate cancer. *Mol Imaging Biol.* 2016;18:411–419.
- Bravaccini S, Puccetti M, Bocchini M, et al. PSMA expression: a potential ally for the pathologist in prostate cancer diagnosis. *Sci Rep.* 2018;8:4254–4254.
- Keam SJ. Piflufolostat F 18: diagnostic first approval. *Mol Diagn Ther.* 2021;25:647–656.
- Yin Y, Werner RA, Higuchi T, et al. Follow-up of lesions with equivocal radiotracer uptake on PSMA-targeted PET in patients with prostate cancer: predictive values of the PSMA-RADS-3A and PSMA-RADS-3B categories. *J Nucl Med.* 2019;60:511–516.
- Grünig H, Maurer A, Thali Y, et al. Focal unspecific bone uptake on [^{18}F]PSMA-1007 PET: a multicenter retrospective evaluation of the distribution, frequency, and quantitative parameters of a potential pitfall in prostate cancer imaging. *Eur J Nucl Med Mol Imaging.* 2021;48:4483–4494.
- Kesler M, Kerzhner K, Druckmann I, et al. Staging ^{68}Ga -PSMA PET/CT in 963 consecutive patients with newly diagnosed prostate cancer: incidence and characterization of skeletal involvement. *Eur J Nucl Med Mol Imaging.* 2022;49:2077–2085.
- Ceci F, Oprea-Lager DE, Emmett L, et al. E-PSMA: the EANM standardized reporting guidelines v1.0 for PSMA-PET. *Eur J Nucl Med Mol Imaging.* 2021;48:1626–1638.
- Eiber M, Herrmann K, Calais J, et al. Prostate cancer molecular imaging standardized evaluation (PROMISE): proposed mTNM classification for the interpretation of PSMA-ligand PET/CT. *J Nucl Med.* 2018;59:469–478.
- Rowe SP, Pienta KJ, Pomper MG, Gorin MA. Proposal for a structured reporting system for prostate-specific membrane antigen-targeted PET imaging: PSMA-RADS version 1.0. *J Nucl Med.* 2018;59:479–485.
- Plouznikoff N, Garcia C, Artigas C, Entezari K, Flamen P. Heterogeneity of ^{68}Ga -PSMA PET/CT uptake in fibrous dysplasia. *Clin Nucl Med.* 2019;44:e593–e594.
- Hofman MS, Hicks RJ, Maurer T, Eiber M. Prostate-specific membrane antigen PET: clinical utility in prostate cancer, normal patterns, pearls, and pitfalls. *Radiographics.* 2018;38:200–217.
- Keidar Z, Gill R, Goshen E, et al. ^{68}Ga -PSMA PET/CT in prostate cancer patients: patterns of disease, benign findings and pitfalls. *Cancer Imaging.* 2018;18:39.
- Sheikhabahai S, Afshar-Oromieh A, Eiber M, et al. Pearls and pitfalls in clinical interpretation of prostate-specific membrane antigen (PSMA)-targeted PET imaging. *Eur J Nucl Med Mol Imaging.* 2017;44:2117–2136.
- De Vincentis G, Monari F, Baldari S, et al. Narrative medicine in metastatic prostate cancer reveals ways to improve patient awareness & quality of care. *Future Oncol.* 2018;14:2821–2832.
- Amfield EG, Thomas PA, Roberts MJ, et al. Clinical insignificance of [^{18}F]PSMA-1007 avid non-specific bone lesions: a retrospective evaluation. *Eur J Nucl Med Mol Imaging.* 2021;48:4495–4507.
- Kuten J, Dekalo S, Mintz I, Yossepowitch O, Mano R, Even-Sapir E. The significance of equivocal bone findings in staging PSMA imaging in the preoperative setting: validation of the PSMA-RADS version 1.0. *EJNMMI Res.* 2021;11:3.
- Rauscher I, Krönke M, König M, et al. Matched-pair comparison of ^{68}Ga -PSMA-11 PET/CT and ^{18}F -PSMA-1007 PET/CT: frequency of pitfalls and detection efficacy in biochemical recurrence after radical prostatectomy. *J Nucl Med.* 2020;61:51–57.
- Chen MY, Franklin A, Yaxley J, et al. Solitary rib lesions showing prostate-specific membrane antigen (PSMA) uptake in pre-treatment staging ^{68}Ga -PSMA-11 positron emission tomography scans for men with prostate cancer: benign or malignant? *BJU Int.* 2020;126:396–401.
- Szabo Z, Mena E, Rowe SP, et al. Initial evaluation of [^{18}F]DCFPyL for prostate-specific membrane antigen (PSMA)-targeted PET imaging of prostate cancer. *Mol Imaging Biol.* 2015;17:565–574.
- Rosner B, Glynn RJ, Lee ML. Extension of the rank sum test for clustered data: two-group comparisons with group membership defined at the subunit level. *Biometrics.* 2006;62:1251–1259.
- Shih JH, Fay MP. Pearson's chi-square test and rank correlation inferences for clustered data. *Biometrics.* 2017;73:822–834.
- Han S, Woo S, Kim YJ, Suh CH. Impact of ^{68}Ga -PSMA PET on the management of patients with prostate cancer: a systematic review and meta-analysis. *Eur Urol.* 2018;74:179–190.
- Fendler WP, Ferdinandus J, Czernin J, et al. Impact of ^{68}Ga -PSMA-11 PET on the management of recurrent prostate cancer in a prospective single-arm clinical trial. *J Nucl Med.* 2020;61:1793–1799.
- Blazak JK, Thomas P. Paget disease: a potential pitfall in PSMA PET for prostate cancer. *Clin Nucl Med.* 2016;41:699–700.
- Vollnberg B, Alberts I, Genitsch V, Rominger A, Afshar-Oromieh A. Assessment of malignancy and PSMA expression of uncertain bone foci in [^{18}F]PSMA-1007 PET/CT for prostate cancer: a single-centre experience of PET-guided biopsies. *Eur J Nucl Med Mol Imaging.* 2022;49:3910–3916.

¹⁷⁷Lu-PSMA-I&T for Treatment of Metastatic Castration-Resistant Prostate Cancer: Prognostic Value of Scintigraphic and Clinical Biomarkers

Amir Karimzadeh^{1,2}, Matthias Heck³, Robert Tauber³, Karina Knorr¹, Bernhard Haller⁴, Calogero D'Alessandria¹, Wolfgang A. Weber¹, Matthias Eiber^{*1}, and Isabel Rauscher^{*1}

¹Department of Nuclear Medicine, School of Medicine, Technical University of Munich, Munich, Germany; ²Department of Diagnostic and Interventional Radiology and Nuclear Medicine, University Medical Center Hamburg-Eppendorf, Hamburg, Germany; ³Department of Urology, School of Medicine, Technical University of Munich, Munich, Germany; and ⁴Institute of AI and Informatics in Medicine, School of Medicine, Technical University of Munich, Munich, Germany

The aim of this retrospective analysis was to determine prostate-specific antigen (PSA) response, PSA progression-free survival (PFS), and overall survival (OS) in a large cohort of patients with metastatic castration-resistant prostate cancer (mCRPC) treated with ¹⁷⁷Lu-PSMA-I&T and to identify clinical and scintigraphic prognostic factors for outcome. **Methods:** In total, 301 consecutive mCRPC patients were included in this analysis. Prognostic factors included clinical parameters, routine laboratory parameters, and findings on posttreatment scintigraphy. Scintigraphic tumor uptake of ¹⁷⁷Lu-PSMA-I&T was compared with salivary gland uptake and classified as high or low. The longest extent of skeletal metastatic disease was measured, and its changes during therapy were used to define scintigraphic progression, response, and stable disease. A PSA response of at least 50%, PSA PFS, and OS were calculated. **Results:** In total, 1,138 cycles (median, 3 cycles per patient) of ¹⁷⁷Lu-PSMA-I&T using a standard activity of 7.4 GBq were applied intravenously every 4–10 wk (median, 6 wk). Overall, 34% (95% CI, 28%–38%) of patients showed a PSA response of at least 50%, and the median PSA PFS and OS of the total patient cohort were 16.0 wk (95% CI, 12.1–19.9) and 13.8 mo (95% CI, 12.4–15.5), respectively. Patients with high scintigraphic tumor uptake showed a higher PSA response rate of at least 50% (45.7% vs. 10.4%; $P < 0.0001$) and a significantly reduced risk of PSA progression (median event time, 24.9 vs. 9.0 wk; hazard ratio, 0.3; 95% CI, 0.2–0.5; $P < 0.0001$). In our data, risk of death was not significantly different between patients with high scintigraphic uptake and those with low scintigraphic uptake (median, 14.4 vs. 12.4 mo; hazard ratio, 0.9; 95% CI, 0.6–1.3; $P = 0.6$). In a multivariable analysis, the following pretherapeutic prognostic factors for OS were identified: alkaline phosphatase, lactate dehydrogenase, and PSA levels; prior chemotherapy; and the presence of visceral metastases. Scintigraphic response was a strong prognostic factor for PSA response, PSA PFS, and OS after 1 treatment cycle. **Conclusion:** This retrospective analysis of a large group of consecutive patients corroborates previous clinical experience for ¹⁷⁷Lu-PSMA-I&T in mCRPC and establishes previously proposed prognostic factors. The skeletal tumor extent and its changes were identified as new potential biomarkers to predict the outcome of therapy after the first treatment cycle.

Key Words: ¹⁷⁷Lu-PSMA-I&T; metastatic castration-resistant prostate cancer (mCRPC); prognostic factors; scintigraphic biomarkers; clinical biomarkers

J Nucl Med 2023; 64:402–409
DOI: 10.2967/jnumed.122.264402

Prostate-specific membrane antigen (PSMA)-targeted radioligand therapy (RLT) has increasingly emerged for therapy of patients with metastatic castration-resistant prostate cancer (mCRPC) who exhausted approved treatment regimens (1,2). For the PSMA ligand ¹⁷⁷Lu-PSMA-617, efficacy and low toxicity have been shown in several retrospective analyses and in 2 phase II prospective trials (1,3,4). Recently, prolonged overall survival (OS) and progression-free survival (PFS) were proven in a randomized phase III clinical trial just recently resulting in Food and Drug Administration approval (5). Further, clinical parameters such as prior chemotherapy, the presence of visceral metastases, and increased levels of serum lactate dehydrogenase (LDH) have been found to be negatively correlated with patient outcome (6).

Another PSMA ligand that has shown promise for therapy of mCRPC is ¹⁷⁷Lu-PSMA-I&T, although clinical experience is more limited (7). ¹⁷⁷Lu-PSMA-I&T is currently being explored in a multicenter, randomized prospective phase III trial in mCRPC prior chemotherapy (SPLASH, NCT04647526) after second-line hormonal treatment, with the first results expected in 2023.

Previously, results on 100 patients who underwent ¹⁷⁷Lu-PSMA-I&T RLT showed mild toxicity and good antitumor activity in late-stage mCRPC (2). A prostate-specific antigen (PSA) decline of at least 50% within 12 wk was associated with longer clinical PFS and OS. A subgroup analysis identified an association of visceral metastasis at baseline and increased LDH with worse outcome.

The first preliminary retrospective analyses indicate that intensity on posttherapeutic ¹⁷⁷Lu-PSMA scintigraphy could be predictive for PSA response, suggesting it as a simple, fast, and widely available imaging biomarker for therapy response (8). However, data are sparse, and impact on OS has not been evaluated. Our clinical experience indicates that the extent of disease and, specifically, infiltration of the appendicular skeleton on posttherapeutic scans and its change during ¹⁷⁷Lu-PSMA RLT also hold promise to serve as a new and potentially prognostic imaging biomarker.

Received May 11, 2022; revision accepted Sep. 14, 2022.
For correspondence or reprints, contact Amir Karimzadeh (amir.karimzadeh@uke.de).

*Contributed equally to this work.

Published online Sep. 22, 2022.

COPYRIGHT © 2023 by the Society of Nuclear Medicine and Molecular Imaging.

Thus, the aim of our retrospective analysis was to update our clinical experience with ^{177}Lu -PSMA-I&T; to evaluate, especially, the prognostic value of clinical and laboratory parameters; and to investigate the use of posttreatment whole-body scintigraphy to predict patient outcome.

MATERIALS AND METHODS

Patients and ^{177}Lu -PSMA-I&T RLT

This retrospective analysis included 301 consecutive mCRPC patients receiving at least 2 cycles of ^{177}Lu -PSMA-I&T between December 2014 and July 2020. All patients had previously received second-line hormonal therapy with abiraterone or enzalutamide and chemotherapy or were unfit for chemotherapy. Patient characteristics are shown in Table 1. Before treatment, sufficient PSMA expression was confirmed by PSMA ligand PET imaging (^{68}Ga -PSMA-11, ^{18}F -PSMA-1007, ^{18}F -rhPSMA-7, or ^{18}F -rhPSMA-7.3). Only patients with PSMA ligand uptake in tumor lesions at least as high as liver background uptake were treated.

TABLE 1
Baseline Patient Characteristics

Characteristic	Data
No. of patients	301
Age (y), $n = 301$	73 (67–77)
PSA (ng/mL), $n = 297$	99.5 (20.4–290.3)
LDH (U/L), $n = 297$	263.5 (218–344)
AP (U/L), $n = 297$	112 (72–231)
Hemoglobin (g/dL), $n = 297$	11.7 (10.3–12.8)
Prior systemic therapies for mCRPC, $n = 301$	
Docetaxel	213
Cabazitaxel	48
Abiraterone	252
Enzalutamide	183
^{223}Ra	41
Previous chemotherapy	214
No. of prior mCRPC therapies, $n = 301$	
1	105
2	109
3	68
4	18
5	4
Site of metastasis, $n = 301$	
Lymph node, overall	216
Lymph node only (N1+/M1a)	22
Bone overall	274
Bone (M1b, without visceral metastases)	215
Visceral, overall (M1c)	64
Liver	26
Lung	31
Adrenal	21

Qualitative data are number and percentage; continuous data are median and interquartile range.

This patient population includes the 100 patients reported by Heck et al. but adds new patients and extended follow-up for the first 100 patients (2).

^{177}Lu -PSMA-I&T was prepared according to good manufacturing practice and the German Medicinal Products Act (arzneimittelgesetz §13 2b). The institutional ethics committee approved this retrospective analysis under reference number 115/18S, and all subjects gave written informed consent. Patients were treated under the conditions of the Declaration of Helsinki, article 37, “Unproven Interventions in Clinical Practice.”

Whole-Body Scintigraphy and Image Analysis

Posttherapeutic whole-body scintigraphy (planar anterior and posterior views) was performed approximately 24 h after injection at every cycle using a Symbia T series camera (Siemens) with a medium-energy parallel-hole collimator, a scan speed of 20 cm/min, and 113 keV \pm 20% and 208 keV \pm 12% photopeak windows. All images were evaluated by one nuclear medicine physician in training under the supervision of one board-certified nuclear medicine physician with more than 7 y of experience in PSMA-targeted imaging and therapy.

The whole-body scans were analyzed for scintigraphic tumor uptake and the extent of skeletal metastatic disease. Tumor uptake of ^{177}Lu -PSMA-I&T on the first posttreatment scan was visually classified as high when most metastatic lesions exceeded the physiologic uptake of the salivary glands. If most lesions equaled or were lower than uptake in the salivary glands, the tumor uptake was classified as low. The extent of skeletal metastatic disease was assessed by a simple quantitative index, as follows. On the first posttherapy scintigram, the longest extent of metastatic disease in a single bone (e.g., femur) contributing to the appendicular skeleton (including clavicle, scapula, humerus, radius, ulna, and the pelvic bones, except the sacrum, femur, tibia, and fibula) was identified and its absolute extent was measured with a ruler. If metastatic bone infiltration was discontinuous in a particular bone, the extents of each site of metastatic disease were measured and summed. On the second posttherapy scintigram, the extent of the same metastatic site was reassessed. The absolute change between the first and second posttherapeutic scans was calculated and defined as change in infiltration length. Scintigraphic progression, response, and stable disease were defined as more than a 0.5-cm increase, more than a 0.5-cm decrease, and a \pm 0.5-cm change in infiltration length between the first and second cycles, respectively.

Clinical Parameters, PSA Response, and PSA Progression

The following pretherapeutic parameters were collected: age, alkaline phosphatase (AP), LDH, hemoglobin, and PSA, as well as their relative changes between the first and second cycles. PSA response was defined as a PSA decline of at least 50% from baseline according to the criteria of Prostate Cancer Clinical Trials Working group 3 (9). PSA progression was defined either as a PSA increase of at least 25% and at least 2 ng/mL above the nadir after an initial PSA decline or a PSA increase of at least 25% and at least 2 ng/mL from baseline in cases with no PSA decline (9).

Prior systemic therapies (including abiraterone, enzalutamide, first- and second-line chemotherapy, and ^{223}Ra) and metastatic patterns (N+/M1a, lymph node only disease; M1b, presence of bone metastases without visceral metastases; and M1c, presence of visceral metastases) derived from PSMA PET imaging were collected.

Statistical Analysis

Primary outcome measures were PSA response, OS, and PSA PFS. The Kaplan–Meier method was used to estimate event time distributions, and log-rank tests were used for group comparisons. To correct for log-rank test α -error accumulation, significance was assumed when P values were less than 0.016 (Bonferroni adjustment for impact

of infiltration length on OS and PSA PFS). Frequencies of PSA response were compared between groups using χ^2 tests.

Univariable and multivariable Cox regression analyses were performed to determine the association of pretherapeutic parameters, relative changes in laboratory parameters, and information from posttherapeutic scintigraphy (scintigraphic tumor uptake and change in infiltration length) with PSA PFS and OS. A subgroup analysis in patients without visceral metastases was performed given the known strong negative association of visceral metastases with outcome. The corresponding hazard ratios (HRs) and 95% CIs are presented. A *P* value of less than 0.05 was considered statistically significant.

For tumor uptake, as well as classification of scintigraphic response, stable disease, and progression, the Cohen κ -coefficient was calculated for intrarater reliability. Strength of agreement for κ values was interpreted according to the Landis and Koch benchmark scale (10).

χ^2 tests, Kaplan–Meier estimation, log-rank tests, and calculation of the Cohen κ -coefficient were performed using Prism (version 8.4.3; GraphPad Software) for Mac (Apple). Uni- and multivariable Cox regression analysis was performed using SPSS Statistics (version 25.0; IBM Corp.) for Windows (Microsoft).

RESULTS

In total, 301 patients were analyzed, and 1,138 cycles of PSMA RLT with a median of 3 cycles per patient (range, 2–20) were applied. The patients received an intravenous treatment using a standard activity of 7.4 GBq of ^{177}Lu -PSMA-I&T every 4–10 wk (median, 6 wk), which could be slightly adapted on the basis of, for example, lab test results and tumor burden. The median time on treatment was 3 mo. Posttherapeutic scintigraphy and complete laboratory results were not available for 2 and 4 patients, respectively. At baseline, pelvic lymph nodes, extrapelvic lymph nodes, bone metastases, and visceral metastases were present in 159 (52.8%), 192 (63.8%), 274 (91.0%), and 64 (21.3%) patients, respectively. The median follow-up was 9 mo (range, 1–63 mo). One hundred one (34%; 95% CI, 28%–38%) patients achieved a PSA response after PSMA-targeted RLT. In the total patient cohort, median OS was 13.8 mo (95% CI, 12.4–15.5 mo) and median PSA PFS was 16.0 wk (95% CI, 12.1–19.9 wk). At the time of analysis, 226 patients had shown PSA progression and 182 patients had died.

Impact of Scintigraphic Tumor Uptake on PSA Response, PSA PFS, and OS

High (>salivary gland level) and low (\leq salivary gland level) scintigraphic tumor uptake was observed in 202 (67.6%) and 97 (32.4%) patients, respectively. The classification as high or low uptake achieved substantial agreement for intrarater reliability ($\kappa = 0.796$). PSA response was achieved in 91 (45.7%) patients with high uptake versus 10 (10.4%) patients with low uptake ($P < 0.0001$; Fig. 1). Examples of patients with high and low uptake are presented in Figure 2.

PSA PFS in patients with high uptake was significantly longer than in those with low uptake (median, 24.9 vs. 9.0 wk; HR, 0.3; 95% CI, 0.2–0.5; $P < 0.0001$; Fig. 3A). OS did not significantly differ between patients with high uptake and those with low uptake (median, 14.4 vs. 12.4 mo; HR, 0.9; 95% CI, 0.6–1.3; $P = 0.6$; Fig. 3B). In the subgroup of patients without visceral metastases, higher rates of PSA response (50.3% vs. 12.5%) were achieved, and PSA PFS and OS were significantly longer in patients with high uptake (median, 26.7 vs. 9.0 wk; HR, 0.3; 95% CI, 0.2–0.4; $P < 0.0001$) than in those with low uptake (15.5 vs. 11.4 mo; HR, 0.6; 95% CI, 0.4–1.0; $P = 0.03$) (Figs. 3C and 3D).

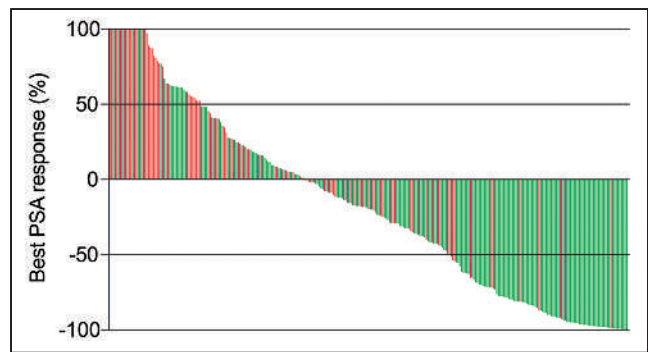


FIGURE 1. Waterfall plot showing response to treatment as measured by serum PSA. Best PSA response is defined as smallest increase or greatest decrease in PSA from baseline compared with color-coded ^{177}Lu -PSMA ligand uptake in posttherapeutic whole-body scintigraphy. First 21 columns represent patients with increase of >100% as best PSA response. Red = patients with low scintigraphic uptake on posttherapeutic scintigraphy; green = patients with high scintigraphic uptake on posttherapeutic scintigraphy.

Impact of Infiltration Length on PSA Response, PSA PFS, and OS

The median extent of metastases on the first and second posttreatment scans was 9.8 cm (range, 1.2–76.9 cm) and 10.3 cm (range, 0.0–78.4 cm), respectively. In 4 patients, the extents of metastatic disease in the femur and the tibia/fibula were summed because of a lack of delimitation of the infiltration path. No significant correlation between quartiles of the extent of disease and PSA PFS ($P = 0.4$) or OS ($P = 0.2$) was observed (Supplemental Fig. 1; supplemental materials are available at <http://jnm.snmjournals.org>).

Overall, 46 (24.7%), 65 (34.9%), and 75 (40.3%) patients showed scintigraphic response, stable disease, and progression, respectively. The classification of scintigraphic response, stable disease, and progression achieved substantial agreement for intrarater reliability (weighted $\kappa = 0.711$). A PSA response was achieved in 64.4%

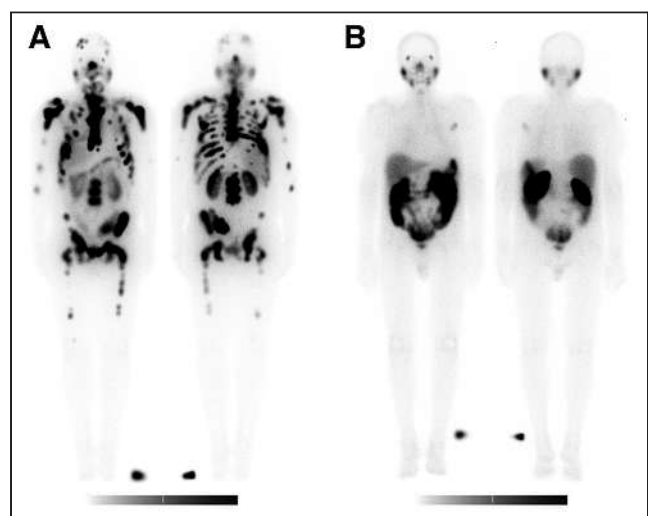


FIGURE 2. A 69-year-old patient with bone metastases presenting with high scintigraphic uptake (A) and a 76-year-old patient with bone and lymph node metastases presenting with low scintigraphic uptake (B) on posttherapeutic whole-body scintigraphy at first cycle of ^{177}Lu -PSMA-I&T. PSA PFS and OS were 58 wk and 24 mo, respectively, in patient A and 17 wk and 10 mo, respectively, in patient B.

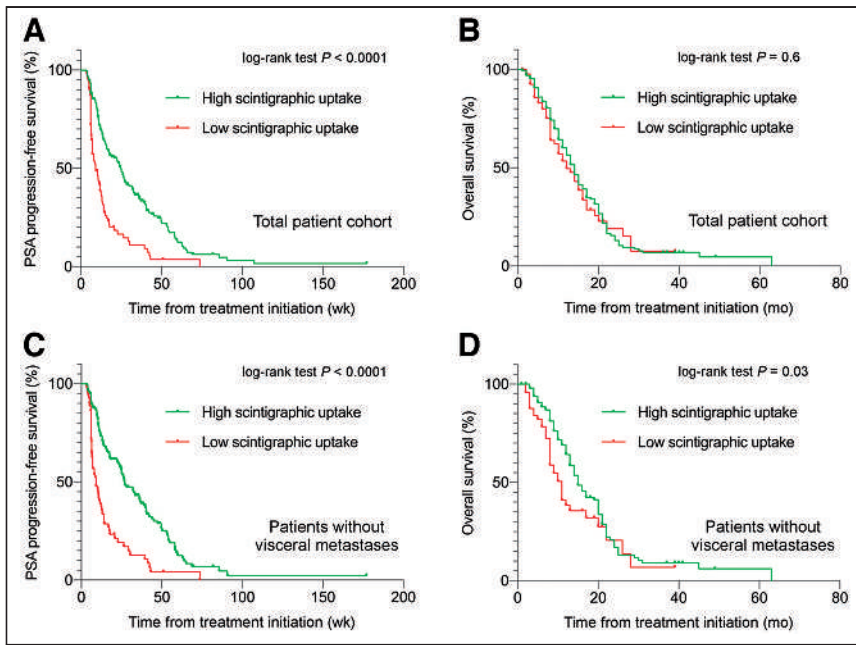


FIGURE 3. Kaplan-Meier survival curves for PSA PFS and OS stratified by high and low uptake on posttherapeutic scintigraphy: PSA PFS (A) and OS (B) in total patient cohort, and PSA PFS (C) and OS (D) in patients without visceral metastases.

($n = 29$) of patients with a scintigraphic response, whereas only 29.7% ($n = 19$) with scintigraphically stable disease and 8.1% ($n = 6$) with scintigraphic progression achieved a PSA response ($P < 0.0001$; Fig. 4). An example of a patient who showed a scintigraphic response is presented in Figure 5.

The distribution of PSA PFS and OS in patients with a scintigraphic response, stable disease, and progression significantly differed (median, 33.1 vs. 16.0 vs. 9.0 wk [$P < 0.0001$] and 16.5 vs. 11.6 vs. 7.4 mo [$P < 0.0001$], respectively; Figs. 6A and 6B).

Uni- and Multivariable Analysis of Prognostic Factors for Outcome

Univariable Cox regression analysis revealed that rising levels of AP, LDH, PSA, as well as prior chemotherapy and the presence of visceral metastases at baseline, were potential negative prognostic factors for OS, whereas the presence of lymph node-only metastases was a significant positive prognostic factor for OS (Table 2). In multivariable analysis, only rising levels of AP, LDH, and PSA and the presence of visceral metastases were identified as significant prognosticators (Table 2).

High tumor uptake was not associated with OS ($P = 0.3$) but was associated with longer PSA PFS in both the univariable and the multivariable analyses ($P < 0.0001$ for each) (Supplemental Table 1). Furthermore, scintigraphic progression was negatively associated with OS on both univariable and multivariable analyses ($P < 0.0001$ for each) (Table 3).

DISCUSSION

^{177}Lu -PSMA-I&T is the second most commonly used PSMA-targeted radiopharmaceutical for palliative treatment of mCRPC; however, significantly fewer data have been published for ^{177}Lu -PSMA-I&T than for ^{177}Lu -PSMA-617 so far (11). Our retrospective analysis of 301 patients treated with ^{177}Lu -PSMA-I&T substantially expands clinical knowledge about it, underlines its

effectiveness, and establishes previously proposed prognostic parameters until the results from the multicenter, randomized prospective phase III trial are published. One important prospective study to which its results might be compared is the SPLASH study (NCT04647526), despite the slight difference in inclusion criteria between that study and ours. Most of our patients also received chemotherapy in addition to second-line hormonal therapy (abiraterone or enzalutamide), contrary to those in SPLASH, who previously received only a single novel androgen receptor axis-targeted therapy but no chemotherapy.

In addition, our analysis underlines the value of PSMA ligand uptake as a noninvasive prognostic imaging biomarker. Specifically, we observed high scintigraphic tumor uptake resulting in a significantly higher PSA response rate and a lower risk of PSA progression. Further, scintigraphic response (defined as a decrease in skeletal infiltration length between 2 cycles) significantly prognosticated a better outcome, with longer PSA PFS and OS.

The number of patients with a 50% PSA decline in our analysis (34%) is well in line with data reported in the literature and, especially, our previous report for ^{177}Lu -PSMA-I&T. A large variation in PSA response rates has been found in the literature, ranging from 20% to 60%, with an estimated PSA response rate of 46% of patients in a recent metaanalysis (11). The lower number of PSA responders in our cohort is most likely explained by differences in the patient population. More than two thirds of the patients in our analysis had received chemotherapy before RLT. In univariable analysis, previous exposure to chemotherapy resulted in a 1.5-fold increased risk of death when compared with patients who had not previously received chemotherapy. In the recent metaanalysis by Sadaghiani et al. (11),

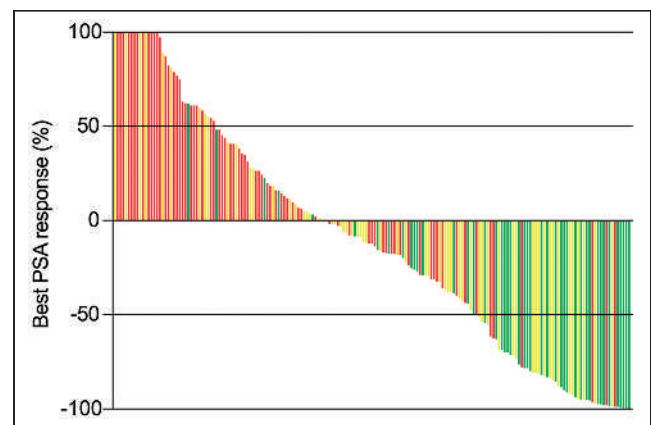


FIGURE 4. Waterfall plot showing response to treatment as measured by serum PSA. Best PSA response is compared with color-coded change in infiltration length on posttherapeutic scintigraphy. First 16 columns represent patients with increase of $>100\%$ as best PSA response. Green = patients with response (>0.5 cm decrease in infiltration length between first and second cycles); yellow = stable disease (± 0.5 -cm change in infiltration length); red = progression (>0.5 cm increase).

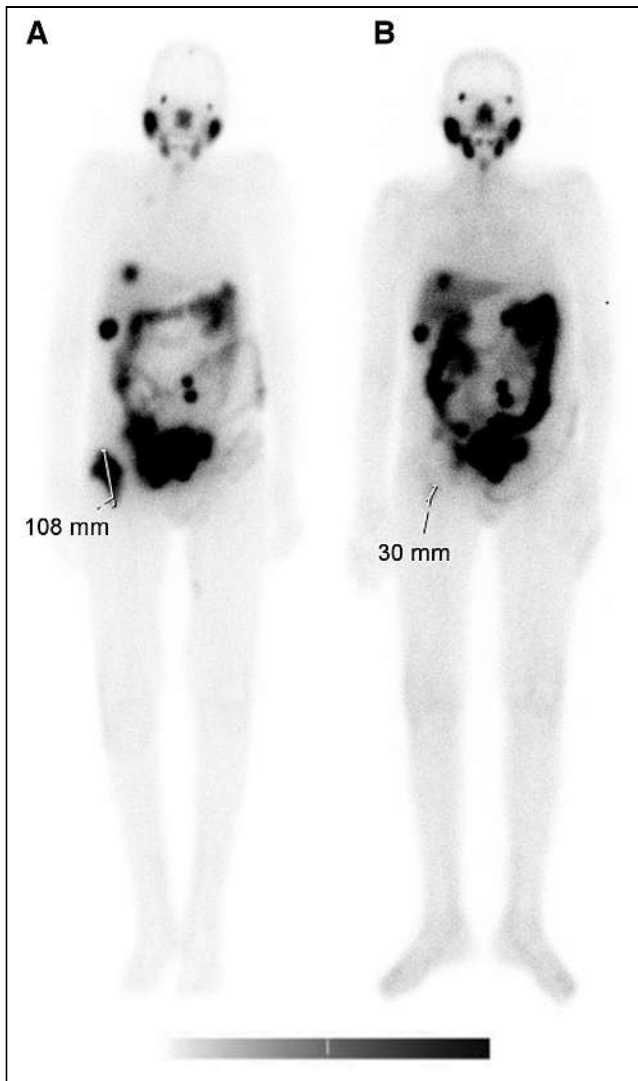


FIGURE 5. (A) An 81-y-old patient with bone, lymph node, and liver metastases presenting with metastatic disease in right femur with extent of 10.8 cm on posttherapeutic whole-body scintigraphy at first cycle of ^{177}Lu -PSMA-I&T. (B) Same patient with decrease in infiltration length to 3.0 cm at second cycle of ^{177}Lu -PSMA-I&T. Change in infiltration length was -7.8 cm, and classification was therefore scintigraphic response. PSA PFS and OS were 24 wk and 22 mo, respectively.

the rate of pretreatment with chemotherapy varied between 0% and 80%. Our data compare well with a retrospective analysis using ^{177}Lu -PSMA-617 RLT in 104 mCRCP posttaxane patients and reporting PSA response in 33% of patients and a median OS of 14 mo (95% CI, 12.6–15.4 mo) (12).

Recently, the VISION trial, an international, open-labeled, phase 3 trial evaluating ^{177}Lu -PSMA-617 in patients presenting with mCRPC, was published (5). OS was significantly prolonged in patients receiving ^{177}Lu -PSMA-617 as compared with standard care alone (median, 15.3 vs. 11.3 mo; $P < 0.001$). Median OS in our patient cohort receiving ^{177}Lu -PSMA-I&T was slightly shorter, at 13.8 mo (95% CI, 12.4–15.5 mo). However, a substantial number of patients (253/551) in the VISION trial undergoing ^{177}Lu -PSMA-617 RLT had also received androgen-receptor–pathway inhibitors with enzalutamide, abiraterone, or apalutamide as part of the standard of care, which might have some additive effect. In our clinical practice,

^{177}Lu -PSMA-I&T was applied in addition to standard application of gonadotropin-releasing hormone analog but without a combination with other active agents.

In addition, discrepancies between treatment outcome in compassionate-use programs and prospective trials might be further explained by an inconsistency in the applied inclusion criteria. The recently published multicenter, randomized prospective phase II trial TheraP reported a significantly higher treatment response in patients receiving ^{177}Lu -PSMA-617 than in patients receiving cabazitaxel (4). However, on the basis of the strict selection criteria, only patients with high ^{68}Ga -PSMA-11 tumor uptake and the absence of ^{18}F -FDG–positive/PSMA ligand–negative lesions were treated. These criteria led to exclusion of 28% of the initially screened patients, with visceral metastases being present in only 7% of the included patient cohort (as compared with 21% of patients in our analysis). The PSA response rate was 66%, compared with 34% in our study.

Our analysis of potential prognostic factors indicated a significant relationship between baseline laboratory parameters (LDH, AP, and PSA) and PSA PFS, and OS, as is in line with previous smaller studies (13). However, these findings still remain controversial, and a variety of other reports lack clear associations in multivariable analyses (14).

Finally, prior therapy with ^{223}Ra was not associated with a worse outcome of ^{177}Lu -PSMA-I&T therapy. One could assume that β -emitting ^{177}Lu -PSMA-I&T is less effective in tumors that have already progressed after α -emitter treatment, with a much higher linear energy transfer than for ^{177}Lu . However, ^{223}Ra may affect predominantly the tumor stroma because it accumulates in the bone matrix surrounding the cancer cells (15). Conversely, ^{177}Lu -PSMA-I&T accumulates directly in prostate cancer cells.

Our data also demonstrate a potential prognostic value of routine posttreatment scintigraphy, as patients with high scintigraphic tumor uptake more frequently achieved PSA response and presented with a reduced risk of PSA progression (PSA PFS, 24.9 vs. 9.0 wk; HR, 0.3; 95% CI, 0.2–0.5; $P < 0.0001$). This finding corroborates a recent retrospective analysis of 50 mCRPC patients showing that high scintigraphic uptake on posttherapeutic scintigraphy was a significant predictor of PSA decline of at least 50% from baseline (OR, 11.77; $P = 0.003$) and PSA PFS (OR, 0.2029; $P = 0.0111$) (16). Similarly, Rathke et al. described intense scintigraphic tumor uptake ($>$ salivary gland level) as a significant predictor of partial remission in univariable analysis (OR, 18.0; 95% CI, 2.230–145.3119; $P = 0.0067$) and multivariable analysis (OR, 60.265; 95% CI, 5.038–720.922; $P = 0.001$) (8). Tumor response in this analysis was defined by a visual decrease in uptake by metastatic lesions during later treatment cycles, and no correlation with independent clinical outcome parameters (e.g., PSA PFS, and OS) was available. Our analysis adds further data on the potential of scintigraphic tumor uptake to predict OS: no significant reduction in risk of death for patients with high scintigraphic tumor uptake was observed (14.4 vs. 12.4 mo; HR, 0.9; 95% CI, 0.6–1.3; $P = 0.6$). Similar results have recently been published by Hotta et al. (17) demonstrating significantly shorter PSA PFS in patients who did not fulfill the VISION criteria but still underwent ^{177}Lu -PSMA-RLT than in those who did fulfill the VISION criteria (2.1 vs. 4.1 mo; HR, 1.6; $P = 0.0025$). Median OS was shorter (9.6 vs. 14.2 mo; HR, 1.4; $P = 0.16$) but not to a statistically significant extent. One potential confounder could be the presence of visceral metastases, which are one of the strongest predictors for OS (18). When excluding patients with visceral metastases from our analysis, median OS was significantly longer for high tumor

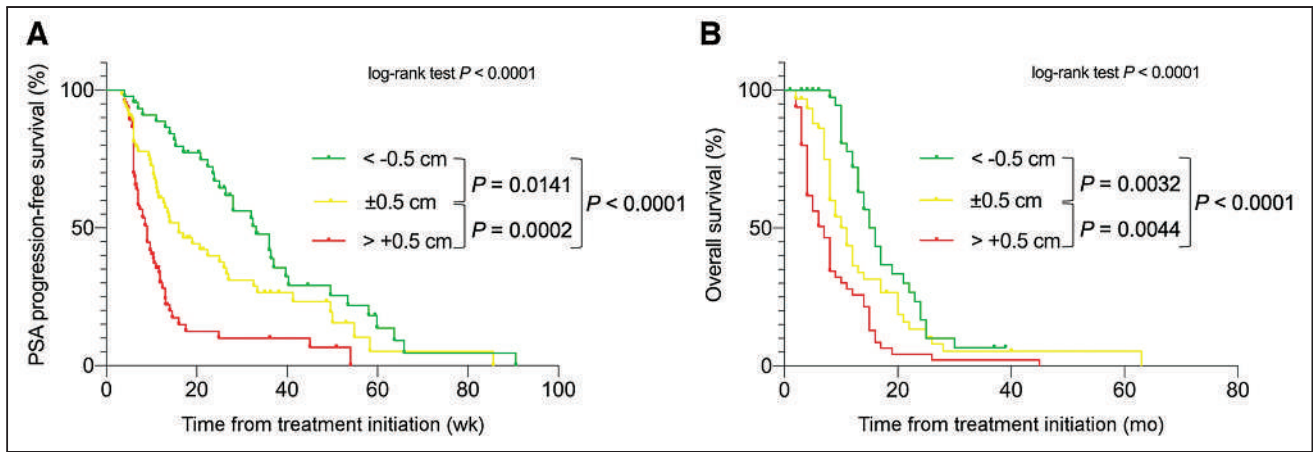


FIGURE 6. Kaplan-Meier survival curves stratified by scintigraphic response (>0.5-cm decrease in infiltration length between first and second cycles), scintigraphically stable disease (± 0.5 -cm change in infiltration length), and scintigraphic progression (>0.5-cm increase) for PSA PFS (A) and OS (B).

uptake than for low tumor uptake (15.5 vs. 11.4 mo; HR, 0.6; 95% CI, 0.4–1.0; $P = 0.03$).

Pretherapeutic PSMA ligand PET/CT is usually performed to assess whether the patient is eligible for PSMA RLT. Depending on the logistic workflow, there may be a potentially substantial

difference in the time to the start of PSMA RLT. Posttherapeutic scintigraphy, usually performed 24 h after injection, offers an intratherapeutic assessment of the disease state and has potential for longitudinal assessment of its changes over time, with no bias due to disease progression in between. Evaluation of posttherapeutic

TABLE 2
Uni- and Multivariable Analysis for Association of Baseline Variables with OS

Variable	No. of patients	Univariable analysis			Multivariable analysis		
		HR	95% CI	P	HR	95% CI	P
High scintigraphic uptake	295						
No	96	Reference					
Yes	199	0.9	0.6–1.2	0.3	0.8	0.6–1.1	0.2
Age, continuous	295	1.0	1.0–1.0	0.3	1.0	1.0–1.0	0.6
AP per 50 U/L increase, continuous	295	1.0	1.0–1.1	0.0001*	1.0	1.0–1.1	0.02*
LDH per 50 U/L increase, continuous	295	1.0	1.0–1.1	<0.0001*	1.0	1.0–1.1	0.001*
Hemoglobin, continuous	295	1.0	1.0–1.0	0.7	1.0	1.0–1.0	0.4
PSA per 50 ng/mL increase, continuous	295	1.0	1.0–1.0	0.0001*	1.0	1.0–1.0	0.01*
≥ 2 pretreatments	295						
No	98	Reference					
Yes	197	1.4	1.0–1.9	0.1	1.3	0.8–2.0	0.3
Previous ^{223}Ra	295						
No	254	Reference					
Yes	41	1.0	0.7–1.5	0.9	0.8	0.5–1.2	0.3
Previous chemotherapy	295						
No	84	Reference					
Yes	211	1.5	1.1–2.2	0.02*	1.1	0.7–1.7	0.7
Bone metastases (M1b, without visceral metastases)	211	Reference			Reference		
Lymph node only metastases (N+/M1a)	21	0.3	0.1–0.7	0.007*	0.4	0.2–1.0	0.05
Visceral metastases (M1c)	63	1.5	1.1–2.0	0.03*	1.5	1.0–2.1	0.02*

*Statistically significant.

TABLE 3
Uni- and Multivariable Analysis for Association of Changes in Various Parameters with OS

Change in ...	No. of patients	Univariable analysis			Multivariable analysis		
		HR	95% CI	P	HR	95% CI	P
Infiltration length per 10-mm increase, continuous	182	1.1	1.1–1.3	<0.0001*	1.2	1.1–1.3	<0.0001*
AP per 20% increase, continuous	182	1.0	1.0–1.1	0.13	1.0	1.0–1.1	0.3
LDH per 20% increase, continuous	182	1.2	1.1–1.3	0.001*	1.2	1.0–1.3	0.01*
Hemoglobin per 20% decrease, continuous	182	1.0	0.8–1.4	0.61	1.0	0.8–1.4	0.8
PSA per 20% increase, continuous	182	1.0	1.0–1.1	0.03*	1.0	1.0–1.0	0.8

*Statistically significant.

scintigraphy is easy to apply and has the potential to yield a useful imaging biomarker for prognosticating treatment outcome.

Finally, we present the extent of disease in the appendicular skeleton on posttherapeutic scintigraphy and its change between the first and second treatment cycles as a potential simple and quickly assessable new biomarker. Patients with a scintigraphic response (defined as a decrease in skeletal infiltration length between 2 cycles) presented with a significantly higher likelihood for a PSA response (64.4%), a significantly longer median PSA PFS (33.1 wk), and a longer median OS (16.5 mo). Moreover, whereas whole-body posttreatment scans allow detection of suggestive tumor uptake from head to toe and therefore enable a potentially powerful and inexpensive way to monitor tumor response, pretherapeutic PET/CT imaging is usually performed from skull base to mid thigh (skull and extremities are not included routinely) and is not suitable for routine assessment of the extent of disease in the appendicular skeleton.

Our study had several limitations, including the retrospective nature of the analysis. Qualitative evaluation of scintigraphic uptake and quantitative measurement of skeletal involvement are prone to potential error. However, all posttherapeutic scintigrams were analyzed and measured by the same reader, providing consistency within our patient cohort. Nevertheless, future studies also analyzing inter-reader agreement are warranted. Finally, the proposed biomarker of scintigraphic response as defined in this analysis is applicable only to patients with metastases in the appendicular skeleton and should be expanded to other organ systems in the future.

CONCLUSION

Our retrospective analysis of a large cohort of consecutive mCRPC patients undergoing ¹⁷⁷Lu-PSMA-I&T corroborates previous clinical data on treatment efficacy. It establishes known clinical and laboratory prognostic factors, such as the presence of visceral metastases, elevated LDH, and elevated AP. The clear association between PSA PFS and OS and posttreatment scintigraphic tumor uptake underlines the value of PSMA expression as a prognostic indicator. Finally, we propose skeletal tumor extent on posttherapeutic scintigraphy as a potential novel and simple prognostic imaging biomarker that should be explored in further prospective studies.

DISCLOSURE

Matthias Eiber reports fees from Blue Earth Diagnostics Ltd. (consultant, research funding), Novartis/AAA (consultant), Telix

(consultant), Bayer (consultant, research funding), RayzeBio (consultant), Point Biopharma (consultant), Janssen Pharmaceuticals (consultant, speakers' bureau), Parexel (image review), and Bioclinica (image review) outside the submitted work and a patent application for rhPSMA. No other potential conflict of interest relevant to this article was reported.

KEY POINTS

QUESTION: Is it possible to predict patient outcome using clinical and laboratory parameters and newly proposed posttreatment whole-body scintigraphy parameters updating our experience in a large number of consecutive mCRPC patients?

PERTINENT FINDINGS: Our retrospective analysis on a large number of mCRPC patients undergoing ¹⁷⁷Lu-PSMA-I&T corroborated previous reports on ¹⁷⁷Lu-PSMA-617 considering PSA response, PSA PFS, and OS. Moreover, it significantly established known prognostic factors, such as the presence of visceral metastases, elevated LDH, and elevated AP, and introduced tumor extent in the appendicular skeleton on posttherapeutic scintigraphy as a significant imaging biomarker predicting patient outcome.

IMPLICATIONS FOR PATIENT CARE: Our retrospective analysis might pave the way for widespread use and better patient selection of ¹⁷⁷Lu-PSMA-I&T in mCRPC patients and potentially introduces a simple and inexpensive imaging tool for tumor response assessment.

REFERENCES

- Hofman MS, Violet J, Hicks RJ, et al. [¹⁷⁷Lu]-PSMA-617 radionuclide treatment in patients with metastatic castration-resistant prostate cancer (LuPSMA trial): a single-centre, single-arm, phase 2 study. *Lancet Oncol*. 2018;19:825–833.
- Heck MM, Tauber R, Schwaiger S, et al. Treatment outcome, toxicity, and predictive factors for radioligand therapy with ¹⁷⁷Lu-PSMA-I&T in metastatic castration-resistant prostate cancer. *Eur Urol*. 2019;75:920–926.
- Rahbar K, Ahmadzadehfard H, Kratochwil C, et al. German multicenter study investigating ¹⁷⁷Lu-PSMA-617 radioligand therapy in advanced prostate cancer patients. *J Nucl Med*. 2017;58:85–90.
- Hofman MS, Emmett L, Sandhu S, et al. [¹⁷⁷Lu]Lu-PSMA-617 versus cabazitaxel in patients with metastatic castration-resistant prostate cancer (TheraP): a randomised, open-label, phase 2 trial. *Lancet*. 2021;397:797–804.
- Sartor O, de Bono J, Chi KN, et al. Lutetium-177-PSMA-617 for metastatic castration-resistant prostate cancer. *N Engl J Med*. 2021;385:1091–1103.

6. Ahmadzadehfar H, Rahbar K, Baum RP, et al. Prior therapies as prognostic factors of overall survival in metastatic castration-resistant prostate cancer patients treated with [¹⁷⁷Lu]Lu-PSMA-617: a WARMTH multicenter study (the 617 trial). *Eur J Nucl Med Mol Imaging*. 2021;48:113–122.
7. Weineisen M, Schottelius M, Simecek J, et al. ⁶⁸Ga- and ¹⁷⁷Lu-labeled PSMA I&T: optimization of a PSMA-targeted theranostic concept and first proof-of-concept human studies. *J Nucl Med*. 2015;56:1169–1176.
8. Rathke H, Holland-Letz T, Mier W, et al. Response prediction of ¹⁷⁷Lu-PSMA-617 radioligand therapy using Prostate-Specific Antigen, Chromogranin A, and Lactate Dehydrogenase. *J Nucl Med*. 2020;61:689–695.
9. Scher HI, Morris MJ, Stadler WM, et al. Trial design and objectives for castration-resistant prostate cancer: updated recommendations from the Prostate Cancer Clinical Trials Working Group 3. *J Clin Oncol*. 2016;34:1402–1418.
10. Landis JR, Koch GG. The measurement of observer agreement for categorical data. *Biometrics*. 1977;33:159–174.
11. Sadaghiani MS, Sheikhabaei S, Werner RA, et al. A systematic review and meta-analysis of the effectiveness and toxicities of lutetium-177-labeled prostate-specific membrane antigen-targeted radioligand therapy in metastatic castration-resistant prostate cancer. *Eur Urol*. 2021;80:82–94.
12. Rahbar K, Boegemann M, Yordanova A, et al. PSMA targeted radioligand therapy in metastatic castration resistant prostate cancer after chemotherapy, abiraterone and/or enzalutamide: a retrospective analysis of overall survival. *Eur J Nucl Med Mol Imaging*. 2018;45:12–19.
13. Yordanova A, Linden P, Hauser S, et al. The value of tumor markers in men with metastatic prostate cancer undergoing [¹⁷⁷Lu]Lu-PSMA therapy. *Prostate*. 2020;80:17–27.
14. Barber TW, Singh A, Kulkarni HR, et al. Clinical outcomes of ¹⁷⁷Lu-PSMA radioligand therapy in earlier and later phases of metastatic castration-resistant prostate cancer grouped by previous taxane chemotherapy. *J Nucl Med*. 2019;60:955–962.
15. Morris MJ, Corey E, Guise TA, et al. Radium-223 mechanism of action: implications for use in treatment combinations. *Nat Rev Urol*. 2019;16:745–756.
16. Derlin T, Werner RA, Lafos M, et al. Neuroendocrine differentiation and response to PSMA-targeted radioligand therapy in advanced metastatic castration-resistant prostate cancer: a single-center retrospective study. *J Nucl Med*. 2020;61:1602–1606.
17. Hotta M, Gafita A, Czernin J, Calais J. Outcome of patients with PSMA PET/CT screen failure by VISION criteria and treated with ¹⁷⁷Lu-PSMA therapy: a multi-center retrospective analysis. *J Nucl Med*. 2022;63:1484–1488.
18. Manafi-Farid R, Harsini S, Saidi B, et al. Factors predicting biochemical response and survival benefits following radioligand therapy with [¹⁷⁷Lu]Lu-PSMA in metastatic castrate-resistant prostate cancer: a review. *Eur J Nucl Med Mol Imaging*. 2021;48:4028–4041.

¹⁷⁷Lu-PSMA SPECT Quantitation at 6 Weeks (Dose 2) Predicts Short Progression-Free Survival for Patients Undergoing ¹⁷⁷Lu-PSMA-I&T Therapy

Nikeith John^{1,2}, Sarennya Pathmanandavel¹, Megan Crumbaker²⁻⁴, William Counter¹, Bao Ho¹, Andrew O. Yam²⁻⁴, Peter Wilson⁵, Remy Niman⁵, Maria Ayers¹, Aron Poole¹, Adam Hickey¹, Shikha Agrawal¹, Gary Perkins¹, Annukka Kallinen¹, Enid Eslick¹, Martin R. Stockler⁶, Anthony M. Joshua²⁻⁴, Andrew Nguyen^{1,2}, and Louise Emmett¹⁻³

¹Department of Theranostics and Nuclear Medicine, St. Vincent's Hospital, Sydney, New South Wales, Australia; ²St. Vincent's Clinical School, University of New South Wales, Sydney, New South Wales, Australia; ³Garvan Institute of Medical Research, Sydney, New South Wales, Australia; ⁴Kinghorn Cancer Centre, St. Vincent's Hospital, Sydney, New South Wales, Australia; ⁵MIM Software, Inc., Cleveland, Ohio; and ⁶NHMRC Clinical Trials Centre, University of Sydney, Sydney, New South Wales, Australia

¹⁷⁷Lu-PSMA is an effective treatment in metastatic castration-resistant prostate cancer (mCRPC). Our ability to assess response rates and adjust treatment may be improved using predictive tools. This study aimed to evaluate change in ¹⁷⁷Lu-PSMA SPECT quantitative parameters to monitor treatment response. **Methods:** One hundred twenty-seven men with progressive mCRPC previously treated with androgen-signaling inhibition (99%) and chemotherapy (71%) received a median of 3 (interquartile range [IQR], 2–5) 8-GBq (IQR, 8–8.5 GBq) doses of ¹⁷⁷Lu-PSMA-I&T. Imaging included ⁶⁸Ga-PSMA-11 PET/CT (SUV_{max} > 15 at a single site and > 10 at all sites > 2 cm), diagnostic CT, and ¹⁷⁷Lu SPECT/CT from vertex to mid thigh (24 h after treatment). ¹⁷⁷Lu SPECT/CT quantitative analysis was undertaken at cycles 1 (baseline) and 2 (week 6) of treatment. Clinical and biochemical results were assessed to evaluate prostate-specific antigen (PSA) progression-free survival (PFS) and overall survival (OS). **Results:** A PSA reduction of more than 50% was seen in 58% (74/127). The median PSA PFS was 6.1 mo (95% CI, 5.5–6.7), and OS was 16.8 mo (95% CI, 13.5–20.1). At the time of analysis, 41% (52/127) were deceased. At baseline and week 6, 76% (96/127) had analyzable serial ¹⁷⁷Lu SPECT/CT imaging. SPECT total tumor volume (TTV) was reduced between baseline and week 6 in 74% (71/96; median, –193; IQR, –486 to –41). Any increase in SPECT TTV between baseline and week 6 was associated with significantly shorter PSA PFS (hazard ratio, 2.5; 95% CI, 1.5–4.2; *P* = 0.0008) but not OS. Median PSA PFS in those with an increase in SPECT TTV was 3.7 mo (95% CI, 2.8–6.8), compared with 6.7 mo (95% CI, 5.8–10.6) in those with no increase in SPECT TTV. An increase in SPECT TTV greater than 20% was also associated with PSA PFS (hazard ratio, 1.9; 95% CI, 1.2–3.0; *P* = 0.008) but less significantly than any change in SPECT TTV. There was a significant difference in PSA PFS between patients with both increased PSA and SPECT TTV and patients with reduced SPECT TTV and PSA (median, 2.8 vs. 9.0 mo; *P* < 0.0001). **Conclusion:** Increasing PSMA SPECT TTV on quantitative ¹⁷⁷Lu SPECT/CT predicts short progression-free survival and may play a future role as an imaging response biomarker, identifying when to cease or intensify ¹⁷⁷Lu-PSMA therapy.

Key Words: metastatic prostate cancer; SPECT; lutetium-PSMA; response biomarker

Received Jul. 16, 2022; revision accepted Sep. 1, 2022.
For correspondence or reprints, contact Louise Emmett (louise.emmett@svha.org.au).
Published online Sep. 8, 2022.
COPYRIGHT © 2023 by the Society of Nuclear Medicine and Molecular Imaging.

J Nucl Med 2023; 64:410–415
DOI: 10.2967/jnumed.122.264677

In metastatic castration-resistant prostate cancer (mCRPC), ¹⁷⁷Lu-PSMA is an effective therapy, although treatment resistance and short response duration remain common (1–4). The ability to monitor early responses to ¹⁷⁷Lu-PSMA therapy may improve patient outcomes by enabling treatment escalation, change in treatment, or a treatment “holiday,” dependent on imaging results. Interim and serial ⁶⁸Ga-HBEDD-PSMA-11 PET/CT (⁶⁸Ga-PSMA) have recently been found predictive of progression-free survival (PFS) with prostate-specific membrane antigen (PSMA)-targeted radionuclide therapy (5). Quantitative ¹⁷⁷Lu SPECT/CT imaging after each ¹⁷⁷Lu-PSMA dose may also be valuable in response monitoring in addition to providing dosimetric information. Increased tumor volume on ¹⁷⁷Lu SPECT/CT at dose 3 (week 12) has been shown to predict early disease progression with ¹⁷⁷Lu-PSMA therapy (6). This study aimed to determine if quantitative parameters on the week 6 ¹⁷⁷Lu SPECT imaging 24 h after ¹⁷⁷Lu-PSMA therapy predicted treatment response and PFS.

MATERIALS AND METHODS

Men with mCRPC treated clinically with ¹⁷⁷Lu-PSMA-I&T were enrolled into a retrospective registry. Enrolled men were treated at a single center with ¹⁷⁷Lu-PSMA-I&T at 6-wk intervals until disease progression or treatment was changed. Information on prior treatment, years since diagnosis, and biochemical and hematologic parameters was collected. Patients were followed up after treatment to document prostate-specific antigen progression-free survival (PSA PFS) and overall survival (OS). ¹⁷⁷Lu SPECT/CT 24 h after each treatment was undertaken for quantification of disease burden. The institutional review board of St. Vincent's Hospital approved this retrospective study (Human Research Ethics Committee approval 2022/ETH00924) and waived the requirement to obtain informed consent.

Screening

Men underwent screening ⁶⁸Ga-PSMA PET/CT; bone scan; and CT of the chest, abdomen, and pelvis. They were eligible if they had an SUV_{max} greater than 15 on ⁶⁸Ga-PSMA PET at one or more sites, an SUV_{max} greater than 10 at all measurable sites of disease not impacted by partial

voluming, and no sites of soft-tissue disease on contrast-enhanced CT without corresponding ^{68}Ga -PSMA uptake. Patients with an Eastern Cooperative Oncology Group (ECOG) performance status of 1–3 were eligible for treatment. A minimum estimated glomerular filtration rate of 35 mL/min, hemoglobin of more than 70 g/L, and platelets of more than 70 (10^9 /unit) were required.

Treatment

Men received treatment with ^{177}Lu -PSMA-I&T at 6-wk intervals (median number of doses, 3; interquartile range [IQR], 2–5) between May 2018 and April 2022. A median of 8 GBq (IQR, 7.5–8 GBq) of ^{177}Lu -PSMA-I&T was administered via slow intravenous injection. Dexamethasone, 8 mg orally, was administered on day 1 for each dose to minimize pain flare and vomiting (7,8). Blood work was routinely performed at 3-wk intervals to assess toxicity, adverse events, and biochemical response. Prior treatments and the date of diagnosis were documented, as was PSA PFS and OS. The clinical protocol included 6 doses of ^{177}Lu -PSMA at 6-week intervals, with a multidisciplinary clinical decision dictating the duration of treatment based on evidence of disease progression or exceptional response. Patients were followed up after cessation of treatment to confirm clinical outcomes.

^{177}Lu -PSMA-I&T PSMA-I&T precursor (ABX/Huayi) in sodium acetate buffer was added to non-carrier-added ^{177}Lu -LuCl₃ according to the institutional production protocol. Radiochemical purity was determined using high-pressure liquid chromatography and thin-layer chromatography.

Imaging Procedures and Analysis

Screening ^{68}Ga -PSMA PET/CT was performed on all patients before consideration for treatment. All treated patients had ^{177}Lu SPECT/CT (vertex to mid thighs) acquired 24 h after ^{177}Lu -PSMA-I&T injection, with the 24-h time point determined on the basis of the TheraP trial protocol (8). SPECT imaging was undertaken with a Discovery 670 system (GE Healthcare) and a Tandem NM/CT 870 DR (GE Healthcare) with the following parameters: medium-energy collimators, 3 bed positions, 60 projections over 360° with an acquisition time of 10 s per frame, 128 × 128 matrix, and 4.42 × 4.42 mm pixel size. An energy window centered on 208 keV ± 10% with a 165 keV ± 6.5% scatter window was used. An unenhanced low-dose CT scan was obtained immediately afterward, using the following parameters: pitch of 1, tube voltage of 120 kV, automatic mAs control (reference mAs, 90), slice thickness of 3.7 mm, matrix of 512 × 512, and field of view of 40 cm. For quantitation, the required SPECT calibration was performed on both cameras with a cylindrical phantom (for determination of sensitivity factor and conversion from counts to units of activity), and CT attenuation correction was performed using a CIRS CT-data-to-electron-density phantom by MIM Software Inc. For images acquired on the Discovery 670, SPECT projection images were reconstructed with an iterative ordered-subset expectation-maximum algorithm with 4 iterations and 10 subsets using SPEC-TRA Quant (MIM Software, Inc.). No pre- or post-reconstruction filters were applied. CT-based attenuation correction, dual-energy-window scatter correction, collimator-based resolution recovery, and quantitative conversion to SUV were performed during the reconstruction. Images acquired on the Tandem NM/CT 870 DR were processed using the same reconstructive parameters on a GE Healthcare SmartConsole for quantitation. Diagnostic contrast CT chest, abdomen and pelvis was undertaken at each treatment cycle to assess for non-PSMA-avid visceral disease progression.

Quantitative Analysis

^{177}Lu SPECT/CT images were analyzed semiquantitatively using MIM (LesionID; MIM Software Inc.) software and a standardized semi-automated workflow to delineate regions of interest with a minimum SUV_{max} cutoff of 3 and lesion size of at least 0.5 mm. All lesions

identified quantitatively were manually reviewed and physiologic activity removed. Whole-body quantitation was used to derive total tumor volume (TTV), SUV_{max}, and SUV_{mean} (9).

Statistical Analysis

We measured PSA decline from baseline ($\geq 50\%$ [PSA50]) at any time point; PSA PFS, as defined by Prostate Cancer Working Group 3 (PCWG3) criteria (with PSA progression defined as a PSA rise of ≥ 2); and OS (10,11). The Kaplan–Meier method was used to characterize time-to-event endpoints and to estimate medians (presented with 95% CIs). We correlated changes in SPECT TTV, SPECT PSMA intensity, and clinical and biochemical parameters with time-to-event outcomes, using univariable and multivariable Cox proportional-hazards regression models (12,13). Variables included increase in SPECT TTV, SUV_{max}, SUV_{mean}, PSA, and radiographic progression. *P* values below 5% were considered significant. Analyses were performed using R (version 4.0.5).

RESULTS

Patient Characteristics

Between May 2019 and April 2022, 127 men underwent ^{177}Lu -PSMA-I&T therapy. All had mCRPC, 99% (126/127) had received prior androgen-signaling inhibitor (ASI) treatment, and 70% (89/127) had received prior docetaxel. The mean age was 75 y (IQR, 70–80 y) (Table 1). Patients received a median of 3 doses up to a maximum of 10 (IQR, 2–5). Seven percent (9/127) had received prior ^{177}Lu -PSMA-617 on trial. Fifty-eight percent (74/127) had a PSA reduction of more than 50% (PSA50). Median PSA PFS was 6.1 mo (IQR, 4.9–8.4 mo; 95% CI, 5.5–6.7 mo), and median OS was 16.8 mo (IQR, 6.3–14.9 mo; 95% CI, 13.5–20.1 mo). At the time of analysis, 41% (52/127) were deceased.

TABLE 1
Patient Characteristics (*n* = 127)

Characteristic	Data
Age (y)	75 (70–80)
Years since diagnosis	6 (3–9)
Prior systemic treatments	
LHRH agonist/antagonist	100% (127/127)
Chemotherapy	70% (89/127)
Docetaxel	70% (89/127)
Cabazitaxel	35% (44/127)
Androgen-signaling inhibitor (ASI)	99% (126/127)
PSA ($\mu\text{g/L}$)	76 (26.7–258.5)
LDH (units/L)	242 (211–301)
Platelets (10^9 /unit)	220 (177–271)
Hemoglobin (g/L)	116 (103–127)
Sites of disease	
Bone	97% (93/96)
Lymph nodes	47% (45/96)
Viscera	20% (19/96)

LHRH = luteinizing hormone-releasing hormone; LDH = lactate dehydrogenase.
Qualitative data are percentage and number; continuous data are median and interquartile range (IQR).

TABLE 2
Baseline Predictive Biomarkers

Biomarker	PSA PFS			OS		
	HR	95% CI	<i>P</i>	HR	95% CI	<i>P</i>
SPECT SUV _{mean}	0.90	0.85–0.96	0.0009	0.94	0.9–1.0	0.06
SPECT SUV _{mean} < 7	2.7	1.6–4.4	0.00003	2.1	1–4	0.03
SPECT TTV	1.0	0.99–1.0	0.17	1.0	0.99–1.001	0.1
Hemoglobin (>100)	0.59	0.32–1.1	0.09	0.92	0.39–2.1	0.83
ALP (>1.5 ULN)	1.8	1.1–3.0	0.03	2.2	1.1–4.5	0.04
LDH (>1.5 ULN)	2.3	1.3–4.1	0.006	1.8	0.85–4.0	0.12

ALP = alkaline phosphatase; ULN = upper limit of normal; LDH = lactate dehydrogenase.

SPECT Quantitation

Seventy-six percent (96/127) of men had analyzable ¹⁷⁷Lu SPECT/CT data at baseline and week 6. ¹⁷⁷Lu SPECT/CT quantitation measures at baseline and week 6, including SPECT TTV, SUV_{max}, and SUV_{mean}, are summarized in Table 2. On the baseline ¹⁷⁷Lu SPECT/CT, median SUV_{mean} was 8.8 (IQR, 7–12), median SUV_{max} was 60 (IQR, 35–88), and median SPECT TTV was 411 cm³ (IQR, 128–1,169 cm³). SPECT TTV was reduced between baseline and week 6 in 74% (71/96; median, –193 cm³; IQR, –486 to –41 cm³) and increased in 25% (24/96; median, 103 cm³; IQR, 42–196 cm³). SUV_{max} was increased in 24% (23/96), and SUV_{mean} was increased in 22% (21/96).

Patient Outcomes

¹⁷⁷Lu SPECT/CT. At baseline, SPECT TTV (dose 1) was not significantly associated with PSA PFS or OS (Table 2). SUV_{mean} measured on dose 1 ¹⁷⁷Lu SPECT/CT was significantly associated with PSA PFS as a continuous variable (hazard ratio [HR], 0.90; 95% CI, 0.85–0.96; *P* = 0.0009) but not with OS (HR, 0.94; 95% CI, 0.9–1.0). When stratified by an SUV_{mean} of more than 7 on dose 1 ¹⁷⁷Lu SPECT/CT, patients with an SUV_{mean} of more than 7 had a median PSA PFS of 6.8 mo (95% CI, 6–9 mo), versus 3.0 mo (95% CI, 2.6–6 mo) in those with an SUV_{mean} of less than 7. An SUV_{mean} of more than 7 was significantly associated with longer PSA PFS (HR, 2.7; 95% CI, 1.6–4.4; *P* < 0.001) and OS (HR, 2.1; 95% CI, 1–4; *P* = 0.03).

Any increase in SPECT TTV between baseline and week 6 was associated with significantly shorter PSA PFS (HR, 2.5; 95% CI, 1.5–4.2; *P* = 0.0008) but not OS. Median PSA PFS in those with an increase in SPECT TTV was 3.7 mo (95% CI, 2.8–6.8 mo), compared with 6.7 mo (95% CI, 5.8–10.6 mo) in those with no increase in SPECT TTV (Fig. 1). An increase in SPECT TTV greater than 20% was also associated with PSA PFS (HR, 1.9; 95% CI, 1.2–3.0; *P* = 0.008), but less significantly than any change

in SPECT TTV. Increases in SUV_{max} and SUV_{mean} were both associated with PSA PFS (respectively: HR of 1.8 and 95% CI of 1.0–3.1 [*P* = 0.04] and HR of 2.1 and 95% CI of 1.2–3.8 [*P* = 0.01]) but not OS (Table 3).

Biochemical. Twenty-three percent (22/96) of patients demonstrated a rise in PSA by week 6. A PSA rise was associated with significantly shorter PSA PFS (HR, 4.0; 95% CI, 2.3–6.9; *P* < 0.0001) and worse OS (HR, 2.4; 95% CI, 1.1–5.1; *P* = 0.02). A baseline lactate dehydrogenase level of more than 1.5 times the upper limit of normal was associated with worse PSA PFS

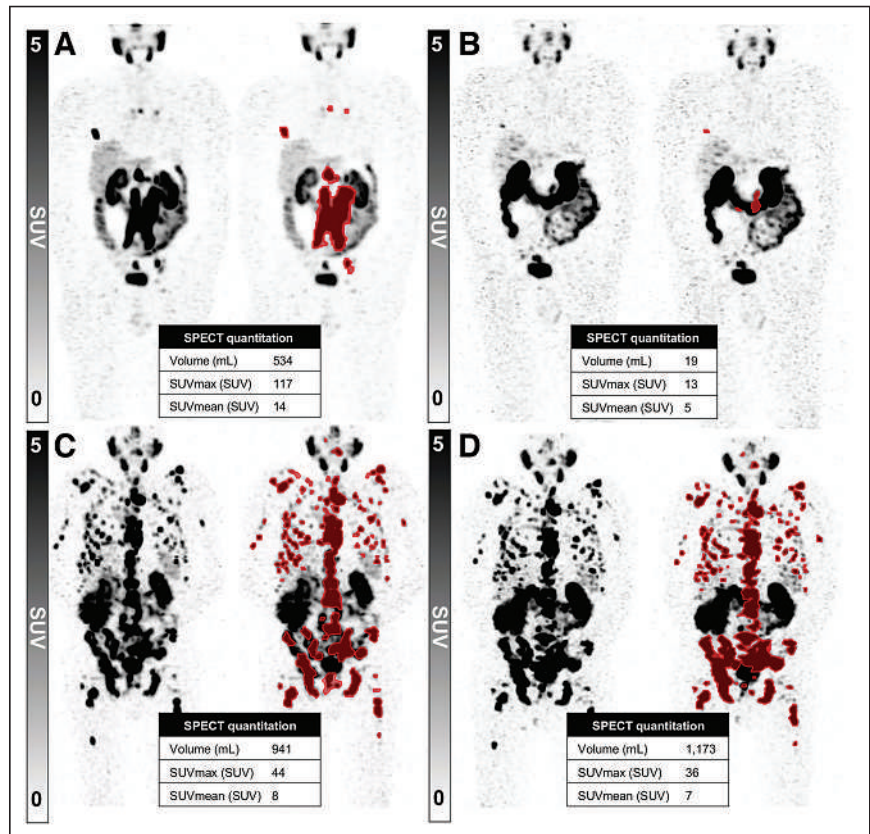


FIGURE 1. (A and B) Reduction between SPECT TTV from baseline (A) to week 6 (B) in patient with PSA PFS at 14 mo. (C and D) Patient with increased SPECT TTV at 6 wk (C) and PSA PFS at 2.0 mo (D).

TABLE 3
Univariable Analysis of Response Biomarkers (Baseline to 6-Week SPECT)

Parameter	PSA PFS			OS		
	HR	95% CI	<i>P</i>	HR	95% CI	<i>P</i>
Δ SPECT TTV	2.5	1.5–4.2	0.0008	1.2	0.6–2.7	0.57
Δ SPECT SUV _{mean}	2.1	1.2–3.8	0.01	1.7	0.7–4.0	0.2
Δ SPECT SUV _{max}	1.8	1.0–3.1	0.04	1.3	0.6–2.8	0.6
Δ PSA	4.0	2.3–6.9	0.0001	2.4	1.1–5.1	0.02

Δ = change in parameter.

(HR, 2.3; 95% CI, 1.3–4.1; *P* = 0.006), and an alkaline phosphatase level of more than 1.5 times the upper limit of normal was associated with both worse PSA PFS and worse OS (respectively: HR of 1.8 and 95% CI of 1.1–3.0 [*P* = 0.03] and HR of 2.2 and 95% CI of 1.1–4.5 [*P* = 0.04]). Baseline hemoglobin was associated with neither PSA PFS nor OS (Table 2).

Combination Biomarkers. Of the 25 patients with SPECT TTV progression at week 6, 44% (11/25) had no concurrent PSA progression (median PSA PFS, 3.7 mo; 95% CI, 2.8–4.7), and 14 men had both PSA and SPECT TTV progression at week 6 (median PSA PFS, 2.8 mo; 95% CI, 1.4–4.7) (Fig. 2). PSA PFS in patients with increased PSA and SPECT TTV differed significantly from that in patients with reduced SPECT TTV and PSA (median, 2.8 mo vs. 9.0 mo; *P* < 0.0001).

Seventy-one men had reduced SPECT TTV by week 6. Eleven percent (8/71) of men had a reduction in SPECT TTV and PSA

progression (median PSA PFS, 2.7 mo; 95% CI, 1.4–4.8). Of these, 2 of 8 had new PSMA-negative hepatic lesions identified on diagnostic CT, and 2 of 8 had new small-volume lesions identified on SPECT, despite a drop in SPECT TTV.

SPECT Multivariable Analysis. Both a baseline SPECT SUV_{mean} of more than 7 and a change in SPECT TTV were found to be independently predictive for PSA PFS, whereas a change in SUV_{mean} or SUV_{max} was not (Table 4).

DISCUSSION

This study demonstrated that a change in tumor volume on ¹⁷⁷Lu SPECT/CT between baseline and 6 wk of ¹⁷⁷Lu-PSMA-617 therapy is predictive of short PFS. Furthermore, the combination of increased SPECT TTV and a PSA rise at 6 wk identified a subgroup of men at high risk of a poor response to ¹⁷⁷Lu SPECT/CT therapy who may benefit from either a change in therapy or the

addition of combination treatments that may have a synergistic benefit in conjunction with ¹⁷⁷Lu-PSMA. Identifying effective response biomarker combinations such as early PSA rise and SPECT TTV, which provide strong information as early as 6 wk into treatment, is a big step toward being able to tailor treatment strategies to individual patients, thereby improving outcomes.

¹⁷⁷Lu-PSMA has proven an effective therapy for mCRPC, with randomized trials demonstrating improved OS and high PSA response rates compared with standard-of-care therapies (2,3). However, responses can be heterogeneous, and a proportion of men with suitable ⁶⁸Ga-PSMA PET screening results may have limited treatment responses. At the same time, combination trials with ¹⁷⁷Lu-PSMA are under way to investigate whether combining ¹⁷⁷Lu-PSMA with other agents may deepen and prolong responses (NCT04419402, NCT03658447, NCT03874884) (7,14). Imaging biochemical and clinical interim response biomarkers will be critical in personalizing treatments to optimize longer-term responses to PSMA-targeted radionuclide therapy and, conversely, in stopping treatment early to mitigate opportunity cost if other treatment options are available.

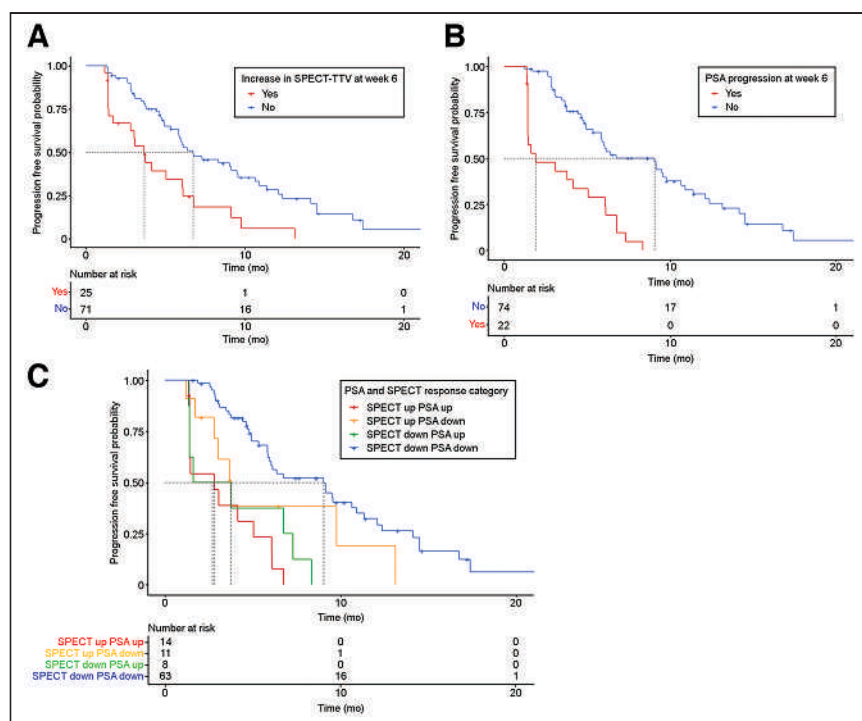


FIGURE 2. Kaplan–Meier curves for PSA PFS in patients with any increase vs. reduced SPECT TTV (A), rise in PSA at 6 wk vs. reduced PSA at 6 wk (B), and combination of reduced SPECT TTV with reduced PSA, rising PSA with reduced SPECT TTV, rising SPECT TTV with reduced PSA, and rising PSA with rising SPECT TTV (C).

TABLE 4
Multivariable Analysis of SPECT Parameter for PSA PFS and OS

Parameter	PSA PFS			OS		
	HR	95% CI	<i>P</i>	HR	95% CI	<i>P</i>
Δ SPECT TTV	1.9	1.1–3.3	0.03	0.85	0.3–2.2	0.7
Δ SUV _{max}	1.0	0.5–2.3	0.9	0.76	0.2–2.6	0.7
Δ SUV _{mean}	1.2	0.5–2.8	0.7	1.3	0.3–6.0	0.70
SUV _{mean} < 7 (baseline)	2.4	1.2–4.6	0.01	2.4	0.9–6.1	0.07

Δ = change in parameter.

The response evaluation criteria in PSMA PET/CT (RECIP) have recently been proposed for response assessment using a 12-wk PSMA PET scan (5). RECIP uses PET/CT quantification to derive volume and intensity scores applying a combination of a 20% increase in PSMA PET TTV and new lesions to determine disease progression. A recent analysis of the LUPIN trial has found that ¹⁷⁷Lu SPECT/CT at week 12 is also predictive of treatment response (6). This study has confirmed this predictive value, also finding that ¹⁷⁷Lu SPECT/CT predicts PFS earlier in treatment (6 wk) without the need for an additional ⁶⁸Ga-PSMA PET scan. This finding has significant cost and availability advantages worldwide, with few countries having approved ⁶⁸Ga-PSMA PET/CT for response assessment. Additionally, the current analysis found that only 4 of 96 patients had new lesions not identified by an increase in SPECT TTV, 2 of 4 of these being new PSMA-negative hepatic lesions not evident on PSMA SPECT/CT. More work is required to determine whether the presence of new lesions on PSMA imaging should be a requirement in classifying disease progression or whether increased tumor volume in conjunction with biochemical parameters is sufficient.

Currently accepted response biomarkers in mCRPC include a sequential rise in PSA (15) and RECIST/PCWG3 criteria progression on diagnostic CT and bone scan (16). Heterogeneity of PSA expression in mCRPC may limit its predictive value in a proportion of men (17). This possibility is reflected by the fact that 25% of the men in this study who had an increase in SPECT TTV did not have a concurrent PSA rise at 6 wk. This percentage is similar to the 21% identified in a previous SPECT TTV study and the 14% demonstrating ⁶⁸Ga-PSMA PET progression before PSA progression by Gafita et al. (5,6). RECIST progression requires serial imaging to determine progression using PCWG3 criteria, limiting its value as an early response biomarker for treatment adjustment. Ongoing evaluation is required to determine whether response evaluation criteria should be modified to include ¹⁷⁷Lu SPECT/CT, although diagnostic CT will remain important in identifying PSMA-negative progression.

Screening PSMA and ¹⁸F-FDG PET parameters have demonstrated strong prognostic value for ¹⁷⁷Lu-PSMA therapy (18,19). In the TheraP trial, patients with a high PSMA SUV_{mean} of more than 10 have an excellent PSA50 response rate (18). SUV_{mean} is an indirect measure of PSMA expression heterogeneity, which impacts treatment effectiveness but cannot assess radiation sensitivity. However, change in SPECT TTV may provide individual information on radiation sensitivity, measuring tumor volume reduction after treatment. This study found that both the screening SUV_{mean} (SPECT) and the change in SPECT TTV were

independently predictive of PSA PFS, raising the possibility of developing effective imaging response nomograms as early as 6 wk into treatment.

Previous work has identified baseline PSMA and biochemical parameters that predict early treatment failure for patients undergoing ¹⁷⁷Lu-PSMA therapy (13). A novel component of our study is the evaluation of baseline PSMA SPECT parameters in addition to the change in SPECT between baseline and after 6 wk of therapy. This study demonstrates that baseline PSMA predictive biomarkers can be derived from SPECT in addition to baseline PET imaging. This ability may be valuable when PSMA PET is not widely available.

This study relied on quantitation of SPECT data rather than visual assessment. This reliance on quantitation for effective predictive and response biomarkers in molecular imaging is increasing, including the highly valuable SUV_{mean} on screening ⁶⁸Ga-PSMA PET for ¹⁷⁷Lu-PSMA therapy (18–20). However, quantitation is not the standard of care and is time-intensive. Further work is needed to streamline quantitation for widespread adoption into routine practice (9).

There were several limitations to this study, a single-center retrospective analysis of a clinical treatment program. Although PSA and survival data were rigorously collected, obtaining routine RECIST/PCWG3 bone scan criteria for radiographic progression was not possible. Additionally, ¹⁷⁷Lu SPECT/CT quantitative measures can vary significantly between centers and systems, and these findings require validation in other clinical databases and quantitative programs (21). This study evaluated only the first 2 SPECT data time points quantitatively, and examination of subsequent time points could provide more comprehensive information on the value of ¹⁷⁷Lu SPECT/CT. Finally, further research with larger patient numbers and outcome data is necessary to better define appropriate volume cutoffs for a significant increase in SPECT TTV that should be used to identify disease progression.

CONCLUSION

Increasing PSMA-SPECT-TTV on quantitative ¹⁷⁷Lu SPECT/CT predicts short PFS and may play a future role as an imaging response biomarker, identifying when to cease or intensify ¹⁷⁷Lu-PSMA therapy.

DISCLOSURE

This investigator-initiated study was sponsored by St. Vincent's Hospital Sydney and supported by a Cancer Institute NSW prostate translational research grant. Sarennya Pathmanandavel received

funding through the Cancer Institute New South Wales and St. Vincent's Clinic Foundation. Louise Emmett has an advisory role with Clarity Pharmaceuticals; receives trial support from Novartis and Astellas; and receives grant funding support from St. Vincent's Clinic Foundation. Anthony Joshua has an advisory role with and receives institutional funding from Novartis. Peter Wilson and Remy Niman are salaried employees of MIM Software, Inc. No other potential conflict of interest relevant to this article was reported.

ACKNOWLEDGMENTS

We thank the patients and the clinical staff at the Department of Theranostics and Nuclear Medicine for their support.

KEY POINTS

QUESTION: Is there value in SPECT imaging of patients after ^{177}Lu -PSMA therapy?

PERTINENT FINDINGS: A change in tumor volume on ^{177}Lu SPECT/CT at week 6 is predictive of short PFS and may have potential as a response biomarker.

IMPLICATIONS FOR PATIENT CARE: ^{177}Lu SPECT/CT has potential as an imaging response biomarker and may assist in the management of men with mCRPC undergoing ^{177}Lu -PSMA therapy.

REFERENCES

- Emmett L, Crumbaker M, Ho B, et al. Results of a prospective phase 2 pilot trial of ^{177}Lu -PSMA-617 therapy for metastatic castration-resistant prostate cancer including imaging predictors of treatment response and patterns of progression. *Clin Genitourin Cancer*. 2019;17:15–22.
- Hofman MS, Emmett L, Sandhu S, et al. [^{177}Lu]Lu-PSMA-617 versus cabazitaxel in patients with metastatic castration-resistant prostate cancer (TheraP): a randomised, open-label, phase 2 trial. *Lancet*. 2021;397:797–804.
- Sartor O, de Bono J, Chi KN, et al. Lutetium-177-PSMA-617 for metastatic castration-resistant prostate cancer. *N Engl J Med*. 2021;385:1091–1103.
- Violet J, Sandhu S, Iravani A, et al. Long-term follow-up and outcomes of retreatment in an expanded 50-patient single-center phase II prospective trial of ^{177}Lu -PSMA-617 theranostics in metastatic castration-resistant prostate cancer. *J Nucl Med*. 2020;61:857–865.
- Gafita A, Rauscher I, Weber M, et al. Novel framework for treatment response evaluation using PSMA PET/CT in patients with metastatic castration-resistant prostate cancer (RECIP 1.0): an international multicenter study. *J Nucl Med*. 2022;63:1651–1658.
- Pathmanandavel S, Crumbaker M, Nguyen A, et al. Evaluation of ^{177}Lu -PSMA SPECT quantitation as a response biomarker within a prospective ^{177}Lu -PSMA-617 and NOX66 combination trial (LuPIN). *J Nucl Med*. August 25, 2022 [Epub ahead of print].
- Emmett L, Subramaniam S, Joshua AM, et al. ENZA-p trial protocol: a randomized phase II trial using prostate-specific membrane antigen as a therapeutic target and prognostic indicator in men with metastatic castration-resistant prostate cancer treated with enzalutamide (ANZUP 1901). *BJU Int*. 2021;128:642–651.
- Hofman MS, Emmett L, Violet J, et al. TheraP: a randomized phase 2 trial of ^{177}Lu -PSMA-617 theranostic treatment vs cabazitaxel in progressive metastatic castration-resistant prostate cancer (Clinical Trial Protocol ANZUP 1603). *BJU Int*. 2019;124(suppl 1):5–13.
- Niman R, Buteau JP, Krutzer A, Turcotte A, Nelson A. Evaluation of a semi-automated whole body PET segmentation method applied to diffuse large B cell lymphoma [abstract]. *J Nucl Med*. 2018;59(suppl 1):592.
- Scher HI, Morris MJ, Stadler WM, et al. Trial design and objectives for castration-resistant prostate cancer: updated recommendations from the Prostate Cancer Clinical Trials Working Group 3. *J Clin Oncol*. 2016;34:1402–1418.
- Eisenhauer EA, Therasse P, Bogaerts J, et al. New response evaluation criteria in solid tumours: revised RECIST guideline (version 1.1). *Eur J Cancer*. 2009;45:228–247.
- Halabi S, Lin CY, Kelly WK, et al. Updated prognostic model for predicting overall survival in first-line chemotherapy with metastatic castration-resistant prostate cancer. *J Clin Oncol*. 2014;32:671–677.
- Gafita A, Calais J, Grogan TR, et al. Nomograms to predict outcomes after ^{177}Lu -PSMA therapy in men with metastatic castration-resistant prostate cancer: an international, multicentre, retrospective study. *Lancet Oncol*. 2021;22:1115–1125.
- Sandhu S, Guo C, Hofman MS. Radionuclide therapy in prostate cancer: from standalone to combination PSMA theranostics. *J Nucl Med*. 2021;62:1660–1668.
- Halabi S, Vogelzang NJ, Ou S-S, Owzar K, Archer L, Small EJ. Progression-free survival as a predictor of overall survival in men with castrate-resistant prostate cancer. *J Clin Oncol*. 2009;27:2766–2771.
- Halabi S, Roy A, Yang Q, Xie W, Kelly WK, Sweeney C. Radiographic progression-free survival as a surrogate endpoint of overall survival in men with metastatic castrate-resistant prostate cancer [abstract]. *J Clin Oncol*. 2021;39(suppl):5057.
- Balk SP, Ko YJ, Bubley GJ. Biology of prostate-specific antigen. *J Clin Oncol*. 2003;21:383–391.
- Buteau JP, Martin AJ, Emmett L, et al. PSMA PET and FDG PET as predictors of response and prognosis in a randomized phase 2 trial of ^{177}Lu -PSMA-617 (LuPSMA) versus cabazitaxel in metastatic, castration-resistant prostate cancer (mCRPC) progressing after docetaxel (TheraP ANZUP 1603) [abstract]. *J Clin Oncol*. 2022;40(suppl):10.
- Pathmanandavel S, Crumbaker M, Yam AO, et al. ^{177}Lu -PSMA-617 and idronoxil in men with end-stage metastatic castration-resistant prostate cancer (LuPIN): patient outcomes and predictors of treatment response in a phase I/II trial. *J Nucl Med*. 2022;63:560–566.
- Kuo P, Hesterman J, Rahbar K, et al. [^{68}Ga]Ga-PSMA-11 PET baseline imaging as a prognostic tool for clinical outcomes to [^{177}Lu]Lu-PSMA-617 in patients with mCRPC: a VISION substudy [abstract]. *J Clin Oncol*. 2022;40(suppl):5002.
- Peters SMB, Meyer Viol SL, van der Werf NR, et al. Variability in lutetium-177 SPECT quantification between different state-of-the-art SPECT/CT systems. *EJNMMI Phys*. 2020;7:9.

Exploring Vessel Wall Biology In Vivo by Ultrasensitive Total-Body PET

Thorsten Derlin¹, Benjamin A. Spencer², Martin Mamach³, Yasser Abdelhafez⁴, Lorenzo Nardo⁴, Ramsey D. Badawi^{2,4}, Simon R. Cherry^{*2,4}, and Frank M. Bengel^{*1}

¹Department of Nuclear Medicine, Hannover Medical School, Hannover, Germany; ²Department of Biomedical Engineering, University of California, Davis, Davis, California; ³Department of Medical Physics and Radiation Protection, Hannover Medical School, Hannover, Germany; and ⁴Department of Radiology, University of California, Davis, Davis, California

Ultrasensitive, high-resolution, extended-field-of-view total-body (TB) PET using the first-of-its-kind 194-cm axial-field-of-view uEXPLORER may facilitate the interrogation of biologic hallmarks of hitherto difficult-to-evaluate low-signal vessel wall pathology in cardiovascular disease. **Methods:** Healthy volunteers were imaged serially for up to 12 h after a standard dose of ¹⁸F-FDG ($n = 15$) or for up to 3 h after injection of a very low dose (about 5% of a standard dose; $n = 15$). A cohort undergoing standard ¹⁸F-FDG PET ($n = 15$) on a conventional scanner with a 22-cm axial field of view served as a comparison group. Arterial wall signal, crosstalk with hematopoietic and lymphoid organs, and image quality were analyzed using standardized techniques. **Results:** TB PET depicted the large vessel walls with excellent quality. The arterial wall could be imaged with high contrast up to 12 h after tracer injection. Ultralow-dose TB ¹⁸F-FDG images yielded a vessel wall signal and target-to-background ratio comparable to those of conventional-dose, short-axial-field-of-view PET. Crosstalk between vessel wall and lymphoid organs was identified with better accuracy in both TB PET cohorts than in conventional PET. **Conclusion:** TB PET enables detailed assessment of in vivo vessel wall biology and its crosstalk with other organs over an extended time window after tracer injection or at an ultralow tracer dose. These initial observations support the feasibility of serial imaging in low-risk populations and will stimulate future mechanistic studies or therapy monitoring in atherosclerosis and other vessel wall pathologies.

Key Words: vessel wall; PET; total-body imaging; inflammation; atherosclerosis

J Nucl Med 2023; 64:416–422
DOI: 10.2967/jnumed.122.264550

Bologic activity of the vessel wall has emerged as an attractive target for noninvasive molecular imaging because of its key role in atherosclerosis (1) but also in other vascular pathologies such as vasculitis or aneurysm (2,3). Specifically, atherosclerosis is recognized today as an inflammatory disease of the arterial wall, for which progression is linked to a tight interplay with the hematopoietic system and various other systemic factors (4).

PET has provided translationally relevant insights into plaque biology; into the crosstalk between vessel wall, hematopoietic

system, and other systemic factors; into the importance of biologic systems activation for disease progression; and into the response to pharmacologic intervention (5–12). The application of PET in atherosclerosis has still, however, been limited mostly to single or dual time points in an individual, because of the radiation exposure derived from standard tracer doses (13). Limited sensitivity for the detection of weak signal from the relatively small vessel-wall target region is considered another challenge, as is the need for sequential imaging of body regions that are not covered by the limited axial field of view of a standard PET scanner.

Total-body (TB) PET is a recent technologic innovation characterized by an extended axial field of view that covers the entire body simultaneously and provides an up to 15–68 times higher detection sensitivity than current conventional PET systems, along with the highest spatial resolution (~3.0 mm) of any current clinical whole-body PET scanner (14). The performance characteristics of the first-of-its-kind 194-cm-long TB PET scanner, the uEXPLORER (United Imaging Healthcare), have recently been reported (15,16). Its capabilities for imaging of the vessel wall, however, have not yet been investigated. Here, we report the usefulness of TB PET for vascular molecular imaging at high contrast and a very low dose and for simultaneous assessment of systemic interaction with the hematopoietic and lymphoid systems.

MATERIALS AND METHODS

This is a condensed version of the methods; the full version is in the supplemental materials, available at <http://jnm.snmjournals.org>.

Study Design and Data Collection

This prospective study included 3 different cohorts (total $n = 45$) (Table 1). The first cohort ($n = 15$) included healthy subjects imaged with a standard dose (372 ± 17 MBq) of ¹⁸F-FDG on the uEXPLORER TB PET scanner at the University of California, Davis, at 1.5, 3, and 12 h after injection, to determine the feasibility of an extended time window for imaging of the vessel wall. The second cohort ($n = 15$) included healthy subjects imaged with an ultralow dose (19.6 ± 1.7 MBq) of ¹⁸F-FDG using the same scanner at 1.5 and 3 h after injection, to determine the potential for disease screening and repeat imaging with minimal radiation to the patient. The third cohort ($n = 15$) included a sex-matched patient group imaged with a standard dose (307 ± 12 MBq) of ¹⁸F-FDG using a conventional PET scanner (Fig. 1) with a 22-cm axial field of view (Biograph mCT flow; Siemens Healthineers). Cardiovascular risk factors and medication were documented (17,18). The study protocol complied with the Declaration of Helsinki and was approved by the institutional review boards of the University of California, Davis (approval 1341792), and Hannover Medical School

Received Jun. 21, 2022; revision accepted Sep. 28, 2022.
For correspondence or reprints, contact Thorsten Derlin (derlin.thorsten@mh-hannover.de).

*Contributed equally to this work.

Published online Sep. 29, 2022.

COPYRIGHT © 2023 by the Society of Nuclear Medicine and Molecular Imaging.

TABLE 1
Characteristics of Conventional and TB PET Cohorts

Parameter	Conventional PET cohort	TB PET cohorts	
		Standard dose	Ultralow dose
Subjects (<i>n</i>)	15	15	15
Sex (%)			
Male	40	40	53
Female	60	60	47
Age (y)			
Mean ± SD	59.0 ± 10.4	49.7 ± 14.7	45.0 ± 11.1
Range	33–72	26–78	26–62
Body mass index (kg/m ²)			
Mean ± SD	25.3 ± 3.1	29.1 ± 5.7	25.8 ± 3.4
Range	19.9–28.7	19.4–37.0	20.4–32.3
Cardiovascular risk factors			
Arterial hypertension (<i>n</i>)	7 (47%)	3 (20%)	1 (7%)
Hypercholesterolemia (<i>n</i>)	3 (20%)	5 (33%)	4 (27%)
Diabetes mellitus (<i>n</i>)	2 (13%)	0	0
History of smoking (<i>n</i>)	9 (60%)	1 (7%)	1 (7%)
Pack-years*			
Mean ± SD	44 ± 22	15	20
Range	10–80		
Prior myocardial infarction (<i>n</i>)	4 (27%)	0	0
Prior stroke (<i>n</i>)	1 (7%)	0	0
Prior cardiovascular intervention (<i>n</i>)	5 (33%)	0	0
Family history of IHD (<i>n</i>)	4 (27%)	4 (27%)	5 (33%)
Statin medication (<i>n</i>)	7 (47%)	2 (13%)	2 (13%)
Injected dose		3 (20%)	1 (7%)
Mean ± SD	307.2 ± 11.5	372.4 ± 17.0	19.6 ± 1.7
Range	291.1–328.6	337.3–393.8	17.2–23.5

*There was only 1 subject with history of smoking within each of these 2 cohorts; there is no SD and range is equal to the mean.
SD = standard deviation; IHD = ischemic heart disease.

Cardiovascular risk factors were available for 11 subjects in standard-dose cohort and 12 subjects in ultralow-dose cohort and in all patients of conventional cohort.

(approval 8774_BO_S_2019). All patients at the University of California, Davis, and Hannover Medical School provided written informed consent.

PET Image Acquisition and Reconstruction

TB PET. Ultralow-dose TB CT scans (5 mAs; 140 kVp; tube current modulation on; effective dose, ~1 mSv) or low-dose TB CT scans (50 mAs; 140 kVp; tube current modulation on; effective dose, ~10 mSv) were acquired for attenuation and scatter correction. The CT matrix size was 512 × 512 × 828 with 0.977 × 0.977 × 2.344 mm voxels. A static PET scan of the entire body without bed motion was obtained for 20 min starting 90, 180, and 720 min (standard dose only) after injection. The administered dose of ¹⁸F-FDG was 372 ± 17 MBq for the standard-dose cohort (*n* = 15) and 19.6 ± 1.7 MBq for the low-dose cohort (*n* = 15). Blood glucose was less than 160 mg/dL in all subjects before injection. Studies were reconstructed from list-mode data with vendor-provided software using an iterative algorithm (20 subsets, 4 iterations) incorporating time-of-flight information but no point-spread

function correction. The reconstruction matrix was 256 × 256 × 828 with isotropic voxels of 2.344 mm. Studies were corrected for attenuation, scatter, randoms, and dead time. No smoothing was applied to the reconstructed images.

Conventional PET. Low-dose whole-body CT (25 mAs, reference; 120 kV; CARE Dose4D [Siemens Healthcare]; 5-mm slice thickness; pitch, 1.4) was performed. Using continuous bed motion to cover the entire body, a static PET scan was obtained at 60–90 min after administration of 307 ± 12 MBq (range, 291–329 MBq) of ¹⁸F-FDG. Blood glucose was less than 120 mg/dL in all patients before injection. Attenuation-corrected studies were reconstructed using Ultra HD (Siemens Healthcare), an iterative algorithm combined with time-of-flight and point-spread function information (2 iterations; 21 subsets; matrix, 200; zoom, 1.0; gaussian filter, 5.0 mm).

Image Analysis

Vessel wall ¹⁸F-FDG signal in major arteries (19) was analyzed as described previously using the average SUV_{max} and the arterial target-to-background ratio (20), yielding a measure for assessment of global

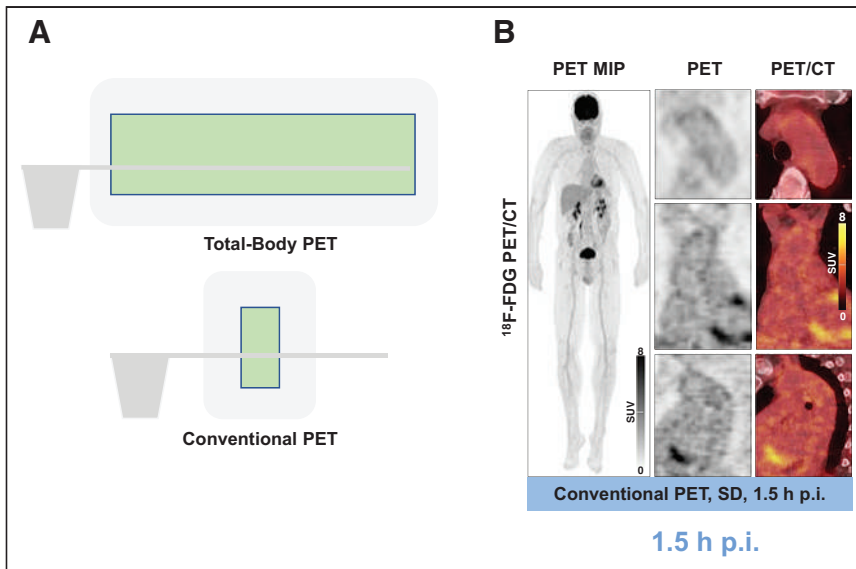


FIGURE 1. Exploring arterial wall biology using ultrasensitive TB PET. (A) Graphical illustration of TB PET scanner vs. conventional short-axial-field-of-view PET scanner. Axial field of view (FOV) of TB PET scanner is 194 cm, providing simultaneous coverage of all tissues and organs in body, with overall increase in effective sensitivity of more than 15- to 68-fold. Axial FOV of conventional PET scanner is typically less than 25 cm. (B) Sample ^{18}F -FDG PET maximum-intensity-projection image and cross-sectional PET and PET/CT images acquired using conventional high-end scanner in 66-y-old man. MIP = maximum-intensity projection; p.i. = after injection; SD = standard dose.

vascular activity for comparison with other surrogate markers of cardiovascular disease (21). Likewise, calcified plaque was assessed (17,19). For characterization of systemic interactions between arterial wall signal and activity of hematopoietic and lymphoid organs (10), spleen signal, bone marrow signal, and lymph node signal were determined. Image noise was assessed using the coefficient of variation of normal liver parenchyma (22).

Statistical Analyses

One-way ANOVA with Šidák multiple-comparisons testing, repeated-measures ANOVA with the Geisser–Greenhouse correction and Šidák multiple-comparisons testing, paired *t* tests, and Pearson correlation coefficients were used for analyses. Statistical significance was established for *P* values of less than 0.05. Analysis was performed using Prism (version 9.0; GraphPad Software) for Microsoft Windows.

RESULTS

Subjects in the TB PET cohorts exhibited a significantly lower number of calcified vessel wall lesions than patients in the conventional PET cohort ($P = 0.011$ for standard-dose cohort; $P = 0.002$ for ultralow-dose cohort), consistent with a lower cardiovascular risk profile (Supplemental Tables 1–3; Table 1). However, a clear-cut vessel wall signal was identified by TB PET in these cohorts despite their lower risk profile.

TB PET Allows for High-Contrast Vessel Wall Imaging by Enabling Imaging Much Later After Tracer Injection

Standard-dose TB PET images yielded excellent image quality up to the final time

point of 12 h after ^{18}F -FDG injection (Fig. 2). For both the aortic wall and other arterial walls, SUV_{max} as a measure of vessel wall signal strength was comparable between early standard-dose TB PET and conventional PET (Supplemental Table 4), albeit the conventional cohort had a higher risk profile. Arterial wall signal (SUV_{max}) increased significantly at very late imaging (1.5 vs. 12 h after injection: SUV_{max} , $P < 0.0001$) in standard-dose TB PET, whereas there were only minor changes in arterial wall signal between 1.5 and 3 h after injection in both TB cohorts. Importantly, blood-pool signal significantly decreased over time ($P < 0.0001$ in all cases), leading to a significant increase in the target-to-background ratio as a measure of vessel wall contrast ($P < 0.0001$ in all cases). Image noise increased at later imaging time points, particularly (and expectedly) on 12-h delayed images (Supplemental Table 4).

TB PET Imaging of the Vessel Wall Is Feasible Using Ultralow Radiotracer Doses

Ultralow-dose TB PET images were of good quality, providing clear visualization of the vessel wall (Fig. 3). Expectedly, there was more noise than for standard-dose images, but the arterial wall signal strength was comparable, and the target-to-background ratio demonstrated the same temporal evolution toward an increase over time (Fig. 4; Supplemental Table 4).

TB PET Improves Analysis of Interorgan Immune Crosstalk

Signal from spleen and bone marrow (Figs. 5 and 6) did not significantly differ between cohorts (lymph node signal was higher in the ultralow-dose cohort). Regarding intraindividual imaging time points, spleen signal decreased over time ($P \leq 0.0143$), whereas bone marrow signal consistently increased over time (standard dose, $P \leq 0.0017$; ultralow dose, $P = 0.0014$) in both TB PET

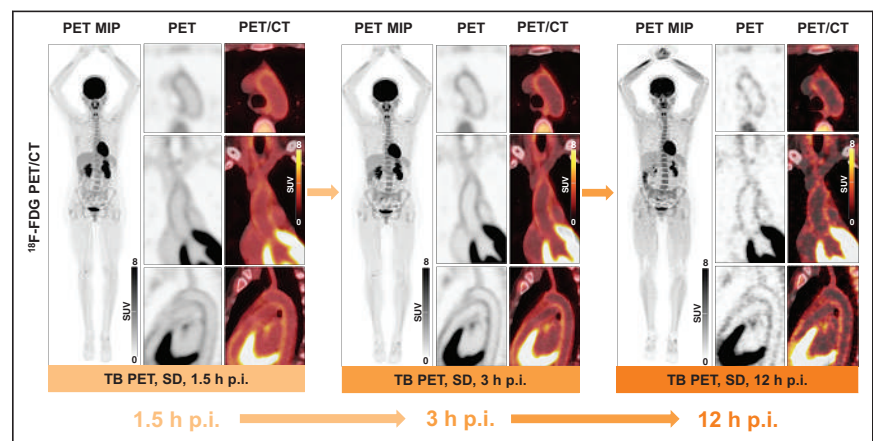


FIGURE 2. Sample TB ^{18}F -FDG PET maximum-intensity-projection images and cross-sectional PET/CT images at different time points using standard radiotracer dose (~370 MBq), ranging from 1.5 h after injection to 12 h after injection. TB PET imaged aortic wall with excellent quality and high contrast, which improved with time. MIP = maximum-intensity projection; p.i. = after injection; SD = standard dose.

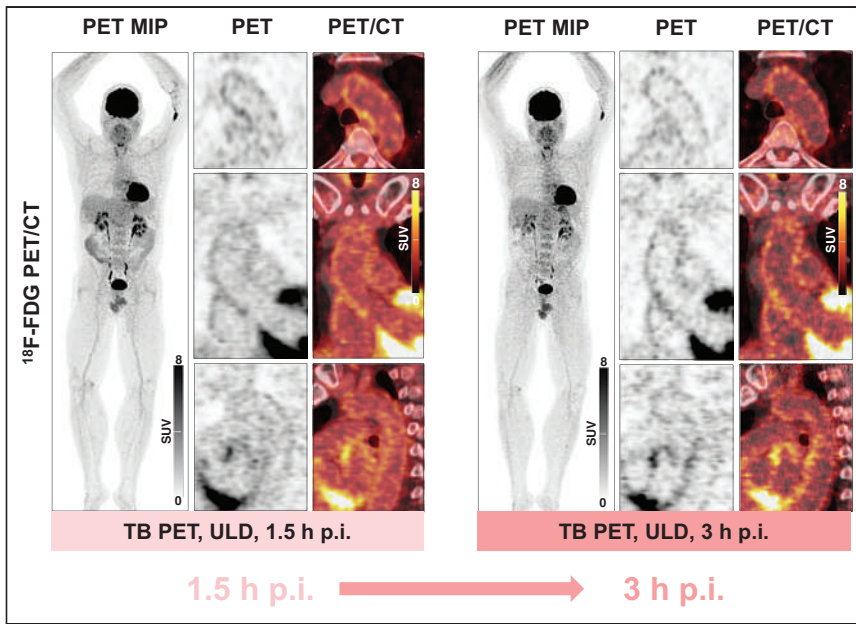


FIGURE 3. Sample TB ^{18}F -FDG PET/CT images at 1.5 and 3 h after injection using very low radio-tracer dose ($\sim 5\%$ of standard dose). Clear vessel wall signal can be obtained using very low radio-tracer doses. MIP = maximum-intensity projection; p.i. = after injection; ULD = ultralow dose.

cohorts (Supplemental Table 5). Importantly, arterial wall signal and activity in lymphoid organs correlated more frequently and more strongly for TB PET than for standard PET (Supplemental Table 6; Fig. 7), particularly in high-quality early images.

DISCUSSION

PET has been used in the past as a powerful tool for noninvasive interrogation of vessel wall biology in vivo. For this use, it has provided valuable insights into disease mechanisms and responses to therapeutic interventions (5–12). However, the arterial wall represents a thin target structure, where target molecules and cell types of interest are more difficult to identify than in larger organs and tissues (10). Using standard PET scanners, robust signal detection remains challenging and is often restricted to large vascular structures or requires high-end motion correction and extended acquisition techniques (23). Our study supports the notion that the recently reported 15- to 68-fold sensitivity gain for TB PET, when compared with current standard systems (15), can be used for improved vessel wall imaging. Intriguingly, the sensitivity of TB PET enables delayed and longitudinal imaging after many half-lives of the radionuclide. For the first time, to our knowledge, we have evaluated the evolution of the arterial wall signal up to 12 h after injection of ^{18}F -FDG, equivalent to about 6.5 half-lives of ^{18}F . The vessel wall signal increased significantly over time. And because blood pool continuously clears over time, the vessel wall target-to-background ratio improves further,

providing superior contrast. Delayed imaging with optimized contrast is therefore one option resulting from the use of ultrasensitive TB PET. Although the target-to-background ratio increased over time, the time point with the highest SUV in arterial wall imaging could not be determined from this study. Images were acquired not continuously but at certain time points.

Another feasible option supported by our study is the use of ultralow-dose imaging. Radiation exposure may be seen as an obstacle to the application of vascular PET imaging, especially in low-risk populations or for serial observations (13,24). The effective dose from a standard activity of 370 MBq of ^{18}F -FDG is about 7 mSv, but using ultralow-dose TB PET, we showed that imaging of the vessel wall is feasible using doses of as low as 5% of a standard dose for up to 3 h after injection, with good image quality and comparable signal strength and vascular contrast compared with standard techniques, although the conventional PET cohort had a higher risk profile, likely associated with a higher true wall signal (12). The

effective dose of 0.4 mSv for the 20 MBq of ^{18}F -FDG in the ultralow-dose protocol is less than 15% of the natural annual radiation exposure, supporting the feasibility of longitudinal studies or broader cross-sectional applications of this technique. Although additional radiation exposure will originate from the CT scan obtained for anatomic coregistration, we expect that there will be solutions for further dose reduction here, too. We note that with the 5-mAs CT protocol used for TB PET in this study, the estimated dose was only 1 mSv. Given the excellent anatomic detail in the stand-alone TB PET images, it may, for example, be conceivable to perform PET-only studies using artificial intelligence-derived maps for

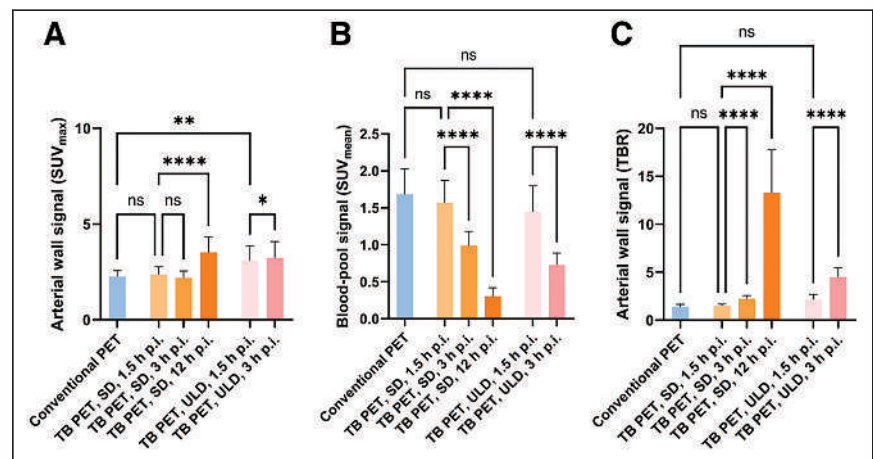


FIGURE 4. Multiple-time-point imaging of arterial wall signal. (A) Arterial wall SUV_{max} increased significantly at very late imaging (12 h after injection, $P < 0.0001$) on standard-dose TB PET, whereas there were only minor changes in arterial wall signal between 1.5 and 3 h after injection in both TB cohorts. (B) By contrast, blood pool SUV_{max} significantly decreased at later imaging time points on TB PET (standard dose, $P < 0.0001$; ultralow dose, $P < 0.0001$). (C) Result was increase in target-to-background ratio over time (standard dose, $P < 0.0001$; ultralow dose, $P < 0.0001$). * $- < 0.05$; ** $- < 0.01$; *** $- < 0.001$; **** $- < 0.0001$. ns = not statistically significant; p.i. = after injection; SD = standard dose; ULD = ultralow dose.

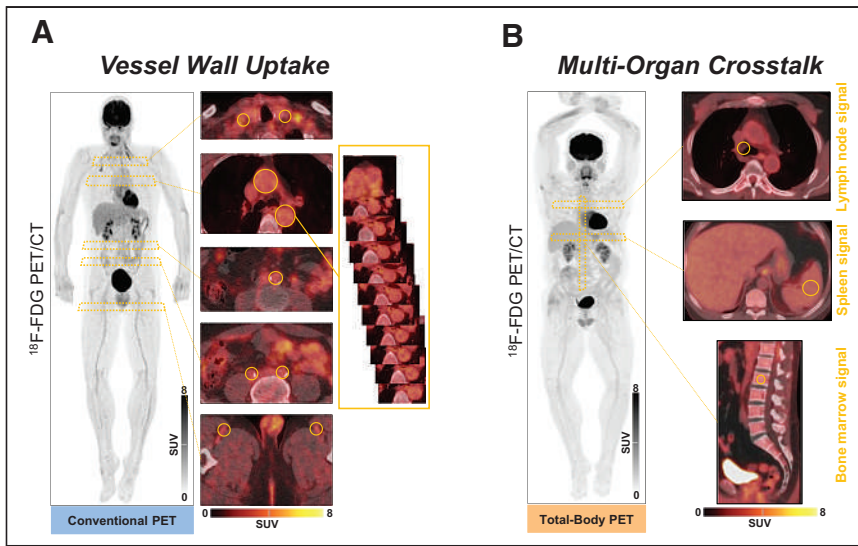


FIGURE 5. Dissecting multiorgan immune crosstalk. (A) Assessment of arterial wall uptake in different large arteries using regions of interest in sample conventional PET. For each arterial localization, uptake was evaluated in 10 slices and then averaged (left panel, PET maximum-intensity-projection image; middle and right panels, transaxial PET/CT images). (B) Sample TB ^{18}F -FDG PET maximum-intensity-projection image (left panel) and cross-sectional PET/CT images (right panel) used for assessment of multiorgan networks.

attenuation correction of PET images (25). Last, further reduction of injected activity was not tested in our study but appears possible if early imaging time points are used. Nevertheless, a detailed analysis of distinct plaques would likely require a higher CT image quality (and dose) for an appropriate analysis of individual plaque structure. Furthermore, we assessed the global vascular activity (21) but not the activity of individual plaques. Analysis of distinct arterial plaques is particularly difficult—and may be less reliable—in the presence of image noise. Importantly, there was more noise using ultralow radiotracer doses than for the standard-dose images in this study, highlighting the need for higher tracer doses when analyzing distinct plaques.

Unlike conventional PET, which is acquired with sequential bed positions alternating between image acquisition and patient table motion, TB PET allows for simultaneous imaging of the entire body, providing a superior measurement technique due to varying imaging time points for different parts of the body. This not only enables accurate and complete coverage of the whole vascular tree but also provides simultaneous information from other organs and tissues that may be interconnected. Our study showed that TB PET may provide more robust information on the relationship between vessel wall signal and activated lymphoid system than standard PET. Simultaneous coverage of the entire body may therefore be superior for analysis of systems-based interactions. The complex, multifaceted systemic interactions between cardiovascular disease and other organs or tissues have gained increasing interest and fostered the

emergence of novel interdisciplinary clinical subspecialties such as neurocardiology, cardiorrheumatology, and cardiooncology (8,26,27). An example is that the local inflammatory tissue response after acute myocardial infarction not only may result in a systemic inflammatory response with exacerbated vessel wall inflammation (28) but also induces neuroinflammation as a potential precursor to cognitive dysfunction (29). TB PET holds the key to providing further and deeper insights into these interorgan interactions at the crossroads between cardiovascular medicine and other fields.

The potential of TB PET for vascular imaging may grow even further. The ultra-high sensitivity will enable ultrafast imaging (30,31), which can be used to obtain parametric images after pixelwise kinetic modeling (32) and may enable real-time motion correction of moving structures such as the coronary arteries. Dynamic TB imaging allows for generation of parametric images using voxel-based Patlak graphical analysis, such as of the metabolic rate of ^{18}F -FDG. Absolute quantification of arterial

wall signal and hematopoietic and lymphoid organ signal may show further improved characterization of systemic organ interactions compared with standard SUV images (33). Such advanced technical developments are expected to yield an even further increase in contrast and accuracy. Additionally, it is important to recognize that although ^{18}F -FDG was used as a tracer example in this study, the methods can be transferred to any other PET tracer. ^{18}F -FDG has been validated as a marker of plaque inflammation (34) but has also been shown to have specificity limitations (7). Other clinically feasible tracers, such as ^{18}F -sodium fluoride (7,17) or ^{68}Ga -pentixafor (19,23), may benefit equally from the advantages of TB PET.

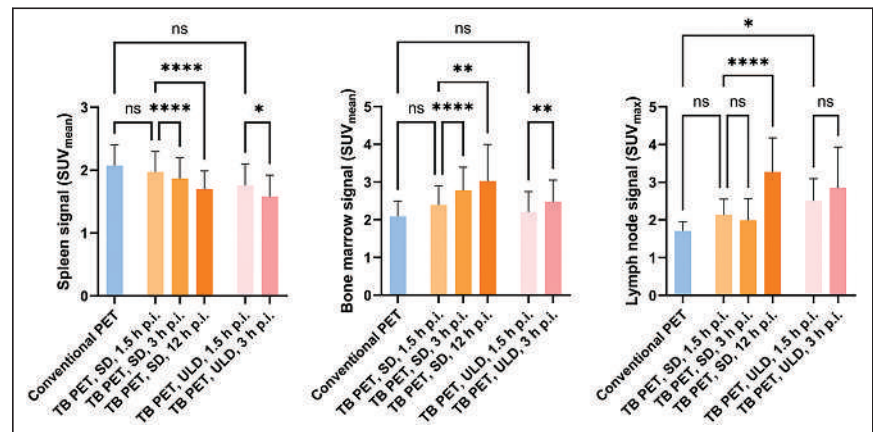


FIGURE 6. Dissecting multiorgan immune crosstalk. Spleen and bone marrow signal did not significantly differ between conventional PET and TB PET cohorts. Regarding intraindividual imaging time points, spleen signal decreased over time (e.g., standard-dose TB PET at 12 h after injection [$P < 0.0001$]), whereas bone marrow signal increased with time (standard dose, $P \leq 0.0017$; ultralow dose, $P = 0.0014$) in both TB PET cohorts. Lymph node signal increased significantly at 12 h after injection ($P < 0.0001$). * - <0.05 ; ** - <0.01 ; *** - <0.001 ; **** - <0.0001 . ns = not statistically significant; p.i. = after injection; SD = standard dose; ULD = ultralow dose.

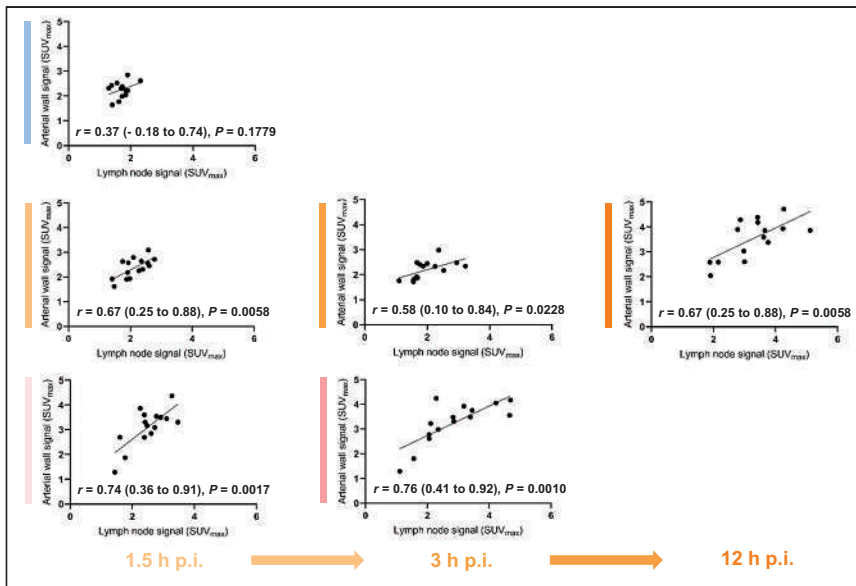


FIGURE 7. Dissecting multiorgan immune crosstalk. Arterial wall signal does not correlate with lymph node signal in conventional PET cohort (top row). By contrast, correlation is significant and consistent in both TB PET cohorts (middle and bottom rows), both at early imaging time points (left column) and at delayed imaging (middle and right columns).

Some limitations of our work should be acknowledged. First, the sample size in the different cohorts was limited, and the TB PET cohorts comprised healthy volunteers with a predominantly low cardiovascular risk profile, precluding a meaningful analysis of the association between arterial wall signal and cardiovascular risk factors in the context of low statistical power to detect such associations. Although imaging of large cohorts of volunteers remains challenging, future analyses may comprise larger clinical samples of patients scanned with TB PET, once the technology has been more broadly applied. Biologic (e.g., the different accepted blood glucose values at the time of PET) and technical factors affecting SUVs may have influenced the study results to some extent but reflect different clinical practices at different sites contributing patients to this study. However, the aim of this study was to demonstrate both principal novel applications and the improved characterization of biologic processes using TB PET. Future studies may also demonstrate an improved relation between PET signal and histopathologic ground truth, that is, inflammation in cases of ^{18}F -FDG (34) or with other inflammatory biomarkers such as C-reactive protein. In particular, correlation with biomarkers may improve at later acquisition times (e.g., at 12 h after injection) and with an optimized target-to-background situation, which might be worthwhile exploring. We provided a first indication of such an improved characterization of biologic processes, given the better correlation between vessel wall signal and hematopoietic and immune organ activity such as spleen and regional lymph nodes in TB PET. Finally, this work focused on demonstrating the initial feasibility of vessel wall imaging using the uEXPLORER scanner, but it was not designed as a controlled trial, such as to monitor the effects of a specific pharmacologic intervention. Our work provides the technologic basis for such studies and should be seen as a stimulus for future more expansive efforts.

CONCLUSION

The first human vessel wall imaging studies using the ultrasensitive, high-resolution TB PET uEXPLORER system highlight the

opportunities for extended-time-window imaging, ultralow-dose imaging, and systems-based analysis of interorgan interaction. Future work will focus on further advances in TB PET data analysis, on additional vessel wall-targeted radiopharmaceuticals, and on clinical feasibility studies using TB PET for such applications as atherosclerosis screening with a global disease activity score, imaging-based stratification for therapy, and repeat imaging in treatment monitoring.

DISCLOSURE

Grant funding was received from the German Research Foundation (BE2217/6-1) and the National Institutes of Health (R01 CA206187). The University of California, Davis, has a revenue-sharing agreement and a research agreement (principal investigators, Ramsey Badawi and Simon Cherry) with United Imaging Healthcare. No other potential conflict of interest relevant to this article was reported.

ACKNOWLEDGMENTS

We are grateful for the invaluable expertise and support of the technologists and clinical research staff involved in this study.

KEY POINTS

QUESTION: Does TB PET improve imaging of vessel wall activity in patients with atherosclerosis?

PERTINENT FINDINGS: TB PET enabled detailed assessment of in vivo vessel wall biology and its crosstalk with other organs, over an extended time window after tracer injection or at an ultralow tracer dose.

IMPLICATIONS FOR PATIENT CARE: TB PET may influence the present clinical practice of cardiovascular PET imaging. These initial observations support the feasibility of serial imaging in low-risk populations, and they will stimulate future mechanistic studies or therapy monitoring in atherosclerosis and other vessel wall pathologies.

REFERENCES

- Daghem M, Bing R, Fayad ZA, et al. Noninvasive imaging to assess atherosclerotic plaque composition and disease activity: coronary and carotid applications. *JACC Cardiovasc Imaging*. 2020;13:1055–1068.
- Slart RHJA, Writing Group, Reviewer Group, et al. FDG-PET/CT(A) imaging in large vessel vasculitis and polymyalgia rheumatica: joint procedural recommendation of the EANM, SNMMI, and the PET Interest Group (PIG), and endorsed by the ASNC. *Eur J Nucl Med Mol Imaging*. 2018;45:1250–1269.
- Malm BJ, Sadeghi MM. Multi-modality molecular imaging of aortic aneurysms. *J Nucl Cardiol*. 2017;24:1239–1245.
- Libby P. The changing landscape of atherosclerosis. *Nature*. 2021;592:524–533.
- Werner RA, Bengel FM, Derlin T. Emerging molecular targets for imaging of atherosclerotic plaque using positron emission tomography. *Curr Radiopharm*. 2021;14:173–183.
- Fayad ZA, Mani V, Woodward M, et al. Safety and efficacy of dalcetrapib on atherosclerotic disease using novel non-invasive multimodality imaging (dal-PLAQUE): a randomised clinical trial. *Lancet*. 2011;378:1547–1559.

7. Joshi NV, Vesey AT, Williams MC, et al. ^{18}F -fluoride positron emission tomography for identification of ruptured and high-risk coronary atherosclerotic plaques: a prospective clinical trial. *Lancet*. 2014;383:705–713.
8. Tawakol A, Ishai A, Takx RA, et al. Relation between resting amygdalar activity and cardiovascular events: a longitudinal and cohort study. *Lancet*. 2017;389:834–845.
9. Keliher EJ, Ye YX, Wojtkiewicz GR, et al. Polyglucose nanoparticles with renal elimination and macrophage avidity facilitate PET imaging in ischaemic heart disease. *Nat Commun*. 2017;8:14064.
10. van der Valk FM, Kuijk C, Verweij SL, et al. Increased haematopoietic activity in patients with atherosclerosis. *Eur Heart J*. 2017;38:425–432.
11. Chowdhury MM, Tarkin JM, Albaghdadi MS, et al. Vascular positron emission tomography and restenosis in symptomatic peripheral arterial disease: a prospective clinical study. *JACC Cardiovasc Imaging*. 2020;13:1008–1017.
12. Singh P, Emami H, Subramanian S, et al. Coronary plaque morphology and the anti-inflammatory impact of atorvastatin: a multicenter ^{18}F -fluorodeoxyglucose positron emission tomographic/computed tomographic study. *Circ Cardiovasc Imaging*. 2016;9:e004195.
13. Meinel FG, Nance JW Jr, Harris BS, et al. Radiation risks from cardiovascular imaging tests. *Circulation*. 2014;130:442–445.
14. Cherry SR, Badawi RD, Karp JS, et al. Total-body imaging: transforming the role of positron emission tomography. *Sci Transl Med*. 2017;9:eaaf6169.
15. Badawi RD, Shi H, Hu P, et al. First human imaging studies with the EXPLORER total-body PET scanner. *J Nucl Med*. 2019;60:299–303.
16. Spencer BA, Berg E, Schmall JP, et al. Performance evaluation of the uEXPLORER total-body PET/CT scanner based on NEMA NU 2-2018 with additional tests to characterize PET scanners with a long axial field of view. *J Nucl Med*. 2021;62:861–870.
17. Derlin T, Wisotzki C, Richter U, et al. In vivo imaging of mineral deposition in carotid plaque using ^{18}F -sodium fluoride PET/CT: correlation with atherogenic risk factors. *J Nucl Med*. 2011;52:362–368.
18. Subramanian S, Emami H, Vucic E, et al. High-dose atorvastatin reduces periodontal inflammation: a novel pleiotropic effect of statins. *J Am Coll Cardiol*. 2013;62:2382–2391.
19. Weiberg D, Thackeray JT, Daum G, et al. Clinical molecular imaging of chemokine receptor CXCR4 expression in atherosclerotic plaque using ^{68}Ga -pentixafor PET: correlation with cardiovascular risk factors and calcified plaque burden. *J Nucl Med*. 2018;59:266–272.
20. Derlin T, Koenecke C, Schultze-Florey C, et al. CD19-targeted immunotherapy attenuates vessel wall inflammation. *JACC Cardiovasc Imaging*. 2021;14:1864–1866.
21. Buceri J, Hyafil F, Verberne HJ, et al. Position paper of the Cardiovascular Committee of the European Association of Nuclear Medicine (EANM) on PET imaging of atherosclerosis. *Eur J Nucl Med Mol Imaging*. 2016;43:780–792.
22. Yan J, Schaefferkoette J, Conti M, et al. A method to assess image quality for low-dose PET: analysis of SNR, CNR, bias and image noise. *Cancer Imaging*. 2016;16:26.
23. Derlin T, Sedding DG, Dutzmann J, et al. Imaging of chemokine receptor CXCR4 expression in culprit and nonculprit coronary atherosclerotic plaque using motion-corrected [^{68}Ga]pentixafor PET/CT. *Eur J Nucl Med Mol Imaging*. 2018;45:1934–1944.
24. Everett BM, MacFadyen JG, Thuren T, et al. Inhibition of interleukin-1 β and reduction in atherothrombotic cardiovascular events in the CANTOS trial. *J Am Coll Cardiol*. 2020;76:1660–1670.
25. Arabi H, Bortolin K, Ginovart N, et al. Deep learning-guided joint attenuation and scatter correction in multitracer neuroimaging studies. *Hum Brain Mapp*. 2020;41:3667–3679.
26. Mantel A, Holmqvist M, Andersson DC, et al. Association between rheumatoid arthritis and risk of ischemic and nonischemic heart failure. *J Am Coll Cardiol*. 2017;69:1275–1285.
27. Campia U, Moslehi JJ, Amiri-Kordestani L, et al. Cardio-oncology: vascular and metabolic perspectives: a scientific statement from the American Heart Association. *Circulation*. 2019;139:e579–e602.
28. Dutta P, Courties G, Wei Y, et al. Myocardial infarction accelerates atherosclerosis. *Nature*. 2012;487:325–329.
29. Thackeray JT, Hupe HC, Wang Y, et al. Myocardial inflammation predicts remodeling and neuroinflammation after myocardial infarction. *J Am Coll Cardiol*. 2018;71:263–275.
30. Zhang X, Xie Z, Berg E, et al. Total-body dynamic reconstruction and parametric imaging on the uEXPLORER. *J Nucl Med*. 2020;61:285–291.
31. Zhang X, Cherry SR, Xie Z, Shi H, Badawi RD, Qi J. Subsecond total-body imaging using ultrasensitive positron emission tomography. *Proc Natl Acad Sci USA*. 2020;117:2265–2267.
32. Wang G, Nardo L, Parikh M, et al. Total-body PET multiparametric imaging of cancer using a voxel-wise strategy of compartmental modeling. *J Nucl Med*. 2022;63:1274–1281.
33. Derlin T, Werner RA, Weiberg D, Derlin K, Bengel FM. Parametric imaging of biologic activity of atherosclerosis using dynamic whole-body positron emission tomography. *JACC Cardiovasc Imaging*. 2022;15:2098–2108.
34. Rudd JH, Warburton EA, Fryer TD, et al. Imaging atherosclerotic plaque inflammation with [^{18}F]fluorodeoxyglucose positron emission tomography. *Circulation*. 2002;105:2708–2711.

PET Imaging of Neutrophil Elastase with ^{11}C -GW457427 in Acute Respiratory Distress Syndrome in Pigs

Emmi Puuvuori¹, Elena Chiodaroli², Sergio Estrada¹, Pierre Cheung¹, Norbert Lubenow³, Jonathan Sigfridsson⁴, Hampus Romelin⁴, Sofie Ingvast³, Mathias Elgland^{1,4}, Francesco Liggieri², Olle Korsgren³, Gaetano Perchiazzi², Olof Eriksson^{*1}, and Gunnar Antoni^{*1,4}

¹Science for Life Laboratory, Department of Medicinal Chemistry, Uppsala University, Uppsala, Sweden; ²Hedenstierna Laboratory, Department of Surgical Sciences, Uppsala University, Uppsala Sweden; ³Department of Immunology, Genetics, and Pathology, Uppsala University, Uppsala, Sweden; and ⁴PET Center, Center for Medical Imaging, Uppsala University Hospital, Uppsala, Sweden

Today, there is a lack of clinically available imaging techniques to detect and quantify specific immune cell populations. Neutrophils are one of the first immune cells at the site of inflammation, and they secrete the serine protease neutrophil elastase (NE), which is crucial in the fight against pathogens. However, the prolonged lifespan of neutrophils increases the risk that patients will develop severe complications, such as acute respiratory distress syndrome (ARDS). Here, we evaluated the novel radiolabeled NE inhibitor ^{11}C -GW457427 in a pig model of ARDS, for detection and quantification of neutrophil activity in the lungs. **Methods:** ARDS was induced by intravenous administration of oleic acid to 5 farm pigs, and 4 were considered healthy controls. The severity of ARDS was monitored by clinical parameters of lung function and plasma biomarkers. Each pig was studied with ^{11}C -GW457427 and PET/CT, before and after pretreatment with the NE inhibitor GW311616 to determine in vivo binding specificity. PET image data were analyzed as SUVs and correlated with immunohistochemical staining for NE in biopsies. **Results:** The binding of ^{11}C -GW457427 was increased in pig lungs with induced ARDS (median SUV_{mean} , 1.91; interquartile range [IQR], 1.67–2.55) compared with healthy control pigs ($P < 0.05$ and $P = 0.03$, respectively; median SUV_{mean} , 1.04; IQR, 0.66–1.47). The binding was especially strong in lung regions with high levels of NE and ongoing inflammation, as verified by immunohistochemistry. The binding was successfully blocked by pretreatment of an NE inhibitor drug, which demonstrated the in vivo specificity of ^{11}C -GW457427 ($P < 0.05$ and $P = 0.04$, respectively; median SUV_{mean} , 0.60; IQR, 0.58–0.77). The binding in neutrophil-rich tissues such as bone marrow ($P < 0.05$ and $P = 0.04$, respectively; baseline median SUV_{mean} , 5.01; IQR, 4.48–5.49; block median SUV_{mean} , 1.57; IQR, 0.95–1.85) and spleen (median SUV_{mean} , 2.14; IQR, 1.19–2.36) was also high in all pigs. **Conclusion:** ^{11}C -GW457427 binds to NE in a porcine model of oleic acid-induced lung inflammation in vivo, with a specific increase in regional lung, bone marrow, and spleen SUV. ^{11}C -GW457427 is a promising tool for localizing, tracking, and quantifying neutrophil-facilitated inflammation in clinical diagnostics and drug development.

Key Words: inflammation; PET; neutrophil elastase; ARDS

J Nucl Med 2023; 64:423–429
DOI: 10.2967/jnumed.122.264306

The acute respiratory distress syndrome (ARDS) is a life-threatening condition characterized by lung injury, infiltration of immune cells, increased permeability, and decreased pulmonary function (1). Inflammation damages the thin-walled alveoli and the alveolar–capillary unit, determining lung edema, decreased lung compliance, and hypoxemia, eventually resulting in the need for mechanical ventilation (2). Different direct (e.g., pneumonia or pulmonary injury) or indirect (e.g., sepsis) mechanisms can lead to ARDS, and despite improvement in treatment, the condition is associated with high mortality (3).

There are several inflammatory biomarkers associated with ARDS, such as cytokines, demonstrating that immune cell recruitment and accumulation are an important path of the pathology (4). Inflammatory processes may affect all major organs and, unresolved, may lead to development of fibrosis and finally organ failure. Even in ARDS induced by intrapulmonary causes such as injurious mechanical ventilation, activation of the inflammatory cascade and mediators carried by the blood circulation can reach remote organs and contribute to multiorgan failure (5).

In this process, immune-active cells such as leukocytes play a key role, and neutrophils are the most abundant leukocytes in the circulation. They are part of the innate immune system, acting as a first line of defense in the immune response, and are recruited to the site of damage within minutes after trauma or acute inflammation. Neutrophils are produced from stem cells in the bone marrow, and they are highly mobile not only in the bloodstream but also in the marginated intravascular pools in the lungs, spleen, and liver (6,7). The lifespan of neutrophils in healthy humans is short, as inactivated neutrophils survive only around 8 h (8). However, the activated neutrophils can prolong their existence up to 5 d (9). The extended life of activated neutrophils promotes chronic inflammation and inflammation-related morbidity in several lung diseases, including ARDS (7,10). On activation, neutrophils can increase the permeability of the blood vessels to proteins and migrate through them into interstitium. Neutrophils can defend the host from invaders by phagocytosis, secretion, and release of antimicrobials (degranulation) and formation of neutrophil extracellular traps (11). One of the biomarkers linked with ARDS is neutrophil extracellular traps, whose purpose is to physically trap microorganisms on the DNA strands to prevent the spread and to disarm pathogens using antimicrobial proteins such as neutrophil elastase (NE) (2).

NE is a serine protease stored in the primary granules of neutrophils and released on neutrophil activation by degranulation and

Received Apr. 18, 2022; revision accepted Sep. 1, 2022.
For correspondence or reprints, contact Olof Eriksson (olof.eriksson@ilk.uu.se) or Gunnar Antoni (gunnar.antoni@akademiska.se).
*Contributed equally to this work.
Published online Sep. 15, 2022.
COPYRIGHT © 2023 by the Society of Nuclear Medicine and Molecular Imaging.

neutrophil extracellular traps. Thus, NE has a key role in mediating tissue remodeling, but it can also damage the lung parenchyma and the airway walls. NE inhibitors such as sivelestat have been investigated as a treatment for acute lung injury and ARDS, with mixed results and no proven efficacy (12). This could potentially be explained by insufficient dosing, exposure, or duration of treatment. No quantitative molecular imaging modality such as PET and a selective PET tracer targeting NE has been used to verify the interaction between drug and drug target and quantify the degree of elastase inhibition *in vivo*. Thus, monitoring the potential of these novel therapeutic strategies requires improved understanding and techniques to monitor disease progression noninvasively.

Currently, the NE activity *in vivo* can be monitored by intravital microscopy, which is limited in depth and field of view and is therefore suitable mainly for preclinical use on small animals (6,13). Clinically, *in vitro* NE levels can be analyzed from sputum and plasma samples; however, the sputum samples are unreliable and plasma samples are not tissue-specific to lungs.

In vivo imaging of NE activity has also been attempted by radiolabeling of a peptide with high affinity for NE (14). The resulting tracer, ^{99m}Tc -mercaptoacetyltryglycine-EPI-human neutrophil elastase inhibitor 2, could visualize inflammation in tissue in nonhuman primates, demonstrating the feasibility of NE *in vivo* imaging by SPECT.

^{11}C -GW457427 (0.44 kDa) is a novel small-molecule PET tracer targeting NE. We have recently reported good-manufacturing-practice-ready production, toxicology, dosimetry, metabolite analysis, and *in vivo* binding data on mice for ^{11}C -GW457427 (15), as well as a pilot clinical study on patients with coronavirus disease 2019 (COVID-19) (16).

The aim of this study was to validate ^{11}C -GW457427 as a PET marker for NE in a translationally relevant large-animal model of ARDS. Porcine and human neutrophils behave similarly and have comparable respiratory mechanics and gas exchange in the lungs (17,18). This makes the pig a relevant model for preclinical studies of NE in ARDS.

MATERIALS AND METHODS

Radiosynthesis of ^{11}C -GW457427

^{11}C -GW457427 was synthesized as described in detail previously (15,16). ^{11}C -GW457427 ($n = 17$) was generated with radiochemical purity of more than 95%.

Animal Handling

The animal experiments were authorized by the Animal Ethics Committee of the Swedish Animal Welfare Agency and performed according to the ARRIVE and institutional guidelines ("Uppsala University Guidelines on Animal Experimentation," UFV 2007/724).

Induction of ARDS in Pig

On the morning of the study day, pigs ($n = 9$; weight, 22–27 kg; Swedish landrace; mean age, 2 mo) were transported to Uppsala University and anesthetized initially by intramuscular administration of tiletamine-zolazepam. Swedish Landrace pigs were chosen because they are a common pig strain in Sweden. Their health is strictly controlled by the veterinarian authorities, but the strain is not genetically modified or the result of inbreeding. The selected age of the pigs was primarily due to logistics, as Swedish Landrace pigs are around 25–30 kg in weight at the age of 2 mo, which is large enough to be suitable for the spatial resolution of the clinical PET scanner used (3–5 mm) but small enough to handle and transport under anesthesia.

Anesthesia was maintained with intravenous ketamine, fentanyl, and midazolam as previously described (19). The experiment was conducted with the animal supine to mimic a patient's position on the intensive care bed. The animals were ventilated in volume-controlled mode, with an inspired oxygen fraction of 0.5, positive end-expiratory pressure of 5 cm H_2O , tidal volume of 6 mL/kg, and respiratory rate of 20/min. Minute volume was adjusted to maintain normocapnia during the experiment by titrating the respiratory frequency. Acute lung damage was induced in 5 pigs by injection of oleic acid (*cis*-9-octadecenoic acid, OA) as described previously in detail (20,21). Approximately a 0.1 mL/kg dose of OA-ethanol solution (1:1 by volume) was given. OA-ethanol solution was administered through a central venous catheter in repeated boluses of around 0.5 mL. Particular attention was paid to obtaining a complete dispersion of the OA into the infusate, avoiding large droplets. Administration of OA was suspended if O_2 saturation fell below 80%. Any fall in systemic arterial pressure during OA injection was countered using epinephrine, in boluses of 0.01 mg.

Of the 9 pigs in this study, 5 had induced lung inflammation and 4 were untreated. The lung function and severity of the ARDS were evaluated by repeatedly monitoring ventilator readouts (in particular lung compliance) and the partial pressure of arterial blood gases together with the oxygen saturation of arterial hemoglobin and the ratio between partial pressure of oxygen in arterial blood and inspired oxygen fraction. The measurements were conducted before the ARDS induction (baseline), directly after ARDS (T1), after the first injection of ^{11}C -GW457427 (T2), and after the administration of blocking compound (T3).

Whole-blood and plasma samples were also acquired at these time points, for analysis of standard peripheral markers at the hospital clinical chemistry core lab. Blood samples were also acquired for thromboelastography analysis of coagulation efficiency. The viscoelastic properties were analyzed using the TEG 6s platform (Haemonetics) (22), analyzing coagulation in citrated whole blood, generating the parameters reaction time (R-time), angle, maximal amplitude, and percentage lysis at 30 min.

^{11}C -GW457427 PET/CT Imaging of Pigs with ARDS

An attenuation CT scan (100 kV; 80–400 mA; noise index, 10; rotation, 1.27 cm [0.5 in]; full spiral; slice thickness, 3.75 mm; pitch, 0.98:1; reconstructed diameter, 50 mm) was initially attained using a digital 4-ring, 64-slice scanner with a 198-mm axial field of view. Afterward, ^{11}C -GW457427 (10 MBq/kg, corresponding to around 3–5 μg of substance) was injected, and a 60-min dynamic PET (Discovery MI; GE Healthcare) scan (4-mm spatial resolution; 30 frames: 12×10 s, 6×30 s, 5×2 min, 5×5 min, and 2×10 min) was simultaneously started over the lungs. A 30-min static scan over the spleen was immediately started after the dynamic study. Both scans were repeated after intravenous pretreatment with a 1 mg/kg dose of NE inhibitor GW311616 (a 1 mL/kg dose of a 1 mg/mL concentration of GW311616 in 0.9% NaCl), administered as a slow bolus 20 min before the tracer, approximately 2 h after the first injection. The dose of inhibitor (1 mg/kg) was based on the dosing used previously in mice (15) and was around 5,000 times higher than the tracer mass dose (in the range of 0.1–0.2 $\mu\text{g}/\text{kg}$).

The baseline scan was started approximately 2.5 h and the blocking scan 4.5 h after the OA treatment was initiated. Radioactivity in arterial plasma and whole blood was determined during the dynamic scans at 5, 30, and 60 min after injection with a γ -well counter. Lastly, a contrast-enhanced CT scan was acquired by late arterial (17 s) and venous phase contrast-enhanced CT (70 mL of iohexol [Omnipaque; GE Healthcare], 350 plus 40 mL of NaCl, 3.5 mL/s, bolus tracking on the descending aorta, threshold of 100 Hounsfield units [HUs]). The PET images were reconstructed using an iterative VPFX-S algorithm (GE Healthcare; ordered-subsets expectation maximization, time of

flight, resolution recovery: 3 iterations, 16 subsets, 3-mm postprocessing filter, and 256×256 matrix).

After the PET scans, each pig was euthanized by intravenous KCl under deep anesthesia. Biopsies were taken from the lung (right and left, apical and basal parts), spleen, and liver, both for snap freezing and for fixation in formalin for immunohistochemical staining.

PET/CT Pig Image Data Analysis

The volumes of interest were manually segmented over the lungs as previously described in detail (23), on SUV-corrected coronal projections using PMOD software (PMOD Technologies LLC). No further kinetic modeling of PET data was performed, because of the lack of assessment of arterial metabolites in the pigs. The HU values over the lungs were obtained from CT images using the same segmentations. In addition, bone and muscle volumes of interest were delineated on dynamic images, and time–activity curves were defined on all organs. The data were summarized and illustrated on Prism (GraphPad Software Inc.) and presented as median and interquartile range (IQR). Baseline, blocking, and control groups were tested for normality by Shapiro–Wilk testing, and since not all groups were normally distributed, the relationship among groups was assessed by Mann–Whitney *U* testing, where *P* values of less than 0.05 were considered significant.

Histology of Pig Biopsies

Postmortem formalin-fixed and paraffin-embedded biopsy samples of the lungs and spleen were acquired after the PET studies and processed into 6- μ m sections. Sections were immunostained for NE using an anti-NE antibody (ab68672, rabbit polyclonal; Abcam) in a concentration of 1 μ g/mL. Bound antibody was visualized by Dako EnVision and diaminobenzidine-based substrate (K4065, Agilent) according to the manufacturer's instructions. Sections were counterstained with hematoxylin, dehydrated, mounted, and analyzed by light microscopy (Leica). Pig spleen sections were used as positive controls, and negative controls had the primary antibody replaced by buffer. Consecutive sections from pig lung and spleen were also stained by sirius red and hematoxylin and eosin according to the routine at the local hospital pathology department (Uppsala University Hospital).

RESULTS

Visual ^{11}C -GW457427 Uptake in ARDS Pigs Compared with Control

NE infiltration was assessed using ^{11}C -GW457427 on pigs after lung damage, in comparison with healthy animals. PET/CT images (from 30 to 60 min after administration), as well as time–activity curves, displayed distinct uptake of ^{11}C -GW457427 in the lungs of pigs with induced ARDS (Figs. 1A and 1E), which was abolished in the second scan by pretreatment with an NE inhibitor (Figs. 1B and 1F). Conversely, lung uptake in control pigs was negligible (Figs. 1C, 1D, 1G, and 1H). Binding of ^{11}C -GW457427 in the lung was consistent with positive immunostaining for NE in the lung from pigs with induced ARDS (Supplemental Fig. 1; supplemental materials are available at <http://jnm.snmjournals.org>). Binding of ^{11}C -GW457427 in the bone marrow was visible in both ARDS and control pigs, and the binding could be blocked by pretreatment with an NE inhibitor (Figs. 1A–1H).

Lung Binding of ^{11}C -GW457427 and ARDS Severity Assessment

On the more damaged dorsal parts, uptake of ^{11}C -GW457427 was significantly higher at baseline (median SUV_{mean} , 1.91; IQR, 1.67–2.55) than after preblocking ($P < 0.05$ and $P = 0.04$, respectively; median SUV_{mean} , 0.60; IQR, 0.58–0.77) or in control pigs ($P < 0.05$ and $P = 0.03$, respectively; median SUV_{mean} , 1.04;

IQR, 0.66–1.47) at 60 min after injection (Fig. 2A). The uptake on the ventral parts was also significantly higher at baseline (median SUV_{mean} , 0.76; IQR, 0.63–0.98) than with blocking ($P < 0.05$ and $P = 0.04$, respectively; median SUV_{mean} , 0.32; IQR, 0.27–0.47) but not between ARDS and healthy control pigs ($P = 0.41$; median SUV_{mean} , 0.66; IQR, 0.47–0.89) (Fig. 2A). The successful induction of ARDS was confirmed by continuous monitoring of lung function (Fig. 2B; Supplemental Table 1). The ratio between partial pressure of oxygen in arterial blood and inspired oxygen fraction decreased with time, dropping below 100 mm Hg at T2, confirming the presence of severe ARDS according to the Berlin definition (1). Oxygen saturation dropped longitudinally, being significantly different between baseline and T3 ($P < 0.05$ and $P = 0.02$, respectively) (Fig. 2B). The damage was also evident in the quantitative analysis of the CT scans (Fig. 2C), with the most dorsal parts of the lungs exhibiting an average density of -63.52 HU, compared with the control dorsal (-495.52 HU), baseline ventral (-528.00 HU), and control ventral (-652.20 HU) parts. Common clinical chemistry laboratory markers were also measured in repeated blood samples from each pig, where changes in peripheral markers were inconclusive (Supplemental Fig. 2). Thromboelastography results under the experiment's duration showed no evidence of coagulopathy, with no significant differences between the ARDS group and control at baseline (Supplemental Fig. 3). Histologic staining for NE, hematoxylin and eosin, and sirius red in tissue biopsy samples taken after death further demonstrated severe inflammation in the lung of the ARDS group, as well as NE-positive cells in the spleen (Supplemental Fig. 1).

The plasma-to-whole-blood ratio for ^{11}C -GW457427 was examined in all pigs throughout the dynamic studies. The plasma-to-blood ratio was below 1 in both ARDS-induced pigs and control pigs after injection of tracer alone and decreased over time (Supplemental Fig. 4A). After preblocking with a pharmacologic dose of an NE inhibitor, the ratio was instead above 1 and was stable over the course of the PET scan in both ARDS and control pigs. This finding indicates more ^{11}C -GW457427 available in plasma for tissue distribution after pretreatment with the inhibitor.

Whole-Body Distribution and Binding of ^{11}C -GW457427

The biodistribution seen in the static whole-body scans from 60 to 90 min after ^{11}C -GW457427 injection supported the finding for the dynamic PET scan. Strong ^{11}C -GW457427 binding was seen on both maximum-intensity projections (Figs. 3A–3B) and coronal projections (Supplemental Figs. 4B–4C) in hemopoietic tissues with a known presence of neutrophils, including spleen, peripheral blood (here measured as heart ventricle), and bone marrow. Importantly, binding in these tissues was decreased after inhibition of NE (Figs. 3B–3C; Supplemental Fig. 4C). The presence of NE in pig spleen (median SUV_{mean} , 2.14; IQR, 1.19–2.36) was also verified by immunohistochemistry of paraffin-embedded biopsy samples (Supplemental Fig. 1). For example, uptake in the bone marrow was significantly blocked ($P < 0.05$ and $P = 0.04$, respectively; baseline median SUV_{mean} , 5.01; IQR, 4.48–5.49; block median SUV_{mean} , 1.57; IQR, 0.95–1.85) in the ARDS model, and binding to bone marrow in control animals (baseline median SUV_{mean} , 3.89; IQR, 2.49–4.23) was similar in magnitude to that in ARDS pigs. Muscle uptake remained unchanged at the background level (baseline median SUV_{mean} , 0.29; IQR, 0.27–0.34). Uptake in kidneys, liver, and muscle was unaffected, consistent with nonspecific uptake due to excretion or background blood contribution to the signal.

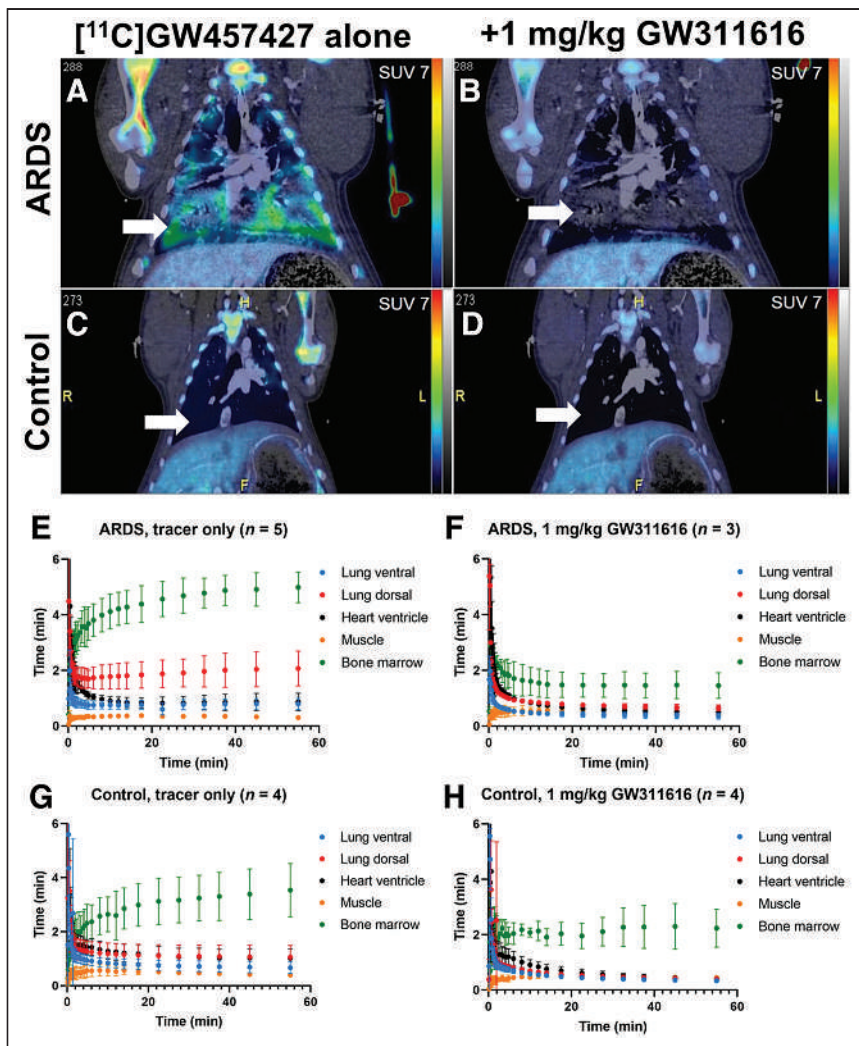


FIGURE 1. (A–D) Representative coronal PET/CT images of ARDS (A and B) and control (C and D) pigs after administration of ^{11}C -GW457427 alone or after pretreatment with NE inhibitor GW311616. Arrows indicate lungs, and SUV scale bar is from 0 to 7. PET images are summed frames from 30 to 60 min after tracer administration. (E–H) Averaged time–activity curves showing distribution and binding of ^{11}C -GW457427 in pigs with induced ARDS (E and F) and control pigs (G and H).

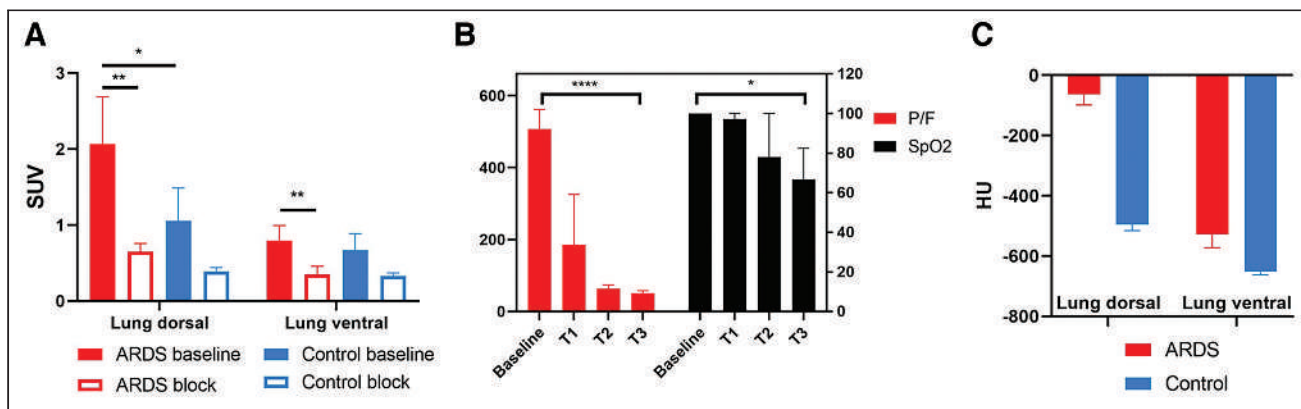


FIGURE 2. (A) Binding of ^{11}C -GW457427 in lung regions in ARDS and control pigs. (B) Lung function over time in ARDS group before ARDS induction (baseline), directly after ARDS induction (T1), after injection of ^{11}C -GW457427 (T2), and after administration of blocking (T3). (C) Damage in lungs in ARDS model was clearly visible on CT and was further confirmed by quantifying lung tissue density by CT.

DISCUSSION

In this study, we validated use of the novel radiotracer ^{11}C -GW457427 for targeting NE in a large-animal model of lung inflammation and ARDS. Neutrophils are the first cells migrating to the lungs during inflammation, and their activation changes the lung pathology by releasing inflammatory mediators and molecules, such as NE. We demonstrated that uptake of ^{11}C -GW457427 in an oleic acid–induced lung inflammation pig model was strong, specific, and reproducible.

In both healthy and ARDS-induced pigs, uptake of ^{11}C -GW457427 was heterogeneously distributed and higher in the more damaged dorsal (gravitationally dependent during the experiment) parts of the lungs. The spread of damage follows the distribution of lung circulation (24) and is supported by HU analysis and histology. In fact, both oleic acid and neutrophils are carried predominantly to the dependent, better-perfused areas of the lung, where it is possible to observe the multifocal and heterogeneous alterations typical of ARDS (25,26). Since the lung injury models also cause permeability changes and vessel leakage, the risk for non-specific uptake gathering in the lungs is always present. However, in this study we were able to block uptake of ^{11}C -GW457427, indicating the specificity of the binding and making us conclude that the dependent, dorsal areas of the lung are the real battleground where the inflammatory reaction takes place. The used tidal volumes, falling in the range of the so-called protective ventilation (27), make us exclude a role of ventilator-induced lung injury (28) in the present experiment.

In addition to the lungs, other organs of interest in this study consisted of hemopoietic

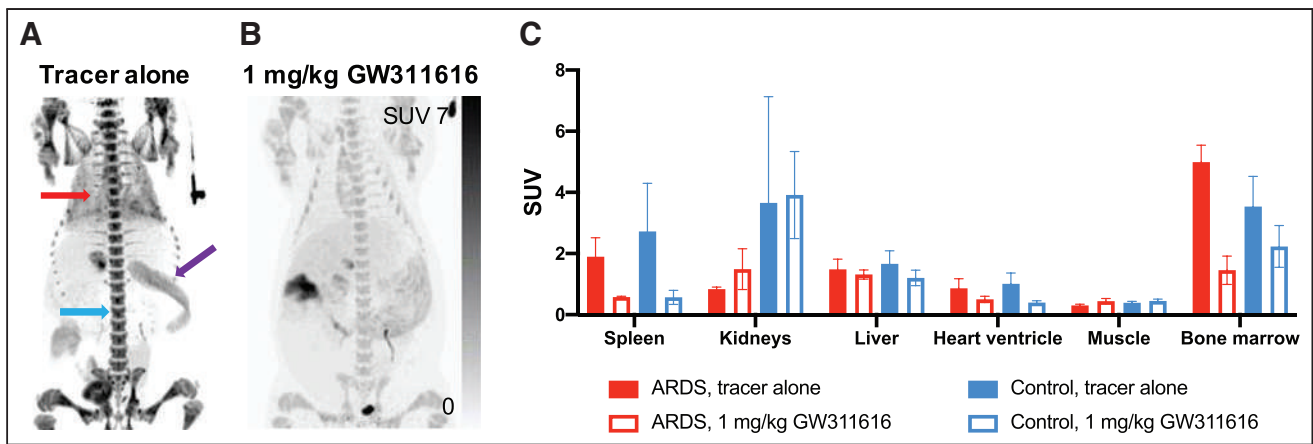


FIGURE 3. Representative images from whole-body scan acquired from 60 to 90 min after ^{11}C -GW457427 administration. (A and B) Maximum-intensity projections for baseline (A) and blocking (B) scans of same pig. Red arrow indicates lung, purple arrow indicates spleen, and blue arrow indicates bone marrow. (C) Bar graph showing binding of ^{11}C -GW457427 in tissues in both ARDS and control pigs during baseline scan or after blocking. Displaceable binding was found in spleen, heart ventricle, and bone marrow.

tissues such as bone marrow and spleen. Since neutrophils are produced in the bone marrow, we expected to see uptake there as well as in the spleen because of the previously described accumulation in the marginated intravascular pools. Uptake was similar in ARDS and control pigs and could be abolished, to a large extent, by pretreatment with the selective NE inhibitor GW311616.

Furthermore, we noticed binding in the blood pool, both by observing the signal in the heart ventricle (estimation of blood concentration) and by measuring the plasma and whole-blood content of radioactivity in blood samples. During the baseline scan, when only ^{11}C -GW457427 was administered, there was a plasma-to-whole-blood ratio lower than 1, which decreased with time. This means that more ^{11}C -GW457427 was present in the cellular components than was free in plasma. After preblocking with GW311616, the plasma-to-whole-blood ratio increased to above 1 and was stable during the PET examination, indicating more tracer available in the plasma component. This was apparent both in the ARDS and in the control groups. We hypothesize that these observations are due to binding of ^{11}C -GW457427 to intracellular NE in circulating neutrophils. The sum of data in hemopoietic tissue spleen, bone marrow, and peripheral blood thus indicates that ^{11}C -GW457427 can cross the cell membrane of both activated and quiescent neutrophils and bind the intracellular pool of NE stored in granules. Such an NE-specific binding in circulating neutrophils could also explain the weakly blockable signal observed also in the lung of control pigs, for example; this signal is at least partially due to neutrophils continually passing through the tissue via the blood.

Analysis of time-dependent uptake in tissues from the dynamic scan showed that uptake remained stable in the lungs in ARDS but increased slowly in bone marrow during the scan. NE in circulating quiescent neutrophils and in the bone marrow is stored in highly condensed granules and is less accessible for binding to ^{11}C -GW457427 than is NE that has been released extracellularly to the tissue after activation or degranulation of the neutrophils at the site of inflammation. The kinetics of binding of ^{11}C -GW457427 to extracellular, easily accessible NE will likely be significantly faster than the kinetics of binding of ^{11}C -GW457427 to stored intracellular NE. To bind intracellular NE, ^{11}C -GW457427 must diffuse through 2 membranes (both the cell and the granule membranes); in addition, accessibility to the active site of NE might

be reduced by packing or storage of the enzyme in the granules. This hypothesis would explain the difference in uptake kinetics (time-activity curve) of radioactivity in lung from that in bone marrow. Additionally, the observation of increased whole-blood-to-plasma ratio with time, in the baseline scans, also fits this hypothesis. Furthermore, we have preliminary data demonstrating that ^{11}C -GW457427 binds NE both in intact and in homogenized neutrophils (Puuvuori et al., unpublished data, March 1, 2022). Thus, ^{11}C -GW457427 will bind both to extracellular activated NE and to inactivated NE inside neutrophils at the site of inflammation. This is important information for correct interpretation of clinical ^{11}C -GW457427 PET images, as it will be challenging to separate extracellular NE from neutrophils at sites of inflammation. Further development to decrease the ability of ^{11}C -GW457427 to diffuse across the cell membrane, such as by increasing hydrophobicity, may lead to a PET tracer more specific for extracellular NE.

In lungs affected by ARDS and inflammation, uptake is rapid and steady—in accordance with a fast on-rate of binding due to the accessibility of NE. In the bone marrow, on the other hand, overall kinetics are slower and increase during the scan, as is in accordance with an apparent slower on-rate of binding driven by the lower intracellular accessibility of the target enzyme.

Previously, ^{18}F -FDG was proposed as a potential marker to assess neutrophilic recruitment in the lungs in inflammatory conditions. Even though neutrophils contribute to the increased uptake of ^{18}F -FDG in lung inflammation, ^{18}F -FDG is inherently nonspecific and will also accumulate in other activated immune cells with increased metabolism, such as macrophages, lymphocytes, and eosinophils. The structural cells in the lungs also increase glucose consumption throughout inflammation, contributing to the increased ^{18}F -FDG uptake. Therefore, ^{18}F -FDG imaging represents the combined inflammatory response during lung inflammation and cannot reliably be used to measure changes in specific immune cell populations, such as neutrophilic accumulation in response to, for example, antiinflammatory treatments (29,30). ^{11}C -GW457427 belongs to a class of selective NE inhibitors originally developed as immunomodulatory drugs. NE is highly specific for neutrophils, and ^{11}C -GW457427 is thus likely to bind to other types of immune cells, such as macrophages.

The performance of ^{11}C -GW457427 in a large-animal model of ARDS is in accordance with previous data on rodents (15). In that

study, strong lung binding of ^{11}C -GW457427 was seen in mice after lipopolysaccharide induction of lung inflammation, which could be blocked by coinjection of a 1 mg/kg dose of unlabeled GW457427. Elevated signal was also found in the spleen and bone marrow, although not to the same extent as in pigs. The pig data presented here are furthermore in line with the first-in-humans results of ^{11}C -GW457427, with strong binding in inflammatory lesions in the lungs of individuals with COVID-19 but not controls (16). Additionally, strong binding was seen in the spleen and bone marrow in both groups, as in pigs. The pig model has the added benefit of allowing intervention by preadministration of an NE inhibitor to demonstrate the specificity of ^{11}C -GW457427. Thus, the in vivo data presented here expand on previous preclinical studies and assist in interpretation of available and future clinical studies on ^{11}C -GW457427.

Limitations of the current study were related mainly to the experimental design and to the restrictions on logistics imposed by the pig model. The strength of the experimental design is that it allows direct comparison between binding of the PET tracer in lung before and after blocking with an NE inhibitor, in each individual. The drawback is instead that postmortem assessment is available only after administration of inhibitor. Furthermore, the complexity and cost of the model, and its combination with the PET scanning, mean that the number of repeated examinations in each group is relatively low ($n = 3$ –5). Finally, the pigs are relatively young and thus may not accurately recapitulate all aspects of the immune response in human adult ARDS.

In the future, ^{11}C -GW457427 might potentially be used to demonstrate the pathophysiology of damage distribution during ventilation-induced lung injury and patient self-induced lung injury (which is still lacking direct morphofunctional proofs) (31) or to monitor the response to neutrophil-targeting therapeutics during acute inflammation, such as COVID-19 treatments in drug development (32). In fact, the recently reported first-in-humans clinical study using ^{11}C -GW457427 did indeed demonstrate strong binding in the lung of individuals with active COVID-19, indicating that NE inhibitors may be a potential treatment strategy given the ample amount of NE in the inflammatory lesions. Neutrophils have also been found to accumulate in several types of tumors, making ^{11}C -GW457427 a potentially attractive noninvasive technique to further elucidate the role of neutrophils and NE in immune oncology (33,34).

CONCLUSION

^{11}C -GW457427 showed significantly higher uptake in a pig model of ARDS lung inflammation than in healthy pigs in vivo using PET. The specificity of ^{11}C -GW457427 binding to NE was verified by blocking studies with an NE inhibitor. ^{11}C -GW457427 is a promising and noninvasive tool for localizing, tracking, and quantifying neutrophil-mediated inflammation in clinical diagnostics and drug development.

DISCLOSURE

This study was supported by grants from the Science for Life Laboratory, the Swedish Research Council (Olof Eriksson, 2020-02312; Olle Korsgren, 2019-01415; and Gaetano Perchiazzi, 2018-02438), the Swedish Heart Lung Foundation (Gaetano Perchiazzi, 20200877 and 20200825), the Ernfors Family Foundation, the Nils Erik Holmstens Foundation for Diabetes Research, ExoDiab, the EFSD/Lilly European Diabetes Research Programme, JDRF (1-SRA-2020-973-S-B), Barndiabetesfonden, Diabetesfonden, and Diabetes Wellness (2409-PG) and by the Alvar Gullstrand research grant (Gaetano

Perchiazzi, ALF-938050). Hampus Romelin is currently an employee of Antaros Medical AB. Olle Korsgren is a cofounder of Antaros Tracer AB. Olof Eriksson is an employee of Antaros Medical AB and cofounder of Antaros Tracer AB. No other potential conflict of interest relevant to this article was reported.

ACKNOWLEDGMENTS

We thank the Hedenstierna Laboratory and the Preclinical PET-MRI Platform (PPP) Core Labs at Uppsala University, as well as the Clinical Pathology R&D Core Lab (FoU), the UAS PET Center, the UAS Blodcentralen, and the Clinical Chemistry Departments at Uppsala University Hospital.

KEY POINTS

QUESTION: Can ^{11}C -GW457427 be used to image NE in a large-animal model?

PERTINENT FINDINGS: The preclinical evaluation of ^{11}C -GW457427 uptake in a pig lung inflammation model was consistent, reproducible, and specific. Uptake in lung in pigs with ARDS was significantly increased compared with healthy control animals and could be abolished by preblocking.

IMPLICATIONS FOR PATIENT CARE: ^{11}C -GW457427 is a novel PET tracer for in vivo imaging of NE—a crucial part of the innate immune system—in inflammatory diseases.

REFERENCES

1. Ranieri VM, Rubenfeld GD, Thompson BT, et al.; ARDS Definition Task Force. Acute respiratory distress syndrome: the Berlin definition. *JAMA*. 2012;307:2526–2533.
2. Matthay MA, Zemans RL, Zimmerman GA, et al. Acute respiratory distress syndrome. *Nat Rev Dis Primers*. 2019;5:18.
3. Bellani G, Laffey JG, Pham T, et al; LUNG SAFE Investigators; ESICM Trials Group. Epidemiology, patterns of care, and mortality for patients with acute respiratory distress syndrome in intensive care units in 50 countries. *JAMA*. 2016;315:788–800.
4. Matthay MA, Ware LB, Zimmerman GA. The acute respiratory distress syndrome. *J Clin Invest*. 2012;122:2731–2740.
5. Plötz FB, Slutsky AS, van Vught AJ, Heijnen CJ. Ventilator-induced lung injury and multiple system organ failure: a critical review of facts and hypotheses. *Intensive Care Med*. 2004;30:1865–1872.
6. Silvestre-Roig C, Hidalgo A, Soehnlein O. Neutrophil heterogeneity: implications for homeostasis and pathogenesis. *Blood*. 2016;127:2173–2181.
7. De Filippo K, Rankin SM. The secretive life of neutrophils revealed by intravital microscopy. *Front Cell Dev Biol*. 2020;8:603230.
8. Summers C, Rankin SM, Condliffe AM, Singh N, Peters AM, Chilvers ER. Neutrophil kinetics in health and disease. *Trends Immunol*. 2010;31:318–324.
9. Gramegna A, Amati F, Terranova L, et al. Neutrophil elastase in bronchiectasis. *Respir Res*. 2017;18:211.
10. Williams AE, Chambers RC. The mercurial nature of neutrophils: still an enigma in ARDS? *Am J Physiol Lung Cell Mol Physiol*. 2014;306:L217–L230.
11. Klopff J, Brostjan C, Eilenberg W, Neumayer C. Neutrophil extracellular traps and their implications in cardiovascular and inflammatory disease. *Int J Mol Sci*. 2021;22:1–17.
12. Iwata K, Doi A, Ohji G, et al. Effect of neutrophil elastase inhibitor (sivelestat sodium) in the treatment of acute lung injury (ALI) and acute respiratory distress syndrome (ARDS): a systematic review and meta-analysis. *Intern Med*. 2010;49:2423–2432.
13. Fisher DT, Muhitch JB, Kim M, et al. Intraoperative intravital microscopy permits the study of human tumour vessels. *Nat Commun*. 2016;7:10684.
14. Ruscowski M, Qu T, Pullman J, et al. Inflammation and infection imaging with a ^{99m}Tc -neutrophil elastase inhibitor in monkeys. *J Nucl Med*. 2000;41:363–374.
15. Estrada S, Elgland M, Selvaraju RK, et al. Preclinical evaluation of [^{11}C]GW457427 as a tracer for neutrophil elastase. *Nucl Med Biol*. 2022;106–107:62–71.

16. Antoni G, Lubberink M, Sörensen J, et al. In vivo visualization and quantification of neutrophil elastase in lungs of COVID-19 patients: a first-in-human positron emission tomography study with ¹¹C-GW457427. *J Nucl Med*. June 9, 2022 [Epub ahead of print].
17. Bréa D, Meurens F, Dubois AV, et al. The pig as a model for investigating the role of neutrophil serine proteases in human inflammatory lung diseases. *Biochem J*. 2012;447:363–370.
18. Monteiro A, Smith RL. Bronchial tree architecture in mammals of diverse body mass. *Int J Morphol*. 2014;32:312–318.
19. Perchiuzzi G, Rylander C, Derosa S, et al. Regional distribution of lung compliance by image analysis of computed tomograms. *Respir Physiol Neurobiol*. 2014;201:60–70.
20. Matute-Bello G, Frevert CW, Martin TR. Animal model of acute lung injury. *Am J Physiol Lung Cell Mol Physiol*. 2008;295:L379–L399.
21. Perchiuzzi G, Rylander C, Pellegrini M, Larsson A, Hedenstierna G. Monitoring of total positive end-expiratory pressure during mechanical ventilation by artificial neural networks. *J Clin Monit Comput*. 2017;31:551–559.
22. Dias JD, Haney EI, Mathew BA, Lopez-Espina CG, Orr AW, Popovsky MA. New-generation thromboelastography: comprehensive evaluation of citrated and heparinized blood sample storage effect on clot-forming variables. *Arch Pathol Lab Med*. 2017;141:569–577.
23. Puuvuori E, Liggieri F, Velikyan I, et al. PET-CT imaging of pulmonary inflammation using [⁶⁸Ga]Ga-DOTA-TATE. *EJNMMI Res*. 2022;12:19.
24. Glenny RW, Robertson HT. Spatial distribution of ventilation and perfusion: mechanisms and regulation. *Compr Physiol*. 2011;1:375–395.
25. Gonçalves-de-Albuquerque CF, Silva AR, Burth P, et al. Acute respiratory distress syndrome: role of oleic acid-triggered lung injury and inflammation. *Mediators Inflamm*. 2015;2015:260465.
26. Kamuf J, Garcia-Bardon A, Ziebart A, et al. Oleic acid-injection in pigs as a model for acute respiratory distress syndrome. *J Vis Exp*. 2018;2018:1–8.
27. Brower RG, Matthay MA, Morris A, Schoenfeld D, Thompson BT, Wheeler A; Acute Respiratory Distress Syndrome Network. Ventilation with lower tidal volumes as compared with traditional tidal volumes for acute lung injury and the acute respiratory distress syndrome. *N Engl J Med*. 2000;342:1301–1308.
28. Slutsky AS, Ranieri VM. Ventilator-induced lung injury. *N Engl J Med*. 2013;369:2126–2136.
29. Aulakh GK, Kaur M, Brown V, Ekanayake S, Khan B, Fonge H. Quantification of regional murine ozone-induced lung inflammation using [¹⁸F]F-FDG microPET/CT imaging. *Sci Rep*. 2020;10:15699.
30. Scherer PM, Chen DL. Imaging pulmonary inflammation. *J Nucl Med*. 2016;57:1764–1770.
31. Brochard L, Slutsky A, Pesenti A. Mechanical ventilation to minimize progression of lung injury in acute respiratory failure. *Am J Respir Crit Care Med*. 2017;195:438–442.
32. Reusch N, De Domenico E, Bonaguro L, et al. Neutrophils in COVID-19. *Front Immunol*. 2021;12:652470.
33. Uribe-Querol E, Rosales C. Neutrophils in cancer: two sides of the same coin. *J Immunol Res*. 2015;2015:983698.
34. Powell DR, Huttenlocher A. Neutrophils in the tumor microenvironment. *Trends Immunol*. 2016;37:41–52.

⁶⁸Ga-DOTA PET for Diagnosis of Spinal Cerebrospinal Fluid Leaks

Petros Evangelou¹, Mohamed Aymen Omrane², Johannes Thurow², Michael Mix², Christian Fung¹, Niklas Lützen³, Ganna Blazhenets², Horst Urbach³, Jürgen Beck*¹, and Philipp T. Meyer*²

¹Department of Neurosurgery, Medical Center, Faculty of Medicine, University of Freiburg, Freiburg, Germany; ²Department of Nuclear Medicine, Medical Center, Faculty of Medicine, University of Freiburg, Freiburg, Germany; and ³Department of Neuroradiology, Medical Center, Faculty of Medicine, University of Freiburg, Freiburg, Germany

Spontaneous intracranial hypotension due to spinal cerebrospinal fluid (CSF) leakage causes substantial disease burden. In many patients, the course is protracted and refractory to conservative treatment, requiring targeted therapy. We propose PET of the CSF space with ⁶⁸Ga-DOTA as a state-of-the-art approach to radionuclide cisternography (RC) and validate its diagnostic value. **Methods:** This study is a retrospective analysis of patients with suspected intracranial hypotension due to spinal CSF leaks and who underwent whole-body PET/CT at 1, 3, and 5 h after intrathecal lumbar injection of ⁶⁸Ga-DOTA. Two independent raters unaware of the clinical data analyzed all scans for direct and indirect RC signs of CSF leakage. Volume-of-interest analysis was performed to assess the biologic half-life of the tracer in the CSF space and the ratio of decay-corrected activity in the CSF space at 5 and 3 h (simplified marker of tracer clearance). Comprehensive stepwise neuroradiologic work-up served as a reference; additional validation was provided by surgical findings and follow-up. **Results:** Of 40 consecutive patients, 39 patients with a working diagnosis of intracranial hypotension due to a spinal CSF leak (spontaneous, $n = 31$; postintervention, $n = 8$) could be analyzed. A spinal CSF leak was verified by the neuroradiologic reference method in 18 of 39 patients. As the only direct and indirect diagnostic signs, extrathecal tracer accumulation at the cervicothoracic junction (67% sensitivity and 90% specificity) and lack of activity over the cerebral convexities (5 h; 94% sensitivity and 67% specificity) revealed a high diagnostic value for spinal CSF leaks. Their combination provided little improvement (71% sensitivity and 95% specificity). Additional quantitative analyses yielded no benefit (94% sensitivity and 53% specificity for biological half-life; 94% sensitivity and 58% specificity for the ratio of total radioactivity within the CSF space at 5 and 3 h). The location of direct signs (extrathecal tracer accumulation) did not correlate with verified sites of spinal CSF leakage. **Conclusion:** We propose CSF PET with ⁶⁸Ga-DOTA as a novel, fast, and convenient approach to RC for verification but not localization of spinal CSF leaks with high sensitivity and specificity. CSF PET may fulfill an important gatekeeper function for stratifying patients toward escalation (ruling in) or deescalation (ruling out) of diagnostic and therapeutic measures. Further prospective studies are needed to validate the present results and determine the potential of the methods to reduce the burden to patients.

Key Words: radionuclide cisternography; spontaneous intracranial hypotension; PET

J Nucl Med 2023; 64:430–436

DOI: 10.2967/jnumed.122.264059

Spontaneous intracranial hypotension (SIH) is an increasingly recognized condition caused by spinal leakage of cerebrospinal fluid (CSF) (1). The clinical situation can be very diverse, especially in individuals with chronic disease, making the diagnosis of SIH difficult (2). Despite its name, it has been reported that only 34%–50% of patients show a low opening pressure on lumbar puncture (2,3). Postural headache and either the presence of stereotypical imaging signs or an opening pressure of <6 cm of H₂O is required for the diagnosis (4). Despite conservative therapy (bed rest, caffeine) and epidural blood patches (EBP), symptoms persist in 10%–30% of patients. This situation warrants verification and localization of leakage to allow for targeted treatment (2,5). Typical diagnostic algorithms propose a combination of different imaging modalities, including often repetitive digital subtraction myelography (1), which misses a substantial fraction of leaks (45%–74%) (3). Considering the invasive nature of and possible extensive radiation exposure with these modalities (6), it is desirable to select patients with a high likelihood for a leak before escalating the diagnostic work-up.

The unsurpassed measurement sensitivity of radionuclide imaging techniques and the ability to repeat imaging for hours without causing additional radiation burden underscore the potential of radionuclide cisternography (RC) in this setting. After seminal reports (e.g., Dichiro (7)) and the introduction of ¹¹¹In-labeled diethylenetriaminepentaacetic acid (DTPA) (8) and ^{99m}Tc-DTPA (9), RC gained rapid acceptance in the field, being considered the diagnostic gold standard for the proof and localization of CSF leaks over the years (10–13). Common criticisms of RC, however, include poor image quality and spatial resolution, low sensitivity and specificity, lack of standardization, and long examination (up to 48 h). Despite methodologic improvements, such as cross-sectional imaging with SPECT (14) and hybrid SPECT/CT (15) and quantitative analysis (10,13,16,17), RC was removed from the International Classification of Headache Disorders, third edition, as a diagnostic imaging tool (4). To date, RC is still commonly performed as planar scintigraphic imaging without taking advantage of state-of-the-art imaging, such as PET/CT, which offers improved sensitivity, spatial resolution, and quantification. In fact, CSF PET (e.g., using ⁶⁸Ga-labeled ethylenediaminetetraacetic acid) was proposed 40 y ago (14) but has only rarely been applied, in single cases (18).

Received Feb. 23, 2022; revision accepted Aug. 13, 2022.
For correspondence or reprints, contact Philipp T. Meyer (philipp.meyer@uniklinik-freiburg.de).
*Contributed equally to this work.
Published online Aug. 18, 2022.
COPYRIGHT © 2023 by the Society of Nuclear Medicine and Molecular Imaging.

Against this background, in the present study we propose a convenient CSF PET methodology and validate its diagnostic value for the presence and localization of spinal CSF leakage.

MATERIALS AND METHODS

Patients

The University of Freiburg institutional review board approved this study, and all subjects gave written informed consent to the examination and the retrospective analysis. Forty consecutive patients referred for CSF PET because of suspected intracranial hypotension due to a spinal CSF leak between May 2020 and March 2021 were eligible, and 39 could be included (see the Results section).

Reference Standard

Patients underwent a standard work-up, including often repeated cranial and spinal MRI, gadolinium MR myelography, and digital subtraction myelography/CT myelography (supplemental materials, available at <http://jnm.snmjournals.org>).

Demonstration of a spinal CSF leak by comprehensive neuroradiologic imaging defined the positivity of the target condition (spinal CSF leak) and its localization. This process involved a stepwise approach aimed at localizing or excluding a spinal CSF leak by dynamic digital subtraction myelography followed by dynamic CT myelography in the prone or lateral decubitus position (1). The result served as a reference for the definition of true-positive, true-negative, false-positive, and false-negative results of various PET outcome measures for the presence or absence of a spinal CSF leak (index test). In patients with verified CSF leaks, localizations provided by the reference method and PET (direct signs) were directly compared. Surgical findings (genuine gold standard, applicable only in those with a positive target condition) and clinical follow-up data were also assessed.

PET Acquisition

PET/CT scans (with low-dose or ultra-low-dose CT) covering the entire CSF space were acquired on a fully digital PET/CT system (Verios; Philips Healthcare) at 1, 3, and 5 h after lumbar intrathecal injection of ^{68}Ga -DOTA (45–50 MBq in 0.5–1.0 mL of saline solution). The preparation of ^{68}Ga -DOTA and the acquisition protocol are described in detail in the supplemental materials.

Visual PET Readings

Two experienced nuclear medicine physicians, unaware of all other clinical and diagnostic data as well as the results of quantitative PET analyses, evaluated all ^{68}Ga -DOTA PET scans independently. Using the 1-, 3-, and 5-h PET/CT datasets, visual readings of direct and indirect RC signs were done and a summary rating was assigned using a 3-step scale (0, none; 1, questionable/mild signal; 2, strong signal) (the supplemental materials provide details).

Direct signs of a spinal CSF leak included uni- or bilateral extrathecal tracer accumulation, witnessed at least at 1 time point and localized according to 28 spinal segments. Extrathecal tracer accumulations in multiple consecutive segments were rated in combination, assuming that they stemmed from the same process.

Indirect signs of a spinal CSF leak included radiotracer accumulation in the bladder (1 h) and radiotracer accumulation in the basal cisterna and over the cerebral convexities. In addition, iatrogenic tracer extravasation at the injection site was assessed.

Finally, a 3-step summary rating was independently recorded by each rater for each individual case (0, 1, and 2 for no, questionable/possible, and probable CSF leakage, respectively). After discussion of discrepant cases, the raters reached a consensus.

Quantitative PET Analysis

The time course of total radioactivity within the CSF space was characterized in terms of biologic half-life ($t_{1/2,\text{biol}}$) and, as a simplified approach, using the ratio of total radioactivity within the CSF space at 5 and 3 h (R5/3; decay-corrected data). Volume-of-interest analyses were performed after coregistration of all 3 PET/CT scans in each patient (supplemental materials).

Statistical analyses are provided in the supplemental materials.

RESULTS

Patient Characteristics

Forty consecutive patients (age, 46.2 ± 14.1 y, 32 women and 8 men) were eligible. Thirty-two patients were diagnosed with SIH (4) (in 1 patient, spinal puncture failed, leaving 31 patients), 4 had a possible persistent/relapsing CSF leak after previous open surgical treatment for SIH, and 4 had questionable SIH; in the latter, a former lumbar puncture or peridural anesthesia was assumed by the referring doctor to be causal. For 37 of 39 included patients (95%), data from a follow-up at 3.6 ± 2.5 mo were available. CSF PET was well tolerated by all patients. There were no side effects, except for those commonly associated with lumbar puncture.

In 18 of 39 patients (46%), stepwise neuroradiologic imaging localized a spinal CSF leak at C7–T3 ($n = 6$) or T7–L1 ($n = 12$)

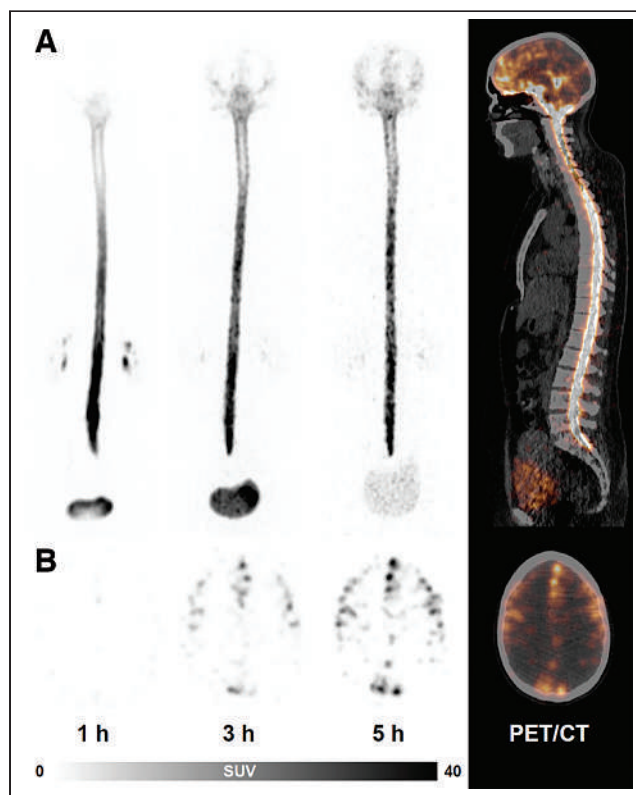


FIGURE 1. Normal CSF PET in patient without verified spinal CSF leak. (A) Maximum-intensity projections of PET images (posterior view; scaled for optimal display) at 1, 3, and 5 h after injection of ^{68}Ga -DOTA and sagittal PET/CT fusion image (at 5 h; far right). (B) Transaxial PET slices at level of centrum semiovale at 1, 3, and 5 h and PET/CT fusion image (far right). Note time-dependent cephalad ascent of tracer with normal accumulation of activity over cerebral hemispheres. Patient (no. 38) was treated with epidural blood patch, without response.

(Suppl. Fig. 1) (supplemental materials are available at <http://jnm.snmjournals.org>). CSF leaks were only verified in patients with SIH but without previous surgery or alternative causes (detection rate, 18/31 [58%]). A ventral dural tear was found in 12 patients (coinciding with a microspur on surgery in 9 patients), whereas a lateral leak and a direct CSF venous fistula were diagnosed in 3 patients each. Except for 1 patient, who refused surgery and was successfully treated with untargeted EBP, all patients with proven leaks underwent surgery; symptom improvement ($n = 10$) or resolution ($n = 6$) was seen in 16 of 17 patients (94%). In the remaining patient, a 60-y-old man with long-standing symptoms, cerebral MRI findings of SIH markedly improved while symptoms remained unchanged.

Of the 21 patients in whom no leak could be identified, 15 were treated with EBP. Follow-up data, which were available for 14 of these 15 patients (27 EBP in total), showed an improvement or resolution of symptoms in only 2 patients each (response rate, 4/14 [29%]). The remaining patients either refused treatment or received alternative diagnoses and treatments. Taken together, the clinical outcomes strongly support the validity of the neuroradiologic reference standard.

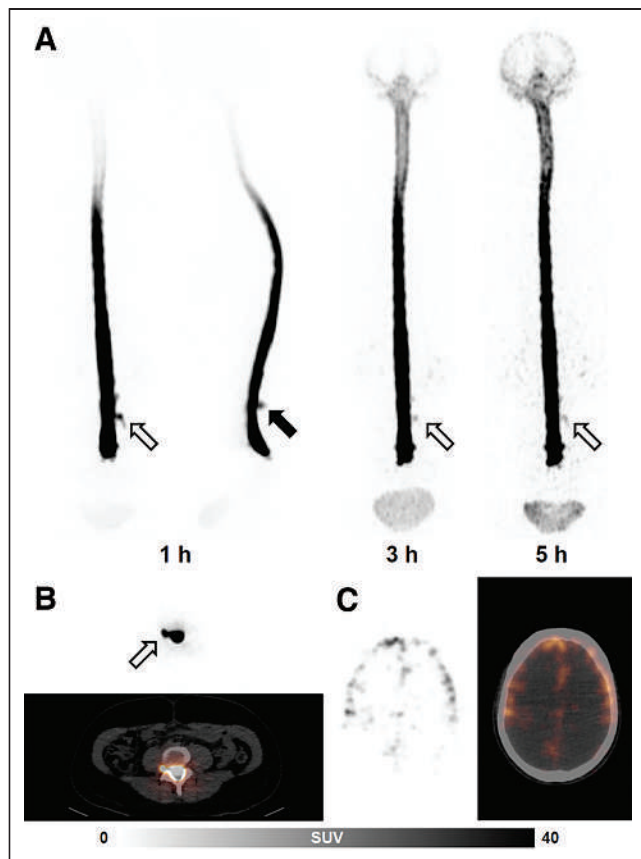


FIGURE 2. CSF PET with iatrogenic extrathecal tracer accumulation in patient without verified spinal CSF leak. (A) Maximum-intensity projections of PET images at 1, 3, and 5 h (posterior view and, at 1 h, lateral view as well; scaled for optimal display) after injection of ^{68}Ga -DOTA. (B and C) Transaxial PET and PET/CT fusion images at levels of L3-L4 (1 h; B) and centrum semiovale (5 h; C). Although strong iatrogenic egression of tracer that was observed in trajectory of injection needle (filled arrow) and to right side at levels of L3-L4 (open arrows) vanished with time, cephalad ascent of tracer was normal, with tracer accumulation over cerebral convexities. Patient (no. 15) was treated with epidural blood patch, without response.

Visual PET Readings

Visual readings (examples are shown in Figs. 1–3 and Suppl. Fig. 2) of direct signs of a spinal CSF leak were highly consistent between both raters (agreement in 86% of ratings; supplemental materials). Supplemental Figure 1 summarizes the sites of extrathecal tracer accumulation. The findings clustered at the craniocervical and cervicothoracic junctions (Fig. 3), over the lower thoracic spine, and in the lumbosacral region (Suppl. Fig. 1). To further analyze the data, we sorted all sites of extrathecal tracer accumulation in these regions (selecting the most prominent if >1 site) (Table 1). Extrathecal tracer accumulation at the craniocervical and cervicothoracic junctions showed no significant dependence on scan time, whereas that in the lower thoracic spine and lumbosacral region decreased significantly with time (supplemental materials).

Mean ratings (across raters and scans) of direct signs at the lower thoracic spine and in the lumbosacral region did not differ between patients without and patients with verified spinal CSF leaks, whereas in the cervicothoracic junction there was a highly significant difference between the groups. This finding allowed for an accurate diagnostic separation of groups (receiver operating

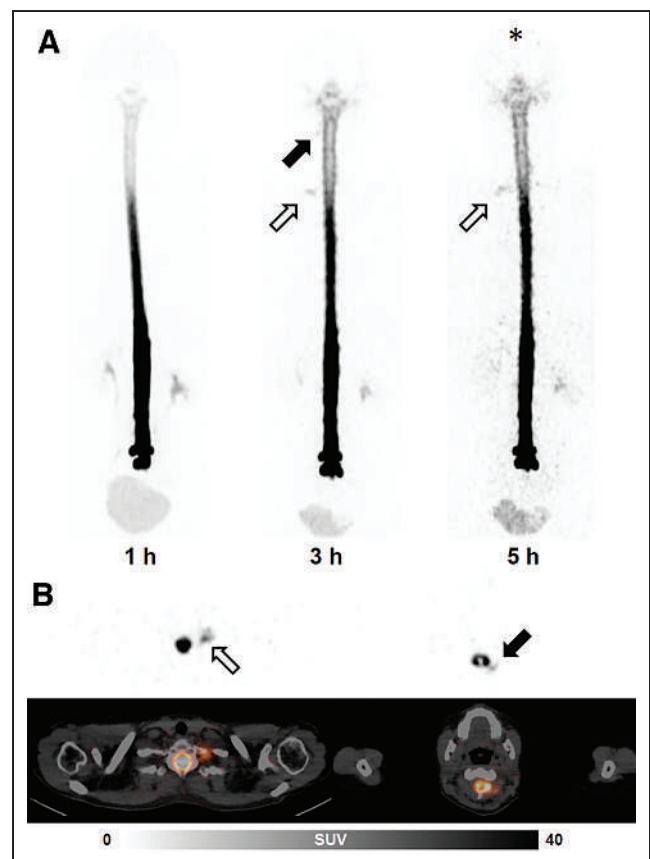


FIGURE 3. Pathologic CSF PET in patient with verified spinal CSF leak. (A) Maximum-intensity projections of PET images at 1, 3, and 5 h (posterior view; scaled for optimal display) after injection of ^{68}Ga -DOTA. (B) Transaxial PET and PET/CT fusion images at levels of C7-T1 and C2 (3 h), respectively. Compatible with surgically verified, lower thoracic lateral CSF leak, there were moderate and mild extrathecal tracer accumulations at level of cervicothoracic junction (open arrows) and in upper cervical region (filled arrows), respectively. There was a lack of tracer accumulation over cerebral convexities (asterisk). Patient (no. 27) was treated by surgery, with improvement of symptoms.

TABLE 1
Results of Visual and Quantitative PET Analyses

Parameter*	Patients without CSF leak (n = 21) [†]	Patients with CSF leak (n = 18) [†]	P [‡]	ROC AUC [§]
Bladder activity at 1 h	1.21 ± 0.68	1.42 ± 0.55	NS	
Basal cisterna at:				
1 h	1.31 ± 0.64	1.53 ± 0.62	NS	
3 h	1.83 ± 0.37	1.74 ± 0.56	NS	
5 h	1.81 ± 0.37	1.71 ± 0.56	NS	
Cerebral convexities at:				
1 h	0.02 ± 0.11	0.03 ± 0.12	NS	
3 h	0.71 ± 0.49	0.50 ± 0.59	NS	
5 h	1.43 ± 0.83	0.50 ± 0.56	0.0016	0.79
Craniocervical (SO–C1)	0.00 ± 0.00	0.19 ± 0.47	(0.055)	(0.58)
Cervicothoracic (C6–T2)	0.06 ± 0.20	0.68 ± 0.58	0.0001	0.81
Lower thoracic (T7–T12)	0.32 ± 0.63	0.44 ± 0.64	NS	
Lumbosacral (L2–S2)	0.75 ± 0.74	0.79 ± 0.81	NS	
Consensus summary reading	0.43 ± 0.68	1.39 ± 0.78	0.0006	0.80
PET quantification				
t _{1/2,biol} (h)	9.47 ± 7.03	4.54 ± 2.45	0.0043	0.70
R5/3	0.79 ± 0.16	0.63 ± 0.18	0.0023	0.78

*Anatomic localizations refer to sites of tracer accumulation (spinal segments). SO = suboccipital.

[†]Except for PET quantification (continuous data), all data represent 3-step ordinal scales given as mean values ± SDs across interpreters and times (if not separated) or consensus of raters.

[‡]For statistical comparisons of patients without and patients with spinal CSF leak. *P* values in parentheses indicate trend effects. NS = not significant.

[§]Reported only for significant and trend (in parentheses) effects.

characteristic [ROC] area under the curve [AUC], 0.81; 67% sensitivity; 90% specificity; cutoff, 0.33; i.e., mild extrathecal tracer accumulation in at least 1 scan) (Table 1). Extrathecal tracer accumulation at the craniocervical junction was rarely observed (3/39 patients) and occurred only in patients with verified spinal CSF leaks (*P* = 0.055). There was no obvious association between the location of verified spinal CSF leaks and extrathecal tracer accumulation on PET. In fact, sites of extrathecal tracer accumulation usually extended over multiple segments and overlapped the site of a verified leak in only 3 of 18 patients (locations differed by only 1 segment in 3 patients and by >1 segment in 12 patients) (Suppl. Fig. 1).

Ratings of indirect signs of CSF leakage and tracer extravasation at the injection site were also highly consistent between observers (agreement on 80%–85% of ratings; supplemental materials). Ratings for the basal cisterna and tracer accumulation over the cerebral hemispheres showed a significant increase with time and dependence on the presence or absence of a spinal CSF leak, whereas tracer extravasation at the injection site decreased significantly with time (supplemental materials).

The only indirect sign that showed a highly significant difference between patients without and patients with verified spinal CSF leaks was a lack of tracer accumulation over the cerebral hemispheres on the 5-h scan. This finding allowed for an accurate diagnostic group separation (ROC AUC, 0.79; 94% sensitivity; 67%

specificity; cutoff, >1.0; i.e., more than only mild tracer accumulation over the cerebral hemispheres at 5 h) (Table 1).

Considering all direct and indirect signs, both raters also filed a summary score that was highly consistent between raters (agreement in 77% of cases; Supplement). The consensus rating of both raters yielded a highly significant group difference between patients without and patients with verified spinal CSF leaks (0.43 ± 0.68 vs. 1.39 ± 0.78; *P* = 0.0006; ROC AUC, 0.80; 83% sensitivity; 67% specificity; cutoff, 1) (Table 1).

Similar results were obtained when analyses were restricted to patients with SIH but without previous surgery or alternative causes (Suppl. Table 1).

Quantitative PET Analysis

Quantification was omitted in 2 patients because of partial epidural tracer injection and out-of-field-of-view artifacts (both scans were still read visually). As expected, t_{1/2,biol} and R5/3 were highly correlated (rho, 0.94; *P* < 0.0001). t_{1/2,biol} and R5/3 showed no significant association with age, sex, body weight, or body height, either in the entire group or in the patients with and the patients without verified spinal CSF leaks. However, t_{1/2,biol} and R5/3 were significantly lower in patients with than in patients without spinal CSF leaks (Table 1). This finding allowed for a diagnostic group separation (for t_{1/2,biol}: ROC AUC, 0.70; 94% sensitivity; 53% specificity; cutoff, <7.9 h; and for R5/3: ROC AUC, 0.78; 94% sensitivity; 58% specificity; cutoff, <0.82).

Combination of Qualitative and Quantitative Analyses

We used stepwise forward regression, including aforementioned significant parameters with the exception of $t_{1/2, \text{biol}}$ (highly correlated to R5/3), to explore which combined parameters best predicted a spinal CSF leak. A minimum Akaike information criterion (36.3) was reached by retaining extrathecal tracer accumulation at the cervicothoracic junction and a lack of tracer accumulation over the cerebral hemispheres (for the resulting multinomial logistic regression model: ROC AUC, 0.88; 71% sensitivity; 95% specificity).

DISCUSSION

We propose CSF PET with ^{68}Ga -DOTA as a novel, state-of-the-art approach to RC that provides several possible advantages over conventional RC. By using a very rigorous diagnostic reference standard in an exceptionally large cohort of patients, we were able not only to validate the diagnostic accuracy of CSF PET for verifying—although not localizing—spinal CSF leakage but also to unravel several misconceptions and controversies concerning RC.

PET provides better spatial resolution (2–3 times higher) and sensitivity (2–3 magnitudes higher) than scintigraphy and SPECT (19), allowing the detection and quantification of the slow cephalad ascent of CSF even with short-lived radionuclides. The entire examination is completed within 5–6 h; in contrast, conventional RC often takes up to 48 h. In addition, individual PET scans are acquired within 20–30 min—thus comparing favorably with whole-body SPECT/CT examinations, which may take up to 1 h. The estimated dose for CSF PET with ^{68}Ga -DOTA is approximately 1.24 mGy/MBq for the spinal cord (highest organ dose), and the effective dose equivalent is 0.16 mSv/MBq; these doses are slightly higher than those for ^{111}In -DTPA (0.95 mGy/MBq and 0.14 mSv/MBq, respectively, assuming the same biokinetic model for both tracers [normal $t_{1/2, \text{biol}}$] and accounting for differences in energy transfer and physical half-lives) (20). Thus, for a typical injected dose of 37 MBq of ^{68}Ga -DOTA, the estimated effective dose is 5.9 mSv. CT scans add about 3–4 mSv, which may be further reduced with dose-sparing techniques. The fast decay of ^{68}Ga -DOTA (as opposed to ^{111}In -DTPA) also implies that there is no relevant radiation exposure to medical personnel if patients undergo spinal surgery shortly after diagnostics (often on the following day at our institution). The synthesis and quality control of ^{68}Ga -DOTA are also very simple and readily available at most larger centers (at least in Europe), rendering it a convenient alternative to ^{111}In -DTPA. Finally, the high image quality of PET/CT scans renders CSF PET with ^{68}Ga -DOTA much more appealing and convincing than conventional RC—factors that, in our experience, strongly improve the acceptance of RC in clinical routines.

The average $t_{1/2, \text{biol}}$ for patients without verified leakage (9.5 ± 7.0 h) is somewhat lower than but still in line with that in the literature (13.5 ± 4.5 h) (10), considering that this group possibly includes patients with missed or iatrogenic leaks. We propose R5/3 as a simpler estimate of tracer clearance, circumventing the need for a 1-h scan and exponential fitting, with slightly higher diagnostic performance. However, quantitative analyses provided no additional benefit over visual readings, in line with findings for conventional RC (21). Still, we routinely perform quantification as a simple adjunct to visual reading, an approach that may be particularly valuable for follow-up assessments (10).

A particular strength of the present study is the use of a rigorous neuroradiologic reference standard that was additionally validated by surgical findings and outcomes. To the best of our knowledge, no previous study on RC included more patients with appropriate

verification (e.g., in the seminal work by Schievink et al. (22), correlation of RC with CT myelography and surgery was available for only 8/11 and 4/11 patients, respectively), with earlier studies often using response to EBP as a reference (10,16,23,24). However, given the uncertainty about the efficacy and mechanism of action of EBP (e.g., success sometimes only after several attempts, targeted vs. nontargeted EBP, often only short-term efficacy, possible placebo effects) (25) as well as the current, improved understanding of SIH pathophysiology (see later text) (3,26–28), we are convinced that the reference standard in current use is the most appropriate. We were able to verify a spinal CSF leak in 18 of 31 patients (58%) with SIH but without previous surgery or alternative causes. Although a few spinal leaks may have been missed (see later text), this fraction is in line with those in the literature (3) and underscores the uncertainty associated with the clinical diagnosis of SIH, which does not require verification of a leak (4).

We made several important observations. First, the site of extrathecal tracer accumulation on CSF PET was not related to the actual location of leakage—something that has not been systematically shown before. We do not believe that this finding is related to the tracer used (e.g., later detection of actual sites of leakage with longer-lived isotopes) but assume that it represents a general shortcoming of RC. In fact, patterns observed in the present study and described in the literature are very similar. However, unlike investigators in earlier studies, we used a rigorous diagnostic reference standard that was a prerequisite for detecting this mismatch. Second, ^{68}Ga -DOTA PET, like conventional RC (10,12,13,17,24), may show several sites of extrathecal tracer accumulation—which, however, do not indicate that there are multiple leaks but rather that the tracer leaves the spinal epidural space at multiple locations. This notion is in line with the current concept that spontaneous spinal CSF leaks most commonly occur in the lower cervical spine and thoracic spine (22,26), frequently being caused by well-defined singular lesions (e.g., dural tears due to diskogenic microspurs) (3,26,27). Thus assumption is also reflected by current excellent surgical outcomes. Third, lumbar/lumbosacral extrathecal tracer accumulations are very rarely (if ever) indicative of leaks in that region but are usually of iatrogenic origin instead, although frequently being reported in the RC literature (10,23). Fourth, early bladder activity as an indirect sign possesses little (if any) diagnostic value, in contrast to early RC reports (11) but in agreement with more recent studies (17,21). Fifth, the term *direct sign* for extrathecal tracer accumulation in the paraspinous space in RC is most likely misleading. In fact, the only direct signs associated with verified leaks in the present study were probably RC equivalents of cervicothoracic extrathecal fluid accumulation on x-ray myelography, commonly referred to as false localizing signs (29). We assume that this finding is simply due to anatomic reasons (e.g., more flexible spinal alignment). To the best of our knowledge, no other systematic studies have provided a detailed (segmental) comparison of neuroradiologic or surgical and RC findings. Even in the aforementioned seminal work (22), anatomic description of CT myelography or RC findings did not pinpoint locations of actual leaks but only provided approximate segmental heights or ranges of extrathecal findings. Given rapid epidural spread and the uncertain mechanism of action of EBP (see earlier text), a therapeutic response to EBP can hardly be taken as a confirmation of an apparent leak localization given by RC, as has frequently been done in the literature (22–24).

CSF PET shows high diagnostic performance in a particularly challenging clinical situation. Extrathecal tracer accumulation at

the cervicothoracic junction provides a high diagnostic specificity (90%) but only a moderate sensitivity (67%) for the verification of spinal CSF leaks. The latter fits the observation that direct signs of CSF leakage on conventional RC might be absent in a highly variable fraction of patients with SIH (10%–70%) (13,22–24). In turn, indirect signs of CSF leakage on conventional RC are found in the vast majority (>90%) of patients (11,13,22,24). A lack of tracer appearance over the cerebral convexities on a 5-h scan provides a very high sensitivity (94%) at a moderate specificity (67%). A very high sensitivity of this sign was also suggested by conventional RC studies (13,17,21). The summary rating of both raters was motivated by clinical practice with conventional RC and comprised all direct and indirect signs (including those of no or little value), with weighting left to the discretion and experience of the rater. Thus, it is not surprising that this consensus reading was not superior to a combination of both aforementioned features by logistic regression.

Given the considerable rate of negative findings of CT and MR myelography in SIH (45%–74%) (3), it is interesting that 4 of 14 patients (29%) with negative neuroradiologic imaging results and treated with EBP showed a clinically relevant response to EBP. All 4 patients fell into the groups of patients who were judged to show “questionable/possible” and “probable” (2 patients each) signs of a spinal CSF leak but in whom no leak could be verified (Suppl. Figs. 1 and 2). Aside from direct and indirect signs suggestive of spinal CSF leaks (in 3 patients and 1 patient, respectively), all 4 patients also showed below-threshold $t_{1/2, \text{biol}}$ and R5/3 values. Thus, it is tempting to speculate that these patients represented false-negative cases on neuroradiologic imaging, leading to an underestimation of the true sensitivity of CSF PET.

In light of these observations, the clinical role of CSF PET is clearly not to localize the site of a spinal CSF leak. CSF PET may, however, play an essential role in verifying spinal CSF leakage with high sensitivity (to rule out) or specificity (to rule in), depending on clinical need. For instance, extrathecal tracer accumulation at the cervicothoracic junction is most likely associated with a spinal CSF leak (90% specificity) and may prompt additional examinations. In turn, sufficient tracer accumulation over the cerebral convexities strongly argues against a spinal CSF leak (>90% sensitivity), leading to a defensive approach (see also Mokri (21)). One motivation would clearly be to minimize the exposure to ionizing radiation in a predominately young and female population. Patients have a long disease history of months to years and have already undergone a plethora of diagnostic and therapeutic actions. In the present study, on average, 2 combined digital subtraction myelography/CT myelography procedures were performed per patient at our institution only. The resulting median radiation exposure in the present study can be estimated to be about 52.6 mSv per patient (6) or, in other words, enough to cause 1 additional radiation-induced cancer death in 250–500 patients (30). This risk may be substantially reduced by including a gatekeeper examination.

The limitations of the present study include its retrospective nature, which warrants prospective validation. In particular, a direct comparison of CSF PET with conventional RC would be desirable (e.g., by coinjection of tracers). Furthermore, the limited number of cases did not allow for detailed statistical contemplation of interesting subgroups (e.g., SIH vs. non-SIH, type of leakage). Finally, the present study summarized the data for the first patients examined with this novel methodology that was developed in parallel. By retrospectively analyzing the data for this set of patients at once in a strictly masked fashion, we minimized possible effects of the raters’ learning curves and bias. However, optimal technical

aspects, such as measures to avoid iatrogenic extrathecal tracer accumulation, still need to be defined. Moreover, although an earlier study showed that upright positioning or exercise does not affect CSF circulation under normal conditions (7), a preliminary report of 2 cases suggested that a sitting position may improve the rate of detection of spinal CSF leaks (31). Further studies are needed to explore whether such efforts or other technical refinements can increase the rate of detection of CSF leakage and possibly improve the localization of spinal CSF leaks by PET.

CONCLUSION

We propose CSF PET with ^{68}Ga -DOTA as a novel, fast, and convenient approach to RC for verification but not localization of CSF leaks with high sensitivity and specificity. CSF PET may fulfill an important gatekeeper function for stratifying patients toward escalation (ruling in) or deescalation (ruling out) of diagnostic and therapeutic measures. Further prospective studies are needed to validate the present results and determine the potential of the methods to reduce the burden to patients.

DISCLOSURE

No potential conflict of interest relevant to this article was reported.

KEY POINTS

QUESTION: Is CSF PET with ^{68}Ga -DOTA a valid method for the diagnosis of spinal CSF leakage when compared with comprehensive, stepwise neuroradiologic imaging?

PERTINENT FINDINGS: The present retrospective study included 39 consecutive adults with suspected intracranial hypotension and who underwent ^{68}Ga -DOTA CSF PET. Extrathecal tracer accumulation at the cervicothoracic junction (67% sensitivity and 90% specificity) and lack of activity over the cerebral convexities (5 h; 94% sensitivity and 67% specificity) revealed a high diagnostic value for spinal CSF leaks.

IMPLICATIONS FOR PATIENT CARE: CSF PET with ^{68}Ga -DOTA may serve as a gatekeeper for stratifying patients toward escalation or deescalation of further diagnostic and therapeutic measures and, thus, reducing the burden to patients.

REFERENCES

1. Luetzen N, Dovi-Akue P, Fung C, Beck J, Urbach H. Spontaneous intracranial hypotension: diagnostic and therapeutic workup. *Neuroradiology*. 2021;63:1765–1772.
2. Beck J, Häni L, Ulrich CT, et al. Diagnostic challenges and therapeutic possibilities in spontaneous intracranial hypotension. *Clinical and Translational Neuroscience*. 2018;2:1–11.
3. Kranz PG, Gray L, Amrhein TJ. Spontaneous intracranial hypotension: 10 myths and misperceptions. *Headache*. 2018;58:948–959.
4. Headache Classification Committee of the International Headache Society (IHS). The International Classification of Headache Disorders, 3rd ed. *Cephalalgia*. 2018; 38:1–211.
5. Schievink WI, Maya MM, Jean-Pierre S, Nuno M, Prasad RS, Moser FG. A classification system of spontaneous spinal CSF leaks. *Neurology*. 2016;87:673–679.
6. Nicholson PJ, Guest WC, van Prooijen M, Farb RI. Digital subtraction myelography is associated with less radiation dose than CT-based techniques. *Clin Neuroradiol*. 2021;31:627–631.
7. Dichiro G. Movement of the cerebrospinal fluid in human beings. *Nature*. 1964; 204:290–291.

8. Hosain F, Som P. Chelated 111 In: an ideal radiopharmaceutical for cisternography. *Br J Radiol*. 1972;45:677–679.
9. Som P, Hosain F, Wagner HN Jr, Scheffel U. Cisternography with chelated complex of ^{99m}Tc. *J Nucl Med*. 1972;13:551–553.
10. Moriyama E, Ogawa T, Nishida A, Ishikawa S, Beck H. Quantitative analysis of radioisotope cisternography in the diagnosis of intracranial hypotension. *J Neurosurg*. 2004;101:421–426.
11. Morioka T, Aoki T, Tomoda Y, et al. Cerebrospinal fluid leakage in intracranial hypotension syndrome: usefulness of indirect findings in radionuclide cisternography for detection and treatment monitoring. *Clin Nucl Med*. 2008;33:181–185.
12. Takahashi K, Mima T. Cerebrospinal fluid leakage after radioisotope cisternography is not influenced by needle size at lumbar puncture in patients with intracranial hypotension. *Cerebrospinal Fluid Res*. 2009;6:5.
13. Hoshino H, Higuchi T, Achmad A, Taketomi-Takahashi A, Fujimaki H, Tsushima Y. A new approach for simple radioisotope cisternography examination in cerebrospinal fluid leakage detection. *Ann Nucl Med*. 2016;30:40–48.
14. Bergstrand G, Larsson S, Bergstrom M, Eriksson L, Edner G. Cerebrospinal fluid circulation: evaluation by single-photon and positron emission tomography. *AJNR*. 1983;4:557–559.
15. Novotny C, Potzi C, Asenbaum S, Peloschek P, Suess E, Hoffmann M. SPECT/CT fusion imaging in radionuclide cisternography for localization of liquor leakage sites. *J Neuroimaging*. 2009;19:227–234.
16. Horikoshi T, Ikegawa H, Uchida M, Takahashi T, Watanabe A, Umeda T. Tracer clearance in radionuclide cisternography in patients with spontaneous intracranial hypotension. *Cephalgia*. 2006;26:1010–1015.
17. Sakurai K, Nishio M, Yamada K, et al. Comparison of the radioisotope cisternography findings of spontaneous intracranial hypotension and iatrogenic cerebrospinal fluid leakage focusing on chronological changes. *Cephalgia*. 2012;32:1131–1139.
18. Freesmeyer M, Schwab M, Besteher B, Grober S, Waschke A, Drescher R. High-resolution PET cisternography with ⁶⁴Cu-DOTA for CSF leak detection. *Clin Nucl Med*. 2019;44:735–737.
19. Cherry S, Sorenson J, Phelps M. *Physics in Nuclear Medicine*. 4th ed. Saunders; 2012.
20. ICRP. ICRP publication 53: radiation dose to patients from radiopharmaceuticals. *Ann ICRP*. 1988;18:1–4.
21. Mokri B. Radioisotope cisternography in spontaneous CSF leaks: interpretations and misinterpretations. *Headache*. 2014;54:1358–1368.
22. Schievink WI, Meyer FB, Atkinson JL, Mokri B. Spontaneous spinal cerebrospinal fluid leaks and intracranial hypotension. *J Neurosurg*. 1996;84:598–605.
23. Yoo HM, Kim SJ, Choi CG, et al. Detection of CSF leak in spinal CSF leak syndrome using MR myelography: correlation with radioisotope cisternography. *AJNR*. 2008;29:649–654.
24. Hyun SH, Lee KH, Lee SJ, et al. Potential value of radionuclide cisternography in diagnosis and management planning of spontaneous intracranial hypotension. *Clin Neurol Neurosurg*. 2008;110:657–661.
25. Häni L, Fung C, Jesse CM, et al. Outcome after surgical treatment of cerebrospinal fluid leaks in spontaneous intracranial hypotension: a matter of time. *J Neurol*. 2022;269:1439–1446.
26. Beck J, Ulrich CT, Fung C, et al. Diskogenic microspurs as a major cause of intractable spontaneous intracranial hypotension. *Neurology*. 2016;87:1220–1226.
27. Kranz PG, Gray L, Malinzak MD, Amrhein TJ. Spontaneous intracranial hypotension: pathogenesis, diagnosis, and treatment. *Neuroimaging Clin N Am*. 2019;29:581–594.
28. Dobrocky T, Nicholson P, Hani L, et al. Spontaneous intracranial hypotension: searching for the CSF leak. *Lancet Neurol*. 2022;21:369–380.
29. Schievink WI, Maya MM, Chu RM, Moser FG. False localizing sign of cervicothoracic CSF leak in spontaneous intracranial hypotension. *Neurology*. 2015;84:2445–2448.
30. UNSCEAR. UNSCEAR 2010 report: summary of low-dose radiation effects on health 2010. Report of the United Nations Scientific Committee on the Effects of Atomic Radiation 2010. UNSCEAR website. <https://www.unscear.org/unscear/en/publications/2010.html>. Accessed November 25, 2022.
31. Lu Y-Y, Wang H-Y, Lin Y, Lin W-Y. The value of changing position in the detection of CSF leakage in spontaneous intracranial hypotension using Tc-99m DTPA scintigraphy: two case reports. *Iran J Radiol*. 2012;9:150–153.

A Head-to-Head Comparison Between Plasma pTau181 and Tau PET Along the Alzheimer's Disease Continuum

Emma M. Coomans¹, Inge M.W. Verberk², Rik Ossenkoppele^{3,4}, Sander C.J. Verfaillie^{1,5}, Denise Visser¹, Mariam Gouda², Hayel Tuncel¹, Emma E. Wolters¹, Tessa Timmers¹, Albert D. Windhorst¹, Sandeep S.V. Golla¹, Philip Scheltens³, Wiesje M. van der Flier^{3,6}, Bart N.M. van Berckel*¹, and Charlotte E. Teunissen*²

¹Department of Radiology and Nuclear Medicine, Amsterdam Neuroscience, Vrije Universiteit Amsterdam, Amsterdam UMC, Amsterdam, The Netherlands; ²Department of Clinical Chemistry, Neurochemistry Laboratory, Amsterdam Neuroscience, Vrije Universiteit Amsterdam, Amsterdam UMC, Amsterdam, The Netherlands; ³Alzheimer Center Amsterdam, Department of Neurology, Amsterdam Neuroscience, Vrije Universiteit Amsterdam, Amsterdam UMC, Amsterdam, The Netherlands; ⁴Clinical Memory Research Unit, Lund University, Lund, Sweden; ⁵Department of Medical Psychology, Amsterdam Public Health Research Institute, University of Amsterdam, Amsterdam UMC, Amsterdam, The Netherlands; and ⁶Department of Epidemiology and Data Science, Vrije Universiteit Amsterdam, Amsterdam UMC, Amsterdam, The Netherlands

Key Words: plasma pTau181; tau PET; Alzheimer's disease

J Nucl Med 2023; 64:437–443

DOI: 10.2967/jnumed.122.264279

Both plasma tau phosphorylated at threonine-181 (pTau181) and tau PET show potential for detecting Alzheimer's disease (AD) pathology and predicting clinical progression. In this study, we performed a head-to-head comparison between plasma pTau181 and tau PET along the AD continuum. **Methods:** We included participants from the Amsterdam Dementia Cohort who underwent ¹⁸F-flortaucipir (tau) PET and had a plasma sample biobanked within 12 mo from tau PET. Fifty subjective cognitive decline (SCD) participants (31 A β -negative and 19 A β -positive) and 60 A β -positive participants with mild cognitive impairment (MCI) or dementia due to AD were included. A subset had 2-y longitudinal plasma pTau181 and tau PET available ($n = 40$). Longitudinal neuropsychological test data covering 3.2 ± 2.7 y from both before and after tau PET were available. Plasma pTau181 and tau PET were compared in their accuracies in discriminating between cognitive stage (MCI/AD vs. SCD) and preclinical A β status (SCD A β -positive vs. SCD A β -negative), their associations with cross-sectional and longitudinal neuropsychological test performance, and their longitudinal changes over time. **Results:** When discriminating between preclinical A β status, the area under the curve (AUC) for plasma pTau181 (0.83) and tau PET (entorhinal, 0.87; temporal, 0.85; neocortical, 0.67) were equally high (all DeLong $P > 0.05$), but tau PET outperformed plasma pTau181 in discriminating MCI/AD from SCD (AUC for plasma pTau181: 0.74; AUCs for tau PET: entorhinal, 0.89; temporal, 0.92; neocortical, 0.89) (all $P < 0.01$). Overall, tau PET showed stronger associations with cognitive decline and was associated with a wider variety of cognitive tests than plasma pTau181 (plasma pTau181, $-0.02 > \beta < -0.12$; tau PET, $-0.01 > \beta < -0.22$). Both plasma pTau181 and tau PET increased more steeply over time in MCI/AD than in SCD ($P < 0.05$), but only tau PET annual changes were associated with cognitive decline. **Conclusion:** Our results suggest that plasma pTau181 and tau PET perform equally well in identifying A β pathology but that tau PET better monitors disease stage and clinical progression.

Neurofibrillary tau tangles consist of hyperphosphorylated tau (pTau) and are a pathologic hallmark of Alzheimer's disease (AD) (1). Tau pathology in AD is closely associated with clinical symptoms and disease severity (2,3). As such, in vivo assessment of tau is expected to provide both accurate diagnostic and accurate prognostic information. Biomarkers for detecting in vivo tau pathology include pTau measurements in cerebrospinal fluid (4), imaging of tracer binding to tau paired helical filaments using PET (5), and, since a few years ago, pTau measurements in blood (6–8). Blood-based biomarkers have major advantages, including easy accessibility, wide applicability, relative noninvasiveness, and low costs and can therefore easily be repeated over time, whereas PET biomarkers, although expensive, have the advantage of providing spatial information on tracer binding throughout the brain.

Studies have shown that plasma tau phosphorylated at threonine-181 (pTau181) can discriminate AD dementia from both non-AD dementias and A β -negative cognitively unimpaired older adults (7–10), and can predict cognitive decline (11,12) and progression to mild cognitive impairment (MCI) or dementia (13,14). Tau PET can also discriminate between AD dementia and both non-AD dementias and cognitively unimpaired older adults (15,16), and strong associations with subsequent cognitive decline and brain atrophy have consistently been reported (17,18). Both plasma pTau181 and tau PET are closely associated with amyloid- β (A β) pathology (7,19). Although both tau biomarkers show potential for AD diagnosis and prognosis, head-to-head comparison studies are limited. With the recent Food and Drug Administration approval of the tau PET tracer ¹⁸F-flortaucipir for clinical use, and intentions for plasma pTau to eventually be used in the clinic, there is a need to compare these biomarkers to guide clinicians in performing their clinical work-up and researchers in designing trials.

The overarching aim of this study was to perform a head-to-head comparison between plasma pTau181 and tau PET in a cohort of participants with subjective cognitive decline (SCD) and MCI or dementia due to AD (MCI/AD) against several clinically relevant measures.

Received Apr. 12, 2022; revision accepted Aug. 23, 2022.

For correspondence or reprints, contact Emma M. Coomans (e.coomans@amsterdamumc.nl).

*Contributed equally to this work.

Published online Oct. 13, 2022.

Immediate Open Access: Creative Commons Attribution 4.0 International License (CC BY) allows users to share and adapt with attribution, excluding materials credited to previous publications. License: <https://creativecommons.org/licenses/by/4.0/>. Details: <http://jnm.snmjournals.org/site/misc/permission.xhtml>.

COPYRIGHT © 2023 by the Society of Nuclear Medicine and Molecular Imaging.

We examined their accuracies in discriminating cognitive stage (MCI/AD vs. SCD) and preclinical A β status (SCD A β -positive vs. SCD A β -negative), their associations with cross-sectional and longitudinal cognition, their longitudinal changes over time, and longitudinal tau biomarker relationships with longitudinal cognition.

MATERIALS AND METHODS

Participants

This study included all individuals from the Amsterdam Dementia Cohort and SCIENCE project with a clinical diagnosis of SCD ($n = 50$), MCI due to AD ($n = 10$), or probable AD dementia ($n = 50$) who underwent ^{18}F -florbetapir (tau) PET and had a plasma sample biobanked within 12 mo from tau PET (median, 5.0 mo; interquartile range, 4.4 mo) (20–23). The supplemental materials available at <http://jnm.snmjournals.org> provide details (20–24). SCD participants underwent ^{18}F -florbetapir (A β) PET for visual assessment of A β status for research purposes (25). All MCI or AD dementia participants were biomarker-defined as A β -positive by means of abnormal cerebrospinal fluid A β 1–42 biomarkers (according to routine thresholds (24)) or a positive A β PET visual read. MCI and AD dementia participants were grouped into a single MCI/AD group. The study protocol was approved by the institutional review board of the Amsterdam UMC. All participants provided written informed consent.

Blood Sampling and Analyses

Ethylenediaminetetraacetic acid plasma samples were collected through venipuncture. A subset ($n = 40$) had 2.2 ± 0.5 y of follow-up samples available.

Samples were measured using the Simoa pTau181 V2 Advantage kit (Quanterix) on the Simoa HDx analyzer (Quanterix) (26). Samples were measured in duplicate, with an average intra-assay coefficient of

variation of $6.1\% \pm 4.6\%$. One SCD participant was a clear outlier longitudinally and therefore excluded from longitudinal analyses (Supplemental Fig. 1).

Tau PET Acquisition and Analyses

Participants underwent dual-time-point dynamic ^{18}F -florbetapir PET scans of at least 100-min duration (27,28). A subset ($n = 40$, the same subset as that with longitudinal plasma) had 2.1 ± 0.1 y of follow-up tau PET available.

We extracted nondisplaceable binding potential (BP_{ND}) from 3 subject-space regions of interest (ROIs) selected a priori and corresponding to postmortem staging of neurofibrillary tangle pathology (29), in line with previous work (30,31). These ROIs included the entorhinal cortex (Braak I); a temporal composite region (Braak III and IV); and a widespread neocortical region (Braak V and VI). Details are described in the supplemental methods (27–29,32–36).

Neuropsychological Assessment

Participants underwent a standardized neuropsychological assessment as part of diagnostic screening, and the assessment was repeated annually (20,25). We used neuropsychological test data from both before and after tau PET and blood collection to accurately estimate slopes in cognitive functioning. The result was longitudinal cognitive data covering 3.2 ± 2.7 y (total of 405 visits; range, 1–13; median, 3; 96 participants ≥ 2) (supplemental methods (25,37)). We a priori selected cognitive tests shown to be sensitive in capturing cognitive decline in early and late stages of AD (38): the Dutch version of the Rey Auditory Verbal Learning Test (RAVLT) delayed recall (episodic memory); the Category Fluency test (CFT) animals (semantic memory); and the Trail-Making Test B (TMT-B) (executive functioning). The Mini-Mental State Examination (MMSE) was used as a measure of global cognition.

TABLE 1
Demographics

Demographic	Total sample	Stratified by diagnosis	
		SCD	MCI/AD
Participants (n)	110 (100%)	50 (45.5%)	60 (55.5%)
Age (y)	65.4 ± 7.4	65.6 ± 7.6	65.3 ± 7.3
Sex, female (n)	53 (48.2%)	25 (50.0%)	28 (46.7%)
Median education	6 (range, 2–7)	6 (range, 2–7)	6 (range, 3–7)
APOE $\epsilon 4$ carrier (n)	61 (56.5%)	18 (37.5%)	43 (71.7%)*
A β -positive status (n)	79 (71.8%)	19 (38.0%)	60 (100%)*
Cognition			
MMSE	25.7 ± 4.2	28.8 ± 1.4	$23.0 \pm 4.0^*$
RAVLT delayed recall	5.7 ± 4.4	9.3 ± 3.3	$2.8 \pm 2.8^*$
CFT animals	19.9 ± 7.3	24.8 ± 5.7	$15.6 \pm 5.7^*$
Trail-making test B	122.5 ± 83.7	78.0 ± 35.8	$174.3 \pm 93.4^*$
Plasma pTau181 (pg/mL)	2.53 ± 1.14	2.08 ± 1.17	$2.91 \pm 0.98^*$
^{18}F -florbetapir PET BP_{ND}			
Entorhinal	0.16 ± 0.26	-0.03 ± 0.17	$0.32 \pm 0.21^*$
Temporal	0.32 ± 0.31	0.10 ± 0.15	$0.50 \pm 0.29^*$
Neocortical	0.22 ± 0.29	0.05 ± 0.07	$0.36 \pm 0.33^*$

*Different from SCD at $P < 0.01$.

Data are mean \pm SD unless specified otherwise. Education reflects Dutch Verhage scale. APOE E4 was missing in 2 SCD patients, CFT animals was missing in 3 MCI/AD patients, and Trail-making test B was missing in 17 MCI/AD patients.

Statistical Analyses

We used R, version 4.0.3, for statistical analyses. A P value of less than 0.05 was considered significant.

Demographic characteristics were compared using t tests, χ^2 tests, and Mann–Whitney U tests. Associations of tau markers with age, sex, and apolipoprotein E (*APOE*) $\epsilon 4$ status were examined using Pearson correlations or t tests. Associations between tau markers were examined using linear regressions adjusted for age, sex, and time between PET and blood collection. We examined between-group differences in tau markers using age- and sex-adjusted analysis of covariances. We performed receiver-operating-characteristic analyses to compare tau marker accuracies in discriminating cognitive stage (SCD vs. MCI/AD) and preclinical $A\beta$ status (SCD $A\beta$ -negative vs. SCD $A\beta$ -positive). Differences between areas under the curve (AUCs) were tested using DeLong tests.

Next, we investigated associations of tau markers with cognitive decline using age-, sex-, and education-adjusted linear mixed models (LMMs) with subject-specific intercepts. For all LMMs, a random slope was added when it improved model fit by comparing the Akaike information criterion using χ^2 statistics. Tau marker (tau PET or plasma pTau181), time (tau PET or blood collection as $T = 0$), and an interaction term of tau marker \times time were entered as fixed variables and neuropsychological test performance as a dependent variable. For all LMMs, we used separate models per tau marker and per cognitive test. Furthermore, tau markers and cognitive scores were scaled within each LMM to compare effect sizes. The fixed effect of tau marker was interpreted as the cross-sectional association, and the fixed effect of tau marker \times time was interpreted as the longitudinal association. P values were corrected for multiple testing by applying the 10% false-discovery rate (FDR).

Lastly, in the subset with longitudinal tau markers, we investigated changes in tau markers over time using age- and sex-adjusted LMMs. Time, diagnosis (SCD or MCI/AD), and an interaction term of diagnosis \times time were entered as fixed variables and tau marker as a dependent variable. We additionally explored associations of tau marker annual changes with cognitive decline, for which tau marker annual changes were calculated as [(follow-up – baseline)/time between measurements in years]. Age-, sex-, and education-adjusted LMMs were performed with tau marker annual change, time (baseline tau PET or blood collection as $T = 0$), and an interaction term of tau marker annual change \times time as a fixed variable and neuropsychologic test performance as a dependent variable. The fixed effect of tau marker annual change \times time was interpreted as the association between tau marker annual change and longitudinal cognition.

RESULTS

Participants

Table 1 shows the participant characteristics. Mean age was 65.4 ± 7.4 y, and 48.2% of participants were female. By study design, all MCI/AD participants were $A\beta$ -positive. Of the 50 SCD participants, 19 (38.0%) were $A\beta$ -positive. There were no group differences in age, sex, or education, but there were more *APOE* $\epsilon 4$ carriers in MCI/AD than in SCD ($P < 0.01$). Supplemental Table 1 shows the characteristics of the longitudinal subset. Plasma pTau181 did not correlate with age or sex in either

SCD or MCI/AD. In SCD, but not MCI/AD, *APOE* $\epsilon 4$ carriers showed higher plasma pTau181 than noncarriers ($P = 0.03$). Tau PET BP_{ND} in the temporal ROI positively correlated with age in SCD ($r = 0.29$, $P = 0.04$), whereas in MCI/AD, tau PET BP_{ND} in all ROIs negatively correlated with age ($-0.37 > r > -0.62$; all ROIs, $P < 0.01$). In MCI/AD, but not SCD, female participants showed higher BP_{ND} than male participants (all ROIs $P < 0.01$). In both SCD and MCI/AD, *APOE* $\epsilon 4$ carriers showed higher entorhinal tau PET BP_{ND} than noncarriers ($P = 0.01$ and $P = 0.03$, respectively) but not in other ROIs (Supplemental Table 2; Supplemental Fig. 2).

Association Between Plasma pTau181 and Tau PET

Across all participants, plasma pTau181 was associated with tau PET in each ROI (range of β , 0.37–0.53; all $P < 0.01$) (Supplemental Tables 3 and 4). Within SCD and MCI/AD separately, plasma pTau181 was associated moderately with tau PET in SCD (range of β , 0.43–0.63; all $P < 0.01$) and associated weakly to moderately with tau PET in MCI/AD (range of β , 0.21–0.29; all $P < 0.05$) (Fig. 1A). Further stratifying SCD participants for $A\beta$ positivity revealed significant positive associations between plasma pTau181 and tau PET in SCD $A\beta$ -positive participants but not in SCD $A\beta$ -negative participants (Fig. 1B).

Comparing Plasma pTau181 and Tau PET for Predicting Cognitive Stage and Preclinical $A\beta$ status

Both plasma pTau181 and tau PET BP_{ND} were higher in MCI/AD than in SCD (all $P < 0.001$), although plasma pTau181 showed considerable between-group overlap (Fig. 2A). The AUC for distinguishing MCI/AD from SCD for plasma pTau181 (AUC, 0.74 [95% CI, 0.65–0.84]) was significantly lower than that for tau PET BP_{ND} in entorhinal (0.89 [95% CI, 0.83–0.96], DeLong $P < 0.001$), temporal (0.92 [95% CI, 0.87–0.98], $P < 0.001$), and neocortical (0.89 [95% CI, 0.83–0.95], $P = 0.005$) ROIs (Fig. 2C).

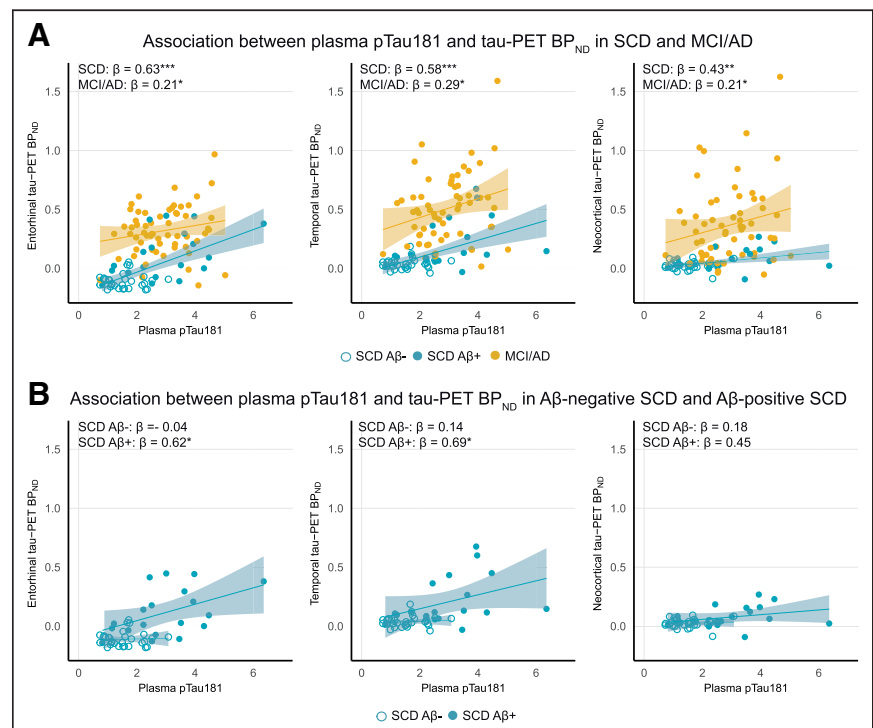


FIGURE 1. Associations between plasma pTau181 and tau PET in SCD and MCI/AD (A) and SCD $A\beta$ -negative and SCD $A\beta$ -positive (B) participants. * $P < 0.05$. ** $P < 0.01$. *** $P < 0.001$.

When the cohort was stratified into SCD A β -negative, SCD A β -positive, MCI, and AD dementia groups, plasma pTau181 was higher in each A β -positive group (SCD A β -positive, MCI, and AD dementia) than in A β -negative SCD (Fig. 2B; Supplemental Table 5). No differences were observed between A β -positive groups. In contrast, tau PET showed more stepwise increases across groups (Fig. 2B; Supplemental Table 5).

Finally, to distinguish preclinical A β status (SCD A β -positive vs. SCD A β -negative), plasma pTau181 showed an AUC of 0.83 (95% CI, 0.70–0.96). Comparable AUCs were observed for tau

PET BP_{ND} in entorhinal (0.87 [95% CI, 0.77–0.98], $P = 0.54$), temporal (0.85 [95% CI, 0.73–0.98], $P = 0.80$), and neocortical (0.67 [95% CI, 0.50–0.84], $P = 0.09$) regions (Fig. 2D).

Comparing Plasma pTau181 and Tau PET for Predicting Cognitive Decline

Next, we investigated associations with cross-sectional and longitudinal cognition. We report associations for plasma pTau181 and temporal tau PET in SCD and MCI/AD that survived FDR correction. Supplemental Table 6 reports all estimates and uncorrected P values.

In SCD, plasma pTau181 was not associated with cross-sectional performance on any of the included neuropsychological tests (FDR $P > 0.05$). Longitudinally, higher plasma pTau181 was associated with a steeper rate of decline on the MMSE ($\beta = -0.05$, FDR $P < 0.01$) and RAVLT delayed recall ($\beta = -0.08$, FDR $P = 0.04$). In SCD, temporal tau PET BP_{ND} was associated with worse cross-sectional performance on the MMSE ($\beta = -0.24$, FDR $P = 0.04$). In addition, temporal tau PET BP_{ND} was associated with a steeper rate of decline on all neuropsychological tests (MMSE: $\beta = -0.12$, FDR $P < 0.01$; RAVLT delayed recall: $\beta = -0.07$, FDR $P = 0.01$; CFT animals: $\beta = -0.08$, FDR $P < 0.01$; trail-making test B: $\beta = -0.07$, FDR $P < 0.01$) (Fig. 3).

In MCI/AD, plasma pTau181 was not associated with cross-sectional or longitudinal performance on any of the included neuropsychological tests (FDR $P > 0.05$). In contrast, in MCI/AD, temporal tau PET BP_{ND} was associated with worse cross-sectional performance on the MMSE ($\beta = -0.45$, FDR $P < 0.01$) and with a steeper rate of decline on the MMSE ($\beta = -0.17$, FDR $P < 0.01$) and on the CFT animals test ($\beta = -0.10$, FDR $P = 0.04$) (Fig. 3).

Comparing Longitudinal Changes in Plasma pTau181 and Tau PET

Finally, in the subset with repeated tau biomarker assessments, an interaction effect of diagnosis \times time was observed for plasma pTau181 ($\beta = 0.35$, $P < 0.001$), meaning plasma pTau181 levels increased more steeply in MCI/AD than in SCD (Fig. 4). For tau PET, we also observed significant interaction effects of diagnosis \times time, with steeper increases in BP_{ND} in MCI/AD than in SCD in temporal ($\beta = 0.08$, $P = 0.049$) and neocortical ($\beta = 0.12$, $P < 0.02$), but not entorhinal ($\beta = 0.08$, $P = 0.14$), regions (Fig. 4). Supplemental Table 7 reports longitudinal changes in tau markers in SCD and MCI/AD separately.

Annual change in plasma pTau181 was not associated with longitudinal cognition (all $P > 0.05$). In contrast, annual change in tau PET BP_{ND} in all ROIs was associated

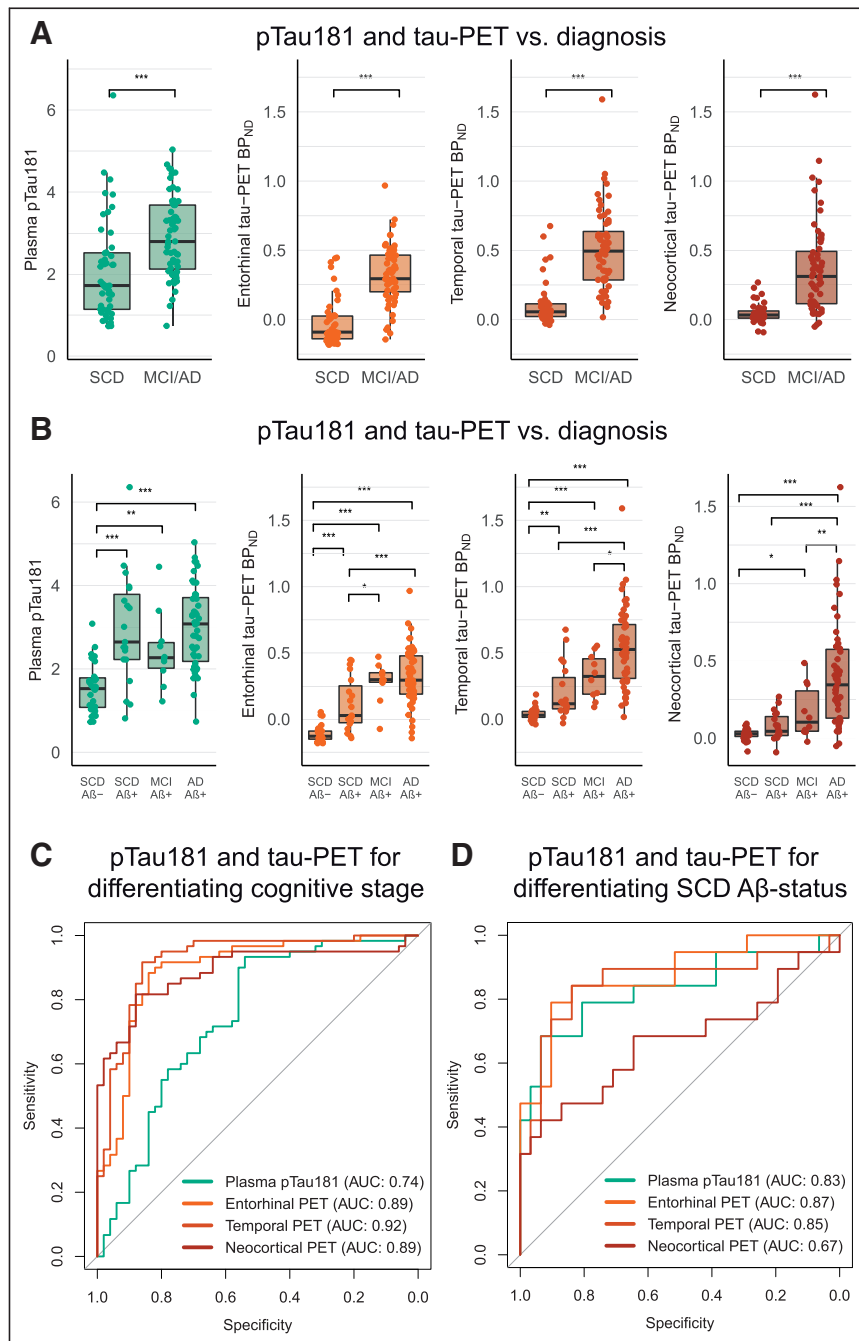


FIGURE 2. (A and C) Plasma pTau181 and tau PET BP_{ND} stratified for SCD and MCI/AD (A) and for SCD A β -negative and SCD A β -positive MCI due to AD and AD dementia (C). (B and D) AUCs for discriminating SCD from MCI/AD (B) and SCD A β -negative from SCD A β -positive (D) participants. * $P < 0.5$. ** $P < 0.01$. *** $P < 0.001$.

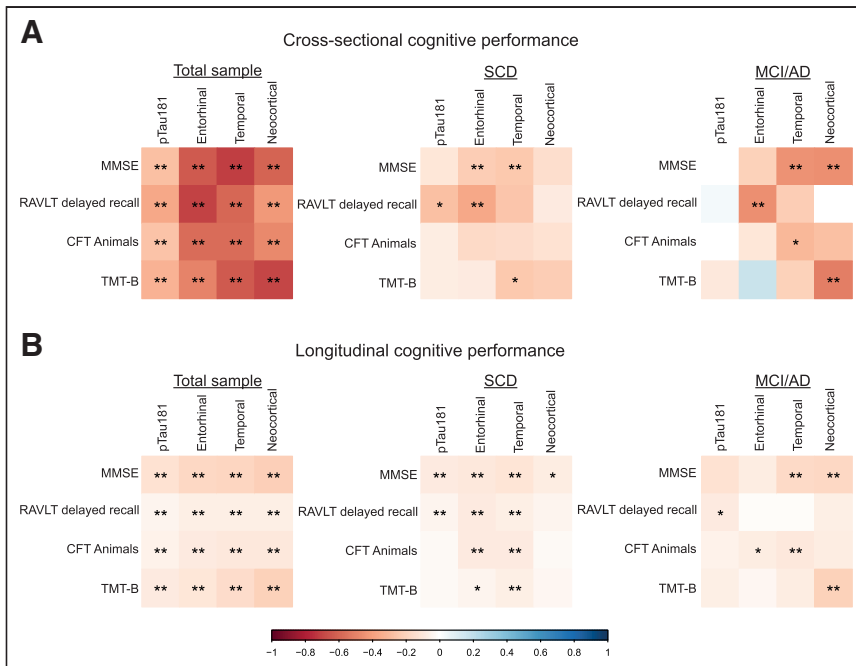


FIGURE 3. Heat plots reflecting standardized β -estimates (color scale) and significance levels from LMMs between plasma pTau181 or tau PET (predictor) and cross-sectional (A) and longitudinal (B) cognitive performance (outcome variables) (age-, sex-, and education-adjusted). *Uncorrected $P < 0.05$. **FDR $P < 0.05$. TMT-B = trail-making test B.

with decline on the RAVLT delayed recall (all $P < 0.05$) (Supplemental Fig. 3). Furthermore, annual change in temporal and neocortical BP_{ND} was associated with decline on the CFT animals, and neocortical BP_{ND} additionally was associated with decline on the MMSE (Supplemental Table 8 shows estimates and P values).

DISCUSSION

In this study, we performed a head-to-head comparison between plasma pTau181 and tau PET in predicting cognitive stage, preclinical A β status, and cross-sectional and longitudinal cognitive functioning. Both plasma pTau181 and tau PET discriminated with high accuracy between SCD A β -negative and SCD A β -positive individuals, but tau PET outperformed plasma pTau181 in discriminating cognitive stage (MCI/AD vs. SCD). Moreover, compared with plasma pTau181, tau PET showed stronger associations with

cognitive decline and was associated with a wider variety of cognitive tests. Both plasma pTau181 and tau PET showed steeper increases over time in MCI/AD than in SCD, but only annual changes in tau PET were associated with longitudinal decline. Our results provide support for both plasma pTau181 and tau PET as biomarkers for identifying A β pathology but indicate that tau PET has better performance for disease staging and clinical progression.

For distinguishing between preclinical A β -positive and A β -negative individuals, plasma pTau181 and tau PET (especially in entorhinal and temporal regions) showed high accuracy and performed equally well (AUCs of 0.83–0.87). This finding highlights the close relationship of both plasma pTau181 and ^{18}F -florotau PET with the presence of A β pathology and underscores the ability of these markers to predict A β status even at a very early stage, in line with previous studies (7,8,14,19). Combined with the practical advantages of plasma biomarkers, our results support the potential of plasma pTau181 for implementation in the clinic as a first step in the diagnostic work-up of AD or as a clinical trial

screening or prescreening tool, before cerebrospinal fluid or PET measurements.

For distinguishing between cognitively impaired and unimpaired individuals, tau PET significantly outperformed plasma pTau181 (AUCs of 0.89–0.92 for tau PET vs. 0.74 for pTau181). A stronger role for tau PET than for plasma pTau181 in disease staging was further strengthened by the comparison of tau marker values between SCD A β -negative, SCD A β -positive, MCI, and AD dementia, which showed stepwise increases in tau PET binding across the groups, whereas no differences in plasma pTau181 were observed among the A β -positive groups of different cognitive stages. In addition, tau PET associations with cross-sectional and longitudinal cognitive functioning were stronger and involved a wider variety of cognitive tests than was observed for plasma pTau181. The observed differences between the tau markers for predicting cognition might be related to biologic differences. Whereas fluid tau markers reflect increased phosphorylation and release of soluble tau (39), tau PET tracers bind to insoluble tau aggregates. Strong associations between tau tracer binding, disease stage, and cognitive decline have also been observed in previous studies (17,40). Overall, our results provide stronger support for tau PET than for plasma pTau181 for tracking disease progression and for use as a potential prognostic biomarker and clinical trial outcome measure.

Our longitudinal analyses showed that both plasma pTau181 and tau PET show steeper increases over time in MCI/AD than in SCD, in line with previous studies and with similar magnitudes (41–43). However, annual increases in only tau PET, not plasma pTau181, were associated with cognitive decline. A previous study investigating plasma

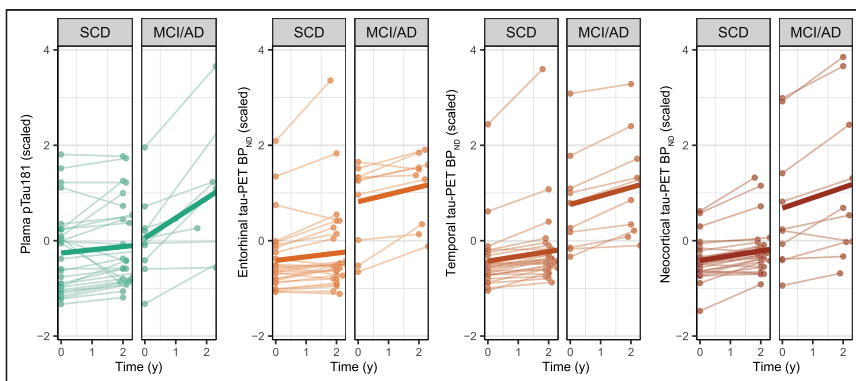


FIGURE 4. Spaghetti plots of scaled longitudinal plasma pTau181 and tau PET in SCD and MCI/AD.

pTau217 did observe associations between annual plasma pTau217 changes and longitudinal cognition (42). This discrepancy could be related to a different plasma pTau isoform or assay (26), and although our longitudinal results should be interpreted with caution because of the small sample size, our finding warrants further investigation as it could have implications for clinical trial designs. Previous studies have suggested that plasma pTau217 might have slightly favorable properties compared with plasma pTau181 in terms of dynamic range (44), prediction of A β status (10), and differentiation between clinical AD dementia and other neurodegenerative dementias (45). However, comparable performance for pTau181 and pTau217 has also been observed, such as in differentiating AD dementia from controls (10,26). Head-to-head comparisons including different plasma pTau isoforms are needed to define the complementarity of these markers.

This study had some limitations. Our cohort consisted of a highly selected sample with a relatively high percentage of A β -positive SCD cases. Head-to-head comparisons between plasma pTau181 and tau PET in unselected cohorts, more diverse populations, and non-AD dementias would be important. Furthermore, we had a relatively small sample size in longitudinal analyses. In addition, we used plasma pTau181 and ¹⁸F-flortaucipir PET, but studies have shown that other plasma pTau isoforms and second-generation PET tracers may be more sensitive for earlier disease stages (26,29,45). Finally, a recent study showed that health conditions such as chronic kidney disease, hypertension, stroke, and myocardial infarction are associated with plasma pTau181 (46). Future studies with larger sample sizes are needed to further investigate this possibility.

CONCLUSION

Plasma pTau181 and tau PET performed equally well in identifying A β pathology, but tau PET better monitored disease stage and clinical progression.

DISCLOSURE

Alzheimer Center Amsterdam is supported by Stichting Alzheimer Nederland and Stichting VUmc fonds. This study was made possible by ZonMW Memorabel, Dioraphte, Avid Radiopharmaceuticals, and Janssen Pharmaceuticals. Albert Windhorst is editor-in-chief of *Nuclear Medicine & Biology*. Philip Scheltens receives consultancy fees (paid to the university) from AC Immune, Alzheon, Brainstorm Cell, ImmunoBrain Checkpoint, Novartis, and Novo Nordisk; is a principal investigator (within university affiliation) of studies with AC Immune, FUJI-film/Toyama, IONIS, UCB, and Vivoryon; and is an employee of Life Sciences Partners Amsterdam. Wiesje van der Flier receives grant support from ZonMW, NWO, EU-FP7, EU-JPND, Alzheimer Nederland, Hersenstichting CardioVascular Onderzoek Nederland, Health~Holland, Topsector Life Sciences & Health, Stichting Dioraphte, Gieskes-Strijbis Fonds, Stichting Equilibrio, Pasman Stichting, Stichting Alzheimer & Neuropsychiatrie Foundation, Philips, Biogen MA Inc., Novartis-NL, Life-MI, AVID, Roche BV, Fujifilm, and Combinostics; holds the Pasman chair; is a recipient of ABOARD (a public-private partnership receiving funding from ZonMW [grant 73305095007] and Health~Holland, Topsector Life Sciences & Health [PPP-allowance LSHM20106]); performs contract research for Biogen MA Inc. and Boehringer Ingelheim; is an invited speaker for Boehringer Ingelheim, Biogen MA Inc., Danone, Eisai, WebMD Neurology (Medscape), and Springer Healthcare; is a consultant to Oxford Health Policy Forum CIC,

Roche, and Biogen MA Inc.; is on the advisory boards of Biogen MA Inc. and Roche, with all funding paid to her institution; was associate editor of *Alzheimer's Research & Therapy*; and is associate editor at *Brain*. Bart van Berckel receives research support from EU-FP7, CTMM, ZonMw, NOW, and Alzheimer Nederland; performed contract research for Rodin, IONIS, AVID, Eli Lilly, UCB, DIAN-TU, and Janssen; was a speaker at a symposium organized by Springer Healthcare; has a consultancy agreement with IXICO for PET visual readings; is a trainer for GE; and receives financial compensation only from Amsterdam UMC. Charlotte Teunissen is on the European Commission (Marie Curie International Training Network, grant 860197 [MIRIADE], and JPND), Health Holland, the Dutch Research Council (ZonMW), the Alzheimer Drug Discovery Foundation, the Selfridges Group Foundation, Alzheimer Netherlands, and the Alzheimer Association; is a recipient of ABOARD (a public-private partnership receiving funding from ZonMW [grant 73305095007] and Health~Holland, Topsector Life Sciences & Health [PPP-allowance LSHM20106]); has collaboration contracts with ADx Neurosciences, Quanterix, and Eli Lilly; performs contract research for AC-Immune, Axon Neurosciences, Biogen, Brainstorm Therapeutics, Celgene, EIP Pharma, Eisai, PeopleBio, Roche, Toyama, and Vivoryon; and is on editorial boards for *Medicaid Neurologie/Springer*, *Alzheimer's Research & Therapy*, and *Neurology: Neuroimmunology & Neuroinflammation*. No other potential conflict of interest relevant to this article was reported.

ACKNOWLEDGMENTS

We thank all participants for their dedication. Research of Alzheimer Center Amsterdam is part of the neurodegeneration research program of Amsterdam Neuroscience.

KEY POINTS

QUESTION: How do cross-sectional and longitudinal plasma pTau181 and tau PET perform in predicting cognitive stage, preclinical A β status, and longitudinal cognition?

PERTINENT FINDINGS: Both plasma pTau181 and tau PET discriminated A β -negative from A β -positive cognitively unimpaired individuals with high accuracy. Tau PET outperformed plasma pTau181 in discriminating cognitively impaired from unimpaired individuals and in predicting cognitive decline. Both plasma pTau181 and tau PET showed steeper longitudinal increases in cognitively impaired than unimpaired individuals, but only annual changes in tau PET were associated with longitudinal cognitive decline.

IMPLICATIONS FOR PATIENT CARE: Both plasma pTau181 and tau PET can be used for predicting A β status, but tau PET better monitors disease stage and predicts cognitive decline.

REFERENCES

- Scheltens P, De Strooper B, Kivipelto M, et al. Alzheimer's disease. *Lancet*. 2021; 397:1577–1590.
- Spires-Jones TL, Hyman BT. The intersection of amyloid beta and tau at synapses in Alzheimer's disease. *Neuron*. 2014;82:756–771.
- Nelson PT, Alafuzoff I, Bigio EH, et al. Correlation of Alzheimer disease neuropathologic changes with cognitive status: a review of the literature. *J Neuropathol Exp Neurol*. 2012;71:362–381.
- Blennox K, Hampel H, Weiner M, Zetterberg H. Cerebrospinal fluid and plasma biomarkers in Alzheimer disease. *Nat Rev Neurol*. 2010;6:131–144.

5. Marquié M, Normandin MD, Vanderburg CR, et al. Validating novel tau positron emission tomography tracer [F-18]-AV-1451 (T807) on postmortem brain tissue. *Ann Neurol*. 2015;78:787–800.
6. Mielke MM, Hagen CE, Xu J, et al. Plasma phospho-tau181 increases with Alzheimer's disease clinical severity and is associated with tau- and amyloid-positron emission tomography. *Alzheimers Dement*. 2018;14:989–997.
7. Thijssen EH, La Joie R, Wolf A, et al. Diagnostic value of plasma phosphorylated tau181 in Alzheimer's disease and frontotemporal lobar degeneration. *Nat Med*. 2020;26:387–397.
8. Janelidze S, Mattsson N, Palmqvist S, et al. Plasma P-tau181 in Alzheimer's disease: relationship to other biomarkers, differential diagnosis, neuropathology and longitudinal progression to Alzheimer's dementia. *Nat Med*. 2020;26:379–386.
9. Karikari TK, Pascoal TA, Ashton NJ, et al. Blood phosphorylated tau 181 as a biomarker for Alzheimer's disease: a diagnostic performance and prediction modelling study using data from four prospective cohorts. *Lancet Neurol*. 2020;19:422–433.
10. Thijssen EH, La Joie R, Strom A, et al. Plasma phosphorylated tau 217 and phosphorylated tau 181 as biomarkers in Alzheimer's disease and frontotemporal lobar degeneration: a retrospective diagnostic performance study. *Lancet Neurol*. 2021;20:739–752.
11. Simrén J, Leuzy A, Karikari TK, et al. The diagnostic and prognostic capabilities of plasma biomarkers in Alzheimer's disease. *Alzheimers Dement*. 2021;17:1145–1156.
12. Pereira JB, Janelidze S, Stomrud E, et al. Plasma markers predict changes in amyloid, tau, atrophy and cognition in non-demented subjects. *Brain*. 2021;144:2826–2836.
13. Palmqvist S, Tideman P, Cullen N, et al. Prediction of future Alzheimer's disease dementia using plasma phospho-tau combined with other accessible measures. *Nat Med*. 2021;27:1034–1042.
14. Karikari TK, Benedet AL, Ashton NJ, et al. Diagnostic performance and prediction of clinical progression of plasma phospho-tau181 in the Alzheimer's Disease Neuroimaging Initiative. *Mol Psychiatry*. 2021;26:429–442.
15. Ossenkoppele R, Rabinovici GD, Smith R, et al. Discriminative accuracy of [¹⁸F]flortaucipir positron emission tomography for Alzheimer disease vs other neurodegenerative disorders. *JAMA*. 2018;320:1151–1162.
16. Leuzy A, Smith R, Ossenkoppele R, et al. Diagnostic performance of RO948 F 18 tau positron emission tomography in the differentiation of Alzheimer disease from other neurodegenerative disorders. *JAMA Neurol*. 2020;77:955–965.
17. Ossenkoppele R, Smith R, Mattsson-Carlgrén N, et al. Accuracy of tau positron emission tomography as a prognostic marker in preclinical and prodromal Alzheimer disease: a head-to-head comparison against amyloid positron emission tomography and magnetic resonance imaging. *JAMA Neurol*. 2021;78:961–971.
18. La Joie R, Visani AV, Baker SL, et al. Prospective longitudinal atrophy in Alzheimer's disease correlates with the intensity and topography of baseline tau-PET. *Sci Transl Med*. 2020;12:eaa5732.
19. Jack CR, Wiste HJ, Botha H, et al. The bivariate distribution of amyloid-beta and tau: relationship with established neurocognitive clinical syndromes. *Brain*. 2019;142:3230–3242.
20. van der Flier WM, Scheltens P. Amsterdam dementia cohort: performing research to optimize care. *J Alzheimers Dis*. 2018;62:1091–1111.
21. Jessen F, Amariglio RE, van Bortel M, et al. A conceptual framework for research on subjective cognitive decline in preclinical Alzheimer's disease. *Alzheimers Dement*. 2014;10:844–852.
22. Albert MS, DeKosky ST, Dickson D, et al. The diagnosis of mild cognitive impairment due to Alzheimer's disease: recommendations from the National Institute on Aging-Alzheimer's Association workgroups on diagnostic guidelines for Alzheimer's disease. *Alzheimers Dement*. 2011;7:270–279.
23. McKhann GM, Knopman DS, Chertkow H, et al. The diagnosis of dementia due to Alzheimer's disease: recommendations from the National Institute on Aging-Alzheimer's Association workgroups on diagnostic guidelines for Alzheimer's disease. *Alzheimers Dement*. 2011;7:263–269.
24. Tijms BM, Willems EAJ, Zwan MD, et al. Unbiased approach to counteract upward drift in cerebrospinal fluid amyloid-beta 1-42 analysis results. *Clin Chem*. 2018;64:576–585.
25. Slot RER, Verfaillie SCJ, Overbeek JM, et al. Subjective Cognitive Impairment Cohort (SCIENCe): study design and first results. *Alzheimers Res Ther*. 2018;10:76.
26. Bayoumy S, Verberk IMW, den Dulk B, et al. Clinical and analytical comparison of six Simoa assays for plasma P-tau isoforms P-tau181, P-tau217, and P-tau231. *Alzheimers Res Ther*. 2021;13:198.
27. Tuncel H, Visser D, Yaqub M, et al. Effect of shortening the scan duration on quantitative accuracy of [¹⁸F]flortaucipir studies. *Mol Imaging Biol*. 2021;23:604–613.
28. Golla SS, Wolters EE, Timmers T, et al. Parametric methods for [¹⁸F]flortaucipir PET. *J Cereb Blood Flow Metab*. 2020;40:365–373.
29. Braak H, Braak E. Neuropathological staging of Alzheimer-related changes. *Acta Neuropathol (Berl)*. 1991;82:239–259.
30. Wolters EE, Ossenkoppele R, Verfaillie SCJ, et al. Regional [¹⁸F]flortaucipir PET is more closely associated with disease severity than CSF p-tau in Alzheimer's disease. *Eur J Nucl Med Mol Imaging*. 2020;47:2866–2878.
31. Coomans EM, Tomassen J, Ossenkoppele R, et al. Genetically identical twins show comparable tau PET load and spatial distribution. *Brain*. 2022;145:3571–3581.
32. Golla SSV, Timmers T, Ossenkoppele R, et al. Quantification of tau load using [¹⁸F]AV1451 PET. *Mol Imaging Biol*. 2017;19:963–971.
33. Vollmar S, Michel C, Treffert JT, et al. HeinzCluster: accelerated reconstruction for FORE and OSEM3D. *Phys Med Biol*. 2002;47:2651–2658.
34. Hammers A, Allom R, Koeppe MJ, et al. Three-dimensional maximum probability atlas of the human brain, with particular reference to the temporal lobe. *Hum Brain Mapp*. 2003;19:224–247.
35. Svarer C, Madsen K, Hasselbalch SG, et al. MR-based automatic delineation of volumes of interest in human brain PET images using probability maps. *Neuroimage*. 2005;24:969–979.
36. Cho H, Choi JY, Hwang MS, et al. In vivo cortical spreading pattern of tau and amyloid in the Alzheimer disease spectrum. *Ann Neurol*. 2016;80:247–258.
37. Ossenkoppele R, van der Flier WM, Verfaillie SC, et al. Long-term effects of amyloid, hypometabolism, and atrophy on neuropsychological functions. *Neurology*. 2014;82:1768–1775.
38. Jutten RJ, Sikkes SAM, Amariglio RE, et al. Identifying sensitive measures of cognitive decline at different clinical stages of Alzheimer's disease. *J Int Neuropsychol Soc*. 2021;27:426–438.
39. Mattsson-Carlgrén N, Andersson E, Janelidze S, et al. Abeta deposition is associated with increases in soluble and phosphorylated tau that precede a positive tau PET in Alzheimer's disease. *Sci Adv*. 2020;6:eaa2387.
40. Hanseeuw BJ, Betensky RA, Jacobs HIL, et al. Association of amyloid and tau with cognition in preclinical Alzheimer disease: a longitudinal study. *JAMA Neurol*. 2019;76:915–924.
41. Jack CR, Wiste HJ, Weigand SD, et al. Predicting future rates of tau accumulation on PET. *Brain*. 2020;143:3136–3150.
42. Mattsson-Carlgrén N, Janelidze S, Palmqvist S, et al. Longitudinal plasma p-tau217 is increased in early stages of Alzheimer's disease. *Brain*. 2020;143:3234–3241.
43. Young CB, Landau SM, Harrison TM, Poston KL, Mormino EC; ADNI. Influence of common reference regions on regional tau patterns in cross-sectional and longitudinal [¹⁸F]-AV-1451 PET data. *Neuroimage*. 2021;243:118553.
44. Barthelemy NR, Horie K, Sato C, Bateman RJ. Blood plasma phosphorylated-tau isoforms track CNS change in Alzheimer's disease. *J Exp Med*. 2020;217:e20200861.
45. Palmqvist S, Janelidze S, Quiroz YT, et al. Discriminative accuracy of plasma phospho-tau217 for Alzheimer disease vs other neurodegenerative disorders. *JAMA*. 2020;324:772–781.
46. Mielke MM, Dage JL, Frank RD, et al. Performance of plasma phosphorylated tau 181 and 217 in the community. *Nat Med*. 2022;28:1398–1405.

A Visual Interpretation Algorithm for Assessing Brain Tauopathy with ^{18}F -MK-6240 PET

John P. Seibyl^{1,2}, Jonathan M. DuBois³, Annie Racine³, Jessica Collins³, Qi Guo⁴, Dustin Wooten³, Eddie Stage⁴, David Cheng², Roger N. Gunn², Lilly Porat², Alex Whittington², Phillip H. Kuo⁵, Masanori Ichise⁶, Robert Comley⁴, Laurent Martarello³, and Cristian Salinas³

¹Institute for Neurodegenerative Disorders, New Haven, Connecticut; ²Invicro, New Haven, Connecticut; ³Biogen, Cambridge, Massachusetts; ⁴AbbVie, North Chicago, Illinois; ⁵University of Arizona, Tucson, Arizona; and ⁶National Institute of Radiological Sciences, National Institutes for Quantum and Radiological Science and Technology, Chiba, Japan

In vivo characterization of pathologic deposition of tau protein in the human brain by PET imaging is a promising tool in drug development trials of Alzheimer disease (AD). 6-(fluoro- ^{18}F)-3-(1H-pyrrolo[2,3-c]pyridin-1-yl)isoquinolin-5-amine (^{18}F -MK-6240) is a radiotracer with high selectivity and subnanomolar affinity for neurofibrillary tangles that shows favorable nonspecific brain penetration and excellent kinetic properties. The purpose of the present investigation was to develop a visual assessment method that provides both an overall assessment of brain tauopathy and regional characterization of abnormal tau deposition. **Methods:** ^{18}F -MK-6240 scans from 102 participants (including cognitively normal volunteers and patients with AD or other neurodegenerative disorders) were reviewed by an expert nuclear medicine physician masked to each participant's diagnosis to identify common patterns of brain uptake. This initial visual read method was field-tested in a separate, nonoverlapping cohort of 102 participants, with 2 additional naïve readers trained on the method. Visual read outcomes were compared with semiquantitative assessments using volume-of-interest SUV ratio. **Results:** For the visual read, the readers assessed 8 gray-matter regions per hemisphere as negative (no abnormal uptake) or positive (1%–25% of the region involved, 25%–75% involvement, or >75% involvement) and then characterized the tau binding pattern as positive or negative for evidence of tau and, if positive, whether brain uptake was in an AD pattern. The readers demonstrated agreement 94% of the time for overall positivity or negativity. Concordance on the determination of regional binary outcomes (negative or positive) showed agreement of 74.3% and a Fleiss κ of 0.912. Using clinical diagnosis as the ground truth, the readers demonstrated a sensitivity of 73%–79% and specificity of 91%–93%, with a combined reader-concordance sensitivity of 80% and specificity of 93%. The average SUV ratio in cortical regions showed a robust correlation with visually derived ratings of regional involvement ($r = 0.73$, $P < 0.0001$). **Conclusion:** We developed a visual read algorithm for ^{18}F -MK-6240 PET offering determination of both scan positivity and the regional degree of cortical involvement. These cross-sectional results show strong interreader concordance on both binary and regional assessments of tau deposition, as well as good sensitivity and excellent specificity supporting use as a tool for clinical trials.

Key Words: neurology; PET; Alzheimer disease; MK-6240; PET; tau proteinopathies

J Nucl Med 2023; 64:444–451
DOI: 10.2967/jnumed.122.264371

Received May 11, 2022; revision accepted Sep. 21, 2022.
For correspondence or reprints, contact John P. Seibyl (jseibyl@seibyl.com).
Published online Sep. 29, 2022.
COPYRIGHT © 2023 by the Society of Nuclear Medicine and Molecular Imaging.

The recent introduction of tau PET imaging biomarkers for clinical and research applications provides a powerful tool for corroborating the patterns of pathologic progression in Alzheimer disease (AD) suggested by postmortem studies (1), as well as potentially offering a way to monitor response to treatments designed to interrupt AD brain pathology (2,3). Tau PET imaging shows a good correlation between regional brain uptake and clinical and psychometric measures in cross-sectional studies (4–7). Indeed, increased density and spread of abnormal uptake in tau PET images is consistent with progression of the disease in patients with early or mild AD and is associated with the degree of neuropsychologic impairment.

Tau PET studies have corroborated findings from pathologic postmortem examination of AD brains, which demonstrated initial cortical uptake in the entorhinal cortex and medial temporal structures, extending to the inferolateral temporal and superolateral temporal structures and to the neocortical occipital, posterior cingulate, parietal, and frontal cortices (8). Temporal lobe structures, especially the mesial temporal gyri and hippocampus, are the earliest neocortical regions to manifest neurofibrillary tangles (9), suggesting that visual read methods might focus particular attention here. The first-generation tau PET agent ^{18}F -flortaucipir (^{18}F -AV-1451), which was used in the largest clinicopathologic study of AD and mild cognitive impairment (MCI) (10), has off-target uptake in areas adjacent to the mesial temporal lobe, limiting the ability to assess the tau pathology of this important region.

6-(fluoro- ^{18}F)-3-(1H-pyrrolo[2,3-c]pyridin-1-yl)isoquinolin-5-amine (^{18}F -MK-6240) is a second-generation tau PET imaging agent with high specificity and low off-target binding in gray and white matter, representing improvements over first-generation tracers (11,12). In cognitively normal individuals, ^{18}F -MK-6240 demonstrates homogeneous uptake such that some structural features such as the ventricles are visualized but without evidence of focal uptake in the neocortex. AD patients show a pattern of cortical uptake that is more intense, asymmetric, and focal (13), consistent with the distribution of the tau pathology reported in postmortem studies (9).

As the utility of tau PET radiotracers such as ^{18}F -MK-6240 expands, potential future clinical applications in AD may include aiding in the differential diagnosis of patients with cognitive impairment, screening for eligibility for long-term treatments to slow disease progression, monitoring the effectiveness of such treatments, assessing the course of disease, and serving as a prognostic biomarker potentially identifying at-risk cohorts. For any of these indications, a robust method for visual assessment will be an important way to evaluate ^{18}F -MK-6240 PET images, especially in the clinical setting, where an interpretation of the

tau PET scan as negative or positive is a primary goal. However, unlike amyloid PET, tau uptake patterns demonstrate dynamic heterogeneity in individuals with AD, both in the spatial extent within the brain and in the intensity of uptake within regions. These patterns offer an opportunity to obtain additional information from the visual read relevant to clinical research trials. Specifically, it may be possible to visually assess changes in the extent of uptake within regions over time, as well as between regions. Thus, it may be possible to elicit tau progression information from the visual interpretation.

The goals of the present study were to develop, field-test, and refine a visual read method for ^{18}F -MK-6240 PET as a potential tool for assessing in vivo brain tau accumulation, providing a read-out of tau positivity and negativity and of the spatial extent of uptake within individual regions. The latter may be relevant to assessing within-patient changes in the context of clinical therapeutic drug trials in which the tau PET signal might be expected to be unchanged or even decrease on serial imaging.

MATERIALS AND METHODS

Imaging Data

Pooled imaging data provided under informed consent from 204 participants with various diagnoses (cognitively normal controls [CNs], patients with MCI due to AD, patients with AD dementia, and patients with non-AD brain disorders) were obtained from Cerevu Technologies, which gathered, curated, organized, and archived the data under contractual agreement from 9 separate studies at 9 clinical sites. All studies had Investigational Review Board approval, and participants provided written informed consent for the procedures, including handling of imaging data. Scans were received as reconstructed anonymized DICOM image volumes corrected for scatter, randoms, and attenuation. Data from each center were acquired according to its own imaging protocol, and scan time windows were therefore not guaranteed to overlap at later postinjection times. Therefore, to generate an average static image for visual assessments, we used the most common overlapping late time-frame window (6×5 -min frames), which was between 60 and 90 min after injection.

Definition of MK-6240 Uptake Patterns

For developing the visual read method, we randomly selected a subset of the original database containing 102 participants (52 CN, 17 MCI, 29 AD, and 4 non-AD neurologic disease). ^{18}F -MK-6240 averaged images, obtained by creating a mean image from the serial static 5-min frames within the 60- to 90-min time window, were reviewed by an experienced nuclear medicine physician-researcher (reader 0) without a pre-specified examination protocol and masked to each participant's diagnosis and imaging site. This process of unguided examination led to the identification and categorization of common uptake patterns that were generally consistent with current understanding of AD tau pathophysiology and patterns that were better described as non-AD or off-target binding. On the basis of this review, an initial visual read procedure was developed for field testing and refinement using the second half of the image dataset (102 different, nonoverlapping participants).

Visual Assessment Algorithm for ^{18}F -MK-6240

The visual assessment of ^{18}F -MK-6240 is a 3-step process involving, first, assessment of

technical adequacy; second, systematic review of neocortical areas for the presence and spatial extent of increased radiotracer uptake; and third, application of a rule set to the findings of step 2 for determination of positivity and classification as an AD pattern or not. Details are described in section S-1 of the supplemental materials (supplemental materials are available at <http://jnm.snmjournals.org>).

Readers focus on 8 prespecified brain regions in each hemisphere of the cerebral cortex (16 regions total): hippocampus, mesial temporal, inferior temporal, lateral temporal, parietal, posterior cingulate, occipital, and frontal lobes (Fig. 1). Temporal regions are grouped under the designation cluster 1, whereas the extratemporal cortical regions are grouped under the designation cluster 2. Cluster 3 comprises subcortical regions (striatum/globus pallidus, thalamus, pons, and dentate nucleus) suggestive of binding related to non-AD tauopathy.

For each of the 16 cortical regions, the reader—informed by training examples—ascertains whether there is abnormally increased radiotracer in the region relative to the cerebellum. The reader also assigns a regional-extent score expressed as the percentage of the region showing abnormal increased uptake: none (0%), 1%–25%, 26%–75%, or more than 75% involvement of the region.

Regional positivity is defined by either focal or confluent uptake involving at least 1%–25% of the region (Table 1). Readers are asked to judge the extent (voxels with increased uptake within each region) rather than the intensity of uptake.

The initial algorithm for assessing positivity was according to 3 rules (Fig. 2). This initial set of rules was refined further on the basis of additional information and experience. Rule 1 is that a scan showing normal findings has no more than one region of focally increased uptake in clusters 1 or 2 (combined) and no regions of focal uptake in cluster 3. Rule 2 is that a scan positive for the AD pattern shows two or more cluster 1–positive or 2–positive regions, with at least one positive region in cluster 1 and no positive regions in cluster 3. Rule 3 is that a scan positive for the non-AD pattern shows two or more cluster 2–positive or cluster 3–positive regions, with no positive regions in cluster 1.

Readers

Two board-certified nuclear medicine physicians with research backgrounds in brain molecular imaging and some experience with flortaucipir PET, but naïve to ^{18}F -MK-6240, served as testers of the read method. First, readers reviewed the scientific background, study rationale, and description of the read method with focus on brain region identification. After a group case review and individual testing for competency, field testing with the 2 independent readers and

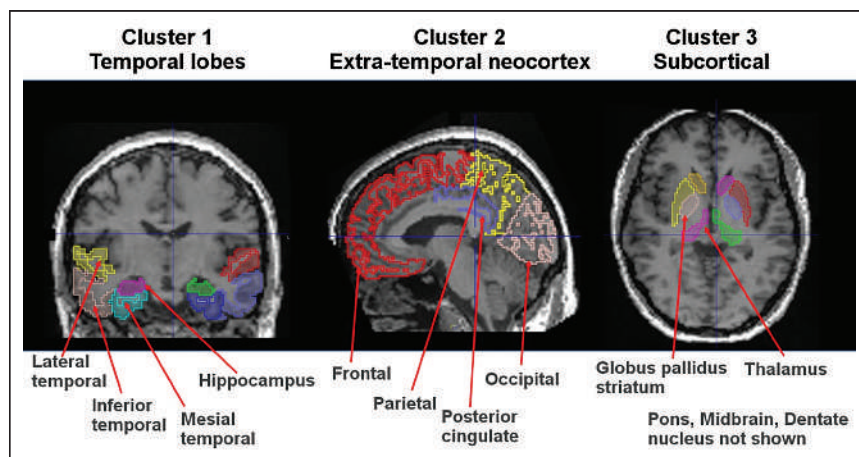


FIGURE 1. Regions for visual read are outlined and overlaid on T1-weighted MR images for anatomic reference.

TABLE 1
Regions for Visual Assessment

Brain area	Included regions	Visual rating	No. regions	Rationale
Cluster 1, temporal lobes	Hippocampus; mesial temporal; inferior temporal; lateral temporal	No uptake (0%); uptake 1%–25%; extension 26%–75%; >75% extension	8 regions: 4 each in left and right hemispheres	Earliest cortical regions involved in AD per Braak staging
Cluster 2, extratemporal neocortex	Occipital; posterior cingulate; parietal; frontal	No uptake (0%); uptake 1%–25%; extension 26%–75%; >75% extension	8 regions: 4 each in left and right hemispheres	Next regions involved in AD
Cluster 3, subcortical area	Striatum-globus; thalamus; dentate nucleus; pons; midbrain	Presence or absence	5 regions	May be positive in non-AD tauopathies

1 in-house expert reader was performed. In total, 112 test scans (102 cases + 10 repeat scans) were randomly presented without clinical or diagnostic information.

Scans were read in either linear gray scale or inverse gray scale. Readers were not provided MRI or CT results or other structural information. Images were maintained on a DICOM server accessed by remote desktop software to run PMOD, version 3.8 (PMOD Technologies), for visual display and adjustment of the PET scans. All interactions with the read platform were logged by PMOD. Readers recorded their findings in an electronic report form, which captured data, time, and user information for each case. Reads were conducted by 2 readers over 2 d and 1 reader over 7 d, all initiated within 1 d of the training.

Evaluation of Read Method

Binary readouts (positive or negative) for tau deposition by the 2 field test readers (readers 1 and 2) were compared with the gold standard read by the internal nuclear medicine reader (reader 0). Concordance for visual assessment among all 3 readers was tallied for positive and negative cases and expressed as a percentage. Cohen κ and Fleiss κ were used to assess reader-by-reader and group agreement, correcting for chance agreement for the overall scan assessment. Agreement was also evaluated on a region-by-region basis among all 3 readers for both the binary determination and regional extent using the Fleiss κ -statistic (14). In addition, an exploratory overall tau visual regional-extent score (VRES) was calculated for each region by

assigning a value to the categoric region score of 1 for visual scores of more than 75%, 0.5 for scores of 26%–75%, 0.25 for scores of less than 25%, and 0 for scores of 0. Hence, a scan with complete bilateral uptake involving greater than 75% extension throughout each region has a total VRES of 16.

Other assessments included intrarater test–retest reliability for scan positivity or negativity, determined for those scans ($n = 10$) that were randomly presented twice to the readers; sensitivity, specificity, and area under the receiver-operating-characteristic curve, determined using the site clinical diagnosis for participants for whom this information was available ($n = 91$); and self-reported reader confidence in their assessments (supplemental materials, section S-2).

Comparison with SUV Ratio (SUVr)

SUVr was used to compare the brain uptake in regions involved in Braak stages 1–6 and the volume-of-interest (VOI) sampling of Jack et al. (15) to binary and VRES reads. T1-weighted MR images and ^{18}F -MK-6240 PET scans were obtained from the Cerveau database. ^{18}F -MK-6240 PET scans were processed and analyzed similarly to visual read images. Details of the image processing are provided in the supplemental materials, section S-3.

Statistical Analysis

Comparison between demographics in the development and testing scan groups used descriptive statistics and unpaired t tests. For visual reads, percentage concordance against the read standard (reader 0) was determined, and pairwise and group reader agreement was assessed with Cohen and Fleiss κ -statistics, respectively. The readers' total VRES (0–16) was compared using ANOVA and post hoc Welch t tests. VRES totals were also correlated with SUVr using Pearson correlation. Further, individual visual reads, VRES analyses, and SUVrs using different VOI strategies underwent receiver-operating-characteristic curve analysis for determination of sensitivity and specificity against the clinical site diagnosis as the truth standard.

Refinement of Algorithm for Assessing Positivity

After the masked read, a study close-out and image review with all readers assessed the adequacy of the initial rule set for describing scans encountered in the presented cases.

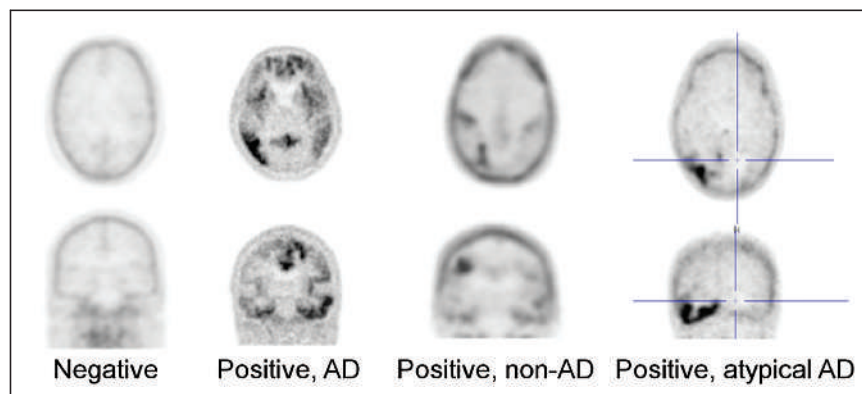


FIGURE 2. ^{18}F -MK-6240 PET in CN volunteer, AD patient, and patient with non-AD tauopathy. “Positive, atypical AD” was added in refined algorithm. Non-AD tauopathy patterns with only subcortical (cluster 3) and no cortical uptake (clusters 1 and 2), as would be expected in progressive supranuclear palsy (PSP), were not encountered in this primarily MCI/AD dataset.

This information was supplemented by other data sources, including published studies on the regional patterns of radiotracer uptake and review of another internal ^{18}F -MK-6240 PET dataset of MCI and mild-AD participants. On this basis, the algorithm was refined. These refinements were then applied to the original dataset for comparison to the preliminary algorithm.

RESULTS

Overall Binary Scan Assessment

The development ($n = 102$) and testing ($n = 102$) datasets were not significantly different with regard to age, self-reported sex, or diagnostic cohort (Table 2). No scans were excluded from review by any reader for technical deficiencies.

Comparing overall binary tau positivity (original rules 2 and 3) against the gold standard by reader 0, both reader 1 and reader 2 had a high level of concordance, with complete agreement on 107 (95%) and 108 (95%) of 112 scans (102 original + 10 repeated), respectively. All 3 readers were in complete agreement on 105 of 112 cases (94%). The Cohen κ for pairwise comparisons was 0.964 and 0.955, respectively, for reader 0 versus reader 1 and reader 0 versus reader 2, indicating excellent agreement. The Fleiss κ for interreader agreement among all 3 readers was 0.912, again indicating excellent agreement. Review of the 7 discordant cases showed 2 primary causes: the first was technical issues such as improper attenuation correction or reconstruction errors due to motion artifacts on scans judged to be still interpretable ($n = 5$), and the second was uptake in the inferior and mesial temporal lobes that was incorrectly attributed to off-target meningeal uptake at the base of the skull ($n = 2$) (Fig. 3). Discrimination of this nonspecific uptake from adjacent cortical regions may be improved by leveraging structural imaging (MRI or CT), which was not allowed in the present study (Supplemental Fig. 1).

Regional Assessments

Assessments were made in 1,792 regions ($112 \text{ cases} \times 16 \text{ regions}$). Evaluation of the 16 regions for reader agreement on the binary determination of positivity or negativity for each region showed that 3 of 3 readers agreed in 1,329 regional reads (74.3% of regions), 2 of 3 readers agreed in 367 regional reads (20.4%), and 96 regions were read (5.3%) with complete discordance. Over the 16 regions, complete agreement among the 3 readers ranged from 69% to 86%. There was excellent agreement for some regions, with the Fleiss κ ranging from 0.726 (left mesial temporal) to 0.945 (right parietal) (Table 3).

TABLE 2
Demographic Data

Group	Development dataset				Test dataset			
	<i>n</i>	Age (y)	Sex (<i>n</i>)		<i>n</i>	Age (y)	Sex (<i>n</i>)	
			M	F			M	F
AD	29	72.4 (9.9)	20	9	24	70.4 (10.7)	12	12
MCI	17	71.2 (7.1)	11	6	21	69.9 (8.0)	12	9
CN	52	66.4 (12.1)	25	27	45	68.6 (7.5)	18	27
Other	4	63.3 (4.6)	0	4	12	65.9 (9.4)	5	7

Age is mean followed by SD in parentheses.

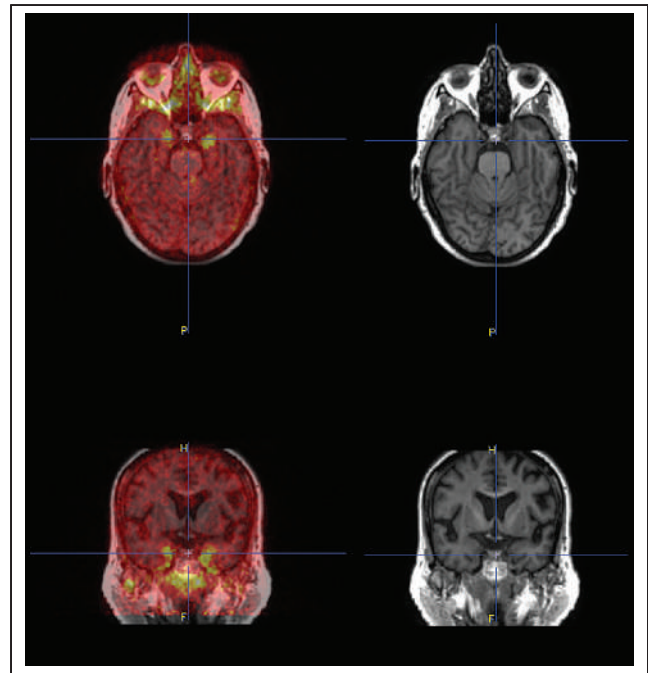


FIGURE 3. Difficult case showing bilateral anterior mesial temporal uptake, which can be confused with off-target uptake in meninges and floor of calvarium. Fused axial image of MK-6240 with the participant's T1-weighted MR image (top left), fused coronal image of MK-6240 with the participant's T1-weighted MR image (bottom left); axial (top right) and coronal (bottom right) views of MRI only.

Evaluation of reader agreement across the 4 possible regional responses (0, <25%, 25%–75%, and >75%) showed substantial agreement for 8 of 16 regions and moderate agreement for the other 8 regions. The regions demonstrating the highest reader agreement were the lateral temporal lobes and posterior cingulate cortex, whereas those regions demonstrating the least reader agreement were the occipital lobes, right hippocampus, and left mesial temporal lobe.

Reproducibility

The reproducibility of the 10 randomly selected cases for binary determination of positive or negative was excellent, with readers 0 and 2 achieving 100% reproducibility and reader 1 achieving 90%. The reproducibility of the binary positive-or-negative determination for the 16 cortical regions for the 10 repeated case pairs was also very good, with readers 0, 1, and 2 showing 93.8%, 95.0%, and 98.8% self-agreement, respectively, for the 10 case pairs of 16 regions. Overall, of the 480 region pairs (10 case pairs of 16 regions each for 3 readers) assessed with the VRES score, 460 (95.8%) of the reads were scored identically. Regions that demonstrated the most intrareader disagreement were the left and right inferior temporal lobes, which together had 8 intrareader disagreements.

Comparison with Clinical Diagnosis

In 91 of the 102 (89%) cases for which a clear, well-supported clinical diagnosis of AD, MCI, or CN was available from the site, we assessed binary visual reads, total VRES, and diagnostic sensitivity and specificity. Among the CN volunteers, 42 of 45 had negative visual reads; positive visual reads were noted in 22 of 28 AD cases and 12 of 18 MCI cases. The consensus read for the overall binary determination of scan positivity (2/3 or 3/3 readers agree) relative to a site diagnosis of cognitive impairment due to AD or

TABLE 3
Reader Agreement on Visual Assessment as Positive or Negative for Regional Tau

Regional binary agreement on positive or negative			Complete agreement on spatial extent scoring		
Agreement	Region	Fleiss κ	Agreement	Region	Fleiss κ
Almost perfect	Right parietal	0.945	Substantial	Right lateral temporal	0.748
	Right frontal	0.929		Left lateral temporal	0.716
	Right lateral temporal	0.907		Right posterior cingulate	0.702
	Left parietal	0.906		Left posterior cingulate	0.678
	Left posterior cingulate	0.904		Right parietal	0.655
	Left lateral temporal	0.888		Left parietal	0.621
	Right posterior cingulate	0.87		Right frontal	0.618
	Substantial	Left frontal		0.801	Left frontal
Left occipital		0.801	Moderate	Right inferior temporal	0.597
Left hippocampus		0.783		Left inferior temporal	0.576
Right inferior temporal		0.782		Right hippocampus	0.552
Right occipital		0.759		Right mesial temporal	0.552
Right hippocampus		0.756		Left hippocampus	0.551
Left inferior temporal		0.753		Left mesial temporal	0.545
Right mesial temporal		0.742		Right occipital	0.537
Left mesial temporal		0.726		Left occipital	0.503

Overall binary assessment, $\kappa = 0.912$.

AD dementia had a sensitivity of 81% and specificity of 93%. Comparing the visual findings of each reader with the site clinical diagnosis as the ground truth demonstrated excellent specificity and moderate to good sensitivity for the visual read method (Table 4).

Comparison with SUVr

SUVr was calculated for 87 subjects who had T1-weighted MR images for coregistration and regional segmentation. When parsed

by visual read status, negative and positive read groups demonstrated a significantly different mean SUVr ($P < 0.001$) for all individual Braak regions, Braak regional combinations (Braak 1–2, 3–4, and 5–6), and VOI regions of Jack et al. (15) (Supplemental Table 1). Individual read data (Fig. 4) demonstrated clustering of negative scans around an SUVr of 1 (no specific binding), whereas visually positive scans showed higher SUVrs spread over a wider range. Although most negative scans clustered around an SUVr of 1, we showed a strong association ($r = 0.73$, $P < 0.0001$) between quantitative SUVrs from Braak 3–4 and semiquantitative VRES summed across all readers (Supplemental Fig. 2). In addition, we examined

TABLE 4
Sensitivity and Specificity of MK-6240 Visual Reads and SUVr Analyses Using Clinical Diagnosis as Standard of Truth

Method	Sensitivity	Specificity	Youden index
Visual read			
Reader 0	0.79	0.93	0.72
Reader 1	0.75	0.93	0.68
Reader 2	0.79	0.91	0.70
Consensus	0.81	0.93	0.74
Visual VRES (cutoff, 1.5)	0.742	0.890	0.63
SUVr			
Braak 1–2 (cutoff, 1.4)	0.649	0.888	0.54
Braak 3–4 (cutoff, 1.3)	0.645	0.963	0.61
Braak 5–6 (cutoff, 1.2)	0.611	0.960	0.57
Jack VOI (cutoff, 1.4)	0.650	0.880	0.53

Jack VOI = VOI regions of Jack et al. (15).

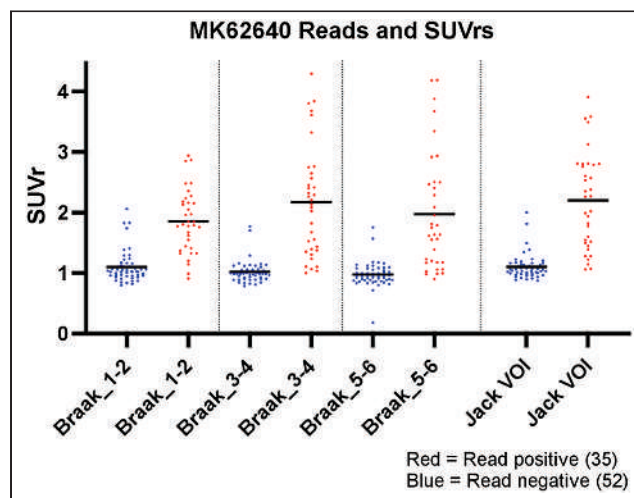


FIGURE 4. SUVr for different regional VOIs parsed by visual read of negative or positive. Jack VOI = VOI regions of Jack et al. (15).

the regional distribution of total VRES and found a Braaklike staging, with a greater number of cases showing higher VRESs in the temporal regions than in the extratemporal cortical regions (Supplemental Fig. 3).

Receiver-operating-characteristic analyses were performed to assess different VOI template sampling for SUVr relative to the clinical site diagnosis as the gold standard. Comparing VOI sampling strategies with the site clinical diagnosis as the truth standard using the highest Youden index for each analysis as the SUVr cut-off (Supplemental Fig. 4) again demonstrated excellent specificity and moderate sensitivity with Braak 3–4. The VOI regions of Jack et al. (15) showed slightly higher sensitivity and specificity than did Braak 1–2 or Braak 5–6 analyses, although the difference did not achieve statistical significance ($P = 0.59$).

Refinement of Algorithm for Assessing Positivity

The original algorithm for assessing positivity performed well in separating tau-positive from tau-negative scans consistently across readers. Nevertheless, a few changes were suggested after reader review, review of additional ^{18}F -MK-6240 PET datasets, and consideration of the published literature (16). These resulted in the adjustments described in Table 5.

The revised algorithm was applied to the regional data, with little effect on the determination of positivity by the readers. The final assessment was changed for only 1 reader in only 2 scans, both of which were reclassified from negative to positive, atypical AD pattern, improving the intrareader concordance from 90% to 100% for that reader. Overall concordance among the 3 readers showed 106 of 112 (95%) to be in complete agreement on the binary assessment of positivity.

DISCUSSION

This paper describes the development, initial evaluation, and refinement of a visual read method for ^{18}F -MK-6240 brain PET assessing the uptake patterns consistent with tau deposition in patients with AD.

The method provides 2 sets of related information: the binary determination of positive or negative for the presence of pathologic tau, and the regional extent of tau deposition in brain areas thought to be involved in the pathologic progression of AD. The utility of this method lies in its potential use in clinical trials, particularly for eligibility assessments to confirm the presence of the targeted pathology, as well as to measure disease progression and treatment effect.

We demonstrated a high reader concordance for binary (positive or negative) and regional assessment of brain uptake consistent with expected tau pathology. Discordance among readers was relatively low and was due primarily to technical artifacts or to confusion of uptake at the base of the skull for uptake in the inferior and mesial temporal lobes. As expected, absolute agreement for VRES (4 possible categories) was lower but still substantial to moderate and varied by region. Agreement among readers was lower in the temporal lobe regions (excepting the lateral temporal lobes) than in other cortical regions (e.g., parietal, posterior cingulate), perhaps because of more difficult anatomic localization relative to the more accessibly definable and larger regions and high meningeal uptake adjacent to inferomedial temporal regions.

Our data show robust test–retest reproducibility and good accuracy relative to clinical site diagnoses. The region with the lowest reproducibility was the inferior temporal lobes; signal in this region was infrequently misattributed to extracerebral uptake in surrounding regions. Off-target uptake of ^{18}F -MK-6240 involves primarily the meninges, as well as uptake at the base of the calvarium, both of which had only a minor impact on scan interpretation in this cohort and were minimized with the aid of structural imaging. This result compares favorably with that of ^{18}F -AV-1451, for which it is typically difficult to evaluate medial temporal structures because of the proximity of off-target uptake within the choroid plexus.

We observed a strong concordance between SUVr and the binary read, with visually negative reads clustered around an SUVr of 1.0, consistent with negligible binding. By contrast, visually positive scans had higher SUVrs that were about twice the value of negative

TABLE 5
Initial and Revised Algorithms for Interpreting MK-6240 PET

Scan assessment	Original algorithm	Refined algorithm	Reason for adjustment
Negative	No more than one region positive in cortex	All clusters negative	Allowing one region to be positive was to prevent interpretation of scans as positive when meningeal uptake near inferolateral temporal lobes could be misread as positive region; this was dropped with improved methods or instructions to identify this confounder
Positive, AD pattern	Evidence of increased uptake in two cortical regions with at least one region in temporal lobes	At least one cluster 1 region positive and no cluster 3 regions positive	Revision was made after observation of multiple cases with isolated cluster 1 abnormality in just one region
Positive, atypical AD pattern	Not assessed	Increased uptake in one or more regions in cluster 2 but not in clusters 1 or 3	This rare pattern was noted from review of other MK-6240 datasets and was expected pattern based on published literature on other tau PET tracers
Positive, non-AD pattern	Any positive scan not fitting AD criteria	Increased uptake in one or more regions in clusters 1–3, with at least one region in cluster 3	Adjustment was made after formalized uniform assessment for regions involved in non-AD tauopathies

reads. Analysis of the semiquantitative VRES found that uptake occurred more frequently in temporal cortical structures than in extratemporal regions, as predicted from the models of tau spread from the postmortem data. However, these differences could also be due to the lack of normalization for region size, which ran from relatively small in the mesial temporal cortex to very large in the frontal lobe. Partial-volume error correction, which was not performed, would be expected to increase the differences between temporal and nontemporal regions.

Relative to clinical diagnosis, both the visual read and SUVR analysis showed excellent specificity and moderate to good sensitivity, with the best combination of sensitivity and specificity (81% and 93%, respectively) in the consensus read. Not surprisingly, the consensus read is the most commonly used PET interpretation method for eligibility assessments in clinical therapeutic trials, where amyloid PET negativity rates may be as high as 10%–20% among individuals thought to have AD on clinical examination (17). In addition, lower sensitivity relative to clinical diagnosis is common in cross-sectional datasets given the observed tendency for the baseline clinical diagnosis to identify AD with higher sensitivity and lower specificity than does imaging when the gold standard is final clinical diagnosis after longitudinal follow-up over a year or more (18). Both the semiquantitative SUVR analysis and the visual read performed similarly for sensitivity and specificity, with visual reads having slightly higher Youden indices. Although the SUVR cutoffs used here represent an optimized Youden index (Supplemental Fig. 2), they may not be ideal for addressing other research questions, which may require a different point on the receiver-operating-characteristic curve.

Limitations

Although the readers were naïve to ^{18}F -MK-6240 PET, they were brain imaging specialists with experience reading other tau and amyloid PET tracers. Reader selection was intentional to evaluate a method designed to visually assess brain tau burden in research and clinical trials, with regional information for tracking change and comparing patients, rather than the simple binary positive/negative determination normally required in clinical routine. Hence, compared with readers who have less experience, the study readers may have more readily handled the difficult task of accurately identifying subregions within the temporal lobes and other neocortical regions. Future studies will aim to evaluate the method and training paradigm on less experienced readers to determine the generalizability of the binary and regional-extent aspects of the method. Perhaps more germane to routine clinical use is that a simpler version of this method can be used for the easier task of determining overall scan positivity.

Limitations of this study are a lack of longitudinal data, no pathologic diagnostic confirmation, and limited data on amyloid status or clinical measures to support the accuracy of clinical diagnosis. Moreover, our development sample included a limited number of MCI patients ($n = 17$), which may limit the applicability of the algorithm to clinical diagnosis and clinical trial inclusion. Specifically, in cases with lower ^{18}F -MK-6240 binding, such as in MCI, off-target binding in meningeal tissue may theoretically lower the accuracy of visual reads in proximal brain regions. Future research will aim to include a better-characterized sample, more representative of patients screened for initial memory complaints. Furthermore, there are exceptions to the rules; specifically, logopenic primary progressive aphasia will score as typical AD because of unilateral left hemispheric uptake in clusters 1 and 2. The case used as an example of positivity for the non-AD pattern (Fig. 2) raises

additional points. The case shows uptake bilaterally in the caudate and also in the right occipital and parietal regions. Is this a case of atypical AD or of non-AD tauopathy? In these rare cases, additional data may prove necessary to clarify and adjust the algorithm.

Finally, we included the midbrain in cluster 3 while instructing readers not to rate the substantia nigra as positive even though it is localized in the midbrain. This may be confusing for some, although the readers very rarely endorsed the midbrain regardless of the evident uptake in the substantia nigra.

The selection of a time window of 60–90 min was driven by the availability of the data and may not be ideal for separating negative from positive scans. In high-binding regions of positive scans, SUVrs may continue to rise past 90 min as washout proceeds (13). When one is visually comparing early versus late PET images, there is some minor residual background uptake in some of the scans. However, this is most apparent in the positive scans, which are typically easier to interpret than negative scans because of the relatively low off-target uptake. In summary, we believe that given the small impact on scan interpretability, it was preferable to open the time window rather than reduce the size of the cohort.

Future Work

Further validation of this read method is needed for greater confidence in the utility of the visual assessment toward the intended research application. The present data have resulted in a minor adjustment of the algorithm to be more reflective of the potential range of cases that a reader may encounter. Although we are confident that the proposed algorithm captures most AD-related cases, minor adjustments may be needed to better marry the scan phenomenology with the intended cohort. Future development should also focus on evaluation of patients who have serial ^{18}F -MK-6240 scans with months to years of longitudinal data, interpretation of scans over a wider range of tauopathies, evaluation in a larger group of readers with a greater range of experience with PET images, and comparison of ^{18}F -MK-6240 PET with clinical metrics and postmortem brain pathology.

CONCLUSION

This work provides a method for the visual interpretation of ^{18}F -MK-6240 brain PET images. This initial cross-sectional study demonstrated that experienced readers can use this algorithm for robust and reproducible visual interpretation of ^{18}F -MK-6240 brain scans. The overall determination of scan positivity may be useful in aiding diagnosis or enhancing the accuracy of clinical trial enrollment. Scan information derived from cortical regional assessment may be most valuable for within-patient evaluation of change over time, as well as for determining the efficacy of new treatments designed to alter the course of progression.

DISCLOSURE

The following investigators and their funding organizations contributed subject data used in this study: Davangere P. Devanand, MD, Department of Psychiatry, Columbia University Irving Medical Center, New York (grant support from R01 AG055422); Eric D. Hostetler, PhD, Merck & Co., Inc.; Keith Johnson, MD, Department of Radiology and Neurology, Massachusetts General Hospital, Harvard Medical School; Sterling C. Johnson, PhD, Alzheimer's Disease Research Center, University of Wisconsin School of Medicine and Public Health (grant support from AG021155, AG062285, AG027161, AG062715, AG062167, and S10OD025245); William C. Kreisl, MD, Taub Institute for Research on Alzheimer's Disease

and the Aging Brain, Columbia University (grant support from R01AG063888 and K23AG052633); Pedro Rosa-Neto, MD, PhD, Translational Neuroimaging Laboratory, McGill University Research Centre for Studies in Aging, Alzheimer's Disease Research Unit, Douglas Research Institute, Le Centre Intégré Universitaire de Santé et de Services Sociaux (CIUSSS) de l'Ouest-de-l'Île-de-Montréal, and Departments of Neurology and Neurosurgery, Psychiatry, and Pharmacology and Therapeutics, McGill University; Christopher C. Rowe, MD, Department of Molecular Imaging and Therapy Austin Health, Australian Dementia Network, University of Melbourne, Australian Imaging, Biomarker, and Lifestyle Study of Aging (AIBL), Florey Institute of Neuroscience and Mental Health (grant support from NHMRC APP1132604, APP1140853, and APP1152623); and Yaa-kov Stern, PhD, Taub Institute for Research on Alzheimer's Disease and the Aging Brain, Columbia University (grant support from 5R01AG038465). This study was funded by Biogen. John Seibyl is a consultant to Biogen and a distinguished scientist at Invicro. David Cheng, Roger Gunn, Lilly Porat, and Alex Whittington are employed by Invicro. Jonathan DuBois, Annie Racine, Jessica Collins, Laurent Martarello, and Cristian Salinas are employed by Biogen. Qi Guo, Dustin Wooten, Eddie Stage, and Robert Comley are employed by AbbVie. Phillip Kuo is a consultant to and employed by Invicro. Masanori Ichise is a consultant. No other potential conflict of interest relevant to this article was reported.

ACKNOWLEDGMENT

We acknowledge the very helpful scientific input and logistic support provided by Megan Stark.

KEY POINTS

QUESTION: Can a visual read method for brain tau deposition using ^{18}F -MK-6240 PET provide robust overall information on positivity or negativity and information about the regional extent of abnormal tracer uptake?

PERTINENT FINDINGS: Readers can use this algorithm for robust and reproducible visual interpretation of ^{18}F -MK-6240 brain scans at the whole-brain and regional levels.

IMPLICATIONS FOR PATIENT CARE: This read method may be a useful tool for AD clinical drug development to enhance the accuracy of clinical trial enrollment, to evaluate within-patient changes over time, and to determine the efficacy of new treatments designed to alter the course of progression.

REFERENCES

- Braak H, Del Tredici K. Top-down projections direct the gradual progression of Alzheimer-related tau pathology throughout the neocortex. *Adv Exp Med Biol.* 2019;1184:291–303.
- Dronse J, Fliessbach K, Bischof GN, et al. In vivo patterns of tau pathology, amyloid-beta burden, and neuronal dysfunction in clinical variants of Alzheimer's disease. *J Alzheimers Dis.* 2017;55:465–471.
- Knopman DS, Lundt ES, Themeau TM, et al. Joint associations of beta-amyloidosis and cortical thickness with cognition. *Neurobiol Aging.* 2018;65:121–131.
- Bao W, Jia H, Finnema S, Cai Z, Carson RE, Huang YH. PET imaging for early detection of Alzheimer's disease: from pathologic to physiologic biomarkers. *PET Clin.* 2017;12:329–350.
- Bejani A, Schonhaut DR, La Joie R, et al. Tau pathology and neurodegeneration contribute to cognitive impairment in Alzheimer's disease. *Brain.* 2017;140:3286–3300.
- Buckley RF, Hanseeuw B, Schultz AP, et al. Region-specific association of subjective cognitive decline with tauopathy independent of global beta-amyloid burden. *JAMA Neurol.* 2017;74:1455–1463.
- Hansson O, Grothe MJ, Strandberg TO, et al. Tau pathology distribution in Alzheimer's disease corresponds differentially to cognition-relevant functional brain networks. *Front Neurosci.* 2017;11:167.
- Schwarz AJ, Yu P, Miller BB, et al. Regional profiles of the candidate tau PET ligand ^{18}F -AV-1451 recapitulate key features of Braak histopathological stages. *Brain.* 2016;139:1539–1550.
- Braak H, Del Tredici K. Potential pathways of abnormal tau and alpha-synuclein dissemination in sporadic Alzheimer's and Parkinson's diseases. *Cold Spring Harb Perspect Biol.* 2016;8:a023630.
- Meyer PF, Pichet Binette A, Gonneaud J, Breitner JCS, Villeneuve S. Characterization of Alzheimer disease biomarker discrepancies using cerebrospinal fluid phosphorylated tau and AV1451 positron emission tomography. *JAMA Neurol.* 2020;77:508–516.
- Hostetler ED, Walji AM, Zeng Z, et al. Preclinical characterization of ^{18}F -MK-6240, a promising PET tracer for in vivo quantification of human neurofibrillary tangles. *J Nucl Med.* 2016;57:1599–1606.
- Koole M, Lohith TG, Valentine JL, et al. Preclinical safety evaluation and human dosimetry of [^{18}F]MK-6240, a novel PET tracer for imaging neurofibrillary tangles. *Mol Imaging Biol.* 2020;22:173–180.
- Beththausen TJ, Cody KA, Zammit MD, et al. In vivo characterization and quantification of neurofibrillary tau PET radioligand ^{18}F -MK-6240 in humans from Alzheimer disease dementia to young controls. *J Nucl Med.* 2019;60:93–99.
- Landis JR, Koch GG. The measurement of observer agreement for categorical data. *Biometrics.* 1977;33:159–174.
- Jack CR, Wiste HJ, Botha H, et al. The bivariate distribution of amyloid-beta and tau: relationship with established neurocognitive clinical syndromes. *Brain.* 2019;142:3230–3242.
- Phillips JS, Nitchie FJ VI, Da Re F, et al. Rates of longitudinal change in ^{18}F -flor-taucipir PET vary by brain region, cognitive impairment, and age in atypical Alzheimer's disease. *Alzheimers Dement.* 2022;18:1235–1247.
- Chapleau M, Iaccarino L, Soleimani-Meigooni D, Rabinovici GD. The role of amyloid PET in imaging neurodegenerative disorders: a review. *J Nucl Med.* 2022;63(suppl 1):13S–19S.
- Veitch DP, Weiner MW, Aisen PS, et al. Using the Alzheimer's Disease Neuroimaging Initiative to improve early detection, diagnosis, and treatment of Alzheimer's disease. *Alzheimers Dement.* 2022;18:824–857.

The Association of Age-Related and Off-Target Retention with Longitudinal Quantification of [¹⁸F]MK6240 Tau PET in Target Regions

Cécile Tissot¹⁻³, Stijn Servaes^{1,2}, Firoza Z. Lussier³, João Pedro Ferrari-Souza^{3,4}, Joseph Therriault^{1,2}, Pâmela C.L. Ferreira³, Gleb Bezgin^{1,2}, Bruna Bellaver^{3,4}, Douglas Teixeira Leffa³, Sulantha S. Mathotaarachchi^{1,2}, Mira Chamoun^{1,2}, Jenna Stevenson^{1,2}, Nesrine Rahmouni^{1,2}, Min Su Kang^{5,6}, Vanessa Pallen^{1,2}, Nina Margherita-Poltronetti^{1,2}, Yi-Ting Wang^{1,2}, Jaime Fernandez-Arias^{1,2}, Andrea L. Benedet⁷, Eduardo R. Zimmer^{4,8}, Jean-Paul Soucy⁹, Dana L. Tudorascu³, Annie D. Cohen³, Madeleine Sharp⁹, Serge Gauthier^{2,10}, Gassan Massarweh¹¹, Brian Lopresti¹², William E. Klunk³, Suzanne L. Baker¹³, Victor L. Villemagne³, Pedro Rosa-Neto^{1,2,9,10}, and Tharick A. Pascoal³

¹McGill University, Montreal, Quebec, Canada; ²McGill University Research Center for Studies in Aging, Montreal, Quebec, Canada; ³Departments of Psychiatry and Neurology, University of Pittsburgh School of Medicine, Pittsburgh, Pennsylvania; ⁴Graduate Program in Biological Sciences: Biochemistry, Porto Alegre, Brazil; ⁵Artificial Intelligence and Computational Neurosciences Lab, Sunnybrook Research Institute, University of Toronto, Toronto, Ontario, Canada; ⁶L.C. Campbell Cognitive Neurology Unit, Hurvitz Brain Sciences Program, Sunnybrook Research Institute, University of Toronto, Toronto, Ontario, Canada; ⁷University of Gothenburg, Gothenburg, Sweden; ⁸Department of Pharmacology, Universidade Federal do Rio Grande do Sul, Porto Alegre, Brazil; ⁹Montreal Neurological Institute, Montreal, Quebec, Canada; ¹⁰Douglas Mental Health Institute, Montreal, Quebec, Canada; ¹¹Department of Radiochemistry, Montreal Neurological Institute, Montreal, Quebec, Canada; ¹²Department of Radiology, University of Pittsburgh School of Medicine, Pittsburgh, Pennsylvania; and ¹³Lawrence Berkeley National Laboratory, Berkeley, California

6-(fluoro-¹⁸F)-3-(1H-pyrrolo[2,3-c]pyridin-1-yl)isoquinolin-5-amine ([¹⁸F]MK6240) tau PET tracer quantifies the brain tau neurofibrillary tangle load in Alzheimer disease. The aims of our study were to test the stability of common reference region estimates in the cerebellum over time and across diagnoses and evaluate the effects of age-related and off-target retention on the longitudinal quantification of [¹⁸F]MK6240 in target regions. **Methods:** We assessed reference, target, age-related, and off-target regions in 125 individuals across the aging and Alzheimer disease spectrum with longitudinal [¹⁸F]MK6240 SUVs and SUV ratios (SUVRs) (mean ± SD, 2.25 ± 0.40 y of follow-up). We obtained SUVR from meninges, exhibiting frequent off-target retention with [¹⁸F]MK6240. Additionally, we compared tracer uptake between 37 cognitively unimpaired young (CUY) (mean age, 23.41 ± 3.33 y) and 27 cognitively unimpaired older (CU) adults (amyloid-β-negative and tau-negative, 58.50 ± 9.01 y) to identify possible nonvisually apparent, age-related signal. Two-tailed *t* testing and Pearson correlation testing were used to determine the difference between groups and associations between changes in region uptake, respectively. **Results:** Inferior cerebellar gray matter SUV did not differ on the basis of diagnosis and amyloid-β status, cross-sectionally and over time. [¹⁸F]MK6240 uptake significantly differed between CUY and CU adults in the putamen or pallidum (affecting ~75% of the region) and in the Braak II region (affecting ~35%). Changes in meningeal and putamen or pallidum SUVRs did not significantly differ from zero, nor did they vary across diagnostic groups. We did not observe significant correlations

between longitudinal changes in age-related or meningeal off-target retention and changes in target regions, whereas changes in all target regions were strongly correlated. **Conclusion:** Inferior cerebellar gray matter was similar across diagnostic groups cross-sectionally and stable over time and thus was deemed a suitable reference region for quantification. Despite not being visually perceptible, [¹⁸F]MK6240 has age-related retention in subcortical regions, at a much lower magnitude but topographically colocalized with significant off-target signal of the first-generation tau tracers. The lack of correlation between changes in age-related or meningeal and target retention suggests little influence of possible off-target signals on longitudinal tracer quantification. Nevertheless, the age-related retention in the Braak II region needs to be further investigated. Future postmortem studies should elucidate the source of the newly reported age-related [¹⁸F]MK6240 signal, and in vivo studies should further explore its impact on tracer quantification.

Key Words: tau; PET; reference region; off-target binding; [¹⁸F]MK6240

J Nucl Med 2023; 64:452–459

DOI: 10.2967/jnumed.122.264434

The accumulation of amyloid-β (Aβ) plaques and hyperphosphorylated tau, forming neurofibrillary tangles (NFTs), is a hallmark of Alzheimer disease (AD) (1) and can be observed in aging and AD dementia (2). The tau levels in the brain are assessed through cerebrospinal fluid and PET imaging. Radiotracers used in PET imaging are considered optimal when they present desirable characteristics such as rapidly equilibrating in vivo kinetics, low off-target retention, no significant lipophilic radiolabeled metabolites able to enter the brain, and high affinity for their target (3).

6-(fluoro-¹⁸F)-3-(1H-pyrrolo[2,3-c]pyridin-1-yl)isoquinolin-5-amine ([¹⁸F]MK6240) is a promising tracer allowing for the quantification of

Received May 26, 2022; revision accepted Sep. 21, 2022.

For correspondence or reprints, contact Tharick Pascoal (pascoal@upmc.edu).
Published online Nov. 17, 2022.

Immediate Open Access: Creative Commons Attribution 4.0 International License (CC BY) allows users to share and adapt with attribution, excluding materials credited to previous publications. License: <https://creativecommons.org/licenses/by/4.0/>. Details: <http://jnm.snmjournals.org/site/misc/permission.xhtml>.

COPYRIGHT © 2023 by the Society of Nuclear Medicine and Molecular Imaging.

fibrillary tau pathology in vivo, with postmortem studies confirming its binding to paired helical fragments of phosphorylated tau (4–7). The tracer binds with high affinity to NFTs, thus making it specific to AD-related tauopathy. As shown in postmortem data, the tracer does not seem to bind to tau aggregates in non-AD tauopathies (5,8), except in rare frontotemporal dementia mutations associated with brain deposition of NFTs (9). [¹⁸F]MK6240 allows for the differentiation between cognitively unimpaired (CU), mild cognitive impairment (MCI), and AD subjects (4). Furthermore, [¹⁸F]MK6240 has been shown to recapitulate in vivo the tau pathologic stages, proposed via postmortem studies by Braak et al. (1,10,11).

Despite several favorable features of [¹⁸F]MK6240, some common challenges in PET studies remain unaddressed for this tracer, such as the choice of a reference region for longitudinal studies and the impact of off-target retention on tracer quantification in target regions (i.e., regions expected to show specific, tau-related retention of [¹⁸F]MK6240). Postmortem and in vivo studies have indicated that [¹⁸F]MK6240 has off-target retention in neuromelanin-containing cells (5). Those are regions, such as the substantia nigra, also observed using first-generation tau PET tracers (12). However, [¹⁸F]MK6240 shows significant off-target retention in the meninges (4,13), a characteristic that is currently the main concern for accurate quantification of NFTs using this tracer.

As longitudinal tracer quantification is critical for clinical trials using tau PET imaging agents as a possible surrogate marker of tau accumulation, exploring the optimal reference region and the effects of off-target retention on longitudinal [¹⁸F]MK6240 quantification are crucial (14,15). Here, we studied longitudinal changes in reference, target, age-related, and off-target regions across diagnostic groups and Aβ status to elucidate the caveats associated with the longitudinal quantification of [¹⁸F]MK6240.

MATERIALS AND METHODS

Participants

We included individuals from the TRIAD cohort (16), with data obtained from December 2017 to November 2021. The study was approved by the Douglas Mental Institute Research Board, and all participants gave written consent. Detailed information gathered from the participants can be found online (<https://triad.tnl-mcgill.com/>). All participants underwent a complete neuropsychologic evaluation, MRI, and acquisition of both [¹⁸F]flutafuranol ([¹⁸F]AZD4694) (Aβ) and [¹⁸F]MK6240 (tau) PET scans. We used 2 distinct subject samples. To assess age-related off-target retention of [¹⁸F]MK6240, we included 37 cognitively unimpaired young (CUY) adults (<35 y old) and 27 cognitively unimpaired older (CU) adults (40–65 y old), both presenting no AD-related pathology (Aβ and tau); this sample was called the age-related sample and included only cross-sectional data. The cutoff for a positive Aβ status was a [¹⁸F]AZD4694 global PET SUVR of less than 1.55 (17), whereas the cutoff for a positive tau status was a [¹⁸F]MK6240 temporal meta-region of interest with an SUVR of less than 1.24, as previously described (18). The longitudinal sample comprised 125 individuals (11 CUY, 66 CU Aβ-negative [Aβ−], 17 CU Aβ-positive [Aβ+], and 31 cognitively impaired [CI] Aβ+, including 22 multidomain amnesic MCI and 9 AD) who underwent a follow-up assessment between 1.5 and 3.5 y after their baseline assessment. Baseline diagnosis was used in the analyses, after clinical assessments, based on the Mini-Mental State Examination (MMSE) and Clinical Dementia Rating (CDR) scoring, according to the criteria of the National Institute of Aging Alzheimer's Association (19). CU individuals did not have objective impairment, had an MMSE score of 26 or more, and had a CDR score of 0 (20). Individuals diagnosed with MCI had subjective or objective cognitive impairment and had relatively

preserved activities of daily life, defined as an MMSE score of 26 or above and a CDR of 0.5 (21). Dementia due to AD was defined as an MMSE score of less than 26 and a CDR score of 0.5 or more. No participant met the criteria for another neurologic or major neuropsychiatric disorder after a clinical interview performed by a trained physician.

PET Image Processing

Participants underwent T1-weighted MRI (3-T; Siemens), as well as [¹⁸F]MK6240 tau PET and [¹⁸F]AZD4694 Aβ PET using the same brain-dedicated Siemens High Resolution Research Tomograph. [¹⁸F]MK6240 images were acquired 90–110 min after tracer injection and reconstructed using an ordered-subset expectation maximization algorithm on a 4-dimensional volume with 4 frames (4 × 300 s) (4). [¹⁸F]AZD4694 images were acquired 40–70 min after tracer injection and reconstructed with the same ordered-subset expectation maximization algorithm with 3 frames (3 × 600 s) (4). Each PET acquisition concluded with a 6-min transmission scan with a rotation ¹³⁷Cs point source for attenuation correction. Images were further corrected for motion, decay, dead time, and random and scattered coincidences. SUV images were calculated considering the injected radionuclide dose and weight of each participant ($\frac{\text{PET}}{\text{dose/weight}}$). Injected dose and weight information can be found in Supplemental Table 1 (supplemental materials are available at <http://jnm.snmjournals.org>). SUVs were extracted from the inferior cerebellar gray matter (CG), superior CG, crus I, and full CG. Information on the masks can be found in Supplemental Table 2. SUVR ratio (SUVR) images were generated using the inferior CG as the reference region for [¹⁸F]MK6240 and the full CG for [¹⁸F]AZD4694. Finally, images were spatially smoothed to achieve a final gaussian kernel of 8 mm in full width at half maximum (22,23). Supplemental Table 3 outlines the mean sensitivity of the scanner at baseline and at follow-up visits. The meninges were not masked at any step of the processing. A population-based meningeal mask was created with the Montreal Neurological Institute MINC tool kit as the region having more than a 90% probability of being part of either telencephalon or cerebellar meninges in CUY individuals (Supplemental Fig. 1). In addition, we categorized individuals as having high or low meningeal retention, based on the meningeal SUV median of the population. SUVRs in Braak regions were extracted following the method of Pascoal et al. (10). Additionally, the Desikan–Killiany–Tourville atlas (24) was used to obtain [¹⁸F]MK6240 SUVR from the putamen and the pallidum. A global [¹⁸F]AZD4694 SUVR was estimated by averaging the SUVR from the precuneus, prefrontal, orbitofrontal, parietal, temporal, anterior, and posterior cingulate cortices (25). The cutoff to classify participants as Aβ+ or Aβ− was a global SUVR of 1.55 (17). The Montreal Neurological Institute MINC tool kit was used to calculate average images of [¹⁸F]MK6240 retention.

TABLE 1
Demographics: Dataset Used to Assess Age-Related Retention

Parameter	CUY (n = 37)	CU Aβ− < 65 y (n = 27)	P
Age (y)	23.41 (3.3)	58.09 (9.2)	<0.001
Female	24 (64.9%)	13 (48.1%)	0.28
Education (y)	16.91 (2.5)	15.41 (3.4)	0.0167
MMSE	29.86 (0.4)	29.22 (0.9)	<0.001
CDR	0.00 (0.0)	0.00 (0.0)	Not applicable

Qualitative data are number and percentage; continuous data are mean and SD.

TABLE 2
Longitudinal Dataset

Parameter	CUY	CU Aβ ⁻	CU Aβ ⁺	CI Aβ ⁺	P
Age (y)	22.65 (1.9)	68.44 (9.8)	74.91 (5.1)	71.44 (5.3)	<0.001
Female (%)	8 (72.7%)	41 (62.1%)	14 (82.4%)	14 (45.2%)	0.0668
Education (y)	16.18 (1.7)	16.27 (4.1)	14.65 (2.4)	15.13 (3.4)	0.2
MMSE	29.82 (0.6)	29.21 (1.1)	29.00 (1.0)	26.06 (4.6)	<0.001
CDR	0.00 (0.0)	0.00 (0.0)	0.00 (0.0)	0.65 (0.4)	<0.001

Qualitative data are number and percentage; continuous data are mean and SD.

Statistical Analysis

R statistical software (version 4.0.0) was used to perform nonimaging statistical analyses. *t* testing or ANOVA was used for continuous variables, and χ^2 or Fisher testing was used for categorical variables for demographic information when appropriate. The coefficient of variation was calculated as the group SD divided by the mean. Longitudinal change (Δ) was calculated as follows: $\frac{\text{follow-up SUV(R)} - \text{baseline SUV(R)}}{\text{time (y)}}$.

Associations between changes in biomarkers were assessed with Pearson correlation. Voxel-wise statistical comparisons were conducted using VoxelStats, a statistical tool box implemented in MATLAB (MathWorks) (26). Age-related retention was evaluated at the voxel level using a 2-sided *t* test between CUY and CU Aβ⁻ and tau-negative elderly individuals aged from 40 to 65 y (Table 1). False-discovery-rate correction was applied with a voxel-level correction of *P* < 0.05.

RESULTS

Participants

In the age-related group analyses, comparing CUY and CU older adults who were both Aβ⁻ and tau-negative, we observed no significant difference in sex and years of education. By definition, subjects had a significant difference in age. We also observed a small but significant difference in the MMSE score, with the CU older adults having a slightly lower score (Table 1). In the longitudinal dataset, as expected, we observed significant differences in age, MMSE scores, and CDR scores across groups. There was no difference in years of education; however, a small but significant difference was observed regarding sex, with more women in the CUY and CU Aβ⁺ groups (Table 2).

Assessment of Stability of Reference Regions over Time for Use in Longitudinal Studies

Our first objective was to ascertain the reference region appropriateness for longitudinal quantification of [¹⁸F]MK6240. Using

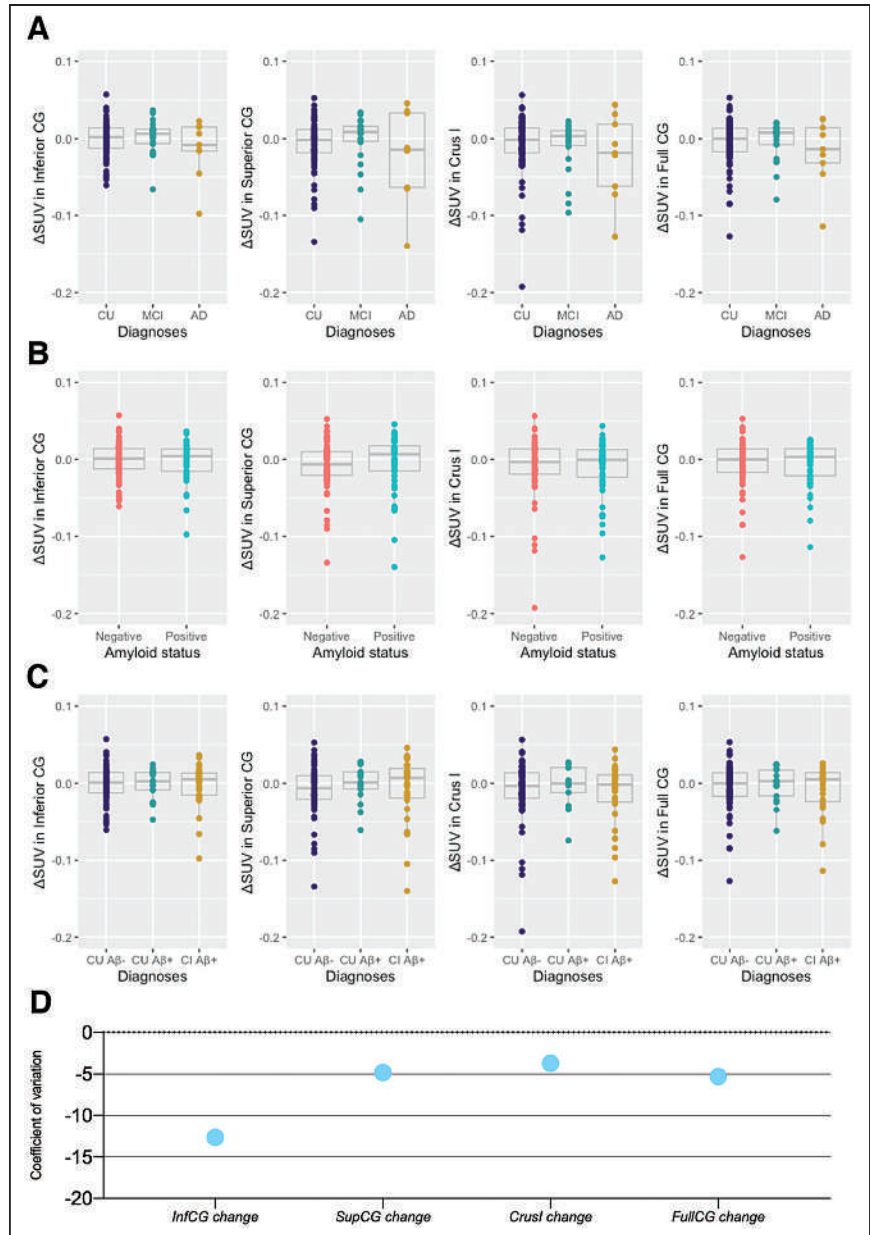


FIGURE 1. Annualized longitudinal changes in [¹⁸F]MK6240 SUV in cerebellar candidate reference regions. (A–C) Δ SUV of [¹⁸F]MK6240 did not significantly differ across diagnosis (A), Aβ status (B), and diagnosis and Aβ status (C). (D) Coefficient of variation of longitudinal changes in SUV within reference regions. Δ = change calculated as $\frac{\text{follow-up SUV} - \text{baseline SUV}}{\text{time (y)}}$. Inf = inferior; sup = superior.

Δ SUV over time, we tested the stability of SUV over the time frame of our study in the inferior CG, superior CG, cerebellar crus I, and full CG. No significant differences in longitudinal changes were observed when individuals were separated on the basis of their clinical diagnosis (Fig. 1A), A β status (Fig. 1B), or both (Fig. 1C). The mean and SD for Δ SUV can be found in Supplemental Table 4. Coefficients of variation for [¹⁸F]MK6240 Δ SUV were similar, being highest for inferior CG longitudinal change (–12.64) and lowest for crus I (–3.71) (Fig. 1D; Table 3). We observed no significant variability in SUV (i.e., between baseline and follow-up measures) in the assessed reference regions (Table 4; Supplemental Table 5).

The supplemental material displays the cross-sectional differences in those SUVs. In the cross-sectional analysis, only superior CG (CU–AD, $P < 0.001$; MCI–AD, $P < 0.001$) and crus I (CU–AD, $P = 0.046$; MCI–AD, $P = 0.051$) presented significant differences between diagnostic groups after correction for multiple comparisons (Supplemental Fig. 2). Cross-sectional coefficients of variation for reference regions are reported in Supplemental Figure 3.

Meningeal and Age-Related Retentions

Figure 2A represents the average [¹⁸F]MK6240 SUVs in the CUY group. First, we detected a strong correlation between telencephalon and cerebellar meninges, cross-sectionally and longitudinally (Supplemental Fig. 4). We observed no significant difference between diagnostic groups in the telencephalon meninges cross-sectionally (CU A β – vs. CU A β +, $P = 0.891$; CU A β – vs. CI A β +, $P = 0.797$; CU A β – vs. CI A β +, $P = 0.999$) or longitudinally (CU A β – vs. CU A β +, $P = 0.150$; CU A β – vs. CI A β +, $P = 0.677$; CU A β – vs. CI A β +, $P = 0.524$). Similarly, no differences were observed in the cerebellar meninges either cross-sectionally (CU A β – vs. CU A β +, $P = 0.946$; CU A β – vs. CI A β +, $P = 0.919$; CU A β – vs. CI A β +, $P = 0.837$) or longitudinally (CU A β – vs. CU A β +, $P = 0.563$; CU A β – vs. CI A β +, $P = 0.631$; CU A β – vs. CI A β +, $P = 0.963$) (Fig. 2B). Finally,

TABLE 3

Coefficient of Variation of Cerebellar Regions Across Diagnosis, at Baseline, and at Follow-Up and Longitudinal Changes

Region	All	CU A β –	CU A β +	CI A β +
Inferior CG BL	0.19	0.18	0.14	0.22
Superior CG BL	0.27	0.24	0.19	0.32
Crus I BL	0.25	0.26	0.19	0.28
Full CG BL	0.22	0.22	0.19	0.24
Inferior CG FU	0.17	0.18	0.16	0.17
Superior CG FU	0.25	0.21	0.21	0.29
Crus I FU	0.22	0.21	0.22	0.25
Full CG FU	0.20	0.20	0.21	0.19
Δ Inferior CG	–12.64	–14.35	–11.12	–11.03
Δ Superior CG	–4.83	–3.79	–52.03	–5.05
Δ Crus I	–3.71	–3.84	–7.48	–2.93
Δ Full CG	–5.30	–5.47	–9.63	–4.28

BL = baseline; FU = follow-up.

Longitudinal change was calculated using formula:

$$\Delta = \frac{(\text{follow-up SUV} - \text{baseline SUV})}{\text{time (y)}}$$

TABLE 4

P Values of 2-Tailed t Test Between Baseline and Follow-up SUV Across Cerebellar Regions in Individuals Categorized by Diagnosis

Region	All	CU A β –	CU A β +	CI A β +
Inferior CG	0.67	0.81	0.72	0.83
Superior CG	0.27	0.21	0.94	0.66
Crus I	0.09	0.18	0.72	0.31
Full CG	0.25	0.40	0.76	0.46

SUVs in the meninges were higher in women than men transversally but not longitudinally (Supplemental Fig. 5).

The average [¹⁸F]MK6240 SUV images of CUY and CU A β – and tau-negative individuals less than 65 y old did not seem to display striking visual differences. However, a t test between the 2 groups revealed significantly higher [¹⁸F]MK6240 retention in the putamen, the pallidum, a parcel of cerebellar white matter, and a few other cortical regions (Fig. 3A). The same test was performed in the longitudinal sample as well (Supplemental Fig. 6). We assessed the percentage of overlap between the age-related signal and brain regions. The most important regional overlaps were with the putamen (75% of the region showing overlap) and the pallidum (72%), followed by the Braak stage II region (38%) (Fig. 3B). SUVs in the putamen and pallidum differed significantly among diagnostic groups, with the CUY having a significantly lower [¹⁸F]MK6240 retention cross-sectionally (CUY vs. CU A β –, $P < 0.001$; CUY vs. CU A β +, $P < 0.001$; CUY vs. CI A β +, $P < 0.001$). Additionally, CI A β – individuals had significantly higher values than CU individuals (A β – and A β +) cross-sectionally (CU A β – vs. CU A β +, $P = 0.926$; CU A β – vs. CI A β –, $P < 0.001$; CU A β – vs. CI A β +, $P < 0.001$). Nevertheless, the longitudinal rate of change (Δ SUV) did not present significant differences among the groups (CUY vs. CU A β –, $P = 0.927$; CUY vs. CU A β +, $P = 0.845$; CUY vs. CI A β –, $P = 0.731$; CU A β – vs. CU A β +, $P = 0.880$; CU A β – vs. CI A β –, $P = 0.728$; CU A β – vs. CI A β +, $P = 0.994$) (Fig. 3C).

Associations of Changes in Target, Age-Related, and Off-Target Retention

Target regions were considered brain regions in which we expect to see [¹⁸F]MK6240 retention based on the pattern of tau distribution extensively reported in the postmortem literature (1,27). We found a strong correlation in Δ SUV among target regions, with each Braak region being more strongly correlated with the adjacent stages. The weakest correlation was between the Braak I and Braak VI regions. When extracting the average SUV in the Braak I–III and Braak IV–VI regions, we also observed a strong positive correlation between regions ($R = 0.62$, $P < 0.001$). We then used SUVs in the telencephalon and cerebellar meninges, as well as in the putamen and pallidum, in the correlations. Δ SUV in those regions did not correlate significantly with Δ SUV in any one of the target regions (Braak I–III and telencephalon meninges: $R = -0.03$, $P = 0.740$; Braak IV–VI and telencephalon meninges: $R = 0.10$, $P = 0.290$; Braak I–III and cerebellar meninges: $R = -0.12$, $P = 0.200$; Braak IV–VI and cerebellar meninges: $R = -0.02$, $P = 0.870$; Braak I–III and putamen and pallidum: $R = 0.12$, $P = 0.200$; Braak IV–VI and putamen and pallidum: $R = 0.05$, $P = 0.600$). Nor did the

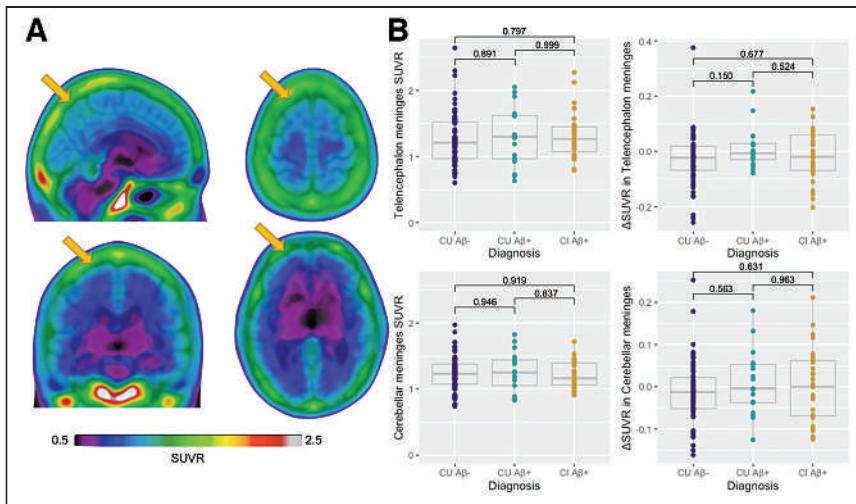


FIGURE 2. Cross-sectional and longitudinal meningeal [¹⁸F]MK6240 SUVR across groups. (A) Representative [¹⁸F]MK6240 average SUVR image in CUY individuals. (B) Cross-sectional and longitudinal changes in [¹⁸F]MK6240 (Δ SUVR) in telencephalon and cerebellar meninges showing no significant differences depending on diagnosis and A β status. Δ = change calculated as $\frac{\text{follow-up SUVR} - \text{baseline SUVR}}{\text{time (y)}}$. Yellow arrows indicate meninges.

meningeal and putamen/pallidum Δ SUVR correlate with each other ($R = 0.01$, $P = 0.920$) (Fig. 4). To further assess the impact of meninges on tracer quantification, we categorized individuals as having high or low meningeal retention (based on SUV median for meninges). We did not find difference in diagnostic groups or longitudinal tracer accumulation between individuals with high and low meningeal retention (Supplemental Table 6). Finally, we assessed the stability of [¹⁸F]MK6240 SUVR in target regions over time when using different reference regions (i.e., inferior CG, crus I, full CG, and superior CG). We extracted Braak IV–VI SUVRs in CUY and

CU A β [−] individuals, for whom we do not expect a significant increase in SUVRs. We observed no difference between baseline and follow-up values when using either reference region (Supplemental Fig. 7; Supplemental Table 7).

DISCUSSION

This study suggested that the most widely used cerebellar reference regions (inferior CG, superior CG, crus I, and full CG) present stability, with no changes over time, and therefore may be suitable for use in longitudinal studies, although differences were observed in the superior CG and crus I cross-sectionally. We found evidence for the existence of an age-related retention in the putamen/pallidum, similar—albeit of much lower magnitude—to the reported off-target retention observed using the first-generation tau PET tracers (12,28). Finally, we demonstrated that there was no association between [¹⁸F]MK6240 Δ SUVR in target

regions and in age-related or meningeal off-target signals over the time frame of our study.

Previous cross-sectional studies have already shown that indices of tau load made using [¹⁸F]MK6240 are amenable to simplified tissue ratio methods using data acquired 90–110 min after injection (4,7). However, questions remain regarding the suitability of the reference region for longitudinal tracer quantification because of the bias often inherent in SUVR data (10). This is of paramount importance because [¹⁸F]MK6240 has been used in clinical trial settings to capture longitudinal changes in tau tangle pathology (29).

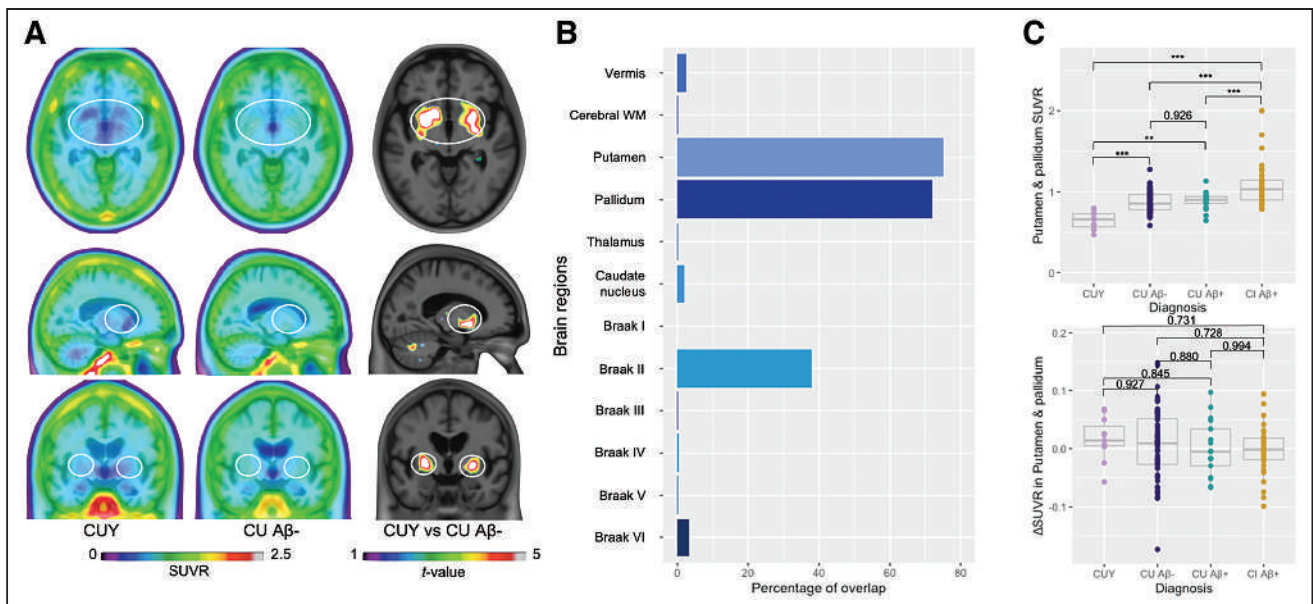


FIGURE 3. [¹⁸F]MK6240 age-related retention. (A) [¹⁸F]MK6240 average SUVR images in CUY and CU A β [−] individuals did not seem to show strong differences visually. *t* test between 2 groups depicts age-related retention in putamen, pallidum, cortical regions, and cerebellar white matter. (B) Percentage of overlap between age-related *t*-map and anatomic brain regions. (C) Longitudinal changes (Δ SUVR) in [¹⁸F]MK6240 SUVR in putamen/pallidum did not present significant differences across groups, whereas cross-sectional SUVR was higher in CI individuals and lower in CUY group. *** $P < 0.001$. ** $P < 0.005$. Δ = change calculated as $\frac{\text{follow-up SUVR} - \text{baseline SUVR}}{\text{time (y)}}$; WM = white matter.

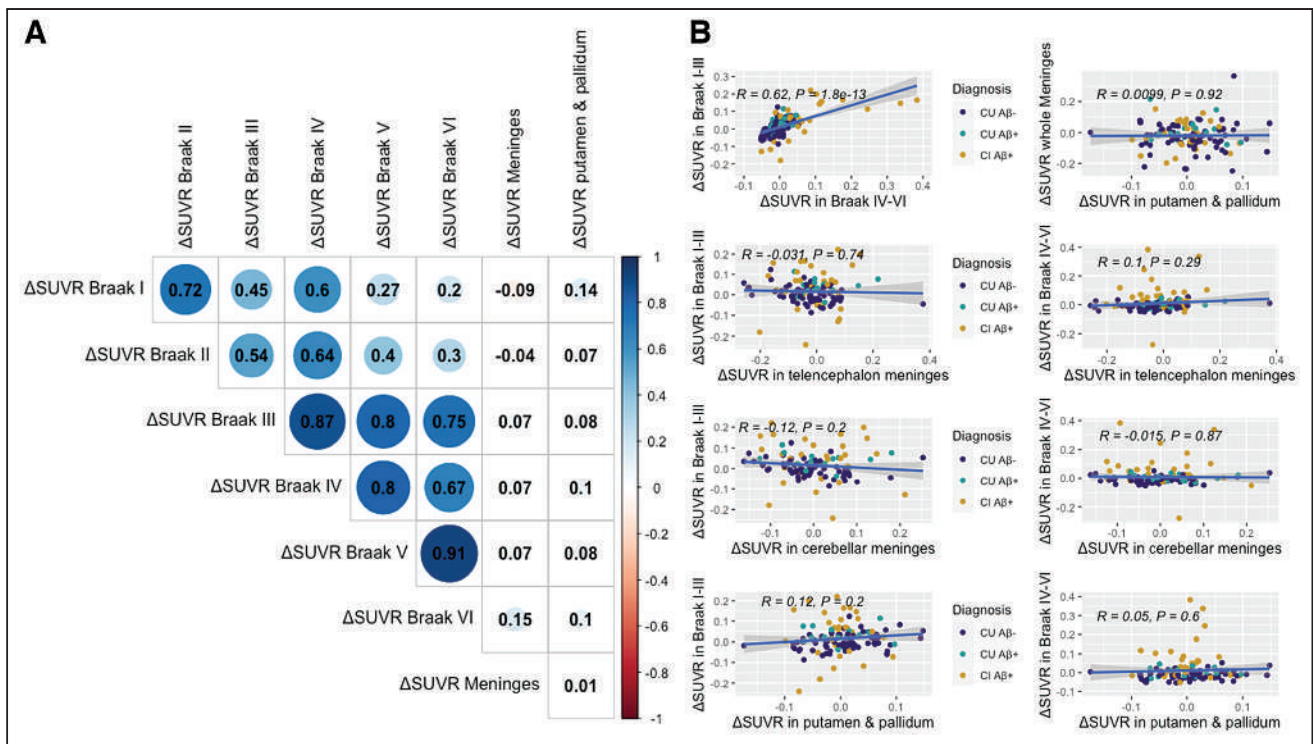


FIGURE 4. Correlations between longitudinal changes in SUVR in age-related, meningeal, and target regions. We assessed Δ SUVR in regions presenting target (Braak I–VI), off-target (both telencephalon and cerebellar meninges), and age-related (putamen/pallidum) tracer uptake. We observed strong Δ SUVR among target regions; however, those did not correlate with Δ SUVRs in off-target and age-related regions. Matrix (A) and plots (B) present estimates of Pearson correlations between regions. Δ = change calculated as $\frac{(\text{follow-up SUVR} - \text{baseline SUVR})}{\text{time (y)}}$.

Extensive research has focused on the cerebellum as the appropriate reference region for tau radiotracers (30,31), as the CG is not expected to harbor significant NFT pathology (1). Although the gold standard method for assessment of the optimal reference region relies on dynamic quantifications with arterial input function, one crucial characteristic of a reference region for longitudinal assessments is not having large variability over time, across diagnostic groups, or in other pathologic features (i.e., A β status in the case of AD research) (32). In this study, we estimated the [18 F]MK6240 SUVs in distinct regions of the CG at baseline, as well as its change over time, based on diagnosis and on A β status. The results indicate that there were small cross-sectional differences between diagnostic groups in the superior CG and crus I but not in the inferior CG and full CG. These differences might be due to spillover effect from the target regions, as individuals with AD dementia inherently have a higher uptake of the tracer. Additionally, we did not observe differences in cerebellar SUVs based on A β status. When examining the differences between baseline and follow-up assessments, we did not observe any significant difference in [18 F]MK6240 SUV for any cerebellar region. Even though all variability was relatively minor, we observed the lowest numeric variability in the SUV levels of the inferior CG cross-sectionally and in the crus I longitudinally. Altogether, our results suggest that tracer retention in the tested reference regions was relatively stable over time and across diagnostic groups, suggesting that all these reference regions could potentially be used for longitudinal [18 F]MK6240 quantification. Given the cross-sectional differences in tracer uptake among diagnostic groups in the superior CG and crus I but not in the inferior CG, this latter region was deemed more appropriate for the cross-sectional and longitudinal

[18 F]MK6240 quantification and thus was used for the remaining analyses. Future studies using the gold standard arterial input function should address other important characteristics of an optimal reference region.

The *t* test comparing young individuals under age 35 y and participants between 40 and 65 y old allowed us to assess age-related retention of [18 F]MK6240. The regions presenting the higher age-related [18 F]MK6240 retention were the putamen and pallidum. Those are often considered off-target regions using other radiotracers for tau (31–33), but the retention seems to be of lower magnitude with [18 F]MK6240 (34). As we included participants younger than 65 y who were CU A β – and tau-negative, we do not expect on-target [18 F]MK6240 retention in subcortical structures based on the postmortem literature (35). Indeed, subcortical regions have been shown to harbor NFT accumulation only at late Braak pathologic stages (27,36), which might explain why we observed a significant cross-sectional difference in putamen and pallidum SUVR between CI A β + individuals and CU individuals (either A β – or A β +). Similar to first-generation tau PET tracers (5), the retention observed with [18 F]MK6240 in the putamen and pallidum may be due to neuromelanin deposition. Although the tracer retention observed in the Braak II region can represent an age-related signal, we cannot entirely exclude that there is some true concentration of NFTs in this region, as modest tau accumulation in CU A β – individuals has already been reported in the hippocampus (2,35). Another possibility is that the marked off-target retention of first-generation tracers in the choroid plexus (12), which contaminates the Braak II region for these tracers, may be a minor age-related problem with [18 F]MK6240 as well. However, it is important to

note that some individuals may have primary age-related tauopathy (37) and may be harboring NFT accumulation in early Braak stages, with little to no A β deposition. Finally, we assessed meningeal retention in both the telencephalon and the cerebellar regions, which have already been characterized as off-target by previous postmortem studies (5). Importantly, we observed no significant difference in the magnitude of meningeal uptake across diagnosis and A β status and no change over time. Nevertheless, we observed sex differences in meningeal retention cross-sectionally but not longitudinally, as previously reported for other tau PET tracers in the meninges and skull (13). Taken together, these results suggest that besides the meningeal retention, [18 F]MK6240 presents a newly described age-related retention in subcortical brain regions, the cause of which needs to be elucidated by future in vitro studies across the aging spectrum.

We observed no association between annualized [18 F]MK6240 SUVR changes in target, age-related regions, and meninges. Braak regions were used to represent target areas for tau tangles, as extensively reported in postmortem studies (1,27). Δ SUVRs in target brain regions correlated strongly with each other, suggesting that changes in tracer retention in these brain regions are influenced by the same brain process, likely NFT accumulation (22). On the other hand, we did not observe a significant correlation between Δ SUVR in meningeal off-target uptake and changes in Braak target regions. Additionally, age-related Δ SUVR in the putamen and pallidum did not correlate with that in target regions. Nor did off-target, meningeal, and age-related subcortical Δ SUVR correlate with each other. This finding suggests that different processes set the pace of progression in target, off-target, and age-related regions and that spillover from off-target regions would not heavily influence rates of progression in [18 F]MK6240 target regions.

This study had limitations. The lack of arterial sampling at baseline and follow-up limits assessments of reference region and accurate tracer retention. We observed a small (close to zero), non-statistically significant decrease in SUVs in cerebellar regions over time. Additionally, all [18 F]MK6240 analyses were conducted using images acquired from 90 to 110 min after injection. Even though this simplified quantitative approach has been validated (4), dynamically acquired PET data with arterial input function would be more appropriate to test the hypotheses of our study. Although there is a possibility that the effect of meninges in reference regions may lead to changes in baseline and follow-up values and, consequently, in rates of change, the fact that meningeal uptake did not change significantly over time or differ between groups defined using cognition or A β status suggests that it does not play a major role in the longitudinal results for this tracer. Moreover, we used spatial smoothing of 8 mm; smaller smoothing would likely cause the meninges to have less impact on the adjacent brain regions. An additional limitation is the lack of partial-volume correction in our study. Postmortem data would validate our findings, as such data would allow us to ensure the absence of NFTs in the cerebellar regions, as well as in the age-related retention regions. Without postmortem confirmation, we cannot exclude that age-related retention in CU adults is caused by tau tangle pathology. Moreover, our sample was restricted to a follow-up of 1.5–3.5 y; using other follow-up durations may give different results. We evaluated only a small subset of reference regions that are frequently reported in the literature; other regions may present better results for [18 F]MK6240 longitudinal quantification. An additional limitation is that we did not provide any evidence about the mechanism through which age-related retention occurs. Arterial and postmortem data are needed to understand our findings.

CONCLUSION

The inferior CG is a suitable reference region for cross-sectional and longitudinal quantification of [18 F]MK6240. [18 F]MK6240 exhibits off-target retention in the meninges and an age-related signal in the putamen and pallidum, also likely representing off-target retention, and in the Braak II region, for which the source needs to be elucidated. The lack of an association between changes in SUVR within age-related, off-target, and target regions suggests that longitudinal changes in [18 F]MK6240 are not heavily driven by changes in age-related or off-target signals. However, future postmortem studies are needed to clarify these findings.

DISCLOSURE

This work was supported by the Weston Brain Institute, Fonds de Recherche Santé Québec, Healthy Brain for Healthy Lives, and the McGill University Faculty of Medicine. Tharick Pascoal is supported by the Alzheimer Association (AACSF-20-648075) and the National Institutes of Health (R01AG073267 and R01AG075336). Serge Gauthier has served as a scientific advisor to Cerveau Therapeutics. No other potential conflicts of interest relevant to this article exist.

ACKNOWLEDGMENT

We thank Cerveau Technologies for providing us with [18 F]MK6240.

KEY POINTS

QUESTION: What is the effect of reference region and nontarget tracer retention on longitudinal quantification of [18 F]MK6240 in target regions?

PERTINENT FINDINGS: The inferior CG and full CG are appropriate reference regions for cross-sectional and longitudinal quantification of [18 F]MK6240. This tracer is already known to present off-target binding in the meninges, but we discovered a so-called age-related binding in the putamen and pallidum. However, the longitudinal changes in nontarget tracer retention did not correlate with longitudinal changes in on-target regions.

IMPLICATIONS FOR PATIENT CARE: [18 F]MK6240 can be used as a surrogate marker in clinical trials, as long as the appropriate reference region is used and off-target and age-related retention are considered.

REFERENCES

1. Braak H, Braak E. Neuropathological staging of Alzheimer-related changes. *Acta Neuropathol (Berl)*. 1991;82:239–259.
2. Jagust W. Imaging the evolution and pathophysiology of Alzheimer disease. *Nat Rev Neurosci*. 2018;19:687–700.
3. Lewis JS, Windhorst AD, Zeglis BM. *Radiopharmaceutical Chemistry*. Springer; 2019.
4. Pascoal TA, Shin M, Kang MS, et al. In vivo quantification of neurofibrillary tangles with [18 F]MK-6240. *Alzheimers Res Ther*. 2018;10(1):74.
5. Aguero C, Dhaynaut M, Normandin MD, et al. Autoradiography validation of novel tau PET tracer [F-18]-MK-6240 on human postmortem brain tissue. *Acta Neuropathol Commun*. 2019;7:37.
6. Hostetler ED, Walji AM, Zeng Z, et al. Preclinical characterization of [18 F]-MK-6240, a promising PET tracer for in vivo quantification of human neurofibrillary tangles. *J Nucl Med*. 2016;57:1599–1606.
7. Bethausen TJ, Cody KA, Zammit MD, et al. In vivo characterization and quantification of neurofibrillary tau PET radioligand [18 F]-MK-6240 in humans from Alzheimer disease dementia to young controls. *J Nucl Med*. 2019;60:93–99.

8. Iqbal K, Del C, Alonso A, et al. Tau pathology in Alzheimer disease and other tauopathies. *Biochim Biophys Acta*. 2005;1739:198–210.
9. Levy JP, Bezgin G, Savard M, et al. ¹⁸F-MK-6240 tau-PET in genetic frontotemporal dementia. *Brain*. 2021;145:1763–1772.
10. Pascoal TA, Therriault J, Benedet AL, et al. ¹⁸F-MK-6240 PET for early and late detection of neurofibrillary tangles. *Brain*. 2020;143:2818–2830.
11. Therriault J, Pascoal TA, Lussier FZ, et al. Biomarker modeling of Alzheimer's disease using PET-based Braak staging. *Nat Aging*. 2022;1-10.P
12. Lee CM, Jacobs HIL, Marquié M, et al. ¹⁸F-flortaucipir binding in choroid plexus: related to race and hippocampus signal. *J Alzheimers Dis*. 2018;62:1691–1702.
13. Smith R, Strandberg O, Leuzy A, et al. Sex differences in off-target binding using tau positron emission tomography. *Neuroimage Clin*. 2021;31:102708.
14. Baker SL, Harrison TM, Maass A, La Joie R, Jagust WJ. Effect of off-target binding on ¹⁸F-flortaucipir variability in healthy controls across the life span. *J Nucl Med*. 2019;60:1444–1451.
15. Chen K, Roontiva A, Thiyyagura P, et al. Improved power for characterizing longitudinal amyloid-β PET changes and evaluating amyloid-modifying treatments with a cerebral white matter reference region. *J Nucl Med*. 2015;56:560–566.
16. Therriault J, Benedet AL, Pascoal TA, et al. APOEε4 potentiates the relationship between amyloid-β and tau pathologies. *Mol Psychiatry*. 2021;26:5977–5988.
17. Therriault J, Benedet AL, Pascoal TA, et al. Determining amyloid-beta positivity using [¹⁸F]AZD4694 PET imaging. *J Nucl Med*. 2021;62:247–252.
18. Therriault J, Pascoal TA, Benedet AL, et al. Frequency of biologically defined Alzheimer disease in relation to age, sex, APOE ε4, and cognitive impairment. *Neurology*. 2021;96:e975–e985.
19. Jack CR, Bennett DA, Blennow K, et al. NIA-AA research framework: toward a biological definition of Alzheimer's disease. *Alzheimers Dement*. 2018;14:535–562.
20. Jack CR, Wiste HJ, Schwarz CG, et al. Longitudinal tau PET in ageing and Alzheimer's disease. *Brain*. 2018;141:1517–1528.
21. Petersen RC. Mild cognitive impairment as a diagnostic entity. *J Intern Med*. 2004;256:183–194.
22. Pascoal TA, Benedet AL, Tudorascu DL, et al. Longitudinal ¹⁸F-MK-6240 tau tangles accumulation follows Braak stages. *Brain*. 2021;144:3517–3528.
23. Joshi A, Koeppe RA, Fessler JA. Reducing between scanner differences in multi-center PET studies. *Neuroimage*. 2009;46:154–159.
24. Desikan RS, Ségonne F, Fischl B, et al. An automated labeling system for subdividing the human cerebral cortex on MRI scans into gyral based regions of interest. *Neuroimage*. 2006;31:968–980.
25. Jack CR, Wiste HJ, Weigand SD, et al. Defining imaging biomarker cut points for brain aging and Alzheimer's disease. *Alzheimers Dement*. 2017;13:205–216.
26. Mathotaarachchi S, Wang S, Shin M, et al. VoxelStats: a MATLAB package for multi-modal voxel-wise brain image analysis. *Front Neuroinform*. 2016;10:20.
27. Braak H, Braak E. Staging of Alzheimer's disease-related neurofibrillary changes. *Neurobiol Aging*. 1995;16:271–278.
28. Leuzy A, Chiotis K, Lemoine L, et al. Tau PET imaging in neurodegenerative tauopathies: still a challenge. *Mol Psychiatry*. 2019;24:1112–1134.
29. Knopman DS, Jones DT, Greicius MD. Failure to demonstrate efficacy of aducanumab: an analysis of the EMERGE and ENGAGE trials as reported by Biogen, December 2019. *Alzheimers Dement*. 2021;17:696–701.
30. Lemoine L, Saint-Aubert L, Marutle A, et al. Visualization of regional tau deposits using ³H-THK5117 in Alzheimer brain tissue. *Acta Neuropathol Commun*. 2015;3:40.
31. Marquié M, Normandin MD, Vanderburg CR, et al. Validating novel tau PET tracer [¹⁸F]-AV-1451 (T807) on postmortem brain tissue. *Ann Neurol*. 2015;78:787–800.
32. Lohith TG, Bennacef I, Vandenberghe R, et al. Brain imaging of Alzheimer dementia patients and elderly controls with ¹⁸F-MK-6240, a PET tracer targeting neurofibrillary tangles. *J Nucl Med*. 2019;60:107–114.
33. Collier TL, Yokell DL, Livni E, et al. cGMP production of the radiopharmaceutical [¹⁸F]MK-6240 for PET imaging of human neurofibrillary tangles. *J Labelled Compd Radiopharm*. 2017;60:263–269.
34. Gogola A, Minhas DS, Villemagne VL, et al. Direct comparison of the tau PET tracers ¹⁸F-flortaucipir and ¹⁸F-MK-6240 in human subjects. *J Nucl Med*. 2022;63:108–116.
35. Braak H, Thal DR, Ghebremedhin E, Del Tredici K. Stages of the pathologic process in Alzheimer disease: age categories from 1 to 100 years. *J Neuropathol Exp Neurol*. 2011;70:960–969.
36. Braak H, Alafuzoff I, Arzberger T, Kretschmar H, Tredici K. Staging of Alzheimer disease-associated neurofibrillary pathology using paraffin sections and immunocytochemistry. *Acta Neuropathol (Berl)*. 2006;112:389–404.
37. Hickman RA, Flowers XE, Wisniewski T. Primary age-related tauopathy (PART): addressing the spectrum of neuronal tauopathic changes in the aging brain. *Curr Neurol Neurosci Rep*. 2020;20:39.

Evaluation of Tau Radiotracers in Chronic Traumatic Encephalopathy

Cassis Varlow and Neil Vasdev

Azrieli Centre for Neuro-Radiochemistry, Brain Health Imaging Centre, Centre for Addiction and Mental Health, and Institute of Medical Science, University of Toronto, Toronto, Ontario, Canada

Chronic traumatic encephalopathy (CTE) is a neurologic disorder associated with head injuries, diagnosed by the perivascular accumulation of hyperphosphorylated tau protein (phospho-tau) identified at autopsy. Tau PET radiopharmaceuticals developed for imaging Alzheimer disease are under evaluation for brain injuries. The goal of this study was to conduct a head-to-head in vitro evaluation of 5 tau PET radiotracers in subjects pathologically diagnosed with CTE. **Methods:** Autoradiography was used to assess the specific binding and distribution of ^3H -flortaucipir (also known as Tauvid, AV-1451, and T807), ^3H -MK-6240 (also known as florquinitalu), ^3H -PI-2620, ^3H -APN-1607 (also known as PM-PBB3 and florzolotau), and ^3H -CBD-2115 (also known as ^3H -OXD-2115) in fresh-frozen human postmortem CTE brain tissue (stages I–IV). Immunohistochemistry was performed for phospho-tau with AT8, 3R tau with RD3, 4R tau with RD4 and amyloid- β with 6F/3D antibodies. Tau target density (maximum specific binding) was quantified by saturation analysis with ^3H -flortaucipir in tissue sections. **Results:** ^3H -flortaucipir demonstrated a positive signal in all CTE cases examined, with varying degrees of specific binding ($68.7\% \pm 10.5\%$; $n = 12$) defined by homologous blockade and to a lesser extent by heterologous blockade with MK-6240 ($27.3\% \pm 13.6\%$; $n = 12$). The ^3H -flortaucipir signal was also displaced by the monoamine oxidase (MAO)–A inhibitor clorgyline ($43.9\% \pm 4.6\%$; $n = 3$), indicating off-target binding to MAO-A. ^3H -APN-1607 was moderately displaced in homologous blocking studies and was not displaced by ^3H -flortaucipir; however, substantial displacement was observed when blocking with the β -amyloid-targeting compound NAV-4694. ^3H -MK-6240 and ^3H -PI-2620 had negligible binding in all but 2 CTE IV cases, and binding may be attributed to pathology severity or mixed Alzheimer disease/CTE pathology. ^3H -CBD-2115 showed moderate binding, displaced under homologous blockade, and aligned with 4R-tau immunostaining. **Conclusion:** In human CTE tissues, ^3H -flortaucipir and ^3H -APN-1607 revealed off-target binding to MAO-A and amyloid- β , respectively, and should be considered if these radiotracers are used in PET imaging studies of patients with brain injuries. ^3H -MK-6240 and ^3H -PI-2620 bind to CTE tau in severe- or mixed-pathology cases, and their respective ^{18}F PET radiotracers warrant further evaluation in patients with severe suspected CTE.

Key Words: CTE; PET; tau; autoradiography; chronic traumatic encephalopathy; traumatic brain injury

J Nucl Med 2023; 64:460–465

DOI: 10.2967/jnumed.122.264404

Chronic traumatic encephalopathy (CTE) is a neurodegenerative disease linked to a history of head injuries, including traumatic brain injuries, repetitive concussive injuries, or subconcussive injuries. Individuals at risk for developing CTE include contact sport athletes, military veterans, and victims of intimate partner violence (1). The lasting implications of CTE have become more prevalent in recent years, with reported symptoms and comorbidities including memory loss, behavioral and mood changes, cognitive deficits, sleep disorders, and substance use disorders (1). Although neurodegeneration can be classified in the clinic on the basis of these cognitive or behavioral presentations, diagnosis of CTE is possible only on postmortem neuropathologic evaluation to identify the presence of perivascular hyperphosphorylated tau protein (phospho-tau) (2,3). CTE diagnosis is categorized into stages ranging from I to IV, where stage I consists of isolated perivascular centers at the depths of sulci in the frontal cortex. The pathology progresses in severity and spreads regionally, with widespread involvement of the neocortex, hippocampus, amygdala, cerebellum, and cervical spinal cord by stage IV (2). The traumatic encephalopathy syndrome criteria of 2014 were proposed for antemortem diagnosis of CTE but have been unable to effectively identify the disease (4). Revisions of these criteria have been proposed to include cognitive symptoms and biomarkers for Alzheimer disease (AD), as CTE and AD share characteristic tau pathology (2,3,5,6). Additionally, it has been suggested that moderate-to-severe traumatic brain injury is also a risk factor for AD, emphasizing the need for differentiation between diagnoses (7).

PET shows promise for antemortem CTE diagnosis, and studies have been conducted on head injury patients using tau PET radiopharmaceuticals optimized for AD, including ^{18}F -FDDNP, ^{18}F -flortaucipir (also known as Tauvid [Eli Lilly and Co.], AV-1451, and T807), ^{11}C -PBB3, and ^{18}F -MK-6240 (also known as florquinitalu), summarized in Table 1 (8–24).

At present, there is no tau PET tracer optimized for CTE (mixed 3-repeat/4-repeat [3R/4R] tau), and considering the heterogeneity of pathology between tauopathies, designing radiotracers for CTE remains a challenge (25). Identifying appropriate radiotracers to successfully image CTE tau in vivo could enable antemortem diagnosis of CTE for the first time and provide opportunities for therapeutic intervention after brain injuries (19,26). The goal of the present study was to conduct a head-to-head in vitro evaluation of 5 tau PET radiotracers in 12 pathologically diagnosed subjects with CTE to determine the suitability of these tracers to image CTE-specific tau inclusions. Autoradiography was used to assess the specific binding and distribution of ^3H -flortaucipir, ^3H -MK-6240, ^3H -PI-2620, ^3H -APN-1607 (also known as PM-PBB3 and florzolotau), and ^3H -CBD-2115 (also known as ^3H -OXD-2115). Immunohistochemistry was validated for phospho-tau with AT8, 3R tau with RD3, 4R tau with RD4, and amyloid- β (A β)

Received May 11, 2022; revision accepted Sep. 6, 2022.

For correspondence or reprints, contact Neil Vasdev (neil.vasdev@utoronto.ca).

Published online Sep. 15, 2022.

COPYRIGHT © 2023 by the Society of Nuclear Medicine and Molecular Imaging.

TABLE 1
Tau PET Studies in Head Injury Patients

Radiotracer	Cohort	<i>n</i>	Findings	Reference
¹⁸ F-FDDNP	Retired NFL players	14	PET correlation with postmortem CTE pathology	(10, 15, 17)
¹⁸ F-flortaucipir	Single moderate-to-severe TBI patients	21	Elevated binding in right occipital cortex, white matter region, and whole brain of TBI subjects	(20)
	Blast-exposed patients	17	Uptake associated with exposure to blast neurotrauma in several regions	(21)
	NFL player and severe-TBI patient	1/1	Increased nigral and striatal uptake in NFL patient; increased subcortical and hippocampal uptake in severe-TBI patient	(11)
	Former NFL players	26	Higher uptake in bilateral superior frontal, bilateral medial temporal, and left parietal regions in NFL players with cognitive/neuropsychiatric symptoms	(19)
	Former NFL player*	1	Uptake observed, but low tau burden quantified, in basal ganglia, thalamus, motor cortex, and calcarine cortex; insignificant correlation between uptake value ratio and tau burden	(9)
	Former NFL player	1	Retention at cortical gray matter–white matter junction; increased uptake bilaterally in cingulate, occipital, and orbitofrontal cortices and in temporal areas	(12)
	TBI patients	2	Significant uptake in occipital lobes	(8)
	Retired athletes, motor vehicle accident patient, and veterans	5/1/2	Heterogeneity in uptake between TBI patients; correlation of regions of higher uptake with decreased white matter integrity and greater functional connectivity	(22)
	Traumatic encephalopathy syndrome patients	11	Mildly elevated tau PET binding in subset of patients at risk for CTE, in distribution consistent with CTE pathology stages III and IV	(23)
	CTE brains	5	No signal in regions with tau aggregates; 2 cases indicating uptake in choroid plexus and meninges; off-target binding in leptomeningeal melanocytes	(14)
¹⁸ F-THK-5317	TBI and repeated sports-related concussions	12/6	Tau aggregation in corpus callosum in athletes with repeated sports-related concussions; tau aggregation in thalami, temporal white matter, and midbrain in TBI patients	(24)
¹¹ C-PBB3	Mild-repetitive or severe TBI patients	27	Increased binding capacity in neocortical gray matter associated with late-onset neuropsychiatric symptoms after TBI; close correlation between psychosis and binding capacity in white matter	(16)
¹⁸ F-MK-6240	Australian Rules football player	1	Poor binding to tau aggregates in non-AD tauopathies; imaging findings of frontally predominant binding significantly different from pattern of prodromal AD	(13, 18)

*In vivo imaging followed by postmortem neuropathologic examination.
NFL = National Football League; TBI = traumatic brain injury.

with 6F/3D antibodies. Tau target density (maximum specific binding [B_{max}]) in postmortem tissue sections was quantified by saturation analysis with ³H-flortaucipir.

MATERIALS AND METHODS

General

³H-flortaucipir (3.515 MBq/μmol, 37 MBq/mL), ³H-APN-1607 (1.998 MBq/μmol, 37 MBq/mL), ³H-MK-6240 (1.536 MBq/μmol,

37 MBq/mL), ³H-PI-2620 (1.554 MBq/μmol, 37 MBq/mL), and ³H-CBD-2115 (1.103 MBq/μmol, 37 MBq/mL) were prepared at Novandi Chemistry AB. Flortaucipir was purchased commercially (Med Chem Express). MK-6240 and NAV-4694 were generously provided by Cerveau Technologies. All other tritium labeling precursors and reference standards except CBD-2115 (Novandi AB and Oxiant Pharmaceuticals) were provided by MedChem Imaging, Inc. All other reagents were purchased from Millipore Sigma unless otherwise stated.

Human Postmortem Brain Tissue

Fresh-frozen human CTE brain tissues were obtained from the Understanding Neurologic Injury and Traumatic Encephalopathy (UNITE) Brain Bank. All AD and healthy control tissue was obtained from the Douglas Bell Canada Brain Bank, and Folio Biosciences, respectively, in accordance with the guidelines put forth by the Centre for Addiction and Mental Health Research Ethics Board (protocol 036-2019). Tissue demographics are summarized in Supplemental Table 1 (supplemental materials are available at <http://jnm.snmjournals.org>).

Detailed autoradiography and immunohistochemistry protocols can be found in the supplemental methods.

RESULTS

Specific Binding and Tau Target Density Quantification with ^3H -Flortaucipir in CTE Tissue

Specific binding of ^3H -flortaucipir in CTE I, II, and IV tissues was evaluated under homologous blocking conditions. Specific binding in whole sections was $68.7\% \pm 10.5\%$ (mean \pm SD), compared with $76.0\% \pm 12.9\%$ in gray matter and $42.1\% \pm 13.1\%$ in white matter ($n = 12$; Fig. 1A). ^3H -flortaucipir binding was also evaluated under heterologous blocking conditions with unlabeled MK-6240, and specific binding was $27.3\% \pm 13.6\%$ (Supplemental Fig. 1; $n = 12$). Off-target binding of ^3H -flortaucipir to monoamine oxidase (MAO)-A/B was investigated by heterologous blocking with clorgyline and lazabemide, inhibitors for MAO-A and MAO-B, respectively. Clorgyline inhibited ^3H -flortaucipir binding by $43.9\% \pm 4.6\%$ ($n = 3$), indicating off-target binding to MAO-A, whereas blocking for MAO-B did not inhibit ^3H -flortaucipir binding (Fig. 1B).

Saturation binding was assayed to quantify a tau B_{max} for the first time (to our knowledge) in CTE. Increasing concentrations of ^3H -flortaucipir allowed for saturability of the target and quantification of a B_{max} , with nonspecific binding defined by homologous blockade, and off-target binding to MAO-A was displaced by clorgyline. Mean saturation curves displaying total, specific, and nonspecific

binding are shown for quantification of tau protein in CTE IV ($n = 4$; Fig. 1C) and AD ($n = 1$; Fig. 1D). With ^3H -flortaucipir in CTE IV, the experimentally determined B_{max} was 99.8 ± 53.8 nM ($n = 4$) and target affinity (K_d) was 14.3 ± 6.6 nM ($n = 4$). Scatchard analysis of these saturation studies is shown in Supplemental Figure 2.

Comparative Binding of ^3H -Flortaucipir, ^3H -MK-6240, and ^3H -PI-2620 in CTE Tissues

^3H -flortaucipir, ^3H -MK-6240, and ^3H -PI-2620 were evaluated for total radiotracer signal in CTE IV cases, compared with an AD-positive control (Fig. 2). The total signal of ^3H -flortaucipir is shown, alongside the addition of clorgyline to eliminate the off-target binding contribution to MAO-A. ^3H -flortaucipir with clorgyline aligned with ^3H -MK-6240, ^3H -PI-2620, and AT8 immunostaining for phospho-tau, with higher signal and antibody density localized to the gray matter. Additional CTE I, CTE II, and CTE IV cases were evaluated with ^3H -MK-6240 and showed negligible binding (Supplemental Fig. 3).

^3H -APN-1607 Distribution in CTE and Off-Target Binding to Amyloid- β

^3H -APN-1607 was evaluated for total radiotracer signal and blocking with self, flortaucipir, or NAV-4694 (also known as flutafuranol and AZD-4694), an $\text{A}\beta$ binding ligand (27), and compared with 6F/3D immunohistochemistry for $\text{A}\beta$ in CTE IV and AD tissues (Fig. 3). ^3H -APN-1607 binding was investigated in CTE I and II cases; however, no signal was observed (Supplemental Fig. 4). Positive ^3H -APN-1607 binding was observed in a subset of CTE IV cases and a positive control AD case. Under homologous blocking conditions, specific binding was highly variable ($52.9\% \pm 19.6\%$; $n = 6$). The ^3H -APN-1607 binding when blocking with flortaucipir revealed increased radiotracer binding in 1 case, whereas the remaining 5 cases demonstrated variable radiotracer displacement ($27.1\% \pm 14.0\%$). Variable displacement of ^3H -APN-1607 binding by NAV-4694 was observed ($31.7\% \pm 22.9\%$; $n = 6$), with higher displacement in samples with greater $\text{A}\beta$ burden. In 1 case (CTE11) with the highest $\text{A}\beta$ burden, ^3H -APN-1607 binding was displaced by 61.4% with NAV-4694, compared with an $\text{A}\beta$ -negative case (CTE9), which had a 10-fold lower displacement (6.3%).

DISCUSSION

Specific Binding and Tau Target Density Quantification with ^3H -Flortaucipir in CTE Tissue

We evaluated specific binding of ^3H -flortaucipir in CTE stages I–IV (Fig. 1A). The highest percentage specific binding of ^3H -flortaucipir was observed by homologous blockade in the gray matter; however, radiotracer signal was maximally displaced by 80%, indicating a degree of nondisplaceable binding with this tracer. The nonspecific binding observed in the white matter can confound PET imaging analysis with ^3H -flortaucipir (14,28).

^3H -flortaucipir binding to MAOs has been reported by in vitro assays, whereas in vivo studies have reported both the presence and the absence of off-target binding (29–32). The reported off-target binding of ^3H -flortaucipir to MAO-A and MAO-B presents a challenge for interpretation of specific binding quantitation and distribution in vitro, as binding of ^3H -flortaucipir to MAO-A/B has been reported with similar affinities to tau (31). MAO-B is considered a biomarker of reactive astrocytes (33), which are involved in the pathogenesis of CTE (34,35). We recently evaluated PET imaging biomarkers for neuroinflammation in pathologically diagnosed cases of

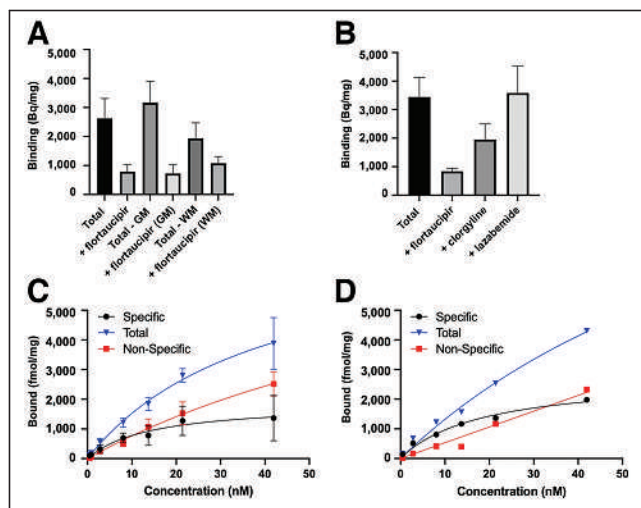


FIGURE 1. ^3H -flortaucipir binding in CTE IV and AD. (A) Quantification of ^3H -flortaucipir (5 nM) total signal compared with homologous block signal in whole section, gray matter, and white matter of CTE cases. Binding is reported in Bq/mg ($n = 12$). (B) Quantification of ^3H -flortaucipir (5 nM) total signal compared with blocking under homologous conditions (10 μM), clorgyline (10 μM) for MAO-A, or lazabemide (10 μM) for MAO-B ($n = 3$) of CTE cases. (C and D) Saturation analysis with increasing ^3H -flortaucipir concentration in CTE ($n = 4$) (C) and AD ($n = 1$) (D) tissue sections to quantify B_{max} and K_d . GM = gray matter; WM = white matter.

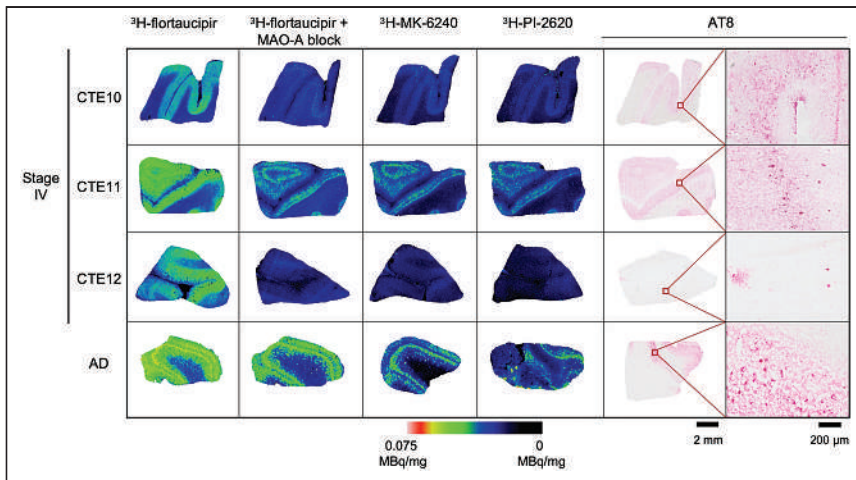


FIGURE 2. ^3H -flortaucipir, ^3H -MK-6240, and ^3H -PI-2620 binding in CTE IV. Total ^3H -flortaucipir signal (5 nM), displacement by $10\ \mu\text{M}$ clorgyline to block off-target binding to MAO-A, total ^3H -MK-6240 (5 nM) binding, and total ^3H -PI-2620 (6 nM) binding are compared with AT8 immunostaining for phospho-tau at 2-mm and 200- μm scales in CTE IV and AD.

CTE and found high variability in the neuroinflammatory pathology of brain injuries (35). No off-target binding of ^3H -flortaucipir to MAO-B was observed under the present assay conditions, whereas off-target binding to MAO-A was identified by blocking with clorgyline ($43.9\% \pm 4.6\%$; $n = 3$; Fig. 1B). Increases in MAO-A availability have been reported in CTE comorbidities (36,37) and could contribute to the off-target binding observed here. The present study quantified a B_{max} ($99.8 \pm 53.8\ \text{nM}$; $n = 4$) and K_d ($14.3 \pm 6.6\ \text{nM}$; $n = 4$; mean \pm SD) for stage IV CTE tau with ^3H -flortaucipir for the first time, to our knowledge (Fig. 1C). The variability observed in

binding in only the most severe CTE IV case, with minimal binding in 2 other CTE IV cases (Fig. 2), despite tau pathology in all CTE stages examined. In the most severe CTE IV case, ^3H -flortaucipir signal blocked with clorgyline strongly aligned with AT8 immunostaining, ^3H -MK-6240, and ^3H -PI-2620 radiotracer binding. ^3H -MK-6240 and ^3H -PI-2620 were evaluated in all CTE stages, although radiotracer binding was again observed only in the most severe CTE IV case. ^{18}F -MK-6240 was previously evaluated in a case study of a single retired Australian Rules football player in whom a CTE-like tau pattern was observed (18). To our knowledge, clinical PET

B_{max} between samples demonstrates how tau abundance within CTE stage subgroups varies, and larger sample sizes would be beneficial to further understand tau aggregation within CTE stages. Although off-target binding of ^3H -flortaucipir to MAO-B may not confound accurate quantification of tau in human PET imaging studies with ^{18}F -flortaucipir, MAO-A binding should be considered for in vivo imaging studies in patients who have sustained repetitive brain injuries or who have been identified as suspected-CTE cases.

Comparative Binding of ^3H -Flortaucipir, ^3H -MK-6240, and ^3H -PI-2620 in CTE Tissues

Radiotracer binding was compared among ^3H -flortaucipir, ^3H -MK-6240, and ^3H -PI-2620 and with AT8 immunostaining for tau aggregate distribution (Fig. 2). Displacing the MAO-A binding contribution of ^3H -flortaucipir resulted in robust radiotracer binding in only the most severe CTE IV case, with minimal binding in 2 other CTE IV cases (Fig. 2), despite tau pathology in all CTE stages examined. In the most severe CTE IV case, ^3H -flortaucipir signal blocked with clorgyline strongly aligned with AT8 immunostaining, ^3H -MK-6240, and ^3H -PI-2620 radiotracer binding. ^3H -MK-6240 and ^3H -PI-2620 were evaluated in all CTE stages, although radiotracer binding was again observed only in the most severe CTE IV case. ^{18}F -MK-6240 was previously evaluated in a case study of a single retired Australian Rules football player in whom a CTE-like tau pattern was observed (18). To our knowledge, clinical PET research studies using ^{18}F -PI-2620 in brain injury populations are yet to be reported; however, ^{18}F -PI-2620 has been proposed for use in in vivo imaging studies of non-AD tauopathies (38,39). The present in vitro autoradiography studies show ^3H -PI-2620 binding is similar to ^3H -MK-6240. This work supports exploring the potential of ^{18}F -MK-6240 and ^{18}F -PI-2620 for PET imaging in patients with suspected mixed AD/CTE pathology or severe suspected CTE; further evaluation of these radiotracers in severe CTE tissues or high at-risk groups is required to determine the utility of this tracer for imaging CTE tau.

Effect of Ethanol Washes on Autoradiography Studies

Our concerns that ethanol washes are not physiologically relevant to evaluation of radiotracer binding in vitro, coupled with the risk of washing away nonspecific binding, led us to investigate the assays in the absence and presence of ethanol. Ethanol has been included in incubation and wash buffers in several in vitro characterization studies of ^{18}F -flortaucipir, ^{18}F -MK-6240, and ^{18}F -PI-2620 (13,14,38). A comparison of autoradiography assay conditions with and

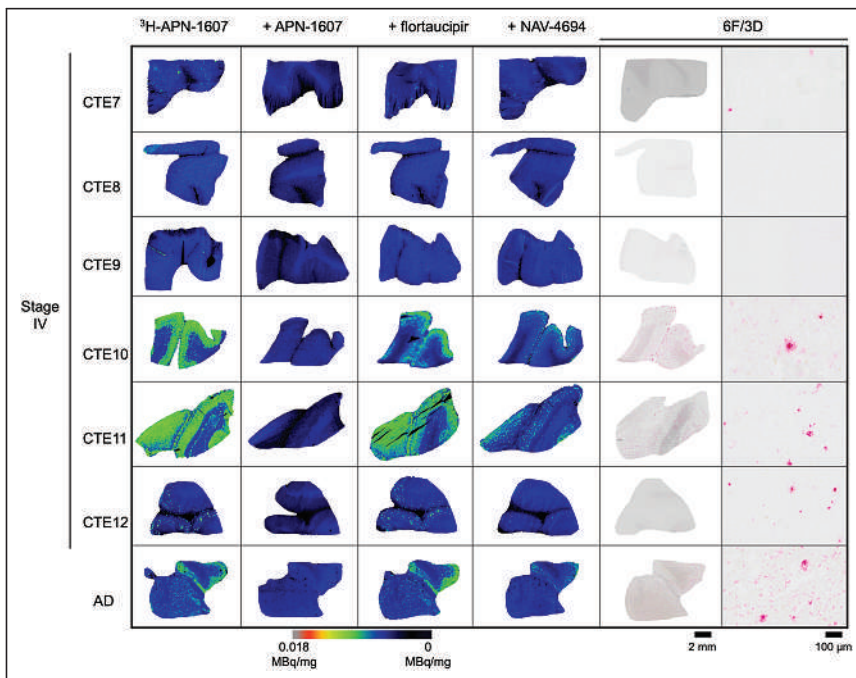


FIGURE 3. Binding of ^3H -APN-1607 in CTE IV and AD. Total ^3H -APN-1607 (5 nM) binding is shown along with displacement by unlabeled APN-1607 ($10\ \mu\text{M}$), flortaucipir ($10\ \mu\text{M}$), and NAV-4694 ($10\ \mu\text{M}$) to indicate $\text{A}\beta$ binding contribution compared with 6F/3D immunohistochemistry for $\text{A}\beta$ shown at 2-mm and 200- μm scales in CTE IV and AD.

without ethanol was performed in the current work (Supplemental Fig. 5). We showed that ethanol is not necessary to demonstrate specific radiotracer distribution and should be used with caution because ethanol washes were found to artificially increase the signal-to-noise ratio, reducing nonspecific binding while risking washing away of specific binding. In addition, ethanol washes cannot be conducted in vivo, therefore limiting the use of radiotracers that require this step to obtain a suitable specific binding window.

³H-APN-1607 Distribution in CTE and Off-Target Binding to Amyloid- β

¹⁸F-APN-1607 is an ¹⁸F-labeled derivative of ¹¹C-PBB3 that has been translated for human PET imaging studies in AD patients and in the 4R-tau dominant tauopathy, progressive supranuclear palsy (40–42). APN-1607 has been shown to bind parallel to the area of A β filaments in tau protein aggregates (43,44). Off-target binding of ¹¹C-PBB3 to A β has been previously described, but ¹⁸F-APN-1607 binding, if any, to A β has not yet been reported. Substantial binding of ³H-APN-1607 to A β was observed in CTE IV cases with a high amyloid plaque burden, as shown by displacement with the A β -targeting compound NAV-4694 (Fig. 3). CTE IV cases with a lower A β burden demonstrated lower total radiotracer binding and displacement by NAV-4694, showing ³H-APN-1607 off-target binding to A β under the present assay conditions.

Despite past reports in which APN-1607 demonstrated binding in 4R-tau dominant conditions (41), ³H-APN-1607 showed no binding in early-stage CTE cases, for which the dominant tau isoform found in neurons is 4R tau (45). These findings indicate limited utility of ³H-APN-1607 to image tau inclusions in early-stage CTE and further limitations of off-target binding in CTE cases with mixed pathology. ¹⁸F-APN-1607 is susceptible to photoisomerization, requiring all experimental procedures to be conducted in the absence of fluorescent light (46). These limitations will hinder the widespread use of ¹⁸F-APN-1607.

³H-CBD-2115 (47) showed elevated signal in CTE IV, compared with CTE I or II, and limitations of meningeal binding (Supplemental Fig. 6). RD3 immunostaining for 3R tau was also performed to show both 3R- and 4R-tau isoforms in CTE (Supplemental Fig. 7).

Heterogeneity of Tauopathies

Limitations of the present study include tissue availability; a larger sample size would allow further interpretation of tau PET radiotracer binding to tau pathology, as this work reveals variability in binding of several radiotracers between and within CTE stage subgroups. It would also be of value to include additional brain regions for analysis in future studies to explore tau PET tracer binding beyond the frontal cortex, for a greater representation of whole-brain imaging achieved with in vivo PET imaging studies. Recent computational studies have revealed different affinity binding sites for tau radiotracers in fibrils associated with different tauopathies (48). However, it was concluded that cryoelectron microscopy is not sufficient for the structure-based tracer discovery for certain targets, as they may have potential-but-hidden binding sites. In addition, variability in pathology is expected within CTE because many factors contribute to disease development and progression, including the type and frequency of brain injury, the anatomic region of impact, and concussive-versus-subconcussive impacts. Investigating these factors will provide opportunities into understanding how brain injuries contribute to CTE disease pathology and progression.

CONCLUSION

We have reported, for the first time to our knowledge, a B_{max} and K_d for CTE tau with ³H-flortaucipir. Off-target binding of ³H-flortaucipir to MAO-A should be considered during in vivo PET imaging studies on patients who have sustained repetitive brain injuries or are suspected of having CTE. Although ³H-MK-6240 and ³H-PI-2620 do not bind optimally to tau aggregates in CTE, the respective ¹⁸F PET radiopharmaceuticals should be evaluated in clinical research studies of severe suspected CTE cases or in the presence of mixed AD/CTE pathology. ³H-APN-1607 showed limited utility to image tau inclusions in early-stage CTE and off-target binding to A β in CTE cases with mixed pathology. All radiotracers evaluated showed binding only in late-stage CTE cases. This study provides critical insights into CTE tau target density, off-target binding of tau PET tracers, and binding of tau PET tracers optimized for AD alongside tau immunostaining to inform in vivo PET imaging studies on suspected-CTE groups, contributing to the ultimate goal of imaging CTE in life.

DISCLOSURE

Cassidy Varlow received a Canada Graduate Scholarship (doctoral) from the Canadian Institutes of Health Research (CIHR). Neil Vasdev received funding from the National Institute on Aging of the National Institutes of Health (NIH; R01AG052414), Azrieli Foundation, Canada Foundation for Innovation, Ontario Research Fund, and Canada Research Chairs Program. Enigma Biomedical Group, Inc., and its affiliates (Cerveau Technologies and Meilleur Technologies) provided radiolabeled or unlabeled MK-6240, CBD-2115, and NAV-4694. Tissue was obtained from the Boston University Alzheimer's Disease Research and CTE Center's brain bank, also referred to as the Understanding Neurologic Injury and Traumatic Encephalopathy (UNITE) or Veterans Affairs–Boston University–Concussion Legacy Foundation (VA-BU-CLF) brain bank (funded by grants P30AG072978, U54NS115266, R01AG062348, and RF1AG057902). Neil Vasdev is a cofounder of MedChem Imaging, Inc. No other potential conflict of interest relevant to this article was reported.

ACKNOWLEDGMENT

We thank Dr. Samuel Svensson from Oxiant Pharmaceuticals for support.

KEY POINTS

QUESTION: Can existing tau PET tracers, optimized for AD, be used to image CTE tau in vitro?

PERTINENT FINDINGS: This study showed that ³H-flortaucipir and ³H-APN-1607 display off-target binding to MAO-A and A β , respectively, in human CTE tissues. ³H-MK-6240 and ³H-PI-2620 bind CTE tau in severe- or mixed-pathology cases.

IMPLICATIONS FOR PATIENT CARE: Off-target binding with ¹⁸F-flortaucipir and ¹⁸F-APN-1607 needs to be considered a confounding factor in PET imaging studies of patients with brain injuries. ¹⁸F-MK-6240 and ¹⁸F-PI-2620 are the most promising tau PET radiotracers for further evaluation in patients with severe suspected CTE.

REFERENCES

1. Banks SJ. Chronic traumatic encephalopathy (CTE). In: Tousi B, Cummings J, eds. *Neuro-Geriatrics: A Clinical Manual*. Springer International Publishing; 2017:183–194.

2. McKee AC, Cairns NJ, Dickson DW, et al. The first NINDS/NIBIB consensus meeting to define neuropathological criteria for the diagnosis of chronic traumatic encephalopathy. *Acta Neuropathol (Berl)*. 2016;131:75–86.
3. Bieniek KF, Cairns NJ, Crary JF, et al. The second NINDS/NIBIB consensus meeting to define neuropathological criteria for the diagnosis of chronic traumatic encephalopathy. *J Neuropathol Exp Neurol*. 2021;80:210–219.
4. Montenegro PH, Baugh CM, Daneshvar DH, et al. Clinical subtypes of chronic traumatic encephalopathy: literature review and proposed research diagnostic criteria for traumatic encephalopathy syndrome. *Alzheimers Res Ther*. 2014;6:68.
5. Omalu B, Hammers J. Letter: recommendation to create new neuropathologic guidelines for the post-mortem diagnosis of chronic traumatic encephalopathy. *Neurosurgery*. 2021;89:E97–E98.
6. Mez J, Alosco ML, Daneshvar DH, et al. Validity of the 2014 traumatic encephalopathy syndrome criteria for CTE pathology. *Alzheimers Dement*. 2021;17:1709–1724.
7. Stein TD, Alvarez VE, McKee AC. Concussion in chronic traumatic encephalopathy. *Curr Pain Headache Rep*. 2015;19:47.
8. Okonkwo DO, Puffer RC, Minhas DS, et al. [¹⁸F]FDG, [¹¹C]PiB, and [¹⁸F]AV-1451 PET imaging of neurodegeneration in two subjects with a history of repetitive trauma and cognitive decline. *Front Neurol*. 2019;10:831.
9. Mantyh WG, Spina S, Lee A, et al. Tau positron emission tomographic findings in a former US football player with pathologically confirmed chronic traumatic encephalopathy. *JAMA Neurol*. 2020;77:517–521.
10. Barrio JR, Small GW, Wong K-P, et al. In vivo characterization of chronic traumatic encephalopathy using [F-18]FDDNP PET brain imaging. *Proc Natl Acad Sci*. 2015;112:E2039–E2047.
11. Mitsis EM, Riggio S, Kostakoglu L, et al. Tauopathy PET and amyloid PET in the diagnosis of chronic traumatic encephalopathies: studies of a retired NFL player and of a man with FTD and a severe head injury. *Transl Psychiatry*. 2014;4:e441.
12. Dickstein DL, Pullman MY, Fernandez C, et al. Cerebral [¹⁸F]T807/AV1451 retention pattern in clinically probable CTE resembles pathognomonic distribution of CTE tauopathy. *Transl Psychiatry*. 2016;6:e900.
13. Aguero C, Dhaynaut M, Normandin MD, et al. Autoradiography validation of novel tau PET tracer [F-18]-MK-6240 on human postmortem brain tissue. *Acta Neuropathol Commun*. 2019;7:37.
14. Marquí M, Agüero C, Amaral AC, et al. [¹⁸F]-AV-1451 binding profile in chronic traumatic encephalopathy: a postmortem case series. *Acta Neuropathol Commun*. 2019;7:164.
15. Omalu B, Small GW, Bailes J, et al. Postmortem autopsy-confirmation of antemortem [F-18]FDDNP-PET scans in a football player with chronic traumatic encephalopathy. *Neurosurgery*. 2018;82:237–246.
16. Takahata K, Kimura Y, Sahara N, et al. PET-detectable tau pathology correlates with long-term neuropsychiatric outcomes in patients with traumatic brain injury. *Brain*. 2019;142:3265–3279.
17. Small GW, Kepe V, Siddarth P, et al. PET scanning of brain tau in retired national football league players: preliminary findings. *Am J Geriatr Psychiatry*. 2013;21:138–144.
18. Krishnadas N, Doré V, Lamb F, et al. Case report: ¹⁸F-MK6240 tau positron emission tomography pattern resembling chronic traumatic encephalopathy in a retired Australian Rules football player. *Front Neurol*. 2020;11:598980.
19. Stern RA, Adler CH, Chen K, et al. Tau positron-emission tomography in former National Football League players. *N Engl J Med*. 2019;380:1716–1725.
20. Gorgoraptis N, Li LM, Whittington A, et al. In vivo detection of cerebral tau pathology in long-term survivors of traumatic brain injury. *Sci Transl Med*. 2019;11:1–14.
21. Robinson ME, McKee AC, Salat DH, et al. Positron emission tomography of tau in Iraq and Afghanistan veterans with blast neurotrauma. *Neuroimage Clin*. 2019;21:101651.
22. Wooten DW, Ortiz-Terán L, Zubcevic N, et al. Multi-modal signatures of tau pathology, neuronal fiber integrity, and functional connectivity in traumatic brain injury. *J Neurotrauma*. 2019;36:3233–3243.
23. Lesman-Segev OH, La Joie R, Stephens ML, et al. Tau PET and multimodal brain imaging in patients at risk for chronic traumatic encephalopathy. *Neuroimage Clin*. 2019;24:102025.
24. Marklund N, Vedung F, Lubberink M, et al. Tau aggregation and increased neuroinflammation in athletes after sports-related concussions and in traumatic brain injury patients: a PET/MR study. *Neuroimage Clin*. 2021;30:102665.
25. Leuzy A, Chiotis K, Lemoine L, et al. Tau PET imaging in neurodegenerative tauopathies: still a challenge. *Mol Psychiatry*. 2019;24:1112–1134.
26. Lin A, Charney M, Shenton ME, Koerte IK. Chapter 29: chronic traumatic encephalopathy—neuroimaging biomarkers. In: Hainline B, Stern RA, eds. *Handbook of Clinical Neurology*. Vol 158. Elsevier; 2018:309–322.
27. Cselényi Z, Jönhagen ME, Forsberg A, et al. Clinical validation of ¹⁸F-AZD4694, an amyloid- β -specific PET radioligand. *J Nucl Med*. 2012;53:415–424.
28. Baker SL, Harrison TM, Maass A, La Joie R, Jagust WJ. Effect of off-target binding on ¹⁸F-flortaucipir variability in healthy controls across the life span. *J Nucl Med*. 2019;60:1444–1451.
29. Hansen AK, Brooks DJ, Borghammer P. MAO-B inhibitors do not block in vivo flortaucipir ([¹⁸F]-AV-1451) binding. *Mol Imaging Biol*. 2018;20:356–360.
30. Murugan NA, Chiotis K, Rodriguez-Vieitez E, Lemoine L, Ågren H, Nordberg A. Cross-interaction of tau PET tracers with monoamine oxidase B: evidence from in silico modelling and in vivo imaging. *Eur J Nucl Med Mol Imaging*. 2019;46:1369–1382.
31. Vermeiren C, Motte P, Viot D, et al. The tau positron-emission tomography tracer AV-1451 binds with similar affinities to tau fibrils and monoamine oxidases. *Mov Disord*. 2018;33:273–281.
32. Drake LR, Pham JM, Desmond TJ, et al. Identification of AV-1451 as a weak, nonselective inhibitor of monoamine oxidase. *ACS Chem Neurosci*. 2019;10:3839–3846.
33. Ekblom J, Jossan SS, Orelund L, Walum E, Aquilonius SM. Reactive gliosis and monoamine oxidase B. In: *Amine Oxidases: Function and Dysfunction*. Springer; 1994:253–258.
34. Chancellor KB, Chancellor SE, Duke-Cohan JE, et al. Altered oligodendroglia and astroglia in chronic traumatic encephalopathy. *Acta Neuropathol (Berl)*. 2021;142:295–321.
35. Varlow C, Knight AC, McQuade P, Vasdev N. Characterization of neuroinflammatory positron emission tomography biomarkers in chronic traumatic encephalopathy. *Brain Commun*. 2022;4:fcac019.
36. Mahar I, Alosco ML, McKee AC. Psychiatric phenotypes in chronic traumatic encephalopathy. *Neurosci Biobehav Rev*. 2017;83:622–630.
37. Meyer JH, Ginovart N, Boovariwala A, et al. Elevated monoamine oxidase A levels in the brain: an explanation for the monoamine imbalance of major depression. *Arch Gen Psychiatry*. 2006;63:1209–1216.
38. Kroth H, Oden F, Molette J, et al. Discovery and preclinical characterization of [¹⁸F]PI-2620, a next-generation tau PET tracer for the assessment of tau pathology in Alzheimer's disease and other tauopathies. *Eur J Nucl Med Mol Imaging*. 2019;46:2178–2189.
39. Brendel M, Barthel H, van Eimeren T, et al. Assessment of ¹⁸F-PI-2620 as a biomarker in progressive supranuclear palsy. *JAMA Neurol*. 2020;77:1408–1419.
40. Zhou XY, Lu JY, Liu FT, et al. In vivo ¹⁸F-APN-1607 tau positron emission tomography imaging in MAPT mutations: cross-sectional and longitudinal findings. *Mov Disord*. 2022;37:525–534.
41. Li L, Liu F-T, Li M, et al. Clinical utility of ¹⁸F-APN-1607 tau PET imaging in patients with progressive supranuclear palsy. *Mov Disord*. 2021;36:2314–2323.
42. Xu X, Ruan W, Liu F, et al. ¹⁸F-APN-1607 tau positron emission tomography imaging for evaluating disease progression in Alzheimer's disease. *Front Aging Neurosci*. 2022;13:789054.
43. Shi Y, Murzin AG, Falcon B, et al. Cryo-EM structures of tau filaments from Alzheimer's disease with PET ligand APN-1607. *Acta Neuropathol (Berl)*. 2021;141:697–708.
44. Zhou Y, Li J, Nordberg A, Ågren H. Dissecting the binding profile of PET tracers to corticobasal degeneration tau fibrils. *ACS Chem Neurosci*. 2021;12:3487–3496.
45. Cherry JD, Kim SH, Stein TD, et al. Evolution of neuronal and glial tau isoforms in chronic traumatic encephalopathy. *Brain Pathol*. 2020;30:913–925.
46. Kawamura K, Hashimoto H, Furutsuka K, et al. Radiosynthesis and quality control testing of the tau imaging positron emission tomography tracer [¹⁸F] PM-PBB3 for clinical applications. *J Labelled Comp Radiopharm*. 2021;64:109–119.
47. Lindberg A, Knight AC, Sohn D, et al. Radiosynthesis, in vitro and in vivo evaluation of [¹⁸F]CBD-2115 as a first-in-class radiotracer for imaging 4R-tauopathies. *ACS Chem Neurosci*. 2021;12:596–602.
48. Murugan NA, Nordberg A, Ågren H. Cryptic sites in tau fibrils explain the preferential binding of the AV-1451 PET tracer toward Alzheimer's tauopathy. *ACS Chem Neurosci*. 2021;12:2437–2447.

Neurovascular Uncoupling: Multimodal Imaging Delineates the Acute Effects of 3,4-Methylenedioxymethamphetamine

Tudor M. Ionescu¹, Mario Amend¹, Tadashi Watabe^{1,2}, Jun Hatazawa², Andreas Maurer¹, Gerald Reischl^{1,3}, Bernd J. Pichler^{1,3}, Hans F. Wehrl^{*1}, and Kristina Herfert^{*1}

¹Werner Siemens Imaging Center, Department of Preclinical Imaging and Radiopharmacy, Eberhard Karls University Tuebingen, Tuebingen, Germany; ²Department of Nuclear Medicine and Tracer Kinetics, Osaka University, Osaka, Japan; and ³Cluster of Excellence iFIT (EXC 2180) "Image Guided and Functionally Instructed Tumor Therapies", University of Tuebingen, Tuebingen, Germany

Psychedelic compounds such as 3,4-methylenedioxymethamphetamine (MDMA) have attracted increasing interest in recent years because of their therapeutic potential in psychiatric disorders. To understand the acute effects of psychedelic drugs *in vivo*, blood-oxygenation-level-dependent (BOLD) functional MRI (fMRI) has been widely used. In particular, fMRI studies have suggested that MDMA leads to inhibition of brain activity, challenging previous hypotheses indicating mainly excitatory effects based, among others, on increased metabolism shown by ¹⁸F-FDG functional PET (fPET). However, interpretation of hemodynamic changes induced by psychedelics is difficult because of their potent vascular effects. **Methods:** We aimed to delineate the acute effects of MDMA using simultaneous PET/fMRI in rats. For this purpose, hemodynamic changes measured by BOLD fMRI were related to alterations in glucose utilization and serotonin transporter (SERT) occupancy using ¹⁸F-FDG fPET/fMRI and ¹¹C-DASB PET/fMRI. **Results:** We show that MDMA induces localized increases in glucose metabolism in limbic projection areas involved in emotional processing. The increased glucose metabolism was accompanied by global cerebral and extracerebral hemodynamic decreases. We further demonstrated a strong correlation between SERT occupancies and regional BOLD reductions after acute MDMA administration. **Conclusion:** Our data indicate that hemodynamic decreases after acute MDMA administration are of a nonneuronal nature and initiate peripherally. Within the brain, MDMA triggers neuronal activation in limbic projection areas, whereas increased serotonin levels induced by SERT blockage cause neurovascular uncoupling through direct vascular effects. Correct understanding of the *in vivo* mechanism of MDMA not only supports ongoing research but also warrants a reassessment of previous studies on neuronal effects of psychedelics relying on neurovascular coupling and recommends ¹⁸F-FDG fPET as a potentially more robust measure for pharmacologic research.

Key Words: methylenedioxymethamphetamine; neurovascular coupling; PET/fMRI; hemodynamics; metabolism; serotonin

J Nucl Med 2023; 64:466–471

DOI: 10.2967/jnumed.122.264391

Psychedelic drugs, including lysergic acid diethylamide, psilocybin, and 3,4-methylenedioxymethamphetamine (MDMA), have recently gained increasing attention because of their potential benefits for treating psychiatric disorders (1). MDMA-assisted psychotherapy is currently in a phase 3 clinical trial to treat severe posttraumatic stress disorder, with encouraging initial results (2). Research in this area is also increasingly associated with the development of imaging techniques as quantitative biomarkers in addition to behavioral parameters (1). To investigate the mechanisms of psychedelic drugs *in vivo*, MRI methods inferring neuronal activity through neurovascular coupling, such as blood-oxygenation-level-dependent (BOLD) functional MRI (fMRI) and arterial spin labeling, have been widely used (3–5). Interestingly, research performed over the last decade using these methods has shown that psychedelic compounds such as MDMA (3) and psilocybin (4) inhibit brain activity, contradicting previous studies that indicated mainly excitatory effects (6–9).

However, the use of hemodynamic methods may be insufficient to understand the effects of psychedelics on neuronal activity. First, psychedelic drugs elicit their effects by strongly affecting one or more neurotransmitter systems (10). Thus, it is crucial to evaluate hemodynamic changes in relation to neurotransmitter alterations. Second, in addition to neuronal effects, an increase in neurotransmitters such as serotonin elicited by psychedelic compounds can have potent vascular effects (11–13). This aspect is particularly critical for methods based on neurovascular coupling, such as BOLD fMRI and arterial spin labeling. The emergence of hybrid PET/MRI allows simultaneous assessment of brain function at multiple physiologic levels. The combination of PET with pharmacologic MRI can offer important complementary insight on drug mechanisms (14,15). Furthermore, recent developments in the administration of ¹⁸F-FDG PET via constant infusion (16) have paved the way toward functional PET (fPET). fPET enables the imaging of changes in glucose metabolism at a resolution of minutes (17), providing a more robust indirect measure of neuronal activity than is possible with fMRI, being largely immune to vascular changes (16).

We aimed to exploit the potential of multimodal imaging to characterize the acute effects of MDMA using PET/fMRI. First, we performed ¹⁸F-FDG fPET/fMRI to simultaneously determine hemodynamic and metabolic changes elicited by MDMA and thereby elucidate potential inhibitory or excitatory actions of this compound. In a second cohort, we used ¹¹C-3-amino-4-(2-dimethylaminomethylphenylsulfanyl)-benzonitrile (¹¹C-DASB) to investigate relationships between hemodynamic alterations and changes in serotonin transporter (SERT) availability, one of the main targets of MDMA (18).

Received May 26, 2022; revision accepted Sep. 14, 2022.
For correspondence or reprints, contact Kristina Herfert (kristina.h erfert@med.uni-tuebingen.de).
*Contributed equally this work.
Published online Sep. 29, 2022.
COPYRIGHT © 2023 by the Society of Nuclear Medicine and Molecular Imaging.

MATERIALS AND METHODS

Animals

Male Lewis rats ($n = 29$) were obtained from Charles River Laboratories and divided into 2 groups: ^{18}F -FDG fPET/fMRI was performed on 17 animals (body weight, 361 ± 19 g), whereas ^{11}C -DASB PET/fMRI was performed on 11 animals (body weight, 365 ± 19 g). Nine fMRI datasets were excluded from the study because of motion during acquisition. One ^{11}C -DASB PET and two ^{18}F -FDG fPET datasets were excluded from the analysis because of paravenous tracer injections. The animals were kept at a room temperature of 22°C and 40%–60% humidity under a 12-h light–dark cycle. The rats were fed with standard diet and received tap water ad libitum. They were kept fasting for 6 h before the start of the experiments. All experiments were performed in accordance with the German Federal Regulations on the Use and Care of Laboratory Animals and approved by the Tübingen regional council. Two additional cohorts scanned under the same ^{18}F -FDG fPET/fMRI and ^{11}C -DASB PET/fMRI protocols, but exposed to phosphate-buffered saline instead of MDMA, are presented in the supplemental materials (available at <http://jnm.snmjournals.org>) (3–6,10,11,15,16,19–36).

Simultaneous PET/fMRI Experiments

The animals were scanned under 1.3% isoflurane and constant monitoring of breathing rate and temperature (Supplemental Fig. 1) using a 7-T small-animal MRI scanner (ClinScan; Bruker). T2-weighted anatomic reference scans and fMRI scans (repetition time, 2,000 ms; echo time, 18 ms) were obtained using a linearly polarized radiofrequency coil for transmission and a 4-channel surface rat brain coil for reception. The PET scans were acquired simultaneously using an in-house–developed insert and reconstructed into 100 frames of 1 min using an ordered-subsets expectation-maximization 2-dimensional algorithm. The MDMA challenge (3.2 mg/kg) was applied 40 min after the start of the acquisition. Additional details on the experimental procedure are provided in the supplemental materials.

Data Analysis

Statistical Parametric Mapping (SPM12, Wellcome Trust Centre for Neuroimaging) via Matlab (The MathWorks) and Analysis of Functional NeuroImages (AFNI, National Institute of Mental Health) were used for data preprocessing as previously reported (37). An extensive description of all preprocessing and analysis steps can be found in the supplemental materials. Average time courses were extracted from all datasets after preprocessing using the MarsBaR toolbox (38) and regions of interest (see Fig. 1 for abbreviations and Supplemental Table 1 for their respective volumes) defined by the atlas of Schiffer et al. (34). Additionally, extracerebral BOLD fMRI signals were extracted using binary masks generated with AFNI. The general linear model available in SPM was applied to determine voxels with significantly altered fMRI and PET signals after MDMA exposure. For all datasets, baseline was defined as 30–40 min after the scan start, when tracer equilibrium had been reached between the regions with high SERT density and high ^{18}F -FDG uptake and the reference regions. The ^{18}F -FDG fPET data were normalized using cerebellar uptake. For ^{11}C -DASB PET, the cerebellar gray matter was chosen as the reference region as previously described (36). For all methods, the signal at baseline was compared with six 10-min blocks between the challenge (40 min after the scan start) and the end of the scan (100 min after the scan start). Group-level T-maps were generated for all cohorts, methods, and time periods. All T-maps were subjected to voxelwise signal quantification to determine the regional contributions of the brain regions selected. The average T-scores of all voxels comprising each region were calculated for each period and modality to compare the respective spatial patterns of MDMA effects on hemodynamics, glucose metabolism, and SERT occupancy.

RESULTS

Metabolic Increases Accompany Hemodynamic Reductions

First, we investigated the relationship between hemodynamic and metabolic changes after acute MDMA administration using simultaneous ^{18}F -FDG fPET/fMRI (Figs. 1 and 2; Supplemental Fig. 2).

The normalized ^{18}F -FDG fPET time–activity curves for all regions and the average whole-brain time–activity curve and voxelwise uptake maps (Fig. 1A) indicated an increase in metabolism in the midbrain and in the anterior subcortical and frontal cortical areas, whereas more minor or no changes occurred in the posterior cortical regions. Notably, we found a simultaneous decrease in hemodynamics, as indicated by BOLD fMRI (Fig. 1B). The whole-brain–averaged BOLD fMRI signal was reduced by 4.5% 15 min after the challenge. Importantly, the data revealed that the decreases were global and occurred in all regions investigated. A temporal comparison of the ^{18}F -FDG fPET and BOLD signal changes relative to baseline is shown in Figure 1C. The highest metabolic increases occurred in frontal areas, including the caudate putamen (22%), insular cortex (21%), medial prefrontal cortex (18%), and amygdala (13.5%). Increases in all regions ($>1\%$) were observed within 5 min of the challenge.

The voxelwise general-linear-model analyses presented in Figure 2 revealed metabolic

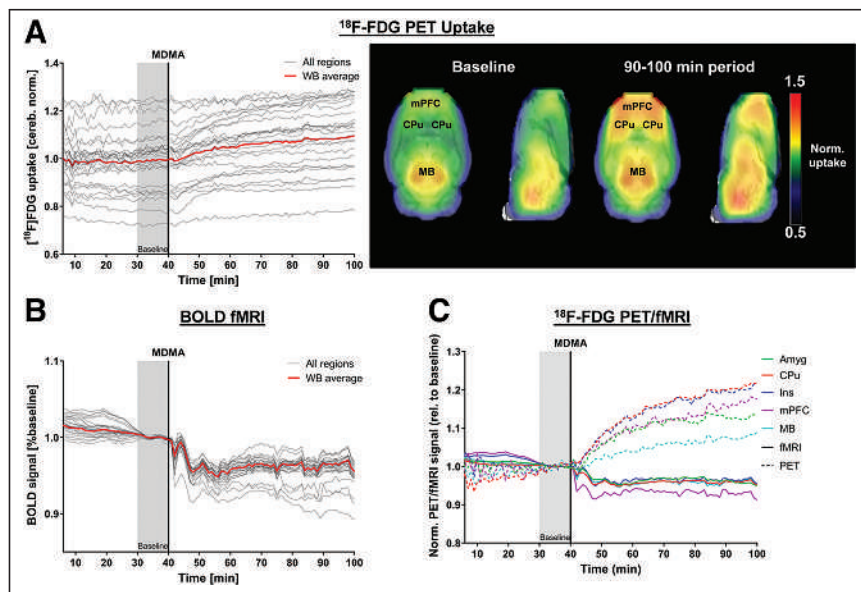


FIGURE 1. Regionwise evaluation of ^{18}F -FDG fPET and BOLD fMRI signal changes. (A) Time–activity curves for all regions and whole-brain average. Voxelwise normalized uptake maps indicate ^{18}F -FDG uptake at baseline and at 90–100 min. (B) Regional BOLD fMRI signals normalized to respective baseline periods. (C) Both signals normalized to baseline period over last 10 min before MDMA administration for common frame of reference. Amyg = amygdala; CPu = caudate putamen; Ins = insular cortex; MB = midbrain; mPFC = medial prefrontal cortex; WB = whole brain.

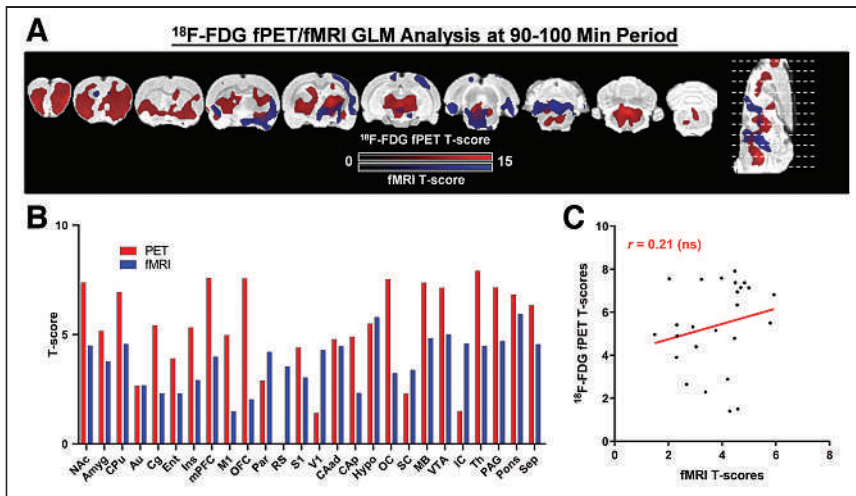


FIGURE 2. General-linear-model analysis of ^{18}F -FDG fPET/fMRI cohort. (A) Voxelwise analysis of both signals at 90–100 min ($P < 0.05$ family-wise error-corrected at voxel level for PET, $P < 0.001$ at voxel level with $P < 0.05$ family-wise error cluster-level correction for fMRI, $n = 15$ for fPET, $n = 9$ for fMRI). (B) Bar diagram indicating average T-scores for each region and modality. (C) Average regional T-scores plotted in scatter diagram to evaluate spatial correlation of both readouts. Amyg = amygdala; Au = auditory cortex; CAad = anterodorsal hippocampus; CAP = posterior hippocampus; Cg = cingulate cortex; CPu = caudate putamen; Ent = entorhinal cortex; GLM = general linear model; Hypo = hypothalamus; IC = inferior colliculus; Ins = insular cortex; M1 = motor cortex; MB = midbrain; mPFC = medial prefrontal cortex; NAc = nucleus accumbens; OC = olfactory cortex; OFC = orbitofrontal cortex; PAG = periaqueductal gray matter; Par = parietal cortex; RS = retrosplenial cortex; S1 = somatosensory cortex; SC = superior colliculus; Sep = septum; Th = thalamus; V1 = visual cortex; VTA = ventral tegmental area.

increases across several subcortical areas and in frontal cortical areas between 90 and 100 min. The medial prefrontal cortex and orbitofrontal cortex ($T = 7.6$ for both), along with the midbrain ($T = 7.4$), thalamus ($T = 7.9$), and nucleus accumbens ($T = 7.4$), exhibited the most

6 min after the challenge (Fig. 3B). Regions with higher baseline SERT availability showed a faster response than regions with lower baseline SERT availability (Fig. 3C). For example, ^{11}C -DASB binding in the midbrain ($\text{BP}_{\text{ND}} = 2.1$) decreased immediately after the challenge. In contrast, ^{11}C -DASB binding in the caudate putamen ($\text{BP}_{\text{ND}} = 1.6$) and medial prefrontal cortex ($\text{BP}_{\text{ND}} = 1.6$) remained stable or increased briefly. After approximately 10 min, ^{11}C -DASB binding decreased in all regions until it reached equilibrium at 30–40 min after the challenge (39% decrease for medial prefrontal cortex, 44% decrease for caudate putamen). BOLD decreases occurred homogeneously, peaking 30 min after the challenge (~8.5% in medial prefrontal cortex, ~5.5% in caudate putamen, and ~6.5% in midbrain).

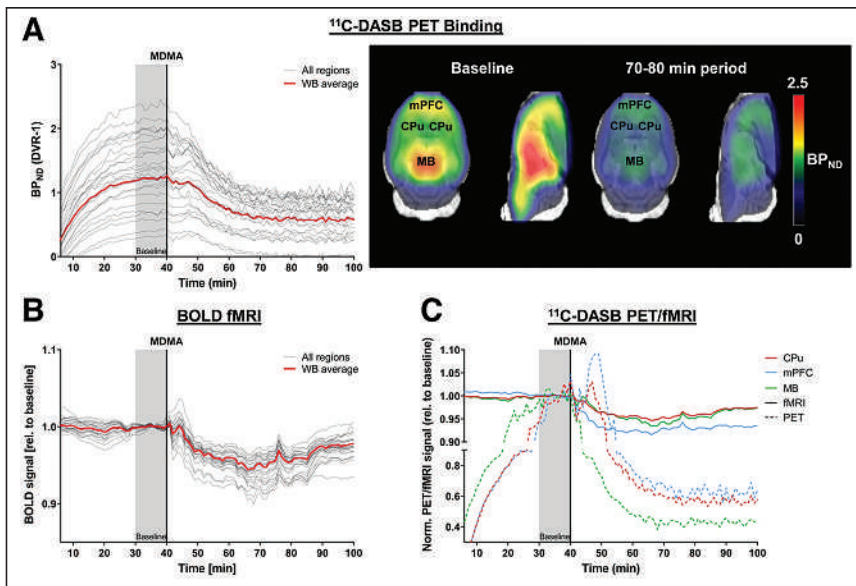


FIGURE 3. Regionwise evaluation of ^{11}C -DASB PET and BOLD fMRI signal changes. (A) Dynamic BP_{ND} for all regions and whole-brain average. Voxelwise maps indicate ^{11}C -DASB binding at baseline, as well as 70–80 min after scan start. (B) Regional BOLD fMRI signals normalized to respective baselines. (C) Temporal comparison of PET and BOLD signal changes (normalized to baseline) in caudate putamen, medial prefrontal cortex, and midbrain. CPU = caudate putamen; DVR = distribution volume ratio; MB = midbrain; mPFC = medial prefrontal cortex; WB = whole brain.

significant ^{18}F -FDG increases. The most significant BOLD fMRI decreases occurred in posterior areas such as the midbrain ($T = 4.8$), ventral tegmental area ($T = 5.0$), hypothalamus ($T = 5.8$), and pons ($T = 5.9$). The T-scores of metabolic increases and hemodynamic decreases did not correlate significantly ($r = 0.21$).

SERT Occupancy Changes Induced by MDMA Correlate with BOLD Decreases

To further elucidate the molecular underpinnings of the observed hemodynamic decreases, we evaluated BOLD fMRI changes concurrently with alterations in SERT availability using ^{11}C -DASB PET/fMRI in a second cohort (Figs. 3 and 4; Supplemental Fig. 3).

The ^{11}C -DASB nondisplaceable binding potential (BP_{ND}) reached equilibrium 30 min after injection (Fig. 3A). After the challenge, binding in all regions decreased either immediately (1–2 min after the challenge) in areas with high binding values ($\text{BP}_{\text{ND}} > 1.8$) or with a delay of approximately 10 min in regions with lower ^{11}C -DASB binding values. At 30 min after the challenge, binding remained stable until the end of the scan. Similarly to the ^{18}F -FDG fPET/fMRI cohort, all regional BOLD signals decreased within

6 min after the challenge (Fig. 3B). Regions with higher baseline SERT availability showed a faster response than regions with lower baseline SERT availability (Fig. 3C). For example, ^{11}C -DASB binding in the midbrain ($\text{BP}_{\text{ND}} = 2.1$) decreased immediately after the challenge. In contrast, ^{11}C -DASB binding in the caudate putamen ($\text{BP}_{\text{ND}} = 1.6$) and medial prefrontal cortex ($\text{BP}_{\text{ND}} = 1.6$) remained stable or increased briefly. After approximately 10 min, ^{11}C -DASB binding decreased in all regions until it reached equilibrium at 30–40 min after the challenge (39% decrease for medial prefrontal cortex, 44% decrease for caudate putamen). BOLD decreases occurred homogeneously, peaking 30 min after the challenge (~8.5% in medial prefrontal cortex, ~5.5% in caudate putamen, and ~6.5% in midbrain).

Figure 4 shows the voxelwise decreases at 70–80 min after the scan start. Regional averages showed the strongest decreases in the ventral tegmental area ($T = 13.7$), periaqueductal gray matter ($T = 12.8$), and midbrain ($T = 12.7$) for ^{11}C -DASB and in the hypothalamus ($T = 7.8$), ventral tegmental area ($T = 7.2$), and thalamus ($T = 6.9$) for BOLD fMRI. Remarkably, regional T-scores of both readouts correlated strongly ($r = 0.79$, $P < 0.001$).

Hemodynamic Reductions Also Occur in Nonneuronal Tissues

The limited spatial extent of hemodynamic changes compared with the metabolic

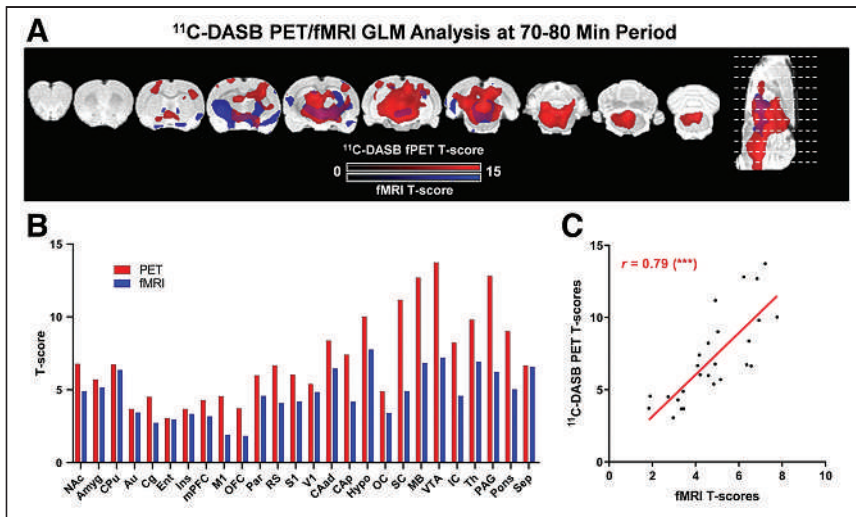


FIGURE 4. General-linear-model analysis of ^{11}C -DASB PET/fMRI cohort. (A) Voxelwise analysis of both signals at 70–80 min. Voxelwise maps are presented ($P < 0.05$, voxel-level family-wise error correction for PET and $P < 0.001$ at voxel level with $P < 0.05$ family-wise error cluster-level correction for fMRI, $n = 11$). (B) Bar diagram indicating average T-scores for each region and modality. (C) Regional T-scores plotted in scatter diagram to evaluate spatial correlation of both readouts. $***P < 0.001$. Amyg = amygdala; Au = auditory cortex; CAad = anterodorsal hippocampus; Cap = posterior hippocampus; Cg = cingulate cortex; CPu = caudate putamen; Ent = entorhinal cortex; GLM = general linear model; Hypo = hypothalamus; IC = inferior colliculus; Ins = insular cortex; M1 = motor cortex; MB = midbrain; mPFC = medial prefrontal cortex; NAc = nucleus accumbens; OC = olfactory cortex; OFC = orbitofrontal cortex; PAG = periaqueductal gray matter; Par = parietal cortex; RS = retrosplenial cortex; S1 = somatosensory cortex; SC = superior colliculus; Sep = septum; Th = thalamus; V1 = visual cortex; VTA = ventral tegmental area.

and SERT occupancy alterations may be due to the smaller magnitudes of the BOLD decreases. To further clarify this aspect, we merged the fMRI scans from both cohorts (Fig. 5). We also extracted the BOLD signals from extracerebral areas to investigate whether the BOLD decreases are specific to neuronal tissue.

After the cohorts were merged, the BOLD fMRI decreases were widespread and, intriguingly, also occurred in nonneuronal areas (Fig. 5). The average extracerebral BOLD signal decreased coherently with the cerebral BOLD signal, both reaching maximum reductions 27 min after the challenge (cerebral BOLD, 4.8%; extracerebral BOLD, 7.4%).

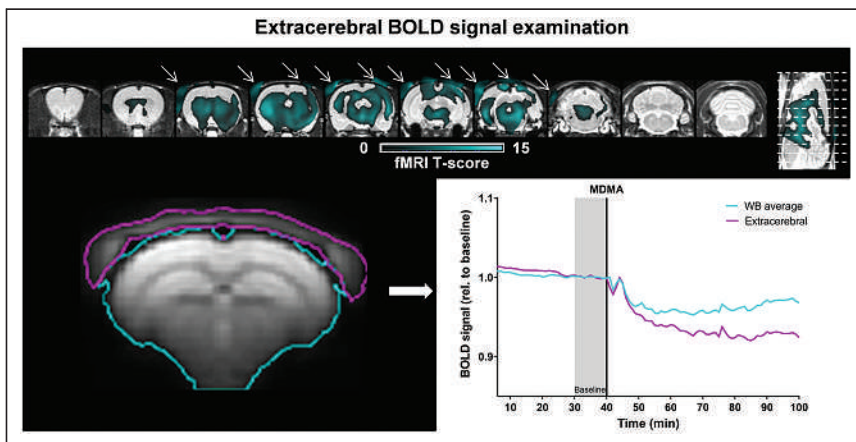


FIGURE 5. General-linear-model analysis of BOLD decreases after merging BOLD fMRI datasets acquired in both cohorts ($n = 20$). Data are shown at $P < 0.05$, family-wise error-corrected at voxel level. Arrows indicate extracerebral decreases. Average BOLD signals were extracted from extracerebellar regions and plotted along with whole-brain signal. WB = whole brain.

Additional Analyses

Analyses of the phosphate-buffered saline cohort and a comparison with the readouts shown after MDMA application are provided in Supplemental Figures 4–5. Furthermore, we extracted general-linear-model alterations induced by MDMA in each subject of both the ^{11}C -DASB cohort and the ^{18}F -FDG cohort to demonstrate the feasibility of subject-level PET inferences using our approach (Supplemental Figs. 6–7). Additionally, we reproduced the metabolic changes using whole-brain normalization and validated the choice of the cerebellum for normalization (Supplemental Fig. 8). Moreover, we examined the robustness of our correlation between hemodynamic and SERT decreases by using β -values and subject-level general-linear-model readouts (Supplemental Fig. 9). Finally, we compared the temporal characteristics of the observed hemodynamic, metabolic, and SERT availability changes (Supplemental Fig. 10).

DISCUSSION

Our data indicate that increased neuronal activity after MDMA is accompanied by neurovascular uncoupling, possibly mediated through the vascular effects of serotonin after SERT blockage.

Simultaneous Uncoupling Between Metabolism and Hemodynamics

Studies measuring glucose utilization after psychedelic challenges have shown mixed results, yet the main result has been increased metabolism (6,7,9,35), suggesting neuronal activation. However, more recent work performed by Carhart-Harris et al. (3), using arterial spin labeling challenged this hypothesis and argued that brain activity is exclusively decreased solely under MDMA. Our study confirmed that this finding also holds true in rodents. Carhart-Harris et al. speculated that MDMA exerts inhibitory effects directly through serotonin receptor (5-HT) 1A (3,39).

Comparable reductions under acute psilocybin reported by the group of Carhart-Harris were attributed to the inhibitory effects of 5-HT_{2A} receptors (4). On a side note, the hemodynamic decreases for MDMA and psilocybin in humans were located predominantly in the right hemisphere (3,4), similarly to our study, thereby supporting the translatability of our readout. Notably, Carhart-Harris et al. argued that possible discrepancies with previous work indicating increased metabolism using ^{18}F -FDG PET (9) might be due to its inferior temporal resolution (4). Therefore, the authors claimed that the reported increases may represent a rebound in glucose metabolism after the acute inhibition captured by fMRI (4). We agree that earlier ^{18}F -FDG PET or ex vivo studies (6,7,9,35) measuring cerebral glucose utilization lacked temporal specificity because

of methodologic limitations on their interpretability in terms of acute effects. An additional confound is that the studies compared different, relatively small cohorts having received either placebo or MDMA. The present work overcomes all these limitations. The constant-infusion protocols used for both tracers enabled delineation of pharmacologic effects immediately after the challenge at 1-min intervals, simultaneously with hemodynamic alterations, and within the same subjects. Therefore, we demonstrated that the uncoupling between flow and metabolism previously shown (6,11,35) does occur simultaneously within the same subjects.

Origin of Peripheral and Cerebral Hemodynamic Decreases

We showed that nonneuronal effects dominate hemodynamic changes induced by MDMA. In particular, our data shed light on 2 separate phenomena. First, the temporal coherence between hemodynamic reductions in cerebral and extracerebral areas suggests that vascular effects occur at the periphery. The 5-HT_{2A} receptor, which is postulated—along with the 5-HT_{1B} receptor—to mediate vasoconstrictive effects (40,41), is one of the main targets of MDMA (5,42). However, because MDMA has a much stronger affinity to the 5-HT_{2A} receptor than to the 5-HT_{1B} receptor (5), direct agonist action of MDMA at 5-HT_{2A} in peripheral blood vessels likely drives our results (40). Previous work has demonstrated the role of 5-HT_{2A} in vasoconstriction of the carotid artery, the main vessel supplying blood to the brain (43,44). In addition to peripheral effects, the cerebral hemodynamic decreases are also likely of a serotonergic nature. Existing publications have indicated that serotonin impacts brain hemodynamics (12,13) and that direct manipulation of the raphe nuclei constricts cerebral microvasculature (11). In contrast to the peripheral hemodynamic reductions, which can be attributed solely to the direct effects of MDMA, the decreases in the brain may additionally be triggered by increased synaptic serotonin levels after SERT blockage. This finding is supported by the high correlation between SERT blockage and hemodynamic decreases in BOLD fMRI, suggesting that increased levels of endogenous serotonin may modulate cerebral hemodynamics. The exact involvement of different receptors needs to be investigated, for instance by combining psychedelic challenges with respective antagonists. Our results warrant a reevaluation of previous data (3,4) and generally call for caution when interpreting findings relying on neurovascular coupling under pharmacologic challenges (3,5,42).

Anatomy and Physiology of Increased Metabolism

We demonstrated that MDMA increases the metabolism of different regions, likely because of neuronal activation, as fPET has been shown to reliably map onto neuronal activity while being independent of hemodynamic changes (16). Interestingly, the metabolic increases were more weighted toward serotonergic projection areas than toward the midbrain regions showing the strongest reductions in SERT availability. First, this finding is in line with the hypothesis that most of the glucose is consumed postsynaptically (45). Second, the areas showing increased metabolism are consistent at a functional level with most previously reported behavioral effects of MDMA. The signals observed in the nucleus accumbens, amygdala, and insula align well with salience changes known from imaging and behavioral studies (3,46). In particular, the nucleus accumbens is involved in responses to numerous drugs (47). The amygdala, insula, and orbitofrontal cortex are strongly involved in emotional processes (48). Activity in the olfactory cortex and olfactory bulb could indicate increased food-seeking or sexual arousal (49,50). Enhanced metabolic activity in the sensory cortices is in concordance with heightened sensations elicited by MDMA (49).

Furthermore, the 5-HT_{2A} receptor exhibits a strong anterior–posterior gradient in the cortex, being strongly expressed in frontal areas of the cortex (51) and overlapping with the activations indicated by fPET, and has been shown to be responsible for serotonergic activation in projection areas such as the prefrontal cortex (52).

Other factors may play a role in the findings, and there are also certain limitations that need to be considered when contemplating our data. The supplemental materials provide a thorough discussion of these aspects.

CONCLUSION

The present study showed the potential of multimodal imaging in drug research. We demonstrated the acute neurovascular uncoupling induced by MDMA, characterized by increased neuronal activity in monoaminergic projection areas and accompanied by vascular depression of a serotonergic nature. Our results provide important insight into the mechanism of action of MDMA and pave the way for the application of ¹⁸F-FDG fPET and hybrid fPET/fMRI in drug research.

DISCLOSURE

This research was supported by funds from the Eberhard Karls University Tübingen Faculty of Medicine (fortune 2209-0-0 and 2409-0-0) to Hans Wehrl, from the Carl Zeiss Foundation to Kristina Herfert, and from the Werner Siemens Foundation to Bernd J. Pichler, as well as by an international exchange grant from the Osaka Medical Research Foundation for Intractable Diseases to Tadashi Watabe. No other potential conflict of interest relevant to this article was reported.

ACKNOWLEDGMENTS

We acknowledge Julia Mannheim, Rebecca Rock, Neele Hübner, Andreas Dieterich, Ines Herbon, Stacy Huang, Sandro Aidone, Linda Schramm, and the Radiopharmacy Department for their administrative and technical support. The graphical abstract was generated using BioRender. This work is part of the PhD thesis of Tudor M. Ionescu.

KEY POINTS

QUESTION: What are the effects of acute administration of MDMA on neuronal activation in the brain?

PERTINENT FINDINGS: Global decreases in BOLD fMRI are of a vascular, rather than a neuronal, nature and strongly correlate with SERT occupancy measured simultaneously using ¹¹C-DASB. In contrast, ¹⁸F-FDG fPET indicates simultaneous increases in limbic glucose consumption, potentially mapping onto neuronal activation.

IMPLICATIONS FOR PATIENT CARE: The study emphasizes the caveats of BOLD fMRI and other hemodynamic methods when strong vascular effects are present and recommends the use of ¹⁸F-FDG fPET as an alternative for tracking neuronal activity in vivo after pharmacologic challenges in drug research.

REFERENCES

1. Andersen KAA, Carhart-Harris R, Nutt DJ, Erritzoe D. Therapeutic effects of classic serotonergic psychedelics: a systematic review of modern-era clinical studies. *Acta Psychiatr Scand.* 2021;143:101–118.

2. Mitchell JM, Bogenschutz M, Lilienstein A, et al. MDMA-assisted therapy for severe PTSD: a randomized, double-blind, placebo-controlled phase 3 study. *Nat Med*. 2021;27:1025–1033.
3. Carhart-Harris RL, Murphy K, Leech R, et al. The effects of acutely administered 3,4-methylenedioxymethamphetamine on spontaneous brain function in healthy volunteers measured with arterial spin labeling and blood oxygen level-dependent resting state functional connectivity. *Biol Psychiatry*. 2015;78:554–562.
4. Carhart-Harris RL, Erritzoe D, Williams T, et al. Neural correlates of the psychedelic state as determined by fMRI studies with psilocybin. *Proc Natl Acad Sci USA*. 2012;109:2138–2143.
5. Dipasquale O, Selvaggi P, Veronese M, Gabay AS, Turkheimer F, Mehta MA. Receptor-enriched analysis of functional connectivity by targets (REACT): a novel, multimodal analytical approach informed by PET to study the pharmacodynamic response of the brain under MDMA. *Neuroimage*. 2019;195:252–260.
6. Quate L, McBean DE, Ritchie IM, Olverman HJ, Kelly PAT. Acute methylenedioxymethamphetamine administration: effects on local cerebral blood flow and glucose utilisation in the dark agouti rat. *Psychopharmacology (Berlin)*. 2004;173:287–295.
7. Soto-Montenegro ML, Vaquero JJ, Arango C, Ricaurte G, García-Barreno P, Desco M. Effects of MDMA on blood glucose levels and brain glucose metabolism. *Eur J Nucl Med Mol Imaging*. 2007;34:916–925.
8. Wilkerson G, London ED. Effects of methylenedioxymethamphetamine on local cerebral glucose utilization in the rat. *Neuropharmacology*. 1989;28:1129–1138.
9. Vollenweider FX, Leenders KL, Scharfetter C, Maguire P, Stadelmann O, Angst J. Positron emission tomography and fluorodeoxyglucose studies of metabolic hyperfrontality and psychopathology in the psilocybin model of psychosis. *Neuropsychopharmacology*. 1997;16:357–372.
10. Gough B, Ali SF, Slikker W, Holson RR. Acute effects of 3,4-methylenedioxymethamphetamine (MDMA) on monoamines in rat caudate. *Pharmacol Biochem Behav*. 1991;39:619–623.
11. Cohen Z, Bonvento G, Lacombe P, Hamel E. Serotonin in the regulation of brain microcirculation. *Prog Neurobiol*. 1996;50:335–362.
12. Kim JG, Leem Y-E, Kwon I, Kang J-S, Bae YM, Cho H. Estrogen modulates serotonin effects on vasoconstriction through Src inhibition. *Exp Mol Med*. 2018;50:1–9.
13. Van Nueten JM, Janssens WJ, Vanhoutte PM. Serotonin and vascular reactivity. *Pharmacol Res Commun*. 1985;17:585–608.
14. Hansen HD, Mandeville JB, Sander CY, et al. Functional characterization of 5-HT(1B) receptor drugs in nonhuman primates using simultaneous PET-MR. *J Neurosci*. 2017;37:10671–10678.
15. Sander CY, Hooker JM, Catana C, et al. Neurovascular coupling to D2/D3 dopamine receptor occupancy using simultaneous PET/functional MRI. *Proc Natl Acad Sci USA*. 2013;110:11169–11174.
16. Villien M, Wey H-Y, Mandeville JB, et al. Dynamic functional imaging of brain glucose utilization using fPET-FDG. *Neuroimage*. 2014;100:192–199.
17. Rischka L, Gryglewski G, Pfaff S, et al. Reduced task durations in functional PET imaging with [¹⁸F]FDG approaching that of functional MRI. *Neuroimage*. 2018;181:323–330.
18. Morefield KM, Keane M, Felgate P, White JM, Irvine RJ. Pill content, dose and resulting plasma concentrations of 3,4-methylenedioxymethamphetamine (MDMA) in recreational ‘ecstasy’ users. *Addiction*. 2011;106:1293–1300.
19. Disselhorst JA, Newport DF, Schmid AM, et al. NEMA NU 4-2008 performance evaluation and MR compatibility tests of an APD-based small animal PET-insert for simultaneous PET/MR imaging. *Phys Med Biol*. 2022;67.
20. Solbach C, Reischl G, Machulla H-J. Determination of reaction parameters for the synthesis of the serotonin transporter ligand [¹¹C]DASB: application to a remotely controlled high yield synthesis. *Radiochim Acta*. 2004;92:341–344.
21. Wilson AA, Ginovart N, Schmidt M, Meyer JH, Threlkeld PG, Houle S. Novel radiotracers for imaging the serotonin transporter by positron emission tomography: synthesis, radiosynthesis, and in vitro and ex vivo evaluation of ¹¹C-labeled 2-(phenylthio)araalkylamines. *J Med Chem*. 2000;43:3103–3110.
22. Hamacher K, Coenen HH, Stocklin G. Efficient stereospecific synthesis of no-carrier-added 2-[¹⁸F]-fluoro-2-deoxy-D-glucose using aminopolyether supported nucleophilic substitution. *J Nucl Med*. 1986;27:235–238.
23. López-González FJ, Silva-Rodríguez J, Paredes-Pacheco J, et al. Intensity normalization methods in brain FDG-PET quantification. *Neuroimage*. 2020;222:117229.
24. Hodkinson DJ, de Groot C, McKie S, Deakin JFW, Williams SR. Differential effects of anaesthesia on the fMRI response to acute ketamine challenge. *Br J Med Res*. 2012;2:373–385.
25. Wehr HF, Hossain M, Lankes K, et al. Simultaneous PET-MRI reveals brain function in activated and resting state on metabolic, hemodynamic and multiple temporal scales. *Nat Med*. 2013;19:1184–1189.
26. Ionescu TM, Amend M, Hafiz R, et al. Elucidating the complementarity of resting-state networks derived from dynamic [¹⁸F]FDG and hemodynamic fluctuations using simultaneous small-animal PET/MRI. *Neuroimage*. 2021;236:118045.
27. Brodde OE. Vascular dopamine receptors: demonstration and characterization by in vitro studies. *Life Sci*. 1982;31:289–306.
28. Passie T, Seifert J, Schneider U, Emrich HM. The pharmacology of psilocybin. *Addict Biol*. 2002;7:357–364.
29. Hutchison RM, Hutchison M, Manning KY, Menon RS, Everling S. Isoflurane induces dose-dependent alterations in the cortical connectivity profiles and dynamic properties of the brain’s functional architecture. *Hum Brain Mapp*. 2014;35:5754–5775.
30. Spangler-Bickell MG, de Laat B, Fulton R, Bormans G, Nuyts J. The effect of isoflurane on ¹⁸F-FDG uptake in the rat brain: a fully conscious dynamic PET study using motion compensation. *EJNMMI Res*. 2016;6:86.
31. Martínez-Maestro M, Labadie C, Möller HE. Dynamic metabolic changes in human visual cortex in regions with positive and negative blood oxygenation level-dependent response. *J Cereb Blood Flow Metab*. 2019;39:2295–2307.
32. Schaller B, Mекle R, Xin L, Kunz N, Gruetter R. Net increase of lactate and glutamate concentration in activated human visual cortex detected with magnetic resonance spectroscopy at 7 tesla. *J Neurosci Res*. 2013;91:1076–1083.
33. Amend M, Ionescu TM, Di X, Pichler BJ, Biswal BB, Wehr HF. Functional resting-state brain connectivity is accompanied by dynamic correlations of application-dependent [¹⁸F]FDG PET-tracer fluctuations. *Neuroimage*. 2019;196:161–172.
34. Schiffer WK, Mirrione MM, Biegen A, Alexoff DL, Patel V, Dewey SL. Serial microPET measures of the metabolic reaction to a microdialysis probe implant. *J Neurosci Methods*. 2006;155:272–284.
35. Ferrington L, Kirilly E, McBean DE, Olverman HJ, Bagdy G, Kelly PAT. Persistent cerebrovascular effects of MDMA and acute responses to the drug. *Eur J Neurosci*. 2006;24:509–519.
36. Walker M, Ehrlichmann W, Stahlschmidt A, Pichler BJ, Fischer K. In vivo evaluation of ¹¹C-DASB for quantitative SERT imaging in rats and mice. *J Nucl Med*. 2016;57:115–121.
37. Amend M. *Multifunctional PET/MR Imaging Decodes Brain Function on Hemodynamic and Metabolic scales*. Dissertation. Eberhard Karls Universität Tübingen; 2019.
38. Brett M, Anton J-L, Valabregue R, Poline J-B. Region of interest analysis using an SPM toolbox [abstract]. *Neuroimage*. 2002;16.
39. Andrade R. Serotonergic regulation of neuronal excitability in the prefrontal cortex. *Neuropharmacology*. 2011;61:382–386.
40. Ullmer C, Schmuck K, Kalkman HO, Lübbert H. Expression of serotonin receptor mRNAs in blood vessels. *FEBS Lett*. 1995;370:215–221.
41. Gamoh S, Hisa H, Yamamoto R. 5-hydroxytryptamine receptors as targets for drug therapies of vascular-related diseases. *Biol Pharm Bull*. 2013;36:1410–1415.
42. Roseman L, Leech R, Feilding A, Nutt DJ, Carhart-Harris RL. The effects of psilocybin and MDMA on between-network resting state functional connectivity in healthy volunteers. *Front Hum Neurosci*. 2014;8:204.
43. Yakovlev DS, Spasov AA, Mal’tsev DV, Anisimova VA. Effect of 5-HT(2A) receptor antagonists on blood flow in the carotid vessels upon elevation of serotonin level. *Bull Exp Biol Med*. 2014;157:350–352.
44. Buchhorn T, Lyons T, Song C, Feilding A, Knöpfel T. The serotonin 2A receptor agonist 25CN-NBOH increases murine heart rate and neck-arterial blood flow in a temperature-dependent manner. *J Psychopharmacol*. 2020;34:786–794.
45. Attwell D, Laughlin SB. An energy budget for signaling in the grey matter of the brain. *J Cereb Blood Flow Metab*. 2001;21:1133–1145.
46. Seeley WW, Menon V, Schatzberg AF, et al. Dissociable intrinsic connectivity networks for salience processing and executive control. *J Neurosci*. 2007;27:2349–2356.
47. Olsen CM. Natural rewards, neuroplasticity, and non-drug addictions. *Neuropharmacology*. 2011;61:1109–1122.
48. Phan KL, Wager T, Taylor SF, Liberzon I. Functional neuroanatomy of emotion: a meta-analysis of emotion activation studies in PET and fMRI. *Neuroimage*. 2002;16:331–348.
49. Sumnall HR, Cole JC, Jerome L. The varieties of ecstatic experience: an exploration of the subjective experiences of ecstasy. *J Psychopharmacol*. 2006;20:670–682.
50. Pfaus JG, Tse TL, Werk CM, et al. Enhanced synaptic responses in the piriform cortex associated with sexual stimulation in the male rat. *Neuroscience*. 2009;164:1422–1430.
51. Weber ET, Andrade R. Htr2a gene and 5-HT(2A) receptor expression in the cerebral cortex studied using genetically modified mice. *Front Neurosci*. 2010;4:36.
52. Puig MV, Gullledge AT. Serotonin and prefrontal cortex function: neurons, networks, and circuits. *Mol Neurobiol*. 2011;44:449–464.

Deep Learning–Based Attenuation Correction Improves Diagnostic Accuracy of Cardiac SPECT

Aakash D. Shanbhag*¹, Robert J.H. Miller*², Konrad Pieszko³, Mark Lemley¹, Paul Kavanagh¹, Attila Feher⁴, Edward J. Miller⁴, Albert J. Sinusas⁴, Philipp A. Kaufmann⁵, Donghee Han¹, Cathleen Huang¹, Joanna X. Liang¹, Daniel S. Berman¹, Damini Dey¹, and Piotr J. Slomka¹

¹Departments of Medicine (Division of Artificial Intelligence in Medicine), Imaging, and Biomedical Sciences, Cedars–Sinai Medical Center, Los Angeles, California; ²Department of Cardiac Sciences, University of Calgary, Calgary, Alberta, Canada; ³Department of Interventional Cardiology and Cardiac Surgery, University of Zielona Góra, Zielona Góra, Poland; ⁴Section of Cardiovascular Medicine, Department of Internal Medicine, Yale University School of Medicine, New Haven, Connecticut; and ⁵Cardiac Imaging, Department of Nuclear Medicine, University Hospital Zurich, Zurich, Switzerland

J Nucl Med 2023; 64:472–478

DOI: 10.2967/jnumed.122.264429

To improve diagnostic accuracy, myocardial perfusion imaging (MPI) SPECT studies can use CT-based attenuation correction (AC). However, CT-based AC is not available for most SPECT systems in clinical use, increases radiation exposure, and is impacted by misregistration. We developed and externally validated a deep-learning model to generate simulated AC images directly from non-AC (NC) SPECT, without the need for CT. **Methods:** SPECT myocardial perfusion imaging was performed using ^{99m}Tc-sestamibi or ^{99m}Tc-tetrofosmin on contemporary scanners with solid-state detectors. We developed a conditional generative adversarial neural network that applies a deep learning model (DeepAC) to generate simulated AC SPECT images. The model was trained with short-axis NC and AC images performed at 1 site ($n = 4,886$) and was tested on patients from 2 separate external sites ($n = 604$). We assessed the diagnostic accuracy of the stress total perfusion deficit (TPD) obtained from NC, AC, and DeepAC images for obstructive coronary artery disease (CAD) with area under the receiver-operating-characteristic curve. We also quantified the direct count change among AC, NC, and DeepAC images on a per-voxel basis. **Results:** DeepAC could be obtained in less than 1 s from NC images; area under the receiver-operating-characteristic curve for obstructive CAD was higher for DeepAC TPD (0.79; 95% CI, 0.72–0.85) than for NC TPD (0.70; 95% CI, 0.63–0.78; $P < 0.001$) and similar to AC TPD (0.81; 95% CI, 0.75–0.87; $P = 0.196$). The normalcy rate in the low-likelihood-of-coronary-disease population was higher for DeepAC TPD (70.4%) and AC TPD (75.0%) than for NC TPD (54.6%, $P < 0.001$ for both). The positive count change (increase in counts) was significantly higher for AC versus NC (median, 9.4; interquartile range, 6.0–14.2; $P < 0.001$) than for AC versus DeepAC (median, 2.4; interquartile range, 1.3–4.2). **Conclusion:** In an independent external dataset, DeepAC provided improved diagnostic accuracy for obstructive CAD, as compared with NC images, and this accuracy was similar to that of actual AC. DeepAC simplifies the task of artifact identification for physicians, avoids misregistration artifacts, and can be performed rapidly without the need for CT hardware and additional acquisitions.

Key Words: attenuation correction; SPECT; myocardial perfusion imaging; deep learning; artificial intelligence

SPECT myocardial perfusion imaging (MPI) is frequently used to evaluate patients for the presence of obstructive coronary artery disease (CAD) (1). Abnormalities of regional perfusion are used to identify patients with a higher likelihood of having obstructive CAD (1,2). However, perfusion abnormalities can be similar in appearance to soft-tissue photon attenuation artifacts.

Attenuation correction (AC) can be provided through CT (CTAC) (3) and has been shown to improve the diagnostic accuracy of SPECT MPI and increase specificity from 81% to 88% (4). AC imaging has been proposed as an important method to significantly increase the proportion of patients who are candidates for rest scan cancellation (5). However, CTAC requires dedicated, expensive SPECT/CT scanners and is associated with additional radiation exposure. Importantly, misregistration of the separately acquired SPECT and CTAC maps is often a source of artifacts, requiring careful quality control and potentially diminishing the clinical value of AC images (6). For these reasons, despite its advantages, CTAC is currently performed on a minority of SPECT MPI scans. This is especially true for the latest generation of solid-state scanners, on which CTAC is performed in less than 5% of sites (written communication between Cory McNeil and Robert Miller, June 9, 2022) and is available from only 1 vendor.

To provide the benefits of AC without the above shortcomings, we developed and evaluated a deep learning model (DeepAC) that applies AC directly to non-AC (NC) short-axis images, without the use of CT (or the need for reconstruction of the data), by generating simulated AC images. DeepAC is a conditional generative adversarial network that comprises 2 competing networks. A generator is tasked with creating DeepAC images, whereas a discriminator differentiates the DeepAC images from actual AC images. The process is repeated until the discriminator network is no longer able to differentiate real AC images from fake AC images. Importantly, physicians are able to better evaluate DeepAC SPECT images for potential artifacts and myocardial segmentation errors.

In this study, we compared image quantification of NC images to CT-based AC and DeepAC images. In an independent external dataset, we compared the diagnostic accuracy of quantitative perfusion

Received Jun. 21, 2022; revision accepted Sep. 16, 2022.

For correspondence or reprints, contact Piotr J. Slomka (piotr.slomka@cshs.org).

*Contributed equally to this work.

Published online Sep. 22, 2022.

COPYRIGHT © 2023 by the Society of Nuclear Medicine and Molecular Imaging.

analysis for obstructive CAD, DeepAC, NC, and CT-based AC imaging. We also performed a change analysis to better understand the potential improvement in DeepAC images compared with actual AC images.

MATERIALS AND METHODS

Patient Populations

We included 2 separate populations from separate centers. The model was trained with 4,886 patients (45% female) from a single center (Yale University) who underwent SPECT MPI with CTAC (details in Supplemental Table 1; supplemental materials are available at <http://jnm.snmjournals.org>). The model was then tested in an external population of 604 patients (48% male) from 2 different centers (University of Zurich and University of Calgary). All data and images were deidentified and transferred to Cedars–Sinai. The study protocol complied with the Declaration of Helsinki and was approved by the institutional review boards at each participating institution. The overall study was approved by the institutional review board at Cedars–Sinai Medical Center. Written informed consent or a waiver of consent was obtained at each institution.

SPECT Image Acquisition

All scans were performed per SPECT/CT MPI guidelines (7), and only stress images were used in the present analysis. In the training population, patients underwent stress–rest/stress-only ($n = 4,112$, 84%), rest–stress ($n = 684$, 14%), or 2-day ($n = 90$, 2%) imaging using ^{99m}Tc -tetrofosmin with a Discovery 570c or Discovery 530c scanner (GE Healthcare). In the external testing populations, patients underwent either a ^{99m}Tc -sestamibi

rest–stress or a ^{99m}Tc -tetrofosmin stress–rest protocol with a Discovery 570c scanner (GE Healthcare). Weight-adjusted (\pm standard deviation) stress imaging doses of 403 ± 207 MBq (4.8 ± 2.5 MBq/kg, 10.9 ± 5.6 mCi) and 413 ± 157 MBq (5.0 ± 1.9 MBq/kg, 11.2 ± 4.2 mCi) were used in the training population and the external population, respectively. Stress images were acquired 15–60 min after stress over a total of 4–6 min (7). Patients underwent exercise or pharmacologic stress using standard clinical parameters. Details of the CT acquisitions and image quality control are available in the supplemental materials.

Model Architecture

The model architecture is outlined in Figure 1. The DeepAC model was developed using 4,886 (training, 4,398; validation, 488) pairs of NC and AC short-axis SPECT slices from stress acquisitions from a single site. Our proposed method focuses on CT-free direct estimation of SPECT AC generation and is independent of any imaging information from CT (8). Ground truth short-axis SPECT AC images (reconstructed at 4×4 mm with a slice thickness of 4 mm) were used to compare DeepAC. Additional details are available in the supplemental materials (9–14).

Processing Speed

Batch mode was used for model testing. Using a graphics processing unit (GeForce RTX 2080; NVIDIA Corp.), the mean time to generate DeepAC image volume from AC volume was 9 ms. Using a computer similar to a standard reporting workstation (AMD Ryzen 9 5950X 16-core processor, 64 Gb of random-access memory), the mean inference time was 66 ms.

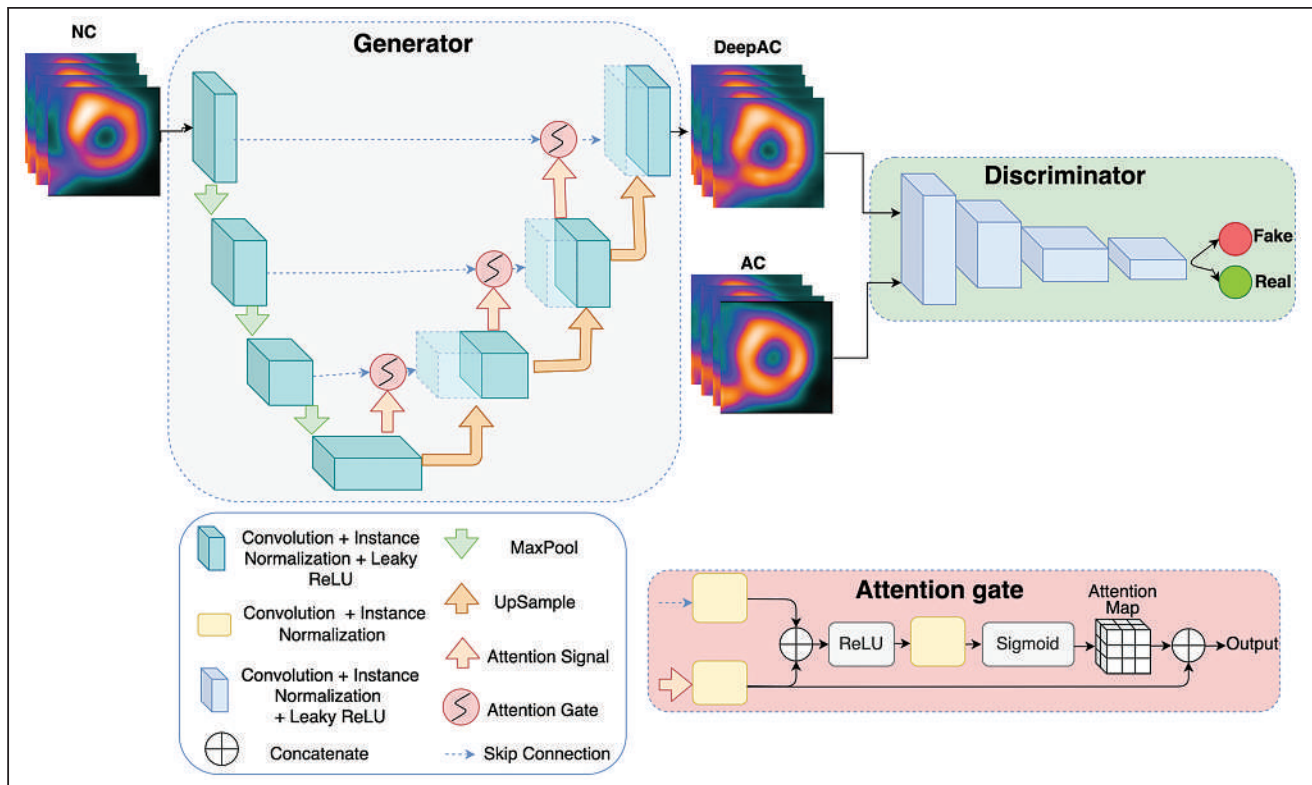


FIGURE 1. Model architecture for conditional generator adversarial network. First, generator network creates simulated AC images from NC images. Discriminator is tasked with differentiating actual AC images (real) from DeepAC images (fake). Generator is attention-gated 3D UNet, for which maximum pooling (MaxPool) downsamples features. Attention gate takes input from lower level (attention signal) with skipped connection; it includes rectified linear unit (ReLU) as nonlinear activation and generates attention map, which is concatenated to upsampled level. This helps generator network focus on essential image structures.

Quantitative Image Analysis

All quantitative image comparisons were performed on the external testing population. Stress total perfusion deficit (TPD) was quantified with Quantitative Perfusion SPECT software (Cedars–Sinai Medical Center) (15). Quantification of TPD for DeepAC images was performed using existing sex-specific databases for AC studies. Additionally, we used change analysis, as implemented in clinical software to perform voxel-by-voxel comparisons among AC, NC, and DeepAC images (16). The change analysis allows derivation of the positive and negative count change between image pairs (sum of absolute voxel-by-voxel count changes in both directions) without normal databases. Positive change integrates image voxels with an increase in counts on AC images, and negative change integrates voxels for which AC images have decreased counts compared with NC images. Thus, positive change identifies perfusion defects that are corrected by the reference technique, and negative change identifies relative perfusion defects unmasked by the reference technique. Change analysis can be used clinically to detect subtle differences in image sets; for example, when comparing stress and rest images, it could be used to identify areas of ischemia (16). This analysis was also performed on a per-vessel basis.

Diagnostic Accuracy for Obstructive CAD

Diagnostic accuracy was assessed in patients with same-day SPECT and coronary CT angiography ($n = 280$) and a low likelihood of coronary disease (LLK) ($n = 324$). Patients from the University of Zurich underwent coronary CT angiography on the same day as SPECT MPI. Obstructive CAD was defined as any stenosis of at least 70% or at least 50% in the left main coronary artery. To ensure that the prevalence of obstructive CAD was similar to that seen in a suspected CAD referral cohort, the population was enriched with an LLK population from the University of Calgary. The LLK population included patients who did not undergo revascularization within 90 days of SPECT MPI and met the following criteria: low probability of CAD based on the Diamond–Forrester model (17), normal findings on expert visual interpretation of perfusion, coronary artery calcium score of 0, and left ventricular ejection fraction of more than 50%. We also evaluated diagnostic accuracy on a per-vessel basis, with left main disease attributed to both the left anterior descending and the left circumflex territories.

Statistical Analysis

Standard descriptive statistics were used. Normality for continuous variables was assessed with the Shapiro–Wilks test. Continuous variables were not found to have a normal distribution, and the difference in median was assessed using the Wilcoxon signed-rank test. The Pitman–Morgan test was used to compare variance between the differences in AC and DeepAC and AC and NC data. Diagnostic accuracy for obstructive CAD was assessed using area under the receiver-operating-characteristic curve (AUC). The DeLong test was used to evaluate for differences in AUC. Lastly, we evaluated normalcy rates in the LLK population, with abnormal quantitative perfusion defined as a stress TPD of more than 3% (integer) (4).

All statistical tests were 2-sided, with a P value of less than 0.05 considered significant. Statistical analyses were performed using R (version 4.1.2) and Stata/IC (version 14.2; StataCorp).

RESULTS

Population Characteristics

The characteristics of the training and external testing populations are shown in Table 1. Patients in the training population were older (median age, 64 vs. 60 y; $P < 0.001$) and more likely to be male (55% vs. 48%, $P < 0.001$) than patients in the testing population.

TABLE 1

Characteristics of Training and External Testing Populations

Characteristic	Training ($n = 4,886$)	External testing ($n = 604$)	P
Age (y)	64 (56–73)	60 (53–68)	<0.001
Male	2,705 (55)	341 (48)	<0.001
Body mass index	29 (26–34)	28 (25–32)	<0.001
Past medical history			
Hypertension	3,204 (67)	255 (36)	<0.001
Diabetes mellitus	1,292 (27)	71 (10)	<0.001
Dyslipidemia	2,649 (55)	195 (28)	<0.001
History of CAD	873 (18)	67 (9)	<0.001
Stress test type			
Exercise	1,775 (36)	393 (56)	<0.001
Pharmacologic	3,106 (64)	313 (44)	<0.001

Qualitative data are number and percentage; continuous data are median and IQR.

Diagnostic Accuracy

Obstructive CAD was present in 64 of 604 (10.6%) patients in the external testing population, compared with 10.7% in a large randomized controlled trial (18). Diagnostic accuracy for obstructive CAD is shown in Figure 2. The AUC for DeepAC stress TPD (AUC, 0.79; 95% CI, 0.72–0.85) was higher than that for NC TPD (0.70; 95% CI, 0.63–0.78; $P < 0.001$). There was no difference between the AUC for DeepAC TPD and that for AC TPD (AUC, 0.81; 95% CI, 0.75–0.87; $P = 0.196$). At 80% sensitivity, the

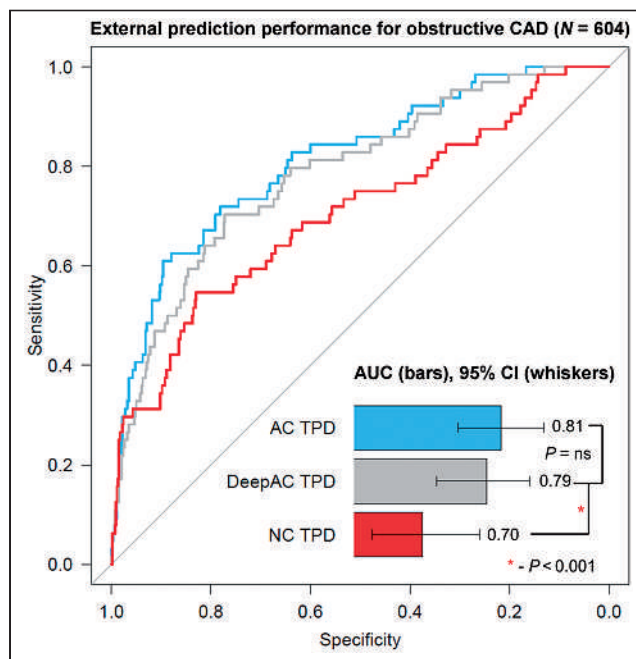


FIGURE 2. Diagnostic accuracy of obstructive CAD. AUC for AC and DeepAC stress TPD was higher than for NC stress TPD. There was no significant (ns) difference between DeepAC stress TPD and AC stress TPD.

specificity of DeepAC TPD was 64% (cut point $\geq 3.6\%$), compared with 65% for AC TPD (cut point $\geq 3.3\%$) and 36% for NC TPD (cut point $\geq 2.0\%$). Using a standard previously established integer TPD threshold of more than 3% for abnormal, DeepAC had sensitivity of 80% and specificity of 63%, compared with sensitivity of 78% and specificity of 66% for AC TPD and sensitivity of 70% and specificity of 56% for NC TPD. The normalcy rate at this threshold in the LLK population was higher for DeepAC TPD (70.4%) and AC TPD (75.0%) than for NC TPD (54.6%, $P < 0.001$ for both).

We also assessed diagnostic accuracy for obstructive CAD on a per-vessel level, with the results in Supplemental Table 2. The diagnostic accuracy for left anterior descending disease was significantly higher for DeepAC stress TPD (AUC, 0.77; 95% CI, 0.69–0.86) than for NC TPD (AUC, 0.69; 95% CI, 0.59–0.79; $P = 0.007$). Diagnostic accuracy was also higher for left circumflex disease for DeepAC stress TPD (AUC, 0.74; 95% CI, 0.60–0.88) than for NC TPD (AUC, 0.60; 95% CI, 0.45–0.76; $P = 0.024$).

Comparison of AC, NC, and DeepAC SPECT Images

The results of the change analysis are shown in Figure 3. Positive change was significantly lower, representing closer agreement, for AC versus DeepAC (median, 2.4; interquartile range [IQR], 1.3–4.2) than for AC versus NC (median, 9.4; IQR, 6.0–14.2; $P < 0.001$). However, negative change was similar for AC versus DeepAC (median, 2.0; IQR, 0.9–3.5) and AC versus NC (median, 2.0; IQR, 1.2–3.6, $P = 0.935$). Similar findings were seen in the subset of patients undergoing stress-first imaging for positive change (AC vs. DeepAC: median, 2.6; IQR, 1.6–4.9; AC vs. NC: median, 12.9; IQR, 8.5–17.8; $P < 0.001$) and negative change (AC vs. DeepAC: median, 2.7; IQR, 1.5–5.1; AC vs. NC: median, 2.5; IQR, 1.5–4.2; $P < 0.001$). Results of the per-vessel change analysis are shown in Supplemental Figure 1. Median positive

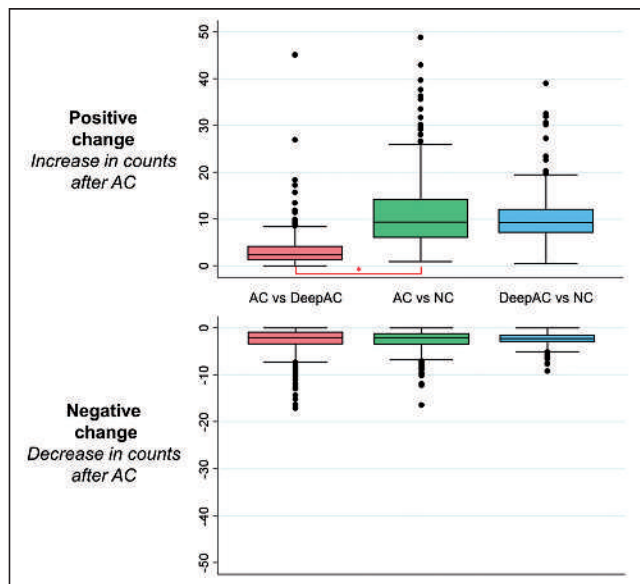


FIGURE 3. Change analysis (voxel-by-voxel analysis after subtraction of coregistered images). Actual AC images were reference image for comparisons of AC vs. DeepAC and AC vs. NC images. DeepAC was used as reference for DeepAC vs. NC. Negative change was not significantly different across all comparisons. However, positive change was significantly lower for AC vs. DeepAC than for AC vs. NC images ($*P < 0.001$).

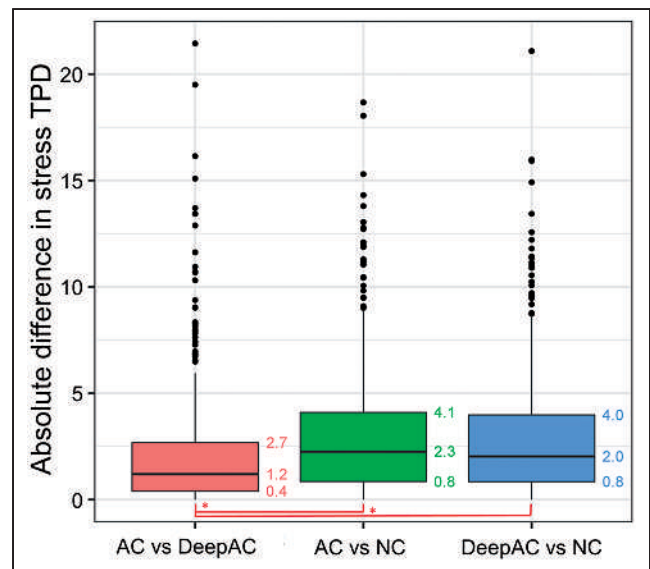


FIGURE 4. Absolute differences in stress TPD between AC, DeepAC, and NC values. Median absolute difference was lower for AC vs. DeepAC than for AC vs. NC or DeepAC vs. NC ($*P < 0.001$).

change was significantly higher with AC versus NC than with AC versus DeepAC in the left anterior descending (2.61 vs. 2.02), left circumflex (4.22 vs. 0.32), and right coronary artery territories (18.96 vs. 1.18, $P < 0.001$ for all).

Absolute differences between AC TPD and DeepAC TPD were lower than absolute differences between AC TPD and NC TPD (median, 1.2 vs. 2.3; $P < 0.001$) (Fig. 4). The Bland–Altman analysis for TPD is outlined in Supplemental Figure 2. Limits of agreement for AC TPD versus DeepAC TPD (bias, -0.2 ; 95% limits of agreement, -6.5 to 6.1 ; Spearman $\rho = 0.78$) were closer than for AC TPD versus NC TPD (bias, -1.0 ; 95% limits of agreement, -8.7 to 6.7 ; Spearman $\rho = 0.55$; $P < 0.001$).

Case Examples

Cases illustrating AC, DeepAC, and NC images, as well as the concept of positive change analysis, are shown in Figures 5–7.

DISCUSSION

We developed a conditional generative adversarial network deep learning model that directly generates DeepAC images, without CT, from NC images. It eliminates the possibility of CT misregistration, leverages optimized vendor-specific reconstruction algorithms for dedicated collimators and solid-state scanners, and allows physicians to evaluate full image sets for potential artifacts using the same approaches as they would for any other clinical study. The model generates DeepAC images in a fraction of a second on standard computer hardware and could readily be implemented in clinical workflows as an automatic preprocessing step.

Critically, for the first time, we demonstrated that the diagnostic accuracy of DeepAC was higher than that of NC using a large external testing population. Additionally, using clinical quantitative analysis, we conclusively demonstrated that DeepAC images are more similar to AC images than are NC images. The significant improvement in positive change suggests that DeepAC corrects attenuation artifacts relative to NC images. Importantly, similar findings were seen in the subset of patients undergoing stress-first imaging, which typically are noisier images. The absence of difference in negative change suggests that it

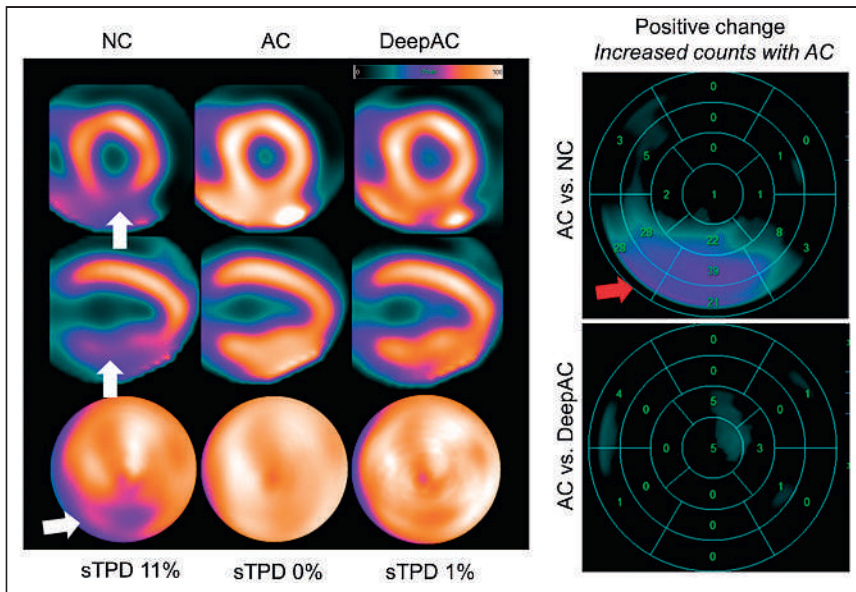


FIGURE 5. NC, AC, and DeepAC images from 53-y-old man with body mass index of 36. On short-axis images (top), vertical long-axis images (middle), and polar maps (bottom), there was defect in inferior wall on NC images only (white arrows), with evidence of adjacent radiotracer activity in abdomen. Standard quantification by stress TPD (sTPD) was 11% (abnormal). After AC correction, sTPD was 0%; DeepAC correction resulted in sTPD of 1% (both normal). There was positive change in inferior wall counts for AC vs. NC (red arrow). There was no change between AC and DeepAC images. Patient had no CAD on coronary CT angiography, and defect most likely represents diaphragmatic attenuation.

is not inducing (or uncovering) defects in a manner that would not be expected with actual AC. DeepAC could be applied clinically in laboratories without dedicated SPECT/CT hardware (majority of SPECT MPI laboratories) to increase normalcy rates and diagnostic accuracy, without affecting existing imaging protocols.

(higher-quality studies) and 8% (lower-quality studies) in internal testing. However, none of these studies included external testing populations. In the present work, we showed higher diagnostic accuracy with DeepAC than with NC images and up to 28% higher specificity, in a large external testing population from 2 different sites using standard clinical quantification of SPECT MPI.

Several AI approaches have been proposed recently to generate simulated AC SPECT MPI (9,19–21). Nguyen et al. developed a generative adversarial network to simulate AC images from non-AC data with data from 491 patients for training and 112 for testing, demonstrating a higher structural similarity index than for 3D UNet (19). Chen et al. proposed a dual squeeze-and-excitation residual dense network, trained and tested with 172 studies, using images from 3 scatter windows together with NC images to predict AC images (9). Yang et al. developed a convolutional network to generate simulated AC images directly from NC images using 100 paired datasets for training and testing and 10-fold cross-validation (20). In the only other study that evaluated the clinical impact of the deep learning AC, Hagio et al. developed a convolutional network that generates simulated AC polar maps from NC maps (rather than images) (21). The authors trained and tested the model in a population from a single center, demonstrating improvement in diagnostic accuracy for CAD either in patients with correlating angiography ($n = 351$) or in LLK cases ($n = 327$). Improvement in specificity was 26%

We also showed improved similarity between AC and DeepAC SPECT images as compared with NC images. There are several aspects of our work that are particularly relevant to future clinical application of the DeepAC model. Our model generates simulated SPECT short-axis images rather than corrected polar maps. This allows physicians to identify potential sources of artifacts such as excessive gut activity and potential errors in myocardial contours. We did not need to exclude cases with surface-mismatch or segmentation errors as was needed in previous polar map-based approaches (21). Our approach leverages existing vendor-specific reconstruction algorithms and could be implemented as a preprocessing step before interpretation with any SPECT MPI interpretation software (22). Importantly, in an independent population, we demonstrated that DeepAC improved diagnostic accuracy for obstructive CAD and normalcy rates, compared with NC SPECT. We used a very conservative definition of LLK, including a coronary artery calcium score of 0 (23), to minimize any chance of misclassifying the presence of obstructive

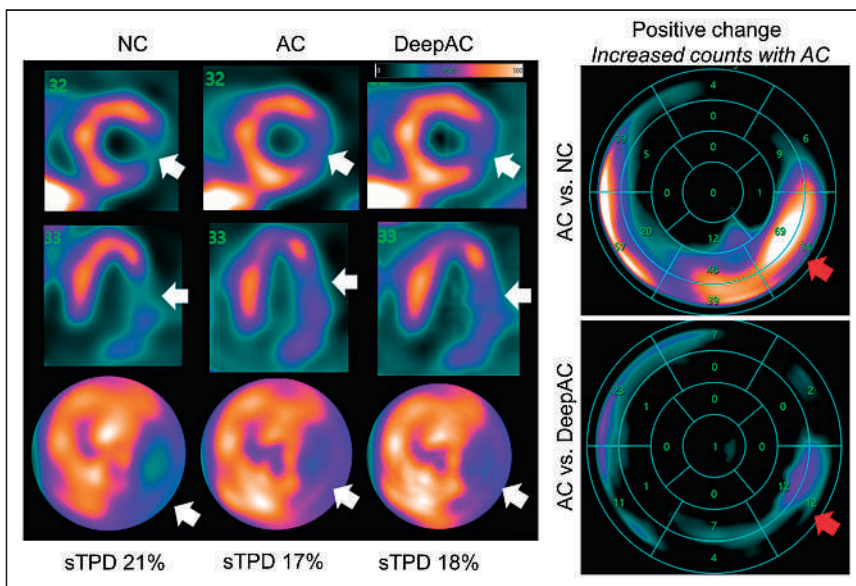


FIGURE 6. NC, AC, and DeepAC images from 63-y-old woman with body mass index of 32. On short-axis images (top), vertical long-axis images (middle), and polar maps (bottom), there was defect in anterolateral, inferolateral, and inferior walls on NC images (white arrows). Standard quantification by stress TPD (sTPD) was 21% (abnormal). After AC correction, sTPD was 17%; DeepAC correction resulted in sTPD of 18% (both abnormal). There was positive change in inferior and inferoseptal walls for AC vs. NC (red arrows). There was only small area of positive change in inferolateral wall for AC vs. DeepAC. Patient had 80% stenosis of proximal left circumflex coronary artery.

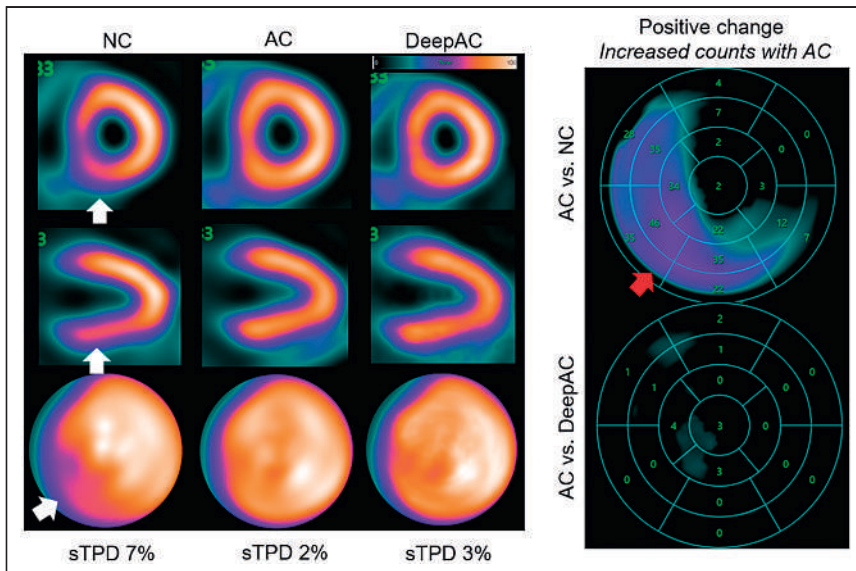


FIGURE 7. NC, AC, and DeepAC images from 62-y-old woman with body mass index of 29. On short-axis images (top), vertical long-axis images (middle), and polar maps (bottom), there was defect in inferior and inferoseptal walls on NC images only (white arrows). Standard quantification by stress TPD (sTPD) was 7% (abnormal). After AC correction, sTPD was 2%; DeepAC correction resulted in sTPD of 3% (both normal). There was positive change in inferior and inferoseptal wall counts for AC vs. NC (red arrow). There was no change between AC and DeepAC images. Patient had no CAD on coronary CT angiography.

CAD in the absence of defined coronary anatomy. We believe this is the first time the utility of simulated AC was demonstrated conclusively with independent, external testing—a critical step toward demonstrating the generalizability of the technique.

DeepAC could be applied clinically to correct for photon attenuation without the additional radiation exposure, cost, and space required for hybrid SPECT/CT. The algorithm could be applied to correct NC SPECT MPI in subsecond times, avoiding potential issues with image misregistration. Importantly, it could be combined with stress-first imaging. We have previously demonstrated that AI can identify low-risk patients for rest scan cancellation (24). DeepAC imaging could be used to further improve the accuracy of these algorithms.

Our study has a few important limitations. Validation of DeepAC on other SPECT camera systems is needed. Further improvements in diagnostic accuracy may be possible by applying dedicated DeepAC databases. Additionally, we did not assess the performance of the DeepAC model on rest images. Although DeepAC allows for soft-tissue AC, it does not provide the additional anatomic information available from CTAC, such as calcium. Therefore, the benefits of implementing this technique to reduce radiation exposure against the added clinical information available from continuing with CTAC imaging need to be carefully weighed (25). Lastly, whereas the population-level results show improved diagnostic accuracy, physicians will still need to review all available data to ensure that the DeepAC results make sense clinically.

CONCLUSION

We developed a deep learning model that generates DeepAC images from NC reconstructed short-axis slices. DeepAC images provide a quantitative assessment of perfusion which is more similar to

actual AC images than NC images are. This translates into improved diagnostic accuracy for obstructive CAD in external testing. DeepAC may simplify the task of artifact identification for physicians compared with NC images alone and can be performed without the need for CTAC hardware.

DISCLOSURE

This research was supported in part by grants R01HL089765 and R35HL161195 from the National Heart, Lung, and Blood Institute/National Institutes of Health (principle investigator, Piotr Slomka). The content is solely the responsibility of the authors and does not necessarily represent the official views of the National Institutes of Health. Robert Miller has received consulting fees and research support from Pfizer. Daniel Berman and Piotr Slomka and Mr. Kavanagh participate in software royalties for Quantitative Perfusion SPECT software at Cedars–Sinai Medical Center. Daniel Berman is a consultant for GE Healthcare, and Edward Miller has served as a GE Healthcare consultant. Piotr Slomka has received research grant support from Siemens Medical Systems.

No other potential conflict of interest relevant to this article was reported.

KEY POINTS

QUESTION: Can deep learning be used to generate AC SPECT images directly from non-AC images?

PERTINENT FINDINGS: We developed a method to generate simulated AC images (DeepAC) and compared them with actual AC and non-AC images using a large external testing population. DeepAC images were more similar to actual AC images than were non-AC images and had high diagnostic accuracy similar to that of actual AC images.

IMPLICATIONS FOR PATIENT CARE: The DeepAC model can be applied clinically to generate AC image sets for improved diagnostic accuracy on SPECT systems without CT capability or to help identify patients for rest scan cancellation.

REFERENCES

- Berman DS, Hachamovitch R, Kiat H, et al. Incremental value of prognostic testing in patients with known or suspected ischemic heart disease. *J Am Coll Cardiol.* 1995;26:639–647.
- Otaki Y, Betancur J, Sharir T, et al. 5-year prognostic value of quantitative versus visual MPI in subtle perfusion defects. *JACC Cardiovasc Imaging.* 2020;13:774–785.
- Huang JY, Huang CK, Yen RF, et al. Diagnostic performance of attenuation-corrected myocardial perfusion imaging for coronary artery disease. *J Nucl Med.* 2016;57:1893–1898.
- Arsanjani R, Xu Y, Hayes SW, et al. Comparison of fully automated computer analysis and visual scoring for detection of coronary artery disease from myocardial perfusion SPECT in a large population. *J Nucl Med.* 2013;54:221–228.

5. van Dijk JD, Mouden M, Ottervanger JP, et al. Value of attenuation correction in stress-only myocardial perfusion imaging using CZT-SPECT. *J Nucl Cardiol*. 2017;24:395–401.
6. Kennedy JA, Israel O, Frenkel A. Directions and magnitudes of misregistration of CT attenuation-corrected myocardial perfusion studies: incidence, impact on image quality, and guidance for registration. *J Nucl Med*. 2009;50:1471–1478.
7. Dorbala S, Di Carli MF, Delbeke D, et al. SNMMI/ASNC/SCCT guideline for cardiac SPECT/CT and PET/CT 1.0. *J Nucl Med*. 2013;54:1485–1507.
8. Torkaman M, Yang J, Shi L, et al. Direct image-based attenuation correction using conditional generative adversarial network for SPECT myocardial perfusion imaging. *Proc SPIE Int Soc Opt Eng*. 2021;11600:116000U.
9. Chen X, Zhou B, Shi LY, et al. CT-free attenuation correction for dedicated cardiac SPECT using a 3D dual squeeze-and-excitation residual dense network. *J Nucl Cardiol*. 2022;29:2235–2250.
10. Jin Q, Meng Z, Sun C, Cui H, Su R. RA-UNet: a hybrid deep attention-aware network to extract liver and tumor in CT scans. *Front Bioeng Biotechnol*. 2020;8:605132.
11. Isola P, Zhu J-Y, Zhou T, Efros AA. Image-to-image translation with conditional adversarial networks. In: *2017 IEEE Conference on Computer Vision and Pattern Recognition (CVPR)*. IEEE;2017:5967–5976.
12. Johnson J, Alahi A, Fei-Fei L. Perceptual losses for real-time style transfer and super-resolution. arXiv website. <https://arxiv.org/abs/1603.08155>. Published March 27, 2016. Accessed November 9, 2022.
13. Kumar SK. On weight initialization in deep neural networks. arXiv website. <https://arxiv.org/abs/1704.08863>. Published April 28, 2017. Revised May 2, 2017. Accessed November 9, 2022.
14. Kingma DP, Adam BJ. A method for stochastic optimization. arXiv website. <https://arxiv.org/abs/1412.6980>. Published December 22, 2014. Revised January 30, 2017. Accessed November 9, 2022.
15. Slomka PJ, Nishina H, Berman DS, et al. Automated quantification of myocardial perfusion SPECT using simplified normal limits. *J Nucl Cardiol*. 2005;12:66–77.
16. Slomka PJ, Nishina H, Berman DS, et al. Automatic quantification of myocardial perfusion stress–rest change: a new measure of ischemia. *J Nucl Med*. 2004;45:183–191.
17. Diamond GA, Forrester JS. Analysis of probability as an aid in the clinical diagnosis of coronary-artery disease. *N Engl J Med*. 1979;300:1350–1358.
18. Douglas PS, Hoffmann U, Patel MR, et al. Outcomes of anatomical versus functional testing for coronary artery disease. *N Engl J Med*. 2015;372:1291–1300.
19. Nguyen TT, Chi TN, Hoang MD, Thai HN, Duc TN. 3D Unet generative adversarial network for attenuation correction of SPECT images. In: *2020 4th International Conference on Recent Advances in Signal Processing, Telecommunications & Computing*. IEEE;2020:93–97.
20. Yang J, Shi L, Wang R, et al. Direct attenuation correction using deep learning for cardiac SPECT: a feasibility study. *J Nucl Med*. 2021;62:1645–1652.
21. Hagio T, Poitrasson-Rivière A, Moody JB, et al. “Virtual” attenuation correction: improving stress myocardial perfusion SPECT imaging using deep learning. *Eur J Med Mol Imaging*. 2022;49:3140–3149.
22. Slomka PJ, Miller RJ, Hu L-H, Germano G, Berman D. Solid-state detector SPECT myocardial perfusion imaging. *J Nucl Med*. 2019;60:1194–1204.
23. Budoff MJ, Blankstein R, Nasir K, Blaha MJ. Power of zero stronger than soft plaque. *J Cardiovasc Comput Tomogr*. 2020;14:279.
24. Hu LH, Miller RJ, Sharir T, et al. Prognostically safe stress-only single-photon emission computed tomography myocardial perfusion imaging guided by machine learning: report from REFINE SPECT. *Eur Heart J Cardiovasc Imaging*. 2021;22:705–714.
25. Trpkov C, Savtchenko A, Liang Z, et al. Visually estimated coronary artery calcium score improves SPECT-MPI risk stratification. *Int J Cardiol Heart Vasc*. 2021;35:100827.

Development of a Lensless Radiomicroscope for Cellular-Resolution Radionuclide Imaging

Justin S. Klein, Tae Jin Kim, and Guillem Pratz

Department of Radiation Oncology, Stanford University, Stanford, California

The action of radiopharmaceuticals takes place at the level of cells. However, existing radionuclide assays can only measure uptake in bulk or in small populations of single cells. This potentially hinders the development of effective radiopharmaceuticals for disease detection, staging, and treatment. **Methods:** We have developed a new imaging modality, the lensless radiomicroscope (LRM), for in vitro, cellular-resolution imaging of β - and α -emitting radionuclides. The palm-sized instrument is constructed from off-the-shelf parts for a total cost of less than \$100, about 500 times less than the radioluminescence microscope, its closest equivalent. The instrument images radiopharmaceuticals by direct detection of ionizing charged particles via a consumer-grade complementary metal-oxide semiconductor detector. **Results:** The LRM can simultaneously image more than 5,000 cells within its 1 cm² field of view, a 100-times increase over state-of-the-art technology. It has spatial resolution of 5 μ m for brightfield imaging and 30 μ m for ¹⁸F positron imaging. We used the LRM to quantify ¹⁸F-FDG uptake in MDA-MB-231 breast cancer cells 72 h after radiation treatment. Cells receiving 3 Gy were 3 times larger (mean = 3,116 μ m²) than their untreated counterparts (mean = 940 μ m²) but had 2 times less ¹⁸F-FDG per area (mean = 217 Bq/mm²), a finding in agreement with the clinical use of this tracer to monitor response. Additionally, the LRM was used to dynamically image the uptake of ¹⁸F-FDG by live cancer cells, and thus measure their avidity for glucose. **Conclusion:** The LRM is a high-resolution, large-field-of-view, and cost-effective approach to image radiotracer uptake with single-cell resolution in vitro.

Key Words: radionuclide imaging; in vitro assays; ¹⁸F-FDG; CMOS detector

J Nucl Med 2023; 64:479–484

DOI: 10.2967/jnumed.122.264021

The past decade has witnessed a significant increase in the number of radiopharmaceuticals approved for diagnostic and therapeutic use in humans. To receive such approval, these radiopharmaceuticals have undergone rigorous evaluation and characterization, including preclinical and clinical studies. During the early phase of this process, in vitro data are often generated to identify and validate promising leads. In addition, existing radiopharmaceuticals continue to be studied even well after they have been approved for human use (1–3). However, most in vitro cell studies are limited in their ability to resolve the action of the radiopharmaceuticals at the

level of individual cells. Most existing assays can only measure the aggregated behavior of millions of cells, complicating efforts to study specific cells of interest within heterogeneous populations (4).

Radioluminescence microscopy (RLM), a technique for in vitro radionuclide imaging, was previously developed to address this need. The method allows dynamic imaging of live cells over a 1 mm² field of view, equating to approximately 50–100 cells simultaneously. RLM consists of a high-sensitivity camera coupled to a microscope objective that images a thin (typically 100–500 μ m) scintillator placed above or below a culture monolayer (2). By imaging β -particle scintillation tracks and applying a reconstruction algorithm (5), high-resolution and quantitative measurements of single cells are achievable (6). RLM has been used to study metabolism with ¹⁸F-FDG (7) and cell proliferation with ¹⁸F-fluorothymidine (1) in cell monolayers. The method can also be applied to image 3-dimensional (3D)-cultured cells including engineered tumor-stroma models (8) and patient-derived tumor organoids (9).

However, the small field of view of RLM presents a challenge for biologic experiments, requiring repeated acquisitions to attain statistical significance, since it is too small to measure sufficient numbers of cells and collect information on rare cell populations, such as tumor progenitor cells (10).

Additionally, it should be noted that building a RLM and successfully executing experiments requires significant technical skill and, to the best of our knowledge, only a few laboratories have adopted this technique. The cost of the necessary equipment is also significant, hindering dissemination and commercialization of the technique to more sites.

Here, we report the development of a lensless radiomicroscope (LRM) for in vitro, cellular-resolution radionuclide imaging of large cell populations. Unlike RLM, the LRM uses neither a scintillator nor a microscope objective. Instead, its design is based on the concept of lensless imaging (Fig. 1A), which was previously demonstrated for imaging cell samples using cell phone cameras or inexpensive photosensor arrays (11). This new microscope can image brightfield and radionuclide uptake of >5,000 cells, a 100 \times increase over RLM, with spatial resolution of 30 μ m for radionuclide imaging and 5 μ m for brightfield imaging. Additionally, the LRM is a simple and compact device built from inexpensive, readily available consumer electronics. With a total price tag of under \$100 USD, it costs approximately 500 \times less than RLM, its predecessor, yet it can acquire radionuclide and brightfield images with similar performance.

To demonstrate the capabilities of this new instrument, we have used the LRM to image the dynamic uptake of ¹⁸F-FDG by MDA-MB-231 breast cancer cells. Additionally, we have demonstrated that it is sensitive to α -particles, enabling its application for imaging therapeutic radiopharmaceuticals in vitro.

Received Mar. 17, 2022; revision accepted Sep. 8, 2022.

For correspondence or reprints, contact Guillem Pratz (pratz@stanford.edu).

Published online Sep. 15, 2022.

COPYRIGHT © 2023 by the Society of Nuclear Medicine and Molecular Imaging.

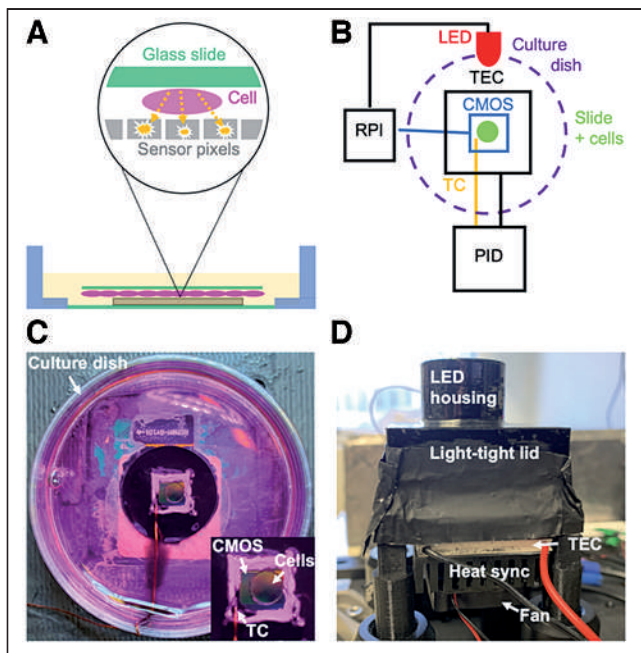


FIGURE 1. Conceptual, physical, and schematic diagram of the LRM. (A) Cells are grown on a glass slide and treated with α - or β -emitting radiopharmaceuticals. The slide is inverted and placed in direct contact with a CMOS imaging sensor. Emitted particles deposit energy in adjacent CMOS pixels, producing a detectable electronic signal. (B) The LRM consists of an imaging sensor (CMOS) that is read out through a compact Raspberry Pi computer (RPI). For live-cell imaging, sensor temperature is regulated by a proportional-integral-derivative (PID) controller connected to a thermocouple (TC) and thermoelectric cooler (TEC). The computer is also connected to an LED, which can be switched on for brightfield imaging. (C) The β -microscope imaging chamber, filled with medium. (D) Light-tight β -microscope enclosure. The LED used for brightfield imaging is housed in the upper cylinder. Attached to the bottom of the enclosure are the thermoelectric cooler, heat sync and fan.

MATERIALS AND METHODS

β -Microscope Design

The β -microscope comprises a light-tight imaging chamber with a removable lid made from 3D-printed parts (Fig. 1D). Inside the imaging chamber (Fig. 1C) is a pixelated Sony IMX219 complementary metal-oxide semiconductor (CMOS) imaging detector (Pi camera V2.1; Raspberry Pi Foundation, U.K.) integrated into a 35-mm-diameter cell-imaging dish (Cellvis). The imager has $3,280 \times 2,464$ square pixels, each $1.12 \mu\text{m}$ in size, and a total active area of $3.79 \times 2.69 \text{ mm}$. The whole imaging dish is easily removable via a J2 FPC connector on the bottom of the dish that mates with the microscope's imaging chamber.

The imaging detector is connected to the camera serial interface of a compact computer (Raspberry Pi Model 3B+; Raspberry Pi Foundation, U.K.). Custom, Python-based software (Python Software Foundation) controls the instrument for brightfield and radionuclide imaging. Microscope software and computer-aided design models are available in our public Git repository: <https://github.com/jstklein/lrm>. Temperature is controlled during cell imaging via a thermoelectric cooler that is coupled to the underside of the Pi camera circuit board. The cooler is controlled by a proportional-integral-derivative controller that is connected to a thermocouple bonded to the CMOS surface (Fig. 1C).

The light-tight enclosure features a 30-mm-long tube and aperture-masked red ($\sim 640 \text{ nm}$) light-emitting diode (LED) that is driven by a 5 V input/output port on the Raspberry Pi computer through a 1 k Ω current-limit resistor (Fig. 1D). The LED provides semicollimated

light for lensless brightfield imaging. We tested other visible wavelength LEDs (green, white) and found all yielded qualitatively similar results and the red LED was arbitrarily chosen. Given the proximity of the cells to the CMOS sensor, brightfield images can be obtained directly from the sensor without any additional reconstruction.

Imaging Dish Construction

The lens assembly of the Pi camera was removed, and the CMOS detector was carefully extracted from the camera housing. Exposed gold bondwires were protected from the aqueous cell culture environment using a waterproof silicon sealant (Marine Adhesive Sealant 5200FC; 3M). The detector was then glued into the hole at the bottom of the plastic imaging dish using 832HD epoxy (MG Chemicals). Finally, a glass coverslip was glued behind the detector, sealing the bottom of the imaging chamber.

Cell Imaging

Cells were grown on glass coverslips that had been prepared for cell culture (12) and subsequently treated with fibronectin (Sigma Aldrich) to improve biocompatibility and facilitate cell attachment. For all imaging experiments, MDA-MB-231 breast cancer cells were grown on round glass coverslips and submerged upside down into the imaging chamber, in direct contact with the CMOS detector. During imaging, the proportional-integral-derivative controller is set to hold the temperature of the cells and medium to 37°C . Without active temperature control, the CMOS imager will exceed physiologic temperatures during operation and potentially interfere with normal cellular processes.

For static images, which capture total uptake at a single time point, cells were incubated in radiopharmaceutical, washed, and then imaged. For dynamic images, which capture the process of radiopharmaceutical transport and accumulation, the radiopharmaceutical was added directly to the imaging chamber and an image time series was captured immediately thereafter to visualize its uptake.

MDA-MB-231 cells (American Type Culture Collection) were cultured in Dulbecco modified eagle medium (DMEM) (catalog no. 11995-065; Thermo Fisher Scientific) supplemented with 10% fetal bovine serum (catalog no. F-0500-A; Atlas Biologicals) and 1% penicillin/streptomycin (cat. no. 15140122; Thermo Fisher Scientific) and incubated at 37°C in a 5% CO_2 environment.

Brightfield images were acquired using autoexposure mode at the maximum resolution of $3,280 \times 2,464$ pixels. Raw RGB images were converted to gray scale and stored as 16-bit JPEG2000 images.

To demonstrate the ability of the microscope to image cell staining, some MDA-MB-231 cells were additionally fixed and stained with crystal violet, first by being rinsed with phosphate-buffered saline, then by being incubated in 5% w/w crystal violet in 6% v/v glutaraldehyde (Sigma-Aldrich), and finally by being rinsed with tap water.

β - and α -images were acquired with the following settings: $3,280 \times 2,464$ pixels, 10-s exposure duration and analog gain of 2.5. A lower threshold of 3 camera counts was applied to each 10-s exposure to remove camera noise. Multiple thresholded exposures were summed in memory to produce output images with effective integration times ranging from approximately 1 to 10 min, depending on the experiment. No other image processing or filtering was performed. Image data were stored as a lossless lz4-compressed 16-bit image matrix. Image data and metadata were combined into a Python data structure, serialized using the Python Pickle format, then saved to file.

α -Imaging

α -emission from a 370-Bq ^{210}Po needle source (United Nuclear Scientific LLC) was imaged by placing the active tip directly on the microscope's CMOS surface. Three 5-min α -images were recorded and summed together. A brightfield image of the needle source was also recorded.

Physical Characterization

β -imaging resolution was assessed by applying the Fourier ring correlation method (13) to a representative image of ^{18}F -FDG uptake by cancer cells. Briefly, 2 images of the same cell population were generated, each constructed from half of the acquired frames. The method estimates the cross-correlation between the 2 images in the spatial frequency domain along concentric rings. A deterministic threshold of 1/7 is then used to yield a quantitative estimate of the spatial resolution of the imager.

In addition, brightfield resolution was characterized by imaging 1- μm amine-modified monodispersed superparamagnetic beads (MonoMag Amine Beads; Ocean NanoTech). The beads were diluted in ethanol and dried onto the surface of a glass microscope coverslip that was imaged using the brightfield mode of the β -microscope. Resolution was measured from the full width at half maximum of a line profile drawn across a single bead in the brightfield image.

Camera Calibration

A flatfield image was captured by illuminating the imaging sensor with uniform white light. This image was used to compute a per-pixel correction factor that was applied to images generated by the instrument. This correction factor accounts for any nonuniformities in the imaging sensor and lens-related calibration factors built into the proprietary camera firmware.

A calibration factor to convert camera units into ^{18}F activity was determined as follows. A drop of ^{18}F -FDG was dried on a glass slide, and activity was measured in a dose calibrator to be 108 kBq. The slide was imaged 397 min (~ 3.6 half-lives) later using the LRM, after it had decayed to 8.9 kBq. This low activity level was used to prevent camera saturation. A region of interest (ROI) was measured around the dried ^{18}F -FDG droplet. The camera calibration factor was computed as $\frac{\text{ROI counts (camera units)} \times \text{pixel area (mm}^2/\text{px)}}{\text{ROI activity (Bq)} \times \text{total imaging time (s)}}$, where pixel area = 1.25×10^{-6} mm 2 /px (based on CMOS pixel pitch).

RESULTS

Characterization

Supplemental Figure 1 (supplemental materials are available at <http://jnm.snmjournals.org>) shows a time-integrated β -microscope image of a dried 8.9-kBq ^{18}F -FDG droplet on a glass slide. The final camera calibration factor was computed using the equation shown above and average measurements from 3 independent, 50 s β -images. The measurements were ROI counts = 422,845,211, ROI activity = 8.9 kBq, and total imaging time = 50 s. The final calibration factor was $840 \frac{\text{camera units} \times \text{mm}^2}{\text{Bq} \times \text{s} \times \text{px}}$, where px is pixels. When divided into ^{18}F β -images on a per-pixel basis, the calibration factor yields quantitative images in units of Bq/mm 2 .

Brightfield resolution was 5.1 μm , based on the full width at half maximum of a 1- μm polystyrene sphere (Fig. 2A). The inset image in Figure 2 shows a line profile drawn across the sphere (dashed blacked line), and arrows show full width at half maximum. β -resolution was 30 μm , based on Fourier ring correlation analysis of ^{18}F -FDG β -images of MDA-MB-231 cells (Fig. 2B). This resolution is equivalent to that of RLM and largely determined by the source-detector distance and the physics of positron transport (6).

Brightfield Imaging

To demonstrate the timelapse capabilities of the LRM and the ability of cells to remain viable over prolonged imaging

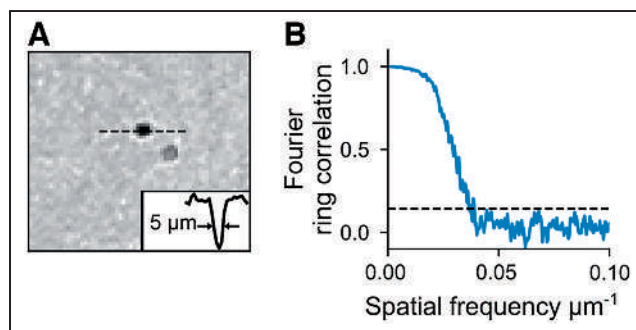


FIGURE 2. LRM physical characterization and calibration. (A) Brightfield image of 1- μm polystyrene sphere with inset line profile showing full width at half maximum. (B) Fourier ring correlation analysis plot showing spatial resolution of LRM.

experiments, MDA-MB-231 cells were grown on a glass slide, then imaged in brightfield mode every 5 min, for 10 h (Supplemental Fig. 2A). Cell migration could be readily observed in a recorded video of the acquisition (Supplemental Video 1), and no adverse effects were detected.

Additionally, the microscope is capable of imaging fixed and stained cells. Supplemental Figure 2A shows enlarged senescent MDA-MB-231 cells after irradiation with 8 Gy (225 kVp x-ray) and subsequent fixing and staining with crystal violet in glutaraldehyde. The use of a stain induces a visible darkening of the cells in the brightfield images.

^{18}F -FDG β -Microscope Imaging

We first demonstrate the LRM technique by imaging ^{18}F -FDG uptake in MDA-MB-231 breast cancer cells (Fig. 3). The β -image is the sum of 13 images, each acquired as a 5-min exposure (65 min total imaging time). The merged image shows that ^{18}F -FDG uptake can be localized to individual cells and matches the brightfield image. Because of the proximity of the cells to the detector, the outline of the cells is clearly resolved, with only overlap between adjacent cells. About 50 cells are shown in the cropped field of view and range in activity from 0 Bq/mm 2 up to 1,800 Bq/mm 2 , indicating a wide range of metabolic activity in this population. Healthier-looking cells (larger, attached, dividing) appear to be more metabolically active than unhealthy ones (detached, granular, shriveled). The images also confirm that background signal is very low in areas where cells are not present, even for extended imaging experiments.

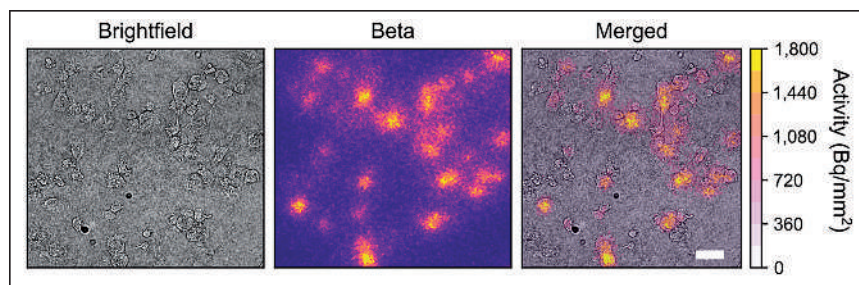


FIGURE 3. High-resolution β -imaging of ^{18}F -FDG in breast cancer cells. MDA-MB-231 cells were imaged using brightfield and β -modes. Images are cropped to $600 \times 600 \mu\text{m}$ from the full 3.7×2.8 mm field of view. Total imaging time for β -imaging was 65 min. Scale bar is 50 μm .

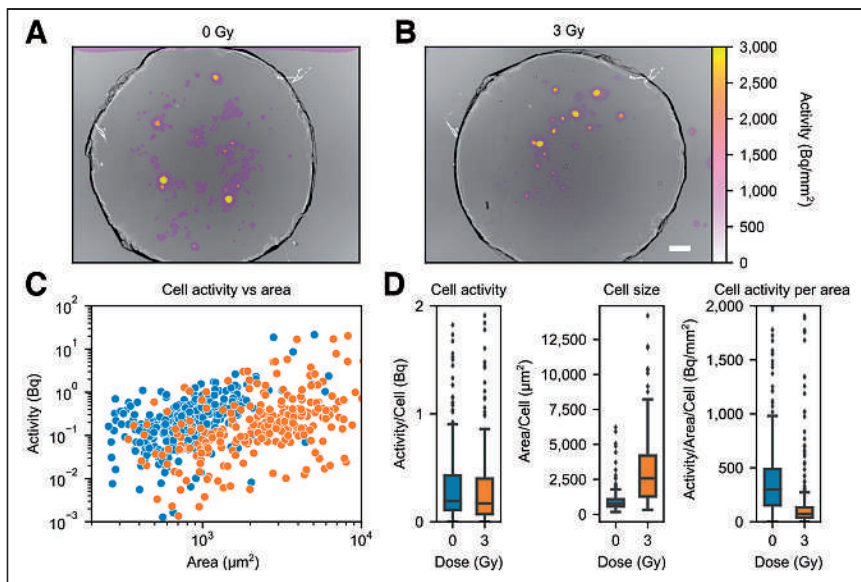


FIGURE 4. ^{18}F -FDG β -imaging of breast cancer cells treated with radiation. β -images of cells receiving 0 Gy (A) and 3 Gy (B). Scale bar is 200 μm . (C) Scatter plot of activity vs. area for treated and untreated cells. (D) Bar graphs of activity per cell, cell size, and cell activity per area.

^{18}F -FDG Imaging of Radiation-Treated Breast Cancer Cells

Figure 4 demonstrates that LRM can be used to determine the response of MDA-MB-231 cells to radiation therapy on the basis of ^{18}F -FDG uptake. Cells were irradiated with 0 and 3 Gy of 225 kVp x-ray 3 d before image acquisition using the LRM.

To quantify the images, ROIs were drawn around cells, and area and activity were measured. Figure 4C shows activity versus area for all cells in the experiment. Data represent ROIs measured from 4 β -images with total integration times of 75 min (0-Gy experiment) and 45, 60, or 105 min (3-Gy experiment).

Figure 4D shows aggregated measurements from cell ROIs. Cells receiving 0 Gy ($n = 301$) had significantly smaller area (mean = 940 μm^2) but overall greater activity per area (mean = 445 Bq/mm^2). Cells receiving 3 Gy ($n = 260$) had larger area (mean = 3116 μm^2), but less activity per area (mean = 217 Bq/mm^2). All results were statistically significant ($P < 0.01$) per Welch's t test. Both groups had similar activity per cell (0-Gy mean = 0.50 Bq; 3-Gy mean = 0.67 Bq; $P > 0.01$).

Dynamic ^{18}F -FDG β -Microscope Imaging

Figure 5 demonstrates dynamic imaging of ^{18}F -FDG uptake by MDA-MB-231 cells over a 190 min period. LRM images were acquired every 10 min, resulting in 19 frames, and the corresponding time-activity curves were computed on the basis of user-defined circular ROIs (Fig. 5B). For this study, ^{18}F -FDG (5 MBq/mL) in DMEM was added to the imaging chamber immediately before imaging the dynamic uptake of the tracer by the cells. The average ^{18}F -FDG distribution over the entire study period is shown in Figure 5B, along with the ROIs that were used. The time-activity curves for the cells were corrected by subtracting the background signal.

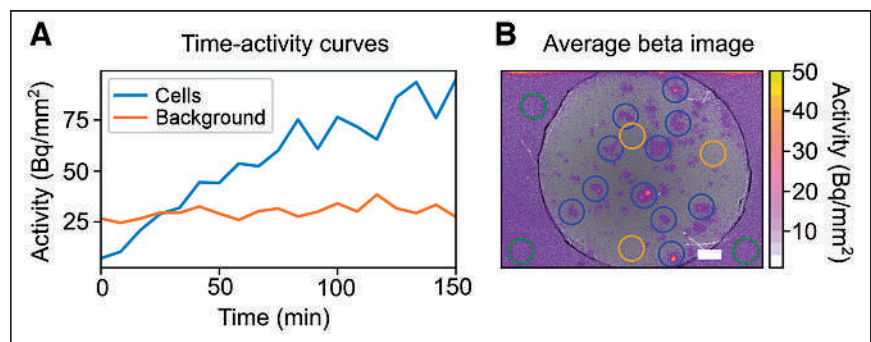


FIGURE 5. Dynamic ^{18}F -FDG imaging of cells. (A) Time-activity curves measured from cell and background ROIs. (B) Cumulative uptake of ^{18}F -FDG by MDA-MB-231 cells, with ROIs shown for cells (blue) and background (orange). Scale bar is 200 μm .

The β -image was merged with the gray scale brightfield image, and ROIs were drawn over clusters of cells (blue) and empty background regions (orange). The image shows regions of significant focal uptake, corresponding to dense clusters of cells. Background signal was significantly lower under the cover glass than outside of it because of the lower volume and shielding by the cover glass.

Time-activity curves of cell and background ROIs (Fig. 5A) show ^{18}F -FDG uptake as a function of time. These curves have been corrected for radioactive decay and drift in detector gain by normalizing them using the background signal outside the circular cover glass region. A movie of ^{18}F -FDG uptake has been included as Supplemental Video 2.

α -Particle Imaging

Figure 6 shows α - and brightfield images of a ^{210}Po needle source. The needle appears as a long dark shadow in the brightfield image. The α -image is the sum of 3 5-min acquisitions. Compared with β -particles, α -particles produce an intense and focal signal on the detector. The merged image shows that the α -signal is readily localized to the needle source.

DISCUSSION

This study presents a novel lensless radiomicroscope that can image commonly used radiotracers at single-cell resolution in 2-dimensional cell cultures. The instrument is compact and inexpensive, yet it can image samples with $>1 \text{ cm}^2$ field of view and 30- μm spatial resolution. The microscope is capable of prolonged, timelapse brightfield in vitro imaging of stained or unstained cells (Supplemental Fig. 2, Supplemental Video 1), and β - (Figs. 3, 4, and 5) or α - (Fig. 6) imaging.

Compared with other solid-state radiation detectors, such as, for instance, a position-sensitive avalanche photodiode (14), a lensless CMOS detector can also be used for imaging cells in brightfield mode, providing images of both the cells and the distribution of the radiotracer. These capabilities could potentially be embedded

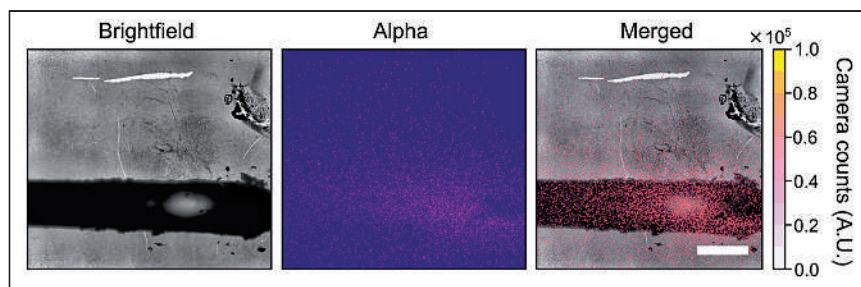


FIGURE 6. α -imaging of Po-210 needle source. The needle is visible as a dark shadow in the brightfield image. α -emission is readily localized to the needle source in the merged image. Scale bar is 500 μm .

within microfluidics devices for in vitro radiobiologic assays (13) or for quality control of radiotracer production (15). Additionally, the system is built from inexpensive consumer-grade components, including a Raspberry Pi minicomputer (\$35), a CMOS camera (\$25), a Peltier cooling system (\$35), and a 3D printed housing (<\$10). The system is therefore highly cost-effective compared with other previously developed imaging methods.

Figure 3 reveals static ^{18}F -FDG β -images of MDA-MB-231 cells and shows that the β -signal is easily localized to individual cells. The spatial resolution of ^{18}F images is estimated to be 30 μm , based on Fourier ring correlation analysis of the LRM images, which is sufficient in most cases to distinguish individual cells. This estimate, which is obtained through a computational method, is consistent with the fact that, in Figure 3, adjacent cells can be readily resolved. Spatial resolution for β -imaging is primarily determined by the physical travel of the positrons before reaching the sensor, regardless of the type and pixel size of the sensor used to detect the ionizing radiation. Thus, although the pixels are very small, the spatial resolution of the LRM is similar to that of other methods that rely on larger pixels, such as RLM (6). The use of CMOS devices with larger pixels could potentially allow improved signal to noise with no loss of resolution, however, the trend in consumer camera electronics is toward smaller form factors and pixels. Additionally, once calibrated, the LRM can be used to provide quantitative estimates of radioactivity distribution in cells. The calibration factor we have provided is relevant only for ^{18}F and the calibration procedure would have to be repeated if other isotopes were imaged.

To illustrate the capabilities of the microscope, we measured ^{18}F -FDG uptake in cells irradiated with 0 or 3 Gy of x-rays (Fig. 4). Radiation is often used as a treatment for solid tumors, with nearly 50% of all cancer patients receiving some form of radiation for their disease. ^{18}F -FDG PET is a common readout of treatment response, but the significance of the PET measurement is unclear because irradiated cells may remain metabolically active, even if they can no longer replicate. To investigate this question, measurements from more than 500 cells were made using the β -microscope in a single experiment. Three days after receiving 3 Gy of x-ray radiation, cells were on average 3 times larger (mean area = 3,116 μm^2) than their untreated counterparts but had half as much ^{18}F -FDG per area. The brightfield images also revealed that the cells treated with 3 Gy had enlarged nuclei, a common occurrence in radiation-treated cells that is due to the failure of these cells to advance through mitosis. The decreased ^{18}F -FDG concentration inside the cells suggests decreased metabolic activity, likely due to radiation-induced damage of the cell's metabolic machinery. Of note,

previous studies noted that cells that survived irradiation actually had higher ^{18}F -FDG uptake than control nonirradiated cells (16,17), based on bulk γ -counting measurements normalized by the number of viable cells. Our study found no substantial difference in uptake between nonirradiated and irradiated, but the difference may be due to the timing and methodology used for measuring this quantity.

Additionally, we demonstrated the feasibility of dynamic ^{18}F -FDG studies using the instrument (Fig. 6). Dynamic images were acquired every 10 min to yield aggregated

time-activity curves that represent the active transport of the tracer by the cells. After decay correction, the measured background due to free ^{18}F -FDG in the culture medium was found to be constant over the course of the experiment. In contrast, the radioactive signal measured at the location of MDA-MB-231 cells rose over time at a nearly constant rate over the 2-h duration of the experiment. The imaged cells initially did not have any detectable radioactivity, but by the end of the experiment, they achieved radiotracer uptake equal to about 6 times the background concentration.

Finally, using a sealed ^{210}Po source, we demonstrated the ability of the LRM to image α -particles. This capability opens the door for imaging therapeutic α -emitting radionuclides, which are an important new class of therapy. The LRM in this context could be used to investigate the distribution of these agents at the level of individual cells in heterogeneous populations of cells and prevent the emergence of resistant subclones.

It should be noted that despite the impressive performance of this instrument, only minimal optimizations for image quality and sensitivity have been made thus far. There are likely significant gains to be had with further software optimization, alone. For example, in previous work, we found that signal-to-noise ratio could be significantly improved by processing the images in pulse-counting mode rather than integration mode (5). Similarly, the CMOS-based LRM could acquire large numbers of frames with short exposures to enumerate individual decay events.

Although the pixelated CMOS sensor provides many advantages for this application, a few limitations of the method should be highlighted. First, the 10 bit A/D converter limits the maximum signal to 1,024 camera units per pixel per frame. At a readout speed of 1 Hz, with ^{18}F , this would limit the maximum detectable activity to 10.8 Bq/px. Additionally, another limitation is that, unlike the previously developed RLM, the LRM lacks fluorescence capabilities. This capability could likely be enabled through harnessing built-in Bayer array or coating the CMOS pixels with a bandpass filter to obtain fluorescence images of cells in a lensless manner (18).

Finally, though we were able to reuse the same CMOS detector for many experiments, we expect that it will eventually degrade due to radiation damage. Given its relatively low cost, it is a consumable component of the microscope that can be regularly replaced.

CONCLUSION

The experiments shown here are a proof-of-concept for the LRM, a new imaging instrument capable of in vitro high-resolution imaging of β - and α -emitting radionuclides. This instrument is simpler and far less costly than current technology while offering an

unprecedentedly large 1 cm² field of view and 30- μ m resolution. Our results demonstrate a variety of potential workflows that could foreseeably be used for radiopharmaceutical development, quality control, and cancer biology investigations. Because the LRM is low cost and constructed from readily available components, we anticipate that this new technology will make in vitro single-cell radionuclide imaging more accessible and enable new investigations in the biologic realm.

DISCLOSURE

Justin Klein was supported by T32CA118681. No other potential conflict of interest relevant to this article was reported.

KEY POINTS

QUESTION: Can a low-cost lensless radiomicroscope visualize cellular-level uptake of radionuclides?

PERTINENT FINDINGS: We have developed a low-cost imaging modality for in vitro imaging of α - and β -emitting radionuclides and imaged quantitative changes in cellular ¹⁸F-FDG uptake after radiation treatment.

IMPLICATIONS FOR PATIENT CARE: The lensless radiomicroscope will aid in the development of effective radiopharmaceuticals by allowing study of their action at the cellular level.

REFERENCES

1. Sengupta D, Pratz G. Single-cell characterization of FLT uptake with radioluminescence microscopy. *J Nucl Med*. 2016;57:1136–1140.
2. Kim TJ, Türkan S, Pratz G. Modular low-light microscope for imaging cellular bioluminescence and radioluminescence. *Nat Protoc*. 2017;12:1055–1076.
3. Liu Z, Lan X. Microfluidic radiobioassays: a radiometric detection tool for understanding cellular physiology and pharmacokinetics. *Lab Chip*. 2019;19:2315–2339.
4. Cherry SR, Sorenson JA, Phelps ME. What is nuclear medicine? In: *Physics in Nuclear Medicine*. Elsevier Health Sciences; 2012:1–6.
5. Pratz G, Chen K, Sun C, et al. High-resolution radioluminescence microscopy of ¹⁸F-FDG uptake by reconstructing the β -ionization track. *J Nucl Med*. 2013;54:1841–1846.
6. Wang Q, Sengupta D, Kim TJ, Pratz G. Performance evaluation of ¹⁸F radioluminescence microscopy using computational simulation. *Med Phys*. 2017;44:1782–1795.
7. Pratz G, Chen K, Sun C, et al. Radioluminescence microscopy: measuring the heterogeneous uptake of radiotracers in single living cells. *PLoS One*. 2012;7:e46285.
8. Khan S, Kim S, Yang YP, Pratz G. High-resolution radioluminescence microscopy of FDG uptake in an engineered 3D tumor-stoma model. *Eur J Nucl Med Mol Imaging*. 2021;48:3400–3407.
9. Khan S, Shin JH, Ferri V, et al. High-resolution positron emission microscopy of patient-derived tumor organoids. *Nat Commun*. 2021;12:5883.
10. Reya T, Morrison SJ, Clarke MF, Weissman IL. Stem cells, cancer, and cancer stem cells. *Nature*. 2001;414:105–111.
11. Ozcan A, McLeod E. Lensless imaging and sensing. *Annu Rev Biomed Eng*. 2016;18:77–102.
12. Fischer AH, Jacobson KA, Rose J, Zeller R. Preparation of slides and coverslips for microscopy. *CSH Protoc*. 2008;2008:pdb.prot4988.
13. Kim TJ, Ha B, Bick AD, Kim M, Tang SKY, Pratz G. Microfluidics-coupled radioluminescence microscopy for in vitro radiotracer kinetic studies. *Anal Chem*. 2021;93:4425–4433.
14. Vu NT, Yu ZTF, Comin-Anduix B, et al. A beta-camera integrated with a microfluidic chip for radioassays based on real-time imaging of glycolysis in small cell populations. *J Nucl Med*. 2011;52:815–821.
15. Ha NS, Sadeghi S, van Dam RM. Recent progress toward microfluidic quality control testing of radiopharmaceuticals. *Micromachines (Basel)*. 2017;8:337.
16. Higashi K, Clavo AC, Wahl RL. In Vitro Assessment of 2-fluoro-2-deoxy-D-glucose, L-methionine and thymidine as agents to monitor the early response of a human adenocarcinoma cell line to radiotherapy. *J Nucl Med*. 1993;34:773–779.
17. Senekowitsch-Schmidtke R, Matzen K, Truckenbrodt R, Mattes J, Heiss P, Schwaiger M. Tumor cell spheroids as a model for evaluation of metabolic changes after irradiation. *J Nucl Med*. 1998;39:1762–1768.
18. Kim M, Pan M, Gai Y, et al. Optofluidic ultrahigh-throughput detection of fluorescent drops. *Lab Chip*. 2015;15:1417–1423.

Adverse Clinical Events at the Injection Site Are Exceedingly Rare After Reported Radiopharmaceutical Extravasation in Patients Undergoing ^{99m}Tc -MDP Whole-Body Bone Scintigraphy: A 12-Year Experience

Ashwin Singh Parihar¹, Lisa R. Schmidt¹, John Crandall¹, Farrokh Dehdashti^{1,2}, and Richard L. Wahl^{1,2}

¹Mallinckrodt Institute of Radiology, Washington University School of Medicine, St. Louis, Missouri; and ²Siteman Cancer Center, Washington University School of Medicine, St. Louis, Missouri

See an invited perspective on this article on page 491.

The deleterious effects of high-dose radiation on normal tissue are sometimes extrapolated to diagnostic (SPECT and PET) radiopharmaceutical extravasation (RPE). It has been hypothesized that diagnostic RPE can have gradually evolving local tissue injury and a potentially increased risk of local dermatologic or oncologic diseases over a longer period. However, data on clinical adverse events after diagnostic RPE are limited. Therefore, our primary aim was to study the occurrence of short-term and long-term clinical adverse events in patients who underwent ^{99m}Tc -methylene diphosphonate (^{99m}Tc -MDP) whole-body bone scintigraphy (WBBS) with reported RPE. **Methods:** The records of ^{99m}Tc -MDP WBBS performed from June 2010 to January 2022 were retrospectively examined for RPE documented in the scan reports. The clinical records of patients with a documented RPE were extensively reviewed for any related short-term adverse events (within 2 wk of the WBBS: local symptoms and care sought for local dermatologic or musculoskeletal issues) and long-term adverse events (until the last follow-up: local deleterious effects and related consults for dermatology, plastic surgery, oncology, or orthopedics). **Results:** Retrospective review of the records of 31,679 ^{99m}Tc -MDP WBBS studies showed RPE documented in 118 (0.37%). Medical records were not retrievable for 22 patients, yielding a final cohort of 96 patients with reported RPE. The median follow-up was 18.9 mo (interquartile range, 7.8–45.7 mo). Short-term events were noted in 4 patients, of whom one was asymptomatic. Of the 3 symptomatic patients, 2 experienced mild discomfort at the injection site, and 1 had tender swelling. Three of the 4 events were in patients who had a prior intravenous contrast extravasation for contrast-enhanced CT performed earlier during the day and a ^{99m}Tc -MDP injection later at the same site, likely leading to RPE. None of the long-term local events had any plausible link with the RPE event. **Conclusion:** Reported RPE was rare, and 3 patients (0.009%) had short-term local symptoms, all of which were likely related to the prior higher-volume intravenous contrast extravasation. The smaller-volume diagnostic radiopharmaceutical injections for WBBS are highly unlikely

to cause local symptoms on their own. No patient had any long-term adverse event with a plausible link to the RPE.

Key Words: extravasation; infiltration; radiotracer; radionuclide; MDP; bone scan

J Nucl Med 2023; 64:485–490

DOI: 10.2967/jnumed.122.264994

Radiopharmaceutical extravasation (RPE) refers to the unintended leakage of the radiopharmaceutical into the tissue surrounding the injection site (frequently during intravenous administration). The consequences of RPE depend on several factors, namely the physical characteristics of the radionuclide (e.g., energy, half-life, and type of emissions), properties of the radiopharmaceutical (e.g., pH, viscosity, osmolality, and adjuvants), volume of injection, fraction of the activity that was extravasated, site of RPE, and multiple patient-related factors (1,2). There is a potential risk of physical harm to the patient, especially with RPE of therapeutic radiopharmaceuticals (2). Further, insufficient delivery of the radiopharmaceutical to the target site may negatively impact image quality and its clinical interpretation, especially when quantitation is involved (2–4).

The detrimental effects of ionizing radiation on normal tissues have been described (5). The physical effects resulting from extravasation of chemotherapy drugs and intravenous iodinated contrast media are also well known (1,6). However, the unique situation with diagnostic radiopharmaceuticals is that they typically involve injections of lower volumes (~0.5–1 mL, compared with >50 mL for iodinated contrast medium), with no direct cytotoxic effect of the pharmaceutical component (compared with the intrinsic cytotoxicity of chemotherapy) and much lower absorbed radiation doses (compared with external-beam radiation therapy) (1,2,5,7). A 2017 systematic review of RPE noted a major deficiency in the literature on the adverse clinical effects of RPE involving diagnostic radiopharmaceuticals, especially with regard to lack of clinical follow-up (2). The authors reported studies with a total of 3,016 cases of diagnostic RPE, out of which only 3 (0.1%) had any follow-up data available. It has been hypothesized that diagnostic RPE can lead to potential complications, either due to the volume effect (e.g., local hematoma and phlebitis) or due to the local effects of radiation (e.g., ulceration and desquamation) (2,8). However, in the absence of any systematically performed study in this space, the association of any adverse clinical effects with diagnostic RPE remains unknown.

Received Oct. 8, 2022; revision accepted Oct. 12, 2022.

For correspondence or reprints, contact Richard L. Wahl (rwahl@wustl.edu).

Published online Oct. 20, 2022.

Immediate Open Access: Creative Commons Attribution 4.0 International License (CC BY) allows users to share and adapt with attribution, excluding materials credited to previous publications. License: <https://creativecommons.org/licenses/by/4.0/>. Details: <http://jnm.snmjournals.org/site/misc/permission.xhtml>.

COPYRIGHT © 2023 by the Society of Nuclear Medicine and Molecular Imaging.

Most cases with diagnostic RPE (85.7%) have been reported with ^{99m}Tc -methylene diphosphonate (^{99m}Tc -MDP) used for skeletal scintigraphy, probably because of the high volume of these studies and the acquisition of whole-body images that frequently capture the injection site (2). Therefore, we sought to review ^{99m}Tc -MDP whole-body bone scintigraphy (WBBS) studies with RPE to determine the occurrence of any clinical adverse events in the patients. The primary objective of this study was to determine whether ^{99m}Tc -MDP RPE in patients undergoing WBBS is associated with adverse clinical events, in the short term or the long term. Secondary objectives were to estimate the rate of RPE in the ^{99m}Tc -MDP WBBS studies performed at the hospitals associated with our institute and to assess the requirement for a repeat scan due to insufficient diagnostic quality of the images.

MATERIALS AND METHODS

We retrospectively reviewed the records of ^{99m}Tc -MDP bone scans performed over 12 y (June 2010 to January 2022) at our medical center to identify WBBS studies for which the scan report documented RPE. The requirement for informed consent was waived for this retrospective analysis. Bone scans other than WBBS, such as limited-field-of-view regional studies, were excluded. The clinical records of patients with a documented RPE during ^{99m}Tc -MDP WBBS were extensively reviewed for any related short-term adverse events (within 2 wk of the study), including local symptoms; any clinical documentation of the RPE (other than radiology and nuclear medicine); and care sought for dermatologic, neurologic, or musculoskeletal issues related to the site of RPE. If no results were found within the 2-wk duration, the next available clinical encounter closest to the scan date was reviewed. Medical admissions, if any, sought after the scan were also reviewed to determine the indication and whether it was related to the RPE. Medical records were also searched for long-term adverse events (through the date of last follow-up) to look for any local deleterious effects and related consults for dermatology, plastic surgery, oncology, or orthopedics. The study workflow is shown in Figure 1.

The Division of Nuclear Medicine at our institute currently routinely uses a small-gauge (23 or 25) butterfly needle (winged infusion

set) for intravenous injections of ^{99m}Tc -MDP. This policy was instituted in September 2017, before which a straight stick technique was more routinely used for intravenous injections. A previously placed peripheral intravenous line may also be used after confirming its patency. An easily palpable superficial vein in the antecubital fossa is the preferred site of cannulation. Proper placement of the needle in the lumen of the vein is verified by confirming adequate blood return before injecting the radiopharmaceutical. Under current institutional policy, if an RPE occurs, the incident is reported to the nuclear medicine physician for further guidance and documented in an online safety report. The nuclear medicine physician then assesses the severity of the RPE by its impact on the patient in terms of likelihood of physical harm and on the study in terms of image quality. It is then determined whether the patient requires further clinical evaluation and whether a repeat study is required.

RESULTS

In total, 38,746 ^{99m}Tc -MDP bone scans were performed over approximately 12 y (June 2010 to January 2022), of which 31,679 were WBBS. RPE was documented in 118 scan reports (0.37%). Medical records were available for 96 of these studies (performed on 96 patients), which formed the final cohort. The medical records of these 96 patients (mean age, 63.8 ± 14.3 y; 48 men, 48 women) were reviewed, with a median follow-up period of 18.9 mo (interquartile range, 7.8–45.7 mo). At the last follow-up, 76 patients were alive and 20 were deceased. The ^{99m}Tc -MDP WBBS studies were performed for initial staging ($n = 26$), restaging ($n = 18$), or evaluation of osseous disease ($n = 52$). All scans except one were performed for an oncologic indication, the most common of which was prostate cancer (35.4%), followed by breast cancer (32.3%) (Table 1). The most common site for the radiopharmaceutical injection was the antecubital fossa (79.2%), followed by the hand or wrist (19.8%). The radiopharmaceutical was injected directly into the central venous catheter in 1 patient. The injections were performed on the left side in 50 patients and on the right side in 46 (including the injection in the central venous catheter). The mean injected activity of ^{99m}Tc -MDP was 791.8 ± 59.2 MBq (21.4 ± 1.6 mCi).

Short-Term Adverse Events

There were 4 RPE-related events, of which 3 were symptomatic. Two patients experienced local discomfort with no blistering or erythema and intact distal pulses and sensation. One patient had local discomfort with tender swelling and intact distal pulses and sensation. One patient who remained asymptomatic was assessed to have normal grip strength and capillary refill. Of these 4 patients, 3 had an intravenous iodinated contrast infiltration previously on the same day while undergoing contrast-enhanced CT (Fig. 2). The RPE occurred at the same site. These 3 patients were recommended to apply cold compresses with arm elevation at home. The recommendation of cold compresses (over hot compresses) was made in view of the high-volume intravenous contrast extravasation earlier during the day of the scan—a volume that was much higher than that of the RPE. Two of these patients had a documented complete resolution of symptoms (one on the same day and the

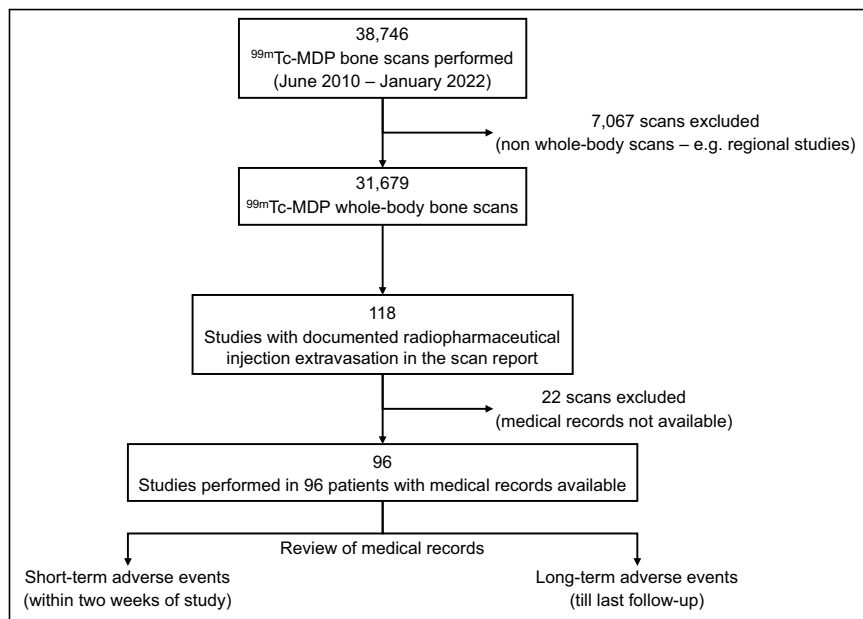


FIGURE 1. Study workflow.

TABLE 1

Primary Clinical Indication for ^{99m}Tc-MDP WBBS in Which RPE Was Reported

Primary clinical condition for bone scan	n	%
Prostate carcinoma	34	35.4
Breast carcinoma	31	32.3
Hepatocellular carcinoma	10	10.4
Renal cell carcinoma	4	4.2
Lung carcinoma	3	3.1
Rectal carcinoma	2	2.1
Neuroendocrine carcinoma	2	2.1
Ovarian carcinoma	2	2.1
Colon carcinoma*	1	1.0
Urinary bladder carcinoma	1	1.0
Melanoma	1	1.0
Esophageal carcinoma	1	1.0
Pancreatic carcinoma*	1	1.0
Osteosarcoma	1	1.0
Rhabdomyosarcoma (cheek)	1	1.0
Paget disease	1	1.0

*One patient had both breast and pancreatic cancer, and one had both breast and colon cancer.

other within a week). An update on the clinical status was not documented for the third patient. The patient with RPE without any prior contrast extravasation did not require any active intervention, and his symptoms resolved on the same day. No appointments or referrals were made for any of these patients with primary care, dermatology, or plastic surgery. None of the patients had any severe RPE-related adverse events that required urgent care or hospital admission.

Long-Term Adverse Events

No long-term local adverse events were observed in 88 of 96 (91.7%) patients. No appointments or referrals were made for any of these 96 patients (with dermatology, plastic surgery, oncology, or orthopedics) related to the RPE. Eight patients experienced adverse events, none of which could be directly attributed to the RPE (Table 2). The most common diagnosis in 3 of these 8 patients was carpal tunnel syndrome. Two patients had a temporary symptom arising from non-RPE-related factors (thrombophlebitis after an intravenous peripheral catheter placement, and contact dermatitis). One patient developed weakness of the upper extremity due to brain metastases from primary renal cell carcinoma. Two patients had paraesthesia in their arm, attributed to cervical radiculopathy in one patient and with an unknown etiology in the other.

Of the 96 studies with documented RPE, 93 (96.9%) were deemed adequate for clinical interpretation and rescanning was not recommended (Fig. 3). A repeat scan was recommended for 3 patients because of the suboptimal diagnostic quality of the initial scan with RPE. A repeat scan was subsequently performed uneventfully for 2 patients.

DISCUSSION

Several prior studies have reported RPE with ^{99m}Tc-MDP or other radiopharmaceuticals for skeletal scintigraphy; however,



FIGURE 2. A 68-y-old woman with left breast cancer. WBBS was performed for restaging. Shortly after intravenous injection of 854.7 MBq (23.1 mCi) of ^{99m}Tc-MDP in right antecubital fossa, patient complained of swelling and tenderness in her arm. Distal pulses and sensation in right upper extremity were intact. She had infiltration of iodinated contrast medium earlier in day in same arm while undergoing contrast-enhanced CT. She was recommended to use cold compresses and arm elevation at home and had experienced complete recovery when evaluated at next visit (4 wk). WBBS images in anterior (A) and posterior (B) projections show site of RPE around right elbow (red arrows). Patient had metastases to right occipital bone and right iliac bone adjacent to sacroiliac joint (solid black arrows). Prior fracture site in left elbow is also visualized (dashed black arrow).

none described any clinical adverse effects associated with the RPE (2). Most prior discussions have focused on the extraskelatal distribution of the radiopharmaceutical after RPE (9–13). In the absence of any significant clinical follow-up data after RPE during diagnostic studies, it has been hypothesized that clinical adverse events might occur but are underreported (2). Our results provide evidence that clinical adverse events reported after ^{99m}Tc-MDP RPE in patients undergoing WBBS are, in fact, rare. Among 96 patients with an RPE documented in the clinical report, only 3 had a short-term clinical adverse event. Of these, only one was potentially directly related to the radiopharmaceutical, whereas the others were almost certainly due to the volume or vesicant effects of an intravenous contrast extravasation earlier during the day.

Among the long-term local adverse events irrespective of etiology, the most common diagnosis was carpal tunnel syndrome (3/8 patients). Carpal tunnel syndrome has a complex pathophysiology, with several genetic and environmental factors involved (14).

TABLE 2
 Long-Term Local Adverse Events (Irrespective of Etiology) in Patients with RPE Documented on Their ^{99m}Tc-MDP
 WBBS Report

Injection site	Short-term symptoms*	Long-term symptoms on follow-up	Site	Scan to symptom onset (mo)	Diagnosis	Intervention	Resolution
R wrist	No	Pain, tenderness	Both hands (L > R)	6	Carpal tunnel syndrome, arthritis	Corticosteroids	No
L ACF	No	Paraesthesia	L arm	0.6	None	None	No
L ACF	No	Numbness	Both hands	33.6	Carpal tunnel syndrome	Surgery	Yes
L ACF	No	Paraesthesia	L arm	47.4	Cervical radiculopathy	None	No
L ACF	No	Weakness	L upper limb	0.6	Brain metastases	Corticosteroids	No
L ACF	No	Swelling, pain	L arm	0.7	Thrombophlebitis	Antibiotics	Yes
R ACF	No	Pain, weakness	R arm	2.8	Carpal tunnel syndrome	Corticosteroids	Yes
R hand	No	Rash, Itching	R arm	1	Eczema/contact allergy	Corticosteroids	Yes

*Within 2 wk of ^{99m}Tc-MDP WBBS.
 ACF = antecubital fossa.

Its prevalence in the general population has been reported to be approximately 3%–5%, with higher rates in workers in specific industries (15,16). The rate of carpal tunnel syndrome in patients with reported RPE in our study was 3%, which conforms to the expected rate in the general population. With a median follow-up of over 18 mo (longest: >8 y), we did not find any long-term local adverse events that could be related to the RPE. This is a significant addition to the existing literature, as most prior studies did not report any follow-up of the patients with RPE. A systematic review published in 2017 showed that only 3 patients of 3,016 (0.1%) with a diagnostic RPE had any follow-up data reported (2). Two case reports included in the review describe ulcer development in 2 patients (after 2 and 3 y) after RPE of ²⁰¹Tl-thallous chloride, although an attempt to establish causation to a radiation-induced injury was not made. One report described an erythematous pruritic plaque after RPE of ¹³¹I-iodocholesterol (2).

Prior studies have reported RPE rates ranging from 2% to 16% for PET/CT (17). Specifically, for ^{99m}Tc-MDP, a study of 225 consecutive WBBS studies across 9 sites in Canada showed a 15% rate of RPE (18). The RPE rate did not change significantly after an educational intervention (postintervention RPE rate, 20%). Notably, they reported that the RPE did not limit clinical interpretation in any of the 450 studies. Another study of 2,435 ^{99m}Tc-MDP WBBS scans performed between 1987 and 1994 reported ipsilateral axillary node visualization with RPE in 2% of the scans (12). In the present study, RPE was documented in the scan reports of 118 of 31,679 (0.37%) ^{99m}Tc-MDP WBBS studies. A repeat study was recommended in 3 of the 96 patients with RPE documented in their reports. Our findings are similar to those of a Canadian study showing no impact of ^{99m}Tc-MDP RPE on the clinical interpretability of 450 scans (18).

Mitigation of the effects of RPE is a relatively unexplored domain. Several techniques such as hot or cold compresses, injection of hyaluronate or steroids, and surgical interventions have

been proposed to manage RPE (2). However, most have relied on the information gained from extravasation of chemotherapy drugs or iodinated contrast medium and extrapolated it to RPE. These extrapolations typically fail to account for the widely different mechanisms of tissue injury with cytotoxic agents and iodinated contrast media (1,7,19). Although some of these approaches may be useful for therapeutic radiopharmaceuticals, they are likely not required for diagnostic RPE (2). It has previously been recommended that RPE with a ^{99m}Tc-labeled radiopharmaceutical does not require an active intervention (8). In the present study, 3 patients with RPE who had a prior iodinated contrast medium extravasation on the same day were recommended to use cold compresses and limb elevation at home. Cold compresses produce vasoconstriction, limit local inflammation and edema, and are effective to prevent contrast medium extravasation–related local injuries (7). The volume of RPE in these patients was minimal compared with the volume of extravasated contrast medium. Therefore, it was deemed appropriate to follow the guidelines related to contrast medium extravasation (6,7). Physiologically, the low bolus volumes of diagnostic RPE (~0.5–1 mL) are unlikely to cause the volume-related adverse effects that are commonly seen with contrast media (~50–200 mL) and chemotherapy infusions (20). The best technique to mitigate RPE-related adverse effects, however rare, is to prevent RPE. The major source of adverse events in our study was injection of the radiopharmaceutical at the same site as a prior intravenous contrast medium injection. It may be useful to ask whether the patient has had a recent intravenous contrast injection (or extravasation) and avoid using that site if injection at another site is feasible and appropriate.

Our study had certain limitations. We chose to identify RPE by searching the scan reports instead of visually reviewing the images of 31,679 WBBS studies. We recognize that this approach has the possibility of missing studies in which an RPE occurred but was not documented in the report. We did not perform any dosimetry

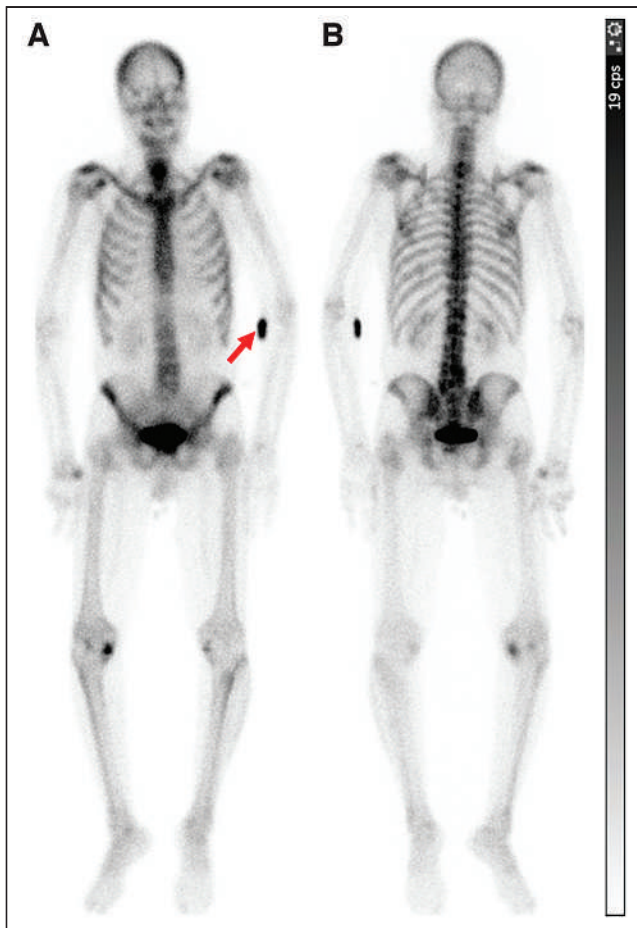


FIGURE 3. A 71-year-old man with prostate cancer. WBBS was performed for metastatic workup. Around 3 h after intravenous injection of 839.9 MBq (22.7 mCi) of ^{99m}Tc -MDP in left antecubital fossa, images were acquired in anterior (A) and posterior (B) projections. RPE was noted at injection site around left elbow (arrow). Study showed increased radiopharmaceutical activity bilaterally in shoulder and knee regions, likely due to degenerative changes. No site suggestive of metastatic disease was seen. Scan was deemed to be of adequate diagnostic quality, and repeat study was not required.

estimations in the current study, as we did not have the time-activity curve data, nor were such estimations directly contributory to our primary objective. Prior studies have proposed methods for estimating local absorbed radiation dose as a surrogate for adverse clinical events (21). Since our approach was to directly look for any adverse clinical events in the patients with RPE, additional information, if any, provided by the dosimetry calculations would have been minimal. We assessed the short-term and long-term adverse events based on a comprehensive review of the medical records instead of interviewing each patient individually. Although our approach may have the potential to miss out on minor details, it is unlikely that a clinically significant adverse event would not have been documented in the medical records. It is also possible that a fraction of patients was not followed up at our center and that an adverse outcome could have been missed by chart review. As one of our secondary objectives, we chose the repeat-scan rates as a surrogate for diagnostic image quality. Although it would have been ideal to have a repeatability experiment with imaging performed “with RPE” and “without RPE” to

assess the impact of RPE on image quality, it was outside the scope of the present study. Nonetheless, the repeat-scan rate is a useful real-world metric, as the interpreting physicians are likely to order a repeat scan if the image quality is suboptimal for clinical interpretation.

Despite these limitations, to our knowledge our study still included the largest cohort of ^{99m}Tc -MDP WBBS studies performed over 12 y and reviewed for RPE-related adverse clinical events with a comprehensive follow-up. Our approach of assessing short-term and long-term adverse events ensured that any anticipated acute and chronic radiation-related injuries were accounted for. Future studies can include visual image review, comparing it with scan reports to determine the RPE rates. Quantitative techniques, including dosimetry, potentially might be used to assess the severity of RPE and correlate it with image quality and occurrence of any adverse events. However, given the rarity of adverse events, such efforts would seem to be of limited yield. The impact of specific interventions, including educational sessions and audits on the RPE rates, should also be explored, as well as the frequency of RPE with other nuclear medicine studies, though we expect that the results would be similar to our observations.

CONCLUSION

Adverse clinical events, both acute and chronic, are exceedingly rare in patients with ^{99m}Tc -MDP RPE during WBBS. Most cases of RPE were not associated with any clinical symptoms and did not require any active intervention. Those few RPE cases with symptoms appeared to be related to injection after intravenous contrast administration extravasations.

DISCLOSURE

No potential conflict of interest relevant to this article was reported.

KEY POINTS

QUESTION: Is ^{99m}Tc -MDP RPE in patients undergoing WBBS associated with adverse clinical events?

PERTINENT FINDINGS: In this retrospective study of 31,679 ^{99m}Tc -MDP WBBS performed over 12 y, we showed that RPE was documented in 118 patients. Of the 96 patients with available medical records, none had a long-term local adverse clinical event attributable to the RPE. Three patients had short-term adverse events, two of which likely resulted from prior intravenous contrast medium extravasation.

IMPLICATIONS FOR PATIENT CARE: Adverse clinical events are rare in patients with ^{99m}Tc -MDP RPE while undergoing WBBS. No long-term local clinical adverse event attributable to the RPE was observed.

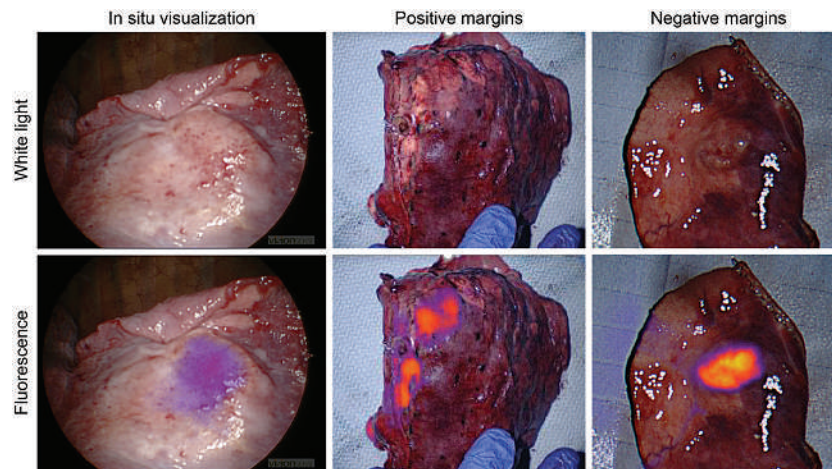
REFERENCES

1. Pérez Fidalgo JA, García Fabregat L, Cervantes A, Margulies A, Vidall C, Roila F. Management of chemotherapy extravasation: ESMO-EONS Clinical Practice Guidelines. *Ann Oncol.* 2012;23:vii167–vii173.
2. van der Pol J, Vöö S, Bucarius J, Mottaghy FM. Consequences of radiopharmaceutical extravasation and therapeutic interventions: a systematic review. *Eur J Nucl Med Mol Imaging.* 2017;44:1234–1243.

3. Osman MM, Muzaffar R, Altinyay ME, Teymouri C. FDG dose extravasations in PET/CT: frequency and impact on SUV measurements. *Front Oncol.* 2011;1:41.
4. Sonoda LI, Ghosh-Ray S, Sanghera B, Dickson J, Wong WL. FDG injection site extravasation. *Clin Nucl Med.* 2012;37:1115–1116.
5. Stone HB, Coleman CN, Anscher MS, McBride WH. Effects of radiation on normal tissue: consequences and mechanisms. *Lancet Oncol.* 2003;4:529–536.
6. Wang CL, Cohan RH, Ellis JH, Adusumilli S, Dunnick NR. Frequency, management, and outcome of extravasation of nonionic iodinated contrast medium in 69,657 intravenous injections. *Radiology.* 2007;243:80–87.
7. Bellin M-F, Jakobsen JÅ, Tomassin I, Thomsen HS, Morcos SK; Contrast Media Safety Committee of the European Society of Urogenital Radiology. Contrast medium extravasation injury: guidelines for prevention and management. *Eur Radiol.* 2002;12:2807–2812.
8. Hung JC, Ponto JA, Hammes RJ. Radiopharmaceutical-related pitfalls and artifacts. *Semin Nucl Med.* 1996;26:208–255.
9. Shih WJ, Collins J, Kiefer V. Visualization in the ipsilateral lymph nodes secondary to extravasation of a bone-imaging agent in the left hand: a case report. *J Nucl Med Technol.* 2001;29:154–155.
10. Giammarile F, Mognetti T, Paycha F. Injection artefact displaying “sock” pattern on bone scan: “glove” sign equivalent resulting from bisphosphonate-(^{99m}Tc) injection in foot venous system. *Eur J Nucl Med Mol Imaging.* 2014;41:1644–1645.
11. Chatterton BE, Vannitambay M, Cook DJ. Lymph node visualisation: an unusual artefact in the ^{99m}Tc-pyrophosphate bone scan. *Eur J Nucl Med.* 1980;5:187–188.
12. Ongseng F, Goldfarb CR, Finestone H. Axillary lymph node uptake of technetium-99m-MDP. *J Nucl Med.* 1995;36:1797–1799.
13. Nguyen BD. Technetium-99m MDP extravasation with cutaneous pattern of ulnar innervation. *Clin Nucl Med.* 2004;29:640–641.
14. Chammas M, Boretto J, Burmann LM, Ramos RM, dos Santos Neto FC, Silva JB. Carpal tunnel syndrome—part I (anatomy, physiology, etiology and diagnosis). *Revista Brasileira de Ortopedia (English ed.).* 2014;49:429–436.
15. Atroshi I. Prevalence of carpal tunnel syndrome in a general population. *JAMA.* 1999;282:153–158.
16. Jackson R, Beckman J, Frederick M, Musolin K, Harrison R. Rates of carpal tunnel syndrome in a state workers’ compensation information system, by industry and occupation—California, 2007–2014. *MMWR Morb Mortal Wkly Rep.* 2018;67:1094–1097.
17. Wong TZ, Benefield T, Masters S, et al. Quality improvement initiatives to assess and improve PET/CT injection infiltration rates at multiple centers. *J Nucl Med Technol.* 2019;47:326–331.
18. McIntosh CJ, Jonathan A. Frequency of interstitial radiotracer injection for patients undergoing bone scan [abstract]. In: *Canadian Association of Radiologists 79th Annual Scientific Meeting Program Book.* Canadian Association of Radiologists; 2016:78.
19. Davenport MS, Wang CL, Bashir MR, Neville AM, Paulson EK. Rate of contrast material extravasations and allergic-like reactions: effect of extrinsic warming of low-osmolality iodinated CT contrast material to 37°C. *Radiology.* 2012;262:475–484.
20. Hannon MG, Lee SK. Extravasation injuries. *J Hand Surg [Am].* 2011;36:2060–2065.
21. Shapiro B, Pillay M, Cox PH. Dosimetric consequences of interstitial extravasation following IV administration of a radiopharmaceutical. *Eur J Nucl Med.* 1987;12:522–523.

Erratum

In the article “Precision Surgery Guided by Intraoperative Molecular Imaging,” by Azari et al. (*J Nucl Med.* 2022;63:1620–1627), Figure 3 contains an error: images in the “In situ visualization” column are switched. The corrected figure appears below. The authors regret the error.



Extravasation of Diagnostic Radiopharmaceuticals: A Wolf in Sheep's Clothing?

Jochem A.J. van der Pol¹ and Felix M. Mottaghy^{1,2}

¹Department of Radiology and Nuclear Medicine, Maastricht University Medical Center, Maastricht, The Netherlands; and

²Department of Nuclear Medicine, University Hospital RWTH Aachen, and Center for Integrated Oncology Aachen Bonn Cologne Düsseldorf, Aachen, Germany

See the associated article on page 485.

Radiopharmaceutical extravasation (RPE) is occurring worldwide on a frequent basis. As we reported in our 2017 literature study, the evidence on the clinical consequences of RPE is scarce (1). Studies we found at that time described clinical follow-up in only a handful of case reports, mostly on incidental therapeutic extravasation. In this issue of *The Journal of Nuclear Medicine*, Parihar and colleagues present the results of their retrospective study focusing on clinical outcome after RPE (2). In their review of 31,679 screened reports of patients who underwent whole-body bone scintigraphy using ^{99m}Tc-methylene diphosphonate, they report clinical follow-up in 96 patients in whom RPE occurred.

One of the conclusions of our work was that adverse events after tracer extravasation might be underreported. On the other hand, if clinical consequences of diagnostic tracer extravasation were to occur in significant numbers, especially with severe or even moderate tissue reactions as a result, more reports would be expected to be published. This study finally adds objective data in a real-world setting to support this hypothesis. The median follow-up duration of 18.9 mo further precludes late-onset adverse events.

The current study evaluated scan reports of a single center over 12 y to detect cases of RPE. Only scanning the reports is certainly a limitation of this study as correctly stated by the authors. An alternative approach would have been a study aimed at detecting extravasation visually on the scans. This would indeed have given a more reliable figure of the frequency of RPE, which seems to be on the very low end in this study (2). As many of us routinely observe in daily clinical practice, many scans already show minor tracer infiltration, which is also illustrated by other studies such as cited by the authors (2). One of the illustrated cases even shows only minor tracer extravasation, which can be expected to occur in relatively high numbers in whole-body bone scintigraphy. The used approach does have the tendency to focus on large tracer extravasations,

which captured the attention of the reading physician and prompted clinical follow-up. One would obviously expect more severe adverse reactions in more prominent RPE. Despite a tendency for lower sensitivity to include tracer extravasation, the study design did, after all, focus on more extended extravasation cases in which clinical consequences of RPE would be most probable.

Since the study was retrospective, patients were not actively checked for any symptoms at planned follow-up checkups. The study also potentially missed patients who presented with mild symptoms to the home practitioner or other health-care professionals.

The authors' conclusion that clinical adverse events after tracer infiltration are rare remains plausible and is in line with our earlier findings based on the literature and our experience in our own clinical setting. However, the methodology of the current study, analyzing only reported cases, inherently does not rule out RPE completely, notably in cases for which it was not reported, therefore potentially missing clinical cases with an adverse reaction.

The discrepancy between extravasation frequency reported in the current study, as opposed to frequencies reported by earlier studies of retrospectively investigated whole-body bone scintigraphy and ¹⁸F-FDG PET scans for tracer extravasation, also emphasizes a current hiatus in the definitions and raises the question of how a clinically significant RPE should be defined.

Of further notable interest is that in 3 of 4 RPE cases for which an event directly attributable to RPE was documented, extravasation of iodinated contrast medium for a contrast-enhanced CT scan earlier on that day had already been documented. This happened despite the standard procedure for intravenous tracer injection in operation in the authors' medical center—a procedure that is carefully explained by the authors, including a patency check by confirming adequate blood return. Circumstances possibly leading to the reuse of an injection site at which extravasation occurred are not elucidated. It does emphasize the importance of a proper patency check and to refrain from reusing an injection location that recently was subject to extravasation.

The authors mention that from September 2017 on, all intravenous injections of ^{99m}Tc-methylene diphosphonate were performed using a small-gauge butterfly needle as opposed to a straight stick technique injection. Unfortunately, no information is given on the frequency of RPE before and after the change in technique.

Studies of RPE cases that report clinical follow up in other abundantly used tracers, such as other ^{99m}Tc-labeled tracers, ¹⁸F-FDG, or ⁶⁸Ga-labeled tracers, are still missing. The same is true for all new diagnostic tracers recently being introduced into the clinic.

Received Nov. 9, 2022; accepted Nov. 15, 2022.

For correspondence or reprints, contact Felix M. Mottaghy (fmottaghy@ukaachen.de).

Published online Dec. 15, 2022.

COPYRIGHT © 2023 by the Society of Nuclear Medicine and Molecular Imaging.

DOI: 10.2967/jnumed.122.265038

A dose estimation assuming the worst case of no clearance of the extravasated radiopharmaceutical in tissue would result in doses that have shown local deleterious effects in external-beam irradiation. However, the real world looks different since there is usually rapid and effective clearance via the lymphatic system. That is the reason that reports on serious adverse events are scarce. Only one recent study has found some cases. The investigators summarize several cases with multiple registered clinically relevant symptoms; however, the cases are not presented with enough detail to find a causal relation to the tracer extravasation (3).

The work of Parihar et al. further supports the hypothesis that clinical consequences of RPE in general are very rare. We encourage handling of clinical extravasation cases according to a standardized operating procedure, such as the local procedure we use and published earlier, in which cases are documented (1). These data can then be aggregated and published as Parihar and colleagues have done. Care should also be taken with image quality, which can suffer from extravasation. Although in only 3 of 122 cases reported by Parihar et al. was a new whole-body bone scintigraphy ordered; for ^{18}F -FDG PET, it was proven earlier that SUVs can vary considerably between scans with and without RPE (4).

Furthermore, in the current time of expansively growing use of therapeutic radioactive compounds, we believe attention should be broadened to include clinical consequences of RPE in radioligand therapy. Since our earlier literature study, some additional cases of therapeutic RPE of ^{177}Lu -labeled compounds have been reported (5–9). None of these reports indicate any serious clinical consequences, however. Furthermore, the European Association of Nuclear Medicine dosimetry committee recently published a guideline on dosimetry of ^{177}Lu -labeled somatostatin and prostate-specific membrane antigen–targeting ligands, in which some practical points are given in the dosimetric approach toward a therapeutic RPE case. The committee also stresses that despite regular use of these compounds, no serious adverse events have been observed after tissue extravasation, as can probably be attributed to rapid clearance from the extravascular space. Estimated absorbed doses to the surrounding tissues did not exceed the dose threshold for ulceration and desquamation (10). These results suggest that a case of ^{177}Lu -labeled compound extravasation should be treated conservatively, although further research is necessary to support this hypothesis.

Large, randomized controlled trials, notably the NETTER-1 and VISION trials that have recently been performed on new therapeutic radiopharmaceuticals, do not report on extravasation (11,12). We encourage future large, randomized controlled trials to actively monitor and report on RPE, preferentially incorporating a detailed standard operating procedure for RPE in the study protocol, including prolonged clinical follow-up in cases of RPE.

In conclusion, RPE is a relatively common event, depending on the definition. The work by Parihar et al. adds more evidence

supporting our earlier conclusion that RPE in abundantly used $^{99\text{m}}\text{Tc}$, ^{123}I , ^{18}F , and ^{68}Ga diagnostic tracers does not require intervention. More research is nevertheless needed, with an emphasis on new diagnostic tracers and therapeutic radiopharmaceuticals.

DISCLOSURE

Felix Mottaghy is a medical advisor for NanoMab Technology Ltd. and Advanced Accelerator Applications (AAA) GmbH; has recently received institutional grants from NanoMab Technology Ltd., Siemens, and GE Precision Healthcare LLC; and is supported by the German Research Foundation (DFG) within the framework of the Research Training Group 2375, “Tumor-Targeted Drug Delivery” (grant 331065168); the Clinical Research Unit CRU 5011, “Integrating Emerging Methods to Advance Translational Kidney Research (InteraKD)” (project 445703531); and the Research Unit 2591, “Severity Assessment in Animal-Based Research” (project 321137804). No other potential conflict of interest relevant to this article was reported.

REFERENCES

1. van der Pol J, Voo S, Bucerius J, Mottaghy FM. Consequences of radiopharmaceutical extravasation and therapeutic interventions: a systematic review. *Eur J Nucl Med Mol Imaging*. 2017;44:1234–1243.
2. Parihar AS, Schmidt LR, Crandall J, Dehdashti F, Wahl RL. Adverse clinical events at the injection site are exceedingly rare after reported radiopharmaceutical extravasation in patients undergoing $^{99\text{m}}\text{Tc}$ -MDP whole-body bone scintigraphy: a 12-year experience. *J Nucl Med*. 2022;64:485–490.
3. Osborne D, Lattanze R, Knowland J, et al. The scientific and clinical case for reviewing diagnostic radiopharmaceutical extravasation long-standing assumptions. *Front Med (Lausanne)*. 2021;8:684157.
4. Osman MM, Muzaffar R, Altinyay ME, Teymour C. FDG dose extravasations in PET/CT: frequency and impact on SUV measurements. *Front Oncol*. 2011;1:41.
5. Berry K, Kendrick J. Lutetium-177 radiopharmaceutical therapy extravasation lessons learned. *Health Phys*. 2022;123:160–164.
6. Jüptner M, Zuhayra M, Assam I, Lutzen U. Successful handling of an accidental extravasation of ^{177}Lu -PSMA-617 in the treatment of advanced prostate cancer. *Nuklearmedizin*. 2018;57:N10–N12.
7. Schlenkhoff CD, Essler M, Ahmadzadehfah H. Possible treatment approach to an extravasation of ^{177}Lu -PSMA-617. *Clin Nucl Med*. 2017;42:639–640.
8. Tyłski P, Pina-Jomir G, Bournaud-Salinas C, Jalade P. Tissue dose estimation after extravasation of ^{177}Lu -DOTATATE. *EJNMMI Phys*. 2021;8:33.
9. Maucherat B, Varmentot N, Fleury V, Senellart H, Rousseau C. Effective management of ^{177}Lu -DOTA⁰-Tyr³-octreotate extravasation. *Clin Nucl Med*. 2021;46:144–145.
10. Sjögreen Gleisner K, Chouin N, Gabina PM, et al. EANM dosimetry committee recommendations for dosimetry of ^{177}Lu -labelled somatostatin-receptor- and PSMA-targeting ligands. *Eur J Nucl Med Mol Imaging*. 2022;49:1778–1809.
11. Sartor O, de Bono J, Chi KN, et al. Lutetium-177-PSMA-617 for metastatic castration-resistant prostate cancer. *N Engl J Med*. 2021;385:1091–1103.
12. Strosberg JR, Caplin ME, Kunz PL, et al. ^{177}Lu -Dotatate plus long-acting octreotide versus high-dose long-acting octreotide in patients with midgut neuroendocrine tumours (NETTER-1): final overall survival and long-term safety results from an open-label, randomised, controlled, phase 3 trial. *Lancet Oncol*. 2021;22:1752–1763.

A Realistic Multiregion Mouse Kidney Dosimetry Model to Support the Preclinical Evaluation of Potential Nephrotoxicity of Radiopharmaceutical Therapy

Clarita Saldarriaga Vargas^{1,2}, Lara Struelens¹, Matthias D'Huyvetter², Vicky Caveliers², and Peter Covens²

¹Radiation Protection Dosimetry and Calibrations, Belgian Nuclear Research Centre (SCK CEN), Mol, Belgium; and ²Department of Medical Imaging, Laboratory for In Vivo Cellular and Molecular Imaging, Vrije Universiteit Brussel, Brussels, Belgium

Suborgan absorbed dose estimates in mouse kidneys are crucial to support preclinical nephrotoxicity analyses of α - and β -particle-emitting radioligands exhibiting a heterogeneous activity distribution in the kidneys. This is, however, limited by the scarcity of reference dose factors (S values) available in the literature for specific mouse kidney tissues. **Methods:** A computational multiregion model of a mouse kidney based on high-resolution MRI data from a healthy mouse kidney was developed. The model was used to calculate S values for 5 kidney tissues (cortex, outer and inner stripes of outer medulla, inner medulla, and papilla and pelvis) for a wide range of β - or α -emitting radionuclides (45 in total) of interest for radiopharmaceutical therapy, using Monte Carlo calculations. Additionally, regional S values were applied for a ¹³¹I-labeled single-domain antibody fragment with predominant retention in the outer stripe of the renal outer medulla. **Results:** The heterogeneous activity distribution in kidneys of considered α - and low- to medium-energy β -emitters considerably affected the absorbed dose estimation in specific suborgan regions. The suborgan tissue doses resulting from the nonuniform distribution of the ¹³¹I-labeled antibody fragment largely deviated (from -40% to 57%) from the mean kidney dose resulting from an assumed uniform activity distribution throughout the whole kidney. The absorbed dose in the renal outer stripe was about 2.0 times higher than in the cortex and in the inner stripe and about 2.6 times higher than in inner tissues. **Conclusion:** The use of kidney regional S values allows a more realistic estimation of the absorbed dose in different renal tissues from therapeutic radioligands with a heterogeneous uptake in the kidneys. This constitutes an improvement from the simplistic (less accurate) renal dose estimates assuming a uniform distribution of activity throughout kidney tissues. Such improvement in dosimetry is expected to support preclinical studies essential for a better understanding of nephrotoxicity in humans. The dosimetric database has added value in the development of new molecular vectors for radiopharmaceutical therapy.

Key Words: multiregion mouse kidney model; suborgan dosimetry; radiopharmaceutical therapy; MIRD; autoradiography

J Nucl Med 2023; 64:493–499

DOI: 10.2967/jnumed.122.264453

In radiopharmaceutical therapy, the transit and temporary retention of radioligand in the kidneys during renal elimination result in

a local irradiation of kidney tissues that can cause absorbed dose-limiting nephrotoxicity. Consequently, nephrotoxicity is often the focus of absorbed dose escalation studies on mice during the preclinical testing of novel radioligands and the preclinical investigation of treatment optimization strategies beyond radioligand design. Additionally, the distribution of a radioligand is often not uniform in the kidney (1–3). Small, fast-clearing radiopharmaceuticals often show increased retention in the proximal tubules of the renal cortex and (or) in the outer stripe of the renal outer medulla (OSOM) (Fig. 1) (2,4,5). This increase can lead to a corresponding nonuniform distribution of absorbed dose and tissue damage across renal regions (1,6) and even in specific substructures within them (7), particularly for radionuclides emitting charged-particle radiation with a limited penetration range in tissue, such as α -particles and low- to medium-energy electrons and β -particles.

Accurate dosimetry of specific mouse kidney tissues is essential for interpreting the outcomes of preclinical nephrotoxicity studies. Understanding the impact in nephrotoxicity of the local tissue damage resulting from the nonuniform dose distribution of radiopharmaceuticals is of increased importance in kidney tissues, which have a complex functional architecture and potentially differ in radiobiologic response (8). An aspect that precludes a more realistic kidney-tissue dosimetry of heterogeneous radioligand distributions is the scarcity of reference radionuclide S values (factors of absorbed dose per radionuclide decay) for relevant tissue regions of the mouse kidney. S values are dependent on the radionuclide radiation emissions and the geometry of the anatomic model used for modeling the radiation source and for absorbed dose calculations. Some dosimetry models of murine kidneys exist that allow an accounting, to some extent, for nonuniform distributions of radionuclides (1,5,6). Their application in preclinical studies is, however, limited by the few compartments used to represent the renal structure and consequently the heterogeneity of the organ activity distribution. Furthermore, S values are available for only a limited number of radionuclides.

The aim of this work was to develop a computational realistic multiregion model of a mouse kidney, based on high-resolution MRI data, to facilitate suborgan kidney dosimetry in preclinical investigations of radiopharmaceutical therapy. Next, the model was used to calculate suborgan regional S values for the kidney for a wide range of radionuclides of interest in radiopharmaceutical therapy. Finally, suborgan kidney dosimetry was demonstrated for a ¹³¹I-radiolabeled single-domain antibody fragment (sdAb) that has predominant retention in the outer stripe of the renal outer medulla and is currently being evaluated clinically for radiopharmaceutical therapy of cancer expressing the human epidermal growth factor receptor type 2 (9).

Received May 26, 2022; revision accepted Sep. 1, 2022.

For correspondence or reprints, contact Clarita Saldarriaga Vargas (csvargas@sckcen.be).

Published online Oct. 13, 2022.

COPYRIGHT © 2023 by the Society of Nuclear Medicine and Molecular Imaging.

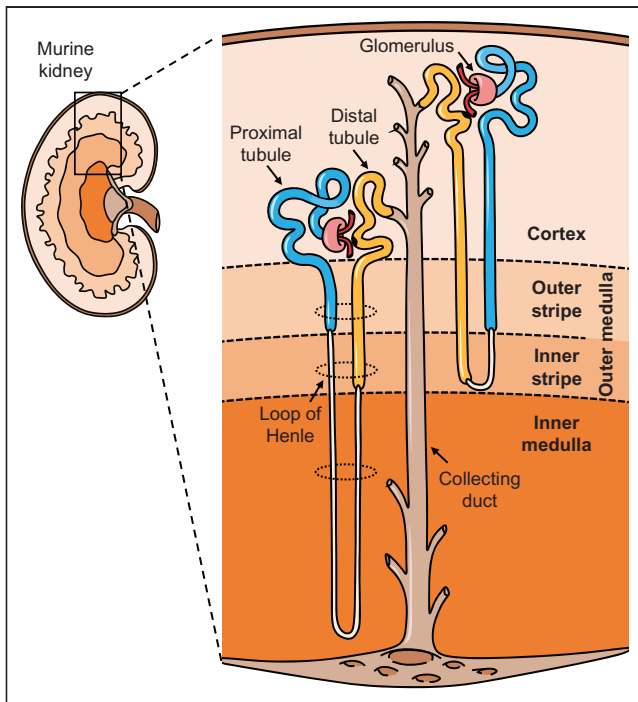


FIGURE 1. Microscopic anatomy of kidney tissues. Main nephron parts and different kidney regions to which they belong are indicated.

MATERIALS AND METHODS

A condensed version of the materials and methods is given here. The complete version can be found in the online supplemental data (supplemental materials are available at <http://jnm.snmjournals.org>).

All animal experiments were conducted in accordance with the guidelines, and after the approval, of the Ethical Committee of the Vrije Universiteit Brussel.

Development of Kidney Model

A schematic overview of the main steps involved in the development of the 3-dimensional (3D) kidney model is shown in Figure 2.

The kidney model was developed using as a reference high-resolution ($43 \times 78 \times 78 \mu\text{m}$ voxels) MRI data obtained ex vivo on a perfusion-fixed kidney excised from a healthy mouse (C57BL/6, female, 9 wk old, 19.5-g body weight). MRI was performed with a horizontal 7-T preclinical scanner (PharmaScan; Bruker BioSpin).

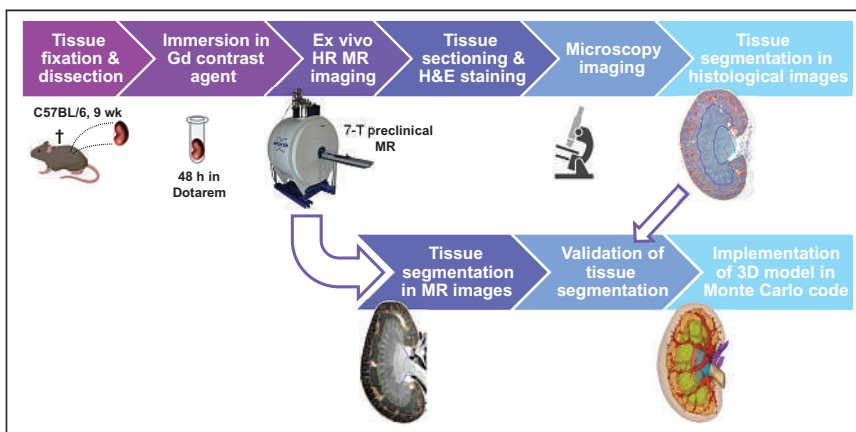


FIGURE 2. Workflow diagram of development of multiregion kidney model. H&E = hematoxylin and eosin; HR = high resolution.

Ten volume regions were segmented on the MR image using 3D-Slicer software (<http://www.slicer.org>). The segmented regions corresponded to 4 tissues of the renal parenchyma (the renal cortex including its vasculature [C], the OSOM including its vasculature [OS], the inner stripe of the outer medulla [IS], and the inner medulla including some vasculature [IM]), the main arteries and veins within the renal parenchyma, the renal papilla, the renal pelvis, part of the external renal vessels, part of the ureter, and uniform surrounding tissue. The kidney model was created by merging all the segmented regions into a single 3D matrix consisting of $127 \times 62 \times 125$ (~ 1 million) voxels, with same voxel dimensions as the MR dataset.

Tissue segmentation was validated against regions of interest drawn on conventional histology images of the same kidney.

Calculation of S Values and Absorbed Energy Fractions

The $S(r_T \leftarrow r_S)$ values (where r_S is source region and r_T is target region) and absorbed energy fractions of different kidney tissues were calculated for the kidney model using Monte Carlo radiation transport simulations with MCNP, version 6.2 (Los Alamos National Laboratory).

Monte Carlo calculations were performed for 12 β -emitting radionuclides (^{32}P , ^{47}Sc , ^{67}Cu , ^{89}Sr , ^{90}Y , ^{131}I , ^{153}Sm , ^{161}Tb , ^{166}Ho , ^{177}Lu , ^{186}Re , and ^{188}Re) and for the α -emitters shown in Supplemental Figure 1 (decay schemes for ^{225}Ac , ^{227}Th , ^{230}U , ^{224}Ra , ^{211}At , and ^{149}Tb) and their progeny, which includes α -, β -, or positron emitters. Radionuclide radiation emission data from International Commission on Radiological Protection report 107 (10) were used for modeling the radiation sources. Absorbed energy fractions for self-irradiation were calculated for monoenergetic electrons (20–2,500 keV), α -particles (3–10 MeV), and photons (10–1,500 keV).

r_S and r_T for S value and absorbed energy fraction calculations include C, OS, IS, IM, and renal papilla and pelvis (PP). These regions, all together, represent the whole kidney region (K), which was used also as an r_S and r_T in the case of a uniform activity distribution throughout kidney tissues. For each radionuclide, the activity was uniformly distributed in each r_S and the absorbed dose per decay was simulated.

Kidney Dosimetry Study

A dosimetry study was performed to demonstrate use of the S values calculated with the kidney model. The radioligand used to derive the mouse kidney biodistribution was the iodinated sdAb 2Rs15d (^{131}I -sdAb) (11).

Healthy mice ($n = 5$; C57BL/6; female; 9 wk old; mean body weight \pm SD, 20.7 ± 1.0 g) were anesthetized by inhalation with 2% isoflurane and were injected in the tail vein with 13.0 ± 3.3 MBq of ^{131}I -sdAb (5 μg of sdAb). At 1, 3, 6, 24, and 70 h after injection, mice ($n = 1$ per time point) were euthanized by cervical dislocation. The kidneys were dissected and weighed, and their activity was measured in a γ -counter using an optimized measurement protocol (12). The fraction of injected activity per gram of dissected kidney tissue was calculated.

The suborgan distribution of ^{131}I -sdAb in kidney tissues was determined with high-resolution quantitative digital autoradiography using an ionizing-radiation quantum imaging detector (13). Each autoradiography image was quantified in ImageJ-Fiji (<https://imagej.net/software/fiji/>) using detailed regions of interest drawn on histologic images of the same section as used for autoradiography or an adjacent kidney section. A region of interest was drawn on each of the 5 tissues considered as r_S in the kidney model (C, OS, IS, IM, and PP), and the mean of the counts per minute of the region-of-interest pixels was estimated.

Suborgan regional dosimetry for kidney tissues was performed following the MIRD methodology. Two source distributions were considered: the first was a time-dependent nonuniform activity distribution based on the relative autoradiography data, and the second was a simplified case in which activity was assumed to be uniformly distributed throughout kidney tissues (i.e., $r_S = r_T = K$).

For each time point, the absorbed dose rate in each r_T delivered by the activities measured in each r_S of the kidney model was based on the S values calculated for the proposed kidney model. The activity of the whole kidney was determined with γ -counting, and the relative suborgan distribution of activity was measured with autoradiography (for the first type of source distribution only).

Absorbed dose rates as a function of time were analyzed by nonlinear least-squares fitting (MATLAB; MathWorks) to a negative power function of time after injection. For each of the 2 source distributions considered, the absorbed dose per unit of injected activity ($D(r_T)/A_0$, where D is absorbed dose and A_0 is injected activity decay corrected to the mouse time of death) was estimated for each r_T , applying mathematic integration of dose rate values from the time of injection (time = 0) to infinity.

RESULTS

Kidney Model

There was good agreement between the histology-based tissue regions of interest and the MR-based regions of interest used to define the kidney model (Fig. 3A, with additional comments in the supplemental data).

The main orthogonal dimensions of the kidney model are around $5.3 \times 4.6 \times 9.5$ mm (excluding ureter and external vessels). In mouse kidneys, unlike human kidneys, medullary tissues are not organized into multiple pyramids and form instead a single bean-shaped body (Fig. 3) (14). As such, there are no renal calyces, and a single renal papilla connects directly and deeply with the renal pelvis. The cortex and the OSOM tissues appear as adjacent rims (each with a thickness of ~ 0.6 mm) surrounding most of the inner tissues. The masses and percentage volume occupancy of each tissue region are listed in Table 1. The 3D dataset of the kidney model can be found in the supplemental file “Kidney_model_dataset.nii.”

S Values

S values for the considered α - and β -emitting radionuclides are listed in Supplemental Tables 1–3. The simulation statistical error of all the reported S values was within 3%, unless otherwise specified. A subset of the S values is graphically shown in Figure 4 for a selection of β - and α -emitters (and their progeny). The absorbed energy fractions for electrons, α -particles, and photons are shown in Supplemental Figure 2.

High-energy β -emitters (e.g., ^{90}Y , ^{188}R , and ^{32}P) typically result in higher S values and more cross-irradiation between the source tissue and surrounding tissues than low-energy β -emitters (e.g., ^{177}Lu , ^{67}Cu , ^{161}Tb , and ^{131}I). Cross-irradiation is nevertheless substantial also for low-energy β -emitters, particularly between adjacent target–source kidney tissue regions (e.g., C \leftarrow OS and IS \leftarrow OS). The S values for self-irradiation (e.g., C \leftarrow C and OS \leftarrow OS) are somewhat higher for radionuclides with an abundant yield of Auger and internal-conversion electrons (^{161}Tb , ^{153}Sm , and ^{166}Ho), as these typically low-energy electrons are absorbed more locally than the more energetic β -particles (Supplemental Figs. 2 and 3).

The energy emitted by α -emitters is absorbed mostly within the r_S itself, and cross-irradiation is small between adjacent tissues and negligible between more distant tissues (e.g., IS \leftarrow C and IM \leftarrow OS). Indeed, the absorbed fractions for self-irradiation with α -particles are mostly 0.90 or more for most tissue regions (Supplemental Fig. 2).

Kidney Dosimetry Study

The pharmacokinetics of ^{131}I -sdAb in mouse kidney tissues are fast. Kidney uptake at 24 h after ^{131}I -sdAb administration is less than 0.5% of that at 1 h after injection (Supplemental Table 4). The autoradiography images (Fig. 5) clearly indicate a nonuniform and time-dependent biodistribution. During the first 24 h after radioligand administration, retention is prominent in the OSOM tissue and then in the cortex tissue (Supplemental Table 4). This observation is likely due to a partial reabsorption of the ^{131}I -sdAb in the proximal tubules located exclusively in these 2 tissues, and particularly in the straight segments that densely

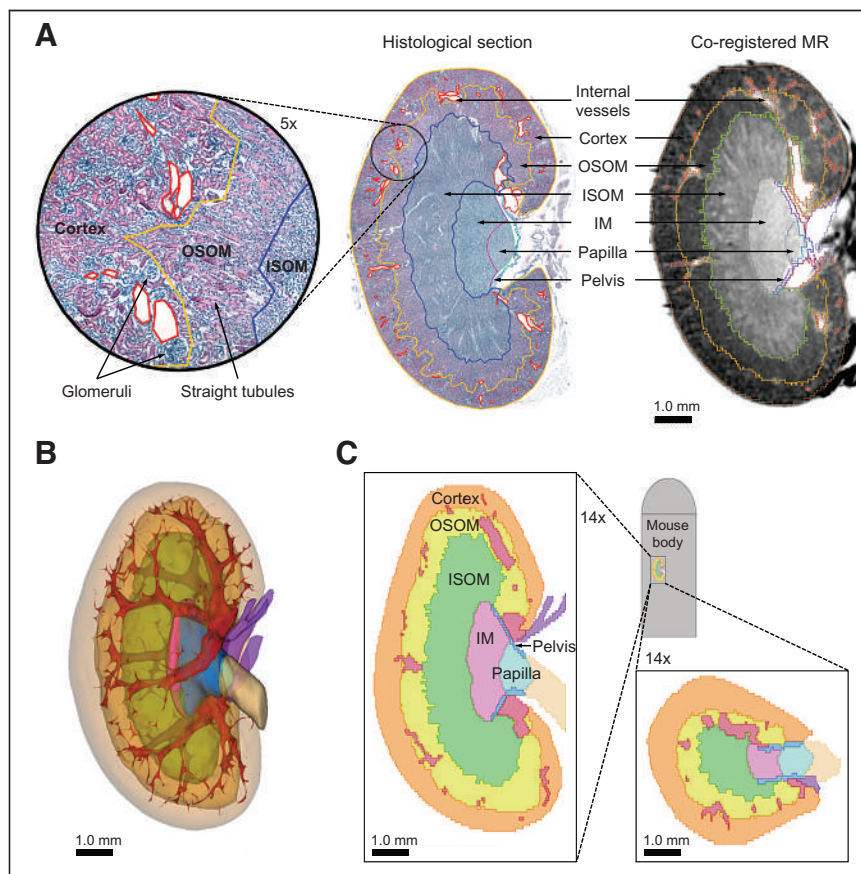


FIGURE 3. (A) Validation of MR-based kidney-tissue segmentation against histology. (B and C) Kidney model 3D rendering with transparency view (B) and coronal (left) and transverse (bottom right) cross-section views (C) of kidney lattice as implemented in Monte Carlo code. ISOM = inner stripe of the renal outer medulla.

TABLE 1

Mass and Percentage Volume Occupancy of Kidney Model Regions Used as r_S or r_T , Including Blood Vessels

r_T or r_S	Mass (mg)		Volume, region (%)
	Region	Vessels	
C	60.2	1.4	51
OS	37.3	3.5	32
IS	16.4	0.4	14
IM	2.0	—	2
PP	1.5	—	1
K	117.5	5.3	100

occupy the OSOM (Fig. 1). From 24 h after injection onward, the little activity that remains in the kidney is more concentrated in the cortex tissue, although the nonuniformity across tissues is less pronounced than at earlier time points. The concentration of activity in the inner tissues (ISOM, papilla and pelvis) is always lower than in the renal cortex and the OSOM tissues.

The distribution of ^{131}I -sdAb activity in kidney tissues has a substantial impact on estimation of time-dependent absorbed dose rates (Fig. 6B) and absorbed doses (Table 2), per unit of injected activity, in specific kidney tissues. Compared with the more realistic nonuniform source distribution, the assumption of a uniform distribution of activity throughout the kidney tissues ($r_S = r_T = \text{K}$) results in a strong underestimation of the absorbed dose rate in the OSOM and an overestimation of the absorbed dose rate in the other tissues (including the renal cortex) at early time points (<24 h after injection). A similar effect

results in the absorbed doses, because for ^{131}I -sdAb the high activities at early time points dominate the estimation of the time-integrated absorbed dose. The absorbed dose is about 2.0 times higher in the OSOM than in the renal cortex and the ISOM tissues, and about 2.6 times higher than in inner tissues.

DISCUSSION

The calculated regional S values indicate that consideration of the heterogeneity in activity distribution in mouse kidneys can have a considerable impact on the absorbed dose estimations of specific tissues, particularly for radionuclides that emit α -particles and low- to medium-energy β -particles. This was demonstrated for the nonuniform mouse kidney biodistribution of a ^{131}I -labeled sdAb that is predominantly and temporarily retained in the OSOM. ^{131}I emits low- to medium-energy β -particles (182 keV on average) with a short penetration range in tissue (~0.4 mm on average) when compared with the size of mouse kidney tissues. Therefore, self-irradiation is the main contributor (~87%) to the absorbed dose rates in the OSOM at early time points (Supplemental Fig. 4). This holds true also for the renal cortex (~71% from self-irradiation), although with an also-important contribution (~29%) of cross-irradiation from activity in the OSOM. This leads to a substantially nonuniform absorbed dose distribution across different kidney tissues in which the OSOM is the most irradiated tissue.

This study presented a realistic 3D model of mouse kidney tissues useful for preclinical internal radiation dosimetry. The regional S values calculated with the proposed model allow a more detailed and realistic estimation of absorbed doses in different renal tissues from β - and α -emitters, accounting for the heterogeneous activity distribution. Exploitation of the full potential of the proposed model would require information on the suborgan activity distribution at the regional-tissue level as a function of time. Such information can be derived from ex

vivo mouse biodistribution studies using quantitative high-resolution autoradiography of β - or α -particles of tissue sections of mice killed at different sampling time points, complemented by γ -counting of the whole kidney to measure kidney activity, as demonstrated in this study. Alternatively, quantitative emission tomography imaging can be used to measure kidney activity thoroughly over time and in vivo (12), which would enable longitudinal studies (such as nephrotoxicity studies) on the same mice as are used for organ-level pharmacokinetic assessment. In such a case, autoradiography measurements may be performed on separate mice at selected time points of the pharmacokinetic profile, chosen, for example, to sample regions of high activity or when the subkidney distribution is more likely to vary (absorption, distribution, elimination phases). The mouse kidney model may be seen as an analog of the model of a human kidney presented in MIRD pamphlet 19 (3), with some differences being that the former is used for preclinical dosimetry of mouse tissues and provides a more realistic representation of kidney tissues, which additionally considers the OSOM as a separate source/target compartment. Modeling of OSOM tissues is

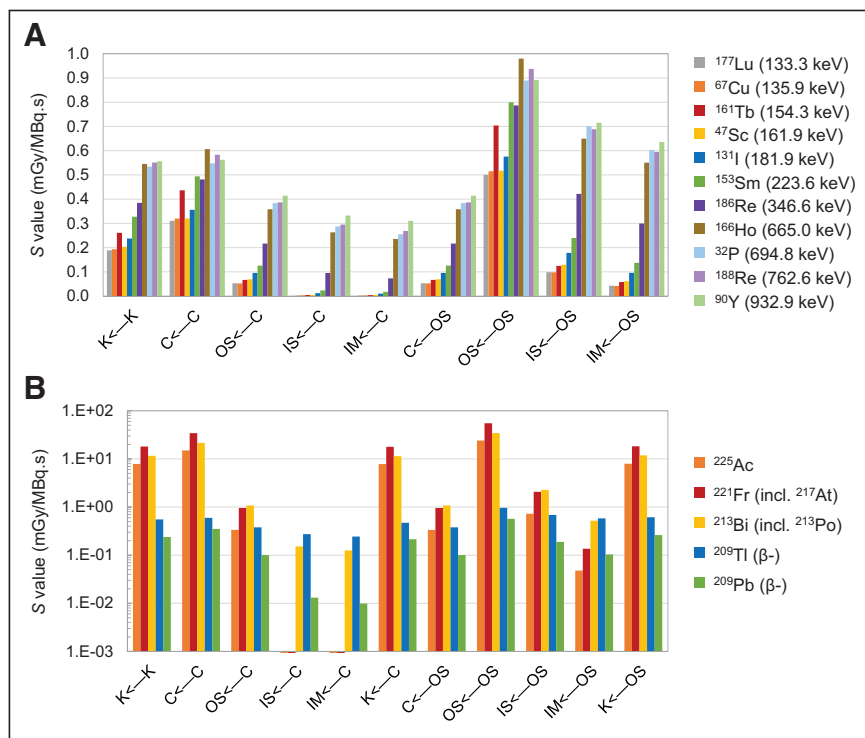


FIGURE 4. S values for some β -emitters (A) and for ^{225}Ac and some of its progeny (B), for selected source and target tissues. For convenience, radionuclide series in A are listed in order of increasing mean β -particle energy per β -decay (values in parentheses in series legends).

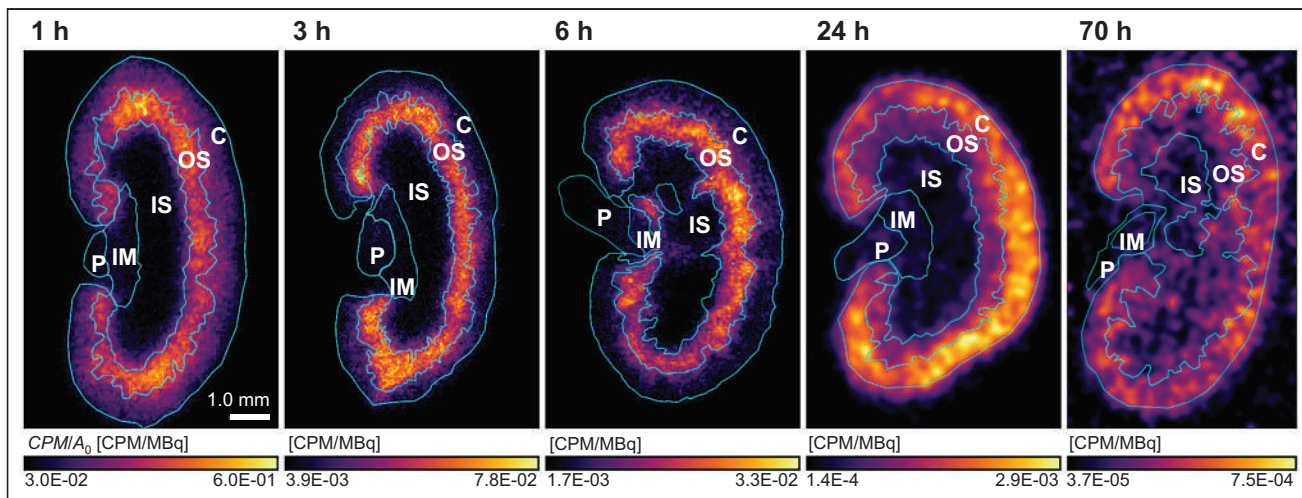


FIGURE 5. Autoradiography images of kidney tissues of mice killed at 1, 3, 6, 24 and 70 h after injection of ^{131}I -sdAb. Autoradiography data at 24 and 70 h after injection were smoothed with $2.0\text{-}\sigma$ gaussian filter for visualization only. Regions of interest used for quantification are shown in cyan. CPM = counts per minute; CPM/A_0 = counts per minute per injected activity decay corrected to the mouse time of death.

pertinent for dosimetry in view of the possible substantial radioligand retention in the straight segments of the proximal tubules, which physically extend from the renal cortex to the OSOM in both humans and rodents. The early biodistribution of ^{131}I -sdAb considered here for the dosimetry study is a good example of such a situation.

For α -particle emitters, subregional dosimetry at the level of mouse nephron substructures (e.g., glomerulus and specific segments of the tubule) can be of interest. Although miniaturized versions of models of a human nephron can be used for that purpose (7), their use in preclinical investigation of radiopharmaceuticals is limited by the difficulty in determining the distribution of radionuclide activity at the level of nephron substructures. The intermediate (i.e., regional) dosimetry of α -particle emitters achievable with the regional S values presented here might be useful when suborgan activity information is available at only a more regional (tissue) level.

S factors are sensitive to the target tissue mass and to the absorbed energy fraction, which is sensitive to the target–source geometry. Besides, the size of kidney tissues may vary with mouse strain, age, health condition, and other factors. Therefore, inaccuracies in absorbed dose estimations might arise from anatomic differences between the

kidney model and the kidneys of mice used in preclinical studies. Mass scaling of the regional S values to the actual (measured) mass of the kidney (factor $M_K/\bar{M}_{\text{kidney}}$ in Supplemental Eq. 1) can compensate for the effect of the r_T mass in the absorbed dose estimations, assuming that the occupancy volumes of the measured tissues is the same as in Table 1. However, mass scaling does not account for deviations in the absorbed energy fractions due to, for example, differences in the thickness of the C rim or of the OS rim associated with tissues with sizes or volumes of occupancy different from the kidney model. The impact of these factors may be investigated using simplified models (such as those based on ellipsoidal shells to represent tissue compartments (6)), and if relevant, correction factors may be determined to be applied to absorbed dose estimations with the regional S values reported here. Such analyses were beyond the scope of this study.

Svensson et al. used a stylized 3-region, 0.15-g kidney model based on spheroids to calculate regional absorbed energy fractions for ^{177}Lu and ^{90}Y β -particles emitted by the renal cortex (5). Compared with that model, the ^{177}Lu and ^{90}Y β -particle absorbed fractions calculated with the more realistic model proposed in this study are, respectively, 6% and 19% lower for self-irradiation of the C (absorbed energy fraction, 0.79 for ^{177}Lu and 0.23 for ^{90}Y) and 62% and 36% higher for cross-irradiation between the renal cortex and the OSOM (absorbed energy fraction, 0.082 for ^{177}Lu and 0.10 for ^{90}Y). These dosimetric discrepancies are likely related to differences in geometry and size of kidney tissue regions between the 2 models.

More realistic absorbed dose estimates of mouse kidney tissues can support the analysis of preclinical nephrotoxicity studies of therapeutic radioligands, such as the investigation of absorbed dose thresholds for toxicity of specific kidney tissues (or substructures) resulting from nonuniform irradiations with radionuclides (5,6,8). Such insight can be relevant for the design of first-in-humans trials with novel radioligands,

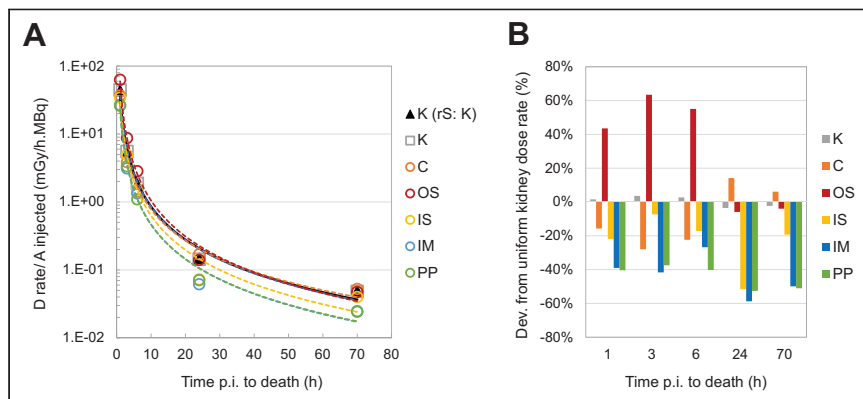


FIGURE 6. (A) Dose rates per unit of injected activity in different tissue regions and in K, as function of time after injection of ^{131}I -sdAb, for heterogeneous activity distribution based on autoradiography data (Supplemental Table 4) and for assumed uniform activity distribution throughout kidney ($r_S = K$). Curves indicate power function fit of each r_T (Supplemental Table 5). (B) Percentage deviations from uniform dose rate throughout kidney tissues ($r_S = K$). A = activity; D = absorbed dose; p.i. = after injection.

TABLE 2

Absorbed Doses Delivered to Different Tissue Regions and to K per Unit of Injected Activity Decay Corrected to the Mouse Time of Death, for Heterogeneous Activity Distribution Based on Autoradiography Data* and for Assumed Uniform Activity Distribution Throughout K

Parameter	Heterogeneous activity distribution						Uniform activity ($r_S = K$), K
	K	C	OS	IS	IM	PP	
Absorbed dose per injected activity, $D(r_T)/A_0$ (mGy·MBq ⁻¹)	73.1	54.8	111.6	62.3	43.0	43.6	71.2
Deviation from $D(r_T = r_S = K)/A_0$ (%)	3	-23	57	-12	-40	-39	-

*Supplemental Table 4.

by informing about potential toxicities due to the predicted absorbed dose distribution in larger kidney tissues such as in humans. The glomeruli are sometimes thought to be the absorbed dose-limiting renal substructures when dealing with β -radiotherapeutics (8,15). Yet, loss of proximal tubules has also been associated with long-term nephrotoxicity in mice with either β - or α -emitting radioligands (5,16). Investigating the absorbed dose dependence of glomerular and proximal tubular damage is therefore of high interest and would benefit from more detailed dosimetry at the level of suborgan regions or even at the level of nephron substructures. Additionally, translational and back-translational research on the renal absorbed dose-toxicity relationships might support the investigation of treatment optimization strategies beyond radioligand design, such as renoprotective agents that reduce reabsorption and internalization by the proximal tubule cells (4,5) and activity fractionation (8,15).

An improved understanding of radiation-induced nephrotoxicity in the presence of absorbed dose (and dose-rate) heterogeneity after radiopharmaceutical therapy should improve the implementation of optimized and patient-specific procedures (8). In peptide receptor radionuclide therapy, for example, the microscopic absorbed dose distribution in human kidneys is thought to play a role in the seemingly lower incidence of nephrotoxicity of ¹⁷⁷Lu-labeled somatostatin analogs than of similar ⁹⁰Y-labeled peptides (2,17). Clinical investigation of the influence of absorbed dose nonuniformity on nephrotoxicity is, however, a challenge, as it would require the availability of a large amount of good-quality patient-specific detailed dosimetry and response data on the kidneys for each therapeutic setting (18). Conversely, animal experiments allow determination of the microscopic distribution of radiopharmaceuticals in tissues *ex vivo* and investigation of the biologic response associated with radiopharmaceutical therapy in a more reproducible and controlled experimental setting. The S values for regions of the mouse kidney presented here could facilitate preclinical absorbed dose estimations required to investigate the contribution to nephrotoxicity of the absorbed dose-dependent damage to different kidney tissues resulting from the nonuniform distribution of radiopharmaceuticals. Such investigations will be essential in the development of complication-probability biophysical models for nephrotoxicity in radiopharmaceutical therapy (8).

CONCLUSION

A computational multiregion model of a mouse kidney was developed and used to create a database of S values for 5 tissue regions and for a wide range of β - and α -emitters of interest in radiopharmaceutical therapy. The comprehensive set of regional S values facilitates preclinical internal radiation dosimetry of mouse

kidney tissues and allows a more realistic estimation of the doses absorbed by different renal tissues from therapeutic radioligands with a nonuniform distribution in the kidneys, such as the ¹³¹I-labeled sdAb investigated. The proposed model and the computed S values represent an improvement from the simplistic (less accurate) renal absorbed dose estimates assuming a uniform distribution of activity throughout the entire kidney. Such dosimetric improvement is expected to support preclinical nephrotoxicity studies essential for a better understanding and prediction of nephrotoxicity in humans.

DISCLOSURE

Matthias D’Huyvetter is employed by Precirix SA, holds ownership interest in sdAb therapeutics, and is a postdoctoral researcher of the Research Foundation Flanders-FWO (12H3619N). No other potential conflict of interest relevant to this article was reported.

ACKNOWLEDGMENTS

We kindly thank Cindy Peleman and Jos Eersels (VUB); Naomi Daems, Jasmine Buset, and Kevin Tabury (SCK CEN); and Brian Miller (University of Arizona) for technically assisting in the animal experiments, histology, microscopy, or autoradiography. We also thank Jörn Engelmann and Elisabeth Jonckers (University of Antwerp) for the small-animal MRI work.

KEY POINTS

QUESTION: How much does the nonuniform distribution of radionuclides used for radiopharmaceutical therapy impact the absorbed dose in mouse kidney tissues?

PERTINENT FINDINGS: A computational multiregion model of a mouse kidney was developed and was used to calculate S values for 5 kidney tissue regions for a wide range of β - and α -particle emitters of interest in radiopharmaceutical therapy. The database of regional S values indicates that consideration of a heterogeneous activity distribution in the kidneys can have a considerable impact on the absorbed dose estimates in specific renal substructures, particularly when dealing with α - and low- to medium-energy β -particle emitters.

IMPLICATIONS FOR PATIENT CARE: An improved dosimetry of therapeutic radiopharmaceuticals in mouse kidney tissues will contribute to a better understanding and prediction of nephrotoxicity in the presence of heterogeneous absorbed dose depositions in human kidneys.

REFERENCES

1. Flynn AA, Pedley RB, Green AJ, et al. The nonuniformity of antibody distribution in the kidney and its influence on dosimetry. *Radiat Res.* 2003;159:182–189.
2. Konijnenberg M, Melis M, Valkema R, Krenning E, de Jong M. Radiation dose distribution in human kidneys by octreotides in peptide receptor radionuclide therapy. *J Nucl Med.* 2007;48:134–142.
3. Bouchet LG, Bolch WE, Blanco HP, et al. MIRD pamphlet no. 19: absorbed fractions and radionuclide S values for six age-dependent multiregion models of the kidney. *J Nucl Med.* 2003;44:1113–1147.
4. Chigoho DM, Bridoux J, Hernot S. Reducing the renal retention of low- to moderate-molecular-weight radiopharmaceuticals. *Curr Opin Chem Biol.* 2021;63:219–228.
5. Svensson J, Mölne J, Forssell-Aronsson E, Konijnenberg M, Bernhardt P. Nephrotoxicity profiles and threshold dose values for [¹⁷⁷Lu]-DOTATATE in nude mice. *Nucl Med Biol.* 2012;39:756–762.
6. Konijnenberg MW, Bijster M, Krenning EP, de Jong M. A stylized computational model of the rat for organ dosimetry in support of preclinical evaluations of PRRT with ⁹⁰Y, ¹¹¹In, or ¹⁷⁷Lu. *J Nucl Med.* 2004;45:1260–1269.
7. Hobbs RF, Song H, Huso DL, Sundel MH, Sgouros G. A nephron-based model of the kidneys for macro-to-micro α -particle dosimetry. *Phys Med Biol.* 2012;57:4403–4424.
8. Wessels BW, Konijnenberg MW, Dale RG, et al. MIRD pamphlet no. 20: the effect of model assumptions on kidney dosimetry and response—implications for radionuclide therapy. *J Nucl Med.* 2008;49:1884–1899.
9. D'Huyvetter M, De Vos J, Caveliers V, et al. Phase I trial of ¹³¹I-GMIB-Anti-HER2-VHH1, a new promising candidate for HER2-targeted radionuclide therapy in breast cancer patients. *J Nucl Med.* 2021;62:1097–1105.
10. Eckerman K, Endo A. ICRP publication 107: nuclear decay data for dosimetric calculations. *Ann ICRP.* 2008;38:7–96.
11. D'Huyvetter M, De Vos J, Xavier C, et al. ¹³¹I-labeled anti-HER2 camelid sdAb as a theranostic tool in cancer treatment. *Clin Cancer Res.* 2017;23:6616–6628.
12. Vargas CS, Struelens L, D'Huyvetter M, Caveliers V, Covens P. Assessment of mouse-specific pharmacokinetics in kidneys based on ¹³¹I activity measurements using micro-SPECT. *EJNMMI Phys.* 2022;9:13.
13. Miller BW, Gregory SJ, Fuller ES, Barrett HH, Barber HB, Furenlid LR. The iQID camera: an ionizing-radiation quantum imaging detector. *Nucl Instrum Methods Phys Res A.* 2014;767:146–152.
14. Treuting PM, Kowalewska J. Urinary system. In: Treuting PM, Dintzis SM, eds. *Comparative Anatomy and Histology: A Mouse and Human Atlas.* Academic Press; 2012:229–251.
15. Barone R, Borson-Chazot F, Valkema R, et al. Patient-specific dosimetry in predicting renal toxicity with ⁹⁰Y-DOTATOC: relevance of kidney volume and dose rate in finding a dose-effect relationship. *J Nucl Med.* 2005;46(suppl 1):99S–106S.
16. Kiess AP, Minn I, Vaidyanathan G, et al. (2S)-2-(3-(1-carboxy-5-(4-²¹¹At-astato-benzamido)pentyl)ureido)-pentanedioic acid for PSMA-targeted α -particle radiopharmaceutical therapy. *J Nucl Med.* 2016;57:1569–1575.
17. Bergsma H, Konijnenberg MW, van der Zwan WA, et al. Nephrotoxicity after PRRT with ¹⁷⁷Lu-DOTA-octreotate. *Eur J Nucl Med Mol Imaging.* 2016;43:1802–1811.
18. Strigari L, Konijnenberg M, Chiesa C, et al. The evidence base for the use of internal dosimetry in the clinical practice of molecular radiotherapy. *Eur J Nucl Med Mol Imaging.* 2014;41:1976–1988.

Progression or Response: New Liver Lesions in a Patient with Responding Hodgkin Lymphoma

Ashwin Singh Parihar, Adeel Haq, Richard L. Wahl, and Amin H. Jahromi

Mallinckrodt Institute of Radiology and Siteman Cancer Center, Washington University School of Medicine, St. Louis, Missouri

A 29-y-old woman with relapsed Hodgkin lymphoma was being assessed for response to ifosfamide, carboplatin, and etoposide therapy. ^{18}F -FDG PET/CT showed progressive hypermetabolic mediastinal lymphadenopathy (Fig. 1A) with diffuse hypermetabolism in the bone marrow, likely secondary to marrow stimulation by granulocyte-colony stimulating factor therapy. Treatment was escalated to gemcitabine, vinorelbine, and doxorubicin and to pembrolizumab. ^{18}F -FDG PET/CT performed 6 wk later showed nearly complete metabolic resolution of the prior mediastinal lymphadenopathy. However, interval development of hepatomegaly with multifocal hypermetabolic lesions throughout the liver was noted (Fig. 1B). In view of the favorable response at the primary site, the new hepatic lesions were favored to represent immune-related hepatitis over progressive lymphomatous involvement of the liver. The patient's laboratory results obtained within 4 d of the PET/CT showed elevated levels of aspartate transaminase (115 U/L) and alanine transaminase (151 U/L) (11 and 15 U/L, respectively, 1 mo beforehand). On the basis of the suggestion of immune-related hepatitis, pembrolizumab was discontinued and prednisone 40 mg daily was started, tapering by 10 mg weekly over 4 wk. The regimen of gemcitabine, vinorelbine, and doxorubicin was continued. Reassessment ^{18}F -FDG PET/CT performed 5 wk later showed continued remission of the mediastinal disease, with marked anatomic and metabolic improvement of the liver lesions (Fig. 1C). The patient received an autologous stem cell transplantation 2 wk later, and reassessment ^{18}F -FDG PET/CT (Fig. 1D) showed continued response by the mediastinal disease and complete resolution of the liver lesions.

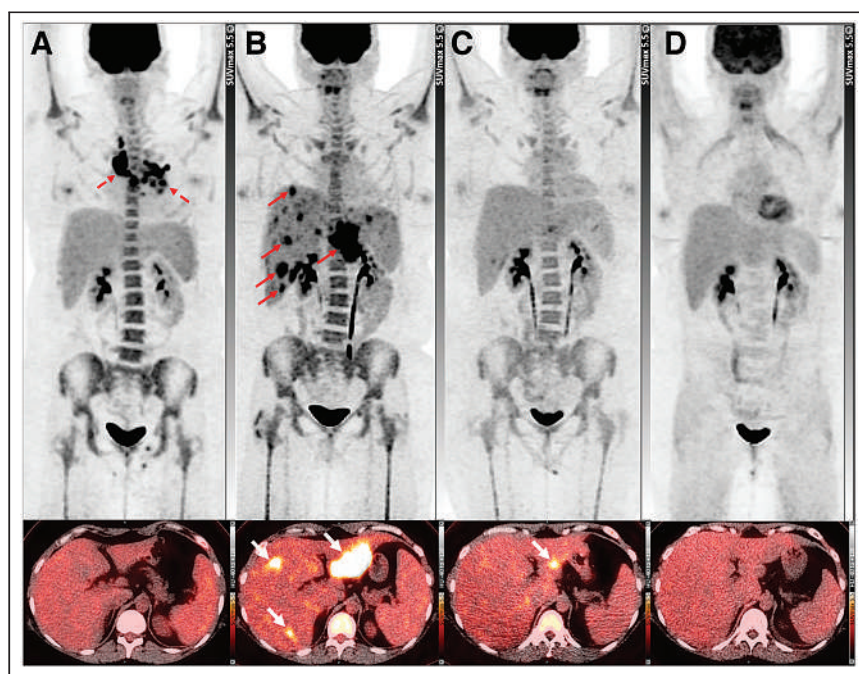


FIGURE 1. (A) ^{18}F -FDG PET/CT maximum-intensity projection (top) and PET/CT transaxial images (bottom) at baseline show hypermetabolic mediastinal lymphadenopathy (dashed arrows). (B) ^{18}F -FDG PET/CT performed 6 wk after treatment with pembrolizumab shows metabolic resolution of mediastinal lymphadenopathy and interval development of multiple discrete hypermetabolic lesions in liver (solid arrows). (C and D) ^{18}F -FDG PET/CT performed 5 wk after discontinuation of pembrolizumab and treatment with prednisone shows significant improvement in liver lesions (C), which resolved completely at 8 wk (D).

Immune-related adverse events, such as hepatitis, are known to occur in patients treated with immune-checkpoint inhibitors. However, the presentation of immune-related hepatitis as multifocal involvement of the liver is uncommon and can mimic the appearance of progressive disease. In such cases, a reassessment ^{18}F -FDG PET/CT performed at least 4 wk after discontinuation of immunotherapy can help improve the diagnostic accuracy. The detection of immune-related adverse events on PET/CT is critical, as patients with severe immune-related adverse events require cessation of immunotherapy and initiation of corticosteroids.

DISCLOSURE

No potential conflict of interest relevant to this article was reported.

Received Oct. 3, 2022; revision accepted Oct. 5, 2022.
For correspondence or reprints, contact Amin H. Jahromi (12345amin@gmail.com).
Published online Oct. 13, 2022.
COPYRIGHT © 2023 by the Society of Nuclear Medicine and Molecular Imaging.
DOI: 10.2967/jnumed.122.264995

Theranostic Digital Twins: An Indispensable Prerequisite for Personalized Cancer Care

TO THE EDITOR: Recently, cancer patient digital twins have been astutely proposed as a conceptual framework with the vision of performing simulations for different treatment options before treatment is started (1). A digital twin is a virtual representation of the patient that uses mathematic and computational models to simulate personalized diagnosis and therapy. We strongly believe an optimal platform for more immediate actualization of the framework for cancer patient digital twins is theranostic nuclear medicine. Here, the theranostic digital twin (TDT) stands on the shoulders of two path-breaking visions: precision medicine and complexity modeling.

Nuclear medicine imaging techniques and the inherent advantage of using theranostic pairs make treatment personalization based on physiologically based pharmacokinetic (PBPK) models readily feasible (2,3). Patient-specific optimization and personalization of radiopharmaceutical therapies (RPTs) can be obtained within the TDT framework, even before the first therapy cycle — a paradigm shift from existing one-size-fits-all therapies.

New technologic developments such as PET scanners with a long axial field of view provide a basis for extended-body PBPK modeling to strengthen TDTs (4). Artificial intelligence complements multiscale modeling (5,6) and offers the unique opportunity to improve every step of data acquisition, generation, and analysis. Theranostic imaging combined with artificial intelligence can be used to predict voxelwise absorbed doses and the effectiveness of RPTs (7).

The five pillars of cancer management can be divided into locoregional treatments (surgery, interventional radiology, and radiation therapy) and systemic treatments (oncology and RPT). Generally, the TDT not only serves as a prerequisite for personalized RPTs but will further support all five pillars. Residual disease after surgery or interventional radiology will result in an increased likelihood of local recurrence; theranostic imaging and TDTs can guide and verify the success. Although radiation therapy and brachytherapy are beneficial for localized diseases, systemic therapies present valuable options for metastasized diseases. TDTs can help in the personalization of systemic therapies by highlighting targets for medical oncology therapies using molecular imaging and PBPK modeling within the TDT. For RPTs, we believe that improvements in outcomes are possible when treatment with a TDT is optimized in terms of radioactivity, tracer amount, number of therapy cycles, and timing to an individual patient's needs, conditions, and preconditions. There is evidence suggesting that with personalization, patient progression-free survival and overall survival can improve (8,9).

TDTs accept the challenge of combining existing multidisciplinary knowledge of cancer management, patient-specific data, and population-based models and create a 3-dimensional digital model representing the individual patient's physiology and disease. Macroscopic observations (organ level, tissue level) are merged with

microscopic effects (cell damage, tumor microenvironment), and the TDT evolves on the basis of (theranostic) imaging and physiologic information (i.e., PBPK). Incorporation of radiomics, personal physiology, and genomics enables rich TDT models. In the future, TDTs may be essential in determining whether a patient will benefit from one therapy and whether a different treatment is advisable, or TDTs may even predict how a particular treatment may inevitably fail, necessitating adjunctive and adjuvant therapies and interventions. TDTs will be updated continuously.

The TDT will facilitate and enhance therapeutic decisions to permit truly personalized cancer care. Being strongly committed to providing cancer patients with the best available treatment, we anticipate different solutions to enable TDTs to proliferate over the next decade. We encourage researchers to unlock the full potential of theranostics to support this important paradigm shift toward precision medicine.

REFERENCES

- Hernandez-Boussard T, Macklin P, Greenspan EJ, et al. Digital twins for predictive oncology will be a paradigm shift for precision cancer care. *Nat Med*. 2021;27:2065–2066.
- Begum NJ, Glatting G, Wester H-J, Eiber M, Beer AJ, Kletting P. The effect of ligand amount, affinity and internalization on PSMA-targeted imaging and therapy: a simulation study using a PBPK model. *Sci Rep*. 2019;9:20041.
- Kletting P, Kull T, Maaß C, et al. Optimized peptide amount and activity for ⁹⁰Y-labeled DOTATATE therapy. *J Nucl Med*. 2016;57:503–508.
- Wang G, Nardo L, Parikh M, et al. Total-body PET multiparametric imaging of cancer using a voxel-wise strategy of compartmental modeling. *J Nucl Med*. 2022;63:1274–1281.
- Alber M, Buganza Tepole A, Cannon WR, et al. Integrating machine learning and multiscale modeling: perspectives, challenges, and opportunities in the biological, biomedical, and behavioral sciences. *NPJ Digit Med*. 2019;2:115.
- Lagergren JH, Nardini JT, Baker RE, Simpson MJ, Flores KB. Biologically-informed neural networks guide mechanistic modeling from sparse experimental data. *PLoS Comput Biol*. 2020;16:e1008462.
- Xue S, Gafita A, Afshar-Oromieh A, Eiber M, Rominger A, Shi K. Voxel-wise prediction of post-therapy dosimetry for ¹⁷⁷Lu-PSMA I&T therapy using deep learning [abstract]. *J Nucl Med*. 2020;61(suppl 1):1424.
- Garin E, Tselikas L, Guiu B, et al. Personalised versus standard dosimetry approach of selective internal radiation therapy in patients with locally advanced hepatocellular carcinoma (DOSISPHERE-01): a randomised, multicentre, open-label phase 2 trial. *Lancet Gastroenterol Hepatol*. 2021;6:17–29.
- Klubo-Gwiedzinska J, Van Nostrand D, Atkins F, et al. Efficacy of dosimetric versus empiric prescribed activity of ¹³¹I for therapy of differentiated thyroid cancer. *J Clin Endocrinol Metab*. 2011;96:3217–3225.

Julia Brosch-Lenz*

Carlos Uribe

Arman Rahmim

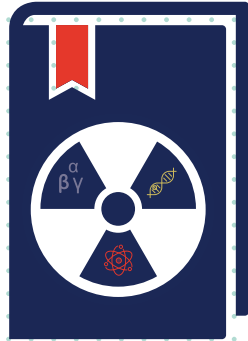
Babak Saboury

*BC Cancer Research Institute Vancouver,
British Columbia, Canada
E-mail: jlbrosch@bccrc.ca

Published online Dec. 8, 2022.
DOI: 10.2967/jnumed.122.264929

Immediate Open Access: Creative Commons Attribution 4.0 International License (CC BY) allows users to share and adapt with attribution, excluding materials credited to previous publications. License: <https://creativecommons.org/licenses/by/4.0/>. Details: <http://jnm.snmjournals.org/site/misc/permission.xhtml>.

COPYRIGHT © 2023 by the Society of Nuclear Medicine and Molecular Imaging.



80 Hour Radionuclide Authorized User TRAINING COURSE

The **ASNC/SNMMI 80 Hour Authorized User Training Course** is designed to provide nuclear medicine physicians with the knowledge needed to establish a culture of safety and quality in their practice.

Featuring more than 40 expert lecturers from across nuclear medicine, the course fulfills the 80 hours of classroom training that the U.S. Nuclear Regulatory Commission (NRC) and Agreement States require for physicians to become authorized users of radioisotopes for imaging and localization studies.

This popular course is available as a standalone program or as a special package for training programs.

LEARN MORE: www.snmmi.org/80HourCourse





2023 ACNM/SNMMI **HOT TOPICS** Webinar Series

SNMMI and ACNM are excited to announce the lineup for the 2023 Hot Topics Webinar Series. These informative webinars will take place at 12:00 pm ET on the second Tuesday of each month and are complimentary for ACNM and SNMMI members.

- ▶ **Theranostics for Prostate Cancer**
On Demand | *Speaker: Stephan Probst, MD*
- ▶ **Theranostics for Pheochromocytoma/Paranglioma**
On Demand | *Speaker: Erik Mittra, MD, PhD*
- ▶ **FDG PET/CT for Infection Imaging**
March 14 | *Speaker: Gad Abikhzer, MDCM, FRCPC*
- ▶ **From Beta to Alpha in Theranostics**
April 11 | *Speaker: Chandrasekhar Bal, MD*
- ▶ **Myocardial Flow Reserve**
May 9 | *Speaker: Ron Schwartz, MD*
- ▶ **PET/MR**
June 25 | *Speaker: Andrei Iagaru, MD*
in-person during the SNMMI 2023 Annual Meeting
- ▶ **Theranostics for Neurodegenerative Disease-Final Frontier for Health Span**
July 11 | *Speaker: Phillip Kuo, MD, PhD*
- ▶ **Cardiac Infection and Inflammation Imaging**
August 8 | *Speaker: Vasken Dilsizian, MD*
- ▶ **Whole Body PET**
September 12 | *Speaker: Ramsey Badawi, PhD*
- ▶ **FAPI PET: Make it or break it?**
October 10 | *Speaker: Ken Herrmann, MD*
- ▶ **Landscape of Molecular Imaging and Fluid Biomarkers in Neurodegeneration**
November 14 | *Speaker: Alexander Drzezga, MD*
- ▶ **PSMA PET**
December 12 | *Speaker: Jeremie Calais, MD*





SPECTRUM
DYNAMICS MEDICAL

VERITON-CT[®]

DIGITAL SPECT/CT



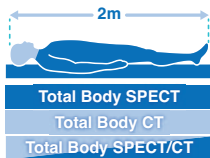
Optimization of Every Step

Spectrum Dynamics has integrated its ground-breaking BroadView Technology design into the VERITON-CT system, providing a digital platform enabling routine 3D imaging in Nuclear Medicine. The result is optimization of every step, from image acquisition to interpretation.

VERITON-CT digital SPECT/CT combines the best-in-class CZT detectors, novel system design, high resolution CT, and advanced software technology to elevate the performance of 360° digital SPECT/CT.



BroadView Technology
Proprietary swiveling detector design provides increased sensitivity for faster scans



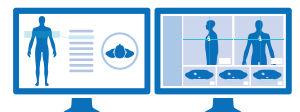
Total Body 3D Imaging
200cm continuous coverage vertex to feet
SPECT | CT | SPECT/CT



80cm NM and CT bore
Wide Bore SPECT/CT
80cm NM and CT bore



Choice of 16/64 slice
Choice of high-resolution CT for diagnostic applications and low dose total body CTAC



TruView Console
One platform, one location for clinical care decision-making:

1. Acquisition
2. Advanced quantitative reconstruction
3. Both 3D and 4D data analysis and review

VERITON-CT Feature Application: 3D Dynamic Imaging

TruFlow for VERITON-CT offers real-time 3D in-vivo fast dynamic imaging to capture the radiopharmaceutical distribution, uptake, or clearance over time in 3D SPECT/CT parametric imaging.

TruFlow

